

nature



MAPPING METASTASIS

Petal plots capture cancer's metastatic potential

Origins of life

How the first living cells solved the water paradox

Conservation

Time to extinguish the fires in Brazil's Pantanal wetlands

High-energy physics

Proton collisions probe nuclear force for exotic particles

Nature

[Fri, 11 Dec 2020]

- [Donation](#)
- [This Week](#)
- [News in Focus](#)
- [Books & Arts](#)
- [Opinion](#)
- [Work](#)
- [Research](#)
- [Amendments & Corrections](#)

Donation

- -> [**打赏 - Donation**](#)

打赏 - JUST FOR FUN

支持分享! 一杯咖啡钱, 打赏金额随意, 感谢大家~ :)

支付宝

微信



支付就用支付宝



打开支付宝[扫一扫]

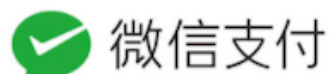
免费寄送收钱码: 拨打95188-6

<https://blog.csdn.net/bboyfelyu>

推荐使用微信支付



Mr.SIMPLE (**辉)



[本书来自: www.github.com/hehonghui](http://www.github.com/hehonghui)

This article was downloaded by **calibre** from <http://economist.cool/donate.html>

This Week

- **[COVID vaccines: the world's medical regulators need access to open data](#)** [08 December 2020]
Editorial • The global race to produce COVID vaccines is a chance for regulators and drug companies to create a more harmonized approvals process.
- **[Accounting for sex and gender makes for better science](#)** [09 December 2020]
Editorial • The European Commission is set to insist on steps that will make research design more inclusive.
- **[Institutions can retool to make research more rigorous](#)** [14 October 2020]
World View • Big moves to rebuild the scientific infrastructure are possible.
- **[Gold diggers put mercury on the menu](#)** [01 December 2020]
Research Highlight • Mining ponds move the toxic element into the food web.
- **[How salt water on Mars could give astronauts a breather](#)** [04 December 2020]
Research Highlight • Water locked away in Martian sediments could be split into the gases needed by humans and their machines.
- **[Presto chango: tiny particles get a chemical makeover but keep their shape](#)** [03 December 2020]
Research Highlight • Self-assembling particles exhibit a mind-boggling array of structure and composition.

EDITORIAL

08 December 2020

COVID vaccines: the world's medical regulators need access to open data

The global race to produce COVID vaccines is a chance for regulators and drug companies to create a more harmonized approvals process.



Medicines regulators, including Emer Cooke (left), the director of the European Medicines Agency, and Stephen Hahn, the commissioner of the US Food and Drug Administration, have an opportunity to further harmonize regulatory processes. Credit: European Medicines Agency, FDA

The roll out of COVID-19 vaccines is under way, but without, it seems, much global coordination. China, Russia and the United Arab Emirates began administering vaccines before the conclusion of clinical trials. Last week, [the United Kingdom issued emergency approval for a vaccine](#) developed by the US biopharmaceutical company Pfizer and BioNTech of Mainz, Germany, following positive results from phase III testing. The US Food and Drug Administration (FDA) has needed longer to make its decision on the same vaccine. And the regulatory agencies of Australia, the European Union and Switzerland are taking longer still.

This patchwork of approvals processes, despite COVID-19 being a common enemy, has revived a long-standing question about how to accelerate harmonization in vaccine regulation. Researchers reviewing the regulatory landscape found at least 51 pathways to various types of accelerated vaccine approval in a group of 24 countries¹.

Greater harmonization would bring many benefits. Drug companies could look forward to agreed definitions for different types of approval, and would benefit from agreed guidelines for criteria that their vaccine candidates would need to meet. If regulators were to ask for broadly the same things, companies could cut the time needed to prepare their drug applications. Companies, for their part, would need to allow — or help to create — a secure way for regulators to share data, which they are often not permitted to do at present.



The COVID vaccine challenges that lie ahead

By assessing the same data, regulators could more easily compare their findings and analyses with those of others, and their decisions would not only be more robust, but also be seen to be more robust. That, in turn, would shore up public confidence in a world in which vaccine hesitancy is rising and in which many citizens already have the means to compare regulatory verdicts. This would be an evolutionary shift, not a revolutionary one, because in recent years — and particularly since the 2014–16 Ebola crisis — regulators have made unprecedented efforts to discuss, coordinate and begin to harmonize some of their processes.

The FDA, which was set up in 1906, is the world's oldest national medicines regulator. But the world has been moving towards greater regulatory coordination for some time. Europe's regulatory system comprises a network of 50 national bodies from 31 European countries. The European Medicines Agency (EMA), created in 1995, sits at the centre of this network. All countries have their own medical regulators, but the EMA provides manufacturers with a single place for scientific evaluation of drug applications, if they want Europe-wide approval.

Although EMA and FDA verdicts are often broadly similar, the authorities differ in key ways. For example, the FDA requires drug companies to submit all the raw data from laboratory, animal and human trials so that it can do its own statistical analysis. By contrast, the EMA relies more on drug companies' own analyses.

In other regions — Africa, for example — countries are also inching towards an approach that allows for the pooling of regulatory expertise. This is the purpose of the African Vaccine Regulatory Forum, set up in 2006.



Why emergency COVID-vaccine approvals pose a dilemma for scientists

And at the global level, in 2012, the member states of the World Health Organization (WHO) agreed to establish the International Coalition of Medicines Regulatory Authorities (ICMRA) to allow regulators to share information and agree on approaches. The ICMRA has 29 members, including regulators from China, Europe and the United States. Through it, members have been able to reach a consensus on the best animal models for testing COVID-19 vaccines, the ideal clinical-trial end points and the complicated issue of continuing placebo-controlled trials after vaccine roll out begins. The coalition's COVID-19 working group is now trying to harmonize the monitoring of vaccines once they have been deployed, because faint signals of adverse effects might be too weak to spot in any one country.

And then there is the WHO itself. Low- and middle-income countries can now benefit from the work that goes into its Emergency Use Listing (EUL) process. On 13 November, the agency issued its first ever such vaccine

listing, for a polio vaccine. National regulators still need to decide whether this vaccine is right for their country, but a recommendation from the WHO — and confidence in its assessment process — means that most are likely to follow its advice.

Around the end of October, the WHO requested that both the FDA and the EMA assess the suitability of COVID-19 vaccines for low- and middle-income countries as they consider whether to issue emergency authorizations. It is not clear whether the regulators will agree — but if either does, the WHO can draw on that analysis and issue its own EUL within days of the decision. That would be collaboration indeed.



COVID vaccine confidence requires radical transparency

These are all important and necessary efforts. The need now is to go one step further and find a path through the many different types of vaccine approval. Before the pandemic, the Coalition for Epidemic Preparedness Innovations, a global group of funding agencies, companies and non-governmental organizations, set up a working group to map out obstacles to better global regulatory alignment, in anticipation of a new infectious disease. This

process confirmed how regulatory agencies differ on issues such as the use of genetic modification in vaccine development, clinical trials in pregnant women, and even vial labelling. But it also meant that inconsistencies were already mapped out and under discussion when the pandemic struck. COVID-19 has intensified these discussions.

The next step will not be easy. Regulators want to be able to exchange data. Their experiences during the pandemic have convinced many that they are moving towards a point at which this will be possible. They want to be able to talk to each other in the same units and about the same end points, and to make decisions based on the same data.

Ultimately, each country must make its own decisions about what's best. But the goal of a harmonized regulatory dossier for vaccines, conforming to an agreed set of international regulatory requirements, would be transformative.

Nature **588**, 195 (2020)

doi: <https://doi.org/10.1038/d41586-020-03458-z>

References

1. 1.

Simpson, S., Chakrabarti, A., Robinson, D., Chirgwin, K. & Lumpkin, M. *npj Vaccines* **5**, 101 (2020).

Jobs from Nature Careers

- - - [All jobs](#)
 -
 - [Perinatal Pathologist](#)

[University of California, San Diego \(UC San Diego\)](#)

[La Jolla, CA, United States](#)

[JOB POST](#)

▪ [**Chief Science and Innovation Officer**](#)

[National Geographic Society](#)

[Washington, United States](#)

[JOB POST](#)

▪ [**Postdoctoral Fellow**](#)

[University of Maryland, Baltimore \(UMB\)](#)

[Baltimore, MD, USA, MD, United States](#)

[JOB POST](#)

▪ [**POSTDOCTORAL SCIENTIST Institute for Experimental Pediatric Endocrinology**](#)

[Charité - University Medicine Berlin](#)

[Berlin, Germany](#)

[JOB POST](#)

This article was downloaded by **calibre** from <https://www.nature.com/articles/d41586-020-03458-z>

EDITORIAL

09 December 2020

Accounting for sex and gender makes for better science

The European Commission is set to insist on steps that will make research design more inclusive.



In Australia's Great Barrier Reef, most sea turtles being born are female because of warming temperatures — a discovery made when researchers analysed male and female populations. Credit: Jonas Gratzer/LightRocket/Getty

At the end of last month, the European Commission announced that its grant recipients will be required to incorporate sex and gender analyses into the design of research studies. The policy will affect researchers applying for grants that are part of the commission's seven-year, 85-billion (US\$100-billion) Horizon Europe programme, which is due to begin next year.

The funding is still awaiting sign-off from the European Union's 27 member states. But if all goes to plan, the commission will be the largest funder to require sex and gender analyses — along with analyses of other aspects of inclusion and how they interact, or intersect, also known as intersectionality — in research design. Such analyses could include disaggregating data by sex when examining cells, or considering how a technology might perpetuate gender stereotypes.

It's a significant achievement. Science will be strengthened by researchers incorporating analyses of sex and gender into their work at every stage — from study design to gathering data, analysing those data and drawing conclusions.

The European Commission is not the first funding agency to make such changes. And this isn't the first time it has requested that studies account for sex and gender. But in Horizon Europe, the requirement becomes a mandate, and is expected to extend, by default, to most grant recipients. Exceptions will be made only for those working on topics for which the commission thinks such studies would not be relevant, such as in pure mathematics. An added benefit of the decision is that public funders in EU member states who work with the commission will take note, creating a window for changes to eventually be applied across the continent.



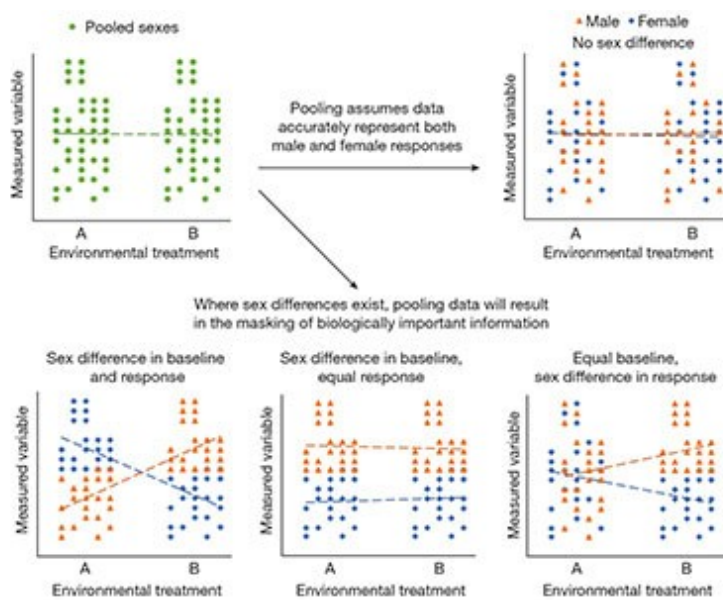
The researcher fighting to embed analysis of sex and gender into science

Science and scientists have a troubled history of failing to account for sex and gender when designing research. For decades, crash test dummies were based on male bodies. Even though smaller models are now used to represent women, they fail to account for some other typical differences, such as neck strength¹. The inclusion of sex and gender analyses can also be revelatory. In Australia's Great Barrier Reef, most sea turtles being born are female because of warming temperatures — a discovery that was made when researchers were able to analyse male and female populations².

In some cases, the results of not accounting for sex and gender have been catastrophic for human health. Between 1997 and 2001, ten prescription drugs were withdrawn from use in the United States, eight of which had been found to be more dangerous for women than men. This had been missed, in part, because women had not been properly represented among trial participants when the drugs were first evaluated.

Although sex and gender analysis is improving in drugs trials, [it remains a work in progress in many fields](#), Londa Schiebinger, a science historian at Stanford University in California, told *Nature*. Researchers have been highlighting the harms caused by failing to account for sex and gender for decades, but it wasn't until after the turn of the millennium that funding bodies really started to address the problem. The Canadian Institutes of Health Research began to mandate that analyses of sex and gender be included in grant applications in 2010, and the US National Institutes of Health followed suit in 2016.

The European Commission began asking grant recipients to include sex and gender analysis in their research design in 2013, a request which covered around one-third of research fields by 2020. But according to later evaluation reports, fewer researchers than expected implemented this request. The current proposal will probably improve these figures. But it needs to be accompanied by other measures — especially those that help to convince researchers that more-inclusive research design is not simply a box-ticking exercise, and leads to better research.



Sex and gender analysis improves science and engineering

An analysis of researchers funded by the Canadian Institutes of Health Research, published in 2014, revealed that some had pushed back when asked to consider sex and gender³. And both this analysis and the European Commission's evaluation highlighted that some grant recipients used sex (which refers to biological characteristics) interchangeably with gender (which is a social construct and is not necessarily aligned with a person's sex). To help researchers to better appreciate the value of sex and gender analysis, the commission's expert advisory group — which Schiebinger chairs — [has published 15 case studies](#) as examples of good practice.

One case study advises researchers on how to integrate gender and other aspects of intersectional analyses into energy research and development; another advises on how such analyses can be done in the design of urban spaces in developed and developing countries.

This kind of analysis should be a fundamental part of research design and therefore the responsibility of every researcher. But in the short term, another positive action could be for research teams to include appropriate specialists to advise on, participate in or lead the design of more-inclusive research. Groups could include researchers from the social or health sciences — the Canadian Institutes of Health Research analysis revealed that health- and social-science researchers are more likely to include sex and gender analyses in project design than are researchers in the biomedical sciences.

Ultimately, inclusive research design cannot be the sole responsibility of funders. Some journals — including Nature — are requesting that authors include sex and gender analyses, when appropriate. Universities and research supervisors also need to incorporate inclusive design into the research methodology training they provide to students.

The European Commission is rightly adding its considerable voice to the effort to ensure that science is designed and carried out in a more inclusive way. But to change practices that have existed for centuries, more researchers — especially research leaders — need to accept what they have been doing wrong, and how research and individuals have suffered as a result. The foundations are being laid for better science, and the more hands that join in this important effort, the better.

Nature **588**, 196 (2020)

doi: <https://doi.org/10.1038/d41586-020-03459-y>

References

1. 1.

Linder, A. & Svedberg, W. *Accid. Anal. Prev.* **127**, 156–162 (2019).

2. 2.

Jensen, M. P. *et al.* *Curr. Biol.* **28**, 154–159 (2018).

3. 3.

Johnson, J. , Sharman, Z., Vissandjée, B. & Stewart, D. E. *PLoS ONE* **9**, e99900 (2014).

Jobs from Nature Careers

- - - [All jobs](#)
 - - [Perinatal Pathologist](#)
 - [University of California, San Diego \(UC San Diego\)](#)
 - [La Jolla, CA, United States](#)
 - [JOB POST](#)
 - [Chief Science and Innovation Officer](#)
 - [National Geographic Society](#)

Washington, United States

JOB POST

▪ **Postdoctoral Fellow**

University of Maryland, Baltimore (UMB)

Baltimore, MD, USA, MD, United States

JOB POST

▪ **POSTDOCTORAL SCIENTIST Institute for
Experimental Pediatric Endocrinology**

Charité - University Medicine Berlin

Berlin, Germany

JOB POST

This article was downloaded by **calibre** from <https://www.nature.com/articles/d41586-020-03459-y>.

| [Section menu](#) | [Main menu](#) |

WORLD VIEW
14 October 2020

Institutions can retool to make research more rigorous



Big moves to rebuild the scientific infrastructure are possible.

Ulrich Dirnagl

Ulrich Dirnagl directs the QUEST Center at the Berlin Institute of Health.
[Contact](#)

Search for this author in:

- [Pub Med](#)
- [Nature.com](#)
- [Google Scholar](#)

Five years ago, I was part of a small group of ‘activists’ who convinced the Berlin Institute of Health (BIH), where I work, to try out a set of reforms intended to improve the trustworthiness, usefulness and ethics of research. Things grew from there: three years ago, with the help of government grants and some nudging by a retired local politician, we secured €2.5 million (US\$2.9 million) per year for efforts to build up incentives and technologies that increase rigour.

We were inspired by initiatives at other universities, such as the reforms that Frank Miedema introduced during his deanship at the University Medical Center Utrecht in the Netherlands. But when the QUEST Center (QUEST stands for Quality, Ethics, Open Science and Translation) launched at the BIH, there was no precedent or blueprint for a programme of this scale.

From the beginning, we presumed that researchers and clinician-scientists are skilled professionals who want to ‘do the right thing’ but are also under pressure to accrue publications to advance their careers. Doing quality research takes time and humility, so unless we changed the system, researchers who pursued quality-enhancing practices could have found themselves at a disadvantage.

What was the solution? We made sure that we were viewed as a resource, not a policing unit. We selected interventions that we thought we could implement. Alongside introducing courses on experimental design and methods aimed at reducing bias, we focused on practices to increase the transparency of research. One push was for the use of electronic laboratory notebooks (ELNs), which improve research documentation and make collaboration easier. We made sure that QUEST, and not individual labs, covered the licence fees and provided plenty of support. So far, nearly 2,000 of our 7,000 researchers, PhD students and technicians are registered ELN users; my guess is that about half of these have an ELN as their primary lab notebook. For many, ELNs are a necessary first step towards systematically managing their research data, which QUEST also supports.

We simultaneously adjusted the incentive and reward system. When hiring professors and awarding institutional funds, we now consider how thoroughly and quickly people share their results. Those who make original

data available in publications are rewarded with a financial bonus that can be spent on research. QUEST works with the BIH and the leadership of the Charité, Berlin’s university medical centre, to ensure that evaluation criteria encompass responsible research practices, including publication of null results, provision of open data and community engagement. A QUEST good-evaluation-practice officer has sat as an independent assessor on hiring commissions for 10 of the past 29 hiring calls.

We tried to craft a system designed for its own improvement. For example, we have developed an anonymous online tool through which researchers have reported hundreds of errors and worrying incidents ([U. Dirnagl et al. PLoS Biol. 14, e2000705; 2016](#)). This has allowed us to learn from errors — for example, a technician realized that ambiguous labelling of cell-culture media by a manufacturer had spoiled her experiment. Her swift reporting prevented others from making the same mistake. The company changed the labels on its flasks and alerted other customers. After we saw many errors stemming from the use of pipettes outside the calibrated range, we set up ‘pipetting exercises’ and saw the rate of these errors fall.

Three years in, we’re seeing more papers published open access and with open data. We’re also seeing greater participation in educational activities and in intramural programmes using responsible selection criteria, such as engagement with patient communities, reuse of data or preregistration. Of course, funders and journals are also pulling in the same direction, so it is impossible to know to which changes are due to the efforts of QUEST.

However, we still have a long way to go. Our benchmarking study found that, within 2 years of completion, only 40% of studies sponsored by the Charité had reported results ([S. Wieschowski et al. J. Clin. Epidemiol. 115, 37–45; 2019](#)). Furthermore, 5 years after completion, more than 30% of results remained unavailable. But we hope to correct this. We use counselling and web tools to offer guidance on how to publish null, inconclusive, negative and other ‘nonstandard’ results, and award monetary research bonuses for the publication of negative results or replication studies.

Most faculty members welcome our activities, and we are working to expand student and researcher engagement.

For example, using funding from the biomedical research charity Wellcome in London, we have established fellowships for mid-career researchers who collaborate to develop and track initiatives for improving science in their own research groups. Our experience shows that structured programmes can be rolled out by any academic institution that is willing and able to improve its research in a systematic fashion. The budget of QUEST is less than 1% of our institution's state funding for research and teaching, not including monies from third-party funders.

QUEST started from scratch. But many institutions already promote activities such as open science, data management and responsible research. If they align their efforts, they can expand them and incorporate scientific ideals into incentive structures. The quality of science and the culture of the workplace will be better off.

Nature 588, 197 (2020)

doi: <https://doi.org/10.1038/d41586-020-02905-1>

Jobs from Nature Careers

- - - [All jobs](#)
 - - [Perinatal Pathologist](#)

[University of California, San Diego \(UC San Diego\)](#)

[La Jolla, CA, United States](#)

[JOB POST](#)

- [Chief Science and Innovation Officer](#)

[National Geographic Society](#)

Washington, United States

JOB POST

▪ **Postdoctoral Fellow**

University of Maryland, Baltimore (UMB)

Baltimore, MD, USA, MD, United States

JOB POST

▪ **POSTDOCTORAL SCIENTIST Institute for Experimental Pediatric Endocrinology**

Charité - University Medicine Berlin

Berlin, Germany

JOB POST

This article was downloaded by **calibre** from <https://www.nature.com/articles/d41586-020-02905-1>



Ponds created by small-scale gold mining in the Madre de Dios region of Peru. Such ponds hasten production of a compound that can poison animals.
Credit: Melissa Marchese

Environmental sciences

01 December 2020

Gold diggers put mercury on the menu

Mining ponds move the toxic element into the food web.

Lake and pond ecosystems created by artisanal gold miners in Peru convert a worrying amount of mercury — a common pollutant from mining operations — into a form that can be ingested by animals and people.

Small-scale and mostly illegal gold-mining operations in the Madre de Dios region of the southern Peruvian Amazon have transformed vast stretches of tropical forest into sandy landscapes pock-marked by ponds and lakes.

Jacqueline Gerson at Duke University in North Carolina, Simon Topp at the University of North Carolina at Chapel Hill and their colleagues wanted to understand how effectively microbes in these ecosystems process mercury into methylmercury, which accumulates in the food web. They analysed landscape changes from 1985 to 2018, and collected water and sediment samples from rivers, natural oxbow lakes and mining ponds, both upstream and downstream of mining operations.

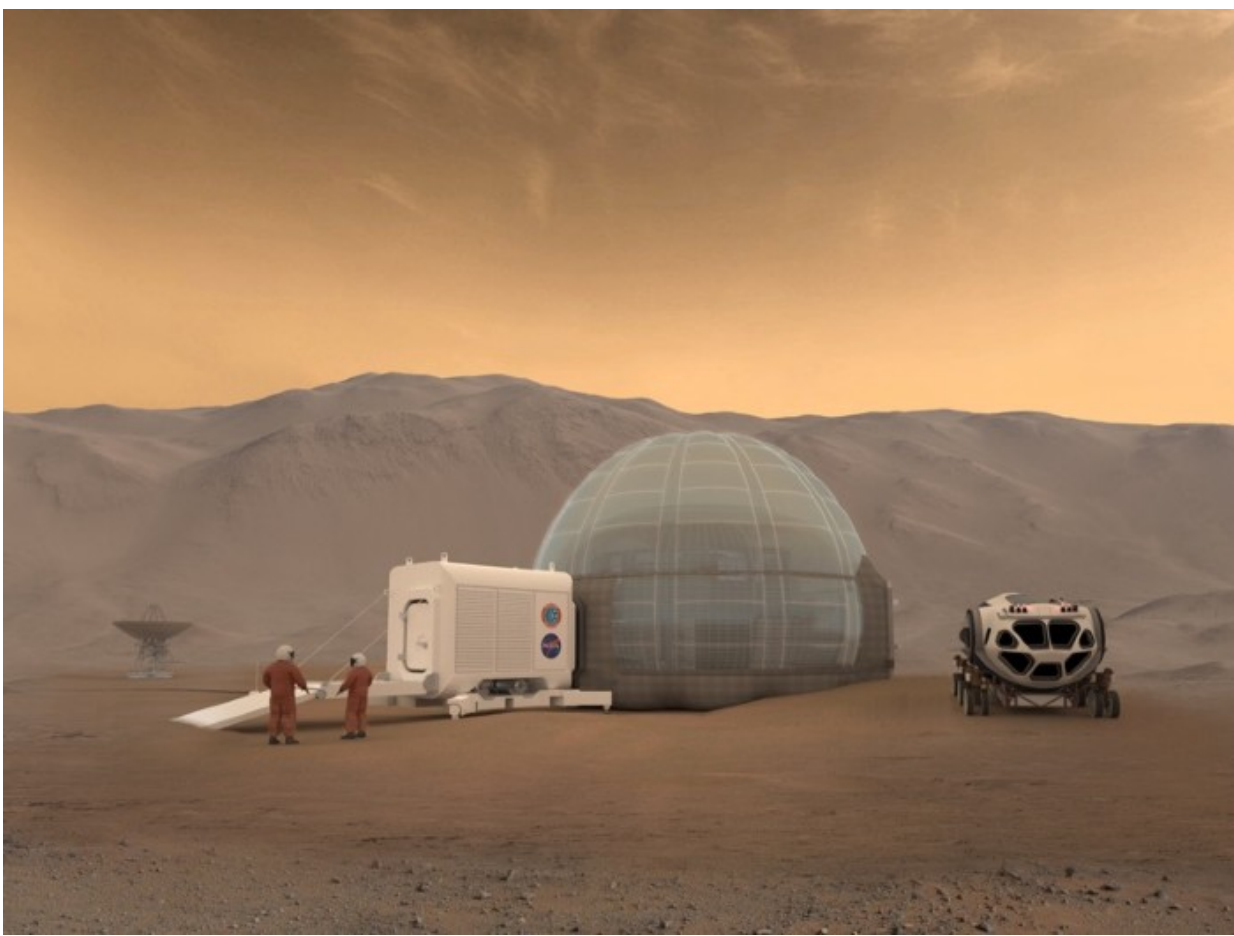
They found that the area covered by ponds and lakes in heavily mined watersheds had increased by 670% since 1985, and that the rate at which mercury pollution is converted into methylmercury is roughly six times greater in lake ecosystems than in rivers.

Landscape changes caused by artisanal mining represent an important and previously unrecognized risk of mercury exposure, the researchers say.

[Sci. Adv. \(2020\)](#)

- [Environmental sciences](#)

This article was downloaded by **calibre** from <https://www.nature.com/articles/d41586-020-03367-1>



Crews living on Mars (artist's impression) could survive on oxygen extracted from the salty water that permeates some of the planet's soils.
Credit: NASA/Clouds AO/SEArch

Chemistry

04 December 2020

How salt water on Mars could give astronauts a breather

Water locked away in Martian sediments could be split into the gases needed by humans and their machines.

A device that uses electricity to decompose water could be used to transform brines on Mars into a supply of hydrogen fuel and life-supporting oxygen.

The red planet's atmosphere is rich in carbon dioxide but contains just 0.14% oxygen. To support a human on Mars, NASA plans to generate oxygen by ripping it from CO₂, creating carbon monoxide and oxygen.

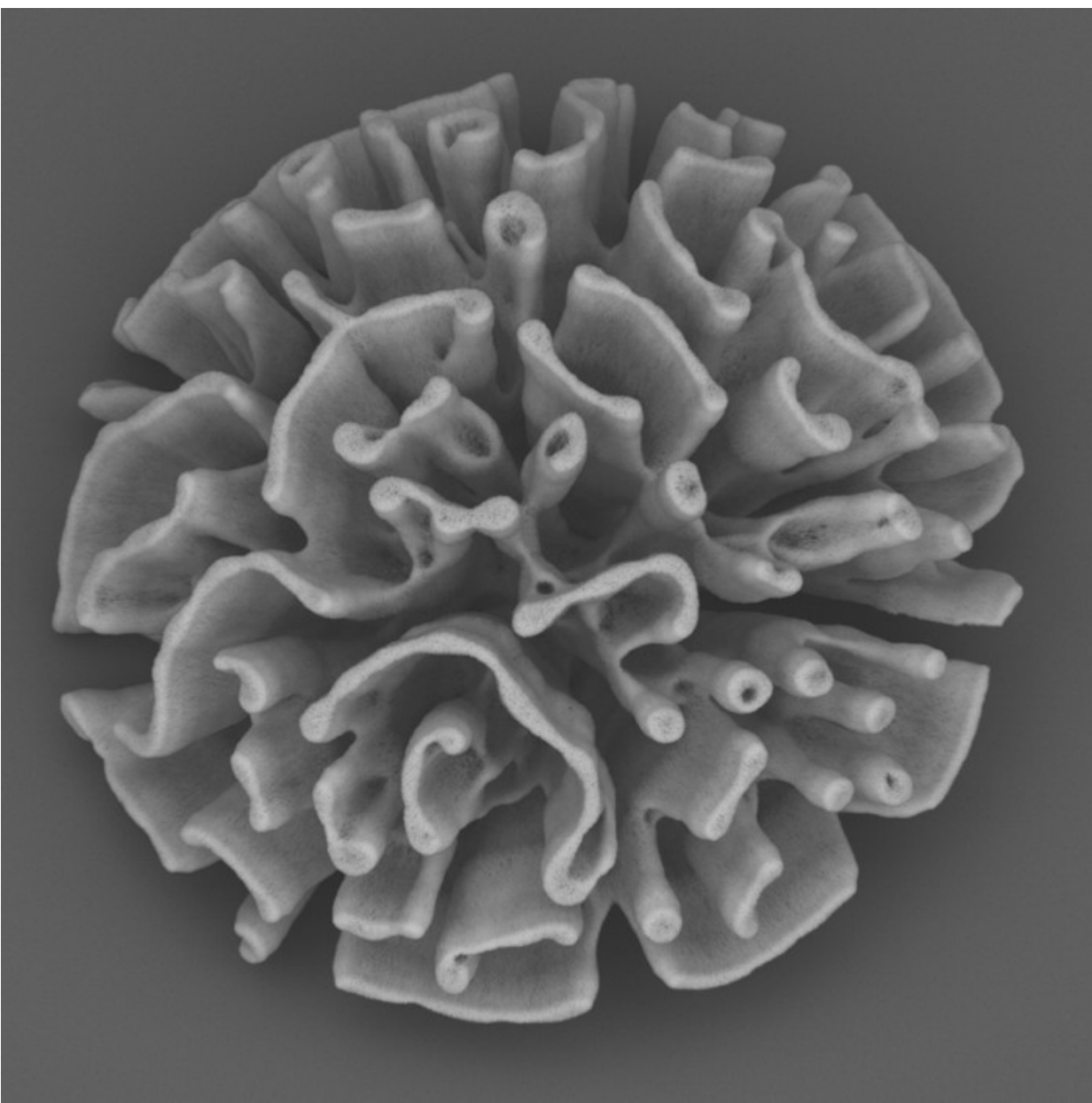
As an alternative strategy, Vijay Ramani and his colleagues at Washington University in St. Louis, Missouri, built an electrolyser, a device that splits liquid water into its constituent gases, hydrogen and oxygen. Most Martian water is frozen, but some areas of the planet have high concentrations of magnesium salts, which help water to remain liquid at low temperatures. The researchers' electrolyser has one electrode made of a lead- and ruthenium-based compound, which promotes oxygen gas generation at the electrode even under salty conditions.

The team tested the electrolyser on a concentrated solution of magnesium salts in a CO₂-rich atmosphere at –36°C, simulating Martian conditions. Compared with NASA's approach, the electrolyser has the potential to produce 25 times the volume of oxygen using the same amount of power.

[Proc. Natl Acad. Sci. USA \(2020\)](#)

- [Chemistry](#)

This article was downloaded by **calibre** from <https://www.nature.com/articles/d41586-020-03430-x>



Scientists can transform a microscopic particle (above) from barium-based to cadmium-based without sacrificing its complex form. Credit: H.C. Hendrikse *et al./Adv. Mater.*

Materials science

03 December 2020

Presto chango: tiny particles get a chemical makeover but keep their shape

Self-assembling particles exhibit a mind-boggling array of structure and composition.

In a neat chemical sleight-of-hand, researchers can swap out the ions in microscopic structures without disturbing the structures' shape, yielding an array of spirals, trumpets and rods with diverse compositions.

Many techniques can be used to guide atoms and ions to self-assemble into various structures, but precise control over both shape and chemical composition of such structures has eluded researchers. Taking up the challenge, Willem Noorduin at AMOLF in Amsterdam and his colleagues first created structures of the desired shapes out of a silica matrix embedded with barium-carbonate crystals.

These were then soaked in a solution containing metal ions, which displaced the barium ones while the rigid silica held the structures in shape. Finally, the structures were heated in a furnace to decompose the carbonate ions, which were replaced by oxide or sulphide ions supplied to the reaction.

One set of nickel oxide ‘corals’ outperformed conventional nickel catalysts at promoting an industrial process for manufacturing hydrogen gas. A porous coral furled and unfurled its petals in response to an electron beam.

[Adv. Mater. \(2020\)](#)

- [Materials science](#)

| [Next section](#) | [Main menu](#) | [Previous section](#) |

News in Focus

| [Next section](#) | [Main menu](#) | [Previous section](#) |

| [Next section](#) | [Main menu](#) | [Previous section](#) |

Books & Arts

| [Next section](#) | [Main menu](#) | [Previous section](#) |

| [Next section](#) | [Main menu](#) | [Previous section](#) |

Opinion

| [Next section](#) | [Main menu](#) | [Previous section](#) |

Work

- **Core curriculum: learning to manage a shared microscopy facility** [08 December 2020]

Technology Feature • High-tech tools are increasingly being consolidated into specialized centres. Running these technological wonderlands takes a unique blend of skills.

- **Ocean explorer** [07 December 2020]

Where I Work • Working on a research vessel means John Fulmer is one of the first to see intriguing discoveries.

TECHNOLOGY FEATURE

08 December 2020

Core curriculum: learning to manage a shared microscopy facility

High-tech tools are increasingly being consolidated into specialized centres. Running these technological wonderlands takes a unique blend of skills.

Sandeep Ravindran

Sandeep Ravindran is a science writer based in Washington DC.

Search for this author in:

- [Pub Med](#)
- [Nature.com](#)
- [Google Scholar](#)

 A man standing in a darkened room surrounded by a large microscope, looking at a screen which illuminates his face

The Advanced Imaging Center in Ashburn, Virginia, provides technical training for core-facility managers. Credit: Advanced Imaging Center, HHMI Janelia Research Campus

It's the long wait for equipment that H. Krishnamurthy remembers from his master's studies at Bangalore University in India. "I used to stand in line to get my turn to use a rusted hammer to nail [down] a frog for dissection," he says.

Today, Krishnamurthy directs a facility so that other researchers in Bengaluru and throughout India need never experience that lack of access. The Central Imaging and Flow Cytometry Lab at the National Center for Biological Sciences in Bengaluru “has helped scientists to take their research to next level”, he says. “Before I started this facility, there was no paper published in *Cell* from India.” Since then, users have published more than half a dozen papers in *Cell*, as well as others in journals such as the *Proceedings of the National Academy of Sciences*.

Over the past 20 years, as instrument costs have risen and funding levels fallen, institutions have increasingly consolidated microscopes, mass spectrometers, flow cytometers and other high-tech equipment in specialized core facilities, where dedicated staff can cost-effectively provide a breadth of expertise and access to equipment beyond what any single laboratory could manage. Numbers are hard to come by, but Peter O’Toole, director of the Bioscience Technology Facility at the University of York, UK, has seen meetings for UK core-facility managers grow from a dozen participants in 2006 to around 200 today. And in Germany, the number of imaging core facilities doubled between 2011 and 2015, from 30 to 60.

The people tasked with running these facilities have a rare collection of skills: in-depth knowledge of the hardware they oversee, managerial and financial acumen to run what is effectively a business, and scientific know-how to guide researchers through a range of experimental systems and designs. The management aspects alone would usually fill three jobs — financial manager, project manager and people manager — says Graham Wright, acting director of the Research Support Centre at the Agency for Science, Technology and Research in Singapore. Krishnamurthy was once asked to list his responsibilities, and says he was shocked at how many he had. “This is not a 9-to-5 job, it’s a 24-hour job,” he says.

Until a few years ago, however, there was no clear career track, and few specialized training opportunities. “All the people in my generation figured it out as we went along,” says Jennifer Waters, director of the Nikon Imaging Center at Harvard Medical School in Boston, Massachusetts.

But things are changing. Waters has launched a programme at Harvard that provides technical training for core-facility managers ([J. C. Waters Trends](#)

[*Cell Biol.* 30, 669–672; 2020](#)), and other institutions have created similar programmes, including the Advanced Imaging Center (AIC) at the Howard Hughes Medical Institute’s Janelia Research Campus in Ashburn, Virginia, and the European Molecular Biology Laboratory (EMBL) in Heidelberg, Germany. And fresh funding opportunities for managers and staff are making the career track easier to navigate.

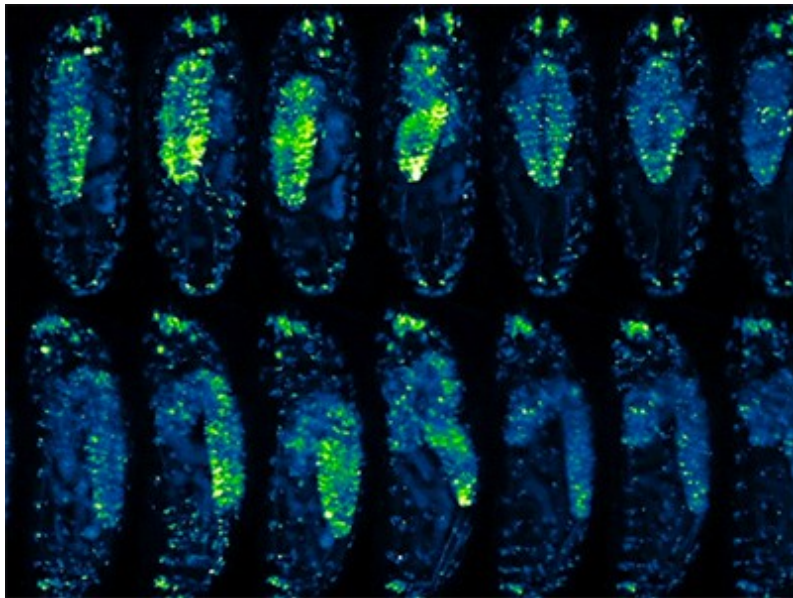
“Probably the most important thing I’m going to do in my career is to help train this next generation,” says Waters.

Combining breadth and depth

At some core facilities, users drop off samples and receive data in return. At others, including Krishnamurthy’s, staff train users, but are not involved in the actual experiments. Many microscopy facilities lie between these extremes, with staff advising users on what imaging techniques are best suited to their projects and working with them as they operate the equipment.

Whatever the operational model, technical expertise is paramount. “The most important prerequisite to work in a core facility is that you really have to be very good at the techniques that you are operating, be it microscopy, flow cytometry or mass spectrometry,” says Teng-Leong Chew, who directs the AIC. That means having not just technical proficiency in that equipment, but also a deep understanding of its theoretical underpinnings, as well as the engineering skills to be able to install, maintain and repair it.

Also required are the skills and experience to weigh in on a diverse array of projects and experimental models. “One minute you’re working on yeast and bacteria and the next minute on brain slices, and that means not only do we see a whole variety of scientific specimens, but also a huge range of microscopy technology,” says Alison North, senior director of the Rockefeller University Bio-Imaging Resource Center in New York City.



The microscope makers putting ever-larger biological samples under the spotlight

Chew, for instance, helps researchers to work out what imaging approach to use, how to design experiments, how to handle the equipment and how to analyse and interpret the resulting images — a process that can take anywhere from hours to days of one-on-one time. “You have to provide very good training, not just in how to use the instrument, but [in] how to make sure that your experiment is accurate, ethical, quantitative and reproducible,” he says.

Staying up to date with technology is crucial, be it through the literature, conferences or word-of-mouth. “That’s part of the job, to scout for new technology and make sure you’re using it earlier,” says Stefanie Reichelt, who runs the light-microscopy core facility at the Cancer Research UK Cambridge Institute at the University of Cambridge. Popular meetings for microscopy core-facility staff include the European Light Microscopy Initiative; Focus on Microscopy; the UK Royal Microscopical Society’s Microscience Microscopy Congress; and the Seeing is Believing conference.

Yet despite their crucial role in the conduct of research, core facilities are often as much businesses as laboratories, and staff rarely receive authorship unless they also provide significant scientific input. Acknowledgements are more common, although not guaranteed. “Sometimes you do hard work, and you will not see that reward directly coming in terms of an acknowledgement,” says Jan Peychl, head of the Light Microscopy Facility (LMF) at the Max Planck Institute of Molecular Cell Biology and Genetics in Dresden, Germany. To help address this, the Royal Microscopical Society and the US Association of Biomolecular Resource Facilities (ABRF) have [developed authorship guidelines](#) that core facilities can provide to their users.

Service providers

As microscopy core facilities become increasingly prevalent, they offer an intriguing career option for PhD and postdoctoral researchers. “I think it is a great career,” says North. But it’s not a position for someone who’s just applying “because they’re worried that they won’t get a job” as a principal investigator, she says.

North looks for applicants who have experience with different types of specimen and in training others in microscopy, and who have been responsible for troubleshooting. The exact scientific training can vary, but a “lack of ego” is a must, she says. “If it’s all about getting credit for the work you’ve done, then this is not the right job for you.”



Harvard Advanced Microscopy Fellows Rylie Walsh and Federico Gasparoli.Credit: Jennifer C. Waters

Indeed, core-facility staff have very different jobs from conventional scientists, and organizations might need to implement performance metrics for core-facility managers to match, says Wright. These metrics “are likely not focused on the number of publications or grants awarded, but more on the users trained, level of user satisfaction, cost recovery, acknowledgements in publications et cetera”, he says.

Facility-director salaries can vary widely, from around £35,000 (US\$47,000) per year for postdoc-like positions to £90,000 for senior managers, says O’Toole. “These can be very different roles with a very similar job title,” he says. Those on the lower end of the scale are likely to have many fewer responsibilities and staff, will not write grant applications and might not fully control their budgets. But they can progress by expanding their core facility or moving to a more senior position at a larger facility.

Before he was a core-facility director, Peychl was a medical doctor, a stage actor and an assistant professor. The common denominator, he says, is people skills: “I deal with hundreds of people, and I need to understand their motivations, and their needs and emotions as well,” he says.

As a junior assistant professor at the Charles University Faculty of Medicine in Hradec Králové in the Czech Republic, Peychl says, he was always the one taking care of his department’s common microscopes. “The person who first goes and fixes it probably is highly qualified to become core-facility manager,” he says. “It’s important that you have this inner drive to support people with cool technologies.”

In 2001, Peychl’s interest in microscopy inspired a career change, and he applied for an imaging-specialist position at the LMF. “Of course, they were surprised that a medical doctor would apply for a technician job, but they immediately offered me a postdoctoral fellowship to support the work of the core imaging facility,” he says.

The business end

Peychl’s experience is unusual in that training opportunities for core-facility management are relatively rare. But they are increasing in number.

The German Society for Microscopy and Image Analysis, known as German BioImaging, has offered a course on core-facility management and leadership in Germany since 2013, and Global BioImaging, an international network of imaging infrastructures and communities coordinated from EMBL Heidelberg, offers similar courses around the world. The ABRF and Core Technologies for Life Sciences, a Paris-based non-profit association of core-facility scientists and staff, have workshops that teach business skills such as accounting and budgeting. Staff can sometimes take business-school classes offered by the universities where their facilities are based. And some managers, including Wright, even complete a master’s of business administration, which he says has been “incredibly useful”.



Core facilities: shared support

German BioImaging and Global BioImaging also organize job-shadowing programmes, which allow staff to pick up skills from their peers. “I see real value in visiting other core facilities to understand how they operate and bring home the relevant bits to help improve our own operations,” says Wright.

Grant-writing skills are essential. “The success of a core facility, to some extent, is reflected by the number of shared instrumentation grants that it secures,” says Chew. In the United States, the National Science Foundation and Department of Defense both fund core facilities, and the National Institutes of Health’s S10 shared instrumentation grant is “almost tailor-made for core-facility directors”, Chew says. Facilities in other parts of the world, including most European countries, are also funded mainly by government grants.

Most of these grants cover only instrumentation, but some, including the German Research Foundation’s core facilities funding programme and the imaging scientists programme from the philanthropic organization the Chan Zuckerberg Initiative in Redwood City, California cover staff, too.

Facility staff positions are often not permanent, which can lead to regular loss of institutional knowledge. “Usually you need minimum of a year to get a person up to speed,” says Peychl. Such turnover presents challenges, he says, but it also encourages flexibility.

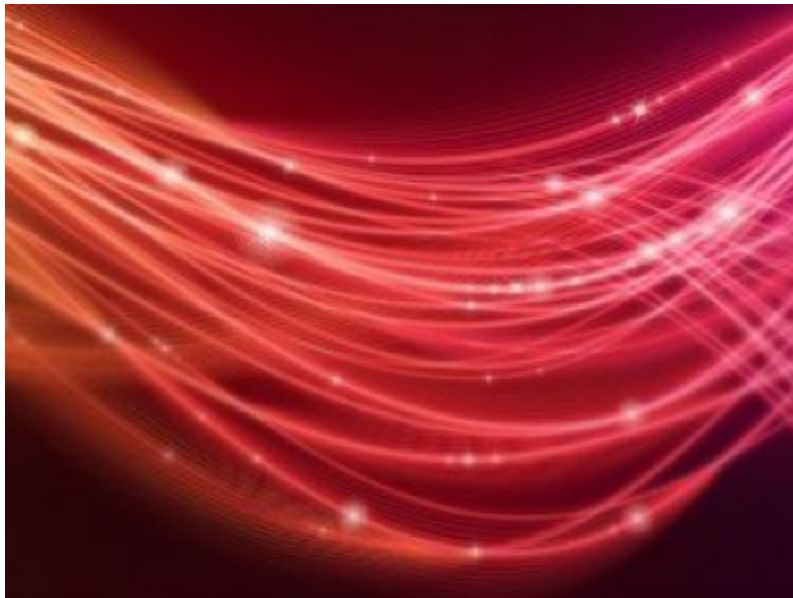
For instance, facility managers had to react quickly when faced with the COVID-19 pandemic, both to keep their staff and users safe and to minimize disruptions.

Peychl, working with Elisa Ferrando-May at the University of Konstanz Bioimaging Center in Germany and others, published COVID-19 guidelines for core facilities, such as avoiding face-to-face training and providing remote support to microscope users ([S. Dietzel et al. *Cytometry A* 97, 882–886; 2020](#)). Roland Nitschke, head of the Life Imaging Center at the University of Freiburg, Germany, set things up at his facility so that he could remotely control microscopes to show users what to do. The set-up required ultra-high-resolution cameras, and scientists started using the same cameras to check in on long-running experiments from home. “Maybe it’s the only good thing to come out of the coronavirus,” says Nitschke.

A core crash course

To bring new recruits up to speed, some managers turn to external courses and workshops. Waters teaches yearly microscopy courses at Cold Spring Harbor Laboratory in New York, and North does the same at the Woods Hole Marine Biological Laboratory in Massachusetts. And Krishnamurthy provides a training programme on confocal microscopy and flow cytometry in Bengaluru. But, “in the end”, says Peychl, “it’s all about hands-on experience”.

Most researchers use just one or two types of microscopy during their PhD or postdoc. “We have everything from single molecules to organoids and embryos coming into the core, and we have 15 different imaging modalities,” says Waters. “The idea of anybody walking out of a postdoc and into a core facility, and being able to immediately know what they’re doing, is ridiculous,” she says.



NatureTech hub

That's what motivated Waters to start Harvard's Advanced Microscopy Fellowship in 2013. Waters originally funded two fellows by reallocating salary for a staff member, but has since been supported by microscope manufacturer Nikon and three departments at Harvard Medical School. The programme costs about US\$80,000 a year for each fellow, and participants are guaranteed two years of funding.

Fellows spend half of their time on core service work, such as training users and maintaining microscopes, and another half on an independent project, such as writing code to assess the quality of microscopy images.

Fellows also learn management and budgeting skills, and work on grants with Waters. And they learn the fine art of dealing with clients. "I want them to have the confidence to sit in a room with a group of faculty and say, 'I know that technology looks interesting, but you don't have the need for it,'" says Waters. "If I have to write an uncomfortable e-mail to a faculty member, I will write it and then forward it to my postdoc so they can see how I worded it," she says. "They get to see how those situations are handled, and they leave with a little bit of a toolkit of how to manage that."

Waters has two current fellows and four alumni who have gone on to work at or run other core facilities. “I want them all to walk out of here being technical experts who deserve respect and are given autonomy,” she explains. Staff might also go into industry, especially to microscopy companies.

Other institutes have created similar programmes. For instance, Janelia’s Advanced Microscopy Fellows spend half of their time getting hands-on experience at the AIC and the other half on self-directed training, whether that’s learning how to code or how to run an international microscopy workshop. “That 50% protected time allows them to hone their skill to become a successful core director in the future,” says Chew.

In Europe, EMBL’s ARISE fellowship programme is launching training for 62 fellows over the next five years, supported by some €12.7 million (US\$15 million) from the European Commission and EMBL. Calls for applications went out in November, and fellows will be hosted at one of six EMBL sites across Europe.

“We want to build through the programme the future heads or senior staff of research infrastructure facilities,” says Tanja Ninkovic, ARISE programme manager at EMBL Heidelberg. As well as learning the ins and outs of core-facility management, fellows will pursue an independent research project and study technology transfer, entrepreneurship and science policy. “These are the skills that are needed by research infrastructure scientists regardless of the technology that the facility is offering,” says Ninkovic.

Peychl, who attended a German BioImaging course for facility managers, sees the increase in core-facility management courses as a sign that these positions are increasingly valued. And he encourages others to consider the role. “For those who like to support others, who are technologically inclined and who have people skills, this could be a rewarding career.”

Nature 588, 358-360 (2020)

doi: <https://doi.org/10.1038/d41586-020-03466-z>

Jobs from Nature Careers

- - - [All jobs](#)
 - - **[Perinatal Pathologist](#)**

[University of California, San Diego \(UC San Diego\)](#)

[La Jolla, CA, United States](#)

[JOB POST](#)

■ **[Chief Science and Innovation Officer](#)**

[National Geographic Society](#)

[Washington, United States](#)

[JOB POST](#)

■ **[Postdoctoral Fellow](#)**

[University of Maryland, Baltimore \(UMB\)](#)

[Baltimore, MD, USA, MD, United States](#)

[JOB POST](#)

■ **[POSTDOCTORAL SCIENTIST Institute for Experimental Pediatric Endocrinology](#)**

[Charité - University Medicine Berlin](#)

[Berlin, Germany](#)

[JOB POST](#)

This article was downloaded by **calibre** from <https://www.nature.com/articles/d41586-020-03466-z>

| [Section menu](#) | [Main menu](#) |

WHERE I WORK

07 December 2020

Ocean explorer

Working on a research vessel means John Fulmer is one of the first to see intriguing discoveries.

Amber Dance

Amber Dance is a freelance writer in Los Angeles, California.

Search for this author in:

- [Pub Med](#)
- [Nature.com](#)
- [Google Scholar](#)



John Fulmer works on ROV SuBastian on the RV *Falkor* near the Great Barrier Reef

John Fulmer, lead technician for the Schmidt Ocean Institute's RV *Falkor*, is currently on leave in Halifax, Canada. Credit: Schmidt Ocean Institute

I have just spent six months in the Great Barrier Reef on the research vessel *Falkor*. Every cruise tackles cutting-edge science and, as lead technician, I've been able to witness so many firsts: the RV *Falkor* is the first ship to map much of this area at high resolution, and to put a remotely operated vehicle (ROV) down in the Great Barrier Reef at depths of up to 2,000 metres. So everything we're seeing is new. With the ROV's two arms, we gather samples of rocks, corals, sediments, jellyfish — everything we come across down there — for collaborators to analyse later.

Recently, we discovered a peculiar knoll rising from the sea floor 2,000 metres down, peaking 300 metres below the surface. The odd thing is that it shouldn't be there. There's little to no volcanic activity in the area to create a mound, and it should have been eroded by water like its surroundings. Analysis of the rock samples we took from the knoll might explain things.

I'm the main liaison between the ship's crew and the scientists travelling with us. Three technicians maintain all the shipboard systems, including an instrument to measure ocean conductivity, temperature and density; a multibeam scanner to map the ocean floor; and the ROV SuBastian, which I'm working on in the photo.

We've been lucky that our institution, the Schmidt Ocean Institute in Palo Alto, California, has kept the work going during the pandemic. Everyone undergoes a two-week hotel quarantine and COVID-19 testing before getting on board. Other researchers haven't been able to get to sea, so we livestream our ROV dives. Collaborators can log in and tell us what looks worth sampling. Anyone can watch and ask the scientists questions, and receive live answers.

Science never sleeps. I work 12-hour shifts every day for 6-month stretches, with no days off, and I'm on call all the time. I'm just starting six months on leave, but sometimes I'll tune in to the dives. It's exciting stuff.

Nature **588**, 362 (2020)

doi: <https://doi.org/10.1038/d41586-020-03467-y>

Jobs from Nature Careers

- - - [All jobs](#)
 - - [Perinatal Pathologist](#)

[University of California, San Diego \(UC San Diego\)](#)

[La Jolla, CA, United States](#)

[JOB POST](#)

▪ [**Chief Science and Innovation Officer**](#)

[National Geographic Society](#)

[Washington, United States](#)

[JOB POST](#)

▪ [**Postdoctoral Fellow**](#)

[University of Maryland, Baltimore \(UMB\)](#)

[Baltimore, MD, USA, MD, United States](#)

[JOB POST](#)

▪ [**POSTDOCTORAL SCIENTIST Institute for Experimental Pediatric Endocrinology**](#)

[Charité - University Medicine Berlin](#)

[Berlin, Germany](#)

[JOB POST](#)

This article was downloaded by **calibre** from <https://www.nature.com/articles/d41586-020-03467-y>.

Research

- **[The changing face of birds from the age of the dinosaurs](#)**

[25 November 2020]

News & Views • The fossil record traces the origin of the modern bird skull as birds evolved from their dinosaurian ancestors. Now the discovery of a bizarre fossil reveals a surprising diversion during this process of facial transformation.

- **[Proton collisions probe the final frontier of the standard model of particle physics](#)** [09 December 2020]

News & Views • The nuclear forces that act on short-lived subatomic particles have been hard to study. This problem has now been solved by smashing high-energy protons together and measuring the momenta of the unstable particles produced.

- **[Cracking the cell access code for the deadly virus VEEV](#)**

[18 November 2020]

News & Views • The discovery that the receptor protein LDLRAD3 is essential for infection of human cells by Venezuelan equine encephalitis virus could inform strategies to combat this potentially lethal infection.

- **[Trade-offs for equitable climate policy assessed](#)** [09 December 2020]

News & Views • Computational models show that regionally varied prices for carbon emissions can greatly reduce the need for poor countries to receive financial assistance to tackle climate change, while still stabilizing global warming.

- **[Detection of large-scale X-ray bubbles in the Milky Way halo](#)** [09 December 2020]

Article • Observations from the eROSITA telescope reveal soft-X-ray-emitting bubbles extending above and below the Galactic plane, which arose from energy injected into the Galactic halo from past activity in the Galactic centre.

- **[Unveiling the strong interaction among hadrons at the LHC](#)** [09 December 2020]

Article • Correlations in momentum space between hadrons created by ultrarelativistic proton-proton collisions at the CERN Large Hadron Collider provide insights into the strong interaction, particularly the short-range dynamics of hyperons—baryons that contain strange quarks.

- **[Dipolar evaporation of reactive molecules to below the Fermi temperature](#)** [09 December 2020]

Article • A strongly interacting gas of polar molecules is created by combining an electric field with two-dimensional optical confinement, enabling evaporative cooling and opening up the exploration of low-entropy many-body phases.

- **Operation of an optical atomic clock with a Brillouin laser subsystem** [09 December 2020]

Article • By using a stimulated Brillouin scattering laser in a strontium-ion optical clock instead of the usual bulk-cavity-stabilized laser, the need for vacuum is removed and resonator volume is substantially reduced.

- **Capillary condensation under atomic-scale confinement** [09 December 2020]

Article • In the tiniest of capillaries, barely larger than a water molecule, condensation is surprisingly predictable from the macroscopic Kelvin condensation equation, a coincidence partially owing to elastic deformation of the capillary walls.

- **Catalytic asymmetric addition of an amine N–H bond across internal alkenes** [03 November 2020]

Article • Hydroamination with high enantio- and regioselectivity is achieved across a wide range of internal alkenes by using a cationic iridium complex that adds an ammonia surrogate containing a pyridine group.

- **Quantification of an efficiency–sovereignty trade-off in climate policy** [09 December 2020]

Article • An integrated assessment model analysis shows that a moderately differentiated carbon price could achieve as much climate mitigation as a uniform carbon tax, avoiding concerns regarding equity between participating countries or sovereignty.

- **Clustered versus catastrophic global vertebrate declines** [18 November 2020]

Article • In the geographically and taxonomically divided systems of vertebrates in the Living Planet Index, a small percentage of clusters showed extreme declines or increases, whereas most vertebrate populations across all systems showed no mean global trend.

- **Late Cretaceous bird from Madagascar reveals unique development of beaks** [25 November 2020]

Article • A crow-sized stem bird, *Falcatakely forsteriae*, possesses a long and deep rostrum—a beak morphology that was previously unknown among Mesozoic birds and is similar to that of some crown-group birds, such as toucans.

- **Multiple wheat genomes reveal global variation in modern breeding** [25 November 2020]

Article • Comparison of multiple genome assemblies from wheat reveals extensive diversity that results from the complex breeding history of wheat and provides a basis for further potential improvements to this important food crop.

- **The barley pan-genome reveals the hidden legacy of mutation breeding** [25 November 2020]

Article • Chromosome-scale sequence assemblies of 20 diverse varieties of barley are used to construct a first-generation pan-genome, revealing previously hidden genetic variation that can be used by studies aimed at crop improvement

- **PIEZ02 in sensory neurons and urothelial cells coordinates urination** [14 October 2020]

Article • PIEZ02 is expressed in the bladder urothelium and sensory neurons innervating the lower urinary tract and is a key mechanosensor for the control of urination.

- **Chemico-genetic discovery of astrocytic control of inhibition in vivo** [11 November 2020]

Article • A cell-surface fragment complementation strategy is used to identify the proteome at the junction of astrocytes and synapses in vivo, and shows that NRCAM expressed in astrocytes has a key role in regulating inhibitory synapse function.

- **The gut microbiota is associated with immune cell dynamics in humans** [25 November 2020]

Article • Influence of the gut microbiome on the human immune system is revealed by systems analysis of vast clinical data from decades of electronic health records paired with massive longitudinal microbiome sequencing.

- **LDLRAD3 is a receptor for Venezuelan equine encephalitis virus** [18 November 2020]

Article • LDLRAD3 is a receptor for infection with Venezuelan equine encephalitis virus, and in mouse models deletion of Ldrrad3 or treatment with a soluble LDLRAD3 decoy molecule abrogates infection and disease caused by this virus.

- **Sex differences in immune responses that underlie COVID-19 disease outcomes** [26 August 2020]

Article • Male patients with COVID-19 have higher plasma levels of innate immune cytokines and chemokines such as IL-8, IL-18 and CCL5 and more non-classical monocytes than female patients, whereas female patients mount robust T cell activation maintained even in older age.

- **Tunable dynamics of B cell selection in gut germinal centres** [28 October 2020]

Article • Antibody selection and maturation within B cells found in gut-associated germinal centres is stimulated by the gut microbiota, to a degree that depends on the presence and composition of the microbes.

- **Receptor binding and priming of the spike protein of SARS-CoV-2 for membrane fusion** [17 September 2020]

Article • Cryo-electron microscopy structures of consecutive binding events of ACE2 in complex with the spike protein of SARS-CoV-2 reveal the mechanisms of receptor binding by the spike protein and activation for membrane fusion by the spike protein of SARS-CoV-2.

- **A metastasis map of human cancer cell lines** [09 December 2020]

Article • A method in which pooled barcoded human cancer cell lines are injected into a mouse xenograft model enables simultaneous mapping of the metastatic potential of multiple cell lines, and shows that breast cancer cells that metastasize to the brain have altered lipid metabolism.

- **A map of cis-regulatory elements and 3D genome structures in zebrafish** [25 November 2020]

Article • A comprehensive map of transcriptomes, cis-regulatory elements, heterochromatin structure, the methylome and 3D genome organization in the zebrafish (*Danio rerio*) enables identification of species-specific and evolutionarily conserved regulatory features, and provides a foundation for modelling studies on human disease and development.

- **Structure of LRRK2 in Parkinson's disease and model for microtubule interaction** [19 August 2020]

Article • The structure of the catalytic half of LRRK2 and an atomic model of microtubule-associated LRRK2 suggest that the conformation of the kinase controls the association of LRRK2 with microtubules.

- **Structures and pH-sensing mechanism of the proton-activated chloride channel** [04 November 2020]

Article • Cryo-electron microscopy structures of the human proton-activated chloride channel (PAC) shed light on its pH-dependent gating mechanism and anion selectivity.

- **Crop asynchrony stabilizes food production** [09 December 2020]

Matters Arising •

- **Reply to: Crop asynchrony stabilizes food production** [09 December 2020]

Matters Arising •

NEWS AND VIEWS

25 November 2020

The changing face of birds from the age of the dinosaurs

The fossil record traces the origin of the modern bird skull as birds evolved from their dinosaurian ancestors. Now the discovery of a bizarre fossil reveals a surprising diversion during this process of facial transformation.

Daniel J. Field

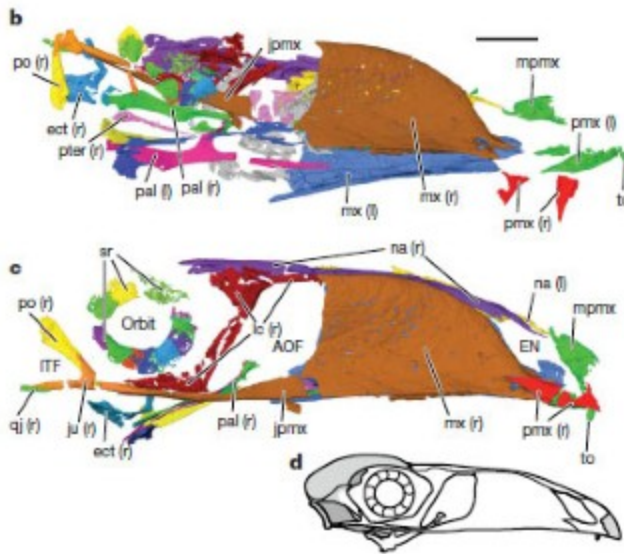
Daniel J. Field is in the Department of Earth Sciences, University of Cambridge, Cambridge CB2 3EQ, UK.

[Contact](#)

Search for this author in:

- [Pub Med](#)
- [Nature.com](#)
- [Google Scholar](#)

As living dinosaurs, birds are the product of a long and complex evolutionary history that has given rise to more than 11,000 living species¹. The past decade has witnessed a surge of interest in the evolution of the avian skull — a structure that is hugely variable across the diversity of living birds². However, our ability to test hypotheses of how and when key transformations of the bird skull took place is limited if we can't incorporate fossils into evolutionary models. [Writing in Nature](#), O'Connor *et al.*³ report a stunning fossil-bird discovery from the age of the dinosaurs that reminds us of the crucial value of fossils for casting light on unexpected complexities in avian evolutionary history.

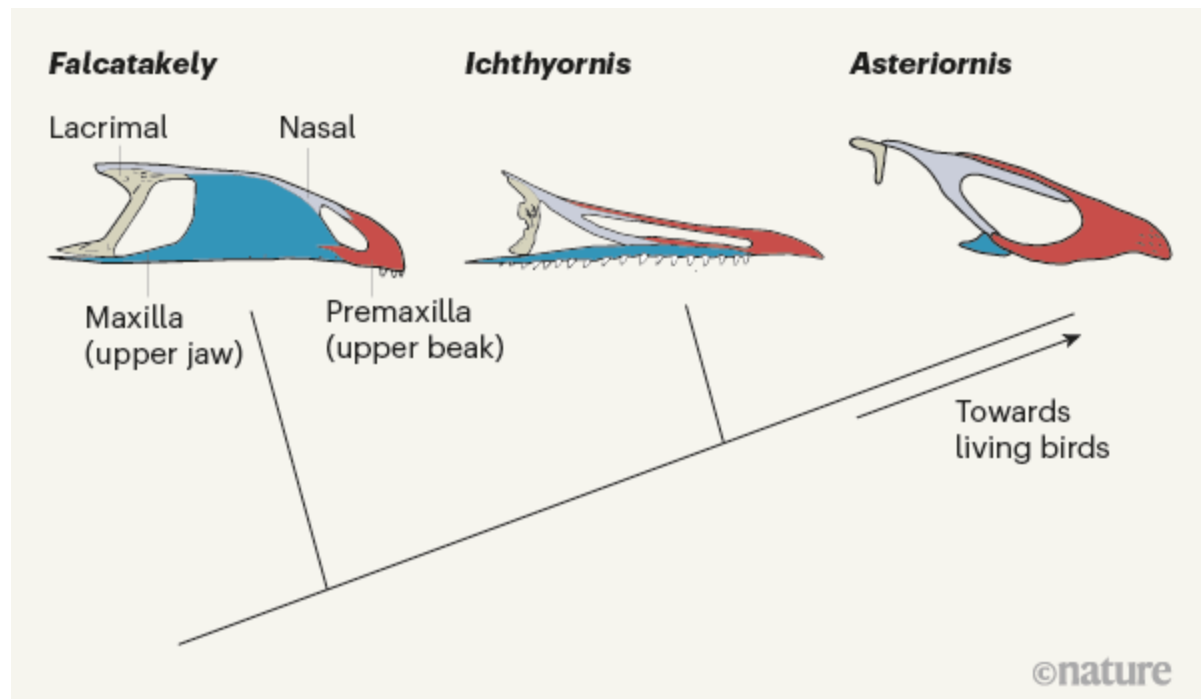


Read the paper: Late Cretaceous bird from Madagascar reveals unique development of beaks

This striking addition to the aviary of the Mesozoic era is between 72 million and 66 million years old (corresponding to the latest stage of the Cretaceous period). It comes from Madagascar, and is named *Falcatakely forsterae*, which roughly translates as Forster's small scythe beak. The name references the distinctive shape of the fossil's bill and honours Catherine Forster's numerous contributions to vertebrate palaeontology in Madagascar. The specimen is small (less than 9 centimetres long) and delicate (paper thin in places), yet the stunning bone preservation provides a spectacular look at this ancient creature's anatomy.

Although the fossil consists of only the front half of a skull, it's clear that *Falcatakely* is more than just a pretty face. The skull is utterly bizarre, characterized by a deep and elongated snout (Fig. 1) unlike those seen in any other Mesozoic birds. The skull's architecture becomes even weirder. The very tip of its snout has one small preserved tooth (the tip possibly had more teeth that were not preserved); however, there are clearly no teeth

anywhere else along its jaws. By contrast, the closest relatives of modern birds from the time of the dinosaurs show the opposite pattern, with teeth found throughout the jaws, but none at the tip of the beak (Fig. 1)⁴. These features give the skull of *Falcatakely* an almost comical profile — imagine a creature resembling a tiny, buck-toothed toucan flitting from branch to branch, occasionally glancing down at Madagascar's formidable Late Cretaceous inhabitants, which included equally bizarre mammals⁵ and giant predatory dinosaurs⁶. Despite the present-day catalogue of approximately 200 Mesozoic bird species from around the world⁷, ranging in age from about 150 million to 66 million years old, none has a skull resembling anything like that of *Falcatakely*. Its discovery reveals a skull shape previously unknown for any bird from the age of the dinosaurs.



©nature

Figure 1 | The evolution of ancient bird skulls. Discoveries of bird skulls from the Mesozoic era (the age of the dinosaurs) have revealed both how the skull of modern birds arose and the surprising variability of these ancient skulls (as illustrated by these fossils, reported between 2018 and 2020). O'Connor *et al.*³ present their discovery of the skull of a bird specimen they name *Falcatakely forsterae*, which shows an unusually deep and elongated snout, with teeth (at least one tooth and possibly more) positioned only at the very tip of the upper jaw in a skull region called the

premaxilla. Like other distant relatives of modern birds, such as non-avian dinosaurs, the upper jaw of *Falcatakely* consists mainly of a region called the maxilla. Closer relatives of modern birds, such as *Ichthyornis*⁴, had teeth throughout the jaws, except at the tip, and retained the ancestrally large maxilla. Early modern birds, including *Asteriornis* (an ancient relative of chickens and ducks)¹³, lost their teeth completely, and had upper jaws dominated by the premaxilla. Nasal bones are shown in grey and lacrimal bones (inferred for *Asteriornis*) are in beige. (Figure adapted from Fig. 2 of ref. 3³, Fig. 3 of ref. 4⁴ and Fig. 1 of ref. 13¹³.)

The exceptional degree of preservation of *Falcatakely* enabled the authors to make other astonishing findings. Imaging using a method called high-resolution micro-computed tomography enabled them to digitally ‘extract’ the fragile skull bones from the surrounding rock. O’Connor and colleagues could then reassemble the delicate components of the bill, including elements such as the paper-thin palate bones, which are rarely found preserved, into a compelling 3D model (see Supplementary Videos 1–8 of ref. 3)³.

Studying the palate, the authors spotted a surprising bone called the ectopterygoid. This is absent in living birds, but is a component of the palate of non-avian dinosaurs and early bird-like forms, such as the iconic early birds *Archaeopteryx* and *Sapeornis*⁸. However, on the basis of detailed analyses, O’Connor *et al.* infer that *Falcatakely* belongs to a group of Mesozoic ‘pre-modern’ birds called Enantiornithes (a name that means ‘opposite birds’, in reference to their atypical shoulder-joint articulations), which occupy a branch of the dinosaur family tree that is much closer to that of modern birds than the branches occupied by either *Archaeopteryx* or *Sapeornis*. The presence of an ectopterygoid in Enantiornithes has been suggested previously⁹, but this identification has been questioned¹⁰. Thus, the detection of an ecto-pterygoid in *Falcatakely* either shows that this ancestral component of the palate was indeed retained in Enantiornithes (at a relatively late stage in avian evolutionary history), or challenges the identification of *Falcatakely* as a member of Enantiornithes, suggesting instead that it belongs on a deeper branch of the family tree of Mesozoic birds.

Although it is impossible to decide definitively between these two options without access to further fossil material, O'Connor *et al.* grapple with this uncertainty to an impressively thorough degree, showing that *Falcatakely* nests with Enantiornithes in evolutionary trees constructed under a range of alternative analytical approaches. Moreover, the identification of *Falcatakely* as a member of Enantiornithes makes sense in light of the previous identification of fragmentary bones assigned to Enantiornithes from the same Madagascan fossil locality¹¹. Nonetheless, some research has indicated that family-tree reconstructions of dinosaurs can return conflicting results when skulls, instead of complete skeletons, are analysed¹². This lack of certainty is all the more reason for the team to continue its productive fieldwork in the hope of discovering more-complete material.

Modern birds originated in the Late Cretaceous¹³, and it has become increasingly apparent that the final 20 million years of the age of the dinosaurs (86 million to 66 million years ago) was a pivotal time in avian evolutionary history. The discovery of *Falcatakely* shows us that the importance of this window in time for bird evolution extends well beyond the origin of modern birds. Apparently, ‘pre-modern’ bird lineages such as Enantiornithes were still experimenting with bold new forms — and possibly previously unfilled ecological niches — well into the terminal stages of the Cretaceous.

The pre-modern birds were wiped out in the end-Cretaceous mass extinction event, along with all other dinosaurs, apart from modern birds¹⁴. Considering the impressive diversity and global distribution of Enantiornithes in the Late Cretaceous, determining why they disappeared in that mass extinction, whereas the earliest modern-bird lineages survived, remains one of the greatest mysteries in avian evolutionary history. The answers to such questions, much like the unexpected anatomy of creatures such as *Falcatakely*, can be revealed only by evidence from the fossil record. So, let’s keep digging.

Nature 588, 221-222 (2020)

doi: <https://doi.org/10.1038/d41586-020-03260-x>

References

1. 1.
del Hoyo, J. *All the Birds of the World* (Lynx, 2020).
2. 2.
Felice, R. N. & Goswami, A. *Proc. Natl Acad. Sci. USA* **115**, 555–560 (2018).
3. 3.
O'Connor, P. M. *et al.* *Nature* **588**, 272–276 (2020).
4. 4.
Field, D. J. *et al.* *Nature* **557**, 96–100 (2018).
5. 5.
Krause, D. W. *et al.* *Nature* **515**, 512–517 (2014).
6. 6.
Lavocat, R. *Bull. Mus. Natl Hist. Nat.* **27**, 256–259 (1955).
7. 7.
Pittman, M. *et al.* in *Pennaraptoran Theropod Dinosaurs: Past Progress and New Frontiers* (eds Pittman, M. & Xing, X.) 37–95 (*Bull. Am. Mus. Natl Hist.* No. 440; Am. Mus. Natl Hist., 2020).
8. 8.
Hu, H. *et al.* *Proc. Natl Acad. Sci. USA* **116**, 19571–19578 (2019).
9. 9.

Elzanowski, A. *Cour. Forschungsinst. Senckenb.* **181**, 37–53 (1995).

10. 10.

Mayr, G. *Avian Evolution: The Fossil Record of Birds and its Paleobiological Significance* (Wiley, 2016).

11. 11.

O'Connor, P. M. & Forster, C. A. *J. Vert. Paleontol.* **30**, 1178–1201 (2010).

12. 12.

Li, Y., Ruta, M. & Wills, M. A. *Syst. Biol.* **69**, 638–659 (2020).

13. 13.

Field, D. J., Benito, J., Chen, A., Jagt, J. W. M. & Ksepka, D. T. *Nature* **579**, 397–401 (2020).

14. 14.

Longrich, N. R., Tokaryk, T. & Field, D. J. *Proc. Natl Acad. Sci. USA* **108**, 15253–15257 (2011).

Jobs from Nature Careers

- - - [All jobs](#)
 - - [Perinatal Pathologist](#)
 - [University of California, San Diego \(UC San Diego\)](#)
 - [La Jolla, CA, United States](#)

JOB POST

- **Chief Science and Innovation Officer**

National Geographic Society

Washington, United States

JOB POST

- **Postdoctoral Fellow**

University of Maryland, Baltimore (UMB)

Baltimore, MD, USA, MD, United States

JOB POST

- **POSTDOCTORAL SCIENTIST Institute for Experimental Pediatric Endocrinology**

Charité - University Medicine Berlin

Berlin, Germany

JOB POST

This article was downloaded by **calibre** from <https://www.nature.com/articles/d41586-020-03260-x>

NEWS AND VIEWS

09 December 2020

Proton collisions probe the final frontier of the standard model of particle physics

The nuclear forces that act on short-lived subatomic particles have been hard to study. This problem has now been solved by smashing high-energy protons together and measuring the momenta of the unstable particles produced.

Manuel Lorenz

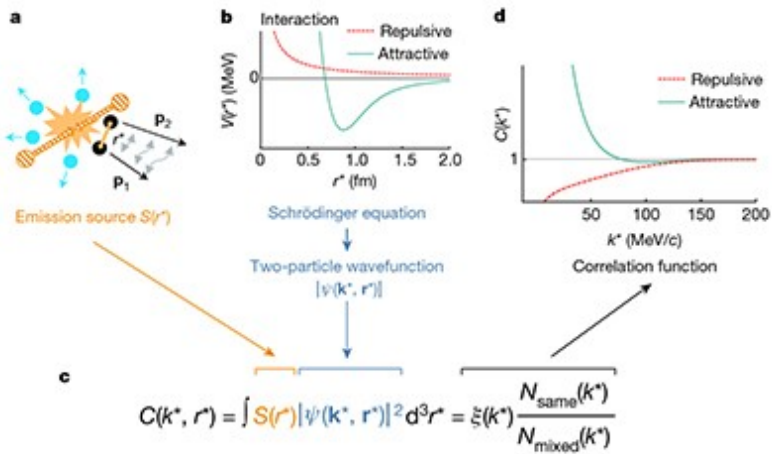
Manuel Lorenz is at the Institute for Nuclear Physics, Goethe University, Frankfurt 60438, Germany.

[Contact](#)

Search for this author in:

- [Pub Med](#)
- [Nature.com](#)
- [Google Scholar](#)

In [a paper in Nature](#), the ALICE Collaboration¹ reports that data from high-energy collisions between protons can be used to investigate the little-understood nuclear forces between protons and subatomic particles called hyperons. The measurements have comparable precision to state-of-the-art numerical calculations of the forces, thereby allowing conclusive quantitative comparisons of experimental data with theory. Accurate knowledge of these forces is needed for various aspects of physics research, for example in efforts to understand the stability of neutron stars.



Read the paper: Unveiling the strong interaction among hadrons at the LHC

The nuclear force between neutrons and protons (which are known collectively as nucleons) is a residual effect of the strong interaction that acts between their elementary constituents (quarks and gluons). First-principles calculations of the nuclear force have been challenging because of the peculiarities of the strong interaction. Our knowledge of this force is, therefore, based largely on simplified models and theories², guided by experimental data³. The strong interaction between hadrons (subatomic particles, such as nucleons, that consist of two or more quarks bound together by the strong interaction) at low energies is therefore often referred to as the final frontier of the standard model of particle physics.

The interaction between nucleons has been measured with high accuracy³, but the interaction of nucleons with their heavier siblings, the hyperons, is less well assessed. Hyperons consist of three quarks, at least one of which must be a type (flavour) known as a strange quark; the other quarks can be up or down, the two lightest quark flavours. Hyperons are not present in the

everyday matter that surrounds us on Earth, but — depending on their interactions with nucleons — might affect the compressibility of nuclear matter at high densities. This means they could be relevant to the stability of neutron stars⁴. Precise knowledge of hyperon–nucleon interactions is therefore of great importance not only for nuclear physics, but also for astrophysics. However, measurements of these interactions are difficult to make in conventional experiments involving direct particle collisions in accelerators, because hyperons are short-lived (their lifetimes are about 10^{-10} s⁵) and fly only a few centimetres, on average, before they decay.

The ALICE Collaboration now reports that proton–hyperon interactions can be investigated using high-energy collisions between protons carried out at the Large Hadron Collider (LHC) at CERN, Europe’s particle physics laboratory near Geneva, Switzerland. The technique depends on measurements of correlations between the momenta of protons and hyperons produced in the collisions.

The process studied in the experiments involves three steps (Fig. 1). First, protons are collided at extremely high energies, taking advantage of the fact that the LHC produces higher collision energies than any other accelerator. Second, hadrons are emitted by a ‘source’ produced by the collision — a volume of space in which quarks and gluons that originally came from the protons interact and become confined within new hadrons. The source emits various types of hadron, including protons and hyperons, some of which form proton–hyperon pairs. Finally, the proton and hyperon in each of these pairs interact with each other in ways that alter the momentum of the paired system. This momentum is measured by a detector and used to determine the momentum correlations.

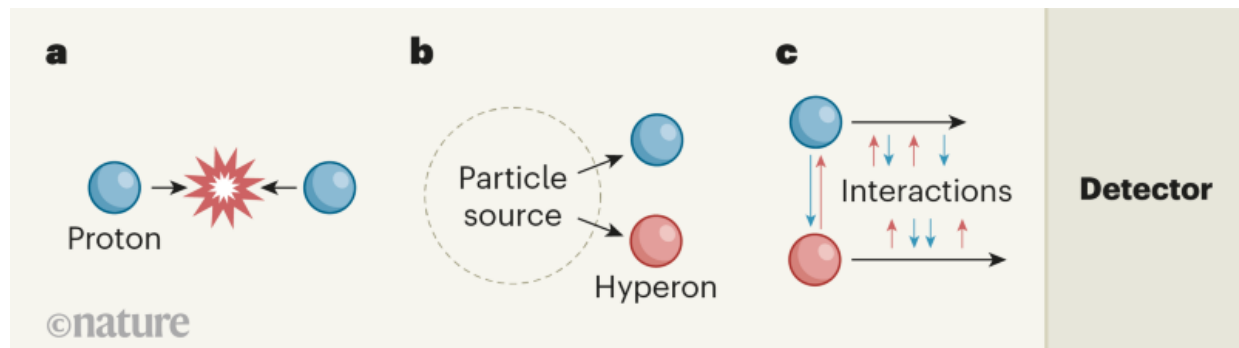
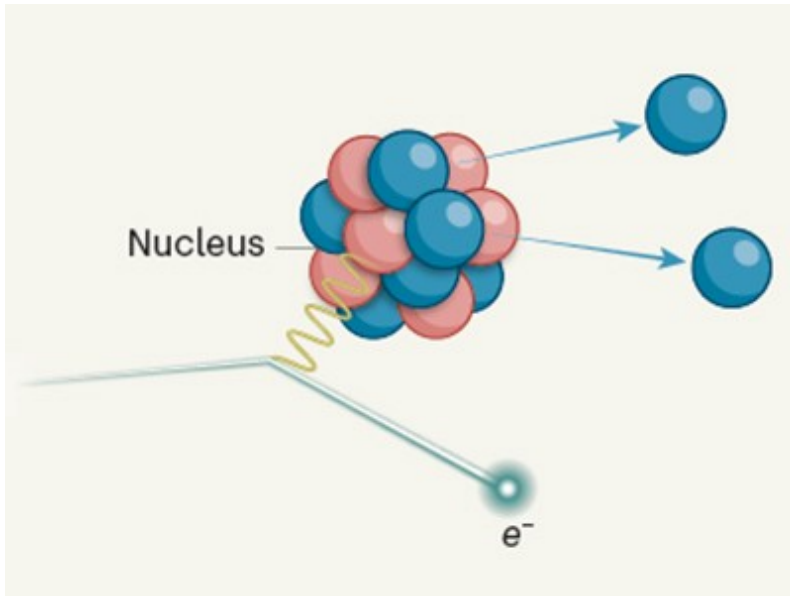


Figure 1 | Investigating the proton–hyperon interaction. **a**, The ALICE Collaboration¹ smashed together high-energy protons in CERN’s Large Hadron Collider. **b**, The collisions generate a ‘particle source’ — a volume of space in which components of the colliding protons interact and become confined within new particles. These new particles are emitted from the source, and include protons that pair up with heavier particles known as hyperons. **c**, The paired-up protons and hyperons interact with each other in a way that alters the relative momentum of the system, which is then measured by a detector. These measurements are then used to determine the nuclear force between the proton–hyperon pair.

The momentum correlations reflect the size of the hadron source and the properties of the interaction between the produced proton–hyperon pairs. Such correlation analyses were originally used to determine the source size in collisions of heavy ions⁶, but in the new work, they are instead used to investigate the interaction between the particles of interest. This approach to studying particle interactions was pioneered by the HADES Collaboration⁷ at the GSI Helmholtz Centre for Heavy Ion Research in Darmstadt, Germany, and was further developed by the ALICE collaboration⁸ at the LHC. The current work depends on the fact that the extremely high-energy proton–proton collisions carried out at the LHC produce a high abundance of hyperons from small-volume hadron sources. The authors used this method to measure the strong force between protons and Ω^- hyperons (which consist of three strange quarks) and between protons and Ξ hyperons (which consist of two strange quarks and one up or down quark).



High-energy-electron scattering probes the strong nuclear interaction at close range

The ALICE Collaboration's findings open up a new 'laboratory' for investigating other nucleon–hyperon interactions, including the little-explored interactions with hyperons that contain two or three strange quarks. This will aid our understanding of metastable states of hyperon pairs or of the compressibility of nuclear matter at high densities. The latter is relevant not only for the stability of neutron stars, but also for neutron-star mergers and heavy-ion collisions.

In a lucky coincidence, recent developments in theoretical physics^{9,10} allow nuclear forces to be calculated from first principles so that the results can be compared with experimental findings. The precision with which nucleon–nucleon interactions can be determined from experimental data is still superior to that obtained from these calculations, but the ALICE Collaboration's measurements of the proton–hyperon interactions almost exactly match those obtained from theory.

A wealth of high-precision measurements of proton–hyperon interactions is expected from the LHC in the next decade, following on from its recent upgrade. Moreover, various other facilities that will study particle collisions at lower energies than those produced at the LHC are expected to go into full operation in the coming years, including NICA in Russia, J-PARC in Japan and FAIR in Germany. Although fewer proton–hyperon pairs are generated per collision in lower-energy collisions, a greater proportion of those pairs will be emitted at low momenta — which might turn out to be advantageous, because more data are needed to reduce the statistical errors in measurements of low-momentum systems. Increases in computing power should also substantially reduce the uncertainties of first-principles calculations of nuclear forces. Taken together, these developments bode well for future research into the final frontier of the standard model of particle physics.

Nature **588**, 222–223 (2020)

doi: <https://doi.org/10.1038/d41586-020-03393-z>

References

1. 1.

ALICE Collaboration. *Nature* **588**, 232–238 (2020).

2. 2.

Epelbaum, E., Hammer, H.-W. & Meissner, U.-G. *Rev. Mod. Phys.* **81**, 1773–1825 (2009).

3. 3.

Stoks, V. & de Swart, J. *Phys. Rev. C* **47**, 761–767 (1993).

4. 4.

Weissenborn, S., Chatterjee, D. & Schaffner-Bielich, J. *Phys. Rev. C* **85**, 065802 (2012).

5. 5.

Tanabashi, M. *et al. Phys. Rev. D* **98**, 030001 (2018).

6. 6.

Lisa, M. A., Pratt, S., Soltz, R. & Wiedemann, U. *Annu. Rev. Nucl. Part. Sci.* **55**, 357–402 (2005).

7. 7.

Adamczewski-Musch, J. *et al. Phys. Rev. C* **94**, 025201 (2016).

8. 8.

Acharya, S. *et al. Phys. Rev. C* **99**, 024001 (2019).

9. 9.

Sasaki, K. *et al. Nucl. Phys. A* **998**, 121737 (2020).

10. 10.

Iritani, T. *et al. Phys. Lett. B* **792**, 284–289 (2019).

Jobs from Nature Careers

- - - [All jobs](#)
 -
 - [Perinatal Pathologist](#)

[University of California, San Diego \(UC San Diego\)](#)

[La Jolla, CA, United States](#)

[JOB POST](#)

- **Chief Science and Innovation Officer**

National Geographic Society

Washington, United States

JOB POST

- **Postdoctoral Fellow**

University of Maryland, Baltimore (UMB)

Baltimore, MD, USA, MD, United States

JOB POST

- **POSTDOCTORAL SCIENTIST Institute for Experimental Pediatric Endocrinology**

Charité - University Medicine Berlin

Berlin, Germany

JOB POST

This article was downloaded by **calibre** from <https://www.nature.com/articles/d41586-020-03393-z>

NEWS AND VIEWS

18 November 2020

Cracking the cell access code for the deadly virus VEEV

The discovery that the receptor protein LDLRAD3 is essential for infection of human cells by Venezuelan equine encephalitis virus could inform strategies to combat this potentially lethal infection.

James Zengel &

James Zengel is in the Department of Microbiology and Immunology, Stanford University School of Medicine, Stanford, California 94305, USA.

Search for this author in:

- [Pub Med](#)
- [Nature.com](#)
- [Google Scholar](#)

Jan E. Carette

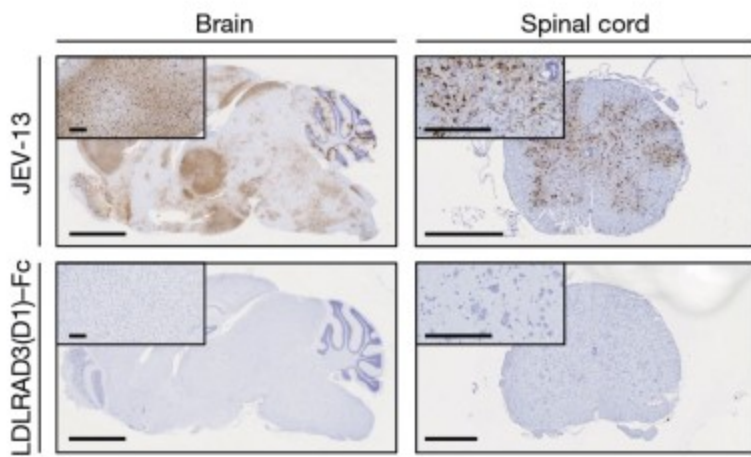
Jan E. Carette is in the Department of Microbiology and Immunology, Stanford University School of Medicine, Stanford, California 94305, USA.
[Contact](#)

Search for this author in:

- [Pub Med](#)
- [Nature.com](#)
- [Google Scholar](#)

When viruses jump from animals to humans, disease outbreaks can follow. A striking example is Venezuelan equine encephalitis virus (VEEV). This virus causes sporadic disease outbreaks in horses in Latin America that frequently spill over into humans, resulting in often-deadly neurological disease¹. Because of its pathogenicity in livestock and humans, VEEV has been studied as a biological weapon by several countries, including the United States². Treatments for the disease are therefore highly desirable. It has been unknown how VEEV co-opts cellular pathways to establish infection in people — in particular, which host receptor protein allows VEEV to cross the cell membrane and initiate its replication cycle. [Writing in Nature](#), Ma *et al.*³ describe the long-sought receptor for VEEV, and show that it is essential for viral replication in both human cells and mouse models.

Interactions between a virus and its host receptor protein can control which tissue types in the body support viral growth, thus influencing the type of disease that results. Furthermore, these interactions can determine how well the virus spreads through a host population. During the continuing SARS-CoV-2 pandemic, for instance, viral strains that had a specific mutation in the virus's spike protein became predominant soon after the virus jumped to humans — this mutation enhances binding between the spike protein and its receptor on human cells, ACE2 (ref. 4)⁴.



Read the paper: LDLRAD3 is a receptor for Venezuelan equine encephalitis virus

Despite the importance of host receptors for understanding infection, their identities for VEEV and other alphaviruses (a category of mainly mosquito-borne RNA viruses) have mostly been elusive . Alphaviruses that infect humans can cause either severe arthritis or — as VEEV does — inflammation of the brain (encephalitis). In 2018, previous work⁵ from some of the authors of the current study uncovered Mxra8 as a mammalian receptor protein for multiple arthritogenic alphaviruses, but not for encephalitis-causing alphaviruses.

Ma *et al.* therefore went in search of the mammalian receptor for VEEV. The authors made use of a gene-editing tool called CRISPR–Cas9 to introduce mutations into more than 20,000 genes in mouse neuronal cells. They then screened the cells to determine which mutations prevented infection by a modified form of VEEV (the version used was less pathogenic than normal, to enable safe experimentation in the laboratory). The screen revealed that *Ldlrad3* was the gene most commonly mutated in infection-resistant cells. Subsequent experiments in a broad range of human and mouse cell types demonstrated that the LDLRAD3 protein is essential for VEEV entry into host cells.

LDLRAD3 is a poorly characterized member of a large group of membrane-bound receptors called the LDL scavenger receptor family. This family is mainly known for its role in bringing lipoprotein particles into the cell in vesicles (a process called endocytosis). Other members of the family have been shown to be co-opted by viruses unrelated to alphaviruses to gain entry into the cell⁶.

Ma and colleagues identified a specific region called domain 1 (D1) in the extracellular portion of LDLRAD3 through which VEEV-like particles directly bind to the receptor (Fig. 1a). But, intriguingly, deletion of the

intracellular domain of LDLRAD3 — which typically mediates endocytosis in this receptor family — did not prevent VEEV entry. This could mean that binding of VEEV to LDLRAD3 triggers fusion of the viral and cell membranes, resulting in direct release of viral RNA into the cell. Alternatively, LDLRAD3 might mainly mediate virus binding, with another, unknown factor controlling endocytosis. Future studies are needed to distinguish between these possibilities.

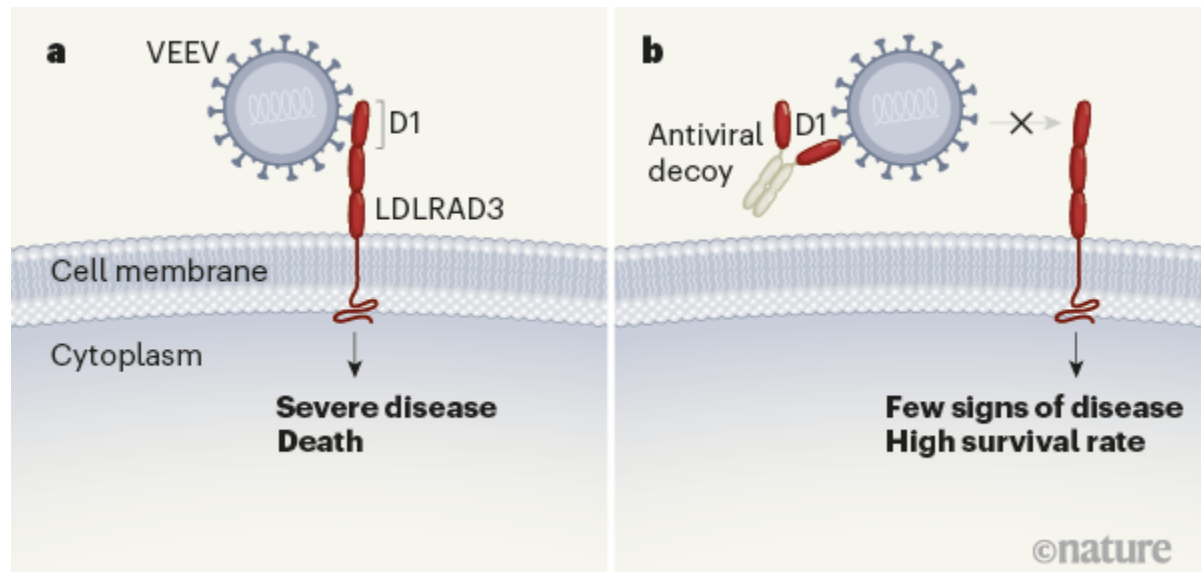


Figure 1 | Preventing infection by Venezuelan equine encephalitis virus (VEEV) in mice. **a**, Ma *et al.*³ report that LDLRAD3 is the mammalian receptor protein for VEEV. Entry of VEEV into cells is mediated by binding to LDLRAD3’s domain 1 (D1). VEEV infection in mice causes severe disease and death in all cases. **b**, The authors fused D1 to part of an antibody. This construct acts as an antiviral decoy, binding to VEEV and so preventing it from interacting with LDLRAD3. The decoy treatment protected mice from VEEV infection — the animals showed few signs of disease and had a much higher survival rate than did untreated animals.

Finally, the authors investigated whether modulating LDLRAD3 could protect mice from VEEV infection. Strikingly, deletion of *Ldlrad3* completely protected the animals from otherwise-lethal infection with highly pathogenic VEEV strains (Fig. 1b). The authors gave wild-type mice a soluble form of LDLRAD3 in which D1 of the receptor was fused to part of an antibody. The construct binds to VEEV, preventing interactions with

LDLRAD3 on cells. Administration of the soluble construct before or after infection with VEEV led to near-complete protection in wild-type mice.

A key question is whether LDLRAD3 mainly mediates infection in the brain, where it causes encephalitis, or whether it also takes part in VEEV infection in the different cell types involved in spreading the virus through the body after an initial mosquito bite. The broad expression pattern of LDLRAD3 in many tissues suggests that the protein has roles in viral spread throughout the body. Indeed, the authors show that soluble LDLRAD3 almost totally blocked virus replication in several tissues that are involved in such spread, including the blood serum, spleen and brain.

In the future, deletion of *Ldlrad3* in specific mouse tissues could help to reveal more about how VEEV spreads and causes disease. By abolishing infection in chosen tissues in this way, one could rigorously test various unknown aspects of disease progression. Are blood cells (specifically, a type called myeloid cells) key in initiating viral spread and fuelling viral infection in the blood after a mosquito bite? Does VEEV reach the central nervous system through the peripheral nervous system, or more directly by crossing the blood–brain barrier⁷? And do these steps require LDLRAD3?

LDLRAD3 mediates cell entry of VEEV, but Ma and colleagues found that it does not control entry of related encephalitic alphaviruses such as Western and Eastern equine encephalitis viruses. This is somewhat unexpected, given the strong similarities in structure⁸ and pathogenesis between the three. An intriguing possibility is that other members of the LDL scavenger receptor family act as receptors for distinct encephalitic alphaviruses. Further structural studies defining the LDLRAD3–VEEV interface will provide clues to why this interaction is seemingly so specific.

What are the therapeutic implications of Ma and colleagues' work? Precise characterization of the LDLRAD3-binding site on VEEV could aid the development of highly neutralizing antibodies that block the VEEV–LDLRAD3 interaction. A similar antibody therapy that prevents interactions between the Ebola virus and its human receptor protein NPC1 has shown success, reducing the mortality from Ebola^{9,10}. Another strategy is to use soluble LDLRAD3 as an antiviral decoy. The authors have

provided strong proof of principle in mice that this might work, although further optimization to enhance the binding affinity and half-life of soluble LDLRAD3 *in vivo* might be required, equivalent to developing engineered ACE2 that has a greatly enhanced potency in blocking SARS-CoV-2 infection¹¹. The discovery of LDLRAD3 has therefore revealed a range of ways in which we might, in the future, combat severe VEEV disease.

Nature **588**, 223-224 (2020)

doi: <https://doi.org/10.1038/d41586-020-03192-6>

References

1. 1.

Weaver, S. C., Ferro, C., Barrera, R., Boshell, J. & Navarro, J.-C. *Annu. Rev. Entomol.* **49**, 141–174 (2004).

2. 2.

Bronze, M. S., Huycke, M. M., Machado, L. J., Voskuhl, G. W. & Greenfield, R. A. *Am. J. Med. Sci.* **323**, 316–325 (2002).

3. 3.

Ma, H. *et al.* Nature **588**, 308–314 (2020).

4. 4.

Yurkovetskiy, L. *et al.* Cell **183**, 739–751 (2020).

5. 5.

Zhang, R. *et al.* Nature **557**, 570–574 (2018).

6. 6.

Hofer, F. *et al.* Proc. Natl Acad. Sci. USA **91**, 1839–1842 (1994).

7. 7.

Charles, P. C., Walters, E., Margolis, F. & Johnston, R. E. *Virology* **208**, 662–671 (1995).

8. 8.

Hasan, S. S. *et al.* *Cell Rep.* **25**, 3136–3147 (2018).

9. 9.

Mulangu, S. *et al.* *N. Engl. J. Med.* **381**, 2293–2303 (2019).

10. 10.

Misasi, J. *et al.* *Science* **351**, 1343–1346 (2016).

11. 11.

Chan, K. K. *et al.* *Science* **369**, 1261–1265 (2020).

Jobs from Nature Careers

- - - [All jobs](#)
 - - [Perinatal Pathologist](#)
 - [University of California, San Diego \(UC San Diego\)](#)
 - [La Jolla, CA, United States](#)
 - [JOB POST](#)
 - [Chief Science and Innovation Officer](#)

National Geographic Society

Washington, United States

JOB POST

▪ **Postdoctoral Fellow**

University of Maryland, Baltimore (UMB)

Baltimore, MD, USA, MD, United States

JOB POST

▪ **POSTDOCTORAL SCIENTIST Institute for Experimental Pediatric Endocrinology**

Charité - University Medicine Berlin

Berlin, Germany

JOB POST

This article was downloaded by **calibre** from <https://www.nature.com/articles/d41586-020-03192-6>

NEWS AND VIEWS

09 December 2020

Trade-offs for equitable climate policy assessed

Computational models show that regionally varied prices for carbon emissions can greatly reduce the need for poor countries to receive financial assistance to tackle climate change, while still stabilizing global warming.

Wei Peng

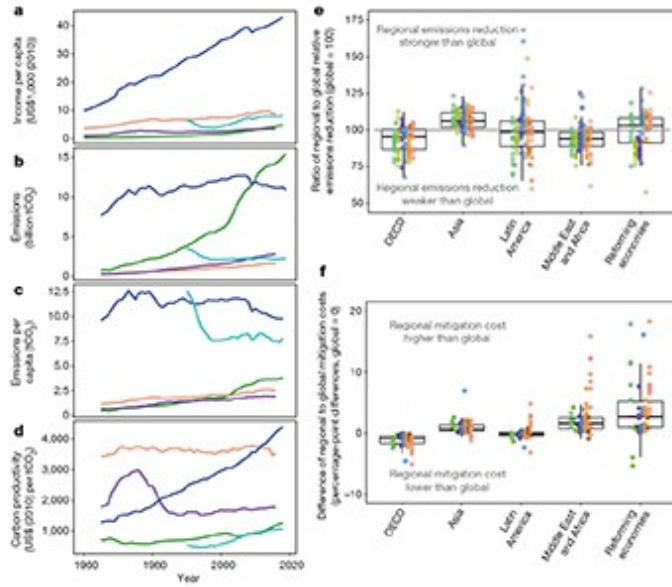
Wei Peng is in the School of International Affairs and the Department of Civil and Environmental Engineering, Pennsylvania State University, University Park, Pennsylvania 16802, USA.

[Contact](#)

Search for this author in:

- [Pub Med](#)
- [Nature.com](#)
- [Google Scholar](#)

International agreements for tackling climate change face many challenges. One of the knottiest is how to allocate mitigation efforts fairly across nations, without increasing the overall global cost, and without asking poor countries to accept large amounts of financial assistance that raise concerns about infringements of national sovereignty. [Writing in Nature](#), Bauer *et al.*¹ report an analysis of the trade-off between cost and sovereignty for various international climate policies. They conclude that sovereignty concerns can be allayed substantially with only slightly higher global costs by using a strategy in which the carbon price — the charge per tonne of carbon dioxide emissions — is varied modestly to account for each country's ability to pay.



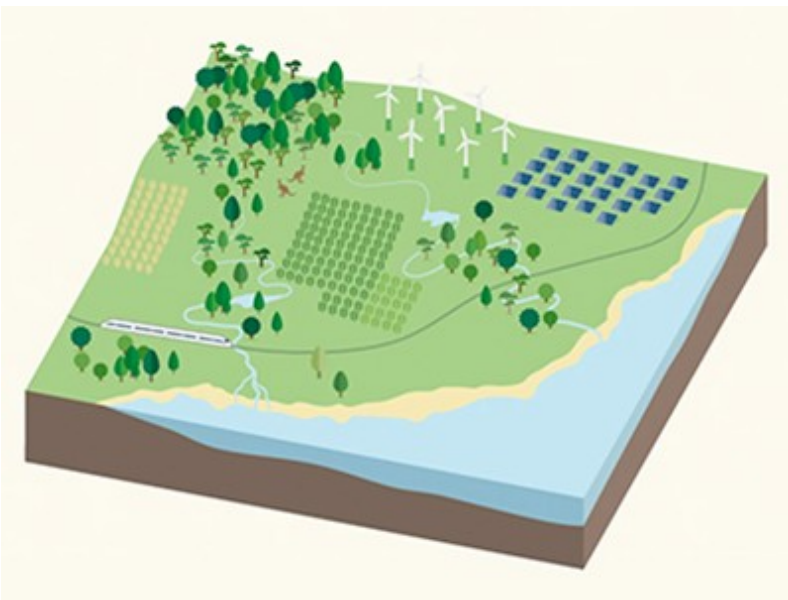
Read the paper: Quantification of an efficiency–sovereignty trade-off in climate policy

After decades of gridlock in climate diplomacy, the 2015 Paris agreement received support from nearly 200 countries for the collective goal of limiting global warming by the end of this century to well below 2 °C above pre-industrial levels. The key to its success was that it provided much-needed flexibility for countries to make their own nationally determined contributions to reducing greenhouse-gas emissions, instead of setting targets through a centralized treaty, as was the case for the 1997 Kyoto Protocol (go.nature.com/3oa6uvl).

By allowing countries to tailor commitments to what can realistically be delivered, the Paris approach reflects the United Nations' equity principle of 'common but differentiated responsibilities and respective capabilities'. It also reduces the need for financial transfer — the provision of money for poor countries to help them tackle climate change and to compensate for the negative economic consequences of mitigating global warming. Reducing this need is politically beneficial for poor countries because they sometimes

perceive a heavy reliance on international financial transfer as undermining their national sovereignty. However, the Paris approach could be more expensive overall than the idealized strategy in which all countries pay a uniform carbon price, because emissions might not be reduced in the places in which it is cheapest to do this. The benefits of the Paris approach for feasibility, equity and sovereignty therefore come at the cost of economic inefficiencies.

Bauer *et al.* quantify the trade-offs between the global cost of climate mitigation (low cost equates to high economic efficiency) and the amount of international financial transfer needed (a proxy for concerns about sovereignty), to find a balance that would enable the 2 °C goal to be achieved with equitable effort-sharing — ensuring the same ratio of mitigation cost to income for all countries. The authors started by analysing two extreme policies. The first involves setting a globally uniform carbon price. This is the cheapest mitigation strategy overall, but requires large international transfer to ensure fair effort-sharing. The second policy is to have widely variable carbon prices across regions to ensure fair effort-sharing. This avoids transfers, but is less economically efficient globally.



Australia at the crossroads

The authors then explored a series of hybrid scenarios in between these two extremes, changing the degree of variation in regional carbon prices and calculating the international transfer required to achieve fair effort-sharing in each case. By combining and comparing these scenarios, the authors plot a curve that depicts the trade-off between global cost and financial transfers (see Fig. 3a of the paper¹).

Bauer *et al.* show that small deviations from a globally uniform carbon price can achieve the 2 °C goal with slightly higher mitigation costs, but much lower transfers. For instance, a modest regional variation in carbon prices with a standard deviation of US\$14 per tonne in 2030 leads to a negligible increase in global mitigation costs, but an 18% reduction in required transfers. This implies that it is highly possible to deliver reasonably good outcomes for equity, economic efficiency and sovereignty, if policymakers are willing to deviate modestly from the economically most efficient strategy (a uniform carbon price).

The authors' findings highlight an advantage of the Paris approach: an equitable outcome can still be achieved when international transfers are reduced. At the 2009 United Nations Climate Change Conference, wealthy countries pledged \$100 billion a year by 2020 to help developing countries tackle climate change. But the total amount collected from public and private sources in 2018 was less than \$80 billion (go.nature.com/39gnts7). US President Donald Trump's decision to withdraw \$2 billion that had been promised to the Green Climate Fund — the largest international fund for financing efforts to mitigate and adapt to climate change (Fig. 1) — contributed to the shortfall. These realities demonstrate the uncertainties in mobilizing large-scale international transfer. By reducing the need for transfer, the Paris approach creates a more collaborative space for engaging both developed and developing countries in climate diplomacy.



Figure 1 | Panel inspection at the Sumber Solar Plant in Mongolia. The construction of this solar plant was supported by the Green Climate Fund, the largest international fund for financing efforts to tackle global warming. However, a heavy reliance on such support is sometimes seen by poor countries as an infringement of their national sovereignty. Bauer *et al.*¹ report an analysis of climate policies that suggests a way to reduce the need for financial support. Credit: GCF/Angeli Mendoza

Bauer and colleagues also point out plausible unintended consequences of the Paris approach for environmental sustainability. If the variation in carbon price across countries is large and the 2 °C target remains the global objective, then developing countries might make only limited efforts to tackle climate change. This could push developed countries to adopt costly options, such as using a technology called bioenergy with carbon capture and storage (BECCS). The authors find that, in this scenario, countries that do not belong to the Organisation for Economic Co-operation and

Development (OECD) will export bioenergy to OECD countries for use in BECCS — exacerbating deforestation and land-use intensification in the global south. The negative effects of BECCS on sustainability have received wide attention², but Bauer and co-workers' study emphasizes that these effects could worsen under the Paris approach, if mitigation efforts shift across countries.

The authors' assessment is based on the REMIND-MAgPIE computational model, which is one of the 'integrated assessment models' (IAMs) used by the Intergovernmental Panel on Climate Change to explore how different policy and technology pathways might affect global emissions and future climate^{3,4}. Such models include representations of economic, energy and land systems, as well as the interactions between them. IAMs have been important analytical tools for designing climate policies⁵, but Bauer and colleagues' study is exemplary in that an IAM is used to evaluate competing considerations faced by climate policymakers.

The new findings are a useful contribution to the high-level debate about the modes and objectives of climate policy, but crucial aspects of the modelling framework lack the granularity needed to inform real-world decision-making. For instance, the model considers just 12 world regions, whereas climate decisions are often made at national and subnational levels. Bauer *et al.* also use carbon prices as a proxy for climate policy, whereas policymakers need to choose from a range of low-carbon policies that vary in cost and feasibility.

Furthermore, countries decide their own carbon prices in the real world, whereas regional carbon prices are not allowed to vary independently in Bauer and colleagues' model. Instead, the authors use a rescaling method to adjust the whole set of regional carbon prices, to make computation easier. Finally, international transfer is modelled as the total financial flow from rich to poor countries, without taking into account specific financing mechanisms. However, a wide range of financing mechanisms exist, such as grants, subsidized loans and private finance, which involve different actors and terms. These limitations do not overshadow the value of the new work, but future efforts should engage model developers and users to bring IAMs closer to real-world problems.

Nature **588**, 225–226 (2020)

doi: <https://doi.org/10.1038/d41586-020-03392-0>

References

1. 1.

Bauer, N. *et al.* *Nature* **588**, 261–266 (2020).

2. 2.

Heck, V., Gerten, D., Lucht, W. & Popp, A. *Nature Clim. Change* **8**, 151–155 (2018).

3. 3.

Clarke, L. *et al.* in *Climate Change 2014: Mitigation of Climate Change. Contribution of Working Group III to the Fifth Assessment Report of the Intergovernmental Panel on Climate Change* (eds Edenhofer, O. *et al.*) Ch. 6, 413–510 (Cambridge Univ. Press, 2014).

4. 4.

Hoegh-Guldberg, O. *et al.* in *Global Warming of 1.5°C* (eds Masson-Delmotte, V. *et al.*) Ch. 3, 175–311 (IPCC, 2018).

5. 5.

van Beek, L., Hajer, M., Pelzer, P., van Vuuren, D. & Cassen, C. *Glob. Environ. Change* **65**, 102191 (2020).

Jobs from Nature Careers

- - - [All jobs](#)
 -

- **Perinatal Pathologist**

University of California, San Diego (UC San Diego)

La Jolla, CA, United States

JOB POST

- **Chief Science and Innovation Officer**

National Geographic Society

Washington, United States

JOB POST

- **Postdoctoral Fellow**

University of Maryland, Baltimore (UMB)

Baltimore, MD, USA, MD, United States

JOB POST

- **POSTDOCTORAL SCIENTIST Institute for Experimental Pediatric Endocrinology**

Charité - University Medicine Berlin

Berlin, Germany

JOB POST

- Article
- [Published: 09 December 2020](#)

Detection of large-scale X-ray bubbles in the Milky Way halo

- [P. Predehl](#) [ORCID: orcid.org/0000-0002-2708-5097](#)¹,
- [R. A. Sunyaev](#) ^{2,3},
- [W. Becker](#) [ORCID: orcid.org/0000-0003-1173-6964](#)^{1,4},
- [H. Brunner](#)¹,
- [R. Burenin](#)²,
- [A. Bykov](#)⁵,
- [A. Cherepashchuk](#)⁶,
- [N. Chugai](#)⁷,
- [E. Churazov](#) ^{2,3},
- [V. Doroshenko](#) [ORCID: orcid.org/0000-0001-8162-1105](#)⁸,
- [N. Eismont](#)²,
- [M. Freyberg](#)¹,
- [M. Gilfanov](#) ^{2,3},
- [F. Haberl](#) [ORCID: orcid.org/0000-0002-0107-5237](#)¹,
- [I. Khabibullin](#)^{2,3},
- [R. Krivonos](#)²,
- [C. Maitra](#)¹,
- [P. Medvedev](#)²,
- [A. Merloni](#) [ORCID: orcid.org/0000-0002-0761-0130](#)¹,
- [K. Nandra](#) [ORCID: orcid.org/0000-0002-7150-9192](#)¹,
- [V. Nazarov](#)²,
- [M. Pavlinsky](#)^{2 na1},
- [G. Ponti](#) [ORCID: orcid.org/0000-0003-0293-3608](#)^{1,9},
- [J. S. Sanders](#) [ORCID: orcid.org/0000-0003-2189-4501](#)¹,

- [M. Sasaki¹⁰](#),
- [S. Sazonov²](#),
- [A. W. Strong¹](#) &
- [J. Wilms](#) ORCID: orcid.org/0000-0003-2065-5410¹⁰

[Nature](#) volume **588**, pages227–231(2020)[Cite this article](#)

- 188 Altmetric
- [Metrics details](#)

Subjects

- [Astronomical instrumentation](#)
- [Galaxies and clusters](#)

Abstract

The halo of the Milky Way provides a laboratory to study the properties of the shocked hot gas that is predicted by models of galaxy formation. There is observational evidence of energy injection into the halo from past activity in the nucleus of the Milky Way^{1,2,3,4}; however, the origin of this energy (star formation or supermassive-black-hole activity) is uncertain, and the causal connection between nuclear structures and large-scale features has not been established unequivocally. Here we report soft-X-ray-emitting bubbles that extend approximately 14 kiloparsecs above and below the Galactic centre and include a structure in the southern sky analogous to the North Polar Spur. The sharp boundaries of these bubbles trace collisionless and non-radiative shocks, and corroborate the idea that the bubbles are not a remnant of a local supernova⁵ but part of a vast Galaxy-scale structure closely related to features seen in γ -rays⁶. Large energy injections from the Galactic centre⁷ are the most likely cause of both the γ -ray and X-ray bubbles. The latter have an estimated energy of around 10^{56} erg, which is sufficient to perturb the structure, energy content and chemical enrichment of the circumgalactic medium of the Milky Way.

[Access through your institution](#)
[Change institution](#)
[Buy or subscribe](#)

Access options

Subscribe to Journal

Get full journal access for 1 year

185,98 €

only 3,58 € per issue

[Subscribe](#)

All prices are NET prices.
VAT will be added later in the checkout.

Rent or Buy article

Get time limited or full article access on ReadCube.

from \$8.99

[Rent or Buy](#)

All prices are NET prices.

Additional access options:

- [Log in](#)
- [Access through your institution](#)
- [Learn about institutional subscriptions](#)

Fig. 1: The Spektr-RG–eROSITA all-sky map.



Fig. 2: The soft-X-ray eROSITA bubbles.



Fig. 3: Comparison of the morphology of the γ -ray and X-ray bubbles.

Data availability

The datasets analysed during this study are not yet publicly available. Their proprietary scientific exploitation rights were granted by the project funding agencies (Roscosmos and DLR) to two consortia led by MPE (Germany)

and IKI (Russia), respectively. The SRG–eROSITA all-sky survey data will be released publicly after a minimum period of 2 years.

References

1. 1.

Su, M., Slatyer, T. R. & Finkbeiner, D. P. Giant gamma-ray bubbles from Fermi-LAT: active galactic nucleus activity or bipolar Galactic wind? *Astrophys. J.* **724**, 1044–1082 (2010).

[ADS](#) [Article](#) [Google Scholar](#)

2. 2.

Ackermann, M. et al. The spectrum and morphology of the Fermi bubbles. *Astrophys. J.* **793**, 64 (2014).

[ADS](#) [Article](#) [Google Scholar](#)

3. 3.

Heywood, I. et al. Inflation of 430-parsec bipolar radio bubbles in the Galactic centre by an energetic event. *Nature* **573**, 235–237 (2019).

[ADS](#) [CAS](#) [Article](#) [Google Scholar](#)

4. 4.

Ponti, G. et al. An X-ray chimney extending hundreds of parsecs above and below the Galactic centre. *Nature* **567**, 347–350 (2019).

[ADS](#) [CAS](#) [Article](#) [Google Scholar](#)

5. 5.

Egger, R. & Aschenbach, B. Interaction of the Loop I supershell with the local hot bubble. *Astron. Astrophys.* **294**, L25–L28 (1995).

[ADS](#) [Article](#) [Google Scholar](#)

6. 6.

Sofue, Y. Bipolar hypershell Galactic center starburst model: further evidence from ROSAT data and new radio and X-ray simulations. *Astrophys. J.* **540**, 224–235 (2000).

[ADS](#) [Article](#) [Google Scholar](#)

7. 7.

Kataoka, J. et al. X-ray and gamma-ray observations of the Fermi bubbles and NPS/Loop I structures. *Galaxies* **6**, 27 (2018).

[ADS](#) [Article](#) [Google Scholar](#)

8. 8.

Merloni, A. et al. eROSITA science book: mapping the structure of the energetic Universe. Preprint at <https://arxiv.org/abs/1209.3114> (2012).

9. 9.

Gaia Collaboration. *Gaia* data release 2. Summary of the contents and survey properties. *Astron. Astrophys.* **616**, A1 (2018).

[Article](#) [Google Scholar](#)

10. 10.

Eisenhardt, P. R. M. et al. The CatWISE preliminary catalog: motions from WISE and NEOWISE data. *Astrophys. J. Suppl. Ser.* **247**, 69 (2020).

[ADS](#) [Article](#) [Google Scholar](#)

11. 11.

Berkhuijsen, E. M. A survey of the continuum radiation at 820 MHz between declinations -7° and $+85^\circ$. A study of the Galactic radiation and the degree of polarization with special reference to the loops and spurs. *Astron. Astrophys.* **14**, 359–386 (1971).

[ADS](#) [Google Scholar](#)

12. 12.

Zubovas, K., King, A. R. & Nayakshin, S. The Milky Way's Fermi bubbles: echoes of the last quasar outburst? *Mon. Not. R. Astron. Soc.* **415**, L21–L25 (2011).

[ADS](#) [Article](#) [Google Scholar](#)

13. 13.

Guo, F. & Mathews, W. G. The Fermi bubbles. I. Possible evidence for recent AGN jet activity in the galaxy. *Astrophys. J.* **756**, 181 (2012).

[ADS](#) [Article](#) [Google Scholar](#)

14. 14.

Mou, G. et al. Fermi bubbles inflated by winds launched from the hot accretion flow in Sgr A*. *Astrophys. J.* **790**, 109 (2014).

[ADS](#) [Article](#) [Google Scholar](#)

15. 15.

Zhang, R. & Guo, F. Simulating the Fermi bubbles as forward shocks driven by AGN jets. *Astrophys. J.* **894**, 117 (2020).

[ADS](#) [CAS](#) [Article](#) [Google Scholar](#)

16. 16.

Crocker, R. M. & Aharonian, F. Fermi bubbles: giant, multibillion-year-old reservoirs of Galactic center cosmic rays. *Phys. Rev. Lett.* **106**, 101102 (2011).

[ADS](#) [Article](#) [Google Scholar](#)

17. 17.

Lacki, B. C. The Fermi bubbles as starburst wind termination shocks. *Mon. Not. R. Astron. Soc.* **444**, L39–L43 (2014).

[ADS](#) [Article](#) [Google Scholar](#)

18. 18.

Crocker, R. M., Bicknell, G. V., Taylor, A. M. & Carretti, E. A unified model of the Fermi bubbles, microwave haze, and polarized radio lobes: reverse shocks in the Galactic center’s giant outflows. *Astrophys. J.* **808**, 107 (2015).

[ADS](#) [Article](#) [Google Scholar](#)

19. 19.

Miller, M. J. & Bregman, J. N. The Interaction of the Fermi Bubbles with the Milky Way’s Hot Gas Halo. *Astrophys. J.* **829**, 9 (2016).

[ADS](#) [Article](#) [Google Scholar](#)

20. 20.

Sofue, Y. Propagation of magnetohydrodynamic waves from the Galactic center. Origin of the 3-kpc arm and the North Polar Spur. *Astron. Astrophys.* **60**, 327–336 (1977).

[ADS](#) [Google Scholar](#)

21. 21.

Lallement, R. et al. On the distance to the North Polar Spur and the local CO-H₂ factor. *Astron. Astrophys.* **595**, A131 (2016).

[Article](#) [Google Scholar](#)

22. 22.

Bland-Hawthorn, J. & Cohen, M. The large-scale bipolar wind in the Galactic center. *Astrophys. J.* **582**, 246–256 (2003).

[ADS](#) [Article](#) [Google Scholar](#)

23. 23.

Nakahira, S. et al. MAXI/SSC all-sky maps from 0.7 keV to 4 keV. *Publ. Astron. Soc. Japan* **72**, 17 (2020).

[ADS](#) [CAS](#) [Article](#) [Google Scholar](#)

24. 24.

Bland-Hawthorn, J. & Gerhard, O. The galaxy in context: structural, kinematic, and integrated properties. *Annu. Rev. Astron. Astrophys.* **54**, 529–596 (2016).

[ADS](#) [CAS](#) [Article](#) [Google Scholar](#)

25. 25.

Casandjian, J.-M. The Fermi-LAT model of interstellar emission for standard point source analysis. Preprint at <https://arxiv.org/abs/1502.07210> (2015).

26. 26.

Carretti, E. et al. Giant magnetized outflows from the centre of the Milky Way. *Nature* **493**, 66–69 (2013).

[ADS](#) [Article](#) [Google Scholar](#)

27. 27.

Böhringer, H. et al. A *ROSAT* HRI study of the interaction of the X-ray emitting gas and radio lobes of NGC 1275. *Mon. Not. R. Astron. Soc.* **264**, L25–L28 (1993).

[ADS](#) [Article](#) [Google Scholar](#)

28. 28.

Kraft, R. et al. X-ray emission from the hot interstellar medium and southwest radio lobe of the nearby radio galaxy Centaurus A. *Astrophys. J.* **592**, 129–146 (2003).

[ADS](#) [Article](#) [Google Scholar](#)

29. 29.

Churazov, E. et al. Asymmetric, arc minute scale structures around NGC 1275. *Astron. Astrophys.* **356**, 788–794 (2000).

[ADS](#) [Article](#) [Google Scholar](#)

30. 30.

Fabian, A. C. et al. Chandra imaging of the complex X-ray core of the Perseus cluster. *Mon. Not. R. Astron. Soc.* **318**, L65–L68 (2000).

[ADS](#) [Article](#) [Google Scholar](#)

31. 31.

Strickland, D. K. & Stevens, I. R. Starburst-driven galactic winds – I. Energetics and intrinsic X-ray emission. *Mon. Not. R. Astron. Soc.* **314**, 511–545 (2000).

[ADS](#) [Article](#) [Google Scholar](#)

32. 32.

Rieke, G. H. et al. The nature of the nuclear sources in M82 and NGC 253. *Astrophys. J.* **238**, 24–40 (1980).

[ADS](#) [CAS](#) [Article](#) [Google Scholar](#)

33. 33.

Tumlinson, J., Peebles, M. S. & Werk, J. K. The circumgalactic medium. *Annu. Rev. Astron. Astrophys.* **55**, 389–432 (2017).

[ADS](#) [Article](#) [Google Scholar](#)

34. 34.

Sanders, J. et al. Annotated version of the eROSITA first all-sky image. <http://www.mpe.mpg.de/7461950/erass1-presskit> (2020).

35. 35.

Selig, M., Vacca, V., Oppermann, N. & Enßlin, T. A. The denoised, deconvolved, and decomposed *Fermi* γ-ray sky. An application of the D³PO algorithm. *Astron. Astrophys.* **581**, 126 (2015).

[ADS](#) [Article](#) [Google Scholar](#)

36. 36.

Predehl, M. et al. The eROSITA X-ray telescope on SRG. *Astron. Astrophys.* <https://doi.org/10.1051/0004-6361/202039313> (2020).

37. 37.

Kataoka, J. et al. *Suzaku* observations of the diffuse X-ray emission across the Fermi bubbles’ edges. *Astrophys. J.* **779**, 57 (2013).

[ADS](#) [Article](#) [Google Scholar](#)

38. 38.

Ursino, E., Galeazzi, M. & Liu, W. Studying the Interstellar medium and the inner region of NPS/LOOP 1 with shadow observations toward MBM36. *Astrophys. J.* **816**, 33 (2016).

[ADS](#) [Article](#) [Google Scholar](#)

39. 39.

Sutherland, M. S. & Dopita, M. A. Cooling functions for low-density astrophysical plasmas. *Astrophys. J. Suppl. Ser.* **88**, 253–327 (1993).

[ADS](#) [CAS](#) [Article](#) [Google Scholar](#)

[Download references](#)

Acknowledgements

This work is based on data from eROSITA, the primary instrument aboard SRG, a joint Russian–German science mission supported by the Russian Space Agency (Roscosmos), in the interests of the Russian Academy of Sciences, represented by its Space Research Institute (IKI), and the Deutsches Zentrum für Luft- und Raumfahrt (DLR). The SRG spacecraft was built by Lavochkin Association (NPOL) and its subcontractors, and is operated by NPOL with support from IKI and the Max Planck Institute for Extraterrestrial Physics (MPE). The development and construction of the eROSITA X-ray instrument was led by MPE, with contributions from the Dr. Karl Remeis Observatory Bamberg and ECAP (FAU Erlangen-Nuernberg), the University of Hamburg Observatory, the Leibniz Institute for Astrophysics Potsdam (AIP), and the Institute for Astronomy and Astrophysics of the University of Tübingen, with the support of DLR and the Max Planck Society. The Argelander Institute for Astronomy of the University of Bonn and the Ludwig Maximilians Universität Munich also participated in the science preparation for eROSITA. The eROSITA data shown here were processed using the eSASS/NRTA software system developed by the German eROSITA consortium. We thank the entire eROSITA collaboration team, in Germany and Russia, who, over many years, have given fundamental contributions to the development of the

mission, the instrument and the science exploitation of the eROSITA data. SRG–eROSITA data processing and calibration and data analyses were performed by a large number of collaboration members in both the German and Russian teams, who also discussed and approved the scientific results presented here. This research made use of Montage. It is funded by the National Science Foundation under grant number ACI-1440620, and was previously funded by NASA’s Earth Science Technology Office, Computation Technologies Project, under cooperative agreement number NCC5-626 between NASA and the California Institute of Technology. G.P. acknowledges funding from the European Research Council (ERC) under the European Union’s Horizon 2020 research and innovation programme (grant agreement number 865637).

Author information

Author notes

1. Deceased: M. Pavlinsky

Affiliations

1. Max-Planck-Institut für Extraterrestrische Physik, Garching, Germany

P. Predehl, W. Becker, H. Brunner, M. Freyberg, F. Haberl, C. Maitra, A. Merloni, K. Nandra, G. Ponti, J. S. Sanders & A. W. Strong

2. Space Research Institute of the Russian Academy of Sciences, Moscow, Russia

R. A. Sunyaev, R. Burenin, E. Churazov, N. Eismont, M. Gilfanov, I. Khabibullin, R. Krivonos, P. Medvedev, V. Nazarov, M. Pavlinsky & S. Sazonov

3. Max-Planck-Institut für Astrophysik, Garching, Germany

R. A. Sunyaev, E. Churazov, M. Gilfanov & I. Khabibullin

4. Max-Planck-Institut für Radioastronomie, Bonn, Germany

W. Becker

5. Ioffe Institute, St Petersburg, Russia

A. Bykov

6. M. V. Lomonosov Moscow State University, P. K. Sternberg
Astronomical Institute, Moscow, Russia

A. Cherepashchuk

7. Institute of Astronomy, Russian Academy of Sciences, Moscow,
Russia

N. Chugai

8. Institut für Astronomie und Astrophysik, Tübingen, Germany

V. Doroshenko

9. INAF-Osservatorio Astronomico di Brera, Merate, Italy

G. Ponti

10. Dr. Karl-Remeis-Sternwarte Bamberg and Erlangen Centre for
Astroparticle Physics, Universität Erlangen-Nürnberg, Bamberg,
Germany

M. Sasaki & J. Wilms

Authors

1. P. Predehl

[View author publications](#)

You can also search for this author in [PubMed](#) [Google Scholar](#)

2. R. A. Sunyaev

[View author publications](#)

You can also search for this author in [PubMed](#) [Google Scholar](#)

3. W. Becker

[View author publications](#)

You can also search for this author in [PubMed](#) [Google Scholar](#)

4. H. Brunner

[View author publications](#)

You can also search for this author in [PubMed](#) [Google Scholar](#)

5. R. Burenin

[View author publications](#)

You can also search for this author in [PubMed](#) [Google Scholar](#)

6. A. Bykov

[View author publications](#)

You can also search for this author in [PubMed](#) [Google Scholar](#)

7. A. Cherepashchuk

[View author publications](#)

You can also search for this author in [PubMed](#) [Google Scholar](#)

8. N. Chugai

[View author publications](#)

You can also search for this author in [PubMed](#) [Google Scholar](#)

9. E. Churazov

[View author publications](#)

You can also search for this author in [PubMed](#) [Google Scholar](#)

10. V. Doroshenko

[View author publications](#)

You can also search for this author in [PubMed](#) [Google Scholar](#)

11. N. Eismont

[View author publications](#)

You can also search for this author in [PubMed](#) [Google Scholar](#)

12. M. Freyberg

[View author publications](#)

You can also search for this author in [PubMed](#) [Google Scholar](#)

13. M. Gilfanov

[View author publications](#)

You can also search for this author in [PubMed](#) [Google Scholar](#)

14. F. Haberl

[View author publications](#)

You can also search for this author in [PubMed](#) [Google Scholar](#)

15. I. Khabibullin

[View author publications](#)

You can also search for this author in [PubMed](#) [Google Scholar](#)

16. R. Krivonos

[View author publications](#)

You can also search for this author in [PubMed](#) [Google Scholar](#)

17. C. Maitra

[View author publications](#)

You can also search for this author in [PubMed](#) [Google Scholar](#)

18. P. Medvedev

[View author publications](#)

You can also search for this author in [PubMed](#) [Google Scholar](#)

19. A. Merloni

[View author publications](#)

You can also search for this author in [PubMed](#) [Google Scholar](#)

20. K. Nandra

[View author publications](#)

You can also search for this author in [PubMed](#) [Google Scholar](#)

21. V. Nazarov

[View author publications](#)

You can also search for this author in [PubMed](#) [Google Scholar](#)

22. M. Pavlinsky

[View author publications](#)

You can also search for this author in [PubMed](#) [Google Scholar](#)

23. G. Ponti

[View author publications](#)

You can also search for this author in [PubMed](#) [Google Scholar](#)

24. J. S. Sanders

[View author publications](#)

You can also search for this author in [PubMed](#) [Google Scholar](#)

25. M. Sasaki

[View author publications](#)

You can also search for this author in [PubMed](#) [Google Scholar](#)

26. S. Sazonov

[View author publications](#)

You can also search for this author in [PubMed](#) [Google Scholar](#)

27. A. W. Strong

[View author publications](#)

You can also search for this author in [PubMed](#) [Google Scholar](#)

28. J. Wilms

[View author publications](#)

You can also search for this author in [PubMed](#) [Google Scholar](#)

Contributions

H.B., M.F., C.M. and J.S.S. developed software to process the eROSITA data and processed the German proprietary data that resulted in the all-sky maps. E.C., M.G., I.K., and P.M. processed the Russian proprietary data. H.B., E.C., M.G., C.M. and J.S.S. performed the analysis that resulted in Fig. 1. V.D., I.K. and J.S.S. performed the image processing that resulted in Figs. 2, 3 and Extended Data Figs. 1, 2. The majority of the text was written by P.P., W.B., M.F., M.G., E.C., G.P., A.W.S., M.S., H.B. and V.D. V.D. and E.C. worked on Fig. 2; Fig. 3 was created by I.K. and V.D. Extended Data Fig. 1 was prepared by A.M. with the support of an MPE graphic design expert. K.N., A.M. and R.A.S. contributed to writing and editing the manuscript. The above-named authors all contributed to the discussion and interpretation of the results and their implications. The remaining co-authors made important contributions to SRG mission planning and operations, eROSITA data acquisition and analysis, and software development for SRG–eROSITA.

Corresponding authors

Correspondence to [P. Predehl](#) or [R. A. Sunyaev](#) or [E. Churazov](#) or [M. Gilfanov](#) or [A. Merloni](#) or [K. Nandra](#).

Ethics declarations

Competing interests

The authors declare no competing interests.

Additional information

Peer review information *Nature* thanks Jun Kataoka and Roland Crocker for their contribution to the peer review of this work. Peer reviewer reports are available.

Publisher's note Springer Nature remains neutral with regard to jurisdictional claims in published maps and institutional affiliations.

Extended data figures and tables

[Extended Data Fig. 1 Schematic of the eROSITA and Fermi bubbles.](#)

Schematic of the geometry of the eROSITA bubbles (EBs; yellow) and Fermi bubbles (FBs; purple) with respect to the Galaxy and the Solar System. The approximate sizes of these structures, as derived from our analysis, are also marked (green and purple arrows).

[Extended Data Fig. 2 Soft-X-ray data compared to a thick-shell model for the eROSITA bubbles.](#)

Comparison between the thick-shell model (cyan line in Fig. 2) and eROSITA data (0.6–1.0-keV band) in a Lambert zenithal equal-area projection. The model is in red; the data are in cyan. The northern bubble is shown on the left (N); the southern bubble is shown on the right (S). The northern bubble is spherical, with an outer radius of 7 kpc and an inner radius of 5 kpc. It is slightly offset from the vertical above the Galactic

centre. The southern shell is instead an ellipse, slightly elongated in the north–south direction (semi-major axis is 7 kpc; semi-minor axis 4.9 kpc).

Supplementary information

[Peer Review File](#)

Rights and permissions

[Reprints and Permissions](#)

About this article



Check for
updates

Cite this article

Predehl, P., Sunyaev, R.A., Becker, W. *et al.* Detection of large-scale X-ray bubbles in the Milky Way halo. *Nature* **588**, 227–231 (2020).
<https://doi.org/10.1038/s41586-020-2979-0>

[Download citation](#)

- Received: 10 July 2020
- Accepted: 25 September 2020
- Published: 09 December 2020
- Issue Date: 10 December 2020
- DOI: <https://doi.org/10.1038/s41586-020-2979-0>

Comments

By submitting a comment you agree to abide by our [Terms](#) and [Community Guidelines](#). If you find something abusive or that does not comply with our terms or guidelines please flag it as inappropriate.

[Access through your institution](#)

[Change institution](#)

[Buy or subscribe](#)

Associated Content

Nature Astronomy | News & Views

[Activity bubbling up](#)

- Jun Kataoka

This article was downloaded by **calibre** from <https://www.nature.com/articles/s41586-020-2979-0>

| [Section menu](#) | [Main menu](#) |

- Article
- [Published: 09 December 2020](#)

Unveiling the strong interaction among hadrons at the LHC

- [ALICE Collaboration](#)

[Nature](#) volume 588, pages 232–238(2020) [Cite this article](#)

- 136 Altmetric
- [Metrics details](#)

Subjects

- [Experimental nuclear physics](#)
- [Experimental particle physics](#)

Abstract

One of the key challenges for nuclear physics today is to understand from first principles the effective interaction between hadrons with different quark content. First successes have been achieved using techniques that solve the dynamics of quarks and gluons on discrete space-time lattices^{1,2}. Experimentally, the dynamics of the strong interaction have been studied by scattering hadrons off each other. Such scattering experiments are difficult or impossible for unstable hadrons^{3,4,5,6} and so high-quality measurements exist only for hadrons containing up and down quarks⁷. Here we demonstrate that measuring correlations in the momentum space between hadron pairs^{8,9,10,11,12} produced in ultrarelativistic proton–proton collisions at the CERN Large Hadron Collider (LHC) provides a precise method with

which to obtain the missing information on the interaction dynamics between any pair of unstable hadrons. Specifically, we discuss the case of the interaction of baryons containing strange quarks (hyperons). We demonstrate how, using precision measurements of proton–omega baryon correlations, the effect of the strong interaction for this hadron–hadron pair can be studied with precision similar to, and compared with, predictions from lattice calculations^{13,14}. The large number of hyperons identified in proton–proton collisions at the LHC, together with accurate modelling¹⁵ of the small (approximately one femtometre) inter-particle distance and exact predictions for the correlation functions, enables a detailed determination of the short-range part of the nucleon-hyperon interaction.

[Access through your institution](#)

[Change institution](#)

[Buy or subscribe](#)

Access options

Subscribe to Journal

Get full journal access for 1 year

185,98 €

only 3,58 € per issue

[Subscribe](#)

All prices are NET prices.

VAT will be added later in the checkout.

Rent or Buy article

Get time limited or full article access on ReadCube.

from \$8.99

[Rent or Buy](#)

All prices are NET prices.

Additional access options:

- [Log in](#)
- [Access through your institution](#)
- [Learn about institutional subscriptions](#)

Fig. 1: Schematic representation of the correlation method.



Fig. 2: Reconstruction of the Ω^- and $\bar{\Omega}^+$ signals.



Fig. 3: Experimental $p-\Xi^-$ and $p-\Omega^-$ correlation functions.

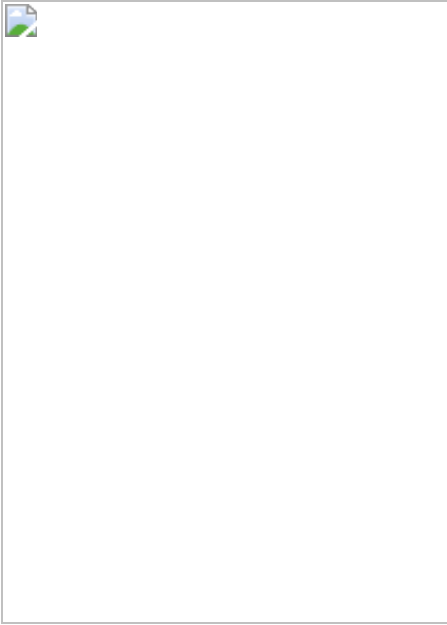
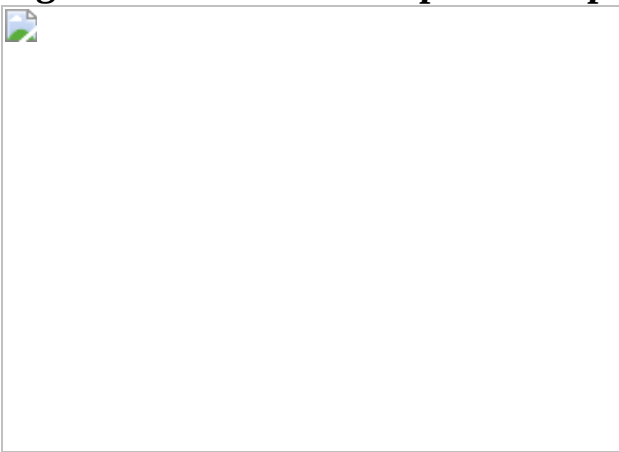


Fig. 4: Potentials for the p - Ξ^- and p - Ω^- interactions.



Data availability

All data shown in histograms and plots are publicly available on the HEPdata repository (<https://hepdata.net>).

Code availability

The source code used in this study is publicly available under the names AliPhysics (<https://github.com/alisw/AliPhysics>) and AliRoot (<https://github.com/alisw/AliROOT>). Further information can be provided by the authors upon reasonable request.

References

1. 1.

NPLQCD Collaboration. Nucleon–nucleon scattering parameters in the limit of SU(3) flavor symmetry. *Phys. Rev. C* **88**, 024003 (2013).

[Google Scholar](#)

2. 2.

Epelbaum, E., Krebs, H., Lee, D. & Meissner, U.-G. Lattice effective field theory calculations for $A = 3, 4, 6, 12$ nuclei. *Phys. Rev. Lett.* **104**, 142501 (2010).

[ADS](#) [PubMed](#) [PubMed Central](#) [Google Scholar](#)

3. 3.

Eisele, F., Filthuth, H., Foehlisch, W., Hepp, V. & Zech, G. Elastic $\Sigma^\pm p$ scattering at low energies. *Phys. Lett. B* **37**, 204–206 (1971).

[ADS](#) [CAS](#) [Google Scholar](#)

4. 4.

Alexander, G. et al. Study of the Λ – N system in low-energy Λ – p elastic scattering. *Phys. Rev.* **173**, 1452–1460 (1968).

[ADS](#) [CAS](#) [Google Scholar](#)

5. 5.

Sechi-Zorn, B., Kehoe, B., Twitty, J. & Burnstein, R. Low-energy Λ –proton elastic scattering. *Phys. Rev.* **175**, 1735–1740 (1968).

[ADS](#) [CAS](#) [Google Scholar](#)

6. 6.

Muller, R. Observation of cascade hyperon interactions. *Phys. Lett. B* **38**, 123–124 (1972).

[ADS](#) [CAS](#) [Google Scholar](#)

7. 7.

Stoks, V. & de Swart, J. Comparison of potential models with the pp scattering data below 350 MeV. *Phys. Rev. C* **47**, 761–767 (1993).

[ADS](#) [CAS](#) [Google Scholar](#)

8. 8.

ALICE Collaboration. p – p , p – Λ and Λ – Λ correlations studied via femtoscopy in pp reactions at $\sqrt{s} = 7$ TeV. *Phys. Rev. C* **99**, 024001 (2019).

[ADS](#) [Google Scholar](#)

9. 9.

ALICE Collaboration. Scattering studies with low-energy kaon–proton femtoscopy in proton–proton collisions at the LHC. *Phys. Rev. Lett.* **124**, 092301 (2020).

[ADS](#) [Google Scholar](#)

10. 10.

ALICE Collaboration. Study of the Λ – Λ interaction with femtoscopy correlations in pp and p – Pb collisions at the LHC. *Phys. Lett. B* **797**, 134822 (2019).

[Google Scholar](#)

11. 11.

ALICE Collaboration. First observation of an attractive interaction between a proton and a cascade baryon. *Phys. Rev. Lett.* **123**, 112002 (2019).

[ADS](#) [Google Scholar](#)

12. 12.

ALICE Collaboration. Investigation of the $p-\Sigma^0$ interaction via femtoscopy in pp collisions. *Phys. Lett. B* **805**, 135419 (2020).

[Google Scholar](#)

13. 13.

HAL QCD Collaboration. $N\Omega$ dibaryon from lattice QCD near the physical point. *Phys. Lett. B* **792**, 284–289 (2019).

[ADS](#) [Google Scholar](#)

14. 14.

Sasaki, K. et al. $\Lambda\Lambda$ and $N\Xi$ interactions from lattice QCD near the physical point. *Nucl. Phys. A* **998**, 121737 (2020).

[CAS](#) [Google Scholar](#)

15. 15.

ALICE Collaboration. Search for a common baryon source in high-multiplicity pp collisions at the LHC. *Phys. Lett. B* **811**, 135849 (2020).

[Google Scholar](#)

16. 16.

Epelbaum, E., Hammer, H.-W. & Meissner, U.-G. Modern theory of nuclear forces. *Rev. Mod. Phys.* **81**, 1773–1825 (2009).

[ADS](#) [CAS](#) [Google Scholar](#)

17. 17.

Hebeler, K., Holt, J., Menendez, J. & Schwenk, A. Nuclear forces and their impact on neutron-rich nuclei and neutron-rich matter. *Annu. Rev. Nucl. Part. Sci.* **65**, 457–484 (2015).

[ADS](#) [CAS](#) [Google Scholar](#)

18. 18.

Gebrerufael, E., Vobig, K., Hergert, H. & Roth, R. Ab initio description of open-shell nuclei: merging no-core shell model and in-medium similarity renormalization group. *Phys. Rev. Lett.* **118**, 152503 (2017).

[ADS](#) [PubMed](#) [PubMed Central](#) [Google Scholar](#)

19. 19.

Klijnsma, T., Bethke, S., Dissertori, G. & Salam, G. P. Determination of the strong coupling constant $\alpha_s(m_Z)$ from measurements of the total cross section for top-antitop quark production. *Eur. Phys. J. C* **77**, 778 (2017).

[ADS](#) [PubMed](#) [PubMed Central](#) [Google Scholar](#)

20. 20.

NPLQCD Collaboration. Two nucleon systems at $m_\pi \sim 450$ MeV from lattice QCD. *Phys. Rev. D* **92**, 114512 (2015).

[ADS](#) [Google Scholar](#)

21. 21.

Wagman, M. L. et al. Baryon–baryon interactions and spin-flavor symmetry from lattice quantum chromodynamics. *Phys. Rev. D* **96**,

114510 (2017).

[ADS](#) [MathSciNet](#) [Google Scholar](#)

22. 22.

Hatsuda, T. Lattice quantum chromodynamics and baryon-baryon interactions. *Front. Phys.* **13**, 132105 (2018).

[ADS](#) [Google Scholar](#)

23. 23.

Hashimoto, O. & Tamura, H. Spectroscopy of Λ hypernuclei. *Prog. Part. Nucl. Phys.* **57**, 564–653 (2006).

[ADS](#) [CAS](#) [Google Scholar](#)

24. 24.

Nakazawa, K. et al. The first evidence of a deeply bound state of $\Xi^- - {}^{14}\text{N}$ system. *Prog. Theor. Exp. Phys.* **2015**, 033D02 (2015).

[ADS](#) [Google Scholar](#)

25. 25.

Nagae, T. et al. Search for a Ξ bound state in the ${}^{12}\text{C}(K^-, K^+)X$ reaction at 1.8 GeV/c. *PoS (INPC2016)* 038 (2017).

26. 26.

Francis, A. et al. Lattice QCD study of the H dibaryon using hexaquark and two-baryon interpolators. *Phys. Rev. D* **99**, 074505, (2019).

[ADS](#) [CAS](#) [Google Scholar](#)

27. 27.

Jaffe, R. L. Perhaps a stable dihyperon. *Phys. Rev. Lett.* **38**, 195–198 (1977); erratum **38**, 617 (1977).

[ADS](#) [CAS](#) [Google Scholar](#)

28. 28.

Nagels, M. M., Rijken, T. A. & de Swart, J. J. Baryon–baryon scattering in a one-boson-exchange-potential approach. II. Hyperon–nucleon scattering. *Phys. Rev. D* **15**, 2547–2564 (1977).

[ADS](#) [CAS](#) [Google Scholar](#)

29. 29.

Nagels, M. M., Rijken, T. A. & de Swart, J. J. Baryon–baryon scattering in a one-boson-exchange-potential approach. III. A nucleon–nucleon and hyperon–nucleon analysis including contributions of a nonet of scalar mesons. *Phys. Rev. D* **20**, 1633–1645 (1979).

[ADS](#) [CAS](#) [Google Scholar](#)

30. 30.

Gongyo, S. et al. Most strange dibaryon from lattice QCD. *Phys. Rev. Lett.* **120**, 212001 (2018).

[ADS](#) [CAS](#) [PubMed](#) [PubMed Central](#) [Google Scholar](#)

31. 31.

ALICE Collaboration. Search for weakly decaying $\overline{\Lambda}\Lambda$ and $\Lambda\Lambda$ exotic bound states in central Pb–Pb collisions at $\sqrt{s_{NN}} = 2.76$ TeV. *Phys. Lett. B* **752**, 267–277 (2016).

[ADS](#) [Google Scholar](#)

32. 32.

Belle Collaboration. Search for an H -dibaryon with mass near $2m_{\Lambda}$ in $\Upsilon(1S)$ and $\Upsilon(2S)$ decays. *Phys. Rev. Lett.* **110**, 222002 (2013).

[Google Scholar](#)

33. 33.

Chrien, R. H particle searches at Brookhaven. *Nucl. Phys. A* **629**, 388–397 (1998).

[ADS](#) [Google Scholar](#)

34. 34.

Yoon, C. et al. Search for the H -dibaryon resonance in ^{12}C (K^- , $K^+\Lambda\Lambda X$). *Phys. Rev. C* **75**, 022201 (2007).

[ADS](#) [Google Scholar](#)

35. 35.

KEK-PS E224 Collaboration. Enhanced $\Lambda\Lambda$ production near threshold in the $^{12}\text{C}(K^-, K^+)$ reaction. *Phys. Lett. B* **444**, 267–272 (1998).

[ADS](#) [Google Scholar](#)

36. 36.

Tolos, L. & Fabbietti, L. Strangeness in nuclei and neutron stars. *Prog. Part. Nucl. Phys.* **112**, 103770 (2020).

[CAS](#) [Google Scholar](#)

37. 37.

HADES Collaboration. The Λp interaction studied via femtoscopy in $p + \text{Nb}$ reactions at $\sqrt{s_{\text{NN}}} = 3.18 \text{ GeV}$. *Phys. Rev. C* **94**, 025201 (2016).

[ADS](#) [Google Scholar](#)

38. 38.

ALICE Collaboration. Enhanced production of multi-strange hadrons in high-multiplicity proton–proton collisions. *Nat. Phys.* **13**, 535–539 (2017).

[Google Scholar](#)

39. 39.

Mihaylov, D. et al. A femtoscopic correlation analysis tool using the Schrödinger equation (CATS). *Eur. Phys. J. C* **78**, 394 (2018).

[ADS](#) [Google Scholar](#)

40. 40.

STAR Collaboration. $\Lambda\Lambda$ correlation function in Au+Au collisions at $\sqrt{s_{NN}} = 200$ GeV. *Phys. Rev. Lett.* **114**, 022301 (2015).

[ADS](#) [Google Scholar](#)

41. 41.

Morita, K., Furumoto, T. & Ohnishi, A. $\Lambda\Lambda$ interaction from relativistic heavy-ion collisions. *Phys. Rev. C* **91**, 024916 (2015).

[ADS](#) [Google Scholar](#)

42. 42.

STAR Collaboration. The proton– Ω correlation function in Au + Au collisions at $\sqrt{s_{NN}} = 200$ GeV. *Phys. Lett. B* **790**, 490–497 (2019).

[ADS](#) [Google Scholar](#)

43. 43.

Pratt, S. Pion interferometry of quark–gluon plasma. *Phys. Rev. D* **33**, 1314–1327 (1986).

[ADS](#) [CAS](#) [Google Scholar](#)

44. 44.

Lisa, M. A., Pratt, S., Soltz, R. & Wiedemann, U. Femtoscopy in relativistic heavy ion collisions. *Annu. Rev. Nucl. Part. Sci.* **55**, 357–402 (2005).

[ADS](#) [CAS](#) [Google Scholar](#)

45. 45.

Haidenbauer, J. & Meißner, U.-G. Phenomenological view on baryon–baryon potentials from lattice QCD simulations. *Eur. Phys. J. A* **55**, 70 (2019).

[ADS](#) [CAS](#) [Google Scholar](#)

46. 46.

Morita, K., Ohnishi, A., Etminan, F. & Hatsuda, T. Probing multistrange dibaryons with proton–omega correlations in high-energy heavy ion collisions. *Phys. Rev. C* **94**, 031901 (2016); erratum **100**, 069902 (2019).

[ADS](#) [Google Scholar](#)

47. 47.

Morita, K. et al. Probing $\Omega\Omega$ and $p\Omega$ dibaryons with femtoscopic correlations in relativistic heavy-ion collisions. *Phys. Rev. C* **101**, 015201 (2020).

[ADS](#) [CAS](#) [Google Scholar](#)

48. 48.

ALICE Collaboration. Upgrade of the ALICE experiment: letter of intent. *J. Phys. G* **41**, 087001 (2014).

[ADS](#) [Google Scholar](#)

49. 49.

Citron, Z. et al. Report from Working Group 5: future physics opportunities for high-density QCD at the LHC with heavy-ion and proton beams. *CERN Yellow Rep. Monogr.* **7**, 1159–1410 (2019).

[Google Scholar](#)

50. 50.

ALICE Collaboration. The ALICE experiment at the CERN LHC. *JINST* **3**, S08002 (2008).

[ADS](#) [Google Scholar](#)

51. 51.

ALICE Collaboration. Performance of the ALICE experiment at the CERN LHC. *Int. J. Mod. Phys. A* **29**, 1430044 (2014).

[ADS](#) [Google Scholar](#)

52. 52.

ALICE Collaboration. Performance of the ALICE VZERO system. *JINST* **8**, P10016 (2013).

[Google Scholar](#)

53. 53.

ALICE Collaboration. Multiplicity dependence of (multi-)strange hadron production in proton-proton collisions at $\sqrt{s} = 13$ TeV. *Eur. Phys. J. C* **80**, 167 (2020).

[ADS](#) [Google Scholar](#)

54. 54.

ALICE Collaboration. Alignment of the ALICE Inner Tracking System with cosmic-ray tracks. *JINST* **5**, P03003 (2010).

[ADS](#) [Google Scholar](#)

55. 55.

Alme, J. et al. The ALICE TPC, a large 3-dimensional tracking device with fast readout for ultra-high multiplicity events. *Nucl. Instrum. Meth. A* **622**, 316–367 (2010).

[ADS](#) [CAS](#) [Google Scholar](#)

56. 56.

Akindinov, A. et al. Performance of the ALICE Time-Of-Flight detector at the LHC. *Eur. Phys. J. Plus* **128**, 44 (2013).

[Google Scholar](#)

57. 57.

Particle Data Group Collaboration. Review of particle physics. *Phys. Rev. D* **98**, 030001 (2018).

[Google Scholar](#)

58. 58.

ALICE Collaboration. Strange particle production in proton–proton collisions at $\sqrt{s} = 0.9$ TeV with ALICE at the LHC. *Eur. Phys. J. C* **71**, 1594 (2011).

[ADS](#) [Google Scholar](#)

59. 59.

Kisiel, A., Zbroszczyk, H. & Szymański, M. Extracting baryon–antibaryon strong-interaction potentials from $\langle p|\bar{\Lambda} \rangle$ femtoscopic correlation functions. *Phys. Rev. C* **89**, 054916 (2014).

[ADS](#) [Google Scholar](#)

[Download references](#)

Acknowledgements

We are grateful to T. Hatsuda and K. Sasaki from the HAL QCD Collaboration for their valuable suggestions and for providing the lattice QCD results regarding the $p-\Xi^-$ and $p-\Omega^-$ interactions. We are also grateful to A. Ohnishi, T. Hyodo, T. Iritani, Y. Kamiya and T. Sekihara for their suggestions and discussions. We thank all the engineers and technicians of the LHC for their contributions to the construction of the experiment and the CERN accelerator teams for the performance of the LHC complex. We acknowledge the resources and support provided by all Grid centres and the Worldwide LHC Computing Grid (WLCG) collaboration. We acknowledge the following funding agencies for their support in building and running the ALICE detector: A. I. Alikhanyan National Science Laboratory (Yerevan Physics Institute) Foundation (ANSL), State Committee of Science and World Federation of Scientists (WFS), Armenia; Austrian Academy of Sciences, Austrian Science Fund (FWF): [M 2467-N36] and Nationalstiftung für Forschung, Technologie und Entwicklung, Austria; Ministry of Communications and High Technologies, National Nuclear Research Center, Azerbaijan; Conselho Nacional de Desenvolvimento Científico e Tecnológico (CNPq), Financiadora de Estudos e Projetos (Finep), Fundação de Amparo à Pesquisa do Estado de São Paulo (FAPESP) and Universidade Federal do Rio Grande do Sul (UFRGS), Brazil; Ministry of Education of China (MOEC), Ministry of Science and Technology of China (MSTC) and National Natural Science Foundation of China (NSFC), China; Ministry of Science and Education and Croatian Science Foundation, Croatia; Centro de Aplicaciones Tecnológicas y Desarrollo Nuclear (CEADEN), Cubaenerga, Cuba; Ministry of Education,

Youth and Sports of the Czech Republic, Czech Republic; The Danish Council for Independent Research | Natural Sciences, the VILLUM FONDEN and Danish National Research Foundation (DNRF), Denmark; Helsinki Institute of Physics (HIP), Finland; Commissariat à l'Energie Atomique (CEA) and Institut National de Physique Nucléaire et de Physique des Particules (IN2P3) and Centre National de la Recherche Scientifique (CNRS), France; Bundesministerium für Bildung und Forschung (BMBF) and GSI Helmholtzzentrum für Schwerionenforschung GmbH, Germany; General Secretariat for Research and Technology, Ministry of Education, Research and Religions, Greece; National Research, Development and Innovation Office, Hungary; Department of Atomic Energy Government of India (DAE), Department of Science and Technology, Government of India (DST), University Grants Commission, Government of India (UGC) and Council of Scientific and Industrial Research (CSIR), India; Indonesian Institute of Science, Indonesia; Centro Fermi – Museo Storico della Fisica e Centro Studi e Ricerche Enrico Fermi and Istituto Nazionale di Fisica Nucleare (INFN), Italy; Institute for Innovative Science and Technology, Nagasaki Institute of Applied Science (IIST), Japanese Ministry of Education, Culture, Sports, Science and Technology (MEXT) and Japan Society for the Promotion of Science (JSPS) KAKENHI, Japan; Consejo Nacional de Ciencia (CONACYT) y Tecnología, through Fondo de Cooperación Internacional en Ciencia y Tecnología (FONCICYT) and Dirección General de Asuntos del Personal Académico (DGAPA), Mexico; Nederlandse Organisatie voor Wetenschappelijk Onderzoek (NWO), Netherlands; The Research Council of Norway, Norway; Commission on Science and Technology for Sustainable Development in the South (COMSATS), Pakistan; Pontificia Universidad Católica del Perú, Peru; Ministry of Science and Higher Education, National Science Centre and WUT ID-UB, Poland; Korea Institute of Science and Technology Information and National Research Foundation of Korea (NRF), Republic of Korea; Ministry of Education and Scientific Research, Institute of Atomic Physics and Ministry of Research and Innovation and Institute of Atomic Physics, Romania; Joint Institute for Nuclear Research (JINR), Ministry of Education and Science of the Russian Federation, National Research Centre Kurchatov Institute, Russian Science Foundation and Russian Foundation for Basic Research, Russia; Ministry of Education, Science, Research and Sport of the Slovak Republic, Slovakia;

National Research Foundation of South Africa, South Africa; Swedish Research Council (VR) and Knut & Alice Wallenberg Foundation (KAW), Sweden; European Organization for Nuclear Research, Switzerland; Suranaree University of Technology (SUT), National Science and Technology Development Agency (NSDTA) and Office of the Higher Education Commission under NRU project of Thailand, Thailand; Turkish Atomic Energy Agency (TAEK), Turkey; National Academy of Sciences of Ukraine, Ukraine; Science and Technology Facilities Council (STFC), United Kingdom; National Science Foundation of the United States of America (NSF) and United States Department of Energy, Office of Nuclear Physics (DOE NP), United States of America.

Author information

Author notes

1. G. Clai

Present address: Italian National Agency for New Technologies, Energy and Sustainable Economic Development (ENEA), Bologna, Italy

2. M. Concas

Present address: Dipartimento DET, Politecnico di Torino, Turin, Italy

3. L. Malinina

Present address: D.V. Skobeltsyn Institute of Nuclear Physics, M.V. Lomonosov Moscow State University, Moscow, Russia

4. M. Mohisin Khan

Present address: Department of Applied Physics, Aligarh Muslim University, Aligarh, India

5. K. Redlich

Present address: Institute of Theoretical Physics, University of Wrocław, Wrocław, Poland

6. Deceased: R. D. Majka

Affiliations

1. Variable Energy Cyclotron Centre, Homi Bhabha National Institute, Kolkata, India

S. Acharya, Z. Ahammed, S. N. Alam, S. Chandra, S. Chattopadhyay, A. K. Dubey, P. Ghosh, S. Muhuri, P. Pareek, S. Sadhu, S. K. Saha, J. Saini, N. Sarkar, V. K. Singh, V. Singhal & S. Thakur

2. Nuclear Physics Institute of the Czech Academy of Sciences, Řež, Czech Republic

D. Adamová, J. Bielčíková, A. Isakov, F. Krizek, S. Kushpil & M. Šumbera

3. Institut für Informatik, Fachbereich Informatik und Mathematik, Johann-Wolfgang-Goethe Universität Frankfurt, Frankfurt am Main, Germany

A. Adler, A. Gomez Ramirez, T. Janson & U. Kebschull

4. Division of Particle Physics, Department of Physics, Lund University, Lund, Sweden

J. Adolfsson, P. Christiansen, O. Matonoha, A. F. Nassirpour, A. Ohlson, A. Oskarsson, T. Richert, O. V. Rueda, D. Silvermyr & E. Stenlund

5. Physics Department, Panjab University, Chandigarh, India

M. M. Aggarwal, S. Dudi, L. Kumar, S. Parmar, A. Sharma & N. Sharma

6. European Organization for Nuclear Research (CERN), Geneva,
Switzerland

G. Aglieri Rinella, A. Alkin, D. Andreou, M. Angeletti, A. Augustinus, K. Barth, F. Bellini, L. Betev, P. Buncic, S. Chapelard, V. Chibante Barroso, P. Chochula, F. Costa, A. Di Mauro, R. Divià, G. Eulisse, A. Festanti, U. Fuchs, C. Gargiulo, C. Grigoras, J. F. Grosse-Oetringhaus, J. A. Hasenbichler, H. Hillemanns, P. Hristov, J. P. Iddon, G. M. Innocenti, N. Jacazio, A. Kalweit, M. Keil, J. Klein, A. Kluge, M. L. Knichel, P. J. Konopka, V. Kučera, M. Lamanna, K. Lapidus, E. Laudi, M. Lettrich, M. Mager, P. Martinengo, N. Mohammadi, A. Morsch, T. Mrnjavac, L. Musa, O. Pinazza, M. Puccio, F. Reidt, P. Riedler, W. Riegler, D. Rohr, R. Shahoyan, G. Simonetti, M. Suljic, A. Tauro, A. Telesca, P. Vande Vyvre, B. Volkel, B. von Haller, A. Wegrzynek, S. C. Wenzel, C. Zampolli & N. Zardoshti

7. Dipartimento DISAT del Politecnico and Sezione INFN, Turin, Italy

M. Agnello, A. Balbino, S. Bufalino, F. Catalano, P. Fecchio & F. Grossa

8. Centro Fermi – Museo Storico della Fisica e Centro Studi e Ricerche
“Enrico Fermi”, Rome, Italy

N. Agrawal, A. Alici, L. Cifarelli, D. De Gruttola, D. Hatzifotiadou, R. Nania, F. Noferini, S. Pisano, J. Wilkinson & A. Zichichi

9. INFN, Sezione di Bologna, Bologna, Italy

N. Agrawal, A. Alici, P. Antonioli, F. Cindolo, G. Clai, D. Hatzifotiadou, N. Jacazio, A. Margotti, R. Nania, F. Noferini, O. Pinazza, R. Preghenella, E. Scapparone & J. Wilkinson

10. Department of Physics, Aligarh Muslim University, Aligarh, India

S. Ahmad, B. Ali, M. D. Azmi, S. Khan, A. Khatun & M. Mohisin Khan

11. Korea Institute of Science and Technology Information, Daejeon,
Republic of Korea

S. U. Ahn

12. Indonesian Institute of Sciences, Jakarta, Indonesia

Z. Akbar & S. Sumowidagdo

13. NRC «Kurchatov» Institute – ITEP, Moscow, Russia

A. Akindinov, S. Kiselev, D. Mal'Kevich, K. Mikhaylov, S.
Shirinkin, R. Sultanov & K. Voloshin

14. Research Division and ExtreMe Matter Institute EMMI, GSI
Helmholtzzentrum für Schwerionenforschung, Darmstadt, Germany

M. Al-Turany, R. Averbeck, X. Bai, P. Braun-Munzinger, A.
Caliva, M. R. Ciupek, A. Dubla, P. Foka, U. Frankenfeld, C.
Garabatos, P. Gasik, P. Giubellino, V. Gonzalez, R. Gross, M. K.
Habib, A. Harlenderova, S. Hornung, M. Ivanov, T. Kollegger, L.
Kreis, C. Lippmann, P. Malzacher, A. Marín, S. Masciocchi, D.
Miśkowiec, C. Schmidt, K. Schwarz, K. Schweda, I.
Selyuzhenkov & J. Zhu

15. Fudan University, Shanghai, China

S. N. Alam, Y. G. Ma, Q. Shou & S. Zhang

16. Universidade Estadual de Campinas (UNICAMP), Campinas, Brazil

D. S. D. Albuquerque, D. D. Chinellato & J. Takahashi

17. National Research Centre Kurchatov Institute, Moscow, Russia

D. Aleksandrov, D. Blau, S. Fokin, M. Ippolitov, A. Kazantsev, V.
Manko, S. Nikolaev, S. Nikulin, A. Nyanin, D. Peresunko, E.
Ryabinkin, Y. Sibiriak, A. Vasiliev & A. Vinogradov

18. INFN, Sezione di Torino, Turin, Italy

B. Alessandro, R. Arnaldi, S. Bagnasco, D. Berzano, E. Bruna, M. Concas, N. De Marco, A. Feliciello, P. Giubellino, F. Gerosa, J. Klein, C. Oppedisano, F. Prino, E. Scomparin & S. Vallero

19. Central China Normal University, Wuhan, China

H. M. Alfanda, M. N. Anaam, P. Bartalini, W. Chang, P. Cui, W. Deng, Y. Ding, F. Fan, M. Hamid, S. Kar, A. M. Khan, X. L. Li, Y. Mao, C. Mengke, H. Pei, X. Peng, X. Ren, S. Tang, R. Xu, Z. Yin, X. Zhang, Z. Zhang, D. Zhou, J. Zhu & Y. Zhu

20. Instituto de Física, Universidad Nacional Autónoma de México,
Mexico City, Mexico

R. Alfaro Molina, L. H. González-Trueba, V. Grabski & A. Menchaca-Rocha

21. COMSATS University Islamabad, Islamabad, Pakistan

Y. Ali, J. B. Butt, Q. U. Hassan, S. A. Hussain, H. Ilyas, M. U. Naru, M. Suleymanov, U. Tabassam & A. Zaman

22. Dipartimento di Fisica e Astronomia dell'Università and Sezione
INFN, Bologna, Italy

A. Alici, S. Arcelli, F. Carnesecchi, L. Cifarelli, M. Colocci, M. Giacalone, G. Scioli & A. Zichichi

23. University of Houston, Houston, TX, USA

N. Alizadehvandchali, R. Bellwied, F. Flor, M. Jin, A. G. Knospe, J. L. Martinez, A. S. Menon, C. J. Myers, S. P. Pathak, L. Pinsky, R. E. Quishpe, O. Sheibani, J. Song, C. Terrevoli, A. R. Timmins & E. N. Umaka

24. Bogolyubov Institute for Theoretical Physics, National Academy of Sciences of Ukraine, Kiev, Ukraine

A. Alkin, V. Trubnikov, V. Yurchenko & G. Zinovjev

25. Department of Physics and Technology, University of Bergen, Bergen, Norway

J. Alme, L. Altenkamper, Ø. Djuvsland, V. N. Eikeland, M. R. Ersdal, F. M. Fionda, O. S. Groettvik, I. M. Lofnes, J. Nystrand, A. Rehman, D. Röhrich, G. J. Tambave, K. Ullaland, B. Wagner, S. Yang, S. Yuan & Z. Zhou

26. Institut für Kernphysik, Johann Wolfgang Goethe-Universität Frankfurt, Frankfurt am Main, Germany

T. Alt, H. Appelhäuser, R. Bailhache, E. Bartsch, C. Blume, L. Bratrud, H. Buesching, P. Dillenseger, B. Dönigus, E. Hellbär, A. Hornung, P. Huhn, J. Jung, M. Jung, S. Kirsch, C. Klein, M. Kleiner, J. Konig, M. Krüger, M. Marquard, A. F. Mechler, R. H. Munzer, R. A. Negrao De Oliveira, F. Pliquet, P. Reichelt, R. Renfordt, H. S. Scheid, N. V. Schmidt, A. Toia & J. Wiechula

27. St. Petersburg State University, St. Petersburg, Russia

I. Altsybeev, A. Erokhin, G. Feofilov, V. Kovalenko, T. Lazareva, D. Nesterov, V. Vechernin, A. Zarochentsev & V. Zhrebchevskii

28. Horia Hulubei National Institute of Physics and Nuclear Engineering, Bucharest, Romania

C. Andrei, A. Bercuci, A. Herghelie, A. Lindner, M. Petrovici, A. Pop, C. Schiaua & M. G. Tarzila

29. Westfälische Wilhelms – Universität Münster, Institut für Kernphysik, Münster, Germany

A. Andronic, A. D. C. Bell Hechavarria, K. Garner, F. Herrmann, J. Honermann, L. A. Husova, F. Jonas, C. Klein-Bösing, J. R. Luhder, D. A. Moreira De Godoy, D. Mühlheim, S. G. Weber, J. P. Wessels & G. A. Willems

30. Physikalisches Institut, Ruprecht-Karls-Universität Heidelberg,
Heidelberg, Germany
- V. Anguelov, M. Arslandok, M. C. Danisch, V. J. G. Feuillard, P.
Glässel, J. Kim, M. Kim, M. K. Köhler, L. Leardini, J. A. Lopez, N. A.
Martin, A. Ohlson, Y. Pachmayer, K. Reygers, R. Schicker, A.
Schmah, M. O. Schmidt, J. Stachel, S. F. Stiefelmaier, B.
Windelband & A. Yuncu
31. Creighton University, Omaha, NB, USA
- C. Anson, R. Hosokawa & J. E. Seger
32. Rudjer Bošković Institute, Zagreb, Croatia
- T. Antičić
33. INFN, Sezione di Padova, Padova, Italy
- F. Antinori, A. Dainese, A. Rossi & R. Turrisi
34. Lawrence Berkeley National Laboratory, Berkeley, CA, USA
- N. Apadula, M. Arratia, A. Collu, L. Greiner, B. Jacak, P. M.
Jacobs, S. Klein, Y. S. Lai, J. D. Mulligan & M. Płoskoń
35. SUBATECH, IMT Atlantique, Université de Nantes, CNRS-IN2P3,
Nantes, France
- L. Aphecetche, G. Batigne, O. Bugnon, F. P. A. Damas, B.
Erazmus, K. Garg, M. Germain, M. Guittiere, G. Martínez García, E.
Masson, P. Pillot, R. Sadek, A. Shabetai, D. Stocco & M. Tarhini
36. Department of Physics, University of Oslo, Oslo, Norway
- I. C. Arsene, O. Dordic, A. Lardeux, S. M. Mahmood, Q. W. Malik, A.
Neagu, M. Richter, K. Røed, T. B. Skaali, T. S. Tveter & J. Wikne

37. Laboratoire de Physique des 2 Infinis, Irène Joliot-Curie, Orsay, France

S. Aziz, Z. Conesa del Valle, B. Espagnon, C. Hadjidakis, C. Huang, L. Massacrier & C. Suire

38. INFN, Sezione di Catania, Catania, Italy

A. Badalà, G. Mandaglio, D. Pistone, A. Rosano & A. Trifirò

39. Gangneung-Wonju National University, Gangneung, Republic of Korea

Y. W. Baek & J. S. Kim

40. Physics Department, University of Jammu, Jammu, India

R. Bala, A. Bhasin, I. R. Bhat, A. Gupta, R. Gupta, S. Rajput, S. Sambyal, A. Sharma, M. Sharma, S. Sharma, R. Singh & V. Sumberia

41. Département de Physique Nucléaire (DPhN), Université Paris-Saclay
Centre d'Etudes de Saclay (CEA), IRFU, Saclay, France

A. Baldisseri, H. Borel, R. Caron, J. Castillo Castellanos, F. P. A. Damas, A. Ferrero, A. M. C. Glaenzer, S. Panebianco, H. Pereira Da Costa, S. Perrin, A. Rakotozafindrabe, M. Winn & S. Yano

42. Helmholtz-Institut für Strahlen- und Kernphysik, Rheinische Friedrich-Wilhelms-Universität Bonn, Bonn, Germany

M. Ball, P. Hauer, B. Ketzer, T. Mahmoud & V. Ratza

43. Physik Department, Technische Universität München, Munich, Germany

S. Balouza, A. Bilandzic, T. Dahms, L. Fabbietti, P. Gasik, S. T. Heckel, B. Hohlweger, S. A. Konigstorfer, A. M. Mathis, D. L. Mihaylov, C. Mordasini, V. M. Sarti, B. Singh, S. F. Taghavi, O. Vázquez Doce & I. Vorobyev

44. Bose Institute, Department of Physics and Centre for Astroparticle Physics and Space Science (CAPSS), Kolkata, India

D. Banerjee, M. A. Bhat, R. Biswas, S. Biswas, P. Das, S. Das, S. K. Ghosh, A. Modak, S. K. Prasad & S. Raha

45. Dipartimento di Fisica e Astronomia dell'Università degli Studi di Catania and Sezione INFN, Catania, Italy

R. Barbera, P. La Rocca, C. Pinto & F. Riggi

46. Dipartimento di Fisica dell'Università degli studi di Torino and Sezione INFN, Turin, Italy

L. Barioglio, S. Beole, A. Bianchi, L. Bianchi, E. Botta, L. D. Cilladi, Y. Corrales Morales, S. Delsanto, A. Ferretti, M. Gagliardi, M. Masera, F. Mazzaschi, L. Micheletti, L. Quaglia, L. Terlizzi & E. Vercellin

47. Wigner Research Centre for Physics, Budapest, Hungary

G. G. Barnaföldi, G. Bencedi, D. Berenyi, G. Biro, L. Boldizsár, G. Hamar, P. Lévai, D. Varga, Z. Varga, M. Varga-Kofarago & R. Vértesi

48. Nuclear Physics Group, STFC Daresbury Laboratory, Daresbury, UK

L. S. Barnby & R. C. Lemmon

49. Université Clermont Auvergne, CNRS/IN2P3, LPC, Clermont-Ferrand, France

V. Barret, N. Bastid, T. Chowdhury, P. Crochet, P. Dupieux, X. Lopez, F. Manso, S. Porteboeuf-Houssais, G. Taillepied & S. Tang

50. University of Liverpool, Liverpool, UK

C. Bartels, M. D. Buckland, M. Chartier, C. Hills, J. P. Iddon, J. Liu & J. Norman

51. Dipartimento di Fisica e Astronomia dell'Università degli Studi di Padova and Sezione INFN, Padua, Italy

F. Baruffaldi, M. Faggin, P. Giubilato, M. Lunardon, A. Rossi, F. Soramel & S. Trogolo

52. Wayne State University, Detroit, MI, USA

S. Basu, V. Gonzalez, W. J. Llope, J. Pan, C. A. Pruneau, J. Putschke, D. Sarkar & S. A. Voloshin

53. Joint Institute for Nuclear Research (JINR), Dubna, Russia

B. Batyunya, C. Ceballos Sanchez, S. Grigoryan, A. Kondratyev, L. Malinina, K. Mikhaylov, P. Nomokonov, V. Pozdniakov, E. Rogochaya, B. Rumyantsev & A. Vodopyanov

54. Indian Institute of Technology Bombay (IIT), Mumbai, India

D. Bauri, H. Bhatt, P. Chakraborty, S. Dash, P. Dhankher, A. Goswami, B. Naik, B. K. Nandi, R. Nayak, S. Padhan, B. Sahoo, P. Sahoo & T. Tripathy

55. Sección Fsica, Departamento de Ciencias, Pontificia Universidad Católica del Perú, Lima, Peru

J. L. Bazo Alba, E. Calvo Villar, A. M. Gago & C. Soncco

56. Niels Bohr Institute, University of Copenhagen, Copenhagen, Denmark

I. G. Bearden, C. H. Christensen, J. J. Gaardhøje, K. Gulbrandsen, Z. Moravcova, B. S. Nielsen, V. Pacik, T. Richert, J. Schukraft, F. Thoresen, V. Vislavicius & Y. Zhou

57. Yale University, New Haven, CT, USA

C. Beattie, H. Bossi, R. Haake, J. W. Harris, L. B. Havener, R. D. Majka, M. H. Oliver & N. Smirnov

58. Institute for Subatomic Physics, Utrecht University/Nikhef, Utrecht, Netherlands

C. Bedda, A. Grelli, M. R. Haque, S. Jaelani, A. P. Mohanty, T. Peitzmann, M. H. P. Sas, R. J. M. Snellings, B. A. Trzeciak, N. van der Kolk, L. V. R. van Doremale, M. van Leeuwen, L. Vermunt, H. Yokoyama & H. J. C. Zanoli

59. Inha University, Incheon, Republic of Korea

N. K. Behera, J. Bok, S. Cho, B. Kim, V. Kučera, M. J. Kweon, J. Y. Kwon, J. Park & J. H. Yoon

60. Université de Strasbourg, CNRS, IPHC UMR 7178, Strasbourg, France

I. Belikov, A. Gal, B. Hippolyte, C. Kuhn, A. Maire, F. Rami, Y. Schutz & S. Senyukov

61. NRNU Moscow Engineering Physics Institute, Moscow, Russia

V. Belyaev, A. Bogdanov, A. Bolozdynya, A. Borissov, V. Grigoriev, V. Kaplin, N. Kondratyeva, V. Loginov, Y. Melikyan, V. Samsonov & I. Selyuzhenkov

62. Petersburg Nuclear Physics Institute, Gatchina, Russia

Y. Berdnikov, V. Ivanov, A. Khanzadeev, E. Kryshen, M. Malaev, V. Nikulin, A. Riabov, V. Riabov, Y. Ryabov, V. Samsonov & M. Zhalov

63. University of Tennessee, Knoxville, TN, USA

R. A. Bertens, A. J. Castro, C. Hughes, C. Nattrass, A. C. Oliveira Da Silva, K. F. Read, A. R. Schmier, S. Sorensen, P. J. Steffanic & W. E. Witt

64. Institute of Space Science (ISS), Bucharest, Romania

M. G. Besoiu, A. Danu, A. Dobrin, C. Ristea, A. Sevcenco & I. Stan

65. Gauhati University, Department of Physics, Guwahati, India

B. Bhattacharjee, N. Hussain & P. Sarma

66. INFN, Laboratori Nazionali di Frascati, Frascati, Italy

N. Bianchi, A. Fantoni, P. Gianotti, P. Larionov, V. Muccifora, S. Pisano, F. Ronchetti & M. Toppi

67. Faculty of Nuclear Sciences and Physical Engineering, Czech Technical University in Prague, Prague, Czech Republic

J. Bielčík, M. Broz, J. G. Contreras, T. Herman, D. Horak, K. Krizkova Gajdosova, R. Lavicka, V. Petráček, K. Šafařík, S. R. Torres & B. A. Trzeciak

68. The University of Texas at Austin, Austin, TX, USA

J. T. Blair, A. N. Flores, E. F. Gauger, R. Hannigan, C. Markert, J. Schambach, D. Thomas & J. R. Wright

69. Università degli Studi di Pavia, Pavia, Italy

G. Boca, S. Costanza, A. Rotondi & N. Valle

70. Oak Ridge National Laboratory, Oak Ridge, TN, USA

F. Bock, T. M. Cormier, L. Cunqueiro, R. J. Ehlers, M. Fasel, H. Hassan, F. Jonas, C. Loizides, M. G. Poghosyan, K. F. Read & N. V. Schmidt

71. Dipartimento di Fisica dell'Università degli studi di Bari Aldo Moro and Sezione INFN, Cagliari, Italy

S. Boi, A. Chauvin, A. De Falco, A. Mulliri, B. Paul & G. L. Usai

72. Faculty of Science, P.J. Šafárik University, Košice, Slovakia

M. Bombara, A. Kravčáková, Z. Rescakova, L. Tropp, M. Vala & J. Vrláková

73. Università di Brescia, Brescia, Italy

G. Bonomi, D. Pagano, J. Pazzini & N. Zurlo

74. Universidade de São Paulo (USP), São Paulo, Brazil

M. Bregant, F. D. M. Canedo, H. F. Degenhardt, C. Jahnke, P. F. T. Matuoka, M. G. Munhoz & A. A. P. Suaide

75. Dipartimento Interateneo di Fisica ‘M. Merlin’, Università degli studi di Bari Aldo Moro and Sezione INFN, Bari, Italy

G. E. Bruno, D. Di Bari, G. Trombetta & G. Volpe

76. Politecnico di Bari, Bari, Italy

G. E. Bruno

77. Russian Federal Nuclear Center (VNIIEF), Sarov, Russia

D. Budnikov, S. Filchagin, R. Ilkaev, A. Kuryakin, S. Nazarenko, A. Tumkin & N. Zaviyalov

78. Stefan Meyer Institut für Subatomare Physik (SMI), Vienna, Austria

P. Buhler, A. A. Capon, S. Lehner, E. Meninno & M. Weber

79. iThemba LABS, National Research Foundation, Somerset West, South Africa

Z. Buthelezi & S. Foertsch

80. University of the Witwatersrand, Johannesburg, South Africa

Z. Buthelezi, S. Delsanto & Z. Vilakazi

81. The Henryk Niewodniczanski Institute of Nuclear Physics, Polish Academy of Sciences, Krakow, Poland

S. A. Bysiak, J. Figiel, L. Görlich, A. Khuntia, M. Kowalski, A. Matyja, C. Mayer, J. Otwinowski, A. Rybicki, H. Sharma & I. Sputowska

82. Nikhef, National Institute for Subatomic Physics, Amsterdam, Netherlands

D. Caffarri, P. Christakoglou, A. Dubla, Z. Khabanova, P. G. Kuijer, S. Qiu, I. Ravasenga & G. Simatovic

83. Universidad Autónoma de Sinaloa, Culiacán, Mexico

J. M. M. Camacho, C. D. Galvan & I. León Monzón

84. High Energy Physics Group, Universidad Autónoma de Puebla, Puebla, Mexico

R. S. Camacho, A. Fernández Téllez, J. R. A. Garcia, I. B. Guzman, E. G. Hernandez, M. I. Martínez, L. A. P. Moreno, S. A. R. Ramirez, M. Rodríguez Cahuantzi, P. F. Rojas, G. Tejeda Muñoz, A. Vargas & S. Vergara Limón

85. Dipartimento di Fisica dell'Università degli studi di Trieste and Sezione INFN, Trieste, Italy

P. Camerini, G. Contin, R. Lea, G. V. Margagliotti, C. D. Martin, R. Rui & V. Zacco

86. INFN, Sezione di Cagliari, Cagliari, Italy

E. A. R. Casula, C. Cicalo, A. Masoni, A. Mulliri & S. Siddhanta

87. Institute of Nuclear Physics, Homi Bhabha National Institute, Kolkata, India

S. Chattopadhyay, D. Das, I. Das, J. Ghosh, H. Hushnud, M. S. Islam, P. Roy, W. Shaikh & T. Sinha

88. Université de Lyon, Université Lyon 1, CNRS/IN2P3, IPN-Lyon, Lyon, France

C. Cheshkov, B. Cheynis, M. Marchisone, L. C. Migliorin, R. Tieulent & A. Uras

89. University of Tsukuba, Tsukuba, Japan

T. Chujo, R. Hosokawa, M. Inaba, B. Kim, J. Lee, Y. Miake, N. Novitzky & S. Sakai

90. University of Cape Town, Cape Town, South Africa

J. Cleymans, T. Dietel, S. Mhlanga & S. Murray

91. INFN, Sezione di Bari, Bari, Italy

F. Colamaria, D. Colella, G. de Cataldo, D. Elia, G. Fiorenza, V. Manzari, A. Mastroserio, M. Mazzilli, E. Nappi & G. Vino

92. Laboratoire de Physique Subatomique et de Cosmologie, Université Grenoble-Alpes, CNRS-IN2P3, Grenoble, France

G. Conesa Balbastre, J. Faivre, C. Furget, R. Guernane & J. Norman

93. INFN, Sezione di Trieste, Trieste, Italy

G. Contin, E. Fragiacomo, G. Luparello & S. Piano

94. Dipartimento di Scienze e Innovazione Tecnologica dell'Università del Piemonte Orientale and INFN Sezione di Torino, Alessandria, Italy

P. Cortese, L. Ramello & M. Sitta

95. Universidade Federal do ABC, Santo Andre, Brazil

M. R. Cosentino

96. Instituto de Ciencias Nucleares, Universidad Nacional Autónoma de México, Mexico City, Mexico

E. Cuautle, A. N. Mishra, L. Nellen, A. Ortiz Velasquez, G. Paić, E. D. Rosas & S. Tripathy

97. Warsaw University of Technology, Warsaw, Poland

D. Dabrowski, K. R. Deja, L. K. Graczykowski, M. J. Jakubowska, M. A. Janik, P. Karczmarczyk, A. Kisiel, G. Kornakov, J. W. Myrcha, L. T. Neumann, P. Nowakowski, J. Oleniacz, P. S. Rokita, K. Roslon, T. P. Trzcinski & H. Zbroszczyk

98. National Institute of Science Education and Research, Homi Bhabha National Institute, Jatni, India

P. Das, A. Dash, S. De, M. Dukhishyam, M. R. Haque, S. Kundu, B. Mohanty, T. K. Nayak & R. Singh

99. Dipartimento di Fisica ‘E.R. Caianiello’ dell’Università and Gruppo Collegato INFN, Salerno, Italy

A. De Caro, S. De Pasquale, M. Fusco Girard, E. Meninno, L. D. Stritto & T. Virgili

100. Frankfurt Institute for Advanced Studies, Johann Wolfgang Goethe-Universität Frankfurt, Frankfurt am Main, Germany

J. de Cuveland, S. Gorbunov, D. Hutter, I. Kisel, M. Krzewicki, S. L. La Pointe, J. Lehrbach, V. Lindenstruth, G. Neskovic & A. R. Redelbach

101. Indian Institute of Technology Indore, Indore, India

S. Deb, P. Pareek, R. Rath, S. P. Rode, A. Roy, R. Sahoo, R. Singh, D. Thakur & S. Tripathy

102. National Centre for Nuclear Research, Warsaw, Poland

A. Deloff, O. Kovalenko, P. Kurashvili, R. Nair, K. Redlich, T. Siemianczuk & G. Wilk

103. Centro de Aplicaciones Tecnológicas y Desarrollo Nuclear
(CEADEN), Havana, Cuba

R. A. Diaz, E. López Torres & G. M. Perez

104. Department of Physics, University of California, Berkeley, CA, USA

D. U. Dixit, E. D. Lesser, A. Liu & F. Torales-Acosta

105. Institute for Nuclear Research, Academy of Sciences, Moscow, Russia

U. Dmitrieva, D. Finogeev, A. Furs, O. Karavichev, T. Karavicheva, E. Karpechev, A. Kurepin, A. B. Kurepin, A. Maevskaia, Y. Melikyan, I. Morozov, I. Pshenichnov, D. Serebryakov, A. Shabanov, A. Tikhonov & N. Topilskaya

106. Physics Department, Faculty of Science, University of Zagreb, Zagreb, Croatia

F. Erhardt, M. Jercic, D. Karatovic, M. Planinic & N. Poljak

107. School of Physics and Astronomy, University of Birmingham,
Birmingham, UK

D. Evans, K. L. Graham, O. Jevons, P. G. Jones, A. Jusko, M. Krivda, J. Kvapil, R. Lietava, S. Ragoni, O. Villalobos Baillie & E. Willsher

108. NRC Kurchatov Institute IHEP, Protvino, Russia

S. Evdokimov, V. Izucheev, Y. Kharlov, E. Kondratyuk, B. Polichtchouk, R. Rogalev, S. Sadovsky & A. Shangaraev

109. Department of Physics, School of Science, National and Kapodistrian University of Athens, Athens, Greece

P. Ganoti & M. Vasileiou

110. Chicago State University, Chicago, IL, USA

E. Garcia-Solis & A. Harton

111. National Nuclear Research Center, Baku, Azerbaijan

A. Garibli & A. Rustamov

112. Instituto de Física, Universidade Federal do Rio Grande do Sul (UFRGS), Porto Alegre, Brazil

M. B. Gay Ducati, L. G. Pereira & R. P. Pezzi

113. Faculty of Electrical Engineering, Mechanical Engineering and Naval Architecture, University of Split, Split, Croatia

S. Gotovac, P. Loncar, E. Mudnic & L. Vickovic

114. A.I. Alikhanyan National Science Laboratory (Yerevan Physics Institute) Foundation, Yerevan, Armenia

A. Grigoryan

115. University of Tokyo, Tokyo, Japan

T. Gunji, S. Hayashi, H. Murakami, Y. Sekiguchi & D. Sekihata

116. Nagasaki Institute of Applied Science, Nagasaki, Japan

H. Hamagaki, M. Ogino & K. Oyama

117. Faculty of Engineering and Science, Western Norway University of Applied Sciences, Bergen, Norway

H. Helstrup, K. F. Hetland, B. Kileng, S. V. Nesbo & M. M. Storetvedt

118. Centro de Investigación y de Estudios Avanzados (CINVESTAV),
Mexico City, Mexico

G. Herrera Corral

119. Ohio State University, Columbus, OH, USA

T. J. Humanic, A. M. Kubera, M. A. Lisa & S. Liu

120. Technical University of Košice, Košice, Slovakia

S. Jadlovska, J. Jadlovsky, L. Koska & D. Voscek

121. Institute of Experimental Physics, Slovak Academy of Sciences,
Košice, Slovakia

P. Kalinak, I. Králik, M. Krivda & J. Musinsky

122. KTO Karatay University, Konya, Turkey

A. Karasu Uysal & S. Yalcin

123. Zentrum für Technologietransfer und Telekommunikation (ZTT),
Hochschule Worms, Worms, Germany

R. Keidel

124. Yonsei University, Seoul, Republic of Korea

D. Kim, J. Kim, J. Kim, T. Kim, T. Kim, Y. Kwon & S. Lee

125. University of Jyväskylä, Jyväskylä, Finland

D. J. Kim, J. E. Parkkila, J. Rak, H. Rytkonen & W. H. Trzaska

126. Jeonbuk National University, Jeonju, Republic of Korea

E. J. Kim & J. Kim

127. Department of Physics, Pusan National University, Pusan, Republic of Korea

H. Kim, B. Lim & I.-K. Yoo

128. Department of Physics, Sejong University, Seoul, Republic of Korea

S. Kim

129. California Polytechnic State University, San Luis Obispo, CA, USA

J. L. Klay

130. Suranaree University of Technology, Nakhon Ratchasima, Thailand

C. Kobdaj & A. Songmoolnak

131. University of South-Eastern Norway, Tønsberg, Norway

R. Langoy & J. Lien

132. China Institute of Atomic Energy, Beijing, China

X. Li & Y. Zhi

133. Dipartimento di Scienze MIFT, Università di Messina, Messina, Italy

G. Mandaglio & A. Trifirò

134. Institute of Physics of the Czech Academy of Sciences, Prague, Czech Republic

J. Mareš & P. Závada

135. Università degli Studi di Foggia, Foggia, Italy

A. Mastroserio

136. INFN, Sezione di Roma, Rome, Italy

M. A. Mazzoni

137. Dipartimento di Fisica dell'Università 'La Sapienza' and Sezione INFN, Rome, Italy

F. Meddi

138. Faculty of Mathematics, Physics and Informatics, Comenius University Bratislava, Bratislava, Slovakia

M. Meres, M. Pikna, B. Sitar, A. Szabo & I. Szarka

139. Budker Institute for Nuclear Physics, Novosibirsk, Russia

Y. Pestov

140. Physics Department, University of Rajasthan, Jaipur, India

R. Raniwala & S. Raniwala

141. Helsinki Institute of Physics (HIP), Helsinki, Finland

S. S. Räsänen, O. A. M. Saarimaki & M. Slupecki

142. Institute of Physics, Homi Bhabha National Institute, Bhubaneswar, India

S. Sahoo, P. K. Sahu & S. Swain

143. Physikalisches Institut, Eberhard-Karls-Universität Tübingen, Tübingen, Germany

H. R. Schmidt, M. Schmidt & M. A. Völkl

144. Hiroshima University, Hiroshima, Japan

K. Shigaki, T. Sugitate, Y. Yamaguchi & K. Yamakawa

145. Nara Women's University (NWU), Nara, Japan

M. Shimomura

146. Centre de Calcul de l'IN2P3, Lyon, France

R. Vernet

147. University of Science and Technology of China, Hefei, China

Y. Wu

Consortia

ALICE Collaboration

- , S. Acharya
- , D. Adamová
- , A. Adler
- , J. Adolfsson
- , M. M. Aggarwal
- , G. Aglieri Rinella
- , M. Agnello
- , N. Agrawal
- , Z. Ahammed
- , S. Ahmad
- , S. U. Ahn
- , Z. Akbar
- , A. Akindinov
- , M. Al-Turany
- , S. N. Alam
- , D. S. D. Albuquerque
- , D. Aleksandrov
- , B. Alessandro
- , H. M. Alfanda
- , R. Alfaro Molina
- , B. Ali
- , Y. Ali
- , A. Alici
- , N. Alizadehvandchali
- , A. Alkin
- , J. Alme
- , T. Alt
- , L. Altenkamper
- , I. Altsybeev
- , M. N. Anaam
- , C. Andrei
- , D. Andreou
- , A. Andronic
- , M. Angeletti

- , V. Anguelov
- , C. Anson
- , T. Antičić
- , F. Antinori
- , P. Antonioli
- , N. Apadula
- , L. Aphecetche
- , H. Appelshäuser
- , S. Arcelli
- , R. Arnaldi
- , M. Arratia
- , I. C. Arsene
- , M. Arslan Dok
- , A. Augustinus
- , R. Averbeck
- , S. Aziz
- , M. D. Azmi
- , A. Badalà
- , Y. W. Baek
- , S. Bagnasco
- , X. Bai
- , R. Bailhache
- , R. Bala
- , A. Balbino
- , A. Baldissari
- , M. Ball
- , S. Balouza
- , D. Banerjee
- , R. Barbera
- , L. Barioglio
- , G. G. Barnaföldi
- , L. S. Barnby
- , V. Barret
- , P. Bartalini
- , C. Bartels
- , K. Barth
- , E. Bartsch

- , F. Baruffaldi
- , N. Bastid
- , S. Basu
- , G. Batigne
- , B. Batyunya
- , D. Bauri
- , J. L. Bazo Alba
- , I. G. Bearden
- , C. Beattie
- , C. Bedda
- , N. K. Behera
- , I. Belikov
- , A. D. C. Bell Hechavarria
- , F. Bellini
- , R. Bellwied
- , V. Belyaev
- , G. Bencedi
- , S. Beole
- , A. Bercuci
- , Y. Berdnikov
- , D. Berenyi
- , R. A. Bertens
- , D. Berzano
- , M. G. Besoiu
- , L. Betev
- , A. Bhasin
- , I. R. Bhat
- , M. A. Bhat
- , H. Bhatt
- , B. Bhattacharjee
- , A. Bianchi
- , L. Bianchi
- , N. Bianchi
- , J. Bielčík
- , J. Bielčíková
- , A. Bilandzic
- , G. Biro

- , R. Biswas
- , S. Biswas
- , J. T. Blair
- , D. Blau
- , C. Blume
- , G. Boca
- , F. Bock
- , A. Bogdanov
- , S. Boi
- , J. Bok
- , L. Boldizsár
- , A. Bolozdynya
- , M. Bombara
- , G. Bonomi
- , H. Borel
- , A. Borissov
- , H. Bossi
- , E. Botta
- , L. Bratrud
- , P. Braun-Munzinger
- , M. Bregant
- , M. Broz
- , E. Bruna
- , G. E. Bruno
- , M. D. Buckland
- , D. Budnikov
- , H. Buesching
- , S. Bufalino
- , O. Bugnon
- , P. Buhler
- , P. Buncic
- , Z. Buthelezi
- , J. B. Butt
- , S. A. Bysiak
- , D. Caffarri
- , A. Caliva
- , E. Calvo Villar

- , J. M. M. Camacho
- , R. S. Camacho
- , P. Camerini
- , F. D. M. Canedo
- , A. A. Capon
- , F. Carnesecchi
- , R. Caron
- , J. Castillo Castellanos
- , A. J. Castro
- , E. A. R. Casula
- , F. Catalano
- , C. Ceballos Sanchez
- , P. Chakraborty
- , S. Chandra
- , W. Chang
- , S. Chapelard
- , M. Chartier
- , S. Chattopadhyay
- , S. Chattopadhyay
- , A. Chauvin
- , C. Cheshkov
- , B. Cheynis
- , V. Chibante Barroso
- , D. D. Chinellato
- , S. Cho
- , P. Chochula
- , T. Chowdhury
- , P. Christakoglou
- , C. H. Christensen
- , P. Christiansen
- , T. Chujo
- , C. Cicalo
- , L. Cifarelli
- , L. D. Cilladi
- , F. Cindolo
- , M. R. Ciuppek
- , G. Clai

- , J. Cleymans
- , F. Colamaria
- , D. Colella
- , A. Collu
- , M. Colocci
- , M. Concas
- , G. Conesa Balbastre
- , Z. Conesa del Valle
- , G. Contin
- , J. G. Contreras
- , T. M. Cormier
- , Y. Corrales Morales
- , P. Cortese
- , M. R. Cosentino
- , F. Costa
- , S. Costanza
- , P. Crochet
- , E. Cuautle
- , P. Cui
- , L. Cunqueiro
- , D. Dabrowski
- , T. Dahms
- , A. Dainese
- , F. P. A. Damas
- , M. C. Danisch
- , A. Danu
- , D. Das
- , I. Das
- , P. Das
- , P. Das
- , S. Das
- , A. Dash
- , S. Dash
- , S. De
- , A. De Caro
- , G. de Cataldo
- , J. de Cuveland

- , A. De Falco
- , D. De Gruttola
- , N. De Marco
- , S. De Pasquale
- , S. Deb
- , H. F. Degenhardt
- , K. R. Deja
- , A. Deloff
- , S. Delsanto
- , W. Deng
- , P. Dhankher
- , D. Di Bari
- , A. Di Mauro
- , R. A. Diaz
- , T. Dietel
- , P. Dillenseger
- , Y. Ding
- , R. Divià
- , D. U. Dixit
- , Ø. Djuvsland
- , U. Dmitrieva
- , A. Dobrin
- , B. Dönigus
- , O. Dordic
- , A. K. Dubey
- , A. Dubla
- , S. Dudi
- , M. Dukhishyam
- , P. Dupieux
- , R. J. Ehlers
- , V. N. Eikeland
- , D. Elia
- , B. Erasmus
- , F. Erhardt
- , A. Erokhin
- , M. R. Ersdal
- , B. Espagnon

- , G. Eulisse
- , D. Evans
- , S. Evdokimov
- , L. Fabbietti
- , M. Faggin
- , J. Faivre
- , F. Fan
- , A. Fantoni
- , M. Fasel
- , P. Fecchio
- , A. Feliciello
- , G. Feofilov
- , A. Fernández Téllez
- , A. Ferrero
- , A. Ferretti
- , A. Festanti
- , V. J. G. Feuillard
- , J. Figiel
- , S. Filchagin
- , D. Finogeev
- , F. M. Fionda
- , G. Fiorenza
- , F. Flor
- , A. N. Flores
- , S. Foertsch
- , P. Foka
- , S. Fokin
- , E. Fragiacomo
- , U. Frankenfeld
- , U. Fuchs
- , C. Furget
- , A. Furs
- , M. Fusco Girard
- , J. J. Gaardhøje
- , M. Gagliardi
- , A. M. Gago
- , A. Gal

- , C. D. Galvan
- , P. Ganoti
- , C. Garabatos
- , J. R. A. Garcia
- , E. Garcia-Solis
- , K. Garg
- , C. Gargiulo
- , A. Garibli
- , K. Garner
- , P. Gasik
- , E. F. Gauger
- , M. B. Gay Ducati
- , M. Germain
- , J. Ghosh
- , P. Ghosh
- , S. K. Ghosh
- , M. Giacalone
- , P. Gianotti
- , P. Giubellino
- , P. Giubilato
- , A. M. C. Glaenzer
- , P. Glässel
- , A. Gomez Ramirez
- , V. Gonzalez
- , L. H. González-Trueba
- , S. Gorbunov
- , L. Görlich
- , A. Goswami
- , S. Gotovac
- , V. Grabski
- , L. K. Graczykowski
- , K. L. Graham
- , L. Greiner
- , A. Grelli
- , C. Grigoras
- , V. Grigoriev
- , A. Grigoryan

- , S. Grigoryan
- , O. S. Groettvik
- , F. Grosa
- , J. F. Grosse-Oetringhaus
- , R. Grosso
- , R. Guernane
- , M. Guittiere
- , K. Gulbrandsen
- , T. Gunji
- , A. Gupta
- , R. Gupta
- , I. B. Guzman
- , R. Haake
- , M. K. Habib
- , C. Hadjidakis
- , H. Hamagaki
- , G. Hamar
- , M. Hamid
- , R. Hannigan
- , M. R. Haque
- , A. Harlenderova
- , J. W. Harris
- , A. Harton
- , J. A. Hasenbichler
- , H. Hassan
- , Q. U. Hassan
- , D. Hatzifotiadou
- , P. Hauer
- , L. B. Havener
- , S. Hayashi
- , S. T. Heckel
- , E. Hellbär
- , H. Helstrup
- , A. Hergheliegiu
- , T. Herman
- , E. G. Hernandez
- , G. Herrera Corral

- , F. Herrmann
- , K. F. Hetland
- , H. Hillemanns
- , C. Hills
- , B. Hippolyte
- , B. Hohlweger
- , J. Honermann
- , D. Horak
- , A. Hornung
- , S. Hornung
- , R. Hosokawa
- , P. Hristov
- , C. Huang
- , C. Hughes
- , P. Huhn
- , T. J. Humanic
- , H. Hushnud
- , L. A. Husova
- , N. Hussain
- , S. A. Hussain
- , D. Hutter
- , J. P. Iddon
- , R. Ilkaev
- , H. Ilyas
- , M. Inaba
- , G. M. Innocenti
- , M. Ippolitov
- , A. Isakov
- , M. S. Islam
- , M. Ivanov
- , V. Ivanov
- , V. Izucheev
- , B. Jacak
- , N. Jacazio
- , P. M. Jacobs
- , S. Jadlovska
- , J. Jadlovsky

- , S. Jaelani
- , C. Jahnke
- , M. J. Jakubowska
- , M. A. Janik
- , T. Janson
- , M. Jercic
- , O. Jevons
- , M. Jin
- , F. Jonas
- , P. G. Jones
- , J. Jung
- , M. Jung
- , A. Jusko
- , P. Kalinak
- , A. Kalweit
- , V. Kaplin
- , S. Kar
- , A. Karasu Uysal
- , D. Karatovic
- , O. Karavichev
- , T. Karavicheva
- , P. Karczmarczyk
- , E. Karpechev
- , A. Kazantsev
- , U. Kebschull
- , R. Keidel
- , M. Keil
- , B. Ketzer
- , Z. Khabanova
- , A. M. Khan
- , S. Khan
- , A. Khanzadeev
- , Y. Kharlov
- , A. Khatun
- , A. Khuntia
- , B. Kileng
- , B. Kim

- , B. Kim
- , D. Kim
- , D. J. Kim
- , E. J. Kim
- , H. Kim
- , J. Kim
- , J. S. Kim
- , J. Kim
- , J. Kim
- , M. Kim
- , S. Kim
- , T. Kim
- , T. Kim
- , S. Kirsch
- , I. Kisel
- , S. Kiselev
- , A. Kisiel
- , J. L. Klay
- , C. Klein
- , J. Klein
- , S. Klein
- , C. Klein-Bösing
- , M. Kleiner
- , A. Kluge
- , M. L. Knichel
- , A. G. Knospe
- , C. Kobdaj
- , M. K. Köhler
- , T. Kollegger
- , A. Kondratyev
- , N. Kondratyeva
- , E. Kondratyuk
- , J. Konig
- , S. A. Konigstorfer
- , P. J. Konopka
- , G. Kornakov

- , L. Koska
- , O. Kovalenko
- , V. Kovalenko
- , M. Kowalski
- , I. Králik
- , A. Kravčáková
- , L. Kreis
- , M. Krivda
- , F. Krizek
- , K. Krizkova Gajdosova
- , M. Krüger
- , E. Kryshen
- , M. Krzewicki
- , A. M. Kubera
- , V. Kučera
- , C. Kuhn
- , P. G. Kuijer
- , L. Kumar
- , S. Kundu
- , P. Kurashvili
- , A. Kurepin
- , A. B. Kurepin
- , A. Kuryakin
- , S. Kushpil
- , J. Kvapil
- , M. J. Kweon
- , J. Y. Kwon
- , Y. Kwon
- , S. L. La Pointe
- , P. La Rocca
- , Y. S. Lai
- , M. Lamanna
- , R. Langoy
- , K. Lapidus
- , A. Lardeux
- , P. Larionov
- , E. Laudi

- , R. Lavicka
- , T. Lazareva
- , R. Lea
- , L. Leardini
- , J. Lee
- , S. Lee
- , S. Lehner
- , J. Lehrbach
- , R. C. Lemmon
- , I. León Monzón
- , E. D. Lesser
- , M. Lettrich
- , P. Lévai
- , X. Li
- , X. L. Li
- , J. Lien
- , R. Lietava
- , B. Lim
- , V. Lindenstruth
- , A. Lindner
- , C. Lippmann
- , M. A. Lisa
- , A. Liu
- , J. Liu
- , S. Liu
- , W. J. Llope
- , I. M. Lofnes
- , V. Loginov
- , C. Loizides
- , P. Loncar
- , J. A. Lopez
- , X. Lopez
- , E. López Torres
- , J. R. Luhder
- , M. Lunardon
- , G. Luparello
- , Y. G. Ma

- , A. Maevskaya
- , M. Mager
- , S. M. Mahmood
- , T. Mahmoud
- , A. Maire
- , R. D. Majka
- , M. Malaev
- , Q. W. Malik
- , L. Malinina
- , D. Mal'Kevich
- , P. Malzacher
- , G. Mandaglio
- , V. Manko
- , F. Manso
- , V. Manzari
- , Y. Mao
- , M. Marchisone
- , J. Mareš
- , G. V. Margagliotti
- , A. Margotti
- , A. Marín
- , C. Markert
- , M. Marquard
- , C. D. Martin
- , N. A. Martin
- , P. Martinengo
- , J. L. Martinez
- , M. I. Martínez
- , G. Martínez García
- , S. Masciocchi
- , M. Masera
- , A. Masoni
- , L. Massacrier
- , E. Masson
- , A. Mastroserio
- , A. M. Mathis
- , O. Matonoha

- , P. F. T. Matuoka
- , A. Matyja
- , C. Mayer
- , F. Mazzaschi
- , M. Mazzilli
- , M. A. Mazzoni
- , A. F. Mechler
- , F. Meddi
- , Y. Melikyan
- , A. Menchaca-Rocha
- , C. Mengke
- , E. Meninno
- , A. S. Menon
- , M. Meres
- , S. Mhlanga
- , Y. Miake
- , L. Micheletti
- , L. C. Migliorin
- , D. L. Mihaylov
- , K. Mikhaylov
- , A. N. Mishra
- , D. Miśkowiec
- , A. Modak
- , N. Mohammadi
- , A. P. Mohanty
- , B. Mohanty
- , M. Mohisin Khan
- , Z. Moravcova
- , C. Mordasini
- , D. A. Moreira De Godoy
- , L. A. P. Moreno
- , I. Morozov
- , A. Morsch
- , T. Mrnjavac
- , V. Muccifora
- , E. Mudnic
- , D. Mühlheim

- , S. Muhuri
- , J. D. Mulligan
- , A. Mulliri
- , M. G. Munhoz
- , R. H. Munzer
- , H. Murakami
- , S. Murray
- , L. Musa
- , J. Musinsky
- , C. J. Myers
- , J. W. Myrcha
- , B. Naik
- , R. Nair
- , B. K. Nandi
- , R. Nania
- , E. Nappi
- , M. U. Naru
- , A. F. Nassirpour
- , C. Nattrass
- , R. Nayak
- , T. K. Nayak
- , S. Nazarenko
- , A. Neagu
- , R. A. Negrao De Oliveira
- , L. Nellen
- , S. V. Nesbo
- , G. Neskovic
- , D. Nesterov
- , L. T. Neumann
- , B. S. Nielsen
- , S. Nikolaev
- , S. Nikulin
- , V. Nikulin
- , F. Noferini
- , P. Nomokonov
- , J. Norman
- , N. Novitzky

- , P. Nowakowski
- , A. Nyanin
- , J. Nystrand
- , M. Ogino
- , A. Ohlson
- , J. Oleniacz
- , A. C. Oliveira Da Silva
- , M. H. Oliver
- , C. Oppedisano
- , A. Ortiz Velasquez
- , A. Oskarsson
- , J. Otwinowski
- , K. Oyama
- , Y. Pachmayer
- , V. Pacik
- , S. Padhan
- , D. Pagano
- , G. Paić
- , J. Pan
- , S. Panebianco
- , P. Pareek
- , J. Park
- , J. E. Parkkila
- , S. Parmar
- , S. P. Pathak
- , B. Paul
- , J. Pazzini
- , H. Pei
- , T. Peitzmann
- , X. Peng
- , L. G. Pereira
- , H. Pereira Da Costa
- , D. Peresunko
- , G. M. Perez
- , S. Perrin
- , Y. Pestov
- , V. Petráček

- , M. Petrovici
- , R. P. Pezzi
- , S. Piano
- , M. Pikna
- , P. Pillot
- , O. Pinazza
- , L. Pinsky
- , C. Pinto
- , S. Pisano
- , D. Pistone
- , M. Płoskoń
- , M. Planinic
- , F. Pliquett
- , M. G. Poghosyan
- , B. Polichtchouk
- , N. Poljak
- , A. Pop
- , S. Porteboeuf-Houssais
- , V. Pozdniakov
- , S. K. Prasad
- , R. Preghenella
- , F. Prino
- , C. A. Pruneau
- , I. Pshenichnov
- , M. Puccio
- , J. Putschke
- , S. Qiu
- , L. Quaglia
- , R. E. Quishpe
- , S. Ragoni
- , S. Raha
- , S. Rajput
- , J. Rak
- , A. Rakotozafindrabe
- , L. Ramello
- , F. Rami
- , S. A. R. Ramirez

- , R. Raniwala
- , S. Raniwala
- , S. S. Räsänen
- , R. Rath
- , V. Ratza
- , I. Ravasenga
- , K. F. Read
- , A. R. Redelbach
- , K. Redlich
- , A. Rehman
- , P. Reichelt
- , F. Reidt
- , X. Ren
- , R. Renfordt
- , Z. Rescakova
- , K. Reygers
- , A. Riabov
- , V. Riabov
- , T. Richert
- , M. Richter
- , P. Riedler
- , W. Riegler
- , F. Riggi
- , C. Ristea
- , S. P. Rode
- , M. Rodríguez Cahuantzi
- , K. Røed
- , R. Rogalev
- , E. Rogochaya
- , D. Rohr
- , D. Röhrich
- , P. F. Rojas
- , P. S. Rokita
- , F. Ronchetti
- , A. Rosano
- , E. D. Rosas
- , K. Roslon

- , A. Rossi
- , A. Rotondi
- , A. Roy
- , P. Roy
- , O. V. Rueda
- , R. Rui
- , B. Rumyantsev
- , A. Rustamov
- , E. Ryabinkin
- , Y. Ryabov
- , A. Rybicki
- , H. Rytkonen
- , O. A. M. Saarimaki
- , R. Sadek
- , S. Sadhu
- , S. Sadovsky
- , K. Šafařík
- , S. K. Saha
- , B. Sahoo
- , P. Sahoo
- , R. Sahoo
- , S. Sahoo
- , P. K. Sahu
- , J. Saini
- , S. Sakai
- , S. Sambyal
- , V. Samsonov
- , D. Sarkar
- , N. Sarkar
- , P. Sarma
- , V. M. Sarti
- , M. H. P. Sas
- , E. Scapparone
- , J. Schambach
- , H. S. Scheid
- , C. Schiaua
- , R. Schicker

- , A. Schmah
- , C. Schmidt
- , H. R. Schmidt
- , M. O. Schmidt
- , M. Schmidt
- , N. V. Schmidt
- , A. R. Schmier
- , J. Schukraft
- , Y. Schutz
- , K. Schwarz
- , K. Schweda
- , G. Scioli
- , E. Scomparin
- , J. E. Seger
- , Y. Sekiguchi
- , D. Sekihata
- , I. Selyuzhenkov
- , S. Senyukov
- , D. Serebryakov
- , A. Sevcenco
- , A. Shabanov
- , A. Shabetai
- , R. Shahoyan
- , W. Shaikh
- , A. Shangaraev
- , A. Sharma
- , A. Sharma
- , H. Sharma
- , M. Sharma
- , N. Sharma
- , S. Sharma
- , O. Sheibani
- , K. Shigaki
- , M. Shimomura
- , S. Shirinkin
- , Q. Shou
- , Y. Sibirjak

- , S. Siddhanta
- , T. Siemiaczuk
- , D. Silvermyr
- , G. Simatovic
- , G. Simonetti
- , B. Singh
- , R. Singh
- , R. Singh
- , R. Singh
- , V. K. Singh
- , V. Singhal
- , T. Sinha
- , B. Sitar
- , M. Sitta
- , T. B. Skaali
- , M. Slupecki
- , N. Smirnov
- , R. J. M. Snellings
- , C. Soncco
- , J. Song
- , A. Songmoolnak
- , F. Soramel
- , S. Sorensen
- , I. Sputowska
- , J. Stachel
- , I. Stan
- , P. J. Steffanic
- , E. Stenlund
- , S. F. Stiefelmaier
- , D. Stocco
- , M. M. Storetvedt
- , L. D. Stritto
- , A. A. P. Suaide
- , T. Sugitate
- , C. Suire
- , M. Suleymanov
- , M. Suljic

- , R. Sultanov
- , M. Šumbera
- , V. Sumberia
- , S. Sumowidagdo
- , S. Swain
- , A. Szabo
- , I. Szarka
- , U. Tabassam
- , S. F. Taghavi
- , G. Taillepied
- , J. Takahashi
- , G. J. Tambave
- , S. Tang
- , M. Tarhini
- , M. G. Tarzila
- , A. Tauro
- , G. Tejeda Muñoz
- , A. Telesca
- , L. Terlizzi
- , C. Terrevoli
- , D. Thakur
- , S. Thakur
- , D. Thomas
- , F. Thoresen
- , R. Tieulent
- , A. Tikhonov
- , A. R. Timmins
- , A. Toia
- , N. Topilskaya
- , M. Toppi
- , F. Torales-Acosta
- , S. R. Torres
- , A. Trifiró
- , S. Tripathy
- , T. Tripathy
- , S. Trogolo
- , G. Trombetta

- , L. Tropp
- , V. Trubnikov
- , W. H. Trzaska
- , T. P. Trzcinski
- , B. A. Trzeciak
- , A. Tumkin
- , R. Turrisi
- , T. S. Tveter
- , K. Ullaland
- , E. N. Umaka
- , A. Uras
- , G. L. Usai
- , M. Vala
- , N. Valle
- , S. Vallero
- , N. van der Kolk
- , L. V. R. van Doremalen
- , M. van Leeuwen
- , P. Vande Vyvre
- , D. Varga
- , Z. Varga
- , M. Varga-Kofarago
- , A. Vargas
- , M. Vasileiou
- , A. Vasiliev
- , O. Vázquez Doce
- , V. Vechernin
- , E. Vercellin
- , S. Vergara Limón
- , L. Vermunt
- , R. Vernet
- , R. Vértesi
- , L. Vickovic
- , Z. Vilakazi
- , O. Villalobos Baillie
- , G. Vino
- , A. Vinogradov

- , T. Virgili
- , V. Vislavicius
- , A. Vodopyanov
- , B. Volkel
- , M. A. Völkl
- , K. Voloshin
- , S. A. Voloshin
- , G. Volpe
- , B. von Haller
- , I. Vorobyev
- , D. Voscek
- , J. Vrláková
- , B. Wagner
- , M. Weber
- , S. G. Weber
- , A. Wegrzynek
- , S. C. Wenzel
- , J. P. Wessels
- , J. Wiechula
- , J. Wikne
- , G. Wilk
- , J. Wilkinson
- , G. A. Willems
- , E. Willsher
- , B. Windelband
- , M. Winn
- , W. E. Witt
- , J. R. Wright
- , Y. Wu
- , R. Xu
- , S. Yalcin
- , Y. Yamaguchi
- , K. Yamakawa
- , S. Yang
- , S. Yano
- , Z. Yin
- , H. Yokoyama

- , I.-K. Yoo
- , J. H. Yoon
- , S. Yuan
- , A. Yuncu
- , V. Yurchenko
- , V. Zaccolo
- , A. Zaman
- , C. Zampolli
- , H. J. C. Zanolli
- , N. Zardoshti
- , A. Zarochentsev
- , P. Závada
- , N. Zaviyalov
- , H. Zbroszczyk
- , M. Zhalov
- , S. Zhang
- , X. Zhang
- , Z. Zhang
- , V. Zhrebchevskii
- , Y. Zhi
- , D. Zhou
- , Y. Zhou
- , Z. Zhou
- , J. Zhu
- , Y. Zhu
- , A. Zichichi
- , G. Zinovjev
- & N. Zurlo

Contributions

All authors have contributed to the publication, being variously involved in the design and the construction of the detectors, in writing software, calibrating subsystems, operating the detectors and acquiring data, and finally analysing the processed data. The ALICE Collaboration members discussed and approved the scientific results. The manuscript was prepared by a subgroup of authors appointed by the collaboration and subject to an

internal collaboration-wide review process. All authors reviewed and approved the final version of the manuscript.

Corresponding author

Correspondence to [L. Musa](#).

Ethics declarations

Competing interests

The authors declare no competing interests.

Additional information

Peer review information *Nature* thanks Kazuya Aoki, Andrzej Kupsc, Manuel Lorenz and the other, anonymous, reviewer(s) for their contribution to the peer review of this work.

Publisher's note Springer Nature remains neutral with regard to jurisdictional claims in published maps and institutional affiliations.

Rights and permissions

[Reprints and Permissions](#)

About this article



Cite this article

ALICE Collaboration., Acharya, S., Adamová, D. *et al.* Unveiling the strong interaction among hadrons at the LHC. *Nature* **588**, 232–238 (2020). <https://doi.org/10.1038/s41586-020-3001-6>

[Download citation](#)

- Received: 03 June 2020
- Accepted: 20 October 2020
- Published: 09 December 2020
- Issue Date: 10 December 2020
- DOI: <https://doi.org/10.1038/s41586-020-3001-6>

Comments

By submitting a comment you agree to abide by our [Terms](#) and [Community Guidelines](#). If you find something abusive or that does not comply with our terms or guidelines please flag it as inappropriate.

[Access through your institution](#)

[Change institution](#)

[Buy or subscribe](#)

Associated Content

Nature | News & Views

[**Proton collisions probe the final frontier of the standard model of particle physics**](#)

- Manuel Lorenz

This article was downloaded by **calibre** from <https://www.nature.com/articles/s41586-020-3001-6>

| [Section menu](#) | [Main menu](#) |

- Article
- [Published: 09 December 2020](#)

Dipolar evaporation of reactive molecules to below the Fermi temperature

- [Giacomo Valtolina](#) ORCID: [orcid.org/0000-0002-5497-958X^{1,2}](https://orcid.org/0000-0002-5497-958X),
- [Kyle Matsuda](#) ORCID: [orcid.org/0000-0001-6861-2386^{1,2}](https://orcid.org/0000-0001-6861-2386),
- [William G. Tobias^{1,2}](#),
- [Jun-Ru Li^{1,2}](#),
- [Luigi De Marco^{1,2}](#) &
- [Jun Ye](#) ORCID: [orcid.org/0000-0003-0076-2112^{1,2}](https://orcid.org/0000-0003-0076-2112)

[Nature](#) volume 588, pages239–243(2020) [Cite this article](#)

- 65 Altmetric
- [Metrics details](#)

Subjects

- [Atomic and molecular collision processes](#)
- [Ultracold gases](#)

Abstract

The control of molecules is key to the investigation of quantum phases, in which rich degrees of freedom can be used to encode information and strong interactions can be precisely tuned¹. Inelastic losses in molecular collisions^{2,3,4,5}, however, have greatly hampered the engineering of low-

entropy molecular systems⁶. So far, the only quantum degenerate gas of molecules has been created via association of two highly degenerate atomic gases^{7,8}. Here we use an external electric field along with optical lattice confinement to create a two-dimensional Fermi gas of spin-polarized potassium–rubidium (KRb) polar molecules, in which elastic, tunable dipolar interactions dominate over all inelastic processes. Direct thermalization among the molecules in the trap leads to efficient dipolar evaporative cooling, yielding a rapid increase in phase-space density. At the onset of quantum degeneracy, we observe the effects of Fermi statistics on the thermodynamics of the molecular gas. These results demonstrate a general strategy for achieving quantum degeneracy in dipolar molecular gases in which strong, long-range and anisotropic dipolar interactions can drive the emergence of exotic many-body phases, such as interlayer pairing and p-wave superfluidity.

[Access through your institution](#)

[Change institution](#)

[Buy or subscribe](#)

Access options

Subscribe to Journal

Get full journal access for 1 year

185,98 €

only 3,58 € per issue

[Subscribe](#)

All prices are NET prices.

VAT will be added later in the checkout.

Rent or Buy article

Get time limited or full article access on ReadCube.

from \$8.99

[Rent or Buy](#)

All prices are NET prices.

Additional access options:

- [Log in](#)
- [Access through your institution](#)
- [Learn about institutional subscriptions](#)

Fig. 1: Experimental setup.

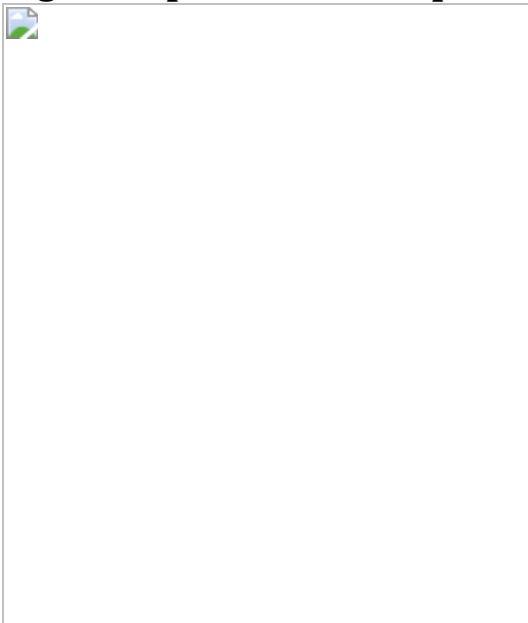


Fig. 2: Long-lived polar molecules in 2D.



Fig. 3: Tuning strong dipolar elastic interactions in a 2D molecular gas.

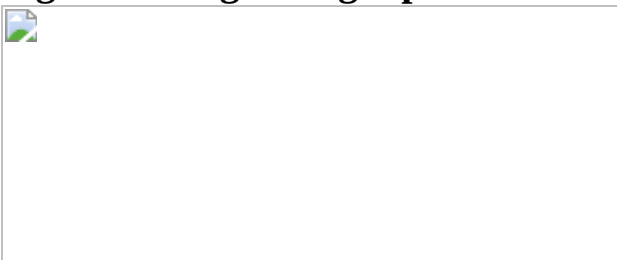


Fig. 4: Evaporative cooling to the quantum degenerate regime.



Data availability

The data that support the findings of this study are available from the corresponding author upon reasonable request. Source data are provided with this paper.

References

1. 1.

Bohn, J. L., Rey, A. M. & Ye, J. Cold molecules: progress in quantum engineering of chemistry and quantum matter. *Science* **357**, 1002–1010 (2017).

[ADS](#) [MathSciNet](#) [CAS](#) [MATH](#) [Google Scholar](#)

2. 2.

Ospelkaus, S. et al. Quantum-state controlled chemical reactions of ultracold potassium-rubidium molecules. *Science* **327**, 853–857 (2010).

[ADS](#) [CAS](#) [Google Scholar](#)

3. 3.

Ni, K.-K. et al. Dipolar collisions of polar molecules in the quantum regime. *Nature* **464**, 1324–1328 (2010).

[ADS](#) [CAS](#) [PubMed](#) [PubMed Central](#) [Google Scholar](#)

4. 4.

Guo, M. et al. Dipolar collisions of ultracold ground-state bosonic molecules. *Phys. Rev. X* **8**, 041044 (2018).

[CAS](#) [Google Scholar](#)

5. 5.

Gregory, P. D. et al. Sticky collisions of ultracold RbCs molecules. *Nat. Commun.* **10**, 3104 (2019).

[ADS](#) [PubMed](#) [PubMed Central](#) [Google Scholar](#)

6. 6.

Moses, S. A. et al. Creation of a low-entropy quantum gas of polar molecules in an optical lattice. *Science* **350**, 659–662 (2015).

[ADS](#) [CAS](#) [PubMed](#) [PubMed Central](#) [Google Scholar](#)

7. 7.

De Marco, L. et al. A degenerate Fermi gas of polar molecules. *Science* **363**, 853–856 (2019).

[ADS](#) [PubMed](#) [PubMed Central](#) [Google Scholar](#)

8. 8.

Tobias, W. G. et al. Thermalization and sub-Poissonian density fluctuations in a degenerate molecular Fermi gas. *Phys. Rev. Lett.* **124**, 033401 (2020).

[ADS](#) [CAS](#) [PubMed](#) [PubMed Central](#) [Google Scholar](#)

9. 9.

André, A. et al. A coherent all-electrical interface between polar molecules and mesoscopic superconducting resonators. *Nat. Phys.* **2**, 636–642 (2006).

[Google Scholar](#)

10. 10.

DeMille, D., Doyle, J. M. & Sushkov, A. O. Probing the frontiers of particle physics with tabletop-scale experiments. *Science* **357**, 990–994 (2017).

[ADS](#) [CAS](#) [PubMed](#) [PubMed Central](#) [Google Scholar](#)

11. 11.

Gregory, P. D., Blackmore, J. A., Bromley, S. L. & Cornish, S. L. Loss of ultracold $^{87}\text{Rb}^{133}\text{Cs}$ molecules via optical excitation of long-lived two-body collision complexes. *Phys. Rev. Lett.* **124**, 163402 (2020).

[ADS](#) [CAS](#) [PubMed](#) [PubMed Central](#) [Google Scholar](#)

12. 12.

Hu, M. G. et al. Direct observation of bimolecular reactions of ultracold KRb molecules. *Science* **366**, 1111–1115 (2019).

[ADS](#) [CAS](#) [PubMed](#) [PubMed Central](#) [Google Scholar](#)

13. 13.

Kirste, M. et al. Quantum-state resolved bimolecular collisions of velocity-controlled OH with NO radicals. *Science* **338**, 1060–1063 (2012).

[ADS](#) [CAS](#) [PubMed](#) [PubMed Central](#) [Google Scholar](#)

14. 14.

Christianen, A., Zwierlein, M. W., Groenenboom, G. C. & Karman, T. Photoinduced two-body loss of ultracold molecules. *Phys. Rev. Lett.* **123**, 123402 (2019).

[ADS](#) [CAS](#) [PubMed](#) [PubMed Central](#) [Google Scholar](#)

15. 15.

Danzl, J. G. et al. Quantum gas of deeply bound ground state molecules. *Science* **321**, 1062–1066 (2008).

[ADS](#) [CAS](#) [PubMed](#) [PubMed Central](#) [Google Scholar](#)

16. 16.

Seßelberg, F. et al. Extending rotational coherence of interacting polar molecules in a spin-decoupled magic trap. *Phys. Rev. Lett.* **121**, 253401 (2018).

[ADS](#) [PubMed](#) [PubMed Central](#) [Google Scholar](#)

17. 17.

Will, S. A., Park, J. W., Yan, Z. Z., Loh, H. & Zwierlein, M. W. Coherent microwave control of ultracold $^{23}\text{Na}^{40}\text{K}$ molecules. *Phys. Rev. Lett.* **116**, 225306 (2016).

[ADS](#) [PubMed](#) [PubMed Central](#) [Google Scholar](#)

18. 18.

Barry, J. F., McCarron, D. J., Norrgard, E. B., Steinecker, M. H. & Demille, D. Magneto-optical trapping of a diatomic molecule. *Nature* **512**, 286–289 (2014).

[ADS](#) [CAS](#) [PubMed](#) [PubMed Central](#) [Google Scholar](#)

19. 19.

Truppe, S. et al. Molecules cooled below the Doppler limit. *Nat. Phys.* **13**, 1173–1176 (2017).

[CAS](#) [Google Scholar](#)

20. 20.

Anderegg, L. et al. An optical tweezer array of ultracold molecules. *Science* **365**, 1156–1158 (2019).

[ADS](#) [CAS](#) [PubMed](#) [PubMed Central](#) [Google Scholar](#)

21. 21.

Ding, S., Wu, Y., Finneran, I. A., Burau, J. J. & Ye, J. Sub-Doppler cooling and compressed trapping of YO molecules at μ K temperatures. *Phys. Rev. X* **10**, 021049 (2020).

[CAS](#) [Google Scholar](#)

22. 22.

Yang, H. et al. Observation of magnetically tunable Feshbach resonances in ultracold $^{23}\text{Na}^{40}\text{K} + ^{40}\text{K}$ collisions. *Science* **363**, 261–264 (2019).

[ADS](#) [CAS](#) [PubMed](#) [PubMed Central](#) [Google Scholar](#)

23. 23.

Son, H., Park, J. J., Ketterle, W. & Jamison, A. O. Collisional cooling of ultracold molecules. *Nature* **580**, 197–200 (2020).

[ADS](#) [CAS](#) [PubMed](#) [PubMed Central](#) [Google Scholar](#)

24. 24.

Segev, Y. et al. Collisions between cold molecules in a superconducting magnetic trap. *Nature* **572**, 189–193 (2019).

[ADS](#) [CAS](#) [PubMed](#) [PubMed Central](#) [Google Scholar](#)

25. 25.

Baranov, M. A., Dalmonte, M., Pupillo, G. & Zoller, P. Condensed matter theory of dipolar quantum gases. *Chem. Rev.* **112**, 5012–5061 (2012).

[CAS](#) [PubMed](#) [PubMed Central](#) [Google Scholar](#)

26. 26.

Aikawa, K. et al. Reaching Fermi degeneracy via universal dipolar scattering. *Phys. Rev. Lett.* **112**, 010404 (2014).

[ADS](#) [CAS](#) [PubMed](#) [PubMed Central](#) [Google Scholar](#)

27. 27.

DeMarco, B. & Jin, D. S. Onset of Fermi degeneracy in a trapped atomic gas. *Science* **285**, 1703–1706 (1999).

[CAS](#) [PubMed](#) [PubMed Central](#) [Google Scholar](#)

28. 28.

Quéméner, G. & Bohn, J. L. Dynamics of ultracold molecules in confined geometry and electric field. *Phys. Rev. A* **83**, 012705 (2011).

[ADS](#) [Google Scholar](#)

29. 29.

Micheli, A. et al. Universal rates for reactive ultracold polar molecules in reduced dimensions. *Phys. Rev. Lett.* **105**, 073202 (2010).

[ADS](#) [PubMed](#) [PubMed Central](#) [Google Scholar](#)

30. 30.

Zhu, B., Quéméner, G., Rey, A. M. & Holland, M. J. Evaporative cooling of reactive polar molecules confined in a two-dimensional geometry. *Phys. Rev. A* **88**, 063405 (2013).

[ADS](#) [Google Scholar](#)

31. 31.

de Miranda, M. H. G. et al. Controlling the quantum stereodynamics of ultracold bimolecular reactions. *Nat. Phys.* **7**, 502–507 (2011).

[Google Scholar](#)

32. 32.

Covey, J. P. *Enhanced Optical and Electric Manipulation of a Quantum Gas of KRb Molecules*. Thesis, Univ. Colorado,
<https://doi.org/10.1007/978-3-319-98107-9> (2018).

33. 33.

Shvarchuck, I. et al. Bose–einstein condensation into nonequilibrium states studied by condensate focusing. *Phys. Rev. Lett.* **89**, 270404 (2002).

[CAS Google Scholar](#)

34. 34.

Hueck, K. et al. Two-dimensional homogeneous Fermi gases. *Phys. Rev. Lett.* **120**, 060402 (2018).

[ADS](#) [CAS](#) [PubMed](#) [PubMed Central](#) [Google Scholar](#)

35. 35.

Ni, K.-K. et al. A high phase-space-density gas of polar molecules. *Science* **322**, 231–235 (2008).

[ADS](#) [CAS](#) [Google Scholar](#)

36. 36.

Quéméner, G. & Bohn, J. L. Strong dependence of ultracold chemical rates on electric dipole moments. *Phys. Rev. A* **81**, 022702 (2010).

[ADS](#) [Google Scholar](#)

37. 37.

Bohn, J. L., Cavagnero, M. & Ticknor, C. Quasi-universal dipolar scattering in cold and ultracold gases. *New J. Phys.* **11**, 055039 (2009).

[ADS](#) [Google Scholar](#)

38. 38.

Ticknor, C. Quasi-two-dimensional dipolar scattering. *Phys. Rev. A* **81**, 042708 (2010).

[ADS](#) [Google Scholar](#)

39. 39.

Bohn, J. L. & Jin, D. S. Differential scattering and rethermalization in ultracold dipolar gases. *Phys. Rev. A* **89**, 022702 (2014).

[ADS](#) [Google Scholar](#)

40. 40.

Aikawa, K. et al. Anisotropic relaxation dynamics in a dipolar Fermi gas driven out of equilibrium. *Phys. Rev. Lett.* **113**, 263201 (2014).

[ADS](#) [CAS](#) [PubMed](#) [PubMed Central](#) [Google Scholar](#)

41. 41.

Babadi, M. & Demler, E. Collective excitations of quasi-two-dimensional trapped dipolar fermions: transition from collisionless to hydrodynamic regime. *Phys. Rev. A* **86**, 063638 (2012).

[ADS](#) [Google Scholar](#)

42. 42.

Giorgini, S., Pitaevskii, L. P. & Stringari, S. Theory of ultracold atomic Fermi gases. *Rev. Mod. Phys.* **80**, 1215 (2008).

[ADS](#) [CAS](#) [Google Scholar](#)

43. 43.

Büchler, H. P. et al. Strongly correlated 2D quantum phases with cold polar molecules: controlling the shape of the interaction potential. *Phys. Rev. Lett.* **98**, 060404 (2007).

[ADS](#) [PubMed](#) [PubMed Central](#) [Google Scholar](#)

44. 44.

Góral, K., Santos, L. & Lewenstein, M. Quantum phases of dipolar bosons in optical lattices. *Phys. Rev. Lett.* **88**, 170406 (2002).

[ADS](#) [PubMed](#) [PubMed Central](#) [Google Scholar](#)

45. 45.

Capogrosso-Sansone, B., Trefzger, C., Lewenstein, M., Zoller, P. & Pupillo, G. Quantum phases of cold polar molecules in 2D optical lattices. *Phys. Rev. Lett.* **104**, 125301 (2010).

[ADS](#) [CAS](#) [PubMed](#) [PubMed Central](#) [Google Scholar](#)

46. 46.

Cooper, N. R. & Shlyapnikov, G. V. Stable topological superfluid phase of ultracold polar fermionic molecules. *Phys. Rev. Lett.* **103**, 155302 (2009).

[ADS](#) [CAS](#) [PubMed](#) [PubMed Central](#) [Google Scholar](#)

47. 47.

Gorshkov, A. V. et al. Tunable superfluidity and quantum magnetism with ultracold polar molecules. *Phys. Rev. Lett.* **107**, 115301 (2011).

[ADS](#) [PubMed](#) [PubMed Central](#) [Google Scholar](#)

48. 48.

Potter, A. C., Berg, E., Wang, D. W., Halperin, B. I. & Demler, E. Superfluidity and dimerization in a multilayered system of fermionic polar molecules. *Phys. Rev. Lett.* **105**, 220406 (2010).

[ADS](#) [PubMed](#) [PubMed Central](#) [Google Scholar](#)

49. 49.

Yao, N. Y. et al. Many-body localization in dipolar systems. *Phys. Rev. Lett.* **113**, 243002 (2014).

[ADS](#) [CAS](#) [PubMed](#) [PubMed Central](#) [Google Scholar](#)

50. 50.

Barbiero, L., Menotti, C., Recati, A. & Santos, L. Out-of-equilibrium states and quasi-many-body localization in polar lattice gases. *Phys. Rev. B* **92**, 180406 (2015).

[ADS](#) [Google Scholar](#)

51. 51.

Zinner, N. T. & Bruun, G. M. Density waves in layered systems with fermionic polar molecules. *Eur. Phys. J. D* **65**, 133–139 (2011).

[ADS](#) [CAS](#) [Google Scholar](#)

52. 52.

Peter, D., Müller, S., Wessel, S. & Büchler, H. P. Anomalous behavior of spin systems with dipolar interactions. *Phys. Rev. Lett.* **109**, 025303 (2012).

[ADS](#) [CAS](#) [PubMed](#) [PubMed Central](#) [Google Scholar](#)

53. 53.

Dalfovo, F., Giorgini, S., Pitaevskii, L. P. & Stringari, S. Theory of Bose–Einstein condensation in trapped gases. *Rev. Mod. Phys.* **71**, 463–512 (1999).

[ADS](#) [CAS](#) [Google Scholar](#)

54. 54.

Inguscio, M., Ketterle, W. & Salomon, C. Ultra-cold Fermi gases. In *Proceedings of the International School of Physics ‘Enrico Fermi’* (2007).

[Download references](#)

Acknowledgements

We acknowledge funding from NIST, DARPA DRINQS, ARO MURI and NSF Phys-1734006. We thank J. L. Bohn, A. M. Kaufman, and C. Miller for careful reading of the manuscript and T. Brown for technical assistance.

Author information

Affiliations

1. JILA, National Institute of Standards and Technology, Boulder, CO, USA

Giacomo Valtolina, Kyle Matsuda, William G. Tobias, Jun-Ru Li, Luigi De Marco & Jun Ye

2. Department of Physics, University of Colorado, Boulder, CO, USA

Giacomo Valtolina, Kyle Matsuda, William G. Tobias, Jun-Ru Li, Luigi De Marco & Jun Ye

Authors

1. Giacomo Valtolina

[View author publications](#)

You can also search for this author in [PubMed](#) [Google Scholar](#)

2. Kyle Matsuda

[View author publications](#)

You can also search for this author in [PubMed](#) [Google Scholar](#)

3. William G. Tobias

[View author publications](#)

You can also search for this author in [PubMed](#) [Google Scholar](#)

4. Jun-Ru Li

[View author publications](#)

You can also search for this author in [PubMed](#) [Google Scholar](#)

5. Luigi De Marco

[View author publications](#)

You can also search for this author in [PubMed](#) [Google Scholar](#)

6. Jun Ye

[View author publications](#)

You can also search for this author in [PubMed](#) [Google Scholar](#)

Contributions

All authors contributed to carrying out the experiments, interpreting the results, and writing the manuscript.

Corresponding authors

Correspondence to [Giacomo Valtolina](#) or [Jun Ye](#).

Ethics declarations

Competing interests

The authors declare no competing interests.

Additional information

Peer review information *Nature* thanks Georgy Shlyapnikov and the other, anonymous, reviewer(s) for their contribution to the peer review of this work.

Publisher's note Springer Nature remains neutral with regard to jurisdictional claims in published maps and institutional affiliations.

Extended data figures and tables

Extended Data Fig. 1 Layer occupancy.

Histogram of the average number per layer (relative population) for the data shown in Fig. 1c.

Extended Data Fig. 2 Trend of $\omega_x/(2\pi)$ versus y .

Grey points are the experimental measurements at $E_{DC} = 5 \text{ kV cm}^{-1}$, the solid grey line is a linear fit to guide the eye, and the dashed line is the prediction (Sim) from the finite-element model. All error bars are 1 standard deviation of the mean.

Extended Data Fig. 3 Evaporation sequence.

a, Ramp in E_{DC} . **b**, Ramp in y . **c**, Trap depth versus time from the finite-element model of electro-optical potential. **d**, Evolution of η , calculated by taking the ratio of the trap depth and temperature at each time point. **e**,

Evolution of T/T_F during the ramp. All error bars are 1 standard error of the mean.

Extended Data Fig. 4 Fermi gas thermometry.

Trend of $T_{\text{out}}/T_{\text{rel}}$ as a function of the excluded region from the centre of the Gaussian fit for $T/T_F = 0.81(15)$ (orange diamonds) and $T/T_F = 2.0(1)$ (black circles). Solid lines are Gaussian fits to simulated density profiles for $T/T_F = 2.0$ (black) and $T/T_F = 0.8$ (orange). All error bars are 1 standard error of the mean.

Rights and permissions

Reprints and Permissions

About this article



Check for
updates

Cite this article

Valtolina, G., Matsuda, K., Tobias, W.G. *et al.* Dipolar evaporation of reactive molecules to below the Fermi temperature. *Nature* **588**, 239–243 (2020). <https://doi.org/10.1038/s41586-020-2980-7>

Download citation

- Received: 20 July 2020
- Accepted: 29 September 2020
- Published: 09 December 2020

- Issue Date: 10 December 2020
- DOI: <https://doi.org/10.1038/s41586-020-2980-7>

Comments

By submitting a comment you agree to abide by our [Terms](#) and [Community Guidelines](#). If you find something abusive or that does not comply with our terms or guidelines please flag it as inappropriate.

[Access through your institution](#)

[Change institution](#)

[Buy or subscribe](#)

This article was downloaded by **calibre** from <https://www.nature.com/articles/s41586-020-2980-7>

| [Section menu](#) | [Main menu](#) |

- Article
- [Published: 09 December 2020](#)

Operation of an optical atomic clock with a Brillouin laser subsystem

- [William Loh](#) [ORCID: orcid.org/0000-0003-1912-6095^{1 na1}](#),
- [Jules Stuart^{1,2 na1}](#),
- [David Reens](#) [ORCID: orcid.org/0000-0002-3317-2402¹](#),
- [Colin D. Bruzewicz¹](#),
- [Danielle Braje¹](#),
- [John Chiaverini](#) [ORCID: orcid.org/0000-0001-7123-8460¹](#),
- [Paul W. Juodawlkis¹](#),
- [Jeremy M. Sage](#) [ORCID: orcid.org/0000-0001-8180-0525^{1,2}](#) &
- [Robert McConnell¹](#)

[Nature](#) volume 588, pages244–249(2020)[Cite this article](#)

- 1 Altmetric
- [Metrics details](#)

Subjects

- [Atom optics](#)

Abstract

Microwave atomic clocks have traditionally served as the ‘gold standard’ for precision measurements of time and frequency. However, over the past

decade, optical atomic clocks^{1,2,3,4,5,6} have surpassed the precision of their microwave counterparts by two orders of magnitude or more. Extant optical clocks occupy volumes of more than one cubic metre, and it is a substantial challenge to enable these clocks to operate in field environments, which requires the ruggedization and miniaturization of the atomic reference and clock laser along with their supporting lasers and electronics^{4,7,8,9}. In terms of the clock laser, prior laboratory demonstrations of optical clocks have relied on the exceptional performance gained through stabilization using bulk cavities, which unfortunately necessitates the use of vacuum and also renders the laser susceptible to vibration-induced noise. Here, using a stimulated Brillouin scattering laser subsystem that has a reduced cavity volume and operates without vacuum, we demonstrate a promising component of a portable optical atomic clock architecture. We interrogate a $^{88}\text{Sr}^+$ ion with our stimulated Brillouin scattering laser and achieve a clock exhibiting short-term stability of 3.9×10^{-14} over one second—an improvement of an order of magnitude over state-of-the-art microwave clocks. This performance increase within a potentially portable system presents a compelling avenue for substantially improving existing technology, such as the global positioning system, and also for enabling the exploration of topics such as geodetic measurements of the Earth, searches for dark matter and investigations into possible long-term variations of fundamental physics constants^{10,11,12}.

[Access through your institution](#)

[Change institution](#)

[Buy or subscribe](#)

Access options

Subscribe to Journal

Get full journal access for 1 year

185,98 €

only 3,58 € per issue

Subscribe

All prices are NET prices.
VAT will be added later in the checkout.

Rent or Buy article

Get time limited or full article access on ReadCube.

from \$8.99

Rent or Buy

All prices are NET prices.

Additional access options:

- [Log in](#)
- [Access through your institution](#)
- [Learn about institutional subscriptions](#)

Fig. 1: SBS laser setup and stabilization scheme.

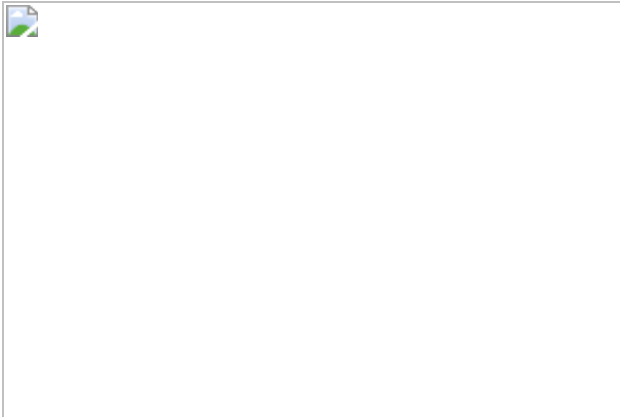


Fig. 2: SBS laser drift cancellation procedure.



Fig. 3: SBS laser subsystem stabilization.



Fig. 4: SBS laser optical clock.



Data availability

The datasets that support this study are available from the corresponding author on reasonable request.

Code availability

The codes used for analysis and simulations are available from the corresponding author on reasonable request.

References

1. 1.

Hinkley, N. et al. An atomic clock with 10^{-18} instability. *Science* **341**, 1215–1218 (2013).

[ADS](#) [CAS](#) [PubMed](#) [PubMed Central](#) [Google Scholar](#)

2. 2.

Bloom, B. J. et al. An optical lattice clock with accuracy and stability at the 10^{-18} level. *Nature* **506**, 71–75 (2014).

[ADS](#) [CAS](#) [PubMed](#) [PubMed Central](#) [Google Scholar](#)

3. 3.

Brewer, S. M. et al. $^{27}\text{Al}^+$ quantum-logic clock with a systematic uncertainty below 10^{-18} . *Phys. Rev. Lett.* **123**, 033201 (2019).

[ADS](#) [CAS](#) [PubMed](#) [PubMed Central](#) [Google Scholar](#)

4. 4.

Koller, S. B. et al. Transportable optical lattice clock with 7×10^{-17} uncertainty. *Phys. Rev. Lett.* **118**, 073601 (2017).

[ADS](#) [CAS](#) [PubMed](#) [PubMed Central](#) [Google Scholar](#)

5. 5.

Godun, R. M. et al. Frequency ratio of two optical clock transitions in $^{171}\text{Yb}^+$ and constraints on the time variation of fundamental constants. *Phys. Rev. Lett.* **113**, 210801 (2014).

[ADS](#) [CAS](#) [Google Scholar](#)

6. 6.

Huntemann, N., Sanner, C., Lipphardt, B., Tamm, Chr. & Peik, E. Single-ion atomic clock with 3×10^{-18} systematic uncertainty. *Phys. Rev. Lett.* **116**, 063001 (2016).

[ADS](#) [CAS](#) [PubMed](#) [PubMed Central](#) [Google Scholar](#)

7. 7.

Leibrandt, D. R., Thorpe, M. J., Bergquist, J. C. & Rosenband, T. Field-test of a robust, portable, frequency-stable laser. *Opt. Express* **19**, 10278–10286 (2011).

[ADS](#) [Google Scholar](#)

8. 8.

Liu, L. et al. In-orbit operation of an atomic clock based on laser-cooled ^{87}Rb . *Nat. Commun.* **9**, 2760 (2018).

[ADS](#) [PubMed](#) [PubMed Central](#) [Google Scholar](#)

9. 9.

Takamoto, M. et al. Test of general relativity by a pair of transportable optical lattice clocks. *Nat. Photon.* **14**, 411–415 (2020).

[ADS](#) [CAS](#) [Google Scholar](#)

10. 10.

Maleki, L. & Prestage, J. Applications of clocks and frequency standards: from the routine to tests of fundamental models. *Metrologia* **42**, S145–S153 (2005).

[ADS](#) [Google Scholar](#)

11. 11.

Ludlow, A. D., Boyd, M. M., Ye, J., Peik, E. & Schmidt, P. O. Optical atomic clocks. *Rev. Mod. Phys.* **87**, 637–701 (2015).

[ADS](#) [CAS](#) [Google Scholar](#)

12. 12.

McGrew, W. F. et al. Atomic clock performance enabling geodesy below the centimetre level. *Nature* **564**, 87–90 (2018).

[ADS](#) [CAS](#) [Google Scholar](#)

13. 13.

Young, B. C., Cruz, F. C., Itano, W. M. & Bergquist, J. C. Visible lasers with subhertz linewidths. *Phys. Rev. Lett.* **82**, 3799–3802 (1999).

[ADS](#) [CAS](#) [Google Scholar](#)

14. 14.

Jiang, Y. Y. et al. Making optical atomic clocks more stable with 10^{-16} -level laser stabilization. *Nat. Photon.* **5**, 158–161 (2011).

[ADS](#) [CAS](#) [Google Scholar](#)

15. 15.

Kessler, T. et al. A sub-40-mHz-linewidth laser based on a silicon single-crystal optical cavity. *Nat. Photon.* **6**, 687–692 (2012).

[ADS](#) [CAS](#) [Google Scholar](#)

16. 16.

Davila-Rodriguez, J. et al. Compact, thermal-noise-limited reference cavity for ultra-low-noise microwave generation. *Opt. Lett.* **42**, 1277–1280 (2017).

[ADS](#) [CAS](#) [Google Scholar](#)

17. 17.

Didier, A. et al. Ultracompact reference ultralow expansion glass cavity. *Appl. Opt.* **57**, 6470–6473 (2018).

[ADS](#) [CAS](#) [Google Scholar](#)

18. 18.

Grudinin, I. S., Matsko, A. B. & Maleki, L. Brillouin lasing with a CaF₂ whispering gallery mode resonator. *Phys. Rev. Lett.* **102**, 043902 (2009).

[ADS](#) [Google Scholar](#)

19. 19.

Lee, H. et al. Chemically etched ultrahigh-Q wedge-resonator on a silicon chip. *Nat. Photon.* **6**, 369–373 (2012).

[ADS](#) [CAS](#) [Google Scholar](#)

20. 20.

Kabakova, I. V. et al. Narrow linewidth Brillouin laser based on chalcogenide photonic chip. *Opt. Lett.* **38**, 3208–3211 (2013).

[ADS](#) [CAS](#) [Google Scholar](#)

21. 21.

Loh, W. et al. Dual-microcavity narrow-linewidth Brillouin laser. *Optica* **2**, 225–232 (2015).

[ADS](#) [CAS](#) [Google Scholar](#)

22. 22.

Otterstrom, N. T., Behunin, R. O., Kittlaus, E. A., Wang, Z. & Rakich, P. T. A silicon Brillouin laser. *Science* **360**, 1113–1116 (2018).

[ADS](#) [MathSciNet](#) [CAS](#) [MATH](#) [Google Scholar](#)

23. 23.

Gundavarapu, S. et al. Sub-hertz fundamental linewidth photonic integrated Brillouin laser. *Nat. Photon.* **13**, 60–67 (2019).

[ADS](#) [CAS](#) [Google Scholar](#)

24. 24.

Geng, J. et al. Highly stable low-noise Brillouin fiber laser with ultranarrow spectral linewidth. *IEEE Photonics Technol. Lett.* **18**, 1813–1815 (2006).

[ADS](#) [Google Scholar](#)

25. 25.

Shee, Y. G., Al-Mansoori, M. H., Ismail, A., Hitam, S. & Mahdi, M. A. Multiwavelength Brillouin-erbium fiber laser with double-Brillouin-frequency spacing. *Opt. Express* **19**, 1699–1706 (2011).

[ADS](#) [CAS](#) [Google Scholar](#)

26. 26.

Tow, K. H. et al. Linewidth-narrowing and intensity noise reduction of the 2nd order Stokes component of a low threshold Brillouin laser made of $\text{Ge}_{10}\text{As}_{22}\text{Se}_{68}$ chalcogenide fiber. *Opt. Express* **20**, B104–B109 (2012).

[CAS](#) [Google Scholar](#)

27. 27.

Debut, A., Randoux, S. & Zemmouri, J. Linewidth narrowing in Brillouin lasers: theoretical analysis. *Phys. Rev. A* **62**, 023803 (2000).

[ADS](#) [Google Scholar](#)

28. 28.

Loh, W., Yegnanarayanan, S., O'Donnell, F. & Juodawlkis, P. W. Ultra-narrow linewidth Brillouin laser with nanokelvin temperature self-referencing. *Optica* **6**, 152–159 (2019).

[ADS](#) [CAS](#) [Google Scholar](#)

29. 29.

Jefferts, S. R., Meekhof, D. M., Shirley, J. H., Stepanovic, M. & Parker, T. E. Accuracy results from NIST-F1 laser-cooled cesium primary frequency standard. In *Proc. IEEE/EIA Int. Frequency Control Symposium and Exhibition* 714–717 (IEEE, 2000).

30. 30.

Madej, A. A., Dubé, P., Zhou, Z., Bernard, J. E. & Gertsvolf, M. $^{88}\text{Sr}^+$ 445-THz single-ion reference at the 10^{-17} level via control and cancellation of systematic uncertainties and its measurement against the SI second. *Phys. Rev. Lett.* **109**, 203002 (2012).

[ADS](#) [PubMed](#) [PubMed Central](#) [Google Scholar](#)

31. 31.

Strelkov, D. V., Thompson, R. J., Baumgartel, L. M., Grudinin, I. S. & Yu, N. Temperature measurement and stabilization in a birefringent whispering gallery mode resonator. *Opt. Express* **19**, 14495–14501 (2011).

[ADS](#) [CAS](#) [PubMed](#) [PubMed Central](#) [Google Scholar](#)

32. 32.

Fescenko, I. et al. Dual-mode temperature compensation technique for laser stabilization to a crystalline whispering gallery mode resonator. *Opt. Express* **20**, 19185–19193 (2012).

[ADS](#) [CAS](#) [PubMed](#) [PubMed Central](#) [Google Scholar](#)

33. 33.

Weng, W. et al. Nanokelvin thermometry and temperature control: beyond the thermal noise limit. *Phys. Rev. Lett.* **112**, 160801 (2014).

[ADS](#) [PubMed](#) [PubMed Central](#) [Google Scholar](#)

34. 34.

Lim, J. et al. Probing 10 μK stability and residual drifts in the cross-polarization dual-mode stabilization of single-crystal ultrahigh- Q optical resonators. *Light Sci. Appl.* **8**, 1 (2019).

[ADS](#) [PubMed](#) [PubMed Central](#) [Google Scholar](#)

35. 35.

Drever, R. W. P. et al. Laser phase and frequency stabilization using an optical resonator. *Appl. Phys. B* **31**, 97–105 (1983).

[ADS](#) [Google Scholar](#)

36. 36.

Storz, R., Braxmaier, C., Jäck, K., Pradl, O. & Schiller, S. Ultrahigh long-term dimensional stability of a sapphire cryogenic optical resonator. *Opt. Lett.* **23**, 1031–1033 (1998).

[ADS](#) [CAS](#) [PubMed](#) [PubMed Central](#) [Google Scholar](#)

37. 37.

Bruzewicz, C. D., McConnell, R., Chiaverini, J. & Sage, J. M. Scalable loading of a two-dimensional trapped-ion array. *Nat. Commun.* **7**, 13005 (2016).

[ADS](#) [CAS](#) [PubMed](#) [PubMed Central](#) [Google Scholar](#)

38. 38.

Wang, S. X., Labaziewicz, J., Ge, Y., Shewmon, R. & Chuang, I. L. Demonstration of a quantum logic gate in a cryogenic surface-electrode ion trap. *Phys. Rev. A* **81**, 062332 (2010).

[ADS](#) [Google Scholar](#)

39. 39.

Ma, L. S., Junger, P., Ye, J. & Hall, J. L. Delivering the same optical frequency at two places: accurate cancellation of phase noise introduced by an optical fiber or other time-varying path. *Opt. Lett.* **19**, 1777–1779 (1994).

[ADS](#) [CAS](#) [PubMed](#) [PubMed Central](#) [Google Scholar](#)

40. 40.

Nicholson, T. L. et al. Comparison of two independent Sr optical clocks with 1×10^{-17} stability at 10^3 s. *Phys. Rev. Lett.* **109**, 230801

(2012).

[ADS](#) [CAS](#) [Google Scholar](#)

41. 41.

Nicholson, T. L. et al. Systematic evaluation of an atomic clock at 2×10^{-18} uncertainty. *Nat. Commun.* **6**, 6896 (2015).

[ADS](#) [CAS](#) [PubMed](#) [PubMed Central](#) [Google Scholar](#)

42. 42.

Dubé, P. et al. Electric quadrupole shift cancellation in single-ion optical frequency standards. *Phys. Rev. Lett.* **95**, 033001 (2005).

[ADS](#) [Google Scholar](#)

43. 43.

Spencer, D. T. et al. An optical frequency synthesizer using integrated photonics. *Nature* **557**, 81–85 (2018).

[ADS](#) [CAS](#) [Google Scholar](#)

44. 44.

Liang, W. et al. Ultralow noise miniature external cavity semiconductor laser. *Nat. Commun.* **6**, 7371 (2015).

[ADS](#) [CAS](#) [PubMed](#) [PubMed Central](#) [Google Scholar](#)

45. 45.

Zhang, W. et al. Ultranarrow linewidth photonic-atomic laser. *Laser Photonics Rev.* **14**, 1900293 (2020).

[ADS](#) [CAS](#) [Google Scholar](#)

46. 46.

Howe, D. A. The total deviation approach to long-term characterization of frequency stability. *IEEE Trans. Ultrason. Ferroelectr. Freq. Control* **47**, 1102–1110 (2000).

[CAS](#) [Google Scholar](#)

47. 47.

Chang, L. et al. Heterogeneous integration of lithium niobate and silicon nitride waveguides for wafer-scale photonic integrated circuits on silicon. *Opt. Lett.* **42**, 803–806 (2017).

[ADS](#) [CAS](#) [Google Scholar](#)

48. 48.

Hjelme, D. R., Mickelson, A. R. & Beausoleil, R. G. Semiconductor laser stabilization by external optical feedback. *IEEE J. Quantum Electron.* **27**, 352–372 (1991).

[ADS](#) [CAS](#) [Google Scholar](#)

49. 49.

Akerman, N., Navon, N., Kotler, S., Glickman, Y. & Ozeri, R. Universal gate-set for trapped-ion qubits using a narrow linewidth diode laser. *New J. Phys.* **17**, 113060 (2015).

[ADS](#) [Google Scholar](#)

50. 50.

Cummins, H. K., Llewellyn, G. & Jones, J. A. Tackling systematic errors in quantum logic gates with composite rotations. *Phys. Rev. A* **67**, 042308 (2003).

[ADS](#) [Google Scholar](#)

[Download references](#)

Acknowledgements

We thank A. Libson, G. N. West and I. L. Chuang for helpful discussions. This work was sponsored by the Under Secretary of Defense for Research and Engineering under Air Force contract number FA8721-05-C-0002. Opinions, interpretations, conclusions and recommendations are those of the authors and are not necessarily endorsed by the US Government.

Author information

Author notes

1. These authors contributed equally: William Loh, Jules Stuart

Affiliations

1. Lincoln Laboratory, Massachusetts Institute of Technology, Lexington, MA, USA

William Loh, Jules Stuart, David Reens, Colin D. Bruzewicz, Danielle Braje, John Chiaverini, Paul W. Juodawlkis, Jeremy M. Sage & Robert McConnell

2. Department of Physics, Massachusetts Institute of Technology, Cambridge, MA, USA

Jules Stuart & Jeremy M. Sage

Authors

1. William Loh

[View author publications](#)

You can also search for this author in [PubMed](#) [Google Scholar](#)

2. Jules Stuart

[View author publications](#)

You can also search for this author in [PubMed](#) [Google Scholar](#)

3. David Reens

[View author publications](#)

You can also search for this author in [PubMed](#) [Google Scholar](#)

4. Colin D. Bruzewicz

[View author publications](#)

You can also search for this author in [PubMed](#) [Google Scholar](#)

5. Danielle Braje

[View author publications](#)

You can also search for this author in [PubMed](#) [Google Scholar](#)

6. John Chiaverini

[View author publications](#)

You can also search for this author in [PubMed](#) [Google Scholar](#)

7. Paul W. Juodawlkis

[View author publications](#)

You can also search for this author in [PubMed](#) [Google Scholar](#)

8. Jeremy M. Sage

[View author publications](#)

You can also search for this author in [PubMed](#) [Google Scholar](#)

9. Robert McConnell

[View author publications](#)

You can also search for this author in [PubMed](#) [Google Scholar](#)

Contributions

W.L., J.S. and R.M. conceived, designed and carried out the experiments with the SBS laser. W.L., J.S., D.R. and R.M. conceived, designed and carried out the experiments with the clock protocol. All authors discussed the results and contributed to the manuscript.

Corresponding author

Correspondence to [William Loh](#).

Ethics declarations

Competing interests

The authors declare no competing interests.

Additional information

Peer review information *Nature* thanks Clément Lacroûte and the other, anonymous, reviewer(s) for their contribution to the peer review of this work.

Publisher's note Springer Nature remains neutral with regard to jurisdictional claims in published maps and institutional affiliations.

Extended data figures and tables

[Extended Data Fig. 1 SBS laser noise.](#)

Shown is the measurement of the 674-nm SBS laser subsystem's frequency noise before and after the application of feedforward stabilization. The SBS laser subsystem features a white noise floor of $3 \text{ Hz}^2 \text{ Hz}^{-1}$ before feedforward and a gradual increase in noise at lower offset frequencies. An integration over the noise spectral density yields a full-width at half-

maximum linewidth of 45 Hz, while a calculation of the white-noise limited linewidth at large offset frequencies yields 9 Hz. With feedforward turned on, the SBS laser subsystem's noise increases slightly and exhibits additional noise peaks that arise from the RF signal generator used for feedforward correction. The integrated linewidth increases to 51 Hz.

Extended Data Fig. 2 Optimization of feedforward stabilization.

a, Measurement of the differential temperature sensitivity of the SBS resonator's two orthogonal-polarization modes. The linewidths of the modes are measured to be 1.2 MHz (blue arrows). For an applied temperature shift of $\Delta T = -0.25^\circ\text{C}$, the centre frequency at 1,348 nm changes by 490 MHz, while the mode separation (black arrows) changes by 11.9 MHz. This corresponds to a feedforward correction ratio of 40:1. **b**, Time series trace of the 1,348-nm SBS laser's frequency with the linear drift removed and the SBS amplitude unservoed. The lack of correspondence between the free-running SBS (red trace) and the polarization beat note ('Pol. beat $\times 39$ '; blue trace) indicates the inability to cancel frequency drift when amplitude noise is present.

Extended Data Fig. 3 Linear drift decay of SBS resonator.

Record of the SBS laser's linear drift at 1,348 nm for two resonators. The first resonator (red circles) is tracked over 79 days, and its linear drift decreases to a value of 200 Hz s^{-1} at the end of the elapsed period of time. The second resonator (blue squares) is tracked over 260 days and reaches a minimum of 30 Hz s^{-1} .

Extended Data Fig. 4 Determining and tracking linear drift.

a, Rabi spectroscopy of the $|5S_{1/2}, m_J = -1/2\rangle \rightarrow |4D_{5/2}, m_J = -3/2\rangle$ clock transition and the first-order motional sidebands at $v_{\text{clock}} \pm v_{\text{trap}}$ (blue and red sideband, respectively) is taken at regular intervals of approximately 25 s. After performing fits to the symmetric sidebands, we can average the two frequencies to obtain an accurate measure of the frequency of the

central feature. Only the spectroscopic data for the final experiment (black line) is shown; for all other datasets, the Gaussian peak fits to the sidebands (red and blue curves) are shown with progressively darkening colour to illustrate the movement of these features over time. For these data, an intentional linear drift of 5 kHz s^{-1} (at 674 nm; equivalently 2.5 kHz s^{-1} at 1,348 nm) was applied to demonstrate the efficacy of this method in cases of high drift, as in the initial few points shown in Extended Data Fig. 3. **b**, Rabi spectroscopy of the clock transition and sidebands after applying a linear drift correction to null out the natural drift of the resonator's frequency. Over the course of 20 min of measurements, very little deviation in the centre frequency is observed. **c**, Linear drift determined from the data presented in **b** and **c**. The linear drift can be obtained from a fit (lines) to the apparent frequency of the clock transition as a function of time (data points). In the first case, with the large drift intentionally applied to the laser frequency, we obtain a drift of 5.2 kHz s^{-1} (at 674 nm) from the fit (green line). After a few iterations of applying a correction and measuring the resulting drift, the drift is driven down to 17 Hz s^{-1} (blue line). **d**, Integrated clock correction signal applied to the laser to keep the frequency resonant with the atom's transition. In this case, we use a simplified clock protocol with an interrogation time of $\tau = 100 \mu\text{s}$ and no interleaving.

Extended Data Fig. 5 BCS laser $^{88}\text{Sr}^+$ ion clock.

Measured interleaved clock performance comprising a BCS laser locked to a $^{88}\text{Sr}^+$ ion operating with 1-ms interrogation time (blue points). The effective dead time is 4.7 ms. The blue points represent the frequency noise at a selection of averaging times, and the vertical blue bars indicate 1σ error. A fit (dashed line) to the data yields a stability of $\sqrt{(3.1 \times 10^{-14}) / \tau}$, which is slightly lower than the same clock operated with a SBS laser.

Extended Data Fig. 6 Schematic of interleaved clock protocol.

A pictorial representation of the interleaved clock procedure is shown. Here the Doppler segments represent the 700- μs duration in which the ion is Doppler cooled. During the OP segments, the ion undergoes 450 μs of

optical pumping in order to prepare the electron in the lower level of the clock transition. The ‘Interrogate’ segments are each 1 ms of interrogation time, bounded by composite $\pi/2$ pulses. Last, the ‘Detect’ segments are 700 μ s of detection time, during which the photons emitted by the ion are detected on a photomultiplier tube and counted by our timing controller. During the ‘Update’ segment, and depending on the number of photons collected, the state of the ion is determined, and the frequency of the clock is either increased or decreased. As discussed in the text, two separate clock signals, $f^{(1)}$ and $f^{(2)}$, are maintained; here these are indicated as Clock 1 and Clock 2. While the frequency of either clock is updated, the experiment begins to prepare the state for the next measurement, as indicated by the black arrows. Each of these clocks is sensitive to laser frequency fluctuation only during the 1 ms interrogation period of the total 5.7 ms cycle time; during all other times, the frequency of the laser must stay within the capture range of the lock.

[Extended Data Fig. 7 Numerical simulation of clock performance.](#)

The measured performance of the stabilized SBS laser (Allan deviation, red curve) is used as an input into a clock protocol simulation incorporating projection noise and dead time. The simulation accurately predicts the measured clock performance via the interleaved self-comparison (green squares) and predicts a single-clock stability of $(2.5 \times 10^{-14}) \sqrt{\tau}$ (blue circles).

Rights and permissions

[Reprints and Permissions](#)

About this article



Check for
updates

Cite this article

Loh, W., Stuart, J., Reens, D. *et al.* Operation of an optical atomic clock with a Brillouin laser subsystem. *Nature* **588**, 244–249 (2020).
<https://doi.org/10.1038/s41586-020-2981-6>

[Download citation](#)

- Received: 16 January 2020
- Accepted: 01 October 2020
- Published: 09 December 2020
- Issue Date: 10 December 2020
- DOI: <https://doi.org/10.1038/s41586-020-2981-6>

Comments

By submitting a comment you agree to abide by our [Terms](#) and [Community Guidelines](#). If you find something abusive or that does not comply with our terms or guidelines please flag it as inappropriate.

[Access through your institution](#)

[Change institution](#)

[Buy or subscribe](#)

This article was downloaded by **calibre** from <https://www.nature.com/articles/s41586-020-2981-6>

- Article
- [Published: 09 December 2020](#)

Capillary condensation under atomic-scale confinement

- [Qian Yang](#) [ORCID: orcid.org/0000-0002-6203-7867](#)^{1,2},
- [P. Z. Sun](#)^{1,2},
- [L. Fumagalli](#)²,
- [Y. V. Stebunov](#)²,
- [S. J. Haigh](#) [ORCID: orcid.org/0000-0001-5509-6706](#)³,
- [Z. W. Zhou](#)⁴,
- [I. V. Grigorieva](#) [ORCID: orcid.org/0000-0001-5991-7778](#)^{1,2},
- [F. C. Wang](#) [ORCID: orcid.org/0000-0002-5954-3881](#)^{1,5} &
- [A. K. Geim](#) [ORCID: orcid.org/0000-0003-2861-8331](#)^{1,2}

[Nature](#) volume 588, pages250–253(2020) [Cite this article](#)

- 143 Altmetric
- [Metrics details](#)

Subjects

- [Condensed-matter physics](#)
- [Nanoscale devices](#)
- [Two-dimensional materials](#)

Abstract

Capillary condensation of water is ubiquitous in nature and technology. It routinely occurs in granular and porous media, can strongly alter such

properties as adhesion, lubrication, friction and corrosion, and is important in many processes used by microelectronics, pharmaceutical, food and other industries^{1,2,3,4}. The century-old Kelvin equation⁵ is frequently used to describe condensation phenomena and has been shown to hold well for liquid menisci with diameters as small as several nanometres^{1,2,3,4,6,7,8,9,10,11,12,13,14}. For even smaller capillaries that are involved in condensation under ambient humidity and so of particular practical interest, the Kelvin equation is expected to break down because the required confinement becomes comparable to the size of water molecules^{1,2,3,4,5,6,7,8,9,10,11,12,13,14,15,16,17,18,19,20,21,22}. Here we use van der Waals assembly of two-dimensional crystals to create atomic-scale capillaries and study condensation within them. Our smallest capillaries are less than four ångströms in height and can accommodate just a monolayer of water. Surprisingly, even at this scale, we find that the macroscopic Kelvin equation using the characteristics of bulk water describes the condensation transition accurately in strongly hydrophilic (mica) capillaries and remains qualitatively valid for weakly hydrophilic (graphite) ones. We show that this agreement is fortuitous and can be attributed to elastic deformation of capillary walls^{23,24,25}, which suppresses the giant oscillatory behaviour expected from the commensurability between the atomic-scale capillaries and water molecules^{20,21}. Our work provides a basis for an improved understanding of capillary effects at the smallest scale possible, which is important in many realistic situations.

[Access through your institution](#)

[Change institution](#)

[Buy or subscribe](#)

Access options

Subscribe to Journal

Get full journal access for 1 year

185,98 €

only 3,58 € per issue

Subscribe

All prices are NET prices.
VAT will be added later in the checkout.

Rent or Buy article

Get time limited or full article access on ReadCube.

from \$8.99

Rent or Buy

All prices are NET prices.

Additional access options:

- [Log in](#)
- [Access through your institution](#)
- [Learn about institutional subscriptions](#)

Fig. 1: Atomic-scale capillaries and water condensation inside.

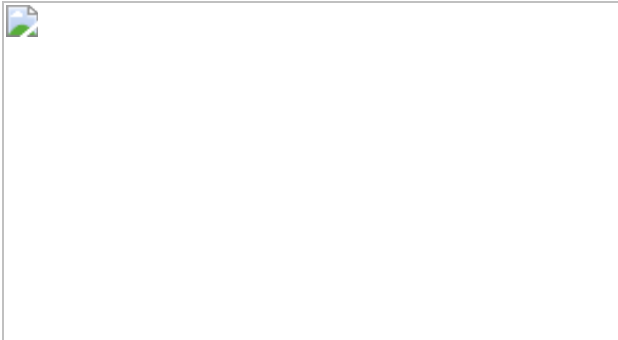
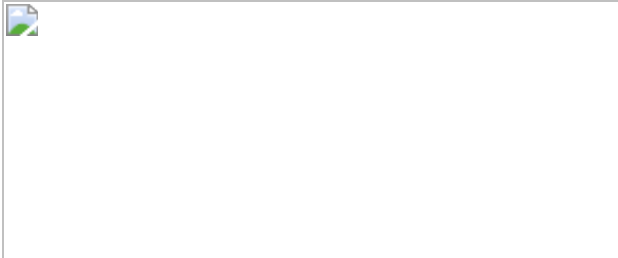


Fig. 2: Condensation transition under extreme 2D confinement.



Data availability

All the mentioned data to support this study and its conclusions are available upon request from Q.Y.

References

1. 1.

Charlaix, E. & Ciccotti, M. *Capillary Condensation in Confined Media* (CRC 2010).

2. 2.

van Honschoten, J. W., Brunets, N. & Tas, N. R. Capillarity at the nanoscale. *Chem. Soc. Rev.* **39**, 1096–1114 (2010).

[Google Scholar](#)

3. 3.

Malijevský, A. & Jackson, G. A perspective on the interfacial properties of nanoscopic liquid drops. *J. Phys. Condens. Matter* **24**, 464121 (2012).

[ADS](#) [Google Scholar](#)

4. 4.

Barsotti, E., Tan, S. P., Saraji, S., Piri, M. & Chen, J.-H. A review on capillary condensation in nanoporous media: implications for hydrocarbon recovery from tight reservoirs. *Fuel* **184**, 344–361 (2016).

[CAS](#) [Google Scholar](#)

5. 5.

Thomson, W. On the equilibrium of vapour at a curved surface of liquid. *Proc. R. Soc. Edinb.* **7**, 63–68 (1872).

[Google Scholar](#)

6. 6.

Aukett, P. N., Quirke, N., Riddiford, S. & Tennison, S. R. Methane adsorption on microporous carbons—a comparison of experiment, theory, and simulation. *Carbon* **30**, 913–924 (1992).

[CAS](#) [Google Scholar](#)

7. 7.

Fisher, L. R., Gamble, R. A. & Middlehurst, J. The Kelvin equation and the capillary condensation of water. *Nature* **290**, 575–576 (1981).

[ADS](#) [CAS](#) [Google Scholar](#)

8. 8.

Kohonen, M. M. & Christenson, H. K. Capillary condensation of water between rinsed mica surfaces. *Langmuir* **16**, 7285–7288 (2000).

[CAS](#) [Google Scholar](#)

9. 9.

Mitropoulos, A. Ch. The Kelvin equation. *J. Colloid Interface Sci.* **317**, 643–648 (2008).

[ADS](#) [CAS](#) [Google Scholar](#)

10. 10.

Zhong, J. et al. Capillary condensation in 8 nm deep channels. *J. Phys. Chem. Lett.* **9**, 497–503 (2018).

[CAS](#) [Google Scholar](#)

11. 11.

Yang, G., Chai, D., Fan, Z. & Li, X. Capillary condensation of single- and multicomponent fluids in nanopores. *Ind. Eng. Chem. Res.* **58**, 19302–19315 (2019).

[CAS](#) [Google Scholar](#)

12. 12.

Kim, S., Kim, D., Kim, J., An, S. & Jhe, W. Direct evidence for curvature-dependent surface tension in capillary condensation: Kelvin equation at molecular scale. *Phys. Rev. X* **8**, 041046 (2018).

[Google Scholar](#)

13. 13.

Gruener, S., Hofmann, T., Wallacher, D., Kityk, A. V. & Huber, P. Capillary rise of water in hydrophilic nanopores. *Phys. Rev. E* **79**, 067301 (2009).

[ADS](#) [Google Scholar](#)

14. 14.

Vincent, O., Marguet, B. & Stroock, A. D. Imbibition triggered by capillary condensation in nanopores. *Langmuir* **33**, 1655–1661 (2017).

[CAS](#) [Google Scholar](#)

15. 15.

Shin, D., Hwang, J. & Jhe, W. Ice-VII-like molecular structure of ambient water nanomeniscus. *Nat. Commun.* **10**, 286 (2019).

[ADS](#) [PubMed](#) [PubMed Central](#) [Google Scholar](#)

16. 16.

Verdaguer, A., Sacha, G. M., Bluhm, H. & Salmeron, M. Molecular structure of water at interfaces: wetting at the nanometer scale. *Chem. Rev.* **106**, 1478–1510 (2006).

[CAS](#) [Google Scholar](#)

17. 17.

Matsuoka, H., Fukui, S. & Kato, T. Nanomeniscus forces in undersaturated vapors: observable limit of macroscopic characteristics. *Langmuir* **18**, 6796–6801 (2002).

[CAS](#) [Google Scholar](#)

18. 18.

Powles, J. G. On the validity of the Kelvin equation. *J. Phys. Math. Gen.* **18**, 1551–1560 (1985).

[ADS](#) [CAS](#) [Google Scholar](#)

19. 19.

Walton, J. P. R. B. & Quirke, N. Capillary condensation: a molecular simulation study. *Mol. Simul.* **2**, 361–391 (1989).

[Google Scholar](#)

20. 20.

Cheng, S. & Robbins, M. O. Nanocapillary adhesion between parallel plates. *Langmuir* **32**, 7788–7795 (2016).

[CAS](#) [Google Scholar](#)

21. 21.

Knežević, M. & Stark, H. Capillary condensation in an active bath. *EPL* **128**, 40008 (2019).

[Google Scholar](#)

22. 22.

Sing, K. S. W. & Williams, R. T. Historical aspects of capillarity and capillary condensation. *Microporous Mesoporous Mater.* **154**, 16–18 (2012).

[CAS](#) [Google Scholar](#)

23. 23.

Schoen, M. & Günther, G. Phase transitions in nanoconfined fluids: synergistic coupling between soft and hard matter. *Soft Matter* **6**, 5832–5838 (2010).

[ADS](#) [CAS](#) [Google Scholar](#)

24. 24.

Gor, G. Y., Huber, P. & Bernstein, N. Adsorption-induced deformation of nanoporous materials—a review. *Appl. Phys. Rev.* **4**, 011303 (2017).

[ADS](#) [Google Scholar](#)

25. 25.

Altabet, Y. E., Haji-Akbari, A. & Debenedetti, P. G. Effect of material flexibility on the thermodynamics and kinetics of hydrophobically induced evaporation of water. *Proc. Natl Acad. Sci. USA* **114**, E2548–E2555 (2017).

[CAS](#) [Google Scholar](#)

26. 26.

Radha, B. et al. Molecular transport through capillaries made with atomic scale precision. *Nature* **538**, 222–225 (2016).

[ADS](#) [CAS](#) [Google Scholar](#)

27. 27.

Gopinadhan, K. et al. Complete steric exclusion of ions and proton transport through confined monolayer water. *Science* **363**, 145–148 (2019).

[ADS](#) [CAS](#) [Google Scholar](#)

28. 28.

Drellich, J., Chibowski, E., Meng, D. D. & Terpilowski, K. Hydrophilic and superhydrophilic surfaces and materials. *Soft Matter* **7**, 9804–9828 (2011).

[ADS](#) [CAS](#) [Google Scholar](#)

29. 29.

Mücksch, C., Rösch, C., Müller-Renno, C., Ziegler, C. & Urbassek, H. M. Consequences of hydrocarbon contamination for wettability and protein adsorption on graphite surfaces. *J. Phys. Chem. C* **119**, 12496–12501 (2015).

[Google Scholar](#)

30. 30.

Fumagalli, L. et al. Anomalously low dielectric constant of confined water. *Science* **360**, 1339–1342 (2018).

[ADS](#) [CAS](#) [Google Scholar](#)

31. 31.

Weeks, B. L. & Vaughn, M. W. Direct imaging of meniscus formation in atomic force microscopy using environmental scanning electron microscopy. *Langmuir* **21**, 8096–8098 (2005).

[CAS](#) [Google Scholar](#)

32. 32.

Malijevský, A. & Parry, A. O. Modified Kelvin equations for capillary condensation in narrow and wide grooves. *Phys. Rev. Lett.* **120**, 135701 (2018).

[ADS](#) [Google Scholar](#)

33. 33.

Christenson, H. K. & Thomson, N. H. The nature of the air-cleaved mica surface. *Surf. Sci. Rep.* **71**, 367–390 (2016).

[ADS](#) [CAS](#) [Google Scholar](#)

34. 34.

Neek-Amal, M., Peeters, F. M., Grigorieva, I. V. & Geim, A. K. Commensurability effects in viscosity of nanoconfined water. *ACS Nano* **10**, 3685–3692 (2016).

[CAS](#) [PubMed](#) [PubMed Central](#) [Google Scholar](#)

35. 35.

Horcas, I. et al. WSXM: a software for scanning probe microscopy and a tool for nanotechnology. *Rev. Sci. Instrum.* **78**, 013705 (2007).

[ADS](#) [CAS](#) [Google Scholar](#)

36. 36.

Gor, G. Y. et al. Elastic response of mesoporous silicon to capillary pressures in the pores. *Appl. Phys. Lett.* **106**, 261901 (2015).

[ADS](#) [Google Scholar](#)

37. 37.

Bangham, D. H. & Fakhouri, N. The expansion of charcoal accompanying sorption of gases and vapours. *Nature* **122**, 681–682 (1928).

[ADS](#) [CAS](#) [Google Scholar](#)

38. 38.

Li, T. & Zhang, Z. Substrate-regulated morphology of graphene. *J. Phys. D* **43**, 075303 (2010).

[ADS](#) [Google Scholar](#)

39. 39.

Scharfenberg, S., Mansukhani, N., Chialvo, C., Weaver, R. L. & Mason, N. Observation of a snap-through instability in graphene. *Appl. Phys. Lett.* **100**, 021910 (2012).

[ADS](#) [Google Scholar](#)

40. 40.

Israelachvili, J. N. *Intermolecular and Surface Forces* (Academic, 2011).

41. 41.

Hibbeler, R. C. *Mechanics of Materials* 814 (Pearson, 2015).

42. 42.

McNeil, L. E. & Grimsditch, M. Elastic moduli of muscovite mica. *J. Phys. Condens. Matter* **5**, 1681–1690 (1993).

[ADS](#) [CAS](#) [Google Scholar](#)

43. 43.

Cost, J. R., Janowski, K. R. & Rossi, R. C. Elastic properties of isotropic graphite. *Phil. Mag.* **17**, 851–854 (1968).

[ADS](#) [CAS](#) [Google Scholar](#)

44. 44.

Ling, F. F., Lai, W. M. & Lucca, D. A. *Fundamentals of Surface Mechanics: With Applications* 96–97 (Springer, 2012).

45. 45.

Plimpton, S. Fast parallel algorithms for short-range molecular dynamics. *J. Comput. Phys.* **117**, 1–19 (1995).

[ADS](#) [CAS](#) [MATH](#) [Google Scholar](#)

46. 46.

Berendsen, H. J. C., Grigera, J. R. & Straatsma, T. P. The missing term in effective pair potentials. *J. Phys. Chem.* **91**, 6269–6271 (1987).

[CAS](#) [Google Scholar](#)

47. 47.

Wu, Y. & Aluru, N. R. Graphitic carbon–water nonbonded interaction parameters. *J. Phys. Chem. B* **117**, 8802–8813 (2013).

[CAS](#) [Google Scholar](#)

48. 48.

Cicero, G., Grossman, J. C., Schwegler, E., Gygi, F. & Galli, G. Water confined in nanotubes and between graphene sheets: a first principle study. *J. Am. Chem. Soc.* **130**, 1871–1878 (2008).

[CAS](#) [Google Scholar](#)

49. 49.

Sendner, C., Horinek, D., Bocquet, L. & Netz, R. R. Interfacial water at hydrophobic and hydrophilic surfaces: slip, viscosity, and diffusion. *Langmuir* **25**, 10768–10781 (2009).

[CAS](#) [Google Scholar](#)

[Download references](#)

Acknowledgements

This work was funded by Lloyd's Register Foundation, the European Research Council, Graphene Flagship and the Royal Society. Q.Y. acknowledges support from the Leverhulme Early Career Fellowship, and F.C.W. from the Strategic Priority Research Program of the Chinese Academy of Sciences (XDB22040402) and the CAS Youth Innovation Promotion Association.

Author information

Affiliations

1. National Graphene Institute, University of Manchester, Manchester, UK

Qian Yang, P. Z. Sun, I. V. Grigorieva, F. C. Wang & A. K. Geim

2. Department of Physics and Astronomy, University of Manchester, Manchester, UK

Qian Yang, P. Z. Sun, L. Fumagalli, Y. V. Stebunov, I. V. Grigorieva & A. K. Geim

3. School of Materials, University of Manchester, Manchester, UK

S. J. Haigh

4. Key Laboratory of Advanced Technologies of Materials, School of Materials Science and Engineering, Southwest Jiaotong University, Chengdu, China

Z. W. Zhou

5. Chinese Academy of Sciences Key Laboratory of Mechanical Behavior and Design of Materials, Department of Modern Mechanics, University of Science and Technology of China, Hefei, China

F. C. Wang

Authors

1. Qian Yang

[View author publications](#)

You can also search for this author in [PubMed](#) [Google Scholar](#)

2. P. Z. Sun

[View author publications](#)

You can also search for this author in [PubMed](#) [Google Scholar](#)

3. L. Fumagalli

[View author publications](#)

You can also search for this author in [PubMed](#) [Google Scholar](#)

4. Y. V. Stebunov

[View author publications](#)

You can also search for this author in [PubMed](#) [Google Scholar](#)

5. S. J. Haigh

[View author publications](#)

You can also search for this author in [PubMed](#) [Google Scholar](#)

6. Z. W. Zhou

[View author publications](#)

You can also search for this author in [PubMed](#) [Google Scholar](#)

7. I. V. Grigorieva

[View author publications](#)

You can also search for this author in [PubMed](#) [Google Scholar](#)

8. F. C. Wang

[View author publications](#)

You can also search for this author in [PubMed](#) [Google Scholar](#)

9. A. K. Geim

[View author publications](#)

You can also search for this author in [PubMed](#) [Google Scholar](#)

Contributions

A.K.G. suggested the project and directed it together with Q.Y. Q.Y. and P.Z.S. fabricated devices. Q.Y. performed measurements and carried out data analysis with help from L.F., Y.V.S., S.J.H. and Z.W.Z. F.C.W. provided theoretical support. A.K.G., Q.Y., F.C.W. and I.V.G. wrote the manuscript. All authors contributed to discussions.

Corresponding authors

Correspondence to [Qian Yang](#) or [F. C. Wang](#) or [A. K. Geim](#).

Ethics declarations

Competing interests

The authors declare no competing interests.

Additional information

Peer review information *Nature* thanks Patrick Huber and the other, anonymous, reviewer(s) for their contribution to the peer review of this work.

Publisher's note Springer Nature remains neutral with regard to jurisdictional claims in published maps and institutional affiliations.

Extended data figures and tables

Extended Data Fig. 1 Nanofabrication of 2D channels.

a, Simplified flow chart for our fabrication procedures. (1) Graphene spacers and the bottom crystal of either mica or graphite (shown in yellow) were assembled on top of an oxidized Si wafer. (2) A suspended SiN membrane with a rectangular hole was prepared separately. (3) The two-layer assembly was transferred from the Si oxide wafer onto the SiN membrane. The opening was extended through the assembly by RIE. (4) The top crystal of mica or graphite was placed on top of graphene spacers. **b**, AFM micrograph of graphene spacers with $N = 5$. The colour scale is given by the height profile (blue curve). **c**, Optical image of a final mica device used in our experiments. The bottom mica crystal shows up in purple on top of the square SiN membrane. Graphene spacers ($N = 3$) and the top mica layer are outlined in blue and yellow, respectively. **d**, Cross-sectional scanning transmission electron microscopy image of a graphite channel with $N = 2$. The blue ticks mark the channel's edges.

Extended Data Fig. 2 Measurements of capillary condensation.

a, Our AFM set-up. Humidified nitrogen gas flows through the bottom chamber made from an aluminium alloy. A silicon wafer of $15 \times 15 \text{ mm}^2$ in size is seen to cover the chamber, flush with its top surface. The white rubber gasket was lowered during AFM measurements to seal the space above the Si wafer. Inset, cross-sectional schematic showing how capillary devices were mounted during AFM measurements. **b**, Schematic of a water plug inside our capillaries. For brevity, the layered structure of water is ignored in this sketch. When the top chamber is at low RH, the meniscus slightly retracts inside the capillary to create a vapour pressure gradient. The RH gradient stabilizes two menisci with the same curvature at both exit and entrance. The distance from the exit meniscus to the opening is expected to be short because, in our atomically flat capillaries, water moves much faster as liquid than vapour²⁶.

Extended Data Fig. 3 Visualization of the condensation transition using AFM.

a–c, Images of a graphite capillary with $N = 3$ at RH of 55%, 70% and 95% (**a**, **b** and **c**, respectively). The upper part of each image shows sagging of the top graphite crystal ($H \approx 80 \text{ nm}$) into the 2D channel. The lower part shows the area immediately outside the channel, which is not covered by the top graphite. The black dotted lines mark a border between the two regions (edge of the top crystal). The colour scales for the lower and upper parts of the AFM images are given by the green and black curves, respectively. The profiles are averaged over $\sim 100 \text{ nm}$ along the y direction, and the curves in the upper parts of all the panels are provided on the same scale given by the black arrows in panel **a**. A small number of horizontal scanning lines (x direction) around the black-dot dividing lines were removed for clarity because they contained numerous instabilities caused by the AFM tip moving along the edge of the top crystal and jumping up and down. Such instabilities are typical for AFM scanning close to edges.

Extended Data Fig. 4 Non-hysteretic capillary condensation with slow dynamics.

a, Sagging profiles for a graphite capillary ($N = 4$) with increasing and decreasing RH between 75% and 80%. Black curve, initial dry-state profile. Red curve, RH was increased to 80%. Then, RH was returned to 75% and maintained at this humidity. AFM profiles were taken after 4 h, 9 h and 16 h (colour coded). **b**, The $N = 6$ graphite capillary was brought from the dry state (black curve) into the state filled with water and kept for an hour at 95% RH (red). The humidity was then decreased to $\sim 30\%$, well below the condensation transition observed at $62.5 \pm 2.5\%$ for this device. The colour-coded curves show the time evolution towards the original dry state. Note that the sagging depths δ for such hysteretic loops were highly reproducible but details of sagging profiles could differ in different RH cycles. For example, the top crystal's adhesion to the right wall was different in the original and final dry states, as seen in **a** (compare black and purple curves). This hysteresis is attributed to irreproducible vdW attachments of top crystals to channel sidewalls.

Extended Data Fig. 5 Capillary condensation in 2D channels with different initial sagging.

a, b, Sagging profiles for two $N = 5$ graphite capillaries with different δ_0 . RH was increased in 5% steps (colour coded). The water condensation transition occurred between 80% and 85% RH in **a** and between 70% and 75% in **b**. The difference in RH_C for the same N is attributed to different h in the two cases.

Extended Data Fig. 6 Remnant sagging above the condensation transition.

a, Schematic of top crystal sagging. **b**, Typical behaviour observed for the sagging depth δ as a function of RH, after the condensation transition occurred at $RH < 60\%$. Symbols: Measurements for two different mica capillaries with $N = 8$. The solid curves are best fits using equations (3) and (4) (colour-coded). The grey symbol with error bars indicates the experimental accuracy.

Extended Data Fig. 7 MD simulations of strongly confined water.

a, Its density profiles at different distances h between two rigid capillary walls with the contact angle $\theta \approx 11^\circ$. **b**, Same calculations but for contact angle 85° . The orange dashed lines mark positions of the surfaces that defined the 2D channels. Water exhibits a pronounced layered structure near each surface, and the structures start to overlap for $h < 15 \text{ \AA}$. Top insets, cross-sectional profiles for water droplets placed on the surfaces with the given θ .

Extended Data Fig. 8 Changes in the solid–liquid surface energy caused by atomic-scale confinement.

Calculated $\Delta\gamma(h)$ for several characteristic θ . The arrows indicate the number of molecular layers of water that fit inside the 2D channels.

Rights and permissions

[Reprints and Permissions](#)

About this article



Check for
updates

Cite this article

Yang, Q., Sun, P.Z., Fumagalli, L. *et al.* Capillary condensation under atomic-scale confinement. *Nature* **588**, 250–253 (2020).
<https://doi.org/10.1038/s41586-020-2978-1>

[Download citation](#)

- Received: 29 April 2020
- Accepted: 21 September 2020
- Published: 09 December 2020
- Issue Date: 10 December 2020
- DOI: <https://doi.org/10.1038/s41586-020-2978-1>

Comments

By submitting a comment you agree to abide by our [Terms](#) and [Community Guidelines](#). If you find something abusive or that does not comply with our terms or guidelines please flag it as inappropriate.

[Access through your institution](#)

[Change institution](#)

[Buy or subscribe](#)

This article was downloaded by **calibre** from <https://www.nature.com/articles/s41586-020-2978-1>

- Article
- [Published: 03 November 2020](#)

Catalytic asymmetric addition of an amine N–H bond across internal alkenes

- [Yumeng Xi](#) ORCID: orcid.org/0000-0003-1285-6036^{1,2},
- [Senjie Ma](#)^{1,2} &
- [John F. Hartwig](#) ORCID: orcid.org/0000-0002-4157-468X^{1,2}

[Nature](#) volume 588, pages254–260(2020) [Cite this article](#)

- 9044 Accesses
- 27 Altmetric
- [Metrics details](#)

Subjects

- [Catalyst synthesis](#)
- [Synthetic chemistry methodology](#)

Abstract

Hydroamination of alkenes, the addition of the N–H bond of an amine across an alkene, is a fundamental, yet challenging, organic transformation that creates an alkylamine from two abundant chemical feedstocks, alkenes and amines, with full atom economy^{1,2,3}. The reaction is particularly important because amines, especially chiral amines, are prevalent

substructures in a wide range of natural products and drugs. Although extensive efforts have been dedicated to developing catalysts for hydroamination, the vast majority of alkenes that undergo intermolecular hydroamination have been limited to conjugated, strained, or terminal alkenes^{2,3,4}; only a few examples occur by the direct addition of the N–H bond of amines across unactivated internal alkenes^{5,6,7}, including photocatalytic hydroamination^{8,9}, and no asymmetric intermolecular additions to such alkenes are known. In fact, current examples of direct, enantioselective intermolecular hydroamination of any type of unactivated alkene lacking a directing group occur with only moderate enantioselectivity^{10,11,12,13}. Here we report a cationic iridium system that catalyses intermolecular hydroamination of a range of unactivated, internal alkenes, including those in both acyclic and cyclic alkenes, to afford chiral amines with high enantioselectivity. The catalyst contains a phosphine ligand bearing trimethylsilyl-substituted aryl groups and a triflimide counteranion, and the reaction design includes 2-amino-6-methylpyridine as the amine to enhance the rates of multiple steps within the catalytic cycle while serving as an ammonia surrogate. These design principles point the way to the addition of N–H bonds of other reagents, as well as O–H and C–H bonds, across unactivated internal alkenes to streamline the synthesis of functional molecules from basic feedstocks.

[Access through your institution](#)

[Change institution](#)

[Buy or subscribe](#)

Access options

Subscribe to Journal

Get full journal access for 1 year

185,98 €

only 3,58 € per issue

[Subscribe](#)

All prices are NET prices.
VAT will be added later in the checkout.

Rent or Buy article

Get time limited or full article access on ReadCube.

from \$8.99

[Rent or Buy](#)

All prices are NET prices.

Additional access options:

- [Log in](#)
- [Access through your institution](#)
- [Learn about institutional subscriptions](#)

Fig. 1: Catalytic asymmetric hydroamination of unactivated internal alkenes.

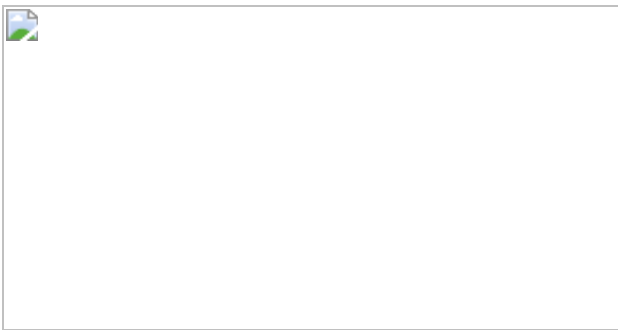


Fig. 2: Development of asymmetric hydroamination of unactivated internal alkenes with 2-amino-6-methylpyridine as an ammonia surrogate.



Fig. 3: Scope of internal alkenes that undergo hydroamination.



Fig. 4: Mechanistic study of the hydroamination.



Data availability

The data that support the findings of this study are available within the article and its Supplementary Information.

References

1. 1.

Müller, T. E. & Beller, M. Metal-initiated amination of alkenes and alkynes. *Chem. Rev.* **98**, 675–704 (1998).

[PubMed](#) [Google Scholar](#)

2. 2.

Müller, T. E., Hultzsch, K. C., Yus, M., Foubelo, F. & Tada, M. Hydroamination: direct addition of amines to alkenes and alkynes. *Chem. Rev.* **108**, 3795–3892 (2008).

[PubMed](#) [Google Scholar](#)

3. 3.

Huang, L., Arndt, M., Gooßen, K., Heydt, H. & Gooßen, L. J. Late transition metal-catalyzed hydroamination and hydroamidation. *Chem. Rev.* **115**, 2596–2697 (2015).

[CAS](#) [PubMed](#) [Google Scholar](#)

4. 4.

Reznichenko, A. L. & Hultzsch, K. C. in *Organic Reactions* 1–554 (Wiley, 2015).

5. 5.

Gurak, J. A., Yang, K. S., Liu, Z. & Engle, K. M. Directed, regiocontrolled hydroamination of unactivated alkenes via protodepalladation. *J. Am. Chem. Soc.* **138**, 5805–5808 (2016).

[CAS](#) [PubMed](#) [Google Scholar](#)

6. 6.

Karshtedt, D., Bell, A. T. & Tilley, T. D. Platinum-based catalysts for the hydroamination of olefins with sulfonamides and weakly basic anilines. *J. Am. Chem. Soc.* **127**, 12640–12646 (2005).

[CAS](#) [PubMed](#) [Google Scholar](#)

7. 7.

Zhang, J., Yang, C.-G. & He, C. Gold(i)-catalyzed intra- and intermolecular hydroamination of unactivated olefins. *J. Am. Chem. Soc.* **128**, 1798–1799 (2006).

[CAS](#) [PubMed](#) [Google Scholar](#)

8. 8.

Musacchio, A. J. et al. Catalytic intermolecular hydroaminations of unactivated olefins with secondary alkyl amines. *Science* **355**, 727–730 (2017).

[ADS](#) [CAS](#) [PubMed](#) [PubMed Central](#) [Google Scholar](#)

9. 9.

Nguyen, T. M., Manohar, N. & Nicewicz, D. A. anti-Markovnikov hydroamination of alkenes catalyzed by a two-component organic photoredox system: direct access to phenethylamine derivatives. *Angew. Chem. Int. Ed.* **53**, 6198–6201 (2014).

[CAS](#) [Google Scholar](#)

10. 10.

Zhang, Z., Lee, S. D. & Widenhoefer, R. A. Intermolecular hydroamination of ethylene and 1-alkenes with cyclic ureas catalyzed by achiral and chiral gold(i) complexes. *J. Am. Chem. Soc.* **131**, 5372–5373 (2009).

[CAS](#) [PubMed](#) [PubMed Central](#) [Google Scholar](#)

11. 11.

Reznichenko, A. L., Nguyen, H. N. & Hultzsch, K. C. Asymmetric intermolecular hydroamination of unactivated alkenes with simple amines. *Angew. Chem. Int. Ed.* **49**, 8984–8987 (2010).

[CAS](#) [Google Scholar](#)

12. 12.

Pan, S., Endo, K. & Shibata, T. Ir(i)-catalyzed intermolecular regio- and enantioselective hydroamination of alkenes with heteroaromatic amines. *Org. Lett.* **14**, 780–783 (2012).

[CAS](#) [PubMed](#) [Google Scholar](#)

13. 13.

Venable, E. P. et al. Rhodium-catalyzed asymmetric hydroamination of allyl amines. *J. Am. Chem. Soc.* **141**, 739–742 (2019).

[CAS](#) [PubMed](#) [PubMed Central](#) [Google Scholar](#)

14. 14.

Nugent, T. C. *Chiral Amine Synthesis: Methods, Developments and Applications* (Wiley VCH, 2010).

15. 15.

Trowbridge, A., Walton, S. M. & Gaunt, M. J. New strategies for the transition-metal catalyzed synthesis of aliphatic amines. *Chem. Rev.* **120**, 2613–2692 (2020).

[CAS](#) [PubMed](#) [Google Scholar](#)

16. 16.

Wang, C. & Xiao, J. in *Stereoselective Formation of Amines* (eds Li, W. & Zhang, X.) 261–282 (Springer, 2014).

17. 17.

Nugent, T. C. & El-Shazly, M. Chiral amine synthesis – recent developments and trends for enamide reduction, reductive amination, and imine reduction. *Adv. Synth. Catal.* **352**, 753–819 (2010).

[CAS](#) [Google Scholar](#)

18. 18.

Patil, M. D., Grogan, G., Bommarius, A. & Yun, H. Oxidoreductase-catalyzed synthesis of chiral amines. *ACS Catal.* **8**, 10985–11015 (2018).

[CAS](#) [Google Scholar](#)

19. 19.

Xie, J.-H., Zhu, S.-F. & Zhou, Q.-L. Transition metal-catalyzed enantioselective hydrogenation of enamines and imines. *Chem. Rev.* **111**, 1713–1760 (2011).

[CAS](#) [PubMed](#) [Google Scholar](#)

20. 20.

Ellman, J. A., Owens, T. D. & Tang, T. P. *N*-*tert*-Butanesulfinyl imines: versatile intermediates for the asymmetric synthesis of amines. *Acc. Chem. Res.* **35**, 984–995 (2002).

[CAS](#) [PubMed](#) [Google Scholar](#)

21. 21.

You, S.-L., Zhu, X.-Z., Luo, Y.-M., Hou, X.-L. & Dai, L.-X. Highly regio- and enantioselective Pd-catalyzed allylic alkylation and amination of monosubstituted allylic acetates with novel ferrocene P,N-ligands. *J. Am. Chem. Soc.* **123**, 7471–7472 (2001).

[CAS](#) [PubMed](#) [Google Scholar](#)

22. 22.

Ohmura, T. & Hartwig, J. F. Regio- and enantioselective allylic amination of achiral allylic esters catalyzed by an iridium–phosphoramidite complex. *J. Am. Chem. Soc.* **124**, 15164–15165 (2002).

[CAS](#) [PubMed](#) [Google Scholar](#)

23. 23.

Löber, O., Kawatsura, M. & Hartwig, J. F. Palladium-catalyzed hydroamination of 1,3-dienes: a colorimetric assay and enantioselective additions. *J. Am. Chem. Soc.* **123**, 4366–4367 (2001).

[PubMed](#) [Google Scholar](#)

24. 24.

Adamson, N. J., Hull, E. & Malcolmson, S. J. Enantioselective intermolecular addition of aliphatic amines to acyclic dienes with a Pd-PHOX catalyst. *J. Am. Chem. Soc.* **139**, 7180–7183 (2017).

[CAS](#) [PubMed](#) [PubMed Central](#) [Google Scholar](#)

25. 25.

Long, J., Wang, P., Wang, W., Li, Y. & Yin, G. Nickel/Brønsted acid-catalyzed chemo- and enantioselective intermolecular hydroamination of conjugated dienes. *iScience* **22**, 369–379 (2019).

[ADS](#) [CAS](#) [PubMed](#) [PubMed Central](#) [Google Scholar](#)

26. 26.

Tran, G., Shao, W. & Mazet, C. Ni-catalyzed enantioselective intermolecular hydroamination of branched 1,3-dienes using primary aliphatic amines. *J. Am. Chem. Soc.* **141**, 14814–14822 (2019).

[CAS](#) [PubMed](#) [Google Scholar](#)

27. 27.

Kawatsura, M. & Hartwig, J. F. Palladium-catalyzed intermolecular hydroamination of vinylarenes using arylamines. *J. Am. Chem. Soc.* **122**, 9546–9547 (2000).

[CAS](#) [Google Scholar](#)

28. 28.

Utsunomiya, M. & Hartwig, J. F. Intermolecular, Markovnikov hydroamination of vinylarenes with alkylamines. *J. Am. Chem. Soc.* **125**, 14286–14287 (2003).

[CAS](#) [PubMed](#) [Google Scholar](#)

29. 29.

Yang, Y., Shi, S.-L., Niu, D., Liu, P. & Buchwald, S. L. Catalytic asymmetric hydroamination of unactivated internal olefins to aliphatic amines. *Science* **349**, 62–66 (2015).

[ADS](#) [CAS](#) [PubMed](#) [PubMed Central](#) [Google Scholar](#)

30. 30.

Gui, J. et al. Practical olefin hydroamination with nitroarenes. *Science* **348**, 886–891 (2015).

[ADS](#) [CAS](#) [PubMed](#) [Google Scholar](#)

31. 31.

Johns, A. M., Sakai, N., Ridder, A. & Hartwig, J. F. Direct measurement of the thermodynamics of vinylarene hydroamination. *J. Am. Chem. Soc.* **128**, 9306–9307 (2006).

[CAS](#) [PubMed](#) [Google Scholar](#)

32. 32.

Liu, Z. & Hartwig, J. F. Mild, rhodium-catalyzed intramolecular hydroamination of unactivated terminal and internal alkenes with primary and secondary amines. *J. Am. Chem. Soc.* **130**, 1570–1571 (2008).

[CAS](#) [PubMed](#) [PubMed Central](#) [Google Scholar](#)

33. 33.

Huang, J.-M., Wong, C.-M., Xu, F.-X. & Loh, T.-P. InBr₃ catalyzed intermolecular hydroamination of unactivated alkenes. *Tetrahedron Lett.* **48**, 3375–3377 (2007).

[CAS](#) [PubMed](#) [Google Scholar](#)

34. 34.

Sevov, C. S., Zhou, J. & Hartwig, J. F. Iridium-catalyzed intermolecular hydroamination of unactivated aliphatic alkenes with amides and sulfonamides. *J. Am. Chem. Soc.* **134**, 11960–11963 (2012).

[CAS](#) [PubMed](#) [Google Scholar](#)

35. 35.

Utsunomiya, M., Kuwano, R., Kawatsura, M. & Hartwig, J. F. Rhodium-catalyzed anti-Markovnikov hydroamination of vinylarenes. *J. Am. Chem. Soc.* **125**, 5608–5609 (2003).

[CAS](#) [PubMed](#) [Google Scholar](#)

36. 36.

Pawlas, J., Nakao, Y., Kawatsura, M. & Hartwig, J. F. A general nickel-catalyzed hydroamination of 1,3-dienes by alkylamines: catalyst selection, scope, and mechanism. *J. Am. Chem. Soc.* **124**, 3669–3679 (2002).

[CAS](#) [PubMed](#) [Google Scholar](#)

37. 37.

Casalnuovo, A. L., Calabrese, J. C. & Milstein, D. Rational design in homogeneous catalysis. Iridium(i)-catalyzed addition of aniline to norbornylene via nitrogen-hydrogen activation. *J. Am. Chem. Soc.* **110**, 6738–6744 (1988).

[CAS](#) [Google Scholar](#)

38. 38.

Dorta, R., Egli, P., Zürcher, F. & Togni, A. The $[\text{IrCl}(\text{diphosphine})]_2/\text{fluoride}$ system. Developing catalytic asymmetric olefin hydroamination. *J. Am. Chem. Soc.* **119**, 10857–10858 (1997).

[CAS](#) [Google Scholar](#)

39. 39.

Zhou, J. & Hartwig, J. F. Intermolecular, catalytic asymmetric hydroamination of bicyclic alkenes and dienes in high yield and enantioselectivity. *J. Am. Chem. Soc.* **130**, 12220–12221 (2008).

[CAS](#) [PubMed](#) [Google Scholar](#)

40. 40.

Sevov, C. S., Zhou, J. & Hartwig, J. F. Iridium-catalyzed, intermolecular hydroamination of unactivated alkenes with indoles. *J. Am. Chem. Soc.* **136**, 3200–3207 (2014).

[CAS](#) [PubMed](#) [Google Scholar](#)

41. 41.

Hanley, P. S. & Hartwig, J. F. Migratory insertion of alkenes into metal–oxygen and metal–nitrogen bonds. *Angew. Chem. Int. Ed.* **52**, 8510–8525 (2013).

[CAS](#) [Google Scholar](#)

42. 42.

Thompson, W. H. & Sears, C. T. Kinetics of oxidative addition to iridium(i) complexes. *Inorg. Chem.* **16**, 769–774 (1977).

[CAS](#) [Google Scholar](#)

43. 43.

Smout, V. et al. Removal of the pyridine directing group from α -substituted *N*-(pyridin-2-yl)piperidines obtained via directed Ru-catalyzed sp^3 C–H functionalization. *J. Org. Chem.* **78**, 9803–9814 (2013).

[CAS](#) [PubMed](#) [Google Scholar](#)

44. 44.

Hanley, P. S. & Hartwig, J. F. Intermolecular migratory insertion of unactivated olefins into palladium–nitrogen bonds. Steric and electronic effects on the rate of migratory insertion. *J. Am. Chem. Soc.* **133**, 15661–15673 (2011).

[CAS](#) [PubMed](#) [Google Scholar](#)

45. 45.

Zhang, M., Hu, L., Lang, Y., Cao, Y. & Huang, G. Mechanism and origins of regio- and enantioselectivities of iridium-catalyzed hydroarylation of alkenyl ethers. *J. Org. Chem.* **83**, 2937–2947 (2018).

[CAS](#) [PubMed](#) [Google Scholar](#)

46. 46.

Xing, D., Qi, X., Marchant, D., Liu, P. & Dong, G. Branched-selective direct α -alkylation of cyclic ketones with simple alkenes. *Angew. Chem. Int. Ed.* **58**, 4366–4370 (2019).

[CAS](#) [Google Scholar](#)

47. 47.

Xi, Y., Butcher, T. W., Zhang, J. & Hartwig, J. F. Regioselective, asymmetric formal hydroamination of unactivated internal alkenes. *Angew. Chem. Int. Ed.* **55**, 776–780 (2016).

[CAS](#) [Google Scholar](#)

48. 48.

Mei, T.-S., Werner, E. W., Burckle, A. J. & Sigman, M. S. Enantioselective redox-relay oxidative heck arylations of acyclic alkenyl alcohols using boronic acids. *J. Am. Chem. Soc.* **135**, 6830–6833 (2013).

[CAS](#) [PubMed](#) [PubMed Central](#) [Google Scholar](#)

49. 49.

Morandi, B., Wickens, Z. K. & Grubbs, R. H. Regioselective Wacker oxidation of internal alkenes: rapid access to functionalized ketones facilitated by cross-metathesis. *Angew. Chem. Int. Ed.* **52**, 9751–9754 (2013).

[CAS](#) [Google Scholar](#)

[Download references](#)

Acknowledgements

The enantioselective aspects of the work were supported by the National Institutes of Health under grant R35GM130387 and the catalyst development was supported by the Director, Office of Science, of the US Department of Energy under contract number DE-AC02-05CH11231. Calculations were performed at the Molecular Graphics and Computation Facility at UC Berkeley funded by the NIH (S10OD023532). We gratefully acknowledge Takasago for gifts of (S)-DTBM-SEGPHOS, and H. Celik for assistance with nuclear magnetic resonance (NMR) experiments. Instruments in the College of Chemistry NMR facility are supported in part by NIH S10OD024998. We thank R. G. Bergman, B. Su and T. Butcher for

discussions. Y.X. thanks Bristol-Myers Squibb for a graduate fellowship, S. Pedram for supply of NaBARF and D. Small for assistance with DFT calculations.

Author information

Affiliations

1. Department of Chemistry, University of California, Berkeley, CA, USA

Yumeng Xi, Senjie Ma & John F. Hartwig

2. Division of Chemical Sciences, Lawrence Berkeley National Laboratory, Berkeley, CA, USA

Yumeng Xi, Senjie Ma & John F. Hartwig

Authors

1. Yumeng Xi

[View author publications](#)

You can also search for this author in [PubMed](#) [Google Scholar](#)

2. Senjie Ma

[View author publications](#)

You can also search for this author in [PubMed](#) [Google Scholar](#)

3. John F. Hartwig

[View author publications](#)

You can also search for this author in [PubMed](#) [Google Scholar](#)

Contributions

Y.X. and J.F.H. conceived the project. Y.X. discovered the reaction and performed experiments and DFT calculations. S.M. performed experiments for revision. Y.X. and J.F.H. wrote the manuscript.

Corresponding author

Correspondence to [John F. Hartwig](#).

Ethics declarations

Competing interests

The authors declare no competing interests.

Additional information

Peer review information *Nature* thanks the anonymous reviewer(s) for their contribution to the peer review of this work.

Publisher's note Springer Nature remains neutral with regard to jurisdictional claims in published maps and institutional affiliations.

Supplementary information

[Supplementary Information](#)

This file contains experimental protocols and spectral data – see contents for details.

Rights and permissions

[Reprints and Permissions](#)

About this article



Check for
updates

Cite this article

Xi, Y., Ma, S. & Hartwig, J.F. Catalytic asymmetric addition of an amine N–H bond across internal alkenes. *Nature* **588**, 254–260 (2020).
<https://doi.org/10.1038/s41586-020-2919-z>

[Download citation](#)

- Received: 26 November 2019
- Accepted: 27 October 2020
- Published: 03 November 2020
- Issue Date: 10 December 2020
- DOI: <https://doi.org/10.1038/s41586-020-2919-z>

Comments

By submitting a comment you agree to abide by our [Terms](#) and [Community Guidelines](#). If you find something abusive or that does not comply with our terms or guidelines please flag it as inappropriate.

[Access through your institution](#)

[Change institution](#)

[Buy or subscribe](#)

This article was downloaded by **calibre** from <https://www.nature.com/articles/s41586-020-2919-z>

- Article
- [Published: 09 December 2020](#)

Quantification of an efficiency–sovereignty trade-off in climate policy

- [Nico Bauer](#) [ORCID: orcid.org/0000-0002-0211-4162¹](#),
- [Christoph Bertram](#) [ORCID: orcid.org/0000-0002-0933-4395¹](#),
- [Anselm Schultes¹](#),
- [David Klein¹](#),
- [Gunnar Luderer](#) [ORCID: orcid.org/0000-0002-9057-6155^{1,2}](#),
- [Elmar Kriegler](#) [ORCID: orcid.org/0000-0002-3307-2647¹](#),
- [Alexander Popp¹](#) &
- [Ottmar Edenhofer](#) [ORCID: orcid.org/0000-0001-6029-5208^{1,2,3}](#)

[Nature](#) volume 588, pages261–266(2020) [Cite this article](#)

- 88 Altmetric
- [Metrics details](#)

Subjects

- [Climate-change mitigation](#)
- [Climate-change policy](#)

Abstract

The Paris Agreement calls for a cooperative response with the aim of limiting global warming to well below two degrees Celsius above pre-

industrial levels while reaffirming the principles of equity and common, but differentiated responsibilities and capabilities¹. Although the goal is clear, the approach required to achieve it is not. Cap-and-trade policies using uniform carbon prices could produce cost-effective reductions of global carbon emissions, but tend to impose relatively high mitigation costs on developing and emerging economies. Huge international financial transfers are required to complement cap-and-trade to achieve equal sharing of effort, defined as an equal distribution of mitigation costs as a share of income^{2,3}, and therefore the cap-and-trade policy is often perceived as infringing on national sovereignty^{2,3,4,5,6,7}. Here we show that a strategy of international financial transfers guided by moderate deviations from uniform carbon pricing could achieve the goal without straining either the economies or sovereignty of nations. We use the integrated assessment model REMIND–MAgPIE to analyse alternative policies: financial transfers in uniform carbon pricing systems, differentiated carbon pricing in the absence of financial transfers, or a hybrid combining financial transfers and differentiated carbon prices. Under uniform carbon prices, a present value of international financial transfers of 4.4 trillion US dollars over the next 80 years to 2100 would be required to equalize effort. By contrast, achieving equal effort without financial transfers requires carbon prices in advanced countries to exceed those in developing countries by a factor of more than 100, leading to efficiency losses of 2.6 trillion US dollars. Hybrid solutions reveal a strongly nonlinear trade-off between cost efficiency and sovereignty: moderate deviations from uniform carbon prices strongly reduce financial transfers at relatively small efficiency losses and moderate financial transfers substantially reduce inefficiencies by narrowing the carbon price spread. We also identify risks and adverse consequences of carbon price differentiation due to market distortions that can undermine environmental sustainability targets^{8,9}. Quantifying the advantages and risks of carbon price differentiation provides insight into climate and sector-specific policy mixes.

[Access through your institution](#)

[Change institution](#)

[Buy or subscribe](#)

Access options

Subscribe to Journal

Get full journal access for 1 year

185,98 €

only 3,58 € per issue

[Subscribe](#)

All prices are NET prices.

VAT will be added later in the checkout.

Rent or Buy article

Get time limited or full article access on ReadCube.

from \$8.99

[Rent or Buy](#)

All prices are NET prices.

Additional access options:

- [Log in](#)
- [Access through your institution](#)
- [Learn about institutional subscriptions](#)

Fig. 1: World economic development and emission mitigation projections.



Fig. 2: Carbon pricing and regional effort.



Fig. 3: Sovereignty versus cost-efficiency trade-off and consequences of differentiated carbon prices.



Data availability

Scenario data have been uploaded in Zenodo with the identifier <https://doi.org/10.5281/zenodo.4010426>. [Source data](#) are provided with this paper.

Code availability

The model codes of REMIND (identifier: ab2c995116e7fb402f6dd0183724496373af996e) and MAgPIE (identifier: 950bc7a08fd0e6c8f790c1399c7837133233e2fc) are open source (<https://github.com/remindmodel/remind> and <https://github.com/magpiemodel/magpie>).

References

1. 1.

Okereke, C. & Coventry, P. Climate justice and the international regime: before, during, and after Paris: climate justice and the international regime. *Wiley Interdiscip. Rev. Clim. Change* **7**, 834–851 (2016).

[Google Scholar](#)

2. 2.

Tavoni, M. et al. Post-2020 climate agreements in the major economies assessed in the light of global models. *Nat. Clim. Change* **5**, 119–126 (2015).

[ADS](#) [Google Scholar](#)

3. 3.

Tavoni, M. et al. The distribution of the major economies' effort in the Durban Platform scenarios. *Clim. Change Econ.* **04**, 1340009 (2013).

[Google Scholar](#)

4. 4.

Leimbach, M. & Giannousakis, A. Burden sharing of climate change mitigation: global and regional challenges under shared socio-economic pathways. *Climatic Change* **155**, 273–291 (2019).

[ADS](#) [Google Scholar](#)

5. 5.

Lüken, M. et al. The role of technological availability for the distributive impacts of climate change mitigation policy. *Energy Policy* **39**, 6030–6039 (2011).

[Google Scholar](#)

6. 6.

Aldy, J. E., Krupnick, A. J., Newell, R. G., Parry, I. W. H. & Pizer, W. A. Designing climate mitigation policy. *J. Econ. Lit.* **48**, 903–934 (2010).

[Google Scholar](#)

7. 7.

Victor, V. *The Collapse of the Kyoto Protocol and the Struggle to Slow Global Warming* (Princeton Univ. Press, 2001).

8. 8.

González-Eguino, M., Capellán-Pérez, I., Arto, I., Ansuategi, A. & Markandya, A. Industrial and terrestrial carbon leakage under climate policy fragmentation. *Clim. Policy* **17**, S148–S169 (2017).

[Google Scholar](#)

9. 9.

Otto, S. A. C. et al. Impact of fragmented emission reduction regimes on the energy market and on CO₂ emissions related to land use: a case study with China and the European Union as first movers. *Technol. Forecast. Soc. Change* **90**, 220–229 (2015).

[Google Scholar](#)

10. 10.

Böhringer, C. & Welsch, H. Burden sharing in a greenhouse: egalitarianism and sovereignty reconciled. *Appl. Econ.* **38**, 981–996 (2006).

[Google Scholar](#)

11. 11.

Nordhaus, W. Climate clubs: overcoming free-riding in international climate policy. *Am. Econ. Rev.* **105**, 1339–1370 (2015).

[Google Scholar](#)

12. 12.

Csereklyei, Z. & Stern, D. I. Global energy use: decoupling or convergence? *Energy Econ.* **51**, 633–641 (2015).

[Google Scholar](#)

13. 13.

International Comparison Program *Purchasing Power Parities and Real Expenditures of World Economies: Summary of Results and Findings of the 2011 International Comparison Program* (World Bank, 2014).

14. 14.

Stern, D. I., Pezzey, J. C. V. & Lambie, N. R. Where in the world is it cheapest to cut carbon emissions? *Aust. J. Agric. Resour. Econ.* **56**, 315–331 (2012).

[Google Scholar](#)

15. 15.

Fujimori, S. et al. Will international emissions trading help achieve the objectives of the Paris Agreement? *Environ. Res. Lett.* **11**, 104001 (2016).

[ADS](#) [Google Scholar](#)

16. 16.

Weyant, J. P. & Hill, J. Introduction and overview. The costs of the Kyoto Protocol: a multi-model evaluation. *Energy J.* (Spec. Issue) vii–xliv (1999).

17. 17.

Zhou, P. & Wang, M. Carbon dioxide emissions allocation: a review. *Ecol. Econ.* **125**, 47–59 (2016).

[Google Scholar](#)

18. 18.

van den Berg, N. J. et al. Implications of various effort-sharing approaches for national carbon budgets and emission pathways. *Climatic Change* <https://doi.org/10.1007/s10584-019-02368-y> (2019).

19. 19.

Höhne, N., den Elzen, M. & Escalante, D. Regional GHG reduction targets based on effort sharing: a comparison of studies. *Clim. Policy* **14**, 122–147 (2014).

[Google Scholar](#)

20. 20.

Manne, A. S. & Stephan, G. Global climate change and the equity–efficiency puzzle. *Energy* **30**, 2525–2536 (2005).

[Google Scholar](#)

21. 21.

Kriegler, E. et al. Making or breaking climate targets: the AMPERE study on staged accession scenarios for climate policy. *Technol. Forecast. Soc. Change* **90**, 24–44 (2015).

[Google Scholar](#)

22. 22.

Aldy, J. et al. Economic tools to promote transparency and comparability in the Paris Agreement. *Nat. Clim. Change* **6**, 1000–1004 (2016).

[ADS](#) [Google Scholar](#)

23. 23.

Jacoby, H. D., Chen, Y.-H. H. & Flannery, B. P. Informing transparency in the Paris Agreement: the role of economic models. *Clim. Policy* **17**, 873–890 (2017).

[Google Scholar](#)

24. 24.

Vandyck, T., Keramidas, K., Saveyn, B., Kitous, A. & Vrontisi, Z. A global stocktake of the Paris pledges: implications for energy systems and economy. *Glob. Environ. Change* **41**, 46–63 (2016).

[Google Scholar](#)

25. 25.

Vrontisi, Z. et al. Enhancing global climate policy ambition towards a 1.5 °C stabilization: a short-term multi-model assessment. *Environ. Res. Lett.* **13**, 044039 (2018).

[ADS](#) [Google Scholar](#)

26. 26.

Rogelj, J. et al. Paris Agreement climate proposals need a boost to keep warming well below 2 °C. *Nature* **534**, 631–639 (2016).

[ADS](#) [CAS](#) [PubMed](#) [PubMed Central](#) [Google Scholar](#)

27. 27.

The Emissions Gap Report 2019 (UNEP, 2019).

28. 28.

Luderer, G. et al. Residual fossil CO₂ emissions in 1.5–2 °C pathways. *Nat. Clim. Change* **8**, 626–633 (2018).

[ADS](#) [CAS](#) [Google Scholar](#)

29. 29.

Kriegler, E. et al. Fossil-fueled development (SSP5): an energy and resource intensive scenario for the 21st century. *Glob. Environ. Change* **42**, 297–315 (2017).

[Google Scholar](#)

30. 30.

Dellink, R., Chateau, J., Lanzi, E. & Magné, B. Long-term economic growth projections in the shared socioeconomic pathways. *Glob. Environ. Change* **42**, 200–214 (2017).

[Google Scholar](#)

31. 31.

Rogelj, J., Forster, P. M., Kriegler, E., Smith, C. J. & Séférian, R. Estimating and tracking the remaining carbon budget for stringent climate targets. *Nature* **571**, 335–342 (2019); correction **580**, E4 (2020).

[ADS](#) [CAS](#) [Google Scholar](#)

32. 32.

Luderer, G. et al. Economic mitigation challenges: how further delay closes the door for achieving climate targets. *Environ. Res. Lett.* **8**, 034033 (2013).

[ADS](#) [Google Scholar](#)

33. 33.

Bauer, N. et al. Shared socio-economic pathways of the energy sector —quantifying the narratives. *Glob. Environ. Change* **42**, 316–330 (2017).

[Google Scholar](#)

34. 34.

Diffenbaugh, N. S. & Burke, M. Global warming has increased global economic inequality. *Proc. Natl Acad. Sci. USA* **116**, 9808–9813 (2019).

[CAS](#) [PubMed](#) [PubMed Central](#) [Google Scholar](#)

35. 35.

Burke, M., Hsiang, S. M. & Miguel, E. Global non-linear effect of temperature on economic production. *Nature* **527**, 235–239 (2015).

[ADS](#) [CAS](#) [Google Scholar](#)

36. 36.

De Cian, E., Hof, A. F., Marangoni, G., Tavoni, M. & van Vuuren, D. P. Alleviating inequality in climate policy costs: an integrated perspective on mitigation, damage and adaptation. *Environ. Res. Lett.* **11**, 074015 (2016).

[ADS](#) [Google Scholar](#)

37. 37.

Evans, D. J. & Sezer, H. Social discount rates for member countries of the European Union. *J. Econ. Stud.* **32**, 47–59 (2005).

[ADS](#) [Google Scholar](#)

38. 38.

Weitzman, M. L. Can negotiating a uniform carbon price help to internalize the global warming externality? *J. Assoc. Environ. Resour. Econ.* **1**, 29–49 (2014).

[Google Scholar](#)

39. 39.

Barrett, S. in *Conflicts and Cooperation in Managing Environmental Resources* (ed. Pethig, R.) 11–35 (Springer, 1991).

40. 40.

Carraro, C. & Siniscalco, D. in *The Economics of Sustainable Development* (eds Goldin, I. & Winters, L. A.) 264–288 (Cambridge Univ. Press, 1995).

41. 41.

Kornek, U. & Edenhofer, O. The strategic dimension of financing global public goods. *Eur. Econ. Rev.* **127**, 103423 (2020).

[Google Scholar](#)

42. 42.

Lazarus, M. & van Asselt, H. Fossil fuel supply and climate policy: exploring the road less taken. *Climatic Change* **150**, 1–13 (2018).

[ADS](#) [Google Scholar](#)

43. 43.

Canadell, J. G. & Raupach, M. R. Managing forests for climate change mitigation. *Science* **320**, 1456–1457 (2008).

[ADS](#) [CAS](#) [PubMed](#) [PubMed Central](#) [Google Scholar](#)

44. 44.

Glachant, M. & Dechezleprêtre, A. What role for climate negotiations on technology transfer? *Clim. Policy* **17**, 962–981 (2017).

[Google Scholar](#)

45. 45.

Schultes, A. et al. Optimal international technology cooperation for the low-carbon transformation. *Clim. Policy* **18**, 1165–1176 (2018).

[Google Scholar](#)

46. 46.

Paroussos, L. et al. Climate clubs and the macro-economic benefits of international cooperation on climate policy. *Nat. Clim. Change* **9**, 542–546 (2019).

[ADS](#) [Google Scholar](#)

47. 47.

Chichilnisky, G. & Heal, G. Who should abate carbon emissions? An international viewpoint. *Econ. Lett.* **44**, 443–449 (1994).

[MATH](#) [Google Scholar](#)

48. 48.

Obersteiner, M. et al. How to spend a dwindling greenhouse gas budget. *Nat. Clim. Change* **8**, 7–10 (2018).

[ADS](#) [Google Scholar](#)

49. 49.

Realmonte, G. et al. An inter-model assessment of the role of direct air capture in deep mitigation pathways. *Nat. Commun.* **10**, 3277 (2019).

[ADS](#) [CAS](#) [PubMed](#) [PubMed Central](#) [Google Scholar](#)

50. 50.

Azar, C., Johansson, D. J. A. & Mattsson, N. Meeting global temperature targets—the role of bioenergy with carbon capture and storage. *Environ. Res. Lett.* **8**, 034004 (2013).

[ADS](#) [Google Scholar](#)

51. 51.

Lundsgaarde, E., Dupuy, K. & Persson, A. *Coordination Challenges in Climate Finance* (Danish Institute for International Studies, 2018);
<https://www.econstor.eu/bitstream/10419/204624/1/1042180393.pdf>

52. 52.

Motty, M. & Ackom, E. K. in *Climate Action* (eds Leal Filho, W. et al.) 1–11 (Springer International Publishing, 2019);
https://doi.org/10.1007/978-3-319-71063-1_104-2

53. 53.

Sharma, A. Precaution and post-caution in the Paris Agreement: adaptation, loss and damage and finance. *Clim. Policy* **17**, 33–47 (2017).

[Google Scholar](#)

54. 54.

BP Statistical Review of World Energy 2020 (BP, 2020);
<https://www.bp.com/en/global/corporate/energy-economics/statistical-review-of-world-energy/downloads.html>

55. 55.

World Development Indicators, DataBank (World Bank, 2020);
<https://databank.worldbank.org/source/world-development-indicators#>

56. 56.

Kriegler, E. et al. The role of technology for achieving climate policy objectives: overview of the EMF 27 study on global technology and climate policy strategies. *Climatic Change* **123**, 353–367 (2014).

[ADS](#) [Google Scholar](#)

57. 57.

Riahi, K. et al. Locked into Copenhagen pledges—implications of short-term emission targets for the cost and feasibility of long-term climate goals. *Technol. Forecast. Soc. Change* **90**, 8–23 (2015).

[Google Scholar](#)

58. 58.

Kriegler, E. et al. Will economic growth and fossil fuel scarcity help or hinder climate stabilization? *Climatic Change* **136**, 7–22 (2016).

[ADS](#) [Google Scholar](#)

59. 59.

Roelfsema, M. et al. Taking stock of national climate policies to evaluate implementation of the Paris Agreement. *Nat. Commun.* **11**, 2096 (2020).

[ADS](#) [CAS](#) [PubMed](#) [PubMed Central](#) [Google Scholar](#)

60. 60.

McCollum, D. L. et al. Energy investment needs for fulfilling the Paris Agreement and achieving the Sustainable Development Goals. *Nat. Energy* **3**, 589–599 (2018); correction **3**, 699 (2018).

[ADS](#) [Google Scholar](#)

61. 61.

Bauer, N. et al. Global energy sector emission reductions and bioenergy use: overview of the bioenergy demand phase of the EMF-33 model comparison. *Climatic Change* <https://doi.org/10.1007/s10584-018-2226-y> (2018).

62. 62.

Riahi, K. et al. in *Global Energy Assessment—Toward a Sustainable Future* 1203–1306 (Cambridge Univ. Press, 2012).

63. 63.

Krey, V. et al. in *IPCC Climate Change 2014: Mitigation of Climate Change* (eds Edenhofer, O. et al.) 1281–1328 (Cambridge Univ. Press, 2014).

64. 64.

Huppmann, D., Rogelj, J., Krey, V., Kriegler, E. & Riahi, K. A new scenario resource for integrated 1.5 °C research. *Nat. Clim. Change* **8**, 1027–1030 (2018)

[ADS](#) [Google Scholar](#)

65. 65.

KC, S. & Lutz, W. The human core of the shared socioeconomic pathways: population scenarios by age, sex and level of education for all countries to 2100. *Glob. Environ. Change* **42**, 181–192 (2017).

[PubMed](#) [PubMed Central](#) [Google Scholar](#)

66. 66.

South, A. rworldmap: a new R package for mapping global data. *The R Journal* **3**, 35–43 (2011).

[Google Scholar](#)

67. 67.

Bauer, N. et al. Bio-energy and CO₂ emission reductions: an integrated land-use and energy sector perspective. *Clim. Change* <https://doi.org/10.1007/s10584-020-02895-z> (2020).

[Download references](#)

Acknowledgements

We acknowledge funding from the German Federal Ministry of Education and Research (BMBF) in the Funding Priority ‘Economics of Climate Change’ (DIPOL: 01LA1809A). This work was supported by the European Union’s Horizon 2020 research and innovation programme under grant agreement numbers 730403 and 821124.

Author information

Affiliations

1. Potsdam Institute for Climate Impact Research (PIK), Member of the Leibniz Association, Potsdam, Germany

Nico Bauer, Christoph Bertram, Anselm Schultes, David Klein, Gunnar Luderer, Elmar Kriegler, Alexander Popp & Ottmar Edenhofer

2. Technical University of Berlin, Berlin, Germany

Gunnar Luderer & Ottmar Edenhofer

3. Mercator Institute on Global Commons and Climate Change (MCC), Berlin, Germany

Ottmar Edenhofer

Authors

1. Nico Bauer

[View author publications](#)

You can also search for this author in [PubMed](#) [Google Scholar](#)

2. Christoph Bertram

[View author publications](#)

You can also search for this author in [PubMed](#) [Google Scholar](#)

3. Anselm Schultes

[View author publications](#)

You can also search for this author in [PubMed](#) [Google Scholar](#)

4. David Klein

[View author publications](#)

You can also search for this author in [PubMed](#) [Google Scholar](#)

5. Gunnar Luderer

[View author publications](#)

You can also search for this author in [PubMed](#) [Google Scholar](#)

6. Elmar Kriegler

[View author publications](#)

You can also search for this author in [PubMed](#) [Google Scholar](#)

7. Alexander Popp

[View author publications](#)

You can also search for this author in [PubMed](#) [Google Scholar](#)

8. Ottmar Edenhofer

[View author publications](#)

You can also search for this author in [PubMed](#) [Google Scholar](#)

Contributions

N.B., C.B., D.K. and A.S. developed the policy analysis framework and designed the experiments. N.B. and A.S. implemented the policy framework. N.B. wrote the manuscript (with assistance from C.B. and G.L.). N.B. led the analysis and writing of the manuscript with contributions from all authors.

Corresponding author

Correspondence to [Nico Bauer](#).

Ethics declarations

Competing interests

The authors declare no competing interests.

Additional information

Peer review information *Nature* thanks Hancheng Dai, Ritu Mathur, Wei Peng and the other, anonymous, reviewer(s) for their contribution to the peer review of this work. Peer reviewer reports are available.

Publisher's note Springer Nature remains neutral with regard to jurisdictional claims in published maps and institutional affiliations.

Extended data figures and tables

[Extended Data Fig. 1](#)

Graphical illustration of the distributional effects between advanced economy A and developing economy B for different policy frameworks characterized by different marginal abatement cost functions f_A and f_B . The case ‘Uniform price w/o transfers’ with carbon prices equal to p in both regions implies different mitigation costs. In the case ‘Uniform price w/ transfers’ these differences are neutralized by transfers T . Alternatively, in the case ‘No transfer’ the differentiation of policies leads to equal costs; this case is not depicted explicitly. The case ‘Hybrid’ differentiates carbon prices to reduce T . The change of global mitigation cost is only the difference between the regional mitigation costs $\Delta AC_a - \Delta AC_b$ (indicated by the red triangles), whereas the changes of transfers are represented by the orange rectangles $p\Delta R$. As long as the differentiation of prices is

relatively small, the decline of transfers exceeds the increase in global mitigation costs.

Extended Data Fig. 2 Illustration of the exponential compression function.

The x axis shows the 2030 carbon prices in the full differentiation case (see Fig. 2a). The example applies the parameter $\alpha = 0.5$ to the compression function $\tilde{p}_r = \tilde{p}^{\min}$ that has been introduced in the Methods. The y axis shows the carbon prices after compression. The figure shows a subset of regions and the light grey line highlights the compression for Latin America and the EU. We note that the set of compressed carbon prices is scaled to comply with the global carbon budget (that is, the relative differences of the carbon price spread remain constant).

Extended Data Fig. 3 Socioeconomic drivers and CO₂ emissions in the no-policy baseline scenario.

a, b, Population (**a**) and economic growth (**b**) from history 1990–2015 and in the SSP2 baseline scenario 2015–2100^{30,65}. **c, d**, Energy and industry CO₂ emissions (**c**) as well as total CO₂ emissions (**d**). See ‘Data availability’ section for more details.

Extended Data Fig. 4 Time path of transfers in the default case with uniform carbon prices.

The transfers are expressed as percentages of GDP in the OECD and the non-OECD regions. The dashed line serves as a point of orientation. It represents the share of the US\$100 billion relative to the OECD’s GDP in 2020.

Extended Data Fig. 5 Effect of carbon price differentiation on primary and final energy use.

a, b, Changes in the global energy mixes distinguished by energy carriers and regions. The figure depicts differences compared with the uniform carbon tax case for the 1,300 GtCO₂ carbon budget. Primary energy (**a**) is measured according to the direct equivalence principle; final energy (**b**) is measured as delivered to final consumer. This means that fossil fuels, biomass and geothermal energy are measured in primary energy input, whereas renewables (hydro, wind and solar) as well as nuclear energy are measured by their electricity output. Notable results are as follows. First, the total amount of energy use increases. Second, OECD countries mostly reduce residual oil and gas consumption, but non-OECD countries mostly increase the use of coal; therefore, the total consumption of coal increases, whereas the global use of oil and gas decreases. Third, the total use of biomass increases due to increasing demand in OCED countries. Fourth, OECD countries accelerate modernization of final energy use by mainly reducing the use of liquids and gases, but increasing electricity and hydrogen. Finally, non-OECD countries delay modernization of energy use by mainly increasing the use of solids, liquids and gases with corresponding implications for air pollution and so on.

Extended Data Fig. 6 Effect of carbon price differentiation on land-use change and investments.

a, b, Changes in global land use (**a**) and investment and regions (**b**). The figure depicts differences compared with the uniform carbon tax case for the 1,300 GtCO₂ carbon budget. The two regions show opposite changes in the variables; for example, OECD countries convert agricultural land into forests to remove carbon by afforestation, whereas non-OECD countries convert forests into cropland to grow biomass that is exported to OECD countries. Moreover, OECD countries increase investments in the energy sector substantially to facilitate the transition to low-carbon technologies and to invest into carbon-removal technologies (which are counted as part of the energy sector). The higher OECD investments crowd-out the macroeconomic investments in OECD countries and energy sector investments in non-OECD countries.

Extended Data Fig. 7 Sensitivity analysis of the trade-off curve.

a, The sensitivity of the ban on bioenergy trade. **b**, The sensitivity with respect to the carbon budget. **c**, The variation of the maximum annual retirement rate of fossil-fuelled infrastructure from 9% to 6% and the delayed availability of technologies that rely on underground geological storage of CO₂ (that is, CCS including direct air capture). **d**, The application of the linear compression function; in this sensitivity analysis the case of uniform taxes and the no-transfer case are identical.

[Extended Data Fig. 8 Regional aggregates used in REMIND and MAgPIE.](#)

Regions and countries belonging to the OECD region are coloured in blue tones. See ‘Data availability’ section for more details. World map based on rworldmap package⁶⁶.

Extended Data Table 1 Overview of data sources for model comparisons

[Full size table](#)

Extended Data Table 2 Overview of selected sensitivity cases

[Full size table](#)

Source data

[Source Data Fig. 1](#)

[Source Data Fig. 2](#)

[Source Data Fig. 3](#)

Rights and permissions

[Reprints and Permissions](#)

About this article



Check for
updates

Cite this article

Bauer, N., Bertram, C., Schultes, A. *et al.* Quantification of an efficiency–sovereignty trade-off in climate policy. *Nature* **588**, 261–266 (2020).
<https://doi.org/10.1038/s41586-020-2982-5>

[Download citation](#)

- Received: 13 March 2020
- Accepted: 29 September 2020
- Published: 09 December 2020
- Issue Date: 10 December 2020
- DOI: <https://doi.org/10.1038/s41586-020-2982-5>

Comments

By submitting a comment you agree to abide by our [Terms](#) and [Community Guidelines](#). If you find something abusive or that does not comply with our terms or guidelines please flag it as inappropriate.

[Access through your institution](#)

[Change institution](#)

[Buy or subscribe](#)

Associated Content

Nature | News & Views

Trade-offs for equitable climate policy assessed

- Wei Peng

This article was downloaded by **calibre** from <https://www.nature.com/articles/s41586-020-2982-5>

| [Section menu](#) | [Main menu](#) |

- Article
- [Published: 18 November 2020](#)

Clustered versus catastrophic global vertebrate declines

- [Brian Leung](#) [ORCID: orcid.org/0000-0002-8323-9628](#)^{1,2},
- [Anna L. Hargreaves](#)¹,
- [Dan A. Greenberg](#) [ORCID: orcid.org/0000-0001-7489-1393](#)³,
- [Brian McGill](#)^{4,5},
- [Maria Dornelas](#) [ORCID: orcid.org/0000-0003-2077-7055](#)⁶ &
- [Robin Freeman](#)⁷

[Nature](#) volume 588, pages267–271(2020) [Cite this article](#)

- 4076 Accesses
- 495 Altmetric
- [Metrics details](#)

Subjects

- [Biodiversity](#)
- [Conservation biology](#)

Abstract

Recent analyses have reported catastrophic global declines in vertebrate populations^{1,2}. However, the distillation of many trends into a global mean index obscures the variation that can inform conservation measures and can be sensitive to analytical decisions. For example, previous analyses have

estimated a mean vertebrate decline of more than 50% since 1970 (Living Planet Index²). Here we show, however, that this estimate is driven by less than 3% of vertebrate populations; if these extremely declining populations are excluded, the global trend switches to an increase. The sensitivity of global mean trends to outliers suggests that more informative indices are needed. We propose an alternative approach, which identifies clusters of extreme decline (or increase) that differ statistically from the majority of population trends. We show that, of taxonomic–geographic systems in the Living Planet Index, 16 systems contain clusters of extreme decline (comprising around 1% of populations; these extreme declines occur disproportionately in larger animals) and 7 contain extreme increases (around 0.4% of populations). The remaining 98.6% of populations across all systems showed no mean global trend. However, when analysed separately, three systems were declining strongly with high certainty (all in the Indo-Pacific region) and seven were declining strongly but with less certainty (mostly reptile and amphibian groups). Accounting for extreme clusters fundamentally alters the interpretation of global vertebrate trends and should be used to help to prioritize conservation efforts.

[Access through your institution](#)

[Change institution](#)

[Buy or subscribe](#)

Access options

Subscribe to Journal

Get full journal access for 1 year

185,98 €

only 3,58 € per issue

[Subscribe](#)

All prices are NET prices.

VAT will be added later in the checkout.

Rent or Buy article

Get time limited or full article access on ReadCube.

from \$8.99

[Rent or Buy](#)

All prices are NET prices.

Additional access options:

- [Log in](#)
- [Access through your institution](#)
- [Learn about institutional subscriptions](#)

Fig. 1: Stylized patterns of system-wide growth rates.



Fig. 2: Effect of extreme populations on the global growth index.



Fig. 3: Population trends by taxonomic groups and realms.



Fig. 4: Effect of the size of the time series.



Fig. 5: Populations in the primary clusters across all systems, after removal of extreme clusters.



Data availability

Data can be obtained from the LPI database (www.livingplanetindex.org), AmphiBio³⁰ (https://figshare.com/articles/Oliveira_et_al_AmphiBIO_v1/4644424), FishBase (www.fishbase.org)²⁸ and life-history traits can be obtained from the amniote life-history database²⁷ (<https://doi.org/10.6084/m9.figshare.c.3308127.v1>).

Code availability

Code for the BHM model is available at:
<https://doi.org/10.5281/zenodo.3901586>.

References

1. 1.

IUCN. *The IUCN Red List of Threatened Species*. version 2019-3
<http://www.iucnredlist.org> (2019).

2. 2.

WWF. *Living Planet Report 2018: Aiming Higher* (eds. Grooten, N. & Almond, R. E. A.) (WWF, 2018).

3. 3.

Rosenberg, K. V. et al. Decline of the North American avifauna.
Science **366**, 120–124 (2019).

[ADS](#) [CAS](#) [Article](#) [Google Scholar](#)

4. 4.

Sánchez-Bayo, F. & Wyckhuys, K. A. G. Worldwide decline of the entomofauna: a review of its drivers. *Biol. Conserv.* **232**, 8–27 (2019).

[Article](#) [Google Scholar](#)

5. 5.

Ceballos, G., Ehrlich, P. R. & Dirzo, R. Biological annihilation via the ongoing sixth mass extinction signaled by vertebrate population losses and declines. *Proc. Natl Acad. Sci. USA* **114**, E6089–E6096 (2017).

[CAS](#) [Article](#) [Google Scholar](#)

6. 6.

Willig, M. R. et al. Populations are not declining and food webs are not collapsing at the Luquillo Experimental Forest. *Proc. Natl Acad. Sci. USA* **116**, 12143–12144 (2019).

[CAS](#) [Article](#) [Google Scholar](#)

7. 7.

Daskalova, G. N., Myers-Smith, I. H. & Godlee, J. L. All is not decline across global vertebrate populations. Preprint at <https://doi.org/10.1101/272898> (2018).

8. 8.

Dornelas, M. et al. A balance of winners and losers in the Anthropocene. *Ecol. Lett.* **22**, 847–854 (2019).

[Article](#) [Google Scholar](#)

9. 9.

Vellend, M. et al. Global meta-analysis reveals no net change in local-scale plant biodiversity over time. *Proc. Natl Acad. Sci. USA* **110**, 19456–19459 (2013).

[ADS](#) [CAS](#) [Article](#) [Google Scholar](#)

10. 10.

Dornelas, M. et al. Assemblage time series reveal biodiversity change but not systematic loss. *Science* **344**, 296–299 (2014).

[ADS](#) [CAS](#) [Article](#) [Google Scholar](#)

11. 11.

Gonzalez, A. et al. Estimating local biodiversity change: a critique of papers claiming no net loss of local diversity. *Ecology* **97**, 1949–1960 (2016).

[Article](#) [Google Scholar](#)

12. 12.

Leung, B., Greenberg, D. A. & Green, D. M. Trends in mean growth and stability in temperate vertebrate populations. *Divers. Distrib.* **23**, 1372–1380 (2017).

[Article](#) [Google Scholar](#)

13. 13.

McGill, B. J., Dornelas, M., Gotelli, N. J. & Magurran, A. E. Fifteen forms of biodiversity trend in the Anthropocene. *Trends Ecol. Evol.* **30**, 104–113 (2015).

[Article](#) [Google Scholar](#)

14. 14.

Anderson, S. C., Branch, T. A., Cooper, A. B. & Dulvy, N. K. Black-swan events in animal populations. *Proc. Natl Acad. Sci. USA* **114**, 3252–3257 (2017).

[CAS](#) [Article](#) [Google Scholar](#)

15. 15.

LPI. *Living Planet Index*. www.livingplanetindex.org/ (2016).

16. 16.

Estes, J. A. et al. Trophic downgrading of planet Earth. *Science* **333**, 301–306 (2011).

[ADS](#) [CAS](#) [Article](#) [Google Scholar](#)

17. 17.

Connors, B. M., Cooper, A. B., Peterman, R. M. & Dulvy, N. K. The false classification of extinction risk in noisy environments. *Proc. R. Soc. Lond. B* **281**, 20132935 (2014).

[Google Scholar](#)

18. 18.

Hanks, E. M., Hooten, M. B. & Baker, F. A. Reconciling multiple data sources to improve accuracy of large-scale prediction of forest disease incidence. *Ecol. Appl.* **21**, 1173–1188 (2011).

[Article](#) [Google Scholar](#)

19. 19.

Youngflesh, C. & Lynch, H. J. Black-swan events: population crashes or temporary emigration? *Proc. Natl Acad. Sci. USA* **114**, E8953–E8954 (2017).

[CAS](#) [Article](#) [Google Scholar](#)

20. 20.

Fournier, A. M. V., White, E. R. & Heard, S. B. Site-selection bias and apparent population declines in long-term studies. *Conserv. Biol.* **33**, 1370–1379 (2019).

[Article](#) [Google Scholar](#)

21. 21.

Newbold, T. et al. Ecological traits affect the response of tropical forest bird species to land-use intensity. *Proc. R. Soc. Lond. B* **280**, 20122131 (2013).

[Google Scholar](#)

22. 22.

Venter, O. et al. Sixteen years of change in the global terrestrial human footprint and implications for biodiversity conservation. *Nat. Commun.* **7**, 12558 (2016).

[ADS](#) [CAS](#) [Article](#) [Google Scholar](#)

23. 23.

Allan, J. R. et al. Hotspots of human impact on threatened terrestrial vertebrates. *PLoS Biol.* **17**, e3000158 (2019).

[Article](#) [Google Scholar](#)

24. 24.

Blowes, S. A. et al. The geography of biodiversity change in marine and terrestrial assemblages. *Science* **366**, 339–345 (2019).

[ADS](#) [CAS](#) [Article](#) [Google Scholar](#)

25. 25.

O'Neill, S. & Nicholson-Cole, S. “Fear won’t do it”: promoting positive engagement with climate change through visual and iconic representations *Sci. Commun.* **30**, 355–379 (2009).

[Article](#) [Google Scholar](#)

26. 26.

Brennan, L. & Binney, W. Fear, guilt, and shame appeals in social marketing. *J. Bus. Res.* **63**, 140–146 (2010).

[Article](#) [Google Scholar](#)

27. 27.

Myhrvold, N. P. et al. An amniote life-history database to perform comparative analyses with birds, mammals, and reptiles. *Ecology* **96**,

3109 (2015).

[Article](#) [Google Scholar](#)

28. 28.

Froese, R. & Pauly, D. *FishBase* version 12/2019 www.fishbase.org (2019).

29. 29.

Boettiger, C., Lang, D. T. & Wainwright, P. C. rfishbase: exploring, manipulating and visualizing FishBase data from R. *J. Fish Biol.* **81**, 2030–2039 (2012).

[CAS Article](#) [Google Scholar](#)

30. 30.

Oliveira, B. F., São-Pedro, V. A., Santos-Barrera, G., Penone, C. & Costa, G. C. AmphiBIO, a global database for amphibian ecological traits. *Sci. Data* **4**, 170123 (2017).

[Article](#) [Google Scholar](#)

31. 31.

Collen, B. et al. Monitoring change in vertebrate abundance: the living planet index. *Conserv. Biol.* **23**, 317–327 (2009).

[Article](#) [Google Scholar](#)

32. 32.

Gelman, A., Hwang, J. & Vehtari, A. Understanding predictive information criteria for Bayesian models. *Stat. Comput.* **24**, 997–1016 (2014).

[MathSciNet Article](#) [Google Scholar](#)

33. 33.

Carpenter, B. et al. Stan: a probabilistic programming language. *J. Stat. Softw.* **76**, 1–32 (2017).

[Article](#) [Google Scholar](#)

34. 34.

R Core Team. *R: A Language and Environment for Statistical Computing* <http://www.R-project.org/> (R Foundation for Statistical Computing, 2016).

35. 35.

McRae, L., Deinet, S. & Freeman, R. The diversity-weighted living planet index: controlling for taxonomic bias in a global biodiversity indicator. *PLoS ONE* **12**, e0169156 (2017).

[Article](#) [Google Scholar](#)

[Download references](#)

Acknowledgements

We thank E. Hudgins, D. Nguyen, S. Varadarajan and A. Jones for discussions, T. Coulson for comments and S. Varadarajan and F. Moyes for help creating the figures. This work was supported by a Natural Sciences and Engineering Research Council (NSERC) Discovery grant to B.L.

Author information

Affiliations

1. Department of Biology, McGill University, Montreal, Quebec, Canada

Brian Leung & Anna L. Hargreaves

2. Bieler School of Environment, McGill University, Montreal, Quebec, Canada

Brian Leung

3. Department of Biological Sciences, Simon Fraser University, Burnaby, British Columbia, Canada

Dan A. Greenberg

4. School of Biology and Ecology, University of Maine, Orono, ME, USA

Brian McGill

5. Mitchell Center for Sustainability Solutions, University of Maine, Orono, ME, USA

Brian McGill

6. Centre for Biological Diversity, University of St Andrews, St Andrews, UK

Maria Dornelas

7. Indicators and Assessments Unit, Institute of Zoology, Zoological Society of London, London, UK

Robin Freeman

Authors

1. Brian Leung

[View author publications](#)

You can also search for this author in [PubMed](#) [Google Scholar](#)

2. Anna L. Hargreaves

[View author publications](#)

You can also search for this author in [PubMed](#) [Google Scholar](#)

3. Dan A. Greenberg

[View author publications](#)

You can also search for this author in [PubMed](#) [Google Scholar](#)

4. Brian McGill

[View author publications](#)

You can also search for this author in [PubMed](#) [Google Scholar](#)

5. Maria Dornelas

[View author publications](#)

You can also search for this author in [PubMed](#) [Google Scholar](#)

6. Robin Freeman

[View author publications](#)

You can also search for this author in [PubMed](#) [Google Scholar](#)

Contributions

Authors are listed in order of their contributions. B.L. formulated the BHM model, conducted analyses and wrote the majority of the paper. A.L.H. discussed and clarified the ideas and had a central role in the writing of the paper. D.A.G. discussed and clarified the ideas, synthesized the data and contributed to the writing of the paper. B.M. discussed and clarified the ideas, and commented on the manuscript. M.D. discussed and clarified the ideas, commented on and improved the presentation of the manuscript. R.F. discussed and clarified the ideas, and provided insight into the LPI data and analyses.

Corresponding author

Correspondence to [Brian Leung](#).

Ethics declarations

Competing interests

The authors declare no competing interests.

Additional information

Peer review information *Nature* thanks Tim Coulson and the other, anonymous, reviewer(s) for their contribution to the peer review of this work.

Publisher's note Springer Nature remains neutral with regard to jurisdictional claims in published maps and institutional affiliations.

Extended data figures and tables

[Extended Data Fig. 1 Theoretical analyses of BHM model.](#)

The p - p plots show that the posterior distributions for each estimated parameter are unbiased and largely follow a 1:1 line for each hyper parameter (σ, τ) as well as the fraction in each cluster ($f_1, f_2 = 1 - f_1$). The 1:1 line is the theoretic expectation, indicating that the true parameter value falls below the 0.01 quantile 1% of the time, the 0.02 quantile 2% of the time, and so on.

[Extended Data Fig. 2 Sensitivity analyses of primary cluster trends.](#)

The trends of the primary clusters (θ_1), for the main analysis (x axis) versus the sensitivity analysis (y axis) for the threshold for extreme clusters (top) and the offset when $n = 0$ was observed (bottom).

Extended Data Fig. 3 Effect of small time series on primary cluster trends.

Each point represents a trend estimate for the primary cluster of a system, with the full dataset (x axis) versus data excluding time series with less than 10 data points (y axis). The red dot indicates the freshwater Indo-Pacific mammals, which was reduced from 22 populations (full) to 2 populations (only data with at least 10 data points).

Extended Data Fig. 4 Mean trends of primary clusters across systems calculated using the BHM model.

Top, all species (14,700 populations). Middle, only large species (9,596 populations). Bottom, only small species (5,103 populations). The small species appear to be declining more than large species, although this finding needs to be interpreted with caution, as most primary distributions did not significantly deviate from zero for small species.

Extended Data Fig. 5 Histograms of observed growth rates and output of the BHM model for systems 1–16.

Blue line, primary cluster; red line, extreme cluster(s) from the model. Grey vertical lines show the range of observed values. In comparing the model output to the data we show the following. (1) The variation of the BHM primary cluster (blue line) is much lower than the raw data, because the BHM separates variation in among-population trends from variation due to within-population fluctuations. (2) The BHM model identifies evidence for extreme clusters in both directions (for example, terrestrial Indo-Pacific birds) or only one direction (for example, terrestrial Neotropical mammals), but not for other apparent clusters (for example, terrestrial Indo-Pacific herps). The BHM integrates the magnitude of within-population fluctuations, time-series sizes, number of populations, among-population variance, and the magnitude and frequency of the extreme populations in determining whether additional (extreme) clusters are needed to account for the observations.

Extended Data Fig. 6 Histograms of observed growth rates and output of the BHM model for systems 17–32.

Blue line, primary cluster; red line, extreme cluster(s) from the model. Grey vertical lines show the range of observed values. For further information, see Extended Data Fig. 5.

Extended Data Fig. 7 Histograms of observed growth rates and output of the BHM model for systems 33–48.

Blue line, primary cluster; red line, extreme cluster(s) from the model. Grey vertical lines show the range of observed values. For further information, see Extended Data Fig. 5.

Extended Data Fig. 8 Histograms of observed growth rates and output of the BHM model for systems 49–57.

Blue line, primary cluster; red line, extreme cluster(s) from the model. Grey vertical lines show the range of observed values. For further information, see Extended Data Fig. 5.

Supplementary information

Supplementary Information

This file contains Supplementary Methods, Supplementary Results, Supplementary Discussion: Effect of small time-series on extreme clusters and Supplementary Tables.

Reporting Summary

Rights and permissions

Reprints and Permissions

About this article



Check for
updates

Cite this article

Leung, B., Hargreaves, A.L., Greenberg, D.A. *et al.* Clustered versus catastrophic global vertebrate declines. *Nature* **588**, 267–271 (2020). <https://doi.org/10.1038/s41586-020-2920-6>

[Download citation](#)

- Received: 28 January 2020
- Accepted: 04 September 2020
- Published: 18 November 2020
- Issue Date: 10 December 2020
- DOI: <https://doi.org/10.1038/s41586-020-2920-6>

Comments

By submitting a comment you agree to abide by our [Terms](#) and [Community Guidelines](#). If you find something abusive or that does not comply with our terms or guidelines please flag it as inappropriate.

[Access through your institution](#)

[Change institution](#)

[Buy or subscribe](#)

| [Section menu](#) | [Main menu](#) |

- Article
- [Published: 25 November 2020](#)

Late Cretaceous bird from Madagascar reveals unique development of beaks

- [Patrick M. O'Connor](#) ORCID: orcid.org/0000-0002-6762-3806^{1,2,3},
- [Alan H. Turner](#) ORCID: orcid.org/0000-0002-4164-6727⁴,
- [Joseph R. Groenke](#)¹,
- [Ryan N. Felice](#) ORCID: orcid.org/0000-0002-9201-9213⁵,
- [Raymond R. Rogers](#)^{3,6},
- [David W. Krause](#)^{3,4} &
- [Lydia J. Rahantarisoa](#)⁷

[Nature](#) volume 588, pages272–276(2020) [Cite this article](#)

- 2718 Accesses
- 1 Citations
- 613 Altmetric
- [Metrics details](#)

Subjects

- [Evolution](#)
- [Palaeontology](#)

Abstract

Mesozoic birds display considerable diversity in size, flight adaptations and feather organization^{1,2,3,4}, but exhibit relatively conserved patterns of beak shape and development^{5,6,7}. Although Neornithine (that is, crown group) birds also exhibit constraint on facial development^{8,9}, they have comparatively diverse beak morphologies associated with a range of feeding and behavioural ecologies, in contrast to Mesozoic birds. Here we describe a crow-sized stem bird, *Falcatakely forsterae* gen. et sp. nov., from the Late Cretaceous epoch of Madagascar that possesses a long and deep rostrum, an expression of beak morphology that was previously unknown among Mesozoic birds and is superficially similar to that of a variety of crown-group birds (for example, toucans). The rostrum of *Falcatakely* is composed of an expansive edentulous maxilla and a small tooth-bearing premaxilla. Morphometric analyses of individual bony elements and three-dimensional rostrum shape reveal the development of a neornithine-like facial anatomy despite the retention of a maxilla–premaxilla organization that is similar to that of nonavialan theropods. The patterning and increased height of the rostrum in *Falcatakely* reveals a degree of developmental lability and increased morphological disparity that was previously unknown in early branching avialans. Expression of this phenotype (and presumed ecology) in a stem bird underscores that consolidation to the neornithine-like, premaxilla-dominated rostrum was not an evolutionary prerequisite for beak enlargement.

[Access through your institution](#)

[Change institution](#)

[Buy or subscribe](#)

Access options

Subscribe to Journal

Get full journal access for 1 year

185,98 €

only 3,58 € per issue

Subscribe

All prices are NET prices.
VAT will be added later in the checkout.

Rent or Buy article

Get time limited or full article access on ReadCube.

from \$8.99

Rent or Buy

All prices are NET prices.

Additional access options:

- [Log in](#)
- [Access through your institution](#)
- [Learn about institutional subscriptions](#)

Fig. 1: Cranium of the Cretaceous enantiornithine bird *Falcatakely forsteriae* (UA 10015, holotype).

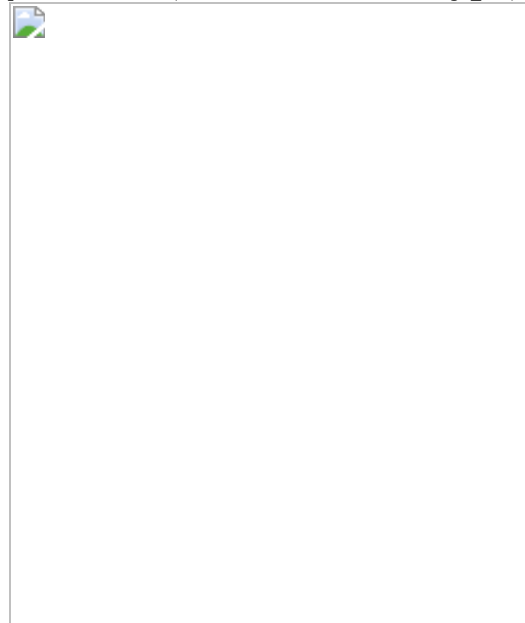


Fig. 2: Mosaic evolution of the avian facial skeleton as depicted among select early branching forms.



Fig. 3: Geometric morphometric analyses of the facial shape of *Falcatakely* among paravians.



Data availability

UA 10015 is catalogued into the collections at the Université d'Antananarivo. Details regarding the development of the digital files and the derivatives of these files (such as DICOM or PLY) used as part of the study are included in the [Supplementary Information](#) and archived on the MorphoSource website (https://www.morphosource.org/Detail/ProjectDetail>Show/project_id/7894). Phylogenetic character information and parameters used in the analyses are provided in the [Supplementary Information](#). Executable files for

phylogenetic analyses, character–taxon matrices, an interactive three-dimensional morphospace plot and interactive three-dimensional PDFs are hosted on DRYAD (<https://doi.org/10.5061/dryad.mkkwh70wg>). This published study, including the novel genus (urn:lsid:zoobank.org:act:5BA26059-B428-4896-BFEA-2475419C61FC) and species (urn:lsid:zoobank.org:act:69314771-F0D8-4C15-946C-524164385FB7) along with the associated nomenclatural acts, have been registered in ZooBank: urn:lsid:zoobank.org:pub:4595D69E-FE12-4DAD-B155-89F084254F73.

References

1. 1.

Xu, X. et al. An integrative approach to understanding bird origins. *Science* **346**, 1253293 (2014).

[PubMed](#) [PubMed Central](#) [Google Scholar](#)

2. 2.

Zhou, Z., Clarke, J. & Zhang, F. Insight into diversity, body size and morphological evolution from the largest Early Cretaceous enantiornithine bird. *J. Anat.* **212**, 565–577 (2008).

[PubMed](#) [PubMed Central](#) [Google Scholar](#)

3. 3.

Brusatte, S. L., O'Connor, J. K. & Jarvis, E. D. The origin and diversification of birds. *Curr. Biol.* **25**, R888–R898 (2015).

[CAS](#) [PubMed](#) [PubMed Central](#) [Google Scholar](#)

4. 4.

O'Connor, J. K. in *The Evolution of Feathers* (eds Foth, C. & Rauhut, O. W. M.) 147–172 (Springer, 2020).

5. 5.

O'Connor, J. K. & Chiappe, L. M. A revision of enantiornithine (Aves: Ornithothoraces) skull morphology. *J. Syst. Palaeontol.* **9**, 135–157 (2011).

[Google Scholar](#)

6. 6.

Huang, J. et al. A new ornithurine from the Early Cretaceous of China sheds light on the evolution of early ecological and cranial diversity in birds. *PeerJ* **4**, e1765 (2016).

[PubMed](#) [PubMed Central](#) [Google Scholar](#)

7. 7.

Bhullar, B.-A. S. et al. How to make a bird skull: major transitions in the evolution of the avian cranium, paedomorphosis, and the beak as a surrogate hand. *Integr. Comp. Biol.* **56**, 389–403 (2016).

[PubMed](#) [PubMed Central](#) [Google Scholar](#)

8. 8.

Young, N. M. et al. Embryonic bauplans and the developmental origins of facial diversity and constraint. *Development* **141**, 1059–1063 (2014).

[CAS](#) [PubMed](#) [PubMed Central](#) [Google Scholar](#)

9. 9.

Mayr, G. Comparative morphology of the avian maxillary bone (os maxillare) based on an examination of macerated juvenile skeletons. *Acta Zool.* **101**, 24–38 (2020).

[Google Scholar](#)

10. 10.

Hu, H., O'Connor, J. K. & Zhou, Z. A new species of Pengornithidae (Aves: Enantiornithes) from the Lower Cretaceous of China suggests a specialized scansorial habitat previously unknown in early birds. *PLoS ONE* **10**, e0126791 (2015).

[PubMed](#) [PubMed Central](#) [Google Scholar](#)

11. 11.

Bailleul, A. M. et al. An Early Cretaceous enantiornithine (Aves) preserving an unlaid egg and probable medullary bone. *Nat. Commun.* **10**, 1275 (2019).

[ADS](#) [PubMed](#) [PubMed Central](#) [Google Scholar](#)

12. 12.

Hou, L., Chiappe, L. M., Zhang, F. & Chuong, C.-M. New Early Cretaceous fossil from China documents a novel trophic specialization for Mesozoic birds. *Naturwissenschaften* **91**, 22–25 (2004).

[ADS](#) [CAS](#) [Google Scholar](#)

13. 13.

O'Connor, J. K. et al. Phylogenetic support for a specialized clade of Cretaceous enantiornithine birds with information from a new species. *J. Vertebr. Paleontol.* **29**, 188–204 (2009).

[Google Scholar](#)

14. 14.

O'Connor, J. K., Chiappe, L. M., Gao, C. & Zhao, B. Anatomy of the Early Cretaceous enantiornithine bird *Rapaxavis pani*. *Acta Palaeontol. Pol.* **56**, 463–475 (2011).

[Google Scholar](#)

15. 15.

O'Connor, J. K., Wang, M. & Hu, H. A new ornithuromorph (Aves) with an elongate rostrum from the Jehol Biota, and the early evolution of rostralization in birds. *J. Syst. Palaeontol.* **14**, 939–948 (2016).

[Google Scholar](#)

16. 16.

Field, D. J. et al. Complete *Ichthyornis* skull illuminates mosaic assembly of the avian head. *Nature* **557**, 96–100 (2018).

[ADS](#) [CAS](#) [Google Scholar](#)

17. 17.

Field, D. J., Benito, J., Chen, A., Jagt, J. W. M. & Ksepka, D. T. Late Cretaceous neornithine from Europe illuminates the origins of crown birds. *Nature* **579**, 397–401 (2020).

[ADS](#) [CAS](#) [Google Scholar](#)

18. 18.

Chiappe, L. M. & Witmer, L. M. *Mesozoic Birds: Above the Heads of Dinosaurs* (Univ. California Press, 2004).

19. 19.

Li, Z., Zhou, Z., Wang, M. & Clarke, J. A. A new specimen of large-bodied basal enantiornithine *Bohaiornis* from the Early Cretaceous of China and the inference of feeding ecology in Mesozoic birds. *J. Paleontol.* **88**, 99–108 (2014).

[Google Scholar](#)

20. 20.

Wang, M., Hu, H. & Li, Z. A new small enantiornithine bird from the Jehol Biota, with implications for early evolution of avian skull morphology. *J. Syst. Palaeontol.* **14**, 481–497 (2016).

[Google Scholar](#)

21. 21.

Wang, M., O'Connor, J. K. & Zhou, Z. A new robust enantiornithine bird from the Lower Cretaceous of China with scansorial adaptations. *J. Vertebr. Paleontol.* **34**, 657–671 (2014).

[Google Scholar](#)

22. 22.

Rogers, R. R., Hartman, J. H. & Krause, D. W. Stratigraphic analysis of Upper Cretaceous rocks in the Mahajanga Basin, northwestern Madagascar: implications for ancient and modern faunas. *J. Geol.* **108**, 275–301 (2000).

[ADS](#) [CAS](#) [PubMed](#) [PubMed Central](#) [Google Scholar](#)

23. 23.

Gauthier, J. A. & de Queiroz, K. in *New Perspectives on the Origin and Early Evolution of Birds: Proceedings of the International Symposium in Honor of John H. Ostrom* (eds Gauthier, J. & Gall, L. F.). 7–41 (Peabody Museum of Natural History, Yale Univ., 2001).

24. 24.

Chiappe, L. M., Norell, M. A. & Clark, J. M. A new skull of *Gobipteryx minuta* (Aves: Enantiornithes) from the Cretaceous of the Gobi Desert. *Am. Mus. Novit.* **3346**, 1–15 (2001).

[Google Scholar](#)

25. 25.

Wang, M. & Zhou, Z. A new enantiornithine (Aves: Ornithothoraces) with completely fused premaxillae from the Early Cretaceous of China. *J. Syst. Palaeontol.* **17**, 1299–1312 (2019).

[Google Scholar](#)

26. 26.

Hieronymus, T. L. & Witmer, L. M. Homology and evolution of avian compound Rhamphothecae. *Auk* **127**, 590–604 (2010).

[Google Scholar](#)

27. 27.

Wang, M., Zhou, Z.-H., O'Connor, J. K. & Zelenkov, N. V. A new diverse enantiornithine family (Bohaiornithidae fam. nov.) from the Lower Cretaceous of China with information from two new species. *Vert. Palasiat.* **52**, 31–76 (2014).

[Google Scholar](#)

28. 28.

Wang, M. & Hu, H. A comparative morphological study of the jugal and quadratojugal in early birds and their dinosaurian relatives. *Anat. Rec.* **300**, 62–75 (2017).

[Google Scholar](#)

29. 29.

Wang, Y. et al. A previously undescribed specimen reveals new information on the dentition of *Sapeornis chaoyangensis*. *Cretac. Res.* **74**, 1–10 (2017).

[Google Scholar](#)

30. 30.

Hu, H., O'Connor, J. K., Wang, M., Wroe, S. & McDonald, P. G. New anatomical information on the bohaiornithid *Longusunguis* and the presence of a plesiomorphic diapsid skull in Enantiornithes. *J. Syst. Palaeontol.* **18**, 1481–1495 (2020).

[Google Scholar](#)

31. 31.

Hu, H. et al. Evolution of the vomer and its implications for cranial kinesis in Paraves. *Proc. Natl Acad. Sci. USA* **116**, 19571–19578 (2019).

[CAS](#) [Google Scholar](#)

32. 32.

Felice, R. N. & Goswami, A. Developmental origins of mosaic evolution in the avian cranium. *Proc. Natl Acad. Sci. USA* **115**, 555–560 (2018).

[CAS](#) [Google Scholar](#)

33. 33.

Bhullar, B.-A. S. et al. A molecular mechanism for the origin of a key evolutionary innovation, the bird beak and palate, revealed by an integrative approach to major transitions in vertebrate history. *Evolution* **69**, 1665–1677 (2015).

[Google Scholar](#)

34. 34.

Mallarino, R. et al. Closely related bird species demonstrate flexibility between beak morphology and underlying developmental programs. *Proc. Natl Acad. Sci. USA* **109**, 16222–16227 (2012).

[ADS](#) [CAS](#) [Google Scholar](#)

35. 35.

Tokita, M., Yano, W., James, H. F. & Abzhanov, A. Cranial shape evolution in adaptive radiations of birds: comparative morphometrics of Darwin's finches and Hawaiian honeycreepers. *Phil. Trans. R. Soc. Lond. B* **372**, 20150481 (2017).

[Google Scholar](#)

36. 36.

Bell, A. & Chiappe, L. M. Statistical approaches for inferring ecology in Mesozoic birds. *J. Syst. Palaeontol.* **9**, 119–133 (2011).

[Google Scholar](#)

37. 37.

O'Connor, J. K. The trophic habits of early birds. *Palaeogeogr. Palaeoclimatol. Palaeoecol.* **513**, 178–195 (2019).

[Google Scholar](#)

38. 38.

Rogers, R. R. Fine-grained debris flows and extraordinary vertebrate burials in the Late Cretaceous of Madagascar. *Geology* **33**, 297–300 (2005).

[ADS](#) [Google Scholar](#)

39. 39.

Rogers, R. R., Krause, D. W., Curry Rogers, K., Rasoamiaramanana, A. H. & Rahantarisoa, L. Paleoenvironment and paleoecology of *Majungasaurus crenatissimus* (Theropoda: Abelisauridae) from the

Late Cretaceous of Madagascar. *J. Vertebr. Paleontol.* **27**, 21–31 (2007).

[Google Scholar](#)

40. 40.

Brusatte, S. L., Lloyd, G. T., Wang, S. C. & Norell, M. A. Gradual assembly of avian body plan culminated in rapid rates of evolution across the dinosaur–bird transition. *Curr. Biol.* **24**, 2386–2392 (2014).

[CAS](#) [PubMed](#) [PubMed Central](#) [Google Scholar](#)

41. 41.

Turner, A. H., Makovicky, P. J. & Norell, M. A. A review of dromaeosaurid systematics and paravian phylogeny. *Bull. Am. Mus. Nat. Hist.* **371**, 1–206 (2012).

[Google Scholar](#)

42. 42.

Ronquist, F. et al. MrBayes 3.2: efficient Bayesian phylogenetic inference and model choice across a large model space. *Syst. Biol.* **61**, 539–542 (2012).

[PubMed](#) [PubMed Central](#) [Google Scholar](#)

43. 43.

Lewis, P. O. A likelihood approach to estimating phylogeny from discrete morphological character data. *Syst. Biol.* **50**, 913–925 (2001).

[CAS](#) [PubMed](#) [PubMed Central](#) [Google Scholar](#)

44. 44.

Clarke, J. A. & Middleton, K. M. Mosaicism, modules, and the evolution of birds: results from a Bayesian approach to the study of morphological evolution using discrete character data. *Syst. Biol.* **57**, 185–201 (2008).

[PubMed](#) [PubMed Central](#) [Google Scholar](#)

45. 45.

Rambaut, A., Suchard, M. A., Xie, D. & Drummond, A. J. Tracer v.1.6. <http://beast.community/tracer> (2014).

46. 46.

O'Reilly, J. E. & Donoghue, P. C. J. The efficacy of consensus tree methods for summarizing phylogenetic relationships from a posterior sample of trees estimated from morphological data. *Syst. Biol.* **67**, 354–362 (2018).

[PubMed](#) [PubMed Central](#) [Google Scholar](#)

47. 47.

Goloboff, P. A., Farris, J. & Nixon, K. TNT, a free program for phylogenetic analysis. *Cladistics* **24**, 774–786 (2008).

[Google Scholar](#)

48. 48.

Goloboff, P. A., Farris, J. S. & Nixon, K. C. TNT: tree analysis using new technology. version 1.1 (Willi Hennig Society Edition) <http://www.lillo.org.ar/phylogeny/tnt/> (2008).

49. 49.

Goloboff, P. A. & Catalano, S. A. TNT version 1.5, including a full implementation of phylogenetic morphometrics. *Cladistics* **32**, 221–238 (2016).

[Google Scholar](#)

[Download references](#)

Acknowledgements

We thank the Université d'Antananarivo, the Mahajanga Basin Project field teams and the villagers of the Berivotra Study Area for support; the ministries of Mines, Higher Education and Culture of the Republic of Madagascar for permission to conduct field research; the National Geographic Society (8597-09) and the US National Science Foundation (EAR-0446488, EAR-1525915, EAR-1664432) for funding; and M. Witton for drafting the line drawings used in Fig. 1 and Extended Data Figs. 1, 2. Collection of avian three-dimensional morphometric data was funded by European Research Council grant no. STG-2014-637171 (to A. Goswami). Full acknowledgments are provided in the Supplementary Information.

Author information

Affiliations

1. Department of Biomedical Sciences, Heritage College of Osteopathic Medicine, Ohio University, Athens, OH, USA

Patrick M. O'Connor & Joseph R. Groenke

2. Ohio Center for Ecological and Evolutionary Studies, Ohio University, Athens, OH, USA

Patrick M. O'Connor

3. Department of Earth Sciences, Denver Museum of Nature & Science, Denver, CO, USA

Patrick M. O'Connor, Raymond R. Rogers & David W. Krause

4. Department of Anatomical Sciences, Stony Brook University, Stony Brook, NY, USA

Alan H. Turner & David W. Krause

5. Centre for Integrative Anatomy, Department of Cell and Developmental Biology, University College London, London, UK

Ryan N. Felice

6. Geology Department, Macalester College, St Paul, MN, USA

Raymond R. Rogers

7. Département de Sciences de la Terre et de l'Environnement, Université d'Antananarivo, Antananarivo, Madagascar

Lydia J. Rahantarisoa

Authors

1. Patrick M. O'Connor

[View author publications](#)

You can also search for this author in [PubMed](#) [Google Scholar](#)

2. Alan H. Turner

[View author publications](#)

You can also search for this author in [PubMed](#) [Google Scholar](#)

3. Joseph R. Groenke

[View author publications](#)

You can also search for this author in [PubMed](#) [Google Scholar](#)

4. Ryan N. Felice

[View author publications](#)

You can also search for this author in [PubMed](#) [Google Scholar](#)

5. Raymond R. Rogers

[View author publications](#)

You can also search for this author in [PubMed](#) [Google Scholar](#)

6. David W. Krause

[View author publications](#)

You can also search for this author in [PubMed](#) [Google Scholar](#)

7. Lydia J. Rahantarisoa

[View author publications](#)

You can also search for this author in [PubMed](#) [Google Scholar](#)

Contributions

P.M.O., A.H.T. and J.R.G. designed the project; P.M.O., A.H.T., J.R.G., R.R.R., D.W.K. and L.J.R. conducted the fieldwork. J.R.G. performed the mechanical preparation of the specimen; J.R.G. and P.M.O. conducted the digital preparation and interpretation of the specimen using microcomputed tomography and carried out the rapid prototyping of UA 10015; R.R.R. and L.J.R. provided geological data and taphonomic interpretation; P.M.O., A.H.T., J.R.G. and R.N.F. completed the laboratory work on and digital representation of the fossil and provided input on descriptions and comparisons; A.H.T. and P.M.O. contributed to the character coding and phylogenetic analysis; R.N.F. completed the morphometric analyses; P.M.O., A.H.T. and J.R.G. developed the manuscript, with contributions and/or editing from all authors.

Corresponding author

Correspondence to [Patrick M. O'Connor](#).

Ethics declarations

Competing interests

The authors declare no competing interests.

Additional information

Peer review information *Nature* thanks Bhart-Anjan Bhullar and Daniel Field for their contribution to the peer review of this work.

Publisher's note Springer Nature remains neutral with regard to jurisdictional claims in published maps and institutional affiliations.

Extended data figures and tables

[Extended Data Fig. 1 Rostrum of the Cretaceous enantiornithine bird *Falcatakely* \(UA 10015, holotype\).](#)

a, Reconstruction (not to scale) illustrating the preserved (in white) elements of the cranium. **b**, Digital polygon surface reconstruction (from microcomputed tomography scans) of the right nasal in rostrodorsal view (caudal to the top) highlighting the midline depression and dimpled surface texture. **c**, Digital polygon surface reconstruction of the right nasal in dorsal view illustrating the dimpled architecture on the frontal and rostral portions, which extends laterally onto the lacrimal. **d**, Digital polygon surface reconstruction of the right facial elements in right lateral view to illustrate the shape and inter-element relationships of the nasal, maxilla and lacrimal (note the surface texture of the right maxilla with neurovascular sulci broadly expressed over the lateral surface, deep to the inferred keratinous covering (that is, beak)). **e**, Digital polygon surface reconstruction of the lower lateral face to highlight arrangement of the maxilla, lacrimal, jugal and postorbital (all elements from the right side). **f**, Digital polygon surface reconstruction of left maxilla and premaxilla articulation (rostral to the left). AOF, antorbital fenestra; cdp, caudodorsal process of the lacrimal; cp, choanal process of the palatine; ect, ectopterygoid; EN, external nares; ITF, infratemporal fenestra; fpn, frontal process of the nasal; inb, internarial bar; jpmx, jugal process of the maxilla; ju, jugal; lbo, lacrimal boot; lc, lacrimal;

ld, lacrimal dimpling; le, lacrimal excavation; lf, lacrimal foramen; mpmx, midline premaxilla; mx, maxilla; mpxj, maxillary process of the jugal; na, nasal; nd, nasal dimpling; nf, nasal fossa; nvs, neurovascular sulci; pal, palatine; pppm, premaxillary process of the maxilla; pmx, premaxilla; po, postorbital; qj, quadratojugal; rdp, rostrodorsal process of the lacrimal; rpn, rostral process of the nasal; tm, tomial margin; to, tooth; vr, ventral ramus of the lacrimal.

Extended Data Fig. 2 Palatal and lateral facial regions of the Cretaceous enantiornithine bird *Falcatakely* (UA 10015, holotype).

a, Digital polygon surface reconstruction (from microcomputed tomography scans) of the palate and lateral face in ventral view. **b**, Reconstructed outline drawing of *Falcatakely* in palatal view (shaded regions are not preserved). **c**, Digital polygon surface reconstruction of internal aspect of left facial skeleton (premaxilla, maxilla and nasal) and palate in right lateral view. The left and right sides are indicated as (l) and (r), respectively. The dashed line in **c** represents the approximate contour of the caudal margin (that is, the ventral ramus of the lacrimal) of the antorbital fenestra. Scale bar, 5 mm; the scale bar is representative for **a** and **c**; the reconstruction in **b** is not to the same scale. AOF, antorbital fenestra; bs, basisphenoid rostrum; cp, choanal process of the (right) palatine; ect, ectopterygoid; EN, external nares; jpmx, jugal process of the maxilla; mpmx, midline premaxilla; mx, maxilla; na, nasal; pal, palatine; pmx, premaxilla; pter, pterygoid; to, tooth; up, uncinate process of the ectopterygoid; vm, vomers.

Extended Data Fig. 3 Majority- rule tree of *Falcatakely* among coelurosaurians from the Bayesian analysis of the TWiG matrix.

Clades outside of the Avialae are collapsed for brevity. Posterior probabilities are placed above the nodes.

Extended Data Fig. 4 Majority -rule tree of *Falcatakely* among avialans from the Bayesian analysis of a modified matrix that was previously published.

A matrix modified from a previous study²⁵ was used. Posterior probabilities are placed above the nodes.

Extended Data Fig. 5 Geometric morphometric analysis of rostrum shape in *Falcatakely* among avians.

Plot of the first two principal components of the three-dimensional landmark analysis of total rostrum shape of *Falcatakely* and extant avian taxa. Whereas the unique configuration of the maxilla and premaxilla in *Falcatakely* is more similar to those of non-avian paravians (Fig. 3), the overall three-dimensional rostrum phenotype occupies the morphospace that is converged on by subsequent radiations of neornithine birds ([Supplementary Data](#)). See [Supplementary Information](#) for analytical protocols.

Extended Data Fig. 6 Landmarking procedure for three-dimensional geometric morphometric analysis in dorsal and lateral views.

a, Dorsal view. **b**, Lateral view. Red spheres represent anatomical (type I) landmarks; yellow spheres are sliding semi-landmarks.

Supplementary information

Supplementary Information

This file includes details related to the provenance of the specimens, preparation (mechanical and digital) of the specimen, and the parameters of both the geometric morphometric and phylogenetic analyses undertaken for the publication. **Location:**[NPG website and DRYAD](#).

Reporting Summary

Supplementary Data

An interactive morphospace plot of *Falcatakely forsteriae* and extant avian taxa (HTML format). Also available at <https://doi.org/10.5061/dryad.mkkwh70wg>.

Video 1

Polygon surface model reconstruction (from CT data) of *Falcatakely forsteriae*, as preserved, with rotation around a dorsoventral axis (relative to left maxilla). **Location: NPG Website and DRYAD.**

Video 2

Polygon surface model reconstruction (from CT data) of *Falcatakely forsteriae*, Beauchêne-style, with rotation around a dorsoventral axis axis (relative to left maxilla). **Location: NPG Website and DRYAD.**

Video 3

Polygon surface model reconstruction (from CT data) of *Falcatakely forsteriae*, as preserved, with rotation around a mediolateral axis (relative to left maxilla). **Location: NPG Website and DRYAD.**

Video 4

Polygon surface model reconstruction (from CT data) of *Falcatakely forsteriae*, Beauchêne-style, with rotation around a mediolateral axis (relative to left maxilla). **Location: NPG Website and DRYAD.**

Video 5

Polygon surface model reconstruction (from CT data) of *Falcatakely forsteriae*, as preserved, with rotation around a rostrocaudal axis (relative to

left maxilla). **Location: NPG Website and DRYAD.**

Video 6

Polygon surface model reconstruction (from CT data) of *Falcatakely forsteriae*, Beauchêne-style, with rotation around a rostrocaudal axis (relative to left maxilla). **Location: NPG Website and DRYAD.**

Video 7

Animation of in-situ to Beauchêne-style state changes in polygon reconstructions (relative to left maxilla). **Location: NPG Website and DRYAD.**

Video 8

Montage highlighting stages of data recovery used for study of *Falcatakely forsteriae*. **Location: NPG Website and DRYAD.**

Rights and permissions

[Reprints and Permissions](#)

About this article



Check for
updates

Cite this article

O'Connor, P.M., Turner, A.H., Groenke, J.R. *et al.* Late Cretaceous bird from Madagascar reveals unique development of beaks. *Nature* **588**, 272–276 (2020). <https://doi.org/10.1038/s41586-020-2945-x>

[Download citation](#)

- Received: 30 April 2020
- Accepted: 14 September 2020
- Published: 25 November 2020
- Issue Date: 10 December 2020
- DOI: <https://doi.org/10.1038/s41586-020-2945-x>

Further reading

- [**The changing face of birds from the age of the dinosaurs**](#)
 - Daniel J. Field

Nature (2020)

Comments

By submitting a comment you agree to abide by our [Terms](#) and [Community Guidelines](#). If you find something abusive or that does not comply with our terms or guidelines please flag it as inappropriate.

[Access through your institution](#)

[Change institution](#)

[Buy or subscribe](#)

Associated Content

Nature | News & Views

[**The changing face of birds from the age of the dinosaurs**](#)

- Daniel J. Field
-

This article was downloaded by **calibre** from <https://www.nature.com/articles/s41586-020-2945-x>

| [Section menu](#) | [Main menu](#) |

- Article
- [Published: 25 November 2020](#)

Multiple wheat genomes reveal global variation in modern breeding

- [Sean Walkowiak^{1,2}](#) na1,
- [Liangliang Gao](#) [ORCID: orcid.org/0000-0002-3864-0631³](#) na1,
- [Cecile Monat](#) [ORCID: orcid.org/0000-0002-0574-3976⁴](#) na1,
- [Georg Haberer⁵](#),
- [Mulualem T. Kassa⁶](#),
- [Jemima Brinton⁷](#),
- [Ricardo H. Ramirez-Gonzalez⁷](#),
- [Markus C. Kolodziej](#) [ORCID: orcid.org/0000-0003-3155-2935⁸](#),
- [Emily Delorean³](#),
- [Dinushika Thambugala⁹](#),
- [Valentyna Klymiuk](#) [ORCID: orcid.org/0000-0001-9308-7886¹](#),
- [Brook Byrns¹](#),
- [Heidrun Gundlach](#) [ORCID: orcid.org/0000-0002-6757-0943⁵](#),
- [Venkat Bandi¹⁰](#),
- [Jorge Nunez Siri¹⁰](#),
- [Kirby Nilsen](#) [ORCID: orcid.org/0000-0002-9477-5549^{1,11}](#),
- [Catharine Aquino¹²](#),
- [Axel Himmelbach⁴](#),
- [Dario Copetti](#) [ORCID: orcid.org/0000-0002-2680-2568^{13,14}](#),
- [Tomohiro Ban¹⁵](#),
- [Luca Venturini¹⁶](#),
- [Michael Bevan](#) [ORCID: orcid.org/0000-0001-8264-2354⁷](#),
- [Bernardo Clavijo¹⁷](#),

- [Dal-Hoe Koo](#)³,
- [Jennifer Ens](#) ORCID: orcid.org/0000-0003-2663-1006¹,
- [Krystalee Wiebe](#)¹,
- [Amidou N'Diaye](#) ORCID: orcid.org/0000-0001-7769-7801¹,
- [Allen K. Fritz](#)³,
- [Carl Gutwin](#)¹⁰,
- [Anne Fiebig](#)⁴,
- [Christine Fosker](#) ORCID: orcid.org/0000-0002-3799-9474¹⁷,
- [Bin Xiao Fu](#)²,
- [Gonzalo Garcia Accinelli](#) ORCID: orcid.org/0000-0001-9647-7935¹⁷,
- [Keith A. Gardner](#) ORCID: orcid.org/0000-0002-4890-301X¹⁸,
- [Nick Fradgley](#)¹⁸,
- [Juan Gutierrez-Gonzalez](#) ORCID: orcid.org/0000-0002-6795-6192¹⁹,
- [Gwyneth Halstead-Nussloch](#)¹³,
- [Masaomi Hatakeyama](#)^{12,13},
- [Chu Shin Koh](#)²⁰,
- [Jasline Deek](#) ORCID: orcid.org/0000-0002-5584-306X²¹,
- [Alejandro C. Costamagna](#)²²,
- [Pierre Fobert](#)⁶,
- [Darren Heavens](#) ORCID: orcid.org/0000-0001-5418-7868¹⁷,
- [Hiroyuki Kanamori](#)²³,
- [Kanako Kawaura](#)¹⁵,
- [Fuminori Kobayashi](#)²³,
- [Ksenia Krasileva](#)¹⁷,
- [Tony Kuo](#)^{24,25},
- [Neil McKenzie](#)⁷,
- [Kazuki Murata](#)²⁶,
- [Yusuke Nabeka](#) ORCID: orcid.org/0000-0002-8692-5981²⁶,
- [Timothy Paape](#)¹³,
- [Sudharsan Padmarasu](#) ORCID: orcid.org/0000-0003-3125-3695⁴,
- [Lawrence Percival-Alwyn](#)¹⁸,
- [Sateesh Kagale](#)⁶,
- [Uwe Scholz](#) ORCID: orcid.org/0000-0001-6113-3518⁴,
- [Jun Sese](#)^{25,27},

- [Philomin Juliana](#) ORCID: [orcid.org/0000-0001-6922-0173²⁸](http://orcid.org/0000-0001-6922-0173),
- [Ravi Singh](#) ORCID: [orcid.org/0000-0002-4676-5071²⁸](http://orcid.org/0000-0002-4676-5071),
- [Rie Shimizu-Inatsugi](#)¹³,
- [David Swarbreck](#)¹⁷,
- [James Cockram](#) ORCID: [orcid.org/0000-0002-1014-6463¹⁸](http://orcid.org/0000-0002-1014-6463),
- [Hikmet Budak](#) ORCID: [orcid.org/0000-0002-2556-2478²⁹](http://orcid.org/0000-0002-2556-2478),
- [Toshiaki Tameshige](#)¹⁵,
- [Tsuyoshi Tanaka](#)²³,
- [Hiroyuki Tsuji](#) ORCID: [orcid.org/0000-0002-6444-559X¹⁵](http://orcid.org/0000-0002-6444-559X),
- [Jonathan Wright](#) ORCID: [orcid.org/0000-0001-6471-8749¹⁷](http://orcid.org/0000-0001-6471-8749),
- [Jianzhong Wu](#) ORCID: [orcid.org/0000-0002-4033-852X²³](http://orcid.org/0000-0002-4033-852X),
- [Burkhard Steuernagel](#)⁷,
- [Ian Small](#) ORCID: [orcid.org/0000-0001-5300-1216³⁰](http://orcid.org/0000-0001-5300-1216),
- [Sylvie Cloutier](#)³¹,
- [Gabriel Keeble-Gagnère](#)³²,
- [Gary Muehlbauer](#)¹⁹,
- [Josquin Tibbets](#)³²,
- [Shuhei Nasuda](#)²⁶,
- [Joanna Melonek](#) ORCID: [orcid.org/0000-0003-4471-2520³⁰](http://orcid.org/0000-0003-4471-2520),
- [Pierre J. Hucl](#)¹,
- [Andrew G. Sharpe](#) ORCID: [orcid.org/0000-0002-1832-4009²⁰](http://orcid.org/0000-0002-1832-4009),
- [Matthew Clark](#) ORCID: [orcid.org/0000-0002-8049-5423¹⁶](http://orcid.org/0000-0002-8049-5423),
- [Erik Legg](#)³³,
- [Arvind Bharti](#)³³,
- [Peter Langridge](#) ORCID: [orcid.org/0000-0001-9494-400X³⁴](http://orcid.org/0000-0001-9494-400X),
- [Anthony Hall](#) ORCID: [orcid.org/0000-0002-1806-020X¹⁷](http://orcid.org/0000-0002-1806-020X),
- [Cristobal Uauy](#) ORCID: [orcid.org/0000-0002-9814-1770⁷](http://orcid.org/0000-0002-9814-1770),
- [Martin Mascher](#) ORCID: [orcid.org/0000-0001-6373-6013^{4,35}](http://orcid.org/0000-0001-6373-6013),
- [Simon G. Krattinger](#) ORCID: [orcid.org/0000-0001-6912-7411^{8,36}](http://orcid.org/0000-0001-6912-7411),
- [Hirokazu Handa](#)^{23,37},
- [Kentaro K. Shimizu](#) ORCID: [orcid.org/0000-0002-6483-1781^{13,15}](http://orcid.org/0000-0002-6483-1781),
- [Assaf Distelfeld](#)³⁸,
- [Ken Chalmers](#)³⁴,
- [Beat Keller](#) ORCID: [orcid.org/0000-0003-2379-9225⁸](http://orcid.org/0000-0003-2379-9225),

- [Klaus F. X. Mayer](#) ORCID: [orcid.org/0000-0001-6484-1077^{5,39}](https://orcid.org/0000-0001-6484-1077),
- [Jesse Poland](#) ORCID: [orcid.org/0000-0002-7856-1399³](https://orcid.org/0000-0002-7856-1399),
- [Nils Stein](#) ORCID: [orcid.org/0000-0003-3011-8731^{4,40}](https://orcid.org/0000-0003-3011-8731),
- [Curt A. McCartney](#) ORCID: [orcid.org/0000-0002-9482-3133⁹](https://orcid.org/0000-0002-9482-3133),
- [Manuel Spannagl](#) ORCID: [orcid.org/0000-0003-0701-7035⁵](https://orcid.org/0000-0003-0701-7035),
- [Thomas Wicker](#) ORCID: [orcid.org/0000-0002-6777-7135⁸](https://orcid.org/0000-0002-6777-7135) &
- [Curtis J. Pozniak](#) ORCID: [orcid.org/0000-0002-7536-3856¹](https://orcid.org/0000-0002-7536-3856)

[Nature](#) volume **588**, pages277–283(2020)[Cite this article](#)

- 15k Accesses
- 1 Citations
- 473 Altmetric
- [Metrics details](#)

Subjects

- [Comparative genomics](#)
- [Haplotypes](#)
- [Plant breeding](#)
- [Structural variation](#)

Abstract

Advances in genomics have expedited the improvement of several agriculturally important crops but similar efforts in wheat (*Triticum* spp.) have been more challenging. This is largely owing to the size and complexity of the wheat genome¹, and the lack of genome-assembly data for multiple wheat lines^{2,3}. Here we generated ten chromosome pseudomolecule and five scaffold assemblies of hexaploid wheat to explore the genomic diversity among wheat lines from global breeding programs. Comparative analysis revealed extensive structural rearrangements, introgressions from wild relatives and differences in gene content resulting

from complex breeding histories aimed at improving adaptation to diverse environments, grain yield and quality, and resistance to stresses^{4,5}. We provide examples outlining the utility of these genomes, including a detailed multi-genome-derived nucleotide-binding leucine-rich repeat protein repertoire involved in disease resistance and the characterization of *Sm1*⁶, a gene associated with insect resistance. These genome assemblies will provide a basis for functional gene discovery and breeding to deliver the next generation of modern wheat cultivars.

[Access through your institution](#)

[Change institution](#)

[Buy or subscribe](#)

Access options

Subscribe to Journal

Get full journal access for 1 year

185,98 €

only 3,58 € per issue

[Subscribe](#)

All prices are NET prices.

VAT will be added later in the checkout.

Rent or Buy article

Get time limited or full article access on ReadCube.

from \$8.99

[Rent or Buy](#)

All prices are NET prices.

Additional access options:

- [Log in](#)
- [Access through your institution](#)
- [Learn about institutional subscriptions](#)

Fig. 1: Patterns of variation in the wheat genome.

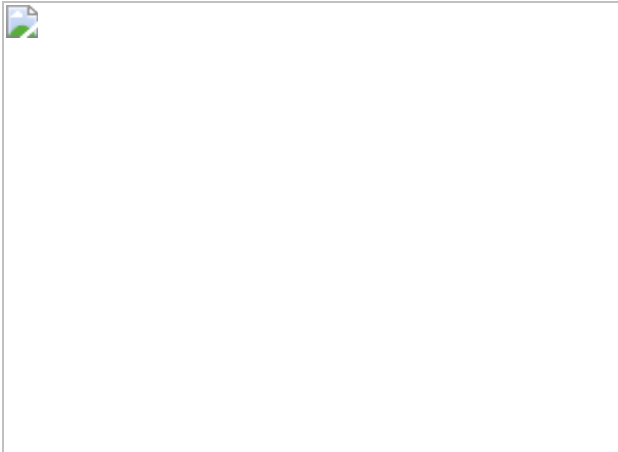


Fig. 2: Introgressions and large-scale structural variation in wheat.

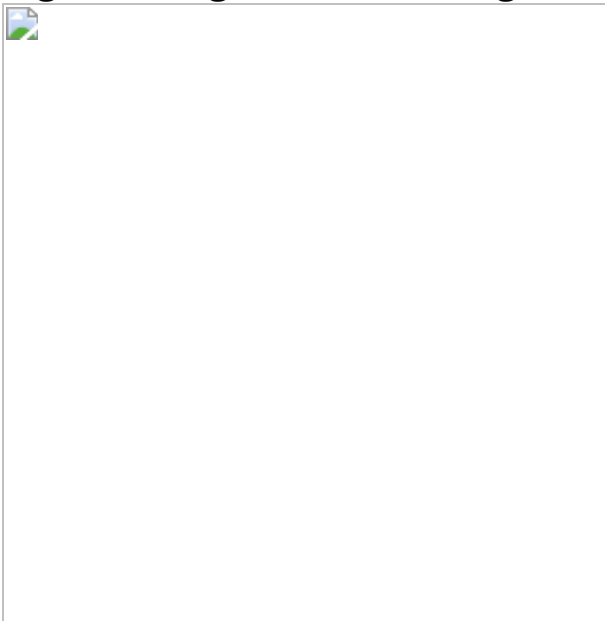
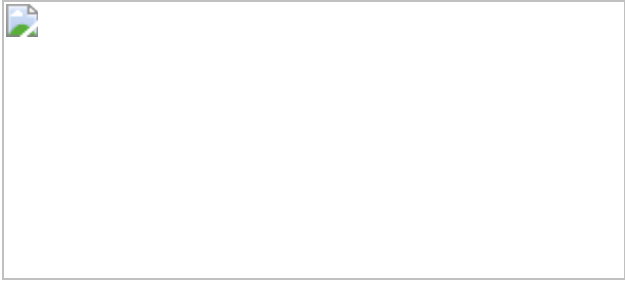


Fig. 3: Cloning of the gene *Sm1*.



Data availability

All sequence reads assemblies have been deposited into the National Center for Biotechnology Information sequence read archive (SRA) (see Supplementary Table 1 for accession numbers). Sequence reads for the RQAs, *T. ponticum*, *A. ventricosa* and *T. timopheevii* have been deposited into the SRA (accession no. [PRJNA544491](#)) and ChIP-seq short read-data used for centromere characterization is deposited under accession no. [PRJNA625537](#). All Hi-C data have been deposited in the European Nucleotide Archive (Supplementary Table 1). The RQAs are available for direct user download at <https://wheat.ipk-gatersleben.de/>. All assemblies and projected annotations are available for comparative analysis at Ensembl Plants (<https://plants.ensembl.org/index.html>). Comparative analysis viewers are also online for synteny (<https://kiranbandi.github.io/10wheatgenomes/>, <http://10wheatgenomes.plantinformatics.io/>) and haplotypes (<http://www.crop-haplotypes.com/>). Seed stocks of the assembled lines are available at the UK Germplasm Resources Unit (<https://www.seedstor.ac.uk/>).

Code availability

Code for custom genome visualizers have been deposited in the public domain for haplotype viewer (<https://github.com/Uauy-Lab/pangenome-haplotypes>), Pretzel (<https://github.com/plantinformatics/pretzel>), AccuSyn (<https://github.com/jorgenunezsiri/accusyn>) and SynVisio (<https://github.com/kiranbandi/synvisio>). Additional scripts used for ChIP-seq analysis of the centromeres are provided at <https://github.com/wheatgenetics/centromere>.

References

1. 1.

The International Wheat Genome Sequencing Consortium. Shifting the limits in wheat research and breeding using a fully annotated reference genome. *Science* **361**, eaar7191 (2018).

[Google Scholar](#)

2. 2.

Montenegro, J. D. et al. The pangenome of hexaploid bread wheat. *Plant J.* **90**, 1007–1013 (2017).

[CAS](#) [PubMed](#) [Google Scholar](#)

3. 3.

International Wheat Genome Sequencing Consortium (IWGSC). A chromosome-based draft sequence of the hexaploid bread wheat (*Triticum aestivum*) genome. *Science* **345**, 1251788 (2014).

[Google Scholar](#)

4. 4.

He, F. et al. Exome sequencing highlights the role of wild-relative introgression in shaping the adaptive landscape of the wheat genome. *Nat. Genet.* **51**, 896–904 (2019); correction **51**, 1194 (2019).

[CAS](#) [PubMed](#) [Google Scholar](#)

5. 5.

Pont, C. et al. Tracing the ancestry of modern bread wheats. *Nat. Genet.* **51**, 905–911 (2019).

[CAS](#) [PubMed](#) [Google Scholar](#)

6. 6.

Kassa, M. T. et al. A saturated SNP linkage map for the orange wheat blossom midge resistance gene Sm1. *Theor. Appl. Genet.* **129**, 1507–1517 (2016).

[CAS](#) [PubMed](#) [Google Scholar](#)

7. 7.

Tadesse, W. et al. Genetic gains in wheat breeding and its role in feeding the world. *Crop Breed. Genet. Genom.* **1**, e190005 (2019).

[Google Scholar](#)

8. 8.

Zhao, Q. et al. Pan-genome analysis highlights the extent of genomic variation in cultivated and wild rice. *Nat. Genet.* **50**, 278–284 (2018).

[CAS](#) [PubMed](#) [Google Scholar](#)

9. 9.

Dubcovsky, J. & Dvorak, J. Genome plasticity a key factor in the success of polyploid wheat under domestication. *Science* **316**, 1862–1866 (2007).

[CAS](#) [PubMed](#) [PubMed Central](#) [Google Scholar](#)

10. 10.

Marcussen, T. et al. Ancient hybridizations among the ancestral genomes of bread wheat. *Science* **345**, 1250092 (2014).

[PubMed](#) [Google Scholar](#)

11. 11.

Avni, R. et al. Wild emmer genome architecture and diversity elucidate wheat evolution and domestication. *Science* **357**, 93–97 (2017).

[ADS](#) [CAS](#) [PubMed](#) [Google Scholar](#)

12. 12.

Maccaferri, M. et al. Durum wheat genome highlights past domestication signatures and future improvement targets. *Nat. Genet.* **51**, 885–895 (2019).

[CAS](#) [PubMed](#) [Google Scholar](#)

13. 13.

Zimin, A. V. et al. The first near-complete assembly of the hexaploid bread wheat genome, *Triticum aestivum*. *Gigascience* **6**, 1–7 (2017).

[ADS](#) [CAS](#) [PubMed](#) [PubMed Central](#) [Google Scholar](#)

14. 14.

Winfield, M. O. et al. Targeted re-sequencing of the allohexaploid wheat exome. *Plant Biotechnol. J.* **10**, 733–742 (2012).

[CAS](#) [PubMed](#) [Google Scholar](#)

15. 15.

Arora, D., Gross, T. & Brueggeman, R. Allele characterization of genes required for rpg4-mediated wheat stem rust resistance identifies *Rpg5* as the R gene. *Phytopathology* **103**, 1153–1161 (2013).

[CAS](#) [PubMed](#) [Google Scholar](#)

16. 16.

Adamski, N. M. et al. A roadmap for gene functional characterisation in crops with large genomes: lessons from polyploid wheat. *eLife* **9**, e55646 (2020).

17. 17.

Uauy, C. Wheat genomics comes of age. *Curr. Opin. Plant Biol.* **36**, 142–148 (2017).

[PubMed](#) [Google Scholar](#)

18. 18.

Mascher, M. et al. A chromosome conformation capture ordered sequence of the barley genome. *Nature* **544**, 427–433 (2017).

[ADS](#) [CAS](#) [PubMed](#) [Google Scholar](#)

19. 19.

Edwards, D. et al. Bread matters: a national initiative to profile the genetic diversity of Australian wheat. *Plant Biotechnol. J.* **10**, 703–708 (2012).

[CAS](#) [PubMed](#) [Google Scholar](#)

20. 20.

Jordan, K. W. et al. A haplotype map of allohexaploid wheat reveals distinct patterns of selection on homoeologous genomes. *Genome Biol.* **16**, 48 (2015).

[PubMed](#) [PubMed Central](#) [Google Scholar](#)

21. 21.

Paape, T. et al. Patterns of polymorphism and selection in the subgenomes of the allotetraploid *Arabidopsis kamchatica*. *Nat. Commun.* **9**, 3909 (2018).

[ADS](#) [PubMed](#) [PubMed Central](#) [Google Scholar](#)

22. 22.

Paape, T. et al. Conserved but attenuated parental gene expression in allopolyploids: Constitutive zinc hyperaccumulation in the allotetraploid *Arabidopsis kamchatica*. *Mol. Biol. Evol.* **33**, 2781–2800 (2016).

[CAS](#) [PubMed](#) [PubMed Central](#) [Google Scholar](#)

23. 23.

Melonek, J., Stone, J. D. & Small, I. Evolutionary plasticity of restorer-of-fertility-like proteins in rice. *Sci. Rep.* **6**, 35152 (2016).

[ADS](#) [CAS](#) [PubMed](#) [PubMed Central](#) [Google Scholar](#)

24. 24.

Bernhard, T., Koch, M., Snowdon, R. J., Friedt, W. & Wittkop, B. Undesired fertility restoration in *msm1* barley associates with two mTERF genes. *Theor. Appl. Genet.* **132**, 1335–1350 (2019).

[CAS](#) [PubMed](#) [Google Scholar](#)

25. 25.

Whitford, R. et al. Hybrid breeding in wheat: technologies to improve hybrid wheat seed production. *J. Exp. Bot.* **64**, 5411–5428 (2013).

[CAS](#) [PubMed](#) [Google Scholar](#)

26. 26.

Keller, B., Wicker, T. & Krattinger, S. G. Advances in wheat and pathogen genomics: Implications for disease control. *Annu. Rev. Phytopathol.* **56**, 67–87 (2018).

[CAS](#) [PubMed](#) [Google Scholar](#)

27. 27.

Steuernagel, B. et al. Rapid cloning of disease-resistance genes in plants using mutagenesis and sequence capture. *Nat. Biotechnol.* **34**, 652–655 (2016).

[CAS](#) [PubMed](#) [Google Scholar](#)

28. 28.

Bariana, H. S. et al. Mapping of durable adult plant and seedling resistances to stripe rust and stem rust diseases in wheat. *Aust. J. Agric. Res.* **52**, 1247–1255 (2001).

[CAS](#) [Google Scholar](#)

29. 29.

Chemayek, B. et al. Tight repulsion linkage between *Sr36* and *Sr39* was revealed by genetic, cytogenetic and molecular analyses. *Theor. Appl. Genet.* **130**, 587–595 (2017).

[CAS](#) [PubMed](#) [Google Scholar](#)

30. 30.

Cruz, C. D. et al. The 2NS translocation from *Aegilops ventricosa* confers resistance to the *Triticum* pathotype of *Magnaporthe oryzae*. *Crop Sci.* **56**, 990–1000 (2016).

[CAS](#) [PubMed](#) [PubMed Central](#) [Google Scholar](#)

31. 31.

Helguera, M. et al. PCR assays for the Lr37-Yr17-Sr38 cluster of rust resistance genes and their use to develop isogenic hard red spring wheat lines. *Crop Sci.* **43**, 1839–1847 (2003).

[CAS](#) [Google Scholar](#)

32. 32.

Li, Y. & Wei, K. Comparative functional genomics analysis of cytochrome P450 gene superfamily in wheat and maize. *BMC Plant Biol.* **20**, 93 (2020).

[CAS](#) [PubMed](#) [PubMed Central](#) [Google Scholar](#)

33. 33.

Gunupuru, L. R. et al. A wheat cytochrome P450 enhances both resistance to deoxynivalenol and grain yield. *PLoS ONE* **13**, e0204992 (2018).

[PubMed](#) [PubMed Central](#) [Google Scholar](#)

34. 34.

Li, B. et al. Wheat centromeric retrotransposons: the new ones take a major role in centromeric structure. *Plant J.* **73**, 952–965 (2013).

[CAS](#) [PubMed](#) [Google Scholar](#)

35. 35.

Gent, J. I., Wang, K., Jiang, J. & Dawe, R. K. Stable patterns of CENH3 occupancy through maize lineages containing genetically similar centromeres. *Genetics* **200**, 1105–1116 (2015).

[PubMed](#) [PubMed Central](#) [Google Scholar](#)

36. 36.

Koo, D. H., Sehgal, S. K., Friebel, B. & Gill, B. S. Structure and stability of telocentric chromosomes in wheat. *PLoS ONE* **10**, e0137747 (2015).

[PubMed](#) [PubMed Central](#) [Google Scholar](#)

37. 37.

Schneider, K. L., Xie, Z., Wolfgruber, T. K. & Presting, G. G. Inbreeding drives maize centromere evolution. *Proc. Natl Acad. Sci. USA* **113**, E987–E996 (2016).

[ADS](#) [CAS](#) [PubMed](#) [Google Scholar](#)

38. 38.

Saxena, R. K., Edwards, D. & Varshney, R. K. Structural variations in plant genomes. *Brief. Funct. Genomics* **13**, 296–307 (2014).

[PubMed](#) [PubMed Central](#) [Google Scholar](#)

39. 39.

Harewood, L. et al. Hi-C as a tool for precise detection and characterisation of chromosomal rearrangements and copy number variation in human tumours. *Genome Biol.* **18**, 125 (2017).

[PubMed](#) [PubMed Central](#) [Google Scholar](#)

40. 40.

Himmelbach, A. et al. Discovery of multi-megabase polymorphic inversions by chromosome conformation capture sequencing in large-genome plant species. *Plant J.* **96**, 1309–1316 (2018).

[CAS](#) [PubMed](#) [Google Scholar](#)

41. 41.

Fradgley, N. et al. A large-scale pedigree resource of wheat reveals evidence for adaptation and selection by breeders. *PLoS Biol.* **17**, e3000071 (2019).

[PubMed](#) [PubMed Central](#) [Google Scholar](#)

42. 42.

Martín, A. C., Rey, M. D., Shaw, P. & Moore, G. Dual effect of the wheat Ph1 locus on chromosome synapsis and crossover. *Chromosoma* **126**, 669–680 (2017).

[PubMed](#) [PubMed Central](#) [Google Scholar](#)

43. 43.

Bevan, M. W. et al. Genomic innovation for crop improvement. *Nature* **543**, 346–354 (2017).

[ADS](#) [CAS](#) [PubMed](#) [Google Scholar](#)

44. 44.

Luján Basile, S. M. et al. Haplotype block analysis of an Argentinean hexaploid wheat collection and GWAS for yield components and adaptation. *BMC Plant Biol.* **19**, 553 (2019).

[PubMed](#) [PubMed Central](#) [Google Scholar](#)

45. 45.

Fox, S. L. et al. Unity hard red spring wheat. *Can. J. Plant Sci.* **90**, 71–78 (2010).

[Google Scholar](#)

46. 46.

Hanks, S. K., Quinn, A. M. & Hunter, T. The protein kinase family: conserved features and deduced phylogeny of the catalytic domains. *Science* **241**, 42–52 (1988).

[ADS](#) [CAS](#) [PubMed](#) [Google Scholar](#)

47. 47.

Brueggeman, R. et al. The stem rust resistance gene *Rpg5* encodes a protein with nucleotide-binding-site, leucine-rich, and protein kinase domains. *Proc. Natl Acad. Sci. USA* **105**, 14970–14975 (2008).

[ADS](#) [CAS](#) [PubMed](#) [Google Scholar](#)

48. 48.

Faris, J. D. et al. A unique wheat disease resistance-like gene governs effector-triggered susceptibility to necrotrophic pathogens. *Proc. Natl Acad. Sci. USA* **107**, 13544–13549 (2010).

[ADS](#) [CAS](#) [PubMed](#) [Google Scholar](#)

49. 49.

Luo, M. C. et al. Genome sequence of the progenitor of the wheat D genome *Aegilops tauschii*. *Nature* **551**, 498–502 (2017).

[ADS](#) [CAS](#) [PubMed](#) [PubMed Central](#) [Google Scholar](#)

50. 50.

Borrill, P., Harrington, S. A. & Uauy, C. Applying the latest advances in genomics and phenomics for trait discovery in polyploid wheat. *Plant J.* **97**, 56–72 (2019).

[CAS](#) [PubMed](#) [Google Scholar](#)

51. 51.

Dvorak, J., Mcguire, P. E. & Cassidy, B. Apparent sources of the A genomes of wheats inferred from polymorphism in abundance and restriction fragment length of repeated nucleotide-sequences. *Genome* **30**, 680–689 (1988).

[CAS](#) [Google Scholar](#)

52. 52.

Watson-Haigh, N. S., Suchecki, R., Kalashyan, E., Garcia, M. & Baumann, U. DAWN: a resource for yielding insights into the diversity among wheat genomes. *BMC Genomics* **19**, 941 (2018).

[CAS](#) [PubMed](#) [PubMed Central](#) [Google Scholar](#)

53. 53.

Kent, W. J. BLAT—the BLAST-like alignment tool. *Genome Res.* **12**, 656–664 (2002).

[CAS](#) [PubMed](#) [PubMed Central](#) [Google Scholar](#)

54. 54.

Slater, G. S. & Birney, E. Automated generation of heuristics for biological sequence comparison. *BMC Bioinformatics* **6**, 31 (2005).

[PubMed](#) [PubMed Central](#) [Google Scholar](#)

55. 55.

Tatusov, R. L., Galperin, M. Y., Natale, D. A. & Koonin, E. V. The COG database: a tool for genome-scale analysis of protein functions and evolution. *Nucleic Acids Res.* **28**, 33–36 (2000).

[CAS](#) [PubMed](#) [PubMed Central](#) [Google Scholar](#)

56. 56.

Thornton, K. Libsequence: a C++ class library for evolutionary genetic analysis. *Bioinformatics* **19**, 2325–2327 (2003).

[CAS](#) [PubMed](#) [Google Scholar](#)

57. 57.

Cheng, S. et al. Redefining the structural motifs that determine RNA binding and RNA editing by pentatricopeptide repeat proteins in land

plants. *Plant J.* **85**, 532–547 (2016).

[CAS](#) [PubMed](#) [Google Scholar](#)

58. 58.

Steuernagel, B. et al. Physical and transcriptional organisation of the bread wheat intracellular immune receptor repertoire. Preprint at <https://doi.org/10.1101/339424> (2018).

59. 59.

Steuernagel, B. et al. The NLR-Annotator tool enables annotation of the intracellular immune receptor repertoire. *Plant Physiol.* **183**, 468–482 (2020).

[CAS](#) [PubMed](#) [PubMed Central](#) [Google Scholar](#)

60. 60.

Spannagl, M. et al. PGSB PlantsDB: updates to the database framework for comparative plant genome research. *Nucleic Acids Res.* **44** (D1), D1141–D1147 (2016).

[CAS](#) [PubMed](#) [Google Scholar](#)

61. 61.

Benson, G. Tandem repeats finder: a program to analyze DNA sequences. *Nucleic Acids Res.* **27**, 573–580 (1999).

[CAS](#) [PubMed](#) [PubMed Central](#) [Google Scholar](#)

62. 62.

Nagaki, K. et al. Chromatin immunoprecipitation reveals that the 180-bp satellite repeat is the key functional DNA element of *Arabidopsis thaliana* centromeres. *Genetics* **163**, 1221–1225 (2003).

[CAS](#) [PubMed](#) [PubMed Central](#) [Google Scholar](#)

63. 63.

Guo, X. et al. De novo centromere formation and centromeric sequence expansion in wheat and its wide hybrids. *PLoS Genet.* **12**, e1005997 (2016).

[PubMed](#) [PubMed Central](#) [Google Scholar](#)

64. 64.

Kim, D., Paggi, J. M., Park, C., Bennett, C. & Salzberg, S. L. Graph-based genome alignment and genotyping with HISAT2 and HISAT-genotype. *Nat. Biotechnol.* **37**, 907–915 (2019).

[CAS](#) [PubMed](#) [PubMed Central](#) [Google Scholar](#)

65. 65.

Wicker, T. et al. Impact of transposable elements on genome structure and evolution in bread wheat. *Genome Biol.* **19**, 103 (2018).

[PubMed](#) [PubMed Central](#) [Google Scholar](#)

66. 66.

Tang, Z., Yang, Z. & Fu, S. Oligonucleotides replacing the roles of repetitive sequences pAs1, pSc119.2, pTa-535, pTa71, CCS1, and pAWRC.1 for FISH analysis. *J. Appl. Genet.* **55**, 313–318 (2014).

[CAS](#) [PubMed](#) [Google Scholar](#)

67. 67.

Zhao, L. et al. Cytological identification of an *Aegilops variabilis* chromosome carrying stripe rust resistance in wheat. *Breed. Sci.* **66**, 522–529 (2016).

[ADS](#) [CAS](#) [PubMed](#) [PubMed Central](#) [Google Scholar](#)

68. 68.

Komuro, S., Endo, R., Shikata, K. & Kato, A. Genomic and chromosomal distribution patterns of various repeated DNA sequences in wheat revealed by a fluorescence *in situ* hybridization procedure. *Genome* **56**, 131–137 (2013).

[CAS](#) [PubMed](#) [Google Scholar](#)

69. 69.

Li, H. Minimap2: pairwise alignment for nucleotide sequences. *Bioinformatics* **34**, 3094–3100 (2018).

[CAS](#) [PubMed](#) [PubMed Central](#) [Google Scholar](#)

70. 70.

Kubaláková, M., Vrána, J., Cíhalíková, J., Simková, H. & Doležel, J. Flow karyotyping and chromosome sorting in bread wheat (*Triticum aestivum* L.). *Theor. Appl. Genet.* **104**, 1362–1372 (2002).

[PubMed](#) [Google Scholar](#)

71. 71.

Brinton, J. et al. A haplotype-led approach to increase the precision of wheat breeding. *Commun. Biol.* <https://doi.org/10.1038/s42003-020-01413-2> (2020).

72. 72.

Thomas, J. et al. Chromosome location and markers of Sm1: a gene of wheat that conditions antibiotic resistance to orange wheat blossom midge. *Mol. Breed.* **15**, 183–192 (2005).

[CAS](#) [Google Scholar](#)

73. 73.

Lamb, R. J. et al. Resistance to *Sitodiplosis mosellana* (Diptera: Cecidomyiidae) in spring wheat (Gramineae). *Can. Entomol.* **132**, 591–605 (2000).

[Google Scholar](#)

74. 74.

la Cour, T. et al. Analysis and prediction of leucine-rich nuclear export signals. *Protein Eng. Des. Sel.* **17**, 527–536 (2004).

[PubMed](#) [Google Scholar](#)

[Download references](#)

Acknowledgements

We are grateful for funding from the Canadian Triticum Applied Genomics research project (CTAG2) funded by Genome Canada, Genome Prairie, the Western Grains Research Foundation, Government of Saskatchewan, Saskatchewan Wheat Development Commission, Alberta Wheat Commission, Viterra and Manitoba Wheat and Barley Growers Association. Funding was also provided by the Biotechnology and Biological Sciences Research Council (BBSRC) via the projects Designing Future Wheat (BB/P016855/1), sLOLA (BB/J003557/1) and MAGIC Pangenome (BB/P010741/1, BB/P010733/1 and BB/P010768/1), by AMED NBRP (JP17km0210142), the German Federal Ministry of Education and Research (FKZ 031B0190, WHEATSeq, 2819103915 and 2819104015), German Network for Bioinformatics and Infrastructure de.NBI (FKZ 031A536A, 031A536B), German Federal Ministry of Food and Agriculture (BMEL FKZ 2819103915 WHEATSEQ), Israel Science Foundation (Grant 1137/17), JST CREST (JPMJCR16O3), US National Science Foundation (1339389), Kansas Wheat Commission and Kansas State University, MEXT KAKENHI, The Birth of New Plant Species (JP16H06469, JP16H06464, JP16H06466 and JP16K21727), National Agriculture and

Food Research Organization (NARO) Vice President Fund, Swiss Federal Office of Agriculture (NAP-PGREL), Agroscope, Delley Seeds and Plants, ETH Zurich Institute of Agricultural Sciences, Fenaco Co-operative, IP-SUISSE, swisssem, JOWA, SGPV-FSPC, Swiss National Science Foundation (31003A_182318 and CRSII5_183578), University of Zurich Research Priority Program Evolution in Action, King Abdullah University of Science and Technology, Grains Research and Development Corporation (GRDC), Australian Research Council (CE140100008) and Groupe Limagrain. We are grateful for the computational support of the Functional Genomics Center Zurich, the Molecular Plant Breeding Group—ETH Zurich, and the Global Institute of Food Security (GIFS), Saskatoon. We acknowledge the contribution of the Australian Wheat Pathogens Consortium (<https://data.bioplatforms.com/organization/edit/bpa-wheat-cultivars>) in the generation of data used in this publication. The Initiative is supported by funding from Bioplatforms Australia through the Australian Government National Collaborative Research Infrastructure Strategy (NCRIS). We thank S. Wu for DNA preparations for assembly and ChIP-seq library preparations; O. Francisco-Pabalan and J. Santos, T. Wisk and S. Wolfe for their provision of OWBM images; M. Knauft, I. Walde, S. König, T. Münch, J. Bauernfeind and D. Schüler for their contribution to Hi-C data generation and sequencing, DNA sequencing and IT administration and sequence data management; J. Vrána for karyotyping the wheat cultivars Arina and Forno; and R. Regier for project management, administration and support.

Author information

Author notes

1. These authors contributed equally: Sean Walkowiak, Liangliang Gao, Cecile Monat

Affiliations

1. Crop Development Centre, University of Saskatchewan, Saskatoon, Saskatchewan, Canada

Sean Walkowiak, Valentyna Klymiuk, Brook Byrns, Kirby Nilsen, Jennifer Ens, Krystalee Wiebe, Amidou N'Diaye, Pierre J. Hucl & Curtis J. Pozniak

2. Grain Research Laboratory, Canadian Grain Commission, Winnipeg, Manitoba, Canada

Sean Walkowiak & Bin Xiao Fu

3. Department of Plant Pathology, Kansas State University, Manhattan, KS, USA

Liangliang Gao, Emily Delorean, Dal-Hoe Koo, Allen K. Fritz & Jesse Poland

4. Leibniz Institute of Plant Genetics and Crop Plant Research (IPK) Gatersleben, Seeland, Germany

Cecile Monat, Axel Himmelbach, Anne Fiebig, Sudharsan Padmarasu, Uwe Scholz, Martin Mascher & Nils Stein

5. Helmholtz Zentrum München—German Research Center for Environmental Health, Neuherberg, Germany

Georg Haberer, Heidrun Gundlach, Klaus F. X. Mayer & Manuel Spannagl

6. Aquatic and Crop Resource Development, National Research Council Canada, Saskatoon, Saskatchewan, Canada

Mulualem T. Kassa, Pierre Fobert & Sateesh Kagale

7. John Innes Centre, Norwich Research Park, Norwich, UK

Jemima Brinton, Ricardo H. Ramirez-Gonzalez, Michael Bevan, Neil McKenzie, Burkhard Steuernagel & Cristobal Uauy

8. Department of Plant and Microbial Biology, University of Zurich,
Zurich, Switzerland

Markus C. Kolodziej, Simon G. Krattinger, Beat Keller & Thomas Wicker

9. Morden Research and Development Centre, Agriculture and Agri-Food Canada, Morden, Manitoba, Canada

Dinushika Thambugala & Curt A. McCartney

10. Department of Computer Science, University of Saskatchewan,
Saskatoon, Saskatchewan, Canada

Venkat Bandi, Jorge Nunez Siri & Carl Gutwin

11. Brandon Research and Development Centre, Agriculture and Agri-Food Canada, Brandon, Manitoba, Canada

Kirby Nilsen

12. Genomics/Transcriptomics group, Functional Genomics Center
Zurich, Zurich, Switzerland

Catharine Aquino & Masaomi Hatakeyama

13. Department of Evolutionary Biology and Environmental Studies,
University of Zurich, Zurich, Switzerland

Dario Copetti, Gwyneth Halstead-Nussloch, Masaomi Hatakeyama, Timothy Paape, Rie Shimizu-Inatsugi & Kentaro K. Shimizu

14. Institute of Agricultural Sciences, ETHZ, Zurich, Switzerland

Dario Copetti

15. Kihara Institute for Biological Research, Yokohama City University,
Yokohama, Japan

Tomohiro Ban, Kanako Kawaura, Toshiaki Tameshige, Hiroyuki
Tsui & Kentaro K. Shimizu

16. Life Sciences Department, Natural History Museum, London, UK

Luca Venturini & Matthew Clark

17. Earlham Institute, Norwich Research Park, Norwich, UK

Bernardo Clavijo, Christine Fosker, Gonzalo Garcia Accinelli, Darren
Heavens, Ksenia Krasileva, David Swarbreck, Jonathan
Wright & Anthony Hall

18. The John Bingham Laboratory, NIAB, Cambridge, UK

Keith A. Gardner, Nick Fradgley, Lawrence Percival-Alwyn & James
Cockram

19. Department of Agronomy and Plant Genetics, University of
Minnesota, Saint Paul, MN, USA

Juan Gutierrez-Gonzalez & Gary Muehlbauer

20. Global Institute for Food Security, University of Saskatchewan,
Saskatoon, Saskatchewan, Canada

Chu Shin Koh & Andrew G. Sharpe

21. School of Plant Sciences and Food Security, Tel Aviv University,
Ramat Aviv, Israel

Jasline Deek

22. Department of Entomology, University of Manitoba, Winnipeg,
Manitoba, Canada

Alejandro C. Costamagna

23. Institute of Crop Science, NARO, Tsukuba, Japan

Hiroyuki Kanamori, Fuminori Kobayashi, Tsuyoshi Tanaka, Jianzhong Wu & Hirokazu Handa

24. Centre for Biodiversity Genomics, University of Guelph, Guelph, Ontario, Canada

Tony Kuo

25. National Institute of Advanced Industrial Science and Technology (AIST), Tokyo, Japan

Tony Kuo & Jun Sese

26. Laboratory of Plant Genetics, Graduate School of Agriculture, Kyoto University, Kyoto, Japan

Kazuki Murata, Yusuke Nabeka & Shuhei Nasuda

27. Humanome Lab, Tokyo, Japan

Jun Sese

28. Global Wheat Program, International Maize and Wheat Improvement Center (CIMMYT), Texcoco, Mexico

Philomin Juliana & Ravi Singh

29. Montana BioAg, Missoula, MT, USA

Hikmet Budak

30. Australian Research Council Centre of Excellence in Plant Energy Biology, School of Molecular Sciences, University of Western Australia, Perth, Western Australia, Australia

Ian Small & Joanna Melonek

31. Ottawa Research and Development Centre, Agriculture and Agri-Food Canada, Ottawa, Ontario, Canada

Sylvie Cloutier

32. Agriculture Victoria, AgriBio, Centre for AgriBioscience, Bundoora, Victoria, Australia

Gabriel Keeble-Gagnère & Josquin Tibbets

33. Syngenta, Durham, NC, USA

Erik Legg & Arvind Bharti

34. School of Agriculture, Food and Wine, University of Adelaide, Adelaide, South Australia, Australia

Peter Langridge & Ken Chalmers

35. German Centre for Integrative Biodiversity Research (iDiv) Halle-Jena-Leipzig, Leipzig, Germany

Martin Mascher

36. Biological and Environmental Science & Engineering Division, King Abdullah University of Science and Technology, Thuwal, Saudi Arabia

Simon G. Krattinger

37. Graduate School of Life and Environmental Sciences, Kyoto Prefectural University, Kyoto, Japan

Hirokazu Handa

38. Institute of Evolution and Department of Evolutionary and Environmental Biology, University of Haifa, Haifa, Israel

Assaf Distelfeld

39. School of Life Sciences Weihenstephan, Technical University of Munich, Freising, Germany

Klaus F. X. Mayer

40. Center for Integrated Breeding Research (CiBreed), Georg-August-University Göttingen, Göttingen, Germany

Nils Stein

Authors

1. Sean Walkowiak

[View author publications](#)

You can also search for this author in [PubMed](#) [Google Scholar](#)

2. Liangliang Gao

[View author publications](#)

You can also search for this author in [PubMed](#) [Google Scholar](#)

3. Cecile Monat

[View author publications](#)

You can also search for this author in [PubMed](#) [Google Scholar](#)

4. Georg Haberer

[View author publications](#)

You can also search for this author in [PubMed](#) [Google Scholar](#)

5. Mulualem T. Kassa

[View author publications](#)

You can also search for this author in [PubMed](#) [Google Scholar](#)

6. Jemima Brinton

[View author publications](#)

You can also search for this author in [PubMed](#) [Google Scholar](#)

7. Ricardo H. Ramirez-Gonzalez

[View author publications](#)

You can also search for this author in [PubMed](#) [Google Scholar](#)

8. Markus C. Kolodziej

[View author publications](#)

You can also search for this author in [PubMed](#) [Google Scholar](#)

9. Emily Delorean

[View author publications](#)

You can also search for this author in [PubMed](#) [Google Scholar](#)

10. Dinushika Thambugala

[View author publications](#)

You can also search for this author in [PubMed](#) [Google Scholar](#)

11. Valentyna Klymiuk

[View author publications](#)

You can also search for this author in [PubMed](#) [Google Scholar](#)

12. Brook Byrns

[View author publications](#)

You can also search for this author in [PubMed](#) [Google Scholar](#)

13. Heidrun Gundlach

[View author publications](#)

You can also search for this author in [PubMed](#) [Google Scholar](#)

14. Venkat Bandi

[View author publications](#)

You can also search for this author in [PubMed](#) [Google Scholar](#)

15. Jorge Nunez Siri

[View author publications](#)

You can also search for this author in [PubMed](#) [Google Scholar](#)

16. Kirby Nilsen

[View author publications](#)

You can also search for this author in [PubMed](#) [Google Scholar](#)

17. Catharine Aquino

[View author publications](#)

You can also search for this author in [PubMed](#) [Google Scholar](#)

18. Axel Himmelbach

[View author publications](#)

You can also search for this author in [PubMed](#) [Google Scholar](#)

19. Dario Copetti

[View author publications](#)

You can also search for this author in [PubMed](#) [Google Scholar](#)

20. Tomohiro Ban

[View author publications](#)

You can also search for this author in [PubMed](#) [Google Scholar](#)

21. Luca Venturini

[View author publications](#)

You can also search for this author in [PubMed](#) [Google Scholar](#)

22. Michael Bevan

[View author publications](#)

You can also search for this author in [PubMed](#) [Google Scholar](#)

23. Bernardo Clavijo

[View author publications](#)

You can also search for this author in [PubMed](#) [Google Scholar](#)

24. Dal-Hoe Koo

[View author publications](#)

You can also search for this author in [PubMed](#) [Google Scholar](#)

25. Jennifer Ens

[View author publications](#)

You can also search for this author in [PubMed](#) [Google Scholar](#)

26. Krystalee Wiebe

[View author publications](#)

You can also search for this author in [PubMed](#) [Google Scholar](#)

27. Amidou N'Diaye

[View author publications](#)

You can also search for this author in [PubMed](#) [Google Scholar](#)

28. Allen K. Fritz

[View author publications](#)

You can also search for this author in [PubMed](#) [Google Scholar](#)

29. Carl Gutwin

[View author publications](#)

You can also search for this author in [PubMed](#) [Google Scholar](#)

30. Anne Fiebig

[View author publications](#)

You can also search for this author in [PubMed](#) [Google Scholar](#)

31. Christine Fosker

[View author publications](#)

You can also search for this author in [PubMed](#) [Google Scholar](#)

32. Bin Xiao Fu

[View author publications](#)

You can also search for this author in [PubMed](#) [Google Scholar](#)

33. Gonzalo Garcia Accinelli

[View author publications](#)

You can also search for this author in [PubMed](#) [Google Scholar](#)

34. Keith A. Gardner

[View author publications](#)

You can also search for this author in [PubMed](#) [Google Scholar](#)

35. Nick Fradgley

[View author publications](#)

You can also search for this author in [PubMed](#) [Google Scholar](#)

36. Juan Gutierrez-Gonzalez

[View author publications](#)

You can also search for this author in [PubMed](#) [Google Scholar](#)

37. Gwyneth Halstead-Nussloch

[View author publications](#)

You can also search for this author in [PubMed](#) [Google Scholar](#)

38. Masaomi Hatakeyama

[View author publications](#)

You can also search for this author in [PubMed](#) [Google Scholar](#)

39. Chu Shin Koh

[View author publications](#)

You can also search for this author in [PubMed](#) [Google Scholar](#)

40. Jasline Deek

[View author publications](#)

You can also search for this author in [PubMed](#) [Google Scholar](#)

41. Alejandro C. Costamagna

[View author publications](#)

You can also search for this author in [PubMed](#) [Google Scholar](#)

42. Pierre Fobert

[View author publications](#)

You can also search for this author in [PubMed](#) [Google Scholar](#)

43. Darren Heavens

[View author publications](#)

You can also search for this author in [PubMed](#) [Google Scholar](#)

44. Hiroyuki Kanamori

[View author publications](#)

You can also search for this author in [PubMed](#) [Google Scholar](#)

45. Kanako Kawaura

[View author publications](#)

You can also search for this author in [PubMed](#) [Google Scholar](#)

46. Fuminori Kobayashi

[View author publications](#)

You can also search for this author in [PubMed](#) [Google Scholar](#)

47. Ksenia Krasileva

[View author publications](#)

You can also search for this author in [PubMed](#) [Google Scholar](#)

48. Tony Kuo

[View author publications](#)

You can also search for this author in [PubMed](#) [Google Scholar](#)

49. Neil McKenzie

[View author publications](#)

You can also search for this author in [PubMed](#) [Google Scholar](#)

50. Kazuki Murata

[View author publications](#)

You can also search for this author in [PubMed](#) [Google Scholar](#)

51. Yusuke Nabeka

[View author publications](#)

You can also search for this author in [PubMed](#) [Google Scholar](#)

52. Timothy Paape

[View author publications](#)

You can also search for this author in [PubMed](#) [Google Scholar](#)

53. Sudharsan Padmarasu

[View author publications](#)

You can also search for this author in [PubMed](#) [Google Scholar](#)

54. Lawrence Percival-Alwyn

[View author publications](#)

You can also search for this author in [PubMed](#) [Google Scholar](#)

55. Sateesh Kagale

[View author publications](#)

You can also search for this author in [PubMed](#) [Google Scholar](#)

56. Uwe Scholz

[View author publications](#)

You can also search for this author in [PubMed](#) [Google Scholar](#)

57. Jun Sese

[View author publications](#)

You can also search for this author in [PubMed](#) [Google Scholar](#)

58. Philomin Juliana

[View author publications](#)

You can also search for this author in [PubMed](#) [Google Scholar](#)

59. Ravi Singh

[View author publications](#)

You can also search for this author in [PubMed](#) [Google Scholar](#)

60. Rie Shimizu-Inatsugi

[View author publications](#)

You can also search for this author in [PubMed](#) [Google Scholar](#)

61. David Swarbreck

[View author publications](#)

You can also search for this author in [PubMed](#) [Google Scholar](#)

62. James Cockram

[View author publications](#)

You can also search for this author in [PubMed](#) [Google Scholar](#)

63. Hikmet Budak

[View author publications](#)

You can also search for this author in [PubMed](#) [Google Scholar](#)

64. Toshiaki Tameshige

[View author publications](#)

You can also search for this author in [PubMed](#) [Google Scholar](#)

65. Tsuyoshi Tanaka

[View author publications](#)

You can also search for this author in [PubMed](#) [Google Scholar](#)

66. Hiroyuki Tsuji

[View author publications](#)

You can also search for this author in [PubMed](#) [Google Scholar](#)

67. Jonathan Wright

[View author publications](#)

You can also search for this author in [PubMed](#) [Google Scholar](#)

68. Jianzhong Wu

[View author publications](#)

You can also search for this author in [PubMed](#) [Google Scholar](#)

69. Burkhard Steuernagel

[View author publications](#)

You can also search for this author in [PubMed](#) [Google Scholar](#)

70. Ian Small

[View author publications](#)

You can also search for this author in [PubMed](#) [Google Scholar](#)

71. Sylvie Cloutier

[View author publications](#)

You can also search for this author in [PubMed](#) [Google Scholar](#)

72. Gabriel Keeble-Gagnère

[View author publications](#)

You can also search for this author in [PubMed](#) [Google Scholar](#)

73. Gary Muehlbauer

[View author publications](#)

You can also search for this author in [PubMed](#) [Google Scholar](#)

74. Josquin Tibbets

[View author publications](#)

You can also search for this author in [PubMed](#) [Google Scholar](#)

75. Shuhei Nasuda

[View author publications](#)

You can also search for this author in [PubMed](#) [Google Scholar](#)

76. Joanna Melonek

[View author publications](#)

You can also search for this author in [PubMed](#) [Google Scholar](#)

77. Pierre J. Hucl

[View author publications](#)

You can also search for this author in [PubMed](#) [Google Scholar](#)

78. Andrew G. Sharpe

[View author publications](#)

You can also search for this author in [PubMed](#) [Google Scholar](#)

79. Matthew Clark

[View author publications](#)

You can also search for this author in [PubMed](#) [Google Scholar](#)

80. Erik Legg

[View author publications](#)

You can also search for this author in [PubMed](#) [Google Scholar](#)

81. Arvind Bharti

[View author publications](#)

You can also search for this author in [PubMed](#) [Google Scholar](#)

82. Peter Langridge

[View author publications](#)

You can also search for this author in [PubMed](#) [Google Scholar](#)

83. Anthony Hall

[View author publications](#)

You can also search for this author in [PubMed](#) [Google Scholar](#)

84. Cristobal Uauy

[View author publications](#)

You can also search for this author in [PubMed](#) [Google Scholar](#)

85. Martin Mascher

[View author publications](#)

You can also search for this author in [PubMed](#) [Google Scholar](#)

86. Simon G. Krattinger

[View author publications](#)

You can also search for this author in [PubMed](#) [Google Scholar](#)

87. Hirokazu Handa

[View author publications](#)

You can also search for this author in [PubMed](#) [Google Scholar](#)

88. Kentaro K. Shimizu

[View author publications](#)

You can also search for this author in [PubMed](#) [Google Scholar](#)

89. Assaf Distelfeld

[View author publications](#)

You can also search for this author in [PubMed](#) [Google Scholar](#)

90. Ken Chalmers

[View author publications](#)

You can also search for this author in [PubMed](#) [Google Scholar](#)

91. Beat Keller

[View author publications](#)

You can also search for this author in [PubMed](#) [Google Scholar](#)

92. Klaus F. X. Mayer

[View author publications](#)

You can also search for this author in [PubMed](#) [Google Scholar](#)

93. Jesse Poland

[View author publications](#)

You can also search for this author in [PubMed](#) [Google Scholar](#)

94. Nils Stein

[View author publications](#)

You can also search for this author in [PubMed](#) [Google Scholar](#)

95. Curt A. McCartney

[View author publications](#)

You can also search for this author in [PubMed](#) [Google Scholar](#)

96. Manuel Spannagl

[View author publications](#)

You can also search for this author in [PubMed](#) [Google Scholar](#)

97. Thomas Wicker

[View author publications](#)

You can also search for this author in [PubMed](#) [Google Scholar](#)

98. Curtis J. Pozniak

[View author publications](#)

You can also search for this author in [PubMed](#) [Google Scholar](#)

Contributions

Project establishment: K.C., A.D., A. Hall, B.K., S.G.K., E.L., P.L., K.F.X.M., J.P., C.J.P., K.K.S., M.S. and N.S. Project coordination: A. Hall, C.J.P. and N.S. Genome assemblies were contributed as follows: CDC Stanley and CDC Landmark: P.J.H., C.J.P., A.G.S., B.B., C.S.K., A.N., K.N. and S.W.; Julius: K.F.X.M., N.S., M.M., C.M. and U.S.; Jagger: G.M., J.P. and L.G.; ArinaLrFor: B.K., S.G.K. and M.C.K.; Mace and LongReach Lancer: K.C., P.L., G.K.-G. and J.T.; Norin 61: K.K.S., H.H., S.N., J.S., K. Kawaura, H.T., T. Tameshige, T.B., D.C., M.H., R.S.-I., C.A., F.K., J.G.-G. and N.S.; SY Mattis: E.L. and A.B.; spelt (PI190962): A.D., C.J.P. and J.D.; Robigus, Claire, Paragon and Cadenza: M.B., M.C., B.C., C.F., N.F. and D.H.; Weebill 1: M.C., B.C., J.C., K.A.G., L.P.-A. and L.V. Sequencing,

assembly and analysis were contributed by WRA2P computational assembly: A. Hall, B.C., G.G.A., K. Krasileva, N.M., D.S. and J. Wright; 10X Genomics: H.B., C.J.P., J.E., S.K. and K.W.; Hi-C and structural analysis: M.M., N.S., A. Himmelbach, C.M., S.P. and L.G.; pseudomolecule assemblies: M.M., C.M. and N.S.; gene projections and TE analysis: K.F.X.M., M.S., H.G. and G.H.; diversity and polymorphism analysis: K.K.S., E.D., T.P., G.H.-N., D.C., M.H., G.H., H.H., H.K., M.S., K.M., T. Tameshige, T. Tanaka, J.S. and J. Wu; centromere diversity: J.P. and D.H.K.; 5B/7B translocation: S.G.K., T.W., J.C. and M.C.K; 2N^VS introgression: J.P., A.K.F., L.G., P.J., C.J.P., R.S. and S.W.; TE-based introgressions: T.W., B.B., J.E., M.C.K., J.P., C.J.P., J.T. and S.W; cytological karyotyping: S.N., K.M., Y.N., J.S. and T.K.; diversification of *Rf* genes: J.M. and I.S.; NLR repertoire: S.G.K. and B.S.; *Sm1* gene cloning: C.A.M., C.J.P., C.U., J.B., A.C.C., S.C., P.F., M.T.K., V.K., D.T. and K.W.; haplotype database: C.U., J.B. and R.H.R.-G.; visualization software: C.G., V.B., G.K.-G., J.N.S., J.T. and J.M.; BLAST server: M.M., A.F. and U.S.; C.J.P and S.W. drafted the manuscript with input from all authors. All co-authors contributed to and edited the final version.

Corresponding authors

Correspondence to [Curt A. McCartney](#) or [Manuel Spannagl](#) or [Thomas Wicker](#) or [Curtis J. Pozniak](#).

Ethics declarations

Competing interests

The authors declare no competing interests.

Additional information

Peer review information *Nature* thanks Victor Albert, Rudi Appels and the other, anonymous, reviewer(s) for their contribution to the peer review of this work.

Publisher's note Springer Nature remains neutral with regard to jurisdictional claims in published maps and institutional affiliations.

Extended data figures and tables

Extended Data Fig. 1 Chromosome-scale collinearity between the RQA.

Genomes were aligned chromosome by chromosome using MUMmer and are represented as dot plots. The introgression on chromosome 2B of LongReach Lancer (red rectangles) and 5B/7B translocation in SY Mattis and ArinaLrFor (purple rectangles) are indicated.

Extended Data Fig. 2 Evaluation of the CDC Landmark RQA using Oxford Nanopore Long Reads.

a, Scaffold-scaffold long read contact map showing shared read IDs between scaffold ends along the ordered scaffolds in the CDC Landmark pseudomolecules. The diagonal pattern indicates that adjacent scaffolds share the same long reads and are therefore properly ordered and oriented by Hi-C in the RQA. **b**, Characterization of inversion events on chromosomes 2A, 3A, and 3D. The directionality biases estimated from alignments of Hi-C data against Chinese Spring (left, top), and chromosome alignment of the inversion events between CDC Landmark and Chinese Spring RQAs (left, bottom) are shown. Long reads spanning the inversion events and magnified views of the reads aligning to the left and right boundaries of the inversions (right) are provided.

Extended Data Fig. 3 Diversity of genes and TEs.

a, Average pairwise genetic diversity of the homeologues (coding sequences only) of the A, B and D subgenomes. The mode of the A, B and D subgenome is 0.00057, 0.00082, and 0.0002, respectively. **b**, Tajima's D estimates of coding sequences for each wheat subgenome. The lower and upper range of the boxplot hinges correspond to the first and third quartiles (the 25th and 75th percentiles). Boxplots show centre line, median; box

limits, upper and lower quartiles; whiskers, $1.5 \times$ interquartile range. **c**, Total gene counts and orthologues for the RQA. Genes in orthologous groups with exactly one gene for each line (Complete; dark brown), genes contained in unambiguous orthologous groups missing an orthologue for at least one line, that is, PAV (2-10 Lines; light brown), and genes with ambiguous orthologues or CNV (Other; pink) are indicated. **d**, Per cent of pairwise shared syntenic fl-LTRs between wheat lines.

Extended Data Fig. 4 Evolutionary relationships among PPR and mTERF gene sequences.

a, The *RFL* clade is in blue and all remaining P-class PPRs are in green. **b**, Clustered mTERF sequences are in blue and the remaining mTERFs are shown in green. The scale bar represents number of substitutions per site. **c**, Sequence inversions and copy number variation at the *Rf3* locus on chromosome 1B. *RFL* genes are shown as light pink triangles above the chromosome scale. Conserved non-PPR genes used as syntenic anchors are shown on the chromosome scale as coloured triangles. The total number (T) and the number of putatively functional *RFL* genes with 10 or more PPR motifs (F) are indicated on the right side of each panel.

Extended Data Fig. 5 Identification of alien introgressions from wheat relatives.

A feature of foreign chromosomal introgressions is that they contain unique patterns of TE insertions. Shown are stretches of >20 Mb containing multiple polymorphic RLC-*Angela* retrotransposons that are found only in one or a few (≤ 4) of the sequenced lines. One representative chromosome for each wheat subgenome is shown. Individual polymorphic retrotransposons are indicated as coloured vertical lines. Colours correspond to the number of cultivars a foreign segment is found in. Regions of particular interest are indicated by black rectangles. These include the 2N^VS alien introgression from *A. ventricosa* at the end of chromosome 2A in Jagger, Mace, SY Mattis and CDC Stanley, as well as introgression in the central region of chromosome 2B from *T. timopheevi* in LongReach Lancer, and introgression at the end of chromosome 3D from *T. ponticum* in LongReach Lancer.

Extended Data Fig. 6 Detailed characterization of the 2N^VS introgression from *A. ventricosa*.

a, Pairwise alignments of the first 50 Mb of chromosome 2A. The black arrow indicates a possible unique haplotype within spelt. **b**, Orthologous

genes between the 2N^vS introgression from *A. ventricosa* in Jagger and the genes on chromosomes 2A, 2B, and 2D in Chinese Spring. **c**, Frequency of 2N^vS introgression carriers in North American datasets from CIMMYT, Kansas State, and the USDA Winter Wheat Regional Performance Nursery (RPN) over time. **d**, Per cent yield difference in lines that carry the 2N^vS introgression. Two sided *t*-tests were performed to test for the significance of the impact of the 2N^vS introgression. ***P* < 0.01; ****P* < 0.001.

Extended Data Fig. 7 Centromere positions and karyotype variation.

Functional centromere positions in the RQA have undergone structural and positional rearrangement. Chromosome alignments showing collinearity (black scaffolds in same orientation, grey scaffolds in opposite orientation) with relative density of CENH3 ChIP-seq mapped to 100 kb genomic bins for Chinese Spring (blue) and a representative genome of comparison (red) for chromosome 4B of CDC Stanley (**a**), and chromosome 5B of Julius (**b**). **c**, Detailed list and clustering of cytological features carried by each wheat line (Supplementary Note 6). Features that are identical (dark grey) or have a gain (black) or loss (light grey) relative to Chinese Spring are indicated.

Extended Data Fig. 8 Hi-C validates inversions identified from pairwise chromosome alignments.

Pairwise alignments of chromosome 6B from the RQA and Chinese Spring are shown. Above each alignment dot plot, the directionality biases estimated from alignments of Hi-C data against Chinese Spring are shown. Boundaries of diagonal segments are indicative of inversions and coincide with inversion boundaries identified from the chromosome alignments.

Extended Data Fig. 9 Characterization of a translocation involving wheat chromosomes 5B and 7B.

a, Cytogenetic karyotypes of Forno (left) and Arina (right), the parents of ArinaLrFor. Note that the large recombinant chromosome 7B is represented by a distinct peak. **b**, Sequence of the translocation breakpoint on

chromosome 7B of Arina*LrFor*. Note that the exact breakpoint lies in a sequence gap (stretch of Ns). The bp positions are indicated at the left. Forward PCR primers are shown in red and reverse primers in blue. The overlap of the two reverse primers is shown in purple. The outer primer pair was used for PCR, while the inner pair was used for a nested PCR. **c**, PCR amplification of the fragment spanning the translocation breakpoint. The nested PCR yielded a ~5 kb fragment that spanned the translocation breakpoint and its identity was confirmed by sequencing. Both PCR and nested PCR were performed in duplicate; both replicates of the nested PCR were sequenced using the Sanger method. For gel source data, see Supplementary Fig. 1. **d**, Mapping of Illumina reads from the cultivars Arina and Forno on to the pseudomolecules of Arina*LrFor*. Sequence derived from Forno is shown in blue, while sequenced derived from Arina is in red. Note that chromosomes 5B and 7B are derived from both parents, indicating that these parental chromosomes can recombine freely, despite the presence of a large 5B/7B translocation in Arina.

Extended Data Fig. 10 Confirmation of gene expression and gene structure for *Sm1*.

a, Critical recombinants from the 99B60-EJ2G/Infinity and 99B60-EJ2D/Thatcher populations used to fine map *Sm1*. The 99B60-EJ2G/Infinity cross had 5,170 F₂ plants, while 99B60-EJ2D/Thatcher cross had 5,264 F₂ plants; only recombinant haplotypes between orange wheat blossom midge resistant (R) and susceptible (S) genotypes are shown. **b**, Oxford Nanopore long read confirmation of the *Sm1* gene candidate in the CDC Landmark RQA (left), and alternative haplotype in Chinese Spring (right). Vertical coloured lines indicate sequence variants. **c**, Amplification of cDNA for the NB-ARC domain of the *Sm1* gene candidate (top) and actin control (bottom) derived from RNA isolated from developing kernels (left) and wheat seedlings (right). Unity and CDC Landmark are carriers of *Sm1*. Waskada carries an alternative haplotype and does not carry *Sm1* (see main text). Thatcher was used as a susceptible parent for fine mapping of *Sm1* and does not contain the associated NB-ARC domain. The experiment was replicated on four independent biological samples for each condition.

d, Distribution of an *Sm1* allele-specific PCR marker in a diverse panel of >300 wheat lines.

Supplementary information

Supplementary Data

Supplementary Figure 1. Original gel source data used for spanning the breakpoint for the 7B/5B translocation.

Reporting Summary

Supplementary Information

This file contains Supplementary Notes 1-8.

Supplementary Tables

This file contains Supplementary Tables 1-27.

Rights and permissions

Reprints and Permissions

About this article



Check for
updates

Cite this article

Walkowiak, S., Gao, L., Monat, C. *et al.* Multiple wheat genomes reveal global variation in modern breeding. *Nature* **588**, 277–283 (2020).

<https://doi.org/10.1038/s41586-020-2961-x>

[Download citation](#)

- Received: 03 April 2020
- Accepted: 09 September 2020
- Published: 25 November 2020
- Issue Date: 10 December 2020
- DOI: <https://doi.org/10.1038/s41586-020-2961-x>

Further reading

- [A haplotype-led approach to increase the precision of wheat breeding](#)
 - Jemima Brinton
 - , Ricardo H. Ramirez-Gonzalez
 - , James Simmonds
 - , Luzie Wingen
 - , Simon Orford
 - , Simon Griffiths
 - , Georg Haberer
 - , Manuel Spannagl
 - , Sean Walkowiak
 - , Curtis Pozniak
 - & Cristobal Uauy

Communications Biology (2020)

Comments

By submitting a comment you agree to abide by our [Terms](#) and [Community Guidelines](#). If you find something abusive or that does not comply with our

terms or guidelines please flag it as inappropriate.

[Access through your institution](#)

[Change institution](#)

[Buy or subscribe](#)

Associated Content

Communications Biology | Article

[A haplotype-led approach to increase the precision of wheat breeding](#)

- Jemima Brinton
- , Ricardo H. Ramirez-Gonzalez
- , James Simmonds
- , Luzie Wingen
- , Simon Orford
- , Simon Griffiths
- , Georg Haberer
- , Manuel Spannagl
- , Sean Walkowiak
- , Curtis Pozniak
- & Cristobal Uauy

This article was downloaded by **calibre** from <https://www.nature.com/articles/s41586-020-2961-x>

- Article
- [Published: 25 November 2020](#)

The barley pan-genome reveals the hidden legacy of mutation breeding

- [Murukarthick Jayakodi](#) ORCID: orcid.org/0000-0003-2951-0541^{1 na1},
- [Sudharsan Padmarasu](#) ORCID: orcid.org/0000-0003-3125-3695^{1 na1},
- [Georg Haberer](#)²,
- [Venkata Suresh Bonthala](#) ORCID: orcid.org/0000-0001-6550-1648²,
- [Heidrun Gundlach](#) ORCID: orcid.org/0000-0002-6757-0943²,
- [Cécile Monat](#) ORCID: orcid.org/0000-0002-0574-3976¹,
- [Thomas Lux](#) ORCID: orcid.org/0000-0002-5543-1911²,
- [Nadia Kamal](#)²,
- [Daniel Lang](#) ORCID: orcid.org/0000-0002-2166-0716²,
- [Axel Himmelbach](#)¹,
- [Jennifer Ens](#) ORCID: orcid.org/0000-0003-2663-1006³,
- [Xiao-Qi Zhang](#)⁴,
- [Tefera T. Angessa](#) ORCID: orcid.org/0000-0002-2400-1732⁴,
- [Gaofeng Zhou](#)^{4,5},
- [Cong Tan](#)⁴,
- [Camilla Hill](#)⁴,
- [Penghao Wang](#)⁴,
- [Miriam Schreiber](#)⁶,
- [Lori B. Boston](#)⁷,
- [Christopher Plott](#)⁷,
- [Jerry Jenkins](#) ORCID: orcid.org/0000-0002-7943-3997⁷,
- [Yu Guo](#)¹,
- [Anne Fiebig](#)¹,
- [Hikmet Budak](#) ORCID: orcid.org/0000-0002-2556-2478⁸,

- [Dongdong Xu⁹](#),
- [Jing Zhang⁹](#),
- [Chunchao Wang⁹](#),
- [Jane Grimwood⁷](#),
- [Jeremy Schmutz](#) [ORCID: orcid.org/0000-0001-8062-9172⁷](#),
- [Ganggang Guo](#) [ORCID: orcid.org/0000-0001-9970-5382⁹](#),
- [Guoping Zhang¹⁰](#),
- [Keiichi Mochida^{11,12,13}](#),
- [Takashi Hirayama](#) [ORCID: orcid.org/0000-0002-3868-2380¹³](#),
- [Kazuhiro Sato](#) [ORCID: orcid.org/0000-0001-8818-5203¹³](#),
- [Kenneth J. Chalmers¹⁴](#),
- [Peter Langridge](#) [ORCID: orcid.org/0000-0001-9494-400X¹⁴](#),
- [Robbie Waugh](#) [ORCID: orcid.org/0000-0003-1045-3065^{6,14,15}](#),
- [Curtis J. Pozniak](#) [ORCID: orcid.org/0000-0002-7536-3856³](#),
- [Uwe Scholz](#) [ORCID: orcid.org/0000-0001-6113-3518¹](#),
- [Klaus F. X. Mayer](#) [ORCID: orcid.org/0000-0001-6484-1077^{2,16}](#),
- [Manuel Spannagl](#) [ORCID: orcid.org/0000-0003-0701-7035²](#),
- [Chengdao Li](#) [ORCID: orcid.org/0000-0002-9653-2700^{4,5,17}](#),
- [Martin Mascher](#) [ORCID: orcid.org/0000-0001-6373-6013^{1,18}](#) &
- [Nils Stein](#) [ORCID: orcid.org/0000-0003-3011-8731^{1,19}](#)

[Nature volume 588](#), pages284–289(2020)[Cite this article](#)

- 13k Accesses
- 255 Altmetric
- [Metrics details](#)

Subjects

- [Genomics](#)
- [Plant genetics](#)
- [Structural variation](#)

Abstract

Genetic diversity is key to crop improvement. Owing to pervasive genomic structural variation, a single reference genome assembly cannot capture the full complement of sequence diversity of a crop species (known as the ‘pan-genome’¹). Multiple high-quality sequence assemblies are an indispensable component of a pan-genome infrastructure. Barley (*Hordeum vulgare* L.) is an important cereal crop with a long history of cultivation that is adapted to a wide range of agro-climatic conditions². Here we report the construction of chromosome-scale sequence assemblies for the genotypes of 20 varieties of barley—comprising landraces, cultivars and a wild barley—that were selected as representatives of global barley diversity. We catalogued genomic presence/absence variants and explored the use of structural variants for quantitative genetic analysis through whole-genome shotgun sequencing of 300 gene bank accessions. We discovered abundant large inversion polymorphisms and analysed in detail two inversions that are frequently found in current elite barley germplasm; one is probably the product of mutation breeding and the other is tightly linked to a locus that is involved in the expansion of geographical range. This first-generation barley pan-genome makes previously hidden genetic variation accessible to genetic studies and breeding.

[Access through your institution](#)

[Change institution](#)

[Buy or subscribe](#)

Access options

Subscribe to Journal

Get full journal access for 1 year

185,98 €

only 3,58 € per issue

[Subscribe](#)

All prices are NET prices.
VAT will be added later in the checkout.

Rent or Buy article

Get time limited or full article access on ReadCube.

from \$8.99

[Rent or Buy](#)

All prices are NET prices.

Additional access options:

- [Log in](#)
- [Access through your institution](#)
- [Learn about institutional subscriptions](#)

Fig. 1: Chromosome-scale sequences of 20 representative barley genotypes reveal large structural variants.

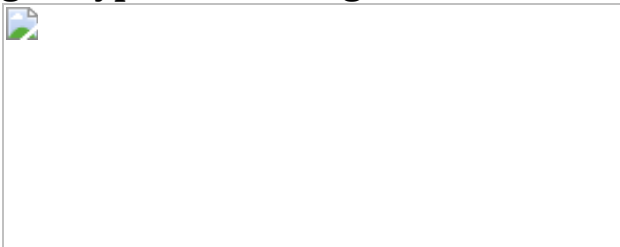


Fig. 2: Single-copy pan-genome and use of PAVs in association mapping.



Fig. 3: Identification and characterization of a large inversion on chromosome 7H.



Fig. 4: Analysis of a frequent inversion on chromosome 2H.



Data availability

All raw sequence data collected in this study and sequence assemblies have been deposited at the European Nucleotide Archive (ENA). Accession codes for raw data and assemblies are listed in Supplementary Tables: Supplementary Table 14 (assemblies), Supplementary Table 10 (assembly raw data), Supplementary Table 4 (whole-genome shotgun sequencing), Supplementary Table 5 (Hi-C) and Supplementary Table 9 (DArT-seq). Assemblies, annotations and analysis results were deposited under a DOI in the PGP repository⁶⁸ using the e!DAL submission system⁶⁹ and are accessible under the URL <https://doi.org/10.5447/ipk/2020/24>. Assemblies and gene annotations can also be downloaded from <https://barley-pangenome.ipk-gatersleben.de>. The Barley Pedigree Catalogue is available at <http://genbank.vurv.cz/barley/pedigree/>.

Code availability

Source code is released in a public Bitbucket repository, at https://bitbucket.org/ipk_dg_public/barley_pangenome/.

References

1. 1.

Bayer, P. E., Golicz, A. A., Scheben, A., Batley, J. & Edwards, D. Plant pan-genomes are the new reference. *Nat. Plants* **6**, 914–920 (2020).

[PubMed](#) [Google Scholar](#)

2. 2.

Dawson, I. K. et al. Barley: a translational model for adaptation to climate change. *New Phytol.* **206**, 913–931 (2015).

[PubMed](#) [Google Scholar](#)

3. 3.

Stein, N. & Muehlbauer, G. J. *The Barley Genome* (Springer, 2018).

4. 4.

International Barley Genome Sequencing Consortium. A physical, genetic and functional sequence assembly of the barley genome. *Nature* **491**, 711–716 (2012).

[ADS](#) [Google Scholar](#)

5. 5.

Mascher, M. et al. A chromosome conformation capture ordered sequence of the barley genome. *Nature* **544**, 427–433 (2017).

[ADS](#) [CAS](#) [PubMed](#) [Google Scholar](#)

6. 6.

Monat, C. et al. TRITEX: chromosome-scale sequence assembly of Triticeae genomes with open-source tools. *Genome Biol.* **20**, 284 (2019).

[CAS](#) [PubMed](#) [PubMed Central](#) [Google Scholar](#)

7. 7.

Mascher, M. et al. Mapping-by-sequencing accelerates forward genetics in barley. *Genome Biol.* **15**, R78 (2014).

[PubMed](#) [PubMed Central](#) [Google Scholar](#)

8. 8.

Russell, J. et al. Exome sequencing of geographically diverse barley landraces and wild relatives gives insights into environmental adaptation. *Nat. Genet.* **48**, 1024–1030 (2016).

[CAS](#) [PubMed](#) [Google Scholar](#)

9. 9.

Milner, S. G. et al. Genebank genomics highlights the diversity of a global barley collection. *Nat. Genet.* **51**, 319–326 (2019).

[CAS](#) [PubMed](#) [Google Scholar](#)

10. 10.

Muñoz-Amatriaín, M. et al. Distribution, functional impact, and origin mechanisms of copy number variation in the barley genome. *Genome Biol.* **14**, R58 (2013).

[PubMed](#) [PubMed Central](#) [Google Scholar](#)

11. 11.

Taketa, S. et al. Barley grain with adhering hulls is controlled by an ERF family transcription factor gene regulating a lipid biosynthesis pathway. *Proc. Natl Acad. Sci. USA* **105**, 4062–4067 (2008).

[ADS](#) [CAS](#) [PubMed](#) [Google Scholar](#)

12. 12.

Tettelin, H. et al. Genome analysis of multiple pathogenic isolates of *Streptococcus agalactiae*: implications for the microbial “pan-genome”. *Proc. Natl Acad. Sci. USA* **102**, 13950–13955 (2005).

[ADS](#) [CAS](#) [PubMed](#) [Google Scholar](#)

13. 13.

Ho, S. S., Urban, A. E. & Mills, R. E. Structural variation in the sequencing era. *Nat. Rev. Genet.* **21**, 171–189 (2019).

[PubMed](#) [PubMed Central](#) [Google Scholar](#)

14. 14.

Danilevicz, M. F., Tay Fernandez, C. G., Marsh, J. I., Bayer, P. E. & Edwards, D. Plant pangenomics: approaches, applications and advancements. *Curr. Opin. Plant Biol.* **54**, 18–25 (2020).

[CAS](#) [PubMed](#) [Google Scholar](#)

15. 15.

Monat, C., Schreiber, M., Stein, N. & Mascher, M. Prospects of pangenomics in barley. *Theor. Appl. Genet.* **132**, 785–796 (2019).

[PubMed](#) [Google Scholar](#)

16. 16.

Coronado, M.-J., Hensel, G., Broeders, S., Otto, I. & Kumlehn, J. Immature pollen-derived doubled haploid formation in barley cv. Golden Promise as a tool for transgene recombination. *Acta Physiol. Plant.* **27**, 591–599 (2005).

[CAS](#) [Google Scholar](#)

17. 17.

Schreiber, M. et al. A genome assembly of the barley ‘transformation reference’ cultivar Golden Promise. *G3* **10**, 1823–1827 (2020).

[CAS](#) [PubMed](#) [Google Scholar](#)

18. 18.

Gottwald, S., Bauer, P., Komatsuda, T., Lundqvist, U. & Stein, N. TILLING in the two-rowed barley cultivar ‘Barke’ reveals preferred sites of functional diversity in the gene *HvHox1*. *BMC Res. Notes* **2**, 258 (2009).

[PubMed](#) [PubMed Central](#) [Google Scholar](#)

19. 19.

Mascher, M. et al. Anchoring and ordering NGS contig assemblies by population sequencing (POPSEQ). *Plant J.* **76**, 718–727 (2013).

[CAS](#) [PubMed](#) [PubMed Central](#) [Google Scholar](#)

20. 20.

Hübner, S. et al. Strong correlation of wild barley (*Hordeum spontaneum*) population structure with temperature and precipitation variation. *Mol. Ecol.* **18**, 1523–1536 (2009).

[PubMed](#) [Google Scholar](#)

21. 21.

Chikhi, R., Limasset, A. & Medvedev, P. Compacting de Bruijn graphs from sequencing data quickly and in low memory. *Bioinformatics* **32**, i201–i208 (2016).

[CAS](#) [PubMed](#) [PubMed Central](#) [Google Scholar](#)

22. 22.

Luo, R. et al. SOAPdenovo2: an empirically improved memory-efficient short-read de novo assembler. *Gigascience* **1**, 18 (2012).

[PubMed](#) [PubMed Central](#) [Google Scholar](#)

23. 23.

Clavijo, B. J. et al. An improved assembly and annotation of the allohexaploid wheat genome identifies complete families of agronomic genes and provides genomic evidence for chromosomal translocations. *Genome Res.* **27**, 885–896 (2017).

[MathSciNet](#) [CAS](#) [PubMed](#) [PubMed Central](#) [Google Scholar](#)

24. 24.

Anderson, S. N. et al. Transposable elements contribute to dynamic genome content in maize. *Plant J.* **100**, 1052–1065 (2019).

[CAS](#) [PubMed](#) [Google Scholar](#)

25. 25.

Brunner, S., Fengler, K., Morgante, M., Tingey, S. & Rafalski, A. Evolution of DNA sequence nonhomologies among maize inbreds. *Plant Cell* **17**, 343–360 (2005).

[CAS](#) [PubMed](#) [PubMed Central](#) [Google Scholar](#)

26. 26.

Nattestad, M. & Schatz, M. C. Assemblytics: a web analytics tool for the detection of variants from an assembly. *Bioinformatics* **32**, 3021–3023 (2016).

[CAS](#) [PubMed](#) [PubMed Central](#) [Google Scholar](#)

27. 27.

Gordon, S. P. et al. Extensive gene content variation in the *Brachypodium distachyon* pan-genome correlates with population structure. *Nat. Commun.* **8**, 2184 (2017).

[ADS](#) [PubMed](#) [PubMed Central](#) [Google Scholar](#)

28. 28.

Yu, S. et al. A single nucleotide polymorphism of *Nud* converts the caryopsis type of barley (*Hordeum vulgare* L.). *Plant Mol. Biol. Report.* **34**, 242–248 (2016).

[CAS](#) [Google Scholar](#)

29. 29.

Arora, S. et al. Resistance gene cloning from a wild crop relative by sequence capture and association genetics. *Nat. Biotechnol.* **37**, 139–143 (2019).

[CAS](#) [PubMed](#) [Google Scholar](#)

30. 30.

Lipka, A. E. et al. GAPIT: genome association and prediction integrated tool. *Bioinformatics* **28**, 2397–2399 (2012).

[CAS](#) [PubMed](#) [Google Scholar](#)

31. 31.

Yu, J. et al. A unified mixed-model method for association mapping that accounts for multiple levels of relatedness. *Nat. Genet.* **38**, 203–208 (2006).

[CAS](#) [PubMed](#) [Google Scholar](#)

32. 32.

Ekberg, I. Cytogenetic studies of three paracentric inversions in barley. *Hereditas* **76**, 1–30 (1974).

[CAS](#) [PubMed](#) [Google Scholar](#)

33. 33.

Ramage, R. & Suneson, C. Translocation-gene linkages on barley chromosome 7. *Crop Sci.* **1**, 319–320 (1961).

[Google Scholar](#)

34. 34.

Himmelbach, A. et al. Discovery of multi-megabase polymorphic inversions by chromosome conformation capture sequencing in large-genome plant species. *Plant J.* **96**, 1309–1316 (2018).

[CAS](#) [PubMed](#) [Google Scholar](#)

35. 35.

Ederveen, A., Lai, Y., van Driel, M. A., Gerats, T. & Peters, J. L. Modulating crossover positioning by introducing large structural changes in chromosomes. *BMC Genomics* **16**, 89 (2015).

[PubMed](#) [PubMed Central](#) [Google Scholar](#)

36. 36.

Bouma, J. & Ohnoutka, Z. *Importance and Application of the Mutant ‘Diamant’ in Spring Barley Breeding* (IAEA, 1991).

37. 37.

Comadran, J. et al. Natural variation in a homolog of *Antirrhinum CENTRORADIALIS* contributed to spring growth habit and environmental adaptation in cultivated barley. *Nat. Genet.* **44**, 1388–1392 (2012).

[CAS](#) [PubMed](#) [Google Scholar](#)

38. 38.

Bustos-Korts, D. et al. Exome sequences and multi-environment field trials elucidate the genetic basis of adaptation in barley. *Plant J.* **99**, 1172–1191 (2019).

[CAS](#) [PubMed](#) [PubMed Central](#) [Google Scholar](#)

39. 39.

Mascher, M. et al. Genebank genomics bridges the gap between the conservation of crop diversity and plant breeding. *Nat. Genet.* **51**, 1076–1081 (2019).

[CAS](#) [PubMed](#) [Google Scholar](#)

40. 40.

Khan, A. W. et al. Super-pangenome by integrating the wild side of a species for accelerated crop improvement. *Trends Plant Sci.* **25**, 148–158 (2020).

[CAS](#) [PubMed](#) [PubMed Central](#) [Google Scholar](#)

41. 41.

Dvorak, J., McGuire, P. E. & Cassidy, B. Apparent sources of the A genomes of wheats inferred from polymorphism in abundance and restriction fragment length of repeated nucleotide sequences. *Genome* **30**, 680–689 (1988).

[CAS](#) [Google Scholar](#)

42. 42.

Himmelbach, A., Walde, I., Mascher, M. & Stein, N. Tethered chromosome conformation capture sequencing in Triticeae: a valuable

tool for genome assembly. *Bio Protoc.* **8**, e2955 (2018).

[CAS](#) [Google Scholar](#)

43. 43.

Padmarasu, S., Himmelbach, A., Mascher, M. & Stein, N. in *Plant Long Non-Coding RNAs* (eds Chekanova, J. & Wang, H.-L.) 441–472 (Springer, 2019).

44. 44.

Matsumoto, T. et al. Comprehensive sequence analysis of 24,783 barley full-length cDNAs derived from 12 clone libraries. *Plant Physiol.* **156**, 20–28 (2011).

[CAS](#) [PubMed](#) [PubMed Central](#) [Google Scholar](#)

45. 45.

Kent, W. J. BLAT—the BLAST-like alignment tool. *Genome Res.* **12**, 656–664 (2002).

[CAS](#) [PubMed](#) [PubMed Central](#) [Google Scholar](#)

46. 46.

Slater, G. S. C. & Birney, E. Automated generation of heuristics for biological sequence comparison. *BMC Bioinformatics* **6**, 31 (2005).

[PubMed](#) [PubMed Central](#) [Google Scholar](#)

47. 47.

Emms, D. M. & Kelly, S. OrthoFinder: solving fundamental biases in whole genome comparisons dramatically improves orthogroup inference accuracy. *Genome Biol.* **16**, 157 (2015).

[PubMed](#) [PubMed Central](#) [Google Scholar](#)

48. 48.

Spannagl, M. et al. PGSB PlantsDB: updates to the database framework for comparative plant genome research. *Nucleic Acids Res.* **44**, D1141–D1147 (2016).

[CAS](#) [PubMed](#) [Google Scholar](#)

49. 49.

Ellinghaus, D., Kurtz, S. & Willhoeft, U. LTRharvest, an efficient and flexible software for de novo detection of LTR retrotransposons. *BMC Bioinformatics* **9**, 18 (2008).

[PubMed](#) [PubMed Central](#) [Google Scholar](#)

50. 50.

Li, H. Minimap2: pairwise alignment for nucleotide sequences. *Bioinformatics* **34**, 3094–3100 (2018).

[CAS](#) [PubMed](#) [PubMed Central](#) [Google Scholar](#)

51. 51.

Gutierrez-Gonzalez, J. J., Mascher, M., Poland, J. & Muehlbauer, G. J. Dense genotyping-by-sequencing linkage maps of two synthetic W7984×Opata reference populations provide insights into wheat structural diversity. *Sci. Rep.* **9**, 1793 (2019).

[ADS](#) [PubMed](#) [PubMed Central](#) [Google Scholar](#)

52. 52.

Pedersen, B. S. & Quinlan, A. R. Mosdepth: quick coverage calculation for genomes and exomes. *Bioinformatics* **34**, 867–868 (2018).

[CAS](#) [PubMed](#) [Google Scholar](#)

53. 53.

Quinlan, A. R. & Hall, I. M. BEDTools: a flexible suite of utilities for comparing genomic features. *Bioinformatics* **26**, 841–842 (2010).

[CAS](#) [PubMed](#) [PubMed Central](#) [Google Scholar](#)

54. 54.

R Core Team. *R: A Language and Environment for Statistical Computing* <http://www.R-project.org> (R Foundation for Statistical Computing, 2013).

55. 55.

Bushnell, B. *BBMap: A Fast, Accurate, Splice-aware Aligner* (Lawrence Berkeley National Laboratory, 2014).

56. 56.

Csardi, G. & Nepusz, T. The igraph software package for complex network research. *InterJournal Complex Syst.* **1695**, 1–9 (2006).

[Google Scholar](#)

57. 57.

Schwartz, S. et al. PipMaker—a web server for aligning two genomic DNA sequences. *Genome Res.* **10**, 577–586 (2000).

[CAS](#) [PubMed](#) [PubMed Central](#) [Google Scholar](#)

58. 58.

Li, H. A statistical framework for SNP calling, mutation discovery, association mapping and population genetical parameter estimation from sequencing data. *Bioinformatics* **27**, 2987–2993 (2011).

[CAS](#) [PubMed](#) [PubMed Central](#) [Google Scholar](#)

59. 59.

Zheng, X. & Gogarten, S. SeqArray: big data management of genome-wide sequence variants. R package version 1.10.6 <https://github.com/zhenxwen/SeqArray> (accessed January 2017).

60. 60.

Zheng, X. et al. A high-performance computing toolset for relatedness and principal component analysis of SNP data. *Bioinformatics* **28**, 3326–3328 (2012).

[CAS](#) [PubMed](#) [PubMed Central](#) [Google Scholar](#)

61. 61.

Akbari, M. et al. Diversity arrays technology (DArT) for high-throughput profiling of the hexaploid wheat genome. *Theor. Appl. Genet.* **113**, 1409–1420 (2006).

[CAS](#) [PubMed](#) [Google Scholar](#)

62. 62.

Hill, C. B. et al. Hybridisation-based target enrichment of phenology genes to dissect the genetic basis of yield and adaptation in barley. *Plant Biotechnol. J.* **17**, 932–944 (2019).

[CAS](#) [PubMed](#) [Google Scholar](#)

63. 63.

Van Ooijen, J. *MapQTL 5, Software for the Mapping of Quantitative Trait Loci in Experimental Populations* (Kyazma, 2004).

64. 64.

Xiao, C. L. et al. MECAT: fast mapping, error correction, and de novo assembly for single-molecule sequencing reads. *Nat. Methods* **14**, 1072–1074 (2017).

[CAS](#) [PubMed](#) [Google Scholar](#)

65. 65.

Chin, C. S. et al. Nonhybrid, finished microbial genome assemblies from long-read SMRT sequencing data. *Nat. Methods* **10**, 563–569 (2013).

[CAS](#) [PubMed](#) [Google Scholar](#)

66. 66.

Li, H. Aligning sequence reads, clone sequences and assembly contigs with BWA-MEM. Preprint at <https://arxiv.org/abs/1303.3997> (2013).

67. 67.

McKenna, A. et al. The Genome Analysis Toolkit: a MapReduce framework for analyzing next-generation DNA sequencing data. *Genome Res.* **20**, 1297–1303 (2010).

[CAS](#) [PubMed](#) [PubMed Central](#) [Google Scholar](#)

68. 68.

Arend, D. et al. PGP repository: a plant phenomics and genomics data publication infrastructure. *Database (Oxford)* **2016**, baw033 (2016).

[Google Scholar](#)

69. 69.

Arend, D. et al. e!DAL—a framework to store, share and publish research data. *BMC Bioinformatics* **15**, 214 (2014).

[PubMed](#) [PubMed Central](#) [Google Scholar](#)

[Download references](#)

Acknowledgements

We thank M. Knauft, I. Walde and S. König for technical assistance; D. Schüler for sequence data management; J. Bauernfeind, T. Münch and H. Miehe for IT administration; D. Arend for help with data submission; M. Bayer for advice on transcriptome analysis; and M. Herz for pedigree information. This research was supported by grants from the German Federal Ministry of Education and Research to N.S., M.M., U.S., M.S. and K.F.X.M. (SHAPE, FKZ 031B0190), to U.S. and K.F.X.M. (de.NBI, FKZ 031A536) and to N.S. (COBRA, FKZ 031A323A); the Australian Grain Research and Development Cooperation (9176507) to C.L., K.C., P.L. and P.W.; JST CREST Japan (no. JPMJCR16O4 to K.M. and T.H.); JST Mirai Program Japan (no. 18076896 to K.S.); the National Key R&D Program of China (2018YFD1000701 and 2018YFD1000700) to D.X. and J.Z.; by funding from the China Agriculture Research System (CARS-05) and the Agricultural Science and Technology Innovation Program to C.W. and G.G. Support for 10X sequencing was provided by a research grant from Genome Canada and Genome Prairie to C.P. and J.E.; and by the Natural Science Foundation of China (31620103912) and the National Key R&D Program of China (2018YFD1000706) to G.Z. We acknowledge support from the European Research Council (ERC Shuffle, project identifier: 66918) to R.W.

Author information

Author notes

1. These authors contributed equally: Murukarthick Jayakodi, Sudharsan Padmarasu

Affiliations

1. Leibniz Institute of Plant Genetics and Crop Plant Research (IPK)
Gatersleben, Seeland, Germany

Murukarthick Jayakodi, Sudharsan Padmarasu, Cécile Monat, Axel
Himmelbach, Yu Guo, Anne Fiebig, Uwe Scholz, Martin
Mascher & Nils Stein

2. Plant Genome and Systems Biology (PGSB), Helmholtz Center
Munich, German Research Center for Environmental Health,
Neuherberg, Germany

Georg Haberer, Venkata Suresh Bonthala, Heidrun Gundlach, Thomas
Lux, Nadia Kamal, Daniel Lang, Klaus F. X. Mayer & Manuel
Spannagl

3. Department of Plant Sciences, University of Saskatchewan, Saskatoon,
Saskatchewan, Canada

Jennifer Ens & Curtis J. Pozniak

4. Western Barley Genetics Alliance, State Agricultural Biotechnology
Centre, College of Science, Health, Engineering and Education,
Murdoch University, Murdoch, Western Australia, Australia

Xiao-Qi Zhang, Tefera T. Angessa, Gaofeng Zhou, Cong Tan, Camilla
Hill, Penghao Wang & Chengdao Li

5. Agriculture and Food, Department of Primary Industries and Regional
Development, South Perth, Western Australia, Australia

Gaofeng Zhou & Chengdao Li

6. The James Hutton Institute, Dundee, UK

Miriam Schreiber & Robbie Waugh

7. HudsonAlpha, Institute for Biotechnology, Huntsville, AL, USA

Lori B. Boston, Christopher Plott, Jerry Jenkins, Jane
Grimwood & Jeremy Schmutz

8. Montana BioAg Inc, Missoula, MT, USA

Hikmet Budak

9. Institute of Crop Sciences, Chinese Academy of Agricultural Sciences
(ICS-CAAS), Beijing, China

Dongdong Xu, Jing Zhang, Chunchao Wang & Ganggang Guo

10. College of Agriculture and Biotechnology, Zhejiang University,
Hangzhou, China

Guoping Zhang

11. Bioproduction Informatics Research Team, RIKEN Center for
Sustainable Resource Science, Yokohama, Japan

Keiichi Mochida

12. Kihara Institute for Biological Research, Yokohama City University,
Yokohama, Japan

Keiichi Mochida

13. Institute of Plant Science and Resources, Okayama University,
Kurashiki, Japan

Keiichi Mochida, Takashi Hirayama & Kazuhiro Sato

14. School of Agriculture, Food and Wine, University of Adelaide, Glen
Osmond, South Australia, Australia

Kenneth J. Chalmers, Peter Langridge & Robbie Waugh

15. School of Life Sciences, University of Dundee, Dundee, UK

Robbie Waugh

16. School of Life Sciences Weihenstephan, Technical University of Munich, Freising, Germany

Klaus F. X. Mayer

17. Hubei Collaborative Innovation Centre for Grain Industry, Yangtze University, Jingzhou, China

Chengdao Li

18. German Centre for Integrative Biodiversity Research (iDiv) Halle-Jena-Leipzig, Leipzig, Germany

Martin Mascher

19. Center for Integrated Breeding Research (CiBreed), Georg-August-University Göttingen, Göttingen, Germany

Nils Stein

Authors

1. Murukarthick Jayakodi

[View author publications](#)

You can also search for this author in [PubMed](#) [Google Scholar](#)

2. Sudharsan Padmarasu

[View author publications](#)

You can also search for this author in [PubMed](#) [Google Scholar](#)

3. Georg Haberer

[View author publications](#)

You can also search for this author in [PubMed](#) [Google Scholar](#)

4. Venkata Suresh Bonthala
[View author publications](#)

You can also search for this author in [PubMed](#) [Google Scholar](#)

5. Heidrun Gundlach
[View author publications](#)

You can also search for this author in [PubMed](#) [Google Scholar](#)

6. Cécile Monat
[View author publications](#)

You can also search for this author in [PubMed](#) [Google Scholar](#)

7. Thomas Lux
[View author publications](#)

You can also search for this author in [PubMed](#) [Google Scholar](#)

8. Nadia Kamal
[View author publications](#)

You can also search for this author in [PubMed](#) [Google Scholar](#)

9. Daniel Lang
[View author publications](#)

You can also search for this author in [PubMed](#) [Google Scholar](#)

10. Axel Himmelbach
[View author publications](#)

You can also search for this author in [PubMed](#) [Google Scholar](#)

11. Jennifer Ens
[View author publications](#)

You can also search for this author in [PubMed](#) [Google Scholar](#)

12. Xiao-Qi Zhang

[View author publications](#)

You can also search for this author in [PubMed](#) [Google Scholar](#)

13. Tefera T. Angessa

[View author publications](#)

You can also search for this author in [PubMed](#) [Google Scholar](#)

14. Gaofeng Zhou

[View author publications](#)

You can also search for this author in [PubMed](#) [Google Scholar](#)

15. Cong Tan

[View author publications](#)

You can also search for this author in [PubMed](#) [Google Scholar](#)

16. Camilla Hill

[View author publications](#)

You can also search for this author in [PubMed](#) [Google Scholar](#)

17. Penghao Wang

[View author publications](#)

You can also search for this author in [PubMed](#) [Google Scholar](#)

18. Miriam Schreiber

[View author publications](#)

You can also search for this author in [PubMed](#) [Google Scholar](#)

19. Lori B. Boston

[View author publications](#)

You can also search for this author in [PubMed](#) [Google Scholar](#)

20. Christopher Plott

[View author publications](#)

You can also search for this author in [PubMed](#) [Google Scholar](#)

21. Jerry Jenkins

[View author publications](#)

You can also search for this author in [PubMed](#) [Google Scholar](#)

22. Yu Guo

[View author publications](#)

You can also search for this author in [PubMed](#) [Google Scholar](#)

23. Anne Fiebig

[View author publications](#)

You can also search for this author in [PubMed](#) [Google Scholar](#)

24. Hikmet Budak

[View author publications](#)

You can also search for this author in [PubMed](#) [Google Scholar](#)

25. Dongdong Xu

[View author publications](#)

You can also search for this author in [PubMed](#) [Google Scholar](#)

26. Jing Zhang

[View author publications](#)

You can also search for this author in [PubMed](#) [Google Scholar](#)

27. Chunchao Wang

[View author publications](#)

You can also search for this author in [PubMed](#) [Google Scholar](#)

28. Jane Grimwood

[View author publications](#)

You can also search for this author in [PubMed](#) [Google Scholar](#)

29. Jeremy Schmutz

[View author publications](#)

You can also search for this author in [PubMed](#) [Google Scholar](#)

30. Ganggang Guo

[View author publications](#)

You can also search for this author in [PubMed](#) [Google Scholar](#)

31. Guoping Zhang

[View author publications](#)

You can also search for this author in [PubMed](#) [Google Scholar](#)

32. Keiichi Mochida

[View author publications](#)

You can also search for this author in [PubMed](#) [Google Scholar](#)

33. Takashi Hirayama

[View author publications](#)

You can also search for this author in [PubMed](#) [Google Scholar](#)

34. Kazuhiro Sato

[View author publications](#)

You can also search for this author in [PubMed](#) [Google Scholar](#)

35. Kenneth J. Chalmers

[View author publications](#)

You can also search for this author in [PubMed](#) [Google Scholar](#)

36. Peter Langridge

[View author publications](#)

You can also search for this author in [PubMed](#) [Google Scholar](#)

37. Robbie Waugh

[View author publications](#)

You can also search for this author in [PubMed](#) [Google Scholar](#)

38. Curtis J. Pozniak

[View author publications](#)

You can also search for this author in [PubMed](#) [Google Scholar](#)

39. Uwe Scholz

[View author publications](#)

You can also search for this author in [PubMed](#) [Google Scholar](#)

40. Klaus F. X. Mayer

[View author publications](#)

You can also search for this author in [PubMed](#) [Google Scholar](#)

41. Manuel Spannagl

[View author publications](#)

You can also search for this author in [PubMed](#) [Google Scholar](#)

42. Chengdao Li

[View author publications](#)

You can also search for this author in [PubMed](#) [Google Scholar](#)

43. Martin Mascher

[View author publications](#)

You can also search for this author in [PubMed](#) [Google Scholar](#)

44. Nils Stein

[View author publications](#)

You can also search for this author in [PubMed](#) [Google Scholar](#)

Contributions

N.S. and M.M. designed the study. N.S. coordinated experiments and sequencing. M.M. supervised sequence assembly. M. Spannagl and K.F.X.M. supervised annotation. U.S. supervised data management and submission. S.P., A.H., J.E., D.X., L.B.B. and J.G. performed sequencing experiments. M.J., C.M., Y.G., C.P., J.J. and J.S. performed sequence assembly. M.J. performed structural variation and genome-wide association scan analysis. A.F. submitted sequence data. G.H., T.L., H.G., V.S.B., N.K. and D.L. annotated and analysed genes and transposable elements. S.P., M.J., X.-Q.Z., T.T.A., G. Zhou, C.T., C.H., P.W., M.M. and C.L. analysed polymorphic inversions. H.B., J.G., J.S., J.Z., C.W., G.G., G. Zhang, K.M., T.H., K.S., K.J.C., P.L., C.J.P., C.L., M. Schreiber, R.W. and N.S. contributed sequence data. M.J., S.P., C.L. and M.M. wrote the paper with input from all co-authors.

Corresponding authors

Correspondence to [Chengdao Li](#) or [Martin Mascher](#) or [Nils Stein](#).

Ethics declarations

Competing interests

The authors declare no competing interests.

Additional information

Peer review information *Nature* thanks Victor Albert, Scott Jackson and the other, anonymous, reviewer(s) for their contribution to the peer review of this work. Peer reviewer reports are available.

Publisher's note Springer Nature remains neutral with regard to jurisdictional claims in published maps and institutional affiliations.

Extended data figures and tables

[Extended Data Fig. 1 Pan-genome selection in the global barley diversity space.](#)

PCA with genotyping-by-sequencing data of 19,778 varieties of domesticated barley sampled from the gene bank of the IPK⁹. The first six principal components are shown. Samples are coloured to highlight the pan-genome selection (first row), or according to geographic origin (second row), row type (third row) or annual growth habit (fourth row). The proportion of variance explained by the principal components is indicated in the axis labels of the first row. The map was created with the R package [mapdata](#)⁵⁴.

Extended Data Fig. 2 Comparison between long-read and short-read assemblies of the Morex cultivar.

a, Co-linearity between Morex V2 (short-read) assembly and the Morex PacBio CLR assembly at the pseudomolecule level. **b**, Summary statistics of the Morex PacBio CLR assembly and Morex V2 assembly. **c**, Alignment of *NUDUM* locus (16 kb) between Morex PacBio CLR and Morex V2. **d**, Structural variants between Morex V2 and Morex PacBio CLR assemblies as detected and classified by Assembllytics. **e**, PAVs between Barke and the Morex V2 and Morex CLR assemblies.

Extended Data Fig. 3 Assessment of contiguity and completeness in 20 genome assemblies.

a, Whole-genome alignments of assemblies of 19 diverse barley accessions to the Morex V2 reference assembly. **b**, Alignment summary of full-length coding sequences (32,878) from the MorexV2 annotation and full-length cDNAs (28,622 full-length cDNAs) in each assembly. Alignments with less than 90% query coverage and 97% (less than 90% for full-length cDNAs) identity were discarded. **c**, Whole-genome alignments show some examples of large chromosomal inversions identified using Hi-C data.

Extended Data Fig. 4 Pairwise shared syntenic full-length LTR locations.

The wild variety B1K-04-12 is set apart as an outlier, as it shares only 19–26% of its still-intact full-length LTR positions with the other landraces and cultivars. The highest similarity is found between the Barke and RGT Planet cultivars (67% shared full-length LTRs).

Extended Data Fig. 5 Gene projection and transposable element annotation.

a, Schematic of the gene projection workflow. TE, transposable element. **b**, Pipeline for annotation and removing transposable elements. **c**, Steps to identify tandemly arrayed gene (TAG) clusters in each assembly. **d**,

Summary of gene projections and transposable element annotation in 20 accessions. **e**, Comparison between de novo annotations and gene projections for three genotypes. Reported counts refer to non-transposable-element genes.

Extended Data Fig. 6 Summary of PAVs detected in pan-genome assemblies.

a, Size distribution of PAVs. **b**, Number of PAVs between 20 genome assemblies. **c**, Distribution of PAVs along the barley genome. **d**, Co-linearity between physical position of PAVs detected between the Morex and Barke cultivars, and mapped genetically in the POPSEQ population.

Extended Data Fig. 7 Analysis of the single-copy pan-genome.

a, Pipeline used to select single-copy k -mers in PAVs as markers for genome-wide association scan analysis. **b**, Summary of single-copy sequence in 20 genome assemblies and results of their clustering. **c**, Copy number of single-copy sequences in a diversity panel comprising 200 domesticated and 100 wild accessions. Frequency ranges from blue (low) to red (high). **d–g**, Comparison of PCA on the basis of PAV and SNP variants in whole-genome shotgun data of 200 diverse accessions (**d, e**) and 19,778 varieties of domesticated barley⁹ (**f, g**). Top panels show PCA results from 160,716 PAVs; bottom panels show PCA results from 779,503 of genotyping-by-sequencing SNPs. The accessions are coloured according to geographical origin and row type (using the colour code defined in Extended Data Fig. 1).

Extended Data Fig. 8 PAV-based genome-wide association scans using whole-genome shotgun and genotyping-by-sequencing data.

a, Manhattan plots of PAV-based genome-wide association scans for morphological traits, including adherence of grain hull, row type, length of rachilla hairs and awn roughness, using whole-genome shotgun data from 200 diverse varieties of domesticated barley. **b**, PAV-based genome-wide

association scan results for these traits using genotyping-by-sequencing data from 1,000 diverse varieties of domesticated barley collected from the gene bank of the IPK⁹. The 200 varieties of barley used for whole-genome shotgun sequencing are a subset of the 1,000 genotyping-by-sequencing genotypes.

Extended Data Fig. 9 Characterization of large inversions in barley.

a, Inversion size distribution. **b**, Recombination in inverted regions. Recombination rate was determined in the Morex × Barke RIL population¹⁹ ($n = 90$ genotypes). **c**, Number of inversions present as singletons or shared between two or more accessions on each chromosome.

Extended Data Table 1 Summary statistics of 20 pan-genome assemblies and annotation

[Full size table](#)

Supplementary information

Supplementary Figure

Supplementary Figure 1 | PCR-based genotyping of the 7H inversion. This is the original gel image from which the blue sections were cropped and used for Fig. 3. Morex and RGT planet were used as controls. All Valticky lines carry Morex allele of 7H inversion. Two Diamant lines (HOR 14972, HOR 4092) carry the RGT Planet allele, one Diamant line (HOR 2073) carries the Morex allele. In another two Diamant lines, neither the RGT Planet allele nor Morex allele was amplified. One cropped section in Fig. 3 does not contain molecular weight marker, but from the original image, it is clear that all correspond to correct fragment sizes.

Reporting Summary

Supplementary Figure 2

| In-depth analysis of two inversions on 2H and 7H. **(a)** Schematic illustration showing precise positions of breakpoints for 7H frequent inversion between Morex and RGT Planet. **(b)** PCR assay for genotyping 7H inversion. The location of three PCR primers are shown in **(a)** with yellow marks (not drawn to scale). **(c)** PCR assay for genotyping the 2H

inversion. Primer locations are shown in Fig. 4c. **(d)** Hi-C contact probability matrix of RGT Planet computed for chromosome 7H. The intensity of pixels represents the normalized Hi-C links counted between 1 Mb windows on chromosome 7H. The frequent 7H inversion was spotted as a pattern of higher than expected interaction frequency against Morex V2 reference genome, marked by blue lines. **(e)** QTL results for grain yield, plant height and different growth stages from multiple sites in RGT Planet x Hindmarsh population.

Supplementary Figure 3

| PCR-based genotyping of the 7H inversion in the pedigree of RGT Planet. Yellow color denotes carriers of RGT Planet allele. Blue colored cultivars are non-carriers. red color cultivars have unknown status as no fragment was amplified. Cultivars shown in white boxes were not assayed because of unavailability of seeds or DNA. Pedigree data were retrieved from the Barley Pedigree Catalogue (<http://genbank.vurv.cz/barley/pedigree/>).

Supplementary Table

Supplementary Table 1. Summary statistics of repetitive elements in twenty barley genomes.

Supplementary Table

Supplementary Table 2. Summary of RNA-seq data used for gene annotation.

Supplementary Table

Supplementary Table 3. Pfam domains most frequently observed in PAV genes.

Supplementary Table

Supplementary Table 4. Summary of whole-genome short-gun (WGS) sequencing for 200 domesticated and 100 wild accessions.

Supplementary Table

Supplementary Table 5. Summary of Hi-C data used in this study.

Supplementary Table

Supplementary Table 6. Inversions detected by Hi-C.

Supplementary Table

Supplementary Table 7. Genetic map of the RGT Planet and Hindmarsh (RxH) population (sheet1) and the Morex and Barke (MxB) population (sheet2).

Supplementary Table

Supplementary Table 8. Screening of the 7H inversion in a large collection of modern varieties and breeding lines (sheet 1) and the 7H inversion in the lines in the pedigree of RGT Planet (sheet 2) and PCR validation of the 2H inversion identified by PCA (Fig. 4b) (sheet 3).

Supplementary Table

Supplementary Table 9. Accession IDs of DArTseq reads of RxH recombinants.

Supplementary Table

Supplementary Table 10. Summary of raw sequencing data generated for pan-genome assemblies.

Supplementary Table

Supplementary Table 11. PacBio library statistics for the libraries included in the Morex genome assembly and their respective assembled sequence coverage levels.

Supplementary Table

Supplementary Table 12. Genomic libraries included in the Morex CLR assembly and their respective assembled sequence coverage levels in the final release.

Supplementary Table

Supplementary Table 13. Summary statistics of the initial output of the Quiver polished MECAT assembly. The table shows total contigs and total assembled basepairs for each set of scaffolds greater than the size listed in the left hand column.

Supplementary Table

Supplementary Table 14. Accessions IDs for 20 pan-genome assemblies and Morex PacBio CLR assembly.

Peer Review File

Rights and permissions

Reprints and Permissions

About this article



Check for
updates

Cite this article

Jayakodi, M., Padmarasu, S., Haberer, G. *et al.* The barley pan-genome reveals the hidden legacy of mutation breeding. *Nature* **588**, 284–289 (2020). <https://doi.org/10.1038/s41586-020-2947-8>

[Download citation](#)

- Received: 03 April 2020
- Accepted: 09 September 2020
- Published: 25 November 2020
- Issue Date: 10 December 2020
- DOI: <https://doi.org/10.1038/s41586-020-2947-8>

Comments

By submitting a comment you agree to abide by our [Terms](#) and [Community Guidelines](#). If you find something abusive or that does not comply with our terms or guidelines please flag it as inappropriate.

[Access through your institution](#)

[Change institution](#)

[Buy or subscribe](#)

This article was downloaded by **calibre** from <https://www.nature.com/articles/s41586-020-2947-8>

- Article
- [Published: 14 October 2020](#)

PIEZ02 in sensory neurons and urothelial cells coordinates urination

- [Kara L. Marshall](#) [ORCID: orcid.org/0000-0003-1722-7941¹](#),
- [Dimah Saade²](#),
- [Nima Ghitani³](#),
- [Adam M. Coombs¹](#),
- [Marcin Szczot³](#),
- [Jason Keller](#) [ORCID: orcid.org/0000-0001-9839-7293⁴](#) nAff5,
- [Tracy Ogata²](#),
- [Ihab Daou¹](#),
- [Lisa T. Stowers](#) [ORCID: orcid.org/0000-0002-4403-1269⁴](#),
- [Carsten G. Bönnemann²](#),
- [Alexander T. Chesler](#) [ORCID: orcid.org/0000-0002-3131-0728^{2,3}](#) &
- [Ardem Patapoutian](#) [ORCID: orcid.org/0000-0003-0726-7034¹](#)

[Nature](#) volume 588, pages290–295(2020) [Cite this article](#)

- 8868 Accesses
- 1 Citations
- 655 Altmetric
- [Metrics details](#)

Subjects

- [Peripheral nervous system](#)
- [Somatosensory system](#)

Abstract

Henry Miller stated that “to relieve a full bladder is one of the great human joys”. Urination is critically important in health and ailments of the lower urinary tract cause high pathological burden. Although there have been advances in understanding the central circuitry in the brain that facilitates urination^{1,2,3}, there is a lack of in-depth mechanistic insight into the process. In addition to central control, micturition reflexes that govern urination are all initiated by peripheral mechanical stimuli such as bladder stretch and urethral flow⁴. The mechanotransduction molecules and cell types that function as the primary stretch and pressure detectors in the urinary tract mostly remain unknown. Here we identify expression of the mechanosensitive ion channel PIEZO2 in lower urinary tract tissues, where it is required for low-threshold bladder-stretch sensing and urethral micturition reflexes. We show that PIEZO2 acts as a sensor in both the bladder urothelium and innervating sensory neurons. Humans and mice lacking functional PIEZO2 have impaired bladder control, and humans lacking functional PIEZO2 report deficient bladder-filling sensation. This study identifies PIEZO2 as a key mechanosensor in urinary function. These findings set the foundation for future work to identify the interactions between urothelial cells and sensory neurons that control urination.

[Access through your institution](#)

[Change institution](#)

[Buy or subscribe](#)

Access options

Subscribe to Journal

Get full journal access for 1 year

185,98 €

only 3,58 € per issue

[Subscribe](#)

All prices are NET prices.
VAT will be added later in the checkout.

Rent or Buy article

Get time limited or full article access on ReadCube.
from \$8.99

[Rent or Buy](#)

All prices are NET prices.

Additional access options:

- [Log in](#)
- [Access through your institution](#)
- [Learn about institutional subscriptions](#)

Fig. 1: Urinary dysfunction in individuals deficient in *PIEZ02*.

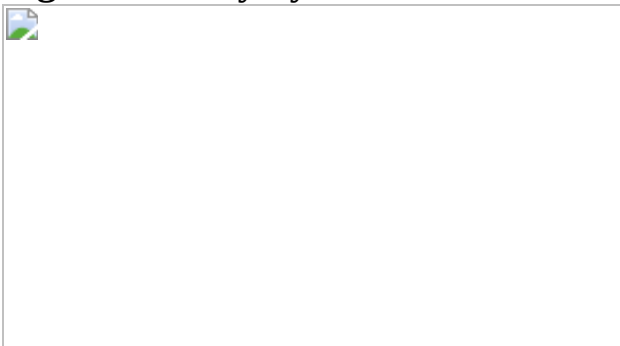


Fig. 2: *Piezo2* is expressed in the lower urinary tract, and sensory neurons require *PIEZ02* to detect low-pressure bladder filling.



Fig. 3: PIEZO2 is required for efficient micturition reflexes.



Fig. 4: PIEZO2 functions in both bladder urothelium and sensory neurons.



Data availability

The raw data that support the findings of this study are available from the corresponding authors upon reasonable request.

Code availability

Code for calcium imaging analysis is previously published¹³. MATLAB (v.2018b) code used for cystometry analysis is available at <https://github.com/PatapoutianLab/cystometry>.

References

1. 1.

de Groat, W. C. & Yoshimura, N. Afferent nerve regulation of bladder function in health and disease. *Handb. Exp. Pharmacol.* **194**, 91–138 (2009).

[Article](#) [Google Scholar](#)

2. 2.

Keller, J. A. et al. Voluntary urination control by brainstem neurons that relax the urethral sphincter. *Nat. Neurosci.* **21**, 1229–1238 (2018).

[CAS](#) [Article](#) [Google Scholar](#)

3. 3.

Hou, X. H. et al. Central control circuit for context-dependent micturition. *Cell* **167**, 73–86 (2016).

[CAS](#) [Article](#) [Google Scholar](#)

4. 4.

Garry, R. C., Roberts, T. D. & Todd, J. K. Reflex responses of the external urethral sphincter of the cat to filling of the bladder. *J. Physiol.* **139**, 13–14 (1957).

[CAS](#) [PubMed](#) [Google Scholar](#)

5. 5.

Cockayne, D. A. et al. Urinary bladder hyporeflexia and reduced pain-related behaviour in P2X₃-deficient mice. *Nature* **407**, 1011–1015 (2000).

[ADS](#) [CAS](#) [Article](#) [Google Scholar](#)

6. 6.

Andersson, K. E., Gratzke, C. & Hedlund, P. The role of the transient receptor potential (TRP) superfamily of cation-selective channels in the management of the overactive bladder. *BJU Int.* **106**, 1114–1127 (2010).

[CAS](#) [Article](#) [Google Scholar](#)

7. 7.

Mochizuki, T. et al. The TRPV4 cation channel mediates stretch-evoked Ca^{2+} influx and ATP release in primary urothelial cell cultures. *J. Biol. Chem.* **284**, 21257–21264 (2009).

[CAS](#) [Article](#) [Google Scholar](#)

8. 8.

Merrill, L., Gonzalez, E. J., Girard, B. M. & Vizzard, M. A. Receptors, channels, and signalling in the urothelial sensory system in the bladder. *Nat. Rev. Urol.* **13**, 193–204 (2016).

[CAS](#) [Article](#) [Google Scholar](#)

9. 9.

Apodaca, G., Balestreire, E. & Birder, L. A. The uroepithelial-associated sensory web. *Kidney Int.* **72**, 1057–1064 (2007).

[CAS](#) [Article](#) [Google Scholar](#)

10. 10.

Zagorodnyuk, V. P., Brookes, S. J., Spencer, N. J. & Gregory, S. Mechanotransduction and chemosensitivity of two major classes of bladder afferents with endings in the vicinity to the urothelium. *J. Physiol.* **587**, 3523–3538 (2009).

[CAS](#) [Article](#) [Google Scholar](#)

11. 11.

Murthy, S. E. et al. The mechanosensitive ion channel Piezo2 mediates sensitivity to mechanical pain in mice. *Sci. Transl. Med.* **10**, (2018).

12. 12.

Ranade, S. S. et al. Piezo2 is the major transducer of mechanical forces for touch sensation in mice. *Nature* **516**, 121–125 (2014).

[ADS](#) [CAS](#) [Article](#) [Google Scholar](#)

13. 13.

Szczot, M. et al. PIEZO2 mediates injury-induced tactile pain in mice and humans. *Sci. Transl. Med.* **10**, (2018).

14. 14.

Woo, S. H. et al. Piezo2 is the principal mechanotransduction channel for proprioception. *Nat. Neurosci.* **18**, 1756–1762 (2015).

[CAS](#) [Article](#) [Google Scholar](#)

15. 15.

Woo, S. H. et al. Piezo2 is required for Merkel-cell mechanotransduction. *Nature* **509**, 622–626 (2014).

[ADS](#) [CAS](#) [Article](#) [Google Scholar](#)

16. 16.

Chesler, A. T. et al. The role of PIEZO2 in human mechanosensation. *N. Engl. J. Med.* **375**, 1355–1364 (2016).

[CAS](#) [Article](#) [Google Scholar](#)

17. 17.

Nonomura, K. et al. Piezo2 senses airway stretch and mediates lung inflation-induced apnoea. *Nature* **541**, 176–181 (2017).

[ADS](#) [CAS](#) [Article](#) [Google Scholar](#)

18. 18.

Zeng, W. Z. et al. PIEZOs mediate neuronal sensing of blood pressure and the baroreceptor reflex. *Science* **362**, 464–467 (2018).

[ADS](#) [CAS](#) [Article](#) [Google Scholar](#)

19. 19.

Afshar, K., Mirbagheri, A., Scott, H. & MacNeily, A. E. Development of a symptom score for dysfunctional elimination syndrome. *J. Urol.* **182**, 1939–1944 (2009).

[Article](#) [Google Scholar](#)

20. 20.

Ehrhardt, A. et al. Urinary retention, incontinence, and dysregulation of muscarinic receptors in male mice lacking *Mras*. *PLoS ONE* **10**, e0141493 (2015).

[Article](#) [Google Scholar](#)

21. 21.

Flum, A. S. et al. Testosterone modifies alterations to detrusor muscle after partial bladder outlet obstruction in juvenile mice. *Front Pediatr.* **5**, 132 (2017).

[Article](#) [Google Scholar](#)

22. 22.

Takezawa, K. et al. Authentic role of ATP signaling in micturition reflex. *Sci. Rep.* **6**, 19585 (2016).

[ADS](#) [CAS](#) [Article](#) [Google Scholar](#)

23. 23.

Takezawa, K., Kondo, M., Nonomura, N. & Shimada, S. Urothelial ATP signaling: what is its role in bladder sensation? *Neurourol. Urodyn.* **36**, 966–972 (2017).

[CAS](#) [Article](#) [Google Scholar](#)

24. 24.

Ferguson, D. R., Kennedy, I. & Burton, T. J. ATP is released from rabbit urinary bladder epithelial cells by hydrostatic pressure changes—a possible sensory mechanism? *J. Physiol.* **505**, 503–511 (1997).

[CAS](#) [Article](#) [Google Scholar](#)

25. 25.

Agarwal, N., Offermanns, S. & Kuner, R. Conditional gene deletion in primary nociceptive neurons of trigeminal ganglia and dorsal root ganglia. *Genesis* **38**, 122–129 (2004).

[CAS](#) [Article](#) [Google Scholar](#)

26. 26.

Sengupta, J. N. & Gebhart, G. F. Mechanosensitive properties of pelvic nerve afferent fibers innervating the urinary bladder of the rat. *J. Neurophysiol.* **72**, 2420–2430 (1994).

[CAS](#) [Article](#) [Google Scholar](#)

27. 27.

Miyamoto, T. et al. Functional role for Piezo1 in stretch-evoked Ca^{2+} influx and ATP release in urothelial cell cultures. *J. Biol. Chem.* **289**, 16565–16575 (2014).

[CAS](#) [Article](#) [Google Scholar](#)

28. 28.

Maksimovic, S. et al. Epidermal Merkel cells are mechanosensory cells that tune mammalian touch receptors. *Nature* **509**, 617–621 (2014).

[ADS](#) [CAS](#) [Article](#) [Google Scholar](#)

29. 29.

Alcaino, C. et al. A population of gut epithelial enterochromaffin cells is mechanosensitive and requires Piezo2 to convert force into serotonin release. *Proc. Natl Acad. Sci. USA* **115**, E7632–E7641 (2018).

[CAS](#) [Article](#) [Google Scholar](#)

30. 30.

Wang, E. C. et al. ATP and purinergic receptor-dependent membrane traffic in bladder umbrella cells. *J. Clin. Invest.* **115**, 2412–2422 (2005).

[CAS](#) [Article](#) [Google Scholar](#)

31. 31.

Chen, T. W. et al. Ultrasensitive fluorescent proteins for imaging neuronal activity. *Nature* **499**, 295–300 (2013).

[ADS](#) [CAS](#) [Article](#) [Google Scholar](#)

[Download references](#)

Acknowledgements

We thank D. Barucha-Goebel, A. R. Foley and S. Donkervoort for help with the clinical assessments; G. Averion, C. Jones and K. Brooks for experimental assistance; S. Ma and S. Simpson-Dworschak for early work on the project; E. Lacefield for helpful discussions; and the Scripps Histology Core for sample preparation. This work was supported by the

Howard Hughes Medical Institute; the NIH grants R35 NS105067 to A.P., F32 DK121494 to K.L.M. and R01 NS108439 to L.S.; and the NIH Intramural Research Program funding from the National Center for Complementary and Integrative Health (A.T.C.) and from the National Institute of Neurological Disorders and Stroke (A.T.C. and C.G.B.).

Author information

Author notes

1. Jason Keller

Present address: Howard Hughes Medical Institute, Janelia Research Campus, Ashburn, VA, USA

Affiliations

1. Howard Hughes Medical Institute, Department of Neuroscience, Dorris Neuroscience Center, The Scripps Research Institute, La Jolla, CA, USA

Kara L. Marshall, Adam M. Coombs, Ihab Daou & Ardem Patapoutian

2. National Institute of Neurological Disorders and Stroke, National Institutes of Health, Bethesda, MD, USA

Dimah Saade, Tracy Ogata, Carsten G. Bönnemann & Alexander T. Chesler

3. National Center for Complementary and Integrative Health, National Institutes of Health, Bethesda, MD, USA

Nima Ghitani, Marcin Szczot & Alexander T. Chesler

4. Department of Neuroscience, Dorris Neuroscience Center, The Scripps Research Institute, La Jolla, CA, USA

Jason Keller & Lisa T. Stowers

Authors

1. Kara L. Marshall

[View author publications](#)

You can also search for this author in [PubMed](#) [Google Scholar](#)

2. Dimah Saade

[View author publications](#)

You can also search for this author in [PubMed](#) [Google Scholar](#)

3. Nima Ghitani

[View author publications](#)

You can also search for this author in [PubMed](#) [Google Scholar](#)

4. Adam M. Coombs

[View author publications](#)

You can also search for this author in [PubMed](#) [Google Scholar](#)

5. Marcin Szczot

[View author publications](#)

You can also search for this author in [PubMed](#) [Google Scholar](#)

6. Jason Keller

[View author publications](#)

You can also search for this author in [PubMed](#) [Google Scholar](#)

7. Tracy Ogata

[View author publications](#)

You can also search for this author in [PubMed](#) [Google Scholar](#)

8. Ihab Daou

[View author publications](#)

You can also search for this author in [PubMed](#) [Google Scholar](#)

9. Lisa T. Stowers

[View author publications](#)

You can also search for this author in [PubMed](#) [Google Scholar](#)

10. Carsten G. Bönnemann

[View author publications](#)

You can also search for this author in [PubMed](#) [Google Scholar](#)

11. Alexander T. Chesler

[View author publications](#)

You can also search for this author in [PubMed](#) [Google Scholar](#)

12. Ardem Patapoutian

[View author publications](#)

You can also search for this author in [PubMed](#) [Google Scholar](#)

Contributions

K.L.M. designed and performed all mouse cystometry, behavioural experiments and tissue histology, analysed data and, together with A.P., wrote the manuscript. D.S., T.O., C.G.B. and A.T.C. designed and performed the human clinical assessments. Calcium imaging and analysis was performed by N.G., K.L.M. and M.S. Retrograde labelling and FISH experiments were performed by K.L.M., A.M.C. and I.D. J.K. and L.T.S. contributed analytical tools for data analysis, technical support and conceptual project design. C.G.B, A.T.C. and A.P. contributed to project design and supervision. All authors discussed results and contributed to manuscript editing.

Corresponding authors

Correspondence to [Alexander T. Chesler](#) or [Ardem Patapoutian](#).

Ethics declarations

Competing interests

The authors declare no competing interests.

Additional information

Peer review information *Nature* thanks Eric Honoré, Jon Levine and Mark Nelson for their contribution to the peer review of this work.

Publisher's note Springer Nature remains neutral with regard to jurisdictional claims in published maps and institutional affiliations.

Extended data figures and tables

[Extended Data Fig. 1 The bladder urothelium expresses multiple mechanosensitive proteins, and PIEZO2 is not required for sensory neuron pinch responses.](#)

a, FISH in bladder tissue with probes against *Krt20* (green) and *Piezo1* (white). DAPI in blue. **b**, FISH in bladder tissue with probes against *Krt20* (green) and *Tmem63b* (white). DAPI in blue. **c**, Z-projection of the standard deviation of responses from genital pinch in WT and **d**, *Piezo2^{cKO}* DRG. **e**, Quantification of peak responses during pinch shown as percent of baseline (each data point is one cell). $n = 3$ DRGs, 40 cells for WT, 4 DRGs and 69 cells for *Piezo2^{cKO}* DRGs.

[Extended Data Fig. 2 PIEZO2 is required for efficient micturition reflexes in male mice.](#)

a, *Hoxb8-cre;Ai9* bladder tissue, fixed, frozen and mounted to show tdTomato (red) throughout the tissue, labelled with DAPI (blue). Scale is 100 μ m. Expression was evaluated in two mice. **b**, Example pressure and urethra activity traces from three wild-type males and **c**, three *Hoxb8-*

cre;Piezo2^{f/f} knockout male littermates. **d**, Heat map of individual bladder contraction events in wild-type and **e**, knockout male mice, with corresponding urethra activity below in **f** and **g** respectively. **h**, Bladder contraction intervals for males. **i**, Bladder pressures five seconds before peak contraction for males. Note: 1,200 s was the length of one recording. These dots represent recording periods in which the animal had no successful urination events. **j**, Total bladder pressure for males and **k**, sum of urethra activity during bladder contractions. *n* = 6 males per group. *P* < 0.0001 for graphs in **h**, **i**, **j** and **k**, two-sided Student's *t*-test with Welch's correction. **l**, Body weights from a subset of mice whose bladder weights are shown in Fig. 2*t*, and **m**, bladder weights from animals in **l**, shown as a percentage of body weight. Red horizontal lines indicate means, vertical red bars indicate +/- standard deviation (shown where possible).

Extended Data Fig. 3 Upk2- and Scn10a-cre expression and bladder weights.

a, *Upk2-cre;Ai9* bladder tissue fixed, frozen and mounted to show tdTomato (red) throughout the urothelium, labelled with DAPI (blue). Expression was evaluated in two mice. **b**, *Scn10a-cre;Ai9* bladder tissue fixed, frozen and mounted to show tdTomato (red) is not present. Expression was evaluated in two mice. Thin cryosections made neuronal endings difficult to visualize. Scale: 200 μ m, applies to **a** and **b**. **c**, *Scn10a-cre;Ai9* DRG tissue showing tdTomato (red) in the majority of neurons, and **d**, a cell backlabelled with CTB-Alexa 488 injected into bladder. **e**, Merge of **c** and **d**, DAPI in blue. 9/9 backlabelled bladder cells analysed from two mice were tdTomato positive. **f**, Quantification of freshly excised bladder weights from four *Upk2-cre;Piezo2*^{f/f} knockout and wild-type littermates. Age-matched littermates were 10–11 months old, which could account for greater variability. **g**, Bladder weights from age-matched *Scn10a-cre;Piezo2*^{f/f} knockout mice and wild-type littermates, 7–8 months old. Red lines indicate mean values.

Supplementary information

Supplementary Table 1

Clinical assessments and notes for all *Piezo2*-deficient patients interviewed. These represent the answers given by patients during clinician interviews, which sometimes differed from the patient's own answers to the questionnaire (Table 1). Patient numbers correspond to the numbers shown in Table 1. Not all patients returned the questionnaire.

[Reporting Summary](#)

Rights and permissions

[Reprints and Permissions](#)

About this article



Check for
updates

Cite this article

Marshall, K.L., Saade, D., Ghitani, N. *et al.* PIEZO2 in sensory neurons and urothelial cells coordinates urination. *Nature* **588**, 290–295 (2020).
<https://doi.org/10.1038/s41586-020-2830-7>

[Download citation](#)

- Received: 18 March 2020
- Accepted: 22 July 2020
- Published: 14 October 2020
- Issue Date: 10 December 2020
- DOI: <https://doi.org/10.1038/s41586-020-2830-7>

Further reading

- [**PIEZ02 in urinary function**](#)

- Tim Thomas

Nature Reviews Urology (2020)

Comments

By submitting a comment you agree to abide by our [Terms](#) and [Community Guidelines](#). If you find something abusive or that does not comply with our terms or guidelines please flag it as inappropriate.

[Access through your institution](#)

[Change institution](#)

[Buy or subscribe](#)

This article was downloaded by **calibre** from <https://www.nature.com/articles/s41586-020-2830-7>

| [Section menu](#) | [Main menu](#) |

- Article
- [Published: 11 November 2020](#)

Chemico-genetic discovery of astrocytic control of inhibition in vivo

- [Tetsuya Takano](#)¹,
- [John T. Wallace](#)¹,
- [Katherine T. Baldwin](#) ORCID: orcid.org/0000-0002-4423-5712¹,
- [Alicia M. Purkey](#)¹,
- [Akiyoshi Uezu](#)¹,
- [Jamie L. Courtland](#) ORCID: orcid.org/0000-0001-6846-3552²,
- [Erik J. Soderblom](#)^{1,3},
- [Tomomi Shimogori](#)⁴,
- [Patricia F. Maness](#)^{5,6},
- [Cagla Eroglu](#) ORCID: orcid.org/0000-0002-7204-0218^{1,2} &
- [Scott H. Soderling](#) ORCID: orcid.org/0000-0001-7808-197X^{1,2}

[Nature](#) volume 588, pages296–302(2020) [Cite this article](#)

- 8312 Accesses
- 230 Altmetric
- [Metrics details](#)

Subjects

- [Astrocyte](#)
- [Cellular neuroscience](#)

- [Synaptic development](#)

Abstract

Perisynaptic astrocytic processes are an integral part of central nervous system synapses^{1,2}; however, the molecular mechanisms that govern astrocyte–synapse adhesions and how astrocyte contacts control synapse formation and function are largely unknown. Here we use an *in vivo* chemico-genetic approach that applies a cell-surface fragment complementation strategy, Split-TurboID, and identify a proteome that is enriched at astrocyte–neuron junctions *in vivo*, which includes neuronal cell adhesion molecule (NRCAM). We find that NRCAM is expressed in cortical astrocytes, localizes to perisynaptic contacts and is required to restrict neuropil infiltration by astrocytic processes. Furthermore, we show that astrocytic NRCAM interacts transcellularly with neuronal NRCAM coupled to gephyrin at inhibitory postsynapses. Depletion of astrocytic NRCAM reduces numbers of inhibitory synapses without altering glutamatergic synaptic density. Moreover, loss of astrocytic NRCAM markedly decreases inhibitory synaptic function, with minor effects on excitation. Thus, our results present a proteomic framework for how astrocytes interface with neurons and reveal how astrocytes control GABAergic synapse formation and function.

[Access through your institution](#)

[Change institution](#)

[Buy or subscribe](#)

Access options

Subscribe to Journal

Get full journal access for 1 year

185,98 €

only 3,58 € per issue

Subscribe

All prices are NET prices.
VAT will be added later in the checkout.

Rent or Buy article

Get time limited or full article access on ReadCube.

from \$8.99

Rent or Buy

All prices are NET prices.

Additional access options:

- [Log in](#)
- [Access through your institution](#)
- [Learn about institutional subscriptions](#)

Fig. 1: Identification of the astrocyte–neuron synaptic cleft proteome using *in vivo* Split-TurboID.

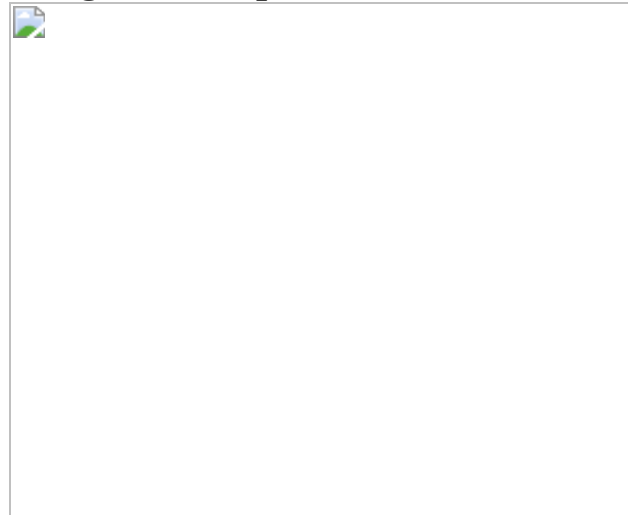


Fig. 2: The astrocyte–neuron synaptic cleft proteome.



Fig. 3: NRCAM controls astrocyte-neuron contacts in vivo.



Fig. 4: Astrocytic NRCAM controls inhibitory synaptic organization and function.



Data availability

Proteomics data are available in the MassIVE database under accession MSV000085821. The data that support the findings of this study are available from the corresponding author upon reasonable request.

References

1. 1.

Yu, X., Nagai, J. & Khakh, B. S. Improved tools to study astrocytes. *Nat. Rev. Neurosci.* **21**, 121–138 (2020).

[CAS](#) [PubMed](#) [Google Scholar](#)

2. 2.

Lanjakornsiripan, D. et al. Layer-specific morphological and molecular differences in neocortical astrocytes and their dependence on neuronal layers. *Nat. Commun.* **9**, 1623 (2018).

[PubMed](#) [PubMed Central](#) [ADS](#) [Google Scholar](#)

3. 3.

Araque, A., Parpura, V., Sanzgiri, R. P. & Haydon, P. G. Tripartite synapses: glia, the unacknowledged partner. *Trends Neurosci.* **22**, 208–215 (1999).

[CAS](#) [PubMed](#) [Google Scholar](#)

4. 4.

Khakh, B. S. & Sofroniew, M. V. Diversity of astrocyte functions and phenotypes in neural circuits. *Nat. Neurosci.* **18**, 942–952 (2015).

[CAS](#) [PubMed](#) [PubMed Central](#) [ADS](#) [Google Scholar](#)

5. 5.

Ma, Z., Stork, T., Bergles, D. E. & Freeman, M. R. Neuromodulators signal through astrocytes to alter neural circuit activity and behaviour. *Nature* **539**, 428–432 (2016).

[CAS](#) [PubMed](#) [PubMed Central](#) [ADS](#) [Google Scholar](#)

6. 6.

Papouin, T., Dunphy, J., Tolman, M., Foley, J. C. & Haydon, P. G. Astrocytic control of synaptic function. *Phil. Trans. R. Soc. Lond. B* **372**, 20160154 (2017).

[Google Scholar](#)

7. 7.

Panatier, A. et al. Astrocytes are endogenous regulators of basal transmission at central synapses. *Cell* **146**, 785–798 (2011).

[CAS](#) [PubMed](#) [Google Scholar](#)

8. 8.

Araque, A. et al. Gliotransmitters travel in time and space. *Neuron* **81**, 728–739 (2014).

[CAS](#) [PubMed](#) [PubMed Central](#) [Google Scholar](#)

9. 9.

Stogsdill, J. A. et al. Astrocytic neuroligins control astrocyte morphogenesis and synaptogenesis. *Nature* **551**, 192–197 (2017).

[CAS](#) [PubMed](#) [PubMed Central](#) [ADS](#) [Google Scholar](#)

10. 10.

Stork, T., Sheehan, A., Tasdemir-Yilmaz, O. E. & Freeman, M. R. Neuron–glia interactions through the Heartless FGF receptor signaling pathway mediate morphogenesis of *Drosophila* astrocytes. *Neuron* **83**, 388–403 (2014).

[CAS](#) [PubMed](#) [PubMed Central](#) [Google Scholar](#)

11. 11.

Sloan, S. A. & Barres, B. A. Mechanisms of astrocyte development and their contributions to neurodevelopmental disorders. *Curr. Opin. Neurobiol.* **27**, 75–81 (2014).

[CAS](#) [PubMed](#) [PubMed Central](#) [Google Scholar](#)

12. 12.

Allen, N. J. & Lyons, D. A. Glia as architects of central nervous system formation and function. *Science* **362**, 181–185 (2018).

[CAS](#) [PubMed](#) [PubMed Central](#) [ADS](#) [Google Scholar](#)

13. 13.

Branon, T. C. et al. Efficient proximity labeling in living cells and organisms with TurboID. *Nat. Biotechnol.* **36**, 880–887 (2018).

[CAS](#) [PubMed](#) [PubMed Central](#) [Google Scholar](#)

14. 14.

Schopp, I. M. et al. Split-BioID a conditional proteomics approach to monitor the composition of spatiotemporally defined protein complexes. *Nat. Commun.* **8**, 15690 (2017).

[CAS](#) [PubMed](#) [PubMed Central](#) [ADS](#) [Google Scholar](#)

15. 15.

De Munter, S. et al. Split-BioID: a proximity biotinylation assay for dimerization-dependent protein interactions. *FEBS Lett.* **591**, 415–424 (2017).

[PubMed](#) [Google Scholar](#)

16. 16.

Kinoshita, N. et al. Genetically encoded fluorescent indicator GRAPHIC delineates intercellular connections. *iScience* **15**, 28–38 (2019).

[CAS](#) [PubMed](#) [PubMed Central](#) [ADS](#) [Google Scholar](#)

17. 17.

Lee, Y., Messing, A., Su, M. & Brenner, M. *GFAP* promoter elements required for region-specific and astrocyte-specific expression. *Glia* **56**, 481–493 (2008).

[PubMed](#) [Google Scholar](#)

18. 18.

Chan, K. Y. et al. Engineered AAVs for efficient noninvasive gene delivery to the central and peripheral nervous systems. *Nat. Neurosci.* **20**, 1172–1179 (2017).

[CAS](#) [PubMed](#) [PubMed Central](#) [Google Scholar](#)

19. 19.

Uezu, A. et al. Identification of an elaborate complex mediating postsynaptic inhibition. *Science* **353**, 1123–1129 (2016).

[CAS](#) [PubMed](#) [PubMed Central](#) [ADS](#) [Google Scholar](#)

20. 20.

Zhang, Y. et al. An RNA-sequencing transcriptome and splicing database of glia, neurons, and vascular cells of the cerebral cortex. *J. Neurosci.* **34**, 11929–11947 (2014).

[CAS](#) [PubMed](#) [PubMed Central](#) [Google Scholar](#)

21. 21.

Zhang, Y. et al. Purification and characterization of progenitor and mature human astrocytes reveals transcriptional and functional differences with mouse. *Neuron* **89**, 37–53 (2016).

[CAS](#) [PubMed](#) [Google Scholar](#)

22. 22.

Sakers, K. & Eroglu, C. Control of neural development and function by glial neuroligins. *Curr. Opin. Neurobiol.* **57**, 163–170 (2019).

[CAS](#) [PubMed](#) [PubMed Central](#) [Google Scholar](#)

23. 23.

Incontro, S., Asensio, C. S., Edwards, R. H. & Nicoll, R. A. Efficient, complete deletion of synaptic proteins using CRISPR. *Neuron* **83**, 1051–1057 (2014).

[CAS](#) [PubMed](#) [PubMed Central](#) [Google Scholar](#)

24. 24.

Custer, A. W. et al. The role of the ankyrin-binding protein NrCAM in node of Ranvier formation. *J. Neurosci.* **23**, 10032–10039 (2003).

[CAS](#) [PubMed](#) [PubMed Central](#) [Google Scholar](#)

25. 25.

Feinberg, K. et al. A glial signal consisting of gliomedin and NrCAM clusters axonal Na⁺ channels during the formation of nodes of Ranvier. *Neuron* **65**, 490–502 (2010).

[CAS](#) [PubMed](#) [PubMed Central](#) [Google Scholar](#)

26. 26.

Demyanenko, G. P. et al. Neural cell adhesion molecule NrCAM regulates Semaphorin 3F-induced dendritic spine remodeling. *J. Neurosci.* **34**, 11274–11287 (2014).

[PubMed](#) [PubMed Central](#) [Google Scholar](#)

27. 27.

Mohan, V. et al. Temporal regulation of dendritic spines through NrCAM-Semaphorin3F receptor signaling in developing cortical pyramidal neurons. *Cereb. Cortex* **29**, 963–977 (2019).

[PubMed](#) [Google Scholar](#)

28. 28.

Mauro, V. P., Krushel, L. A., Cunningham, B. A. & Edelman, G. M. Homophilic and heterophilic binding activities of Nr-CAM, a nervous system cell adhesion molecule. *J. Cell Biol.* **119**, 191–202 (1992).

[CAS](#) [PubMed](#) [Google Scholar](#)

29. 29.

Derouiche, A., Anlauf, E., Aumann, G., Mühlstädt, B. & Lavialle, M. Anatomical aspects of glia-synapse interaction: the perisynaptic glial sheath consists of a specialized astrocyte compartment. *J. Physiol. Paris* **96**, 177–182 (2002).

[CAS](#) [PubMed](#) [Google Scholar](#)

30. 30.

Lavialle, M. et al. Structural plasticity of perisynaptic astrocyte processes involves ezrin and metabotropic glutamate receptors. *Proc. Natl Acad. Sci. USA* **108**, 12915–12919 (2011).

[CAS](#) [PubMed](#) [ADS](#) [Google Scholar](#)

31. 31.

Scheiffele, P., Fan, J., Choih, J., Fetter, R. & Serafini, T. Neuroligin expressed in nonneuronal cells triggers presynaptic development in contacting axons. *Cell* **101**, 657–669 (2000).

[CAS](#) [PubMed](#) [Google Scholar](#)

32. 32.

Graf, E. R., Zhang, X., Jin, S. X., Linhoff, M. W. & Craig, A. M. Neurexins induce differentiation of GABA and glutamate postsynaptic specializations via neuroligins. *Cell* **119**, 1013–1026 (2004).

[CAS](#) [PubMed](#) [PubMed Central](#) [Google Scholar](#)

33. 33.

Chih, B., Gollan, L. & Scheiffele, P. Alternative splicing controls selective trans-synaptic interactions of the neuroligin–neurexin complex. *Neuron* **51**, 171–178 (2006).

[CAS](#) [PubMed](#) [Google Scholar](#)

34. 34.

Tremblay, R., Lee, S. & Rudy, B. GABAergic interneurons in the neocortex: from cellular properties to circuits. *Neuron* **91**, 260–292 (2016).

[CAS](#) [PubMed](#) [PubMed Central](#) [Google Scholar](#)

35. 35.

Miles, R., Tóth, K., Gulyás, A. I., Hájos, N. & Freund, T. F. Differences between somatic and dendritic inhibition in the hippocampus. *Neuron* **16**, 815–823 (1996).

[CAS](#) [PubMed](#) [Google Scholar](#)

36. 36.

Wierenga, C. J. & Wadman, W. J. Miniature inhibitory postsynaptic currents in CA1 pyramidal neurons after kindling epileptogenesis. *J. Neurophysiol.* **82**, 1352–1362 (1999).

[CAS](#) [PubMed](#) [Google Scholar](#)

37. 37.

Martell, J. D. et al. A split horseradish peroxidase for the detection of intercellular protein-protein interactions and sensitive visualization of synapses. *Nat. Biotechnol.* **34**, 774–780 (2016).

[CAS](#) [PubMed](#) [PubMed Central](#) [Google Scholar](#)

38. 38.

Loh, K. H. et al. Proteomic analysis of unbounded cellular compartments: synaptic clefts. *Cell* **166**, 1295–1307 (2016).

[CAS](#) [PubMed](#) [PubMed Central](#) [Google Scholar](#)

39. 39.

Cijssouw, T. et al. Mapping the proteome of the synaptic cleft through proximity labeling reveals new cleft proteins. *Proteomes* **6**, E48 (2018).

[PubMed](#) [Google Scholar](#)

40. 40.

Li, J. et al. Cell-surface proteomic profiling in the fly brain uncovers wiring regulators. *Cell* **180**, 373–386 (2020).

[CAS](#) [PubMed](#) [Google Scholar](#)

41. 41.

Cho, K. F. et al. Split-TurboID enables contact-dependent proximity labeling in cells. *Proc. Natl Acad. Sci. USA* **117**, 12143–12154 (2020).

[CAS](#) [PubMed](#) [Google Scholar](#)

42. 42.

Elmariah, S. B., Oh, E. J., Hughes, E. G. & Balice-Gordon, R. J. Astrocytes regulate inhibitory synapse formation via Trk-mediated modulation of postsynaptic GABA_A receptors. *J. Neurosci.* **25**, 3638–3650 (2005).

[CAS](#) [PubMed](#) [PubMed Central](#) [Google Scholar](#)

43. 43.

Hughes, E. G., Elmariah, S. B. & Balice-Gordon, R. J. Astrocyte secreted proteins selectively increase hippocampal GABAergic axon length, branching, and synaptogenesis. *Mol. Cell. Neurosci.* **43**, 136–145 (2010).

[CAS](#) [PubMed](#) [Google Scholar](#)

44. 44.

Turrigiano, G. G., Leslie, K. R., Desai, N. S., Rutherford, L. C. & Nelson, S. B. Activity-dependent scaling of quantal amplitude in neocortical neurons. *Nature* **391**, 892–896 (1998).

[CAS](#) [PubMed](#) [ADS](#) [Google Scholar](#)

45. 45.

O'Brien, R. J. et al. Activity-dependent modulation of synaptic AMPA receptor accumulation. *Neuron* **21**, 1067–1078 (1998).

[PubMed](#) [Google Scholar](#)

46. 46.

Spence, E. F. et al. In vivo proximity proteomics of nascent synapses reveals a novel regulator of cytoskeleton-mediated synaptic maturation. *Nat. Commun.* **10**, 386 (2019).

[PubMed](#) [PubMed Central](#) [ADS](#) [Google Scholar](#)

47. 47.

Shin, J. H., Yue, Y. & Duan, D. Recombinant adeno-associated viral vector production and purification. *Methods Mol. Biol.* **798**, 267–284 (2012).

[CAS](#) [PubMed](#) [PubMed Central](#) [Google Scholar](#)

48. 48.

Takano, T. et al. LMTK1 regulates dendritic formation by regulating movement of Rab11A-positive endosomes. *Mol. Biol. Cell* **25**, 1755–1768 (2014).

[PubMed](#) [PubMed Central](#) [Google Scholar](#)

49. 49.

Takano, T. et al. Discovery of long-range inhibitory signaling to ensure single axon formation. *Nat. Commun.* **8**, 33 (2017).

[PubMed](#) [PubMed Central](#) [ADS](#) [Google Scholar](#)

50. 50.

Ippolito, D. M, Eroglu, C. Quantifying synapses: an immunocytochemistry-based assay to quantify synapse number. *J. Vis. Exp.* **16**, 2270 (2010).

[Google Scholar](#)

51. 51.

Dani, A., Huang, B., Bergan, J., Dulac, C. & Zhuang, X. Superresolution imaging of chemical synapses in the brain. *Neuron* **68**, 843–856 (2010).

[CAS](#) [PubMed](#) [PubMed Central](#) [Google Scholar](#)

[Download references](#)

Acknowledgements

We thank H. Katsura for modifying the promoter of the surface and split TurboID plasmids for HEK 293T cell expression, and B. Duncan for technical support. This work was supported by Brain initiative RO1DA047258 from NIH (S.H.S. and C.E.), R01MH113280 from NIH (P.F.M.), Kahn Neurotechnology Award (S.H.S. and C.E.), a Grant-in-Aid

for JSPS Fellows (PD) 20153173 from the Japan Society for the Promotion of Science (T.T.), The Uehara memorial Foundation (T.T.), and National Institute of Mental Health Fellowship F30MH117851 (J.L.C).

Author information

Affiliations

1. The Department of Cell Biology, Duke University Medical School, Durham, NC, USA

Tetsuya Takano, John T. Wallace, Katherine T. Baldwin, Alicia M. Purkey, Akiyoshi Uezu, Erik J. Soderblom, Cagla Eroglu & Scott H. Soderling

2. Department of Neurobiology, Duke University Medical School, Durham, NC, USA

Jamie L. Courtland, Cagla Eroglu & Scott H. Soderling

3. Duke Proteomics and Metabolomics Shared Resource and Duke Center for Genomic and Computational Biology, Duke University Medical School, Durham, NC, USA

Erik J. Soderblom

4. Molecular Mechanisms of Brain Development, Center for Brain Science (CBS), RIKEN, Saitama, Japan

Tomomi Shimogori

5. Department of Biochemistry, University of North Carolina School of Medicine, Chapel Hill, NC, USA

Patricia F. Maness

6. Department of Biophysics, University of North Carolina School of Medicine, Chapel Hill, NC, USA

Patricia F. Maness

Authors

1. Tetsuya Takano

[View author publications](#)

You can also search for this author in [PubMed](#) [Google Scholar](#)

2. John T. Wallace

[View author publications](#)

You can also search for this author in [PubMed](#) [Google Scholar](#)

3. Katherine T. Baldwin

[View author publications](#)

You can also search for this author in [PubMed](#) [Google Scholar](#)

4. Alicia M. Purkey

[View author publications](#)

You can also search for this author in [PubMed](#) [Google Scholar](#)

5. Akiyoshi Uezu

[View author publications](#)

You can also search for this author in [PubMed](#) [Google Scholar](#)

6. Jamie L. Courtland

[View author publications](#)

You can also search for this author in [PubMed](#) [Google Scholar](#)

7. Erik J. Soderblom

[View author publications](#)

You can also search for this author in [PubMed](#) [Google Scholar](#)

8. Tomomi Shimogori

[View author publications](#)

You can also search for this author in [PubMed](#) [Google Scholar](#)

9. Patricia F. Maness

[View author publications](#)

You can also search for this author in [PubMed](#) [Google Scholar](#)

10. Cagla Eroglu

[View author publications](#)

You can also search for this author in [PubMed](#) [Google Scholar](#)

11. Scott H. Soderling

[View author publications](#)

You can also search for this author in [PubMed](#) [Google Scholar](#)

Contributions

T.T., C.E. and S.H.S. designed the study. T.T., J.T.W., A.P., C.E. and S.H.S. wrote the manuscript. T.T., J.T.W., A.U. and E.J.S. performed *in vivo* BioID-proteomics analysis. T.T., J.T.W., J.L.C., T.S. and P.F.M. produced the constructs. T.T., J.T.W. and K.T.B. performed imaging analysis and the morphological analysis of the astrocytes. A.P. performed electrophysiological analysis. T.T. and K.T.B. performed the biological experiments. All authors discussed the results and commented on the manuscript text.

Corresponding authors

Correspondence to [Tetsuya Takano](#) or [Cagla Eroglu](#) or [Scott H. Soderling](#).

Ethics declarations

Competing interests

The authors declare no competing interests.

Additional information

Peer review information *Nature* thanks Thomas Biederer, Peter Scheiffele and the other, anonymous, reviewer(s) for their contribution to the peer review of this work.

Publisher's note Springer Nature remains neutral with regard to jurisdictional claims in published maps and institutional affiliations.

Extended data figures and tables

[Extended Data Fig. 1 The reconstituted activity of Split-TurboID in neurons and astrocytes in vitro.](#)

a, Schematics of constructs tested. **b**, Immunoblot analysis of construct expression and biotinylation activity. **c**, Schematic of neuron-astrocyte mixed-culture assay for Split-TurboID with cell-type-specific AAVs in vitro. **d**, Cultured neurons and astrocytes were infected with AAV1/2-GfaABC1D-TurboID-HA-surface, AAV1/2-hSynI-V5-N-TurboID and/or AAV1/2-GfaABC1D-C-TurboID-HA. Representative images of neuron and astrocyte at DIV14 after the treatment of 500 µM biotin for 6h are shown. $n = 3$ biological repeats.

[Extended Data Fig. 2 Split-TurboID maps excitatory and inhibitory perisynaptic proteins.](#)

a–d, Representative images demonstrating that proteins biotinylated by astrocytic TurboID-surface or Split-TurboID (cyan) are adjacent to excitatory presynaptic marker VGLUT1 (**a**), postsynaptic marker HOMER1 (**b**), inhibitory presynaptic marker VGAT (**c**), and postsynaptic marker

gephyrin (**d**). Astrocytes were visualized with GfaABC1D-mCherry-CAAX. $n = 3$ biological repeats.

Extended Data Fig. 3 Brain-wide transduction of astrocytes and neurons.

a, Schematic of AAV PHP.eB viruses for neuronal-EGFP or astrocyte-mCherry-CAAX and retro-orbital injection. **b**, Sagittal section of mouse brain showing expression throughout the cortex and other structures. **c**, Representative image from cortex, hippocampus or cerebellum showing high coverage of neuronal and astrocytic expression.

Extended Data Fig. 4 Mapping and identification of tripartite synaptic cleft proteins by Split-TurboID in vivo.

a, Biotinylation activity of Split-TurboID in vivo. Lysates of mouse brain infected with cell-type-specific TurboID-surface-HA, V5-N-TurboID and/or C-TurboID-HA. Brain lysates were analysed by immunoblotting with anti-Streptavidin, anti-V5, anti-HA and anti-Tubulin antibodies. **b**, The graph indicates the ratio of biotinylation activity in vivo ($n = 4$ brains per each condition). **c, d**, The biotinylation of Split-TurboID in mouse cortex. **e, f**, Quantification of average number of excitatory or inhibitory synaptic colocalized puncta in layer 2/3 of the visual cortex. $n = 15$ slices per each condition from 3 mice. **g**, Chart summarizing proteomic data set identified by mass spectrometry and filters used to identify top candidates. **h**, Venn diagram comparing proteome list of Split-TurboID and TurboID-surface. **i**, Scale-free network of Split-TurboID (green) and TurboID-surface (blue) identified proteins. High-confidence proteins enriched in both Split-TurboID and TurboID-surface fractions are shown in red. Neuronal enriched proteins (RNA-seq expression ratio <1) and astrocyte enriched proteins (RNA-seq expression ratio ≥ 1.0) are represented as circle or diamond, respectively. At least $n = 4$ biological repeats. One-way ANOVA (Dunnett's multiple comparison, $P < 0.0001, 0.001$). Data are means \pm s.e.m.

Extended Data Fig. 5 The validation of candidate proteins with CRISPR-based astrocytic candidate gene depletion strategy.

a, Schematic of CRISPR-based deletion of astrocytic NrCAM in vitro. **b**, Immunoblots showing loss of NrCAM with sgRNA. AAV1/2-U6-empty sgRNA or AAV1/2-U6-NrCAM sgRNA was co-infected with AAV1/2-GfaABC1D-Cas9 to cultured neurons and astrocytes at DIV14. The cells were subjected to immunoblot analysis with an anti-NrCAM antibody. Tubulin was used as a loading control. **c**, The bar graph indicates the expression level of NrCAM from 3 independent experiments. **d**, Schematic of CRISPR-based deletion strategy of candidate gene. **e**, Experimental timeline of AAV-mediated CRISPR-based astrocytic gene deletion strategy in Flex-TdTomato mice. **f**, AAV PHP.eB-U6-NrCAM sgRNA was co-infected with AAV PHP.eB-GfaABC1D-Cas9 in Flex-TdTomato mice at P21. Coronal sections were prepared and immunostained with an anti-TdTomato antibody. **g**, A High-magnification image is shown. **h**, Images of Tenm2-, Tenm4- or NrCAM-deleted astrocytes (cyan) and their territories (red outlines) in visual cortices of juvenile mice. **i**, Average territory volumes at P42 of Tenm2-, Tenm4- or NrCAM-deleted astrocytes. Between 20-25 cells per condition from 3 mice. **j**, Images of Tenm2-, Tenm4- or NrCAM-deleted astrocytes (cyan) and their NIV reconstructions (orange) in visual cortices of juvenile mice. **k**, Average NIV at P42 of Tenm2-, Tenm4- or NrCAM-deleted astrocytes. 51 cells per each condition from 3 mice. $n = 3$ biological repeats. One-way ANOVA (Dunnett's multiple comparison, $P < 0.0001, 0.01$). Data are means \pm s.e.m.

Extended Data Fig. 6 NrCAM is a novel tripartite synaptic protein.

a, A high magnification STED image showing that endogenous NrCAM was enriched at biotinylated proteins in vivo. **b**, Immunoblot analysis of endogenous NrCAM, astrocyte marker GFAP, neuronal marker b-Tubulin III or loading control α -Tubulin from mouse brain or purified astrocyte lysate. **c**, Schematic of the visualization of astrocytic membrane and endogenous NrCAM in vivo. **d**, STED images demonstrating the localization of endogenous NrCAM in vivo. Coronal sections were

immunostained with anti-NrCAM antibody (cyan). High magnification image was shown (right panel). **e**, Schematic of the visualization of both astrocytic and neuronal NrCAM in vivo. **f**, STED images demonstrating that the colocalization of astrocytic NrCAM with neuronal NrCAM in vivo. Coronal sections were prepared and co-immunostained with an anti-V5 (cyan) and anti-HA (magenta) antibody. A high-magnification image is shown in the right. $n = 3$ biological repeats. Data represent means \pm s.e.m.

Extended Data Fig. 7 The role of astrocytic NrCAM in astrocytic morphogenesis in vivo.

a, Schematic of CRISPR-based NrCAM deletion in vivo. **b**, Schematic of hNrCAM domains and fragments. SP, signal peptide; IG, immunoglobulin; FN, fibronectin; TMD, transmembrane domain; ECD, extracellular domains. **c**, Immunoblots showing the expression of each NrCAM fragments in HEK293T cells. **d, f, h, j**, Images of astrocytes following deletion of astrocyte NrCAM alone (NrCAM sgRNA), with coexpression with indicated constructs of sgRNA-resistant human NrCAM, neuronal NrCAM deletion (neuroNrCAM sgRNA), or following neuronal NrCAM deletion alone. Images at indicated ages represent. **e, i**, Analysis of astrocyte territory, 15–29 cells per each condition from 3 mice; **g, k**, Analysis of neuropil infiltration volume. 50–51 cells per each condition from 3 mice. $n = 3$ biological repeats. One-way ANOVA (Dunnett's multiple comparison, $P < 0.0001$). Data represent means \pm s.e.m.

Extended Data Fig. 8 NrCAM controls inhibitory synaptic specializations through binding the gephyrin.

a, Immunoblot analysis of endogenous NrCAM, astrocyte marker GFAP, Neuroligin 2, Neuroligin 3, Kir4.1 or EAAT2 (GLT1) from purified astrocyte lysate. **b**, The bar graph indicates the expression level. **c**, The interaction of NrCAM with PSD95 and gephyrin in HEK293T cells. Cell lysates coexpressing NrCAM-HA with GFP, PSD95-GFP or GFP-gephyrin were incubated with anti-GFP-bound beads. Immunoprecipitated (right) or total (left) NrCAM, GFP, PSD95-GFP or GFP-gephyrin were detected by immunoblotting with anti-HA and anti-GFP antibodies. **d**, Schematic of

HEK293T/neuronal mixed-cultured assay in vitro. **e–h**, Images of in vitro inhibitory synapse formation assays. The graph shows average of the total integrated intensity of VGAT (Cont = 258, NL2 = 222, NrCAM = 242, NrCAM-ΔIG = 288, NrCAM-ΔECD = 303 cells) or GABA_A receptor (Cont = 313, NRX1β4(-) = 310, NrCAM = 300, NrCAM-ΔIG = 278, NrCAM-ΔECD = 278 cells) clusters that contact transfected HEK293T cells. **i–l**, Images of in vitro excitatory synapse formation assay. The graph shows average of the total integrated intensity of VGLUT1 (Cont = 259, NL2 = 306, NrCAM = 286, NrCAM-ΔIG = 321, NrCAM-ΔECD = 196 cells) or HOMER1 (Cont = 471, NRX1β4(-) = 214, NrCAM = 247, NrCAM-ΔIG = 387, NrCAM-ΔECD = 251 cells) clusters that contact transfected HEK293T cells. $n = 3$ biological repeats. One-way ANOVA (Dunnett's multiple comparison, $P < 0.0001$). Data are means ± s.e.m.

[Extended Data Fig. 9 The effect of NrCAM on excitatory synapse formation and function in vivo.](#)

a, Images of postsynapse PSD95 and presynapse VGLUT1 within NrCAM-deletion astrocytes in L1 of the visual cortex. High magnification images (bottom) correspond to boxes (above). **b**, Quantification of average number of excitatory synaptic colocalized puncta within astrocyte territories. $n = 15$ cells per each condition from 3 mice. **c**, mEPSC traces from L2/3 pyramidal neurons following astrocyte control empty sgRNA or NrCAM sgRNA expression. **d–g**, Quantification of mEPSC amplitude (**d, e**, Cont = 16, NrCAM sgRNA = 14 cells from 4 mice) and frequency (**f, g**, Cont = 14, NrCAM sgRNA = 17 cells from each of 4 mice). At least $n = 3$ biological repeats. Student's *t*-test (paired, $P < 0.05$). Data represent means ± s.e.m.

[Extended Data Fig. 10 In vivo chemogenetics method, Split-TurboID, reveals a novel astrocytic cell adhesion molecule, NrCAM, that controls inhibitory synaptic organization.](#)

Development of in vivo chemo-affinity codes, Split-TurboID, and a working model of astrocytic NrCAM influencing inhibitory synaptic function. Split-TurboID can map the molecular composition of such intercellular contacts, even within the highly complex structure of the

tripartite synapse in vivo. Mapping this interface, we discovered a new molecular mechanism by which astrocytes influence inhibitory synapses within the tripartite synaptic cleft via NrCAM. NrCAM is expressed in cortical astrocytes where it interacts with neuronal NrCAM that is coupled to gephyrin at inhibitory postsynapses. Loss of astrocytic NrCAM dramatically alters inhibitory synaptic organization and function in vivo.

Supplementary information

Supplementary Information

This file contains Supplementary Figure 1 (uncropped blots) and Supplementary Table 4 (Primers used for constructions or sequences).

Reporting Summary

Supplementary Table 1

Split-TurboID Enriched Proteins.

Supplementary Table 2

Astrocyte TurboID-Surface Enriched Proteins.

Supplementary Table 3

High Confidence Tri-partite Synapse Proteome.

Supplementary Table 5

Raw Data of Split-TurboID and Astrocyte TurboID-surface Proteome.

Supplementary Table 6

Contaminating Proteins.

Supplementary Table 7

Summary of Statistical Analysis.

Rights and permissions

Reprints and Permissions

About this article



Check for
updates

Cite this article

Takano, T., Wallace, J.T., Baldwin, K.T. *et al.* Chemico-genetic discovery of astrocytic control of inhibition in vivo. *Nature* **588**, 296–302 (2020).
<https://doi.org/10.1038/s41586-020-2926-0>

Download citation

- Received: 23 January 2020
- Accepted: 19 August 2020
- Published: 11 November 2020
- Issue Date: 10 December 2020
- DOI: <https://doi.org/10.1038/s41586-020-2926-0>

Comments

By submitting a comment you agree to abide by our [Terms](#) and [Community Guidelines](#). If you find something abusive or that does not comply with our

terms or guidelines please flag it as inappropriate.

[Access through your institution](#)

[Change institution](#)

[Buy or subscribe](#)

This article was downloaded by **calibre** from <https://www.nature.com/articles/s41586-020-2926-0>

| [Section menu](#) | [Main menu](#) |

- Article
- [Published: 25 November 2020](#)

The gut microbiota is associated with immune cell dynamics in humans

- [Jonas Schluter](#) [ORCID: orcid.org/0000-0002-6214-9367^{1,2}](#),
- [Jonathan U. Peled](#) [ORCID: orcid.org/0000-0002-4029-7625^{3,4}](#),
- [Bradford P. Taylor²](#),
- [Kate A. Markey^{3,4}](#),
- [Melody Smith](#) [ORCID: orcid.org/0000-0002-2702-0381^{3,4}](#),
- [Ying Taur⁵](#),
- [Rene Niehus](#) [ORCID: orcid.org/0000-0002-6751-4124⁶](#),
- [Anna Staffas⁷](#),
- [Anqi Dai³](#),
- [Emily Fontana⁵](#),
- [Luigi A. Amoretti⁵](#),
- [Roberta J. Wright⁵](#),
- [Sejal Morjaria⁵](#),
- [Maly Fenelus⁸](#),
- [Melissa S. Pessin](#) [ORCID: orcid.org/0000-0003-3990-6494⁸](#),
- [Nelson J. Chao⁹](#),
- [Meagan Lew⁹](#),
- [Lauren Bohannon⁹](#),
- [Amy Bush⁹](#),
- [Anthony D. Sung⁹](#),
- [Tobias M. Hohl](#) [ORCID: orcid.org/0000-0002-9097-5412⁵](#),
- [Miguel-Angel Perales](#) [ORCID: orcid.org/0000-0002-5910-4571^{3,4}](#),

- [Marcel R. M. van den Brink](#) ORCID: [orcid.org/0000-0003-0696-4401^{3,4}](https://orcid.org/0000-0003-0696-4401) &
- [Joao B. Xavier](#) ORCID: [orcid.org/0000-0003-3592-1689²](https://orcid.org/0000-0003-3592-1689)

[Nature](#) volume **588**, pages303–307(2020)[Cite this article](#)

- 11k Accesses
- 255 Altmetric
- [Metrics details](#)

Subjects

- [Bone marrow transplantation](#)
- [Computational biology and bioinformatics](#)
- [Evolution](#)
- [Immunology](#)
- [Microbiome](#)

Abstract

The gut microbiota influences development^{1,2,3} and homeostasis^{4,5,6,7} of the mammalian immune system, and is associated with human inflammatory⁸ and immune diseases^{9,10} as well as responses to immunotherapy^{11,12,13,14}. Nevertheless, our understanding of how gut bacteria modulate the immune system remains limited, particularly in humans, where the difficulty of direct experimentation makes inference challenging. Here we study hundreds of hospitalized—and closely monitored—patients with cancer receiving haematopoietic cell transplantation as they recover from chemotherapy and stem-cell engraftment. This aggressive treatment causes large shifts in both circulatory immune cell and microbiota populations, enabling the relationships between the two to be studied simultaneously. Analysis of observed daily changes in circulating neutrophil, lymphocyte and monocyte counts and more than 10,000 longitudinal microbiota samples revealed consistent associations between gut bacteria and immune cell dynamics. High-resolution clinical metadata and Bayesian inference

allowed us to compare the effects of bacterial genera in relation to those of immunomodulatory medications, revealing a considerable influence of the gut microbiota—together and over time—on systemic immune cell dynamics. Our analysis establishes and quantifies the link between the gut microbiota and the human immune system, with implications for microbiota-driven modulation of immunity.

[Access through your institution](#)

[Change institution](#)

[Buy or subscribe](#)

Access options

Subscribe to Journal

Get full journal access for 1 year

185,98 €

only 3,58 € per issue

[Subscribe](#)

All prices are NET prices.

VAT will be added later in the checkout.

Rent or Buy article

Get time limited or full article access on ReadCube.

from \$8.99

[Rent or Buy](#)

All prices are NET prices.

Additional access options:

- [Log in](#)
- [Access through your institution](#)
- [Learn about institutional subscriptions](#)

Fig. 1: Immune reconstitution and microbiome dynamics after HCT.

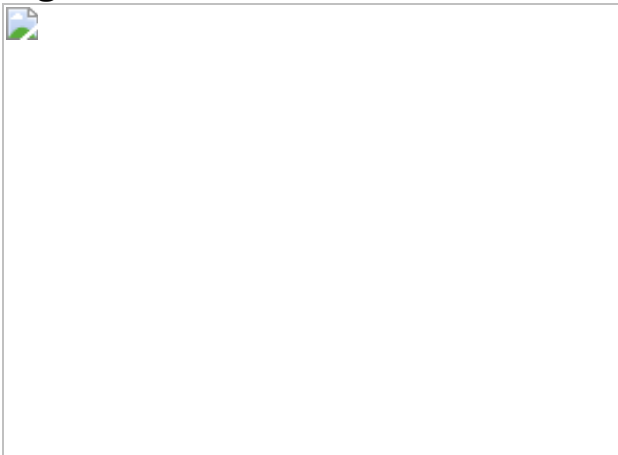


Fig. 2: Neutrophil, lymphocyte and monocyte counts increased in FMT-treated individuals in the weeks following treatment.

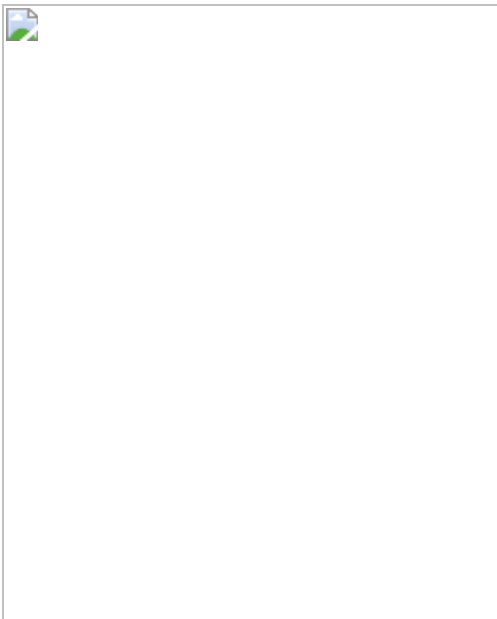
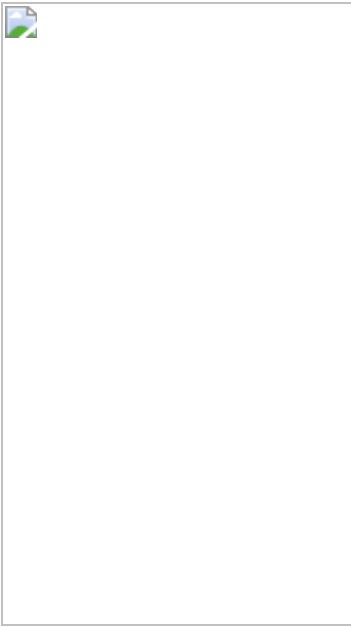


Fig. 3: Bayesian inference reveals associations between the microbiota and dynamics of circulatory WBC counts.



Data availability

All data supporting the findings of this study are available within the paper and its [Supplementary Information files](#). The data used in our study are organized in Excel-compatible comma-separated value files as [Supplementary Tables \(data-tables.zip\)](#). All sequencing data have been made available publicly, and the NCBI SRA accession numbers are listed in the Supplementary Tables. Metadata and processed sequencing data are made available on a public repository via Figshare: meta data, <https://doi.org/10.6084/m9.figshare.12016986.v4>; samples, <https://doi.org/10.6084/m9.figshare.12016983.v4>; 16S counts, <https://doi.org/10.6084/m9.figshare.12016989.v3>; and 16S taxonomy, <https://doi.org/10.6084/m9.figshare.12016992.v1>.

Code availability

All of the steps of the analyses that were performed in this study are described in detail to allow reproduction of the results. Relevant analysis code is available publicly at https://github.com/jsevo/wbcdynamics_microbiome.

References

1. 1.

Mazmanian, S. K., Liu, C. H., Tzianabos, A. O. & Kasper, D. L. An immunomodulatory molecule of symbiotic bacteria directs maturation of the host immune system. *Cell* **122**, 107–118 (2005).

[CAS](#) [PubMed](#) [Google Scholar](#)

2. 2.

Gomez de Agüero, M. et al. The maternal microbiota drives early postnatal innate immune development. *Science* **351**, 1296–1302 (2016).

[PubMed](#) [ADS](#) [Google Scholar](#)

3. 3.

Olin, A. et al. Stereotypic immune system development in newborn children. *Cell* **174**, 1277–1292 (2018).

[CAS](#) [PubMed](#) [PubMed Central](#) [Google Scholar](#)

4. 4.

Tan, T. G. et al. Identifying species of symbiont bacteria from the human gut that, alone, can induce intestinal Th17 cells in mice. *Proc. Natl Acad. Sci. USA* **113**, E8141–E8150 (2016).

[CAS](#) [PubMed](#) [Google Scholar](#)

5. 5.

Deshmukh, H. S. et al. The microbiota regulates neutrophil homeostasis and host resistance to *Escherichia coli* K1 sepsis in neonatal mice. *Nat. Med.* **20**, 524–530 (2014).

[CAS](#) [PubMed](#) [PubMed Central](#) [Google Scholar](#)

6. 6.

Ivanov, I. I. et al. Specific microbiota direct the differentiation of IL-17-producing T-helper cells in the mucosa of the small intestine. *Cell Host Microbe* **4**, 337–349 (2008).

[CAS](#) [PubMed](#) [PubMed Central](#) [Google Scholar](#)

7. 7.

Geva-Zatorsky, N. et al. Mining the human gut microbiota for immunomodulatory organisms. *Cell* **168**, 928–943 (2017).

[CAS](#) [PubMed](#) [Google Scholar](#)

8. 8.

Lloyd-Price, J. et al. Multi-omics of the gut microbial ecosystem in inflammatory bowel diseases. *Nature* **569**, 655–662 (2019).

[CAS](#) [PubMed](#) [PubMed Central](#) [ADS](#) [Google Scholar](#)

9. 9.

Markey, K. A. et al. The microbe-derived short-chain fatty acids butyrate and propionate are associated with protection from chronic GVHD. *Blood* **136**, 130–136 (2020).

[PubMed](#) [Google Scholar](#)

10. 10.

Azzouz, D. et al. Lupus nephritis is linked to disease-activity associated expansions and immunity to a gut commensal. *Ann. Rheum. Dis.* **78**, 947–956 (2019).

[CAS](#) [PubMed](#) [PubMed Central](#) [Google Scholar](#)

11. 11.

Routy, B. et al. Gut microbiome influences efficacy of PD-1-based immunotherapy against epithelial tumors. *Science* **359**, 91–97 (2018).

[CAS](#) [PubMed](#) [PubMed Central](#) [ADS](#) [Google Scholar](#)

12. 12.

Gopalakrishnan, V. et al. Gut microbiome modulates response to anti-PD-1 immunotherapy in melanoma patients. *Science* **359**, 97–103 (2018).

[CAS](#) [PubMed](#) [PubMed Central](#) [ADS](#) [Google Scholar](#)

13. 13.

Vétizou, M. et al. Anticancer immunotherapy by CTLA-4 blockade relies on the gut microbiota. *Science* **350**, 1079–1084 (2015).

[PubMed](#) [PubMed Central](#) [ADS](#) [Google Scholar](#)

14. 14.

Matson, V. et al. The commensal microbiome is associated with anti-PD-1 efficacy in metastatic melanoma patients. *Science* **359**, 104–108 (2018).

[CAS](#) [PubMed](#) [PubMed Central](#) [ADS](#) [Google Scholar](#)

15. 15.

Tanoue, T. et al. A defined commensal consortium elicits CD8 T cells and anti-cancer immunity. *Nature* **565**, 600–605 (2019).

[CAS](#) [PubMed](#) [ADS](#) [Google Scholar](#)

16. 16.

Brandi, G. & Frega, G. Microbiota: overview and implication in immunotherapy-based cancer treatments. *Int. J. Mol. Sci.* **20**, 2699 (2019).

[CAS](#) [PubMed Central](#) [Google Scholar](#)

17. 17.

Xin Yu, J., Hubbard-Lucey, V. M. & Tang, J. The global pipeline of cell therapies for cancer. *Nat. Rev. Drug Discov.* **18**, 821–822 (2019).

[Google Scholar](#)

18. 18.

Morjaria, S. et al. Antibiotic-induced shifts in fecal microbiota density and composition during hematopoietic stem cell transplantation. *Infect. Immun.* **87**, e00206-19 (2019).

[CAS](#) [PubMed](#) [PubMed Central](#) [Google Scholar](#)

19. 19.

Peled, J. U. et al. Microbiota as predictor of mortality in allogeneic hematopoietic-cell transplantation. *N. Engl. J. Med.* **382**, 822–834 (2020).

[CAS](#) [PubMed](#) [PubMed Central](#) [Google Scholar](#)

20. 20.

Taur, Y. et al. Reconstitution of the gut microbiota of antibiotic-treated patients by autologous fecal microbiota transplant. *Sci. Transl. Med.* **10**, eaap9489 (2018).

[PubMed](#) [PubMed Central](#) [Google Scholar](#)

21. 21.

Staffas, A. et al. Nutritional support from the intestinal microbiota improves hematopoietic reconstitution after bone marrow transplantation in mice. *Cell Host Microbe* **23**, 447–457. (2018).

[CAS](#) [PubMed](#) [PubMed Central](#) [Google Scholar](#)

22. 22.

Savani, B. N. et al. Absolute lymphocyte count on day 30 is a surrogate for robust hematopoietic recovery and strongly predicts outcome after T cell-depleted allogeneic stem cell transplantation. *Biol. Blood Marrow Transplant.* **13**, 1216–1223 (2007).

[PubMed](#) [PubMed Central](#) [Google Scholar](#)

23. 23.

Scheiermann, C., Frenette, P. S. & Hidalgo, A. Regulation of leucocyte homeostasis in the circulation. *Cardiovasc. Res.* **107**, 340–351 (2015).

[CAS](#) [PubMed](#) [PubMed Central](#) [Google Scholar](#)

24. 24.

Thompson, P. A. et al. Umbilical cord blood graft engineering: challenges and opportunities. *Bone Marrow Transplant.* **50** (Suppl 2), S55–S62 (2015).

[PubMed](#) [Google Scholar](#)

25. 25.

Gabrilove, J. L. et al. Effect of granulocyte colony-stimulating factor on neutropenia and associated morbidity due to chemotherapy for transitional-cell carcinoma of the urothelium. *N. Engl. J. Med.* **318**, 1414–1422 (1988).

[CAS](#) [PubMed](#) [Google Scholar](#)

26. 26.

Belkaid, Y. & Hand, T. W. Role of the microbiota in immunity and inflammation. *Cell* **157**, 121–141 (2014).

[CAS](#) [PubMed](#) [PubMed Central](#) [Google Scholar](#)

27. 27.

Schirmer, M. et al. Linking the human gut microbiome to inflammatory cytokine production capacity. *Cell* **167**, 1125–1136 (2016).

[CAS](#) [PubMed](#) [PubMed Central](#) [Google Scholar](#)

28. 28.

McLoughlin, K., Schluter, J., Rakoff-Nahoum, S., Smith, A. L. & Foster, K. R. Host selection of microbiota via differential adhesion. *Cell Host Microbe* **19**, 550–559 (2016).

[CAS](#) [PubMed](#) [Google Scholar](#)

29. 29.

Hooper, L. V., Littman, D. R. & Macpherson, A. J. Interactions between the microbiota and the immune system. *Science* **336**, 1268–1273 (2012).

[CAS](#) [PubMed](#) [PubMed Central](#) [ADS](#) [Google Scholar](#)

30. 30.

Palm, N. W. et al. Immunoglobulin A coating identifies colitogenic bacteria in inflammatory bowel disease. *Cell* **158**, 1000–1010 (2014).

[CAS](#) [PubMed](#) [PubMed Central](#) [Google Scholar](#)

31. 31.

Henke, M. T. et al. *Ruminococcus gnavus*, a member of the human gut microbiome associated with Crohn's disease, produces an inflammatory polysaccharide. *Proc. Natl Acad. Sci. USA* **116**, 12672–12677 (2019).

[CAS](#) [PubMed](#) [Google Scholar](#)

32. 32.

Okba, A. M. et al. Neutrophil/lymphocyte ratio and lymphocyte/monocyte ratio in ulcerative colitis as non-invasive biomarkers of disease activity and severity. *Auto Immun. Highlights* **10**, 4 (2019).

[PubMed](#) [PubMed Central](#) [Google Scholar](#)

33. 33.

Choi, S.-J. et al. High neutrophil-to-lymphocyte ratio predicts short survival duration in amyotrophic lateral sclerosis. *Sci. Rep.* **10**, 428 (2020).

[CAS](#) [PubMed](#) [PubMed Central](#) [ADS](#) [Google Scholar](#)

34. 34.

Gao, Y. et al. Neutrophil/lymphocyte ratio is a more sensitive systemic inflammatory response biomarker than platelet/lymphocyte ratio in the prognosis evaluation of unresectable pancreatic cancer. *Oncotarget* **8**, 88835–88844 (2017).

[PubMed](#) [PubMed Central](#) [Google Scholar](#)

35. 35.

Hergott, C. B. et al. Peptidoglycan from the gut microbiota governs the lifespan of circulating phagocytes at homeostasis. *Blood* **127**, 2460–2471 (2016).

[CAS](#) [PubMed](#) [PubMed Central](#) [Google Scholar](#)

36. 36.

Smith, P. M. et al. The microbial metabolites, short-chain fatty acids, regulate colonic Treg cell homeostasis. *Science* **341**, 569–573 (2013).

[CAS](#) [PubMed](#) [ADS](#) [Google Scholar](#)

37. 37.

Balmer, M. L. et al. Microbiota-derived compounds drive steady-state granulopoiesis via MyD88/TICAM signaling. *J. Immunol.* **193**, 5273–5283 (2014).

[CAS](#) [PubMed](#) [Google Scholar](#)

38. 38.

Ze, X., Duncan, S. H., Louis, P. & Flint, H. J. *Ruminococcus bromii* is a keystone species for the degradation of resistant starch in the human colon. *ISME J.* **6**, 1535–1543 (2012).

[CAS](#) [PubMed](#) [PubMed Central](#) [Google Scholar](#)

39. 39.

Foster, K. R., Schluter, J., Coyte, K. Z. & Rakoff-Nahoum, S. The evolution of the host microbiome as an ecosystem on a leash. *Nature* **548**, 43–51 (2017).

[CAS](#) [PubMed](#) [PubMed Central](#) [ADS](#) [Google Scholar](#)

40. 40.

Fu, Y.-Y. et al. T cell recruitment to the intestinal stem cell compartment drives immune-mediated intestinal damage after allogeneic transplantation. *Immunity* **51**, 90–103 (2019).

[CAS](#) [PubMed](#) [PubMed Central](#) [Google Scholar](#)

41. 41.

Gerber, G. K. The dynamic microbiome. *FEBS Lett.* **588**, 4131–4139 (2014).

[CAS](#) [PubMed](#) [Google Scholar](#)

42. 42.

Jobin, C. Precision medicine using microbiota. *Science* **359**, 32–34 (2018).

[CAS](#) [PubMed](#) [ADS](#) [Google Scholar](#)

43. 43.

The Integrative HMP (iHMP) Research Network Consortium. The integrative human microbiome project. *Nature* **569**, 641–648 (2019).

[ADS](#) [Google Scholar](#)

44. 44.

Walter, J., Armet, A. M., Finlay, B. B. & Shanahan, F. Establishing or exaggerating causality for the gut microbiome: lessons from human microbiota-associated rodents. *Cell* **180**, 221–232 (2020).

[CAS](#) [PubMed](#) [Google Scholar](#)

45. 45.

Caporaso, J. G. et al. Ultra-high-throughput microbial community analysis on the Illumina HiSeq and MiSeq platforms. *ISME J.* **6**, 1621–1624 (2012).

[CAS](#) [PubMed](#) [PubMed Central](#) [Google Scholar](#)

46. 46.

Callahan, B. J. et al. DADA2: high-resolution sample inference from Illumina amplicon data. *Nat. Methods* **13**, 581–583 (2016).

[CAS](#) [PubMed](#) [PubMed Central](#) [Google Scholar](#)

47. 47.

Murali, A., Bhargava, A. & Wright, E. S. IDTAXA: a novel approach for accurate taxonomic classification of microbiome sequences. *Microbiome* **6**, 140 (2018).

[PubMed](#) [PubMed Central](#) [Google Scholar](#)

48. 48.

Quast, C. et al. The SILVA ribosomal RNA gene database project: improved data processing and web-based tools. *Nucleic Acids Res.* **41**, D590–D596 (2013).

[CAS](#) [PubMed](#) [PubMed Central](#) [Google Scholar](#)

49. 49.

Pinheiro, J. C., Bates, D. M., DebRoy, S. S. & Sarkar, D. nlme: Linear and Nonlinear Mixed Effects Models. *R package version 3.1-150* (2013).

[Google Scholar](#)

50. 50.

Tibshirani, R. Regression shrinkage and selection via the lasso. *J. R. Stat. Soc. B* **58**, 267–288 (1996).

[MathSciNet](#) [MATH](#) [Google Scholar](#)

51. 51.

Pedregosa, F. et al. Scikit-learn: machine learning in Python. *J. Mach. Learn. Res.* **12**, 2825 (2011).

[MathSciNet](#) [MATH](#) [Google Scholar](#)

52. 52.

Salvatier, J., Wiecki, T. V. & Fonnesbeck, C. *Probabilistic programming in Python using PyMC3*. *PeerJ Comput. Sci.* **2**, e55 (2016).

[Google Scholar](#)

53. 53.

Hoffman, M. D. & Gelman, A. The No-U-turn sampler: adaptively setting path lengths in Hamiltonian Monte Carlo. *J. Mach. Learn. Res.* **15**, 1593–1623 (2014).

[MathSciNet](#) [MATH](#) [Google Scholar](#)

54. 54.

Franzosa, E. A. et al. Species-level functional profiling of metagenomes and metatranscriptomes. *Nat. Methods* **15**, 962–968 (2018).

[CAS](#) [PubMed](#) [PubMed Central](#) [Google Scholar](#)

[Download references](#)

Acknowledgements

We thank M. Lipsitch, S. B. Andersen, K. R. Foster, J. K. Sia, E. G. Pamer, K. Coyte, S. Mitschka and the members of the Xavier lab for helpful discussion and comments on the manuscript. This work was supported by the National Institutes of Health (NIH) grants U01 AI124275, R01 AI137269 and U54 CA209975 to JBX, by the MSKCC Cancer Center Core

Grant P30 CA008748, the Parker Institute for Cancer Immunotherapy at Memorial Sloan Kettering Cancer Center, the Sawiris Foundation, the Society of Memorial Sloan Kettering Cancer Center, MSKCC Cancer Systems Immunology Pilot Grant and Empire Clinical Research Investigator Program. M.S. received funding from the Burroughs Wellcome Fund Postdoctoral Enrichment Program, the Damon Runyon Physician-Scientist Award, and the Robert Wood Johnson Foundation. T.M.H. is investigator in the Pathogenesis of Infectious Diseases from the Burroughs Wellcome Fund, and funded via an award from Geoffrey Beene Foundation, and NIH RO1 AI093808. The funders had no role in study design, data collection and analysis, decision to publish or preparation of the manuscript.

Author information

Affiliations

1. Institute for Computational Medicine, NYU Langone Health, New York, NY, USA

Jonas Schluter

2. Computational and Systems Biology Program, Sloan Kettering Institute, Memorial Sloan Kettering Cancer Center, New York, NY, USA

Jonas Schluter, Bradford P. Taylor & Joao B. Xavier

3. Adult Bone Marrow Transplantation Service, Department of Medicine, Memorial Sloan Kettering Cancer Center, New York, NY, USA

Jonathan U. Peled, Kate A. Markey, Melody Smith, Anqi Dai, Miguel-Angel Perales & Marcel R. M. van den Brink

4. Weill Cornell Medical College, New York, NY, USA

Jonathan U. Peled, Kate A. Markey, Melody Smith, Miguel-Angel Perales & Marcel R. M. van den Brink

5. Infectious Disease Service, Department of Medicine, and Immunology Program, Sloan Kettering Institute, New York, NY, USA

Ying Taur, Emily Fontana, Luigi A. Amoretti, Roberta J. Wright, Sejal Morjaria & Tobias M. Hohl

6. Harvard University, T. H. Chan School of Public Health, Boston, MA, USA

Rene Niehus

7. Sahlgrenska Cancer Center, Department of Microbiology and Immunology, Institute of Biomedicine, University of Gothenburg, Gothenburg, Sweden

Anna Staffas

8. Department of Laboratory Medicine, Memorial Sloan Kettering Cancer Center, New York, NY, USA

Maly Fenelus & Melissa S. Pessin

9. Division of Hematologic Malignancies and Cellular Therapy, Duke University School of Medicine, Durham, NC, USA

Nelson J. Chao, Meagan Lew, Lauren Bohannon, Amy Bush & Anthony D. Sung

Authors

1. Jonas Schluter

[View author publications](#)

You can also search for this author in [PubMed](#) [Google Scholar](#)

2. Jonathan U. Peled

[View author publications](#)

You can also search for this author in [PubMed](#) [Google Scholar](#)

3. Bradford P. Taylor

[View author publications](#)

You can also search for this author in [PubMed](#) [Google Scholar](#)

4. Kate A. Markey

[View author publications](#)

You can also search for this author in [PubMed](#) [Google Scholar](#)

5. Melody Smith

[View author publications](#)

You can also search for this author in [PubMed](#) [Google Scholar](#)

6. Ying Taur

[View author publications](#)

You can also search for this author in [PubMed](#) [Google Scholar](#)

7. Rene Niehus

[View author publications](#)

You can also search for this author in [PubMed](#) [Google Scholar](#)

8. Anna Staffas

[View author publications](#)

You can also search for this author in [PubMed](#) [Google Scholar](#)

9. Anqi Dai

[View author publications](#)

You can also search for this author in [PubMed](#) [Google Scholar](#)

10. Emily Fontana

[View author publications](#)

You can also search for this author in [PubMed](#) [Google Scholar](#)

11. Luigi A. Amoretti

[View author publications](#)

You can also search for this author in [PubMed](#) [Google Scholar](#)

12. Roberta J. Wright

[View author publications](#)

You can also search for this author in [PubMed](#) [Google Scholar](#)

13. Sejal Morjaria

[View author publications](#)

You can also search for this author in [PubMed](#) [Google Scholar](#)

14. Maly Fenelus

[View author publications](#)

You can also search for this author in [PubMed](#) [Google Scholar](#)

15. Melissa S. Pessin

[View author publications](#)

You can also search for this author in [PubMed](#) [Google Scholar](#)

16. Nelson J. Chao

[View author publications](#)

You can also search for this author in [PubMed](#) [Google Scholar](#)

17. Meagan Lew

[View author publications](#)

You can also search for this author in [PubMed](#) [Google Scholar](#)

18. Lauren Bohannon

[View author publications](#)

You can also search for this author in [PubMed](#) [Google Scholar](#)

19. Amy Bush

[View author publications](#)

You can also search for this author in [PubMed](#) [Google Scholar](#)

20. Anthony D. Sung

[View author publications](#)

You can also search for this author in [PubMed](#) [Google Scholar](#)

21. Tobias M. Hohl

[View author publications](#)

You can also search for this author in [PubMed](#) [Google Scholar](#)

22. Miguel-Angel Perales

[View author publications](#)

You can also search for this author in [PubMed](#) [Google Scholar](#)

23. Marcel R. M. van den Brink

[View author publications](#)

You can also search for this author in [PubMed](#) [Google Scholar](#)

24. Joao B. Xavier

[View author publications](#)

You can also search for this author in [PubMed](#) [Google Scholar](#)

Contributions

J.S. and J.B.X. wrote the manuscript. J.S. and J.B.X. designed the analyses with expert help from R.N. J.U.P. and Y.T. contributed to the clinical data

preparation, B.P.T. provided the 16S data-processing pipelines, K.A.M., M.S., A.S., S.M., M.F., M.S.P., T.M.H., M.-A.P. and M.R.M.v.d.B. provided clinical context and helped with variable selection, N.J.C., M.L., L.B., A.B. and A.D.S. provided clinical and other data from Duke, A.D. provided the shotgun processing pipelines. E.F., L.A.A. and R.J.W. processed patients' stool samples, including for 16S sequencing, shotgun metagenomics and qPCR quantification of total 16S rRNA gene. All authors contributed to the writing and interpretation of the results.

Corresponding authors

Correspondence to [Jonas Schluter](#) or [Joao B. Xavier](#).

Ethics declarations

Competing interests

M.R.M.v.d.B. and J.U.P. received financial support from Seres Therapeutics. M.-A.P. has received honoraria from AbbVie, Bellicum, Bristol-Myers Squibb, Incyte, Merck, Novartis, Nektar Therapeutics, and Takeda, research support for clinical trials from Incyte, Kite (Gilead) and Miltenyi Biotec, and serves on data and safety monitoring boards for Servier and Medigene and scientific advisory boards for MolMed and NexImmune.

Additional information

Peer review information *Nature* thanks Henrik Nielsen and the other, anonymous, reviewer(s) for their contribution to the peer review of this work.

Publisher's note Springer Nature remains neutral with regard to jurisdictional claims in published maps and institutional affiliations.

Extended data figures and tables

Extended Data Fig. 1 Blood cell counts over time.

a, WBC counts and platelet counts per graft source over the first 100 days post HCT per day relative to HCT from $N = 2,235$ adult patients (detailed demographics in supplementary Table 1); lines: mean, shaded: \pm standard deviations. **b**, Data exclusion diagram.

Extended Data Fig. 2 FMT increases WBC counts.

a, HCT patient who received an autologous faecal microbiota transplant (auto-FMT, dashed red line) that restored commensal microbial families and ecological diversity in the gut microbiota, with concurrent cell counts of peripheral neutrophils, lymphocytes and monocytes and immunomodulatory drug administrations. **b**, Total WBC counts in 24 enrolled patients (10 control, 14 treated) post-neutrophil engraftment; vertical lines indicate randomization dates. **c**, Weekly mean WBC counts aligned to the randomization date (FMT-treated: red, control: black). Line: mean per week, shaded region: 95% CI. **d**, Coefficient estimates (mean vs. mean + FMT effect) from linear mixed effects models of total WBC counts over time indicate an auto-FMT-induced increase of WBCs (β_{FMT} : $P = 7 \times 10^{-14}$). **e–g**, Respectively: neutrophil, lymphocyte and monocyte count trajectories of 24 FMT trial patients. Thin lines: raw data (blue: post-FMT); thick black: mean per day, thick blue: mean+post-FMT coefficient. Means and confidence intervals (shaded region) without (black) and after FMT (blue), as well as the coefficient estimate for FMT treatment and its P value from a linear mixed effects model relating cell counts over time to the FMT treatment (Methods).

Extended Data Fig. 3 Results of the feature selection stage 1 regression.

a–c, Stage 1 regression on neutrophil, lymphocyte, and monocyte dynamics, respectively, on patients without microbiome data. Coefficients from tenfold cross-validated elastic net regression daily changes in neutrophils. gr: intercept; TCD: T cell depleted graft (ex-vivo) by CD34⁺ selection; PBSC: peripheral blood stem cells; BM: bone marrow;

cord: umbilical cord blood; NONABL: Nonmyeloablative; REDUCE: reduced-intensity conditioning regimen; F: female; N: patients, n: samples (daily changes in neutrophils).

Extended Data Fig. 4 Additional coefficients, posterior convergence evaluation and validation.

a–c, Additional posterior coefficient estimates of medications, additional genera and HCT metadata from the Bayesian stage 2 regression, see also Fig. 3. REDUCE: reduced-intensity conditioning regimen; NONABL: non-myeloablative conditioning regimen. F: female. **d–f**, posterior sampling convergence. Histograms of the ranked posterior draws from the model of neutrophil, lymphocyte and monocyte dynamics, respectively, in PBSC patients (ranked over all chains), plotted separately for each chain show no substantial differences between chains. **g–i**, Predictors of WBC dynamics using data from patients treated at Duke. Heatmaps indicate the slope coefficients from individual univariate regressions of microbiome and clinical predictors with changes in neutrophils, lymphocytes and monocyte, and for comparison the corresponding coefficients signs from the Bayesian multiple linear regressions in stage 2 of the analysis of WBC dynamics in MSK patients (Fig. 3). Pvalues were adjusted for multiple hypothesis testing using Bonferroni correction: *** $P < 0.001$, ** $P < 0.01$, * $P < 0.05$; $P > 0.05$: n.s. Sign of coefficients from MSK PBSC patients for comparison. **j**, Equivalent validation analysis from patients treated at Duke using partial least squares regression of microbiome and clinical predictors identified in stage 2 of our analysis on daily changes in neutrophils, lymphocytes and monocyte.

Extended Data Fig. 5 Validation using absolute instead of relative abundance bacterial genus data.

a–d, Validation analysis of the main model using absolute bacterial abundances as predictors instead of relative abundances in Fig. 3. Results show inferred coefficients and P values from multiple linear regressions. One regression per analysed WBC type dynamics, that is, neutrophil, lymphocyte and monocyte daily log-changes, was conducted, and

coefficients for medications (**a**), WBC feedbacks (**b**) metadata (**c**) and total genus abundances (**d**) are shown. This was only possible for only a subset of the data used in the main analysis for which we obtained absolute bacterial abundance estimates (Methods), n: samples, N: patients.

Extended Data Fig. 6 Jointly inferred association network between WBC and bacterial genus dynamics.

Strong regularization yields few non-zero coefficients and antibiotics dominate the dynamics.

Extended Data Fig. 7 Jointly inferred association network between WBC and bacterial genus dynamics with reduced regularization.

Reducing regularization strength (Methods) indicates potential bidirectional feedbacks, for example, between lymphocytes and *[Ruminococcus] gnatus group* (highlighter green boxes, and cartoon).

Extended Data Fig. 8 Functional analysis of microbiota samples.

To distinguish samples predicted to increase rates of WBCs, a microbiota potency score was calculated from posterior coefficients (Fig. 3, Methods) and the relative abundance of taxa in samples. Bars show linear discriminant analysis (LDA) scores of MetaCyc pathway profiles from 124 shotgun sequenced samples that distinguished positive and negative potency samples the most (LDA-score magnitude in the 95th percentile). Highlighted pathways are discussed in the main text. For each pathway, we tested whether pathway presence was enriched (depleted) in positive (negative) potency samples using one-sided Fisher's exact test; *** $P < 0.001$, ** $P < 0.01$, * $P < 0.05$.

Extended Data Fig. 9 Abundance profiles of bacterial genera across analysed samples.

a, The relative non-zero abundance of *Staphylococcus* is inversely related to microbiome alpha diversity, bold line: regression line from a linear model of the mean of the \log_{10} *Staphylococcus* relative abundance, shaded: 95% confidence intervals ($n = 1,381$ samples with non-zero *Staphylococcus* abundances). **b**, Abundance profiles of the two genera, *Faecalibacterium* and *Ruminococcus* 2, most strongly associated with WBC increase; number of times detected (left) and \log_{10} abundance distribution when above detection (right).

[Extended Data Fig. 10 Survival analysis and confirmation of model results with different priors.](#)

a, Kaplan–Meier plot of patient 3-year survival with sufficient available blood data ([Supplementary Information](#), Extended Data Fig. 1). **b**, posterior association coefficients do not depend on the choice of prior for σ in the main Bayesian model. Plotted are the posterior means from our main analysis against the equivalent inference with an inverse Gamma prior (alpha = 1, beta = 1).

Supplementary information

[Supplementary Information](#)

This file contains Supplementary Tables 1-5 and Supplementary Methods.

[Reporting Summary](#)

[Supplementary Data](#)

This zip file contains Data Tables.

Rights and permissions

[Reprints and Permissions](#)

About this article



Check for
updates

Cite this article

Schluter, J., Peled, J.U., Taylor, B.P. *et al.* The gut microbiota is associated with immune cell dynamics in humans. *Nature* **588**, 303–307 (2020).
<https://doi.org/10.1038/s41586-020-2971-8>

[Download citation](#)

- Received: 03 May 2019
- Accepted: 30 September 2020
- Published: 25 November 2020
- Issue Date: 10 December 2020
- DOI: <https://doi.org/10.1038/s41586-020-2971-8>

Comments

By submitting a comment you agree to abide by our [Terms](#) and [Community Guidelines](#). If you find something abusive or that does not comply with our terms or guidelines please flag it as inappropriate.

[Access through your institution](#)

[Change institution](#)

[Buy or subscribe](#)

| [Section menu](#) | [Main menu](#) |

- Article
- [Published: 18 November 2020](#)

LDLRAD3 is a receptor for Venezuelan equine encephalitis virus

- [Hongming Ma](#) ORCID: orcid.org/0000-0001-5105-1332^{1 na1},
- [Arthur S. Kim](#) ORCID: orcid.org/0000-0003-4101-6642^{1,2 na1},
- [Natasha M. Kafai](#) ORCID: orcid.org/0000-0002-3115-3400^{1,2},
- [James T. Earnest](#) ORCID: orcid.org/0000-0002-5904-8733¹,
- [Aadit P. Shah](#) ORCID: orcid.org/0000-0001-8672-6643¹,
- [James Brett Case](#) ORCID: orcid.org/0000-0001-7331-5511¹,
- [Katherine Basore](#) ORCID: orcid.org/0000-0001-5974-0968²,
- [Theron C. Gilliland](#)³,
- [Chengqun Sun](#)³,
- [Christopher A. Nelson](#) ORCID: orcid.org/0000-0001-8730-4768²,
- [Larissa B. Thackray](#) ORCID: orcid.org/0000-0002-9380-6569¹,
- [William B. Klimstra](#)³,
- [Daved H. Fremont](#) ORCID: orcid.org/0000-0002-8544-2689^{2,4,5,6} &
- [Michael S. Diamond](#) ORCID: orcid.org/0000-0002-8791-3165^{1,2,5,6}

[Nature](#) volume 588, pages308–314(2020)[Cite this article](#)

- 3411 Accesses
- 122 Altmetric
- [Metrics details](#)

Subjects

- [Alphaviruses](#)
- [Viral pathogenesis](#)

Abstract

Venezuelan equine encephalitis virus (VEEV) is a neurotropic alphavirus transmitted by mosquitoes that causes encephalitis and death in humans¹. VEEV is a biodefence concern because of its potential for aerosol spread and the current lack of sufficient countermeasures. The host factors that are required for VEEV entry and infection remain poorly characterized. Here, using a genome-wide CRISPR–Cas9-based screen, we identify low-density lipoprotein receptor class A domain-containing 3 (LDLRAD3)—a highly conserved yet poorly characterized member of the scavenger receptor superfamily—as a receptor for VEEV. Gene editing of mouse *Ldlrad3* or human *LDLRAD3* results in markedly reduced viral infection of neuronal cells, which is restored upon complementation with LDLRAD3. LDLRAD3 binds directly to VEEV particles and enhances virus attachment and internalization into host cells. Genetic studies indicate that domain 1 of LDLRAD3 (LDLRAD3(D1)) is necessary and sufficient to support infection by VEEV, and both anti-LDLRAD3 antibodies and an LDLRAD3(D1)–Fc fusion protein block VEEV infection in cell culture. The pathogenesis of VEEV infection is abrogated in mice with deletions in *Ldlrad3*, and administration of LDLRAD3(D1)–Fc abolishes disease caused by several subtypes of VEEV, including highly virulent strains. The development of a decoy-receptor fusion protein suggests a strategy for the prevention of severe VEEV infection and associated disease in humans.

[Access through your institution](#)

[Change institution](#)

[Buy or subscribe](#)

Access options

Subscribe to Journal

Get full journal access for 1 year

185,98 €

only 3,58 € per issue

[Subscribe](#)

All prices are NET prices.
VAT will be added later in the checkout.

Rent or Buy article

Get time limited or full article access on ReadCube.

from \$8.99

[Rent or Buy](#)

All prices are NET prices.

Additional access options:

- [Log in](#)
- [Access through your institution](#)
- [Learn about institutional subscriptions](#)

Fig. 1: LDLRAD3 is required for efficient VEEV infection in cells.

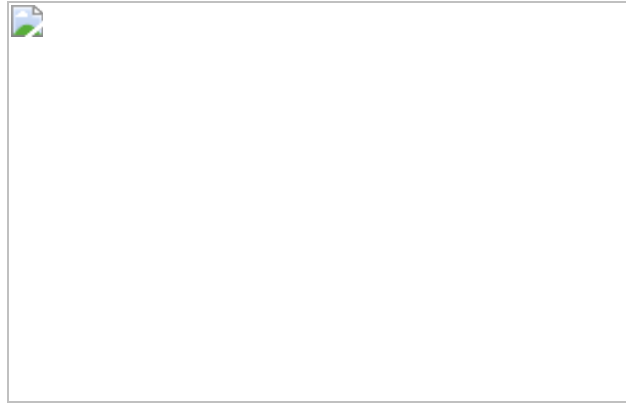


Fig. 2: LDLRAD3 modulates VEEV attachment and internalization.



Fig. 3: Direct binding of LDLRAD3 to VEEV.



Fig. 4: LDLRAD3 is required for VEEV pathogenesis in mice.



Data availability

All data that support the findings of this study are available within the Article and its Supplementary Information. The Supplementary Tables provide data for the CRISPR–Cas9 screen. Any other relevant data are available from the corresponding author upon reasonable request. [Source data](#) are provided with this paper.

References

1. 1.

Sharma, A. & Knollmann-Ritschel, B. Current understanding of the molecular basis of Venezuelan equine encephalitis virus pathogenesis and vaccine development. *Viruses* **11**, 164 (2019).

[CAS](#) [Article](#) [Google Scholar](#)

2. 2.

Weaver, S. C. & Barrett, A. D. Transmission cycles, host range, evolution and emergence of arboviral disease. *Nat. Rev. Microbiol.* **2**, 789–801 (2004).

[CAS](#) [Article](#) [Google Scholar](#)

3. 3.

Aguilar, P. V. et al. Endemic Venezuelan equine encephalitis in the Americas: hidden under the dengue umbrella. *Future Virol.* **6**, 721–740 (2011).

[Article](#) [Google Scholar](#)

4. 4.

Zhang, R. et al. Mxra8 is a receptor for multiple arthritogenic alphaviruses. *Nature* **557**, 570–574 (2018).

[ADS](#) [CAS](#) [Article](#) [Google Scholar](#)

5. 5.

Basore, K. et al. Cryo-EM structure of Chikungunya virus in complex with the Mxra8 receptor. *Cell* **177**, 1725–1737.e16 (2019).

[CAS](#) [Article](#) [Google Scholar](#)

6. 6.

Malygin, A. A. et al. C-terminal fragment of human laminin-binding protein contains a receptor domain for Venezuelan equine encephalitis and tick-borne encephalitis viruses. *Biochemistry (Mosc)* **74**, 1328–1336 (2009).

[CAS](#) [Article](#) [Google Scholar](#)

7. 7.

Ludwig, G. V., Kondig, J. P. & Smith, J. F. A putative receptor for Venezuelan equine encephalitis virus from mosquito cells. *J. Virol.* **70**, 5592–5599 (1996).

[CAS](#) [Article](#) [Google Scholar](#)

8. 8.

Klimstra, W. B., Nangle, E. M., Smith, M. S., Yurochko, A. D. & Ryman, K. D. DC-SIGN and L-SIGN can act as attachment receptors for alphaviruses and distinguish between mosquito cell- and mammalian cell-derived viruses. *J. Virol.* **77**, 12022–12032 (2003).

[CAS](#) [Article](#) [Google Scholar](#)

9. 9.

Bernard, K. A., Klimstra, W. B. & Johnston, R. E. Mutations in the E2 glycoprotein of Venezuelan equine encephalitis virus confer heparan sulfate interaction, low morbidity, and rapid clearance from blood of mice. *Virology* **276**, 93–103 (2000).

[CAS](#) [Article](#) [Google Scholar](#)

10. 10.

Yin, J., Gardner, C. L., Burke, C. W., Ryman, K. D. & Klimstra, W. B. Similarities and differences in antagonism of neuron alpha/beta interferon responses by Venezuelan equine encephalitis and Sindbis alphaviruses. *J. Virol.* **83**, 10036–10047 (2009).

[CAS](#) [Article](#) [Google Scholar](#)

11. 11.

Ryman, K. D. et al. Heparan sulfate binding can contribute to the neurovirulence of neuroadapted and nonneuroadapted Sindbis viruses. *J. Virol.* **81**, 3563–3573 (2007).

[CAS](#) [Article](#) [Google Scholar](#)

12. 12.

Gardner, C. L., Ebel, G. D., Ryman, K. D. & Klimstra, W. B. Heparan sulfate binding by natural eastern equine encephalitis viruses promotes neurovirulence. *Proc. Natl Acad. Sci. USA* **108**, 16026–16031 (2011).

[ADS](#) [CAS](#) [Article](#) [Google Scholar](#)

13. 13.

Tanaka, A. et al. Genome-wide screening uncovers the significance of N-sulfation of heparan sulfate as a host cell factor for Chikungunya virus infection. *J. Virol.* **91**, e00432-17 (2017).

[CAS](#) [Article](#) [Google Scholar](#)

14. 14.

Li, W. et al. MAGeCK enables robust identification of essential genes from genome-scale CRISPR/Cas9 knockout screens. *Genome Biol.* **15**, 554 (2014).

[Article](#) [Google Scholar](#)

15. 15.

Diez-Roux, G. et al. A high-resolution anatomical atlas of the transcriptome in the mouse embryo. *PLoS Biol.* **9**, e1000582 (2011).

[CAS](#) [Article](#) [Google Scholar](#)

16. 16.

Ranganathan, S. et al. LRAD3, a novel low-density lipoprotein receptor family member that modulates amyloid precursor protein trafficking. *J. Neurosci.* **31**, 10836–10846 (2011).

[CAS](#) [Article](#) [Google Scholar](#)

17. 17.

Noyes, N. C., Hampton, B., Migliorini, M. & Strickland, D. K. Regulation of itch and Nedd4 E3 ligase activity and degradation by LRAD3. *Biochemistry* **55**, 1204–1213 (2016).

[CAS](#) [Article](#) [Google Scholar](#)

18. 18.

Smith, S. A. et al. Isolation and characterization of broad and ultrapotent human monoclonal antibodies with therapeutic activity against Chikungunya virus. *Cell Host Microbe* **18**, 86–95 (2015).

[CAS](#) [Article](#) [Google Scholar](#)

19. 19.

Ryman, K. D., Meier, K. C., Gardner, C. L., Adegboyega, P. A. & Klimstra, W. B. Non-pathogenic Sindbis virus causes hemorrhagic fever in the absence of alpha/beta and gamma interferons. *Virology* **368**, 273–285 (2007).

[CAS](#) [Article](#) [Google Scholar](#)

20. 20.

Sun, C., Gardner, C. L., Watson, A. M., Ryman, K. D. & Klimstra, W. B. Stable, high-level expression of reporter proteins from improved alphavirus expression vectors to track replication and dissemination during encephalitic and arthritogenic disease. *J. Virol.* **88**, 2035–2046 (2014).

[Article](#) [Google Scholar](#)

21. 21.

Davis, N. L., Willis, L. V., Smith, J. F. & Johnston, R. E. In vitro synthesis of infectious Venezuelan equine encephalitis virus RNA from a cDNA clone: analysis of a viable deletion mutant. *Virology* **171**, 189–204 (1989).

[CAS](#) [Article](#) [Google Scholar](#)

22. 22.

Kinney, R. M. et al. Attenuation of Venezuelan equine encephalitis virus strain TC-83 is encoded by the 5'-noncoding region and the E2 envelope glycoprotein. *J. Virol.* **67**, 1269–1277 (1993).

[CAS](#) [Article](#) [Google Scholar](#)

23. 23.

Anishchenko, M. et al. Generation and characterization of closely related epizootic and enzootic infectious cDNA clones for studying interferon sensitivity and emergence mechanisms of Venezuelan equine encephalitis virus. *J. Virol.* **78**, 1–8 (2004).

[CAS](#) [Article](#) [Google Scholar](#)

24. 24.

Kim, A. S. et al. Protective antibodies against Eastern equine encephalitis virus bind to epitopes in domains A and B of the E2 glycoprotein. *Nat. Microbiol.* **4**, 187–197 (2019).

[CAS](#) [Article](#) [Google Scholar](#)

25. 25.

Lubman, O. Y. et al. Rodent herpesvirus Peru encodes a secreted chemokine decoy receptor. *J. Virol.* **88**, 538–546 (2014).

[Article](#) [Google Scholar](#)

26. 26.

Sanjana, N. E., Shalem, O. & Zhang, F. Improved vectors and genome-wide libraries for CRISPR screening. *Nat. Methods* **11**, 783–784 (2014).

[CAS](#) [Article](#) [Google Scholar](#)

27. 27.

Willnow, T. E. et al. RAP, a specialized chaperone, prevents ligand-induced ER retention and degradation of LDL receptor-related endocytic receptors. *EMBO J.* **15**, 2632–2639 (1996).

[CAS](#) [Article](#) [Google Scholar](#)

28. 28.

Ko, S. Y. et al. A virus-like particle vaccine prevents equine encephalitis virus infection in nonhuman primates. *Sci. Transl. Med.* **11**, eaav3113 (2019).

[CAS Article](#) [Google Scholar](#)

29. 29.

Pal, P. et al. Development of a highly protective combination monoclonal antibody therapy against Chikungunya virus. *PLoS Pathog.* **9**, e1003312 (2013).

[CAS Article](#) [Google Scholar](#)

[Download references](#)

Acknowledgements

This study was supported by NIH grants R01 AI143673 (M.S.D. and D.H.F.), U19 AI142790 (M.S.D. and D.H.F.), U19 AI142759 (M.S.D.), R01 AI095436 (W.B.K.), HHSN272201700060C (D.H.F.), T32 AI007172 (N.M.K. and K.B.), Defense Reduction Threat Agency grants HDTRA1-15-1-0013 (M.S.D.), and HDTRA1-15-1-0047 (W.B.K.). We thank G. Bu for discussions, J. Lai for anti-E1 human monoclonal antibodies, N. Ihenacho for technical assistance, M. Elam-Noll for animal husbandry, the Washington University Morphology Core, K. Carlton and J. Mascola for a gift of the VEEV VLPs and S. Whelan for providing comments on the manuscript.

Author information

Author notes

1. These authors contributed equally: Hongming Ma, Arthur S. Kim

Affiliations

1. Department of Medicine, Washington University School of Medicine, St Louis, MO, USA

Hongming Ma, Arthur S. Kim, Natasha M. Kafai, James T. Earnest, Aadit P. Shah, James Brett Case, Larissa B. Thackray & Michael S. Diamond

2. Department of Pathology and Immunology, Washington University School of Medicine, St Louis, MO, USA

Arthur S. Kim, Natasha M. Kafai, Katherine Basore, Christopher A. Nelson, Daved H. Fremont & Michael S. Diamond

3. Department of Immunology, Center for Vaccine Research University of Pittsburgh, Pittsburgh, PA, USA

Theron C. Gilliland, Chengqun Sun & William B. Klimstra

4. Department of Biochemistry and Molecular Biophysics, Washington University School of Medicine, St Louis, MO, USA

Daved H. Fremont

5. Andrew M. and Jane M. Bursky Center for Human Immunology and Immunotherapy Program, Washington University School of Medicine, St Louis, MO, USA

Daved H. Fremont & Michael S. Diamond

6. Department of Molecular Microbiology, Washington University School of Medicine, St Louis, MO, USA

Daved H. Fremont & Michael S. Diamond

Authors

1. Hongming Ma

[View author publications](#)

You can also search for this author in [PubMed](#) [Google Scholar](#)

2. Arthur S. Kim

[View author publications](#)

You can also search for this author in [PubMed](#) [Google Scholar](#)

3. Natasha M. Kafai

[View author publications](#)

You can also search for this author in [PubMed](#) [Google Scholar](#)

4. James T. Earnest

[View author publications](#)

You can also search for this author in [PubMed](#) [Google Scholar](#)

5. Aadit P. Shah

[View author publications](#)

You can also search for this author in [PubMed](#) [Google Scholar](#)

6. James Brett Case

[View author publications](#)

You can also search for this author in [PubMed](#) [Google Scholar](#)

7. Katherine Basore

[View author publications](#)

You can also search for this author in [PubMed](#) [Google Scholar](#)

8. Theron C. Gilliland

[View author publications](#)

You can also search for this author in [PubMed](#) [Google Scholar](#)

9. Chengqun Sun

[View author publications](#)

You can also search for this author in [PubMed](#) [Google Scholar](#)

10. Christopher A. Nelson
[View author publications](#)

You can also search for this author in [PubMed](#) [Google Scholar](#)

11. Larissa B. Thackray
[View author publications](#)

You can also search for this author in [PubMed](#) [Google Scholar](#)

12. William B. Klimstra
[View author publications](#)

You can also search for this author in [PubMed](#) [Google Scholar](#)

13. Daved H. Fremont
[View author publications](#)

You can also search for this author in [PubMed](#) [Google Scholar](#)

14. Michael S. Diamond
[View author publications](#)

You can also search for this author in [PubMed](#) [Google Scholar](#)

Contributions

H.M. performed CRISPR–Cas9 screening, validation and infection studies with assistance from A.S.K., J.T.E. and A.S. A.S.K., K.B. and C.A.N. generated recombinant proteins and performed binding experiments. C.S. created SINV chimaeras and other GFP-expressing alphavirus reagents. N.M.K., J.B.C. and T.C.G. performed the experiments in mice. A.S.K. and L.B.T. designed and analysed the LDLRAD3-deficient mice. H.M., A.S.K., N.M.K., J.T.E., W.B.K., D.H.F. and M.S.D. designed experiments. H.M., A.S.K., N.M.K., J.T.E., K.B. and C.A.N. performed data analysis. H.M.,

A.S.K. and M.S.D. wrote the initial draft, and the other authors provided editing comments.

Corresponding author

Correspondence to [Michael S. Diamond](#).

Ethics declarations

Competing interests

M.S.D. is a consultant for Inbios, Vir Biotechnology, NGM Biopharmaceuticals and Carnival Corporation, and is on the Scientific Advisory Board of Moderna and Immunome. The Diamond laboratory at Washington University School of Medicine has received unrelated sponsored research agreements from Moderna, Vir Biotechnology and Emergent BioSolutions. D.H.F. is a founder of Courier Therapeutics.

Additional information

Peer review information *Nature* thanks Suresh Mahalingam, Berend Jan Bosch and Jan Carette for their contribution to the peer review of this work. Peer reviewer reports are available.

Publisher's note Springer Nature remains neutral with regard to jurisdictional claims in published maps and institutional affiliations.

Extended data figures and tables

[Extended Data Fig. 1 CRISPR–Cas9-based screen identifying LDLRAD3 as a required factor for VEEV infectivity.](#)

a, $\Delta B4galt7$ N2a cells were transfected separately with two half libraries containing 130,209 sgRNAs, puromycin-selected and then inoculated with SINV–VEEV–GFP (TrD strain) at an MOI of 1. After 24 h, GFP-negative

cells were sorted, expanded in the presence of anti-VEEV monoclonal antibodies (VEEV-57, VEEV-67 and VEEV-68 (2 µg/ml)) and re-inoculated with SINV–VEEV–GFP. The infection and sorting process were repeated twice. Genomic DNA from GFP-negative cells was sequenced for sgRNA abundance. **b**, Representative flow cytometry histogram of parental N2a (grey) and $\Delta B4galt7$ N2a (red) cells stained for heparan sulfate surface expression using R17²⁵, a rodent herpesvirus immune evasion protein that binds to heparan sulfate. **c**, Schematic of chimeric SINV–VEEV virus. The chimaera contains the non-structural genes from SINV (strain TR339), structural genes from VEEV (IAB strain TrD, IC strain INH9813 or ID strain ZPC738) and an eGFP gene (green) between the capsid and E3 protein. The insertion of GFP has minimal effects on virus infection and replication^{20,24}. **d**, Sequence alignment of mouse (*M. musculus*), mouse $\Delta 32$ N-terminus isoform, human (*Homo sapiens*), rhesus macaque (*Macaca mulatta*), cattle (*Bos taurus*), horse (*Equus caballus*), dog (*Canis lupus familiaris*) and chicken (*Gallus gallus*) LDLRAD3 ectodomain using ESPript 3. Red boxes indicate conserved residues between orthologues. The predicted domains based on sequence similarity to other related proteins and the transmembrane domains are indicated below the sequence.

Extended Data Fig. 2 Gene editing of LDLRAD3 expression.

a, Parental and gene-edited $\Delta B4galt7$ N2a (top) and BV2 (bottom) cells were subjected to next-generation sequencing to confirm gene editing of *Ldlrad3*. Sequences were aligned to the *Ldlrad3* gene to identify nucleotide insertions or deletions (indels). Allele frequency is indicated next to each sequence. **b**, Viability of $\Delta B4galt7$ (control, black), $\Delta B4galt7 \Delta Ldlrad3$ (red) and *Ldlrad3*-complemented $\Delta B4galt7 \Delta Ldlrad3$ (blue) N2a (left) and BV2 (right) cells as determined by Cell-Titer Glo assay. Mean ± s.d. of three to six experiments (N2a: $n = 12$; BV2: control, $n = 17$; $\Delta Ldlrad3 +$ vector, $n = 17$; $\Delta Ldlrad3 + Ldlrad3$, $n = 9$). **c**, Anti-Flag staining of $\Delta B4galt7$ N2a cells (control, black) and lentivirus-complemented $\Delta B4galt7 \Delta Ldlrad3$ N2a cells with empty vector (red) or *Ldlrad3* cDNA (blue) containing an N-terminal Flag-tag sequence (left). Schematic of the Flag-tagged LDLRAD3 protein (bottom) indicating the signal peptide (orange), Flag tag (red), GGS linker (grey) and LDLRAD3 coding region (blue). Cells were stained with an anti-Flag monoclonal antibody and analysed by

flow cytometry. Mean \pm s.d. of two experiments ($n = 6$). Representative flow cytometry histograms (right) showing LDLRAD3 surface expression of empty vector (red) and *Ldlrad3* (blue)-complemented $\Delta Ldlrad3$ cells. **d**, Next-generation sequencing confirmation of *Ldlrad3* gene editing in N2a (top) and BV2 (bottom) cells retaining heparan sulfate biosynthetic capacity. Allele frequency is indicated next to each sequence. **e**, Left, *B4galt7^{+/+}* (control, black), *B4galt7^{+/+}* $\Delta Ldlrad3$ (red) and *B4galt7^{+/+}* $\Delta Ldlrad3$ complemented with *Ldlrad3* cDNA (blue) N2a cells were analysed for surface expression of LDLRAD3 by flow cytometry using an anti-Flag monoclonal antibody. Mean \pm s.d. of two experiments ($n = 6$). Representative flow cytometry histograms (right) showing LDLRAD3 surface expression of empty vector (red) and *Ldlrad3* (blue)-complemented $\Delta Ldlrad3$ cells. **f**, Next-generation sequencing of *LDLRAD3* gene editing in two independent SH-SY5Y cell lines. Allele frequency is indicated next to each sequence. **g**, Two clonal $\Delta LDLRAD3$ SH-SY5Y cell populations were complemented with full-length *Ldlrad3* or truncated *Ldlrad3* isoform (N-terminal 32 amino acid deletion, isoform 2) cDNA containing an N-terminal Flag-tag sequence, stained with an anti-Flag monoclonal antibody and analysed by flow cytometry. Representative flow cytometry histograms are shown. **h**, A second clonal population of $\Delta LDLRAD3$ SH-SY5Y (red) cells were complemented with full-length *Ldlrad3* (blue) or the truncated *Ldlrad3* isoform (orange), inoculated with SINV–VEEV–GFP (TrD) and infection was assessed by flow cytometry. Mean \pm s.d. of three experiments ($n = 9$; one-way ANOVA with Dunnett's post-test: **** $P < 0.0001$). **i**, $\Delta B4galt7$ (control, black), $\Delta B4galt7$ $\Delta Ldlrad3$ (red), *Ldlrad3*-complemented $\Delta B4galt7$ $\Delta Ldlrad3$ (blue), *LDLRAD3*-complemented $\Delta B4galt7$ $\Delta Ldlrad3$ (light blue) and N-terminal Flag-tagged *Ldlrad3*-complemented *B4galt7* $\Delta Ldlrad3$ (teal) N2a cells were analysed for LDLRAD3 cell surface expression with anti-LDLRAD3 polyclonal serum. Mean \pm s.d. of three experiments ($n = 9$; one-way ANOVA with Dunnett's post-test: **** $P < 0.0001$). [Source data](#)

Extended Data Fig. 3 Surface expression of LDLRAD3 and VEEV infection of human lymphocyte cell lines.

a, Representative flow cytometry histograms of LDLRAD3 surface expression using anti-LDLRAD3 polyclonal serum (left) and contour plots

of SINV–VEEV–GFP infection (right) of Jurkat cells. **b**, *LDLRAD3*-complemented Jurkat cells were assessed for *LDLRAD3* surface expression (left) and infection by SINV–VEEV–GFP (TrD) (middle and right). Representative flow cytometry histograms and contour plots are shown. Mean \pm s.d. of three experiments ($n = 9$; Mann–Whitney test: **** $P < 0.0001$). **c**, Representative flow cytometry histograms of *LDLRAD3* surface expression using anti-*LDLRAD3* polyclonal serum (left) and contour plots of SINV–VEEV–GFP infection (right) of Raji cells. **d**, *LDLRAD3*-complemented Raji cells were assessed for *LDLRAD3* surface expression (left) and infection by SINV–VEEV–GFP (TrD) (middle and right). Representative flow cytometry histograms are shown. Mean \pm s.d. of three experiments ($n = 9$; Mann–Whitney test: **** $P < 0.0001$). [Source data](#)

Extended Data Fig. 4 Surface expression of *LDLRAD3* and VEEV infection in different cell lines.

a, b, Representative flow cytometry histograms of *LDLRAD3* surface expression using anti-*LDLRAD3* polyclonal serum (**a**) and contour plots of SINV–VEEV–GFP infection (**b**) of 293T, 3T3, A549, HAP1, HeLa, hCMEC/D3, HT1080, Huh7.5, K562, LADMAC, MRC-5 and U2OS cells. The population of infected cells are indicated for each cell line (**b**). Data are representative of two or three experiments.

Extended Data Fig. 5 Assessment of *LDLRAD3* surface expression and VEEV infection in gene-edited cell lines and primary cells.

a, Control and Δ *LDLRAD3* or Δ *Ldlrad3* 293T, 3T3, HeLa and hCMEC/D3 cells were assessed for *LDLRAD3* surface expression (left) and SINV–VEEV–GFP (TrD) infection via GFP expression by flow cytometry (right). Two independent *Ldlrad3* or *LDLRAD3* gene-edited cell lines were generated (sgRNAs no. 1 and no. 2) and evaluated. Mean \pm s.d. of three experiments (*LDLRAD3* surface expression, $n = 6$; VEEV infection, $n = 9$; one-way ANOVA with Dunnett’s post-test: **** $P < 0.0001$). **b**, Primary cell lines (CADMEC, HDF, HPBM and HPBT) were assessed for

LDLRAD3 surface expression using anti-LDLRAD3 polyclonal serum (left) (red). Cells were inoculated with SINV–VEEV–GFP (TrD) and assessed for infection via GFP expression by flow cytometry (right) (orange). The population of infected cells are indicated for each cell line. Data are representative of two or three experiments. [Source data](#)

Extended Data Fig. 6 Expression and characterization of recombinant LDLRAD3–Fc, VEEV structural proteins and domain-truncated forms of LDLRAD3 proteins.

a, b, Coomassie-stained SDS–PAGE under non-reducing (NR) and reducing (R) conditions of mouse LDLRAD3 domain variants (D1, D1-HRV, D2 and D1+D2) fused to mouse IgG2b Fc domain (**a**) and LDLRAD3(D1) fused to human IgG1 Fc domain (**b**). Data are representative of two experiments. **c**, Binding of human LDLRAD3(D1)–Fc, CHIKV positive control (humanized CHK-152 (CHK-152)), or negative control (humanized E16 (E16)) to VEEV (top) or CHIKV (bottom) VLPs by ELISA. Mean \pm s.d. of two experiments ($n = 8$). **d**, Silver-stained SDS–PAGE of LDLRAD3(D1-HRV)–Fc ((–)HRV protease) and HRV 3C protease-digested LDLRAD3(D1) ((+)HRV protease) under non-reducing conditions. Data are representative of three experiments. **e**, Coomassie-stained SDS–PAGE of baculovirus-generated VEEV p62–E1 under non-reducing and reducing conditions. Data are representative of two experiments. **f**, Binding of LDLRAD3(D1) (2,000 nM starting concentration, twofold dilutions) to CHIKV p62–E1 by surface plasmon resonance. LDLRAD3(D1) does not bind appreciably to CHIKV p62–E1. Cartoon diagram (inset) and sensograms of HRV-cleaved monovalent LDLRAD3(D1) (purple) binding to CHIKV p62–E1 (E3, yellow; E2, cyan; E1, grey). Data are representative of three experiments. **g, h**, $\Delta Ldlrad3 \Delta B4galt7$ N2a cells were complemented with either full-length *Ldlrad3* (black), *Ldlrad3* domain truncations D1+D2 (cyan), D2+D3 (purple) or an *Ldlrad3* isoform that lacks 32 N-terminal residues (orange). Cells were assessed for LDLRAD3 surface expression by N-terminal Flag-tag staining (**g**) and SINV–VEEV–GFP (TrD) infection (**h**) by flow cytometry analysis. The population of infected cells are indicated for each cell line. Data are representative of three experiments. **i**, $\Delta B4galt7 \Delta Ldlrad3$ N2a cells were complemented with either empty vector (red) or LDLRAD3 D1 truncation

(blue), inoculated with SINV–VEEV–GFP, and infection was assessed by flow cytometry (left). A representative flow cytometry plot of LDLRAD3(D1)-complemented $\Delta B4galt7 \Delta Ldlrad3$ N2a cells infected with SINV–VEEV–GFP (TrD) infection is shown. Mean \pm s.d. of three experiments ($n = 9$; one-way ANOVA with Dunnett's post-test: **** $P < 0.0001$). Flow cytometry histogram of LDLRAD3(D1) surface expression as assessed by N-terminal Flag-tag staining and flow cytometry analysis (middle). Data are representative of two experiments. SINV–VEEV–GFP (TrD) infection of $\Delta B4galt7$ (control, black), $\Delta B4galt7 \Delta Ldlrad3$ (red) and $Ldlrad3$ (D1)-complemented $\Delta B4galt7 \Delta Ldlrad3$ (blue) cells was normalized for Flag-positive cells (right). Mean \pm s.d. of three experiments ($n = 9$; one-way ANOVA with Dunnett's post-test: **** $P < 0.0001$). For gel source data, see Supplementary Fig. 1. [Source data](#)

Extended Data Fig. 7 Weight change and clinical assessment of C57BL/6J and CD-1 mice treated with LDLRAD3(D1)–Fc.

a, b, Four-week-old C57BL/6J mice were administered 750 μ g of anti-IFNAR1 monoclonal antibody via intraperitoneal (i.p.) route 24 h before virus inoculation. Two hundred and fifty μ g of LDLRAD3(D1)–Fc or isotype control monoclonal antibody JEV-13 was given 6 h before (**a**) or 24 h after (**b**) i.p. inoculation with 10^5 FFU of SINV–VEEV TrD. Mice were monitored for weight change. Mean \pm s.d. from two or three experiments (**a**: $n = 15$; **b**: $n = 10$; two-way ANOVA with Dunnett's post-test: * $P < 0.05$; ** $P < 0.01$, **** $P < 0.0001$; n.s., not significant). **a**, One day post infection (dpi), $P = 0.0271$; **b**, 1 dpi, $P = 0.9978$; 2 dpi, $P = 0.9940$; 3 dpi, $P = 0.0082$. **c**, Six-week-old C57BL/6J mice were administered 250 μ g of LDLRAD3(D1)–Fc or isotype control monoclonal antibody JEV-13 via i.p. route 6 h before subcutaneous inoculation with 10^2 FFU of VEEV ZPC738. Mice were monitored for weight change. Data are mean \pm s.d. from two experiments ($n = 10$; two-way ANOVA with Dunnett's post-test for weight change: * $P < 0.05$, *** $P < 0.001$, **** $P < 0.0001$; n.s., not significant). One dpi, $P > 0.9999$; 2 dpi, $P = 0.05$; 8 dpi, $P = 0.0001$. **d–f**, Six-week-old CD-1 mice were administered 200 μ g of LDLRAD3(D1)–Fc or isotype control monoclonal antibody JEV-13 via i.p. route 6 h before subcutaneous (**d**) or intracranial (**e, f**) inoculation with 10^3 PFU of VEEV TrD. Mice were

monitored for weight change (left) and clinical disease (right) was assessed over time (healthy, ruffled fur, hunched posture, seizures, ataxia, moribund or death). Mean \pm s.d. from two experiments (two-way ANOVA with Dunnett's post-test for weight change: $*P < 0.05$, $****P < 0.0001$; n.s., not significant; **d**, JEV-13, $n = 7$; LDLRAD3(D1)-Fc, $n = 8$; **e**, $n = 10$). **d**, One dpi, $P = 0.8267$; 2 dpi, $P = 0.0531$; 3 dpi, $P = 0.032$; **e**, 1 dpi, $P > 0.9999$; 2 dpi, $P = 0.2961$; 3 dpi, $P = 0.0482$. At 4.5, 5.5, 8 and 14 dpi, IVIS imaging was used to visual VEEV TrD luciferase infection in CD-1 mice that received LDLRAD3(D1)-Fc or isotype control monoclonal antibody JEV-13 prophylactic treatment and were challenged via intracranial inoculation (**f**). Isotype control treated mice became moribund at 4.5 dpi. The total flux (photons s^{-1}) in the head region of each mouse was quantified. IVIS images shown are representative images from two experiments ($n = 10$). [Source data](#)

Extended Data Fig. 8 RNA in situ hybridization and histopathological analysis of VEEV infection in LDLRAD3(D1)-Fc- or isotype-control-treated mice.

a–d. Six-week-old C57BL/6J mice were administered 250 μ g of isotype control monoclonal antibody JEV-13 (**a**, **b**) or LDLRAD3(D1)-Fc (**c**, **d**) via intraperitoneal route 6 h before subcutaneous inoculation of 10^2 FFU of VEEV ZPC738. Six days post-infection, brain tissues were collected, fixed, paraffin-embedded and subjected to RNA in situ hybridization using VEEV ZPC738-specific probes (**a**, **c**) and haematoxylin and eosin staining (**b**, **d**). Scale bars, 2 mm. Representative high-power (10 \times) magnification insets of the olfactory bulb (1), cortex/midbrain (2), thalamus (3), cerebellum (4) and hippocampus (5) are shown for isotype control (**a**, top) or LDLRAD3(D1)-Fc (**c**, bottom) treated mice. Scale bars, 100 μ m. Haematoxylin and eosin staining of brain sections from isotype control- (**b**) or LDLRAD3(D1)-Fc (**d**)-treated mice. Scale bars, 2 mm. Representative high-power (10 \times) magnification insets of the cerebral cortex (6), thalamus (7), cerebellum (8) and hippocampus (9) are shown for isotype control- (**b**, top) or LDLRAD3(D1)-Fc (**d**, bottom)-treated mice. Scale bars, 100 μ m. Representative images from one experiment ($n = 5$ per group) are shown. [Source data](#)

Extended Data Fig. 9 Generation and clinical assessment of C57BL/6 mice with deletions in *Ldlrad3* by CRISPR–Cas9 gene targeting.

a, Scheme of *Ldlrad3* gene locus with two sgRNA targeting guides for a site in exon 2 of both isoforms. The full-length and truncated Δ32 N terminus residue *Ldlrad3* isoforms are coloured red (top) and orange (bottom), respectively. **b**, Sequencing and alignment of *Ldlrad3* sgRNA targeting region in exon 2 (11- and 14-nucleotide frameshift deletions) in gene-edited *Ldlrad3* mice. The amino acid residues and the two sgRNA guides used for gene-editing (blue and orange arrows) are indicated above. **c, d**, Seven-week-old male and female mice with deletions in *Ldlrad3* (Δ11 or Δ14 nucleotides; homozygous or compound heterozygous) or wild-type C57BL/6 mice were inoculated subcutaneously with 10^3 PFU of VEEV TrD (**c**, left) or 10^2 FFU of VEEV ZPC738 (**d**). Mice were monitored for weight change. Data are from two experiments (VEEV TrD: WT, $n = 12$; Δ*Ldlrad3*, $n = 10$; VEEV ZPC738: WT, $n = 9$; Δ*Ldlrad3*, $n = 8$; two-way ANOVA with Dunnett's post-test: ** $P < 0.01$, **** $P < 0.0001$; n.s., not significant). **c**, One dpi, $P > 0.999$; 2 dpi, $P = 0.2136$; 3 dpi, $P = 0.5489$; 4 dpi, $P = 0.0065$; 8 dpi, $P = 0.0014$. **d**, One dpi, $P = 0.8383$; 2 dpi, $P = 0.001$. Clinical disease (right) was assessed over time (healthy, ruffled fur, hunched posture, seizures, ataxia, moribund or death) in mice inoculated with VEEV TrD (**c**, right).

Extended Data Fig. 10 *Ldlrad3* mRNA expression in tissues from mice.

a, Generation of a TaqMan primer/ probe set against the *Ldlrad3* gene targeting exons 2 and 3. **b, c**, Profile of *Ldlrad3* mRNA expression in different mice tissues (**b**) and the brains of wild-type and *Ldlrad3*-deficient mice (**c**). Data are the mean ± s.d. of one experiment (**b**, spinal cord, kidney, superior cervical lymph node, heart, brain, lung, colon, liver, muscle, jejunum, spleen, inguinal lymph node, ileum and pancreas, $n = 5$; testis and ovary, $n = 3$; **c**, $n = 3$). **d**, In situ hybridization (brown) of *Ldlrad3* (olfactory bulb, cortex, thalamus, and hippocampus) from wild-type mice (left). *Ldlrad3* RNA puncta are indicated by left-pointing red arrows. A Zika virus

(ZIKV) RNA in situ hybridization probe was used as a negative control (right). Slides were counterstained with Gill's haematoxylin. Representative high-power ($63\times$) magnification images from $n = 5$ per group are shown. Scale bar, 10 μm . [Source data](#)

Supplementary information

[Supplementary Figure](#)

Supplementary Figure 1. Uncropped gels for indicated Extended Data Figures.

[Reporting Summary](#)

[Supplementary Table](#)

Supplementary Table 1. List of genes and scores after MAGeCK analysis.

[Peer Review File](#)

Source data

[Source Data Fig. 1](#)

[Source Data Fig. 2](#)

[Source Data Fig. 3](#)

[Source Data Fig. 4](#)

[Source Data Extended Data Fig. 2](#)

[Source Data Extended Data Fig. 3](#)

[Source Data Extended Data Fig. 5](#)

[Source Data Extended Data Fig. 6](#)

[Source Data Extended Data Fig. 7](#)

[Source Data Extended Data Fig. 8](#)

[Source Data Extended Data Fig. 10](#)

Rights and permissions

[Reprints and Permissions](#)

About this article



Check for
updates

Cite this article

Ma, H., Kim, A.S., Kafai, N.M. *et al.* LDLRAD3 is a receptor for Venezuelan equine encephalitis virus. *Nature* **588**, 308–314 (2020).
<https://doi.org/10.1038/s41586-020-2915-3>

[Download citation](#)

- Received: 27 April 2020
- Accepted: 30 September 2020
- Published: 18 November 2020
- Issue Date: 10 December 2020

- DOI: <https://doi.org/10.1038/s41586-020-2915-3>

Comments

By submitting a comment you agree to abide by our [Terms](#) and [Community Guidelines](#). If you find something abusive or that does not comply with our terms or guidelines please flag it as inappropriate.

[Access through your institution](#)

[Change institution](#)

[Buy or subscribe](#)

Associated Content

Nature | News & Views

[Cracking the cell access code for the deadly virus VEEV](#)

- James Zengel
- & Jan E. Carette

This article was downloaded by **calibre** from <https://www.nature.com/articles/s41586-020-2915-3>

| [Section menu](#) | [Main menu](#) |

Sex differences in immune responses that underlie COVID-19 disease outcomes
[Download PDF](#)

- Article
- [Published: 26 August 2020](#)

Sex differences in immune responses that underlie COVID-19 disease outcomes

- [Takehiro Takahashi^{1 na1}](#),
- [Mallory K. Ellingson ORCID: orcid.org/0000-0003-2729-0661^{2 na1}](#),
- [Patrick Wong^{1 na1}](#),
- [Benjamin Israelow ORCID: orcid.org/0000-0002-1308-8246^{1,3 na1}](#),
- [Carolina Lucas ORCID: orcid.org/0000-0003-4590-2756^{1 na1}](#),
- [Jon Klein ORCID: orcid.org/0000-0002-3552-7684^{1 na1}](#),
- [Julio Silva^{1 na1}](#),
- [Tianyang Mao ORCID: orcid.org/0000-0001-9251-8592^{1 na1}](#),
- [Ji Eun Oh¹](#),
- [Maria Tokuyama¹](#),
- [Peiwen Lu ORCID: orcid.org/0000-0001-6118-872X¹](#),
- [Arvind Venkataraman¹](#),
- [Annsea Park¹](#),
- [Feimei Liu^{1,4}](#),
- [Amit Meir ORCID: orcid.org/0000-0001-9635-1021⁵](#),
- [Jonathan Sun⁶](#),
- [Eric Y. Wang¹](#),
- [Arnaud Casanovas-Massana ORCID: orcid.org/0000-0002-3301-6143²](#),
- [Anne L. Wyllie ORCID: orcid.org/0000-0001-6015-0279²](#),
- [Chantal B. F. Vogels²](#),
- [Rebecca Ernest²](#),
- [Sarah Lapidus²](#),
- [Isabel M. Ott^{2,7}](#),
- [Adam J. Moore²](#),

- [Yale IMPACT Research Team](#),
- [Albert Shaw³](#),
- [John B. Fournier³](#),
- [Camila D. Odio³](#),
- [Shelli Farhadian³](#),
- [Charles Dela Cruz⁸](#),
- [Nathan D. Grubaugh²](#),
- [Wade L. Schulz^{9,10}](#),
- [Aaron M. Ring ORCID: orcid.org/0000-0003-3699-2446¹](#),
- [Albert I. Ko ORCID: orcid.org/0000-0001-9023-2339²](#),
- [Saad B. Omer^{2,3,11,12}](#) &
- [Akiko Iwasaki ORCID: orcid.org/0000-0002-7824-9856^{1,13}](#)

Nature volume 588, pages315–320(2020)[Cite this article](#)

- 339k Accesses
- 22 Citations
- 2545 Altmetric
- [Metrics details](#)

Subjects

- [Acute inflammation](#)
- [SARS-CoV-2](#)
- [Viral infection](#)

Abstract

There is increasing evidence that coronavirus disease 2019 (COVID-19) produces more severe symptoms and higher mortality among men than among women^{1,2,3,4,5}. However, whether immune responses against severe acute respiratory syndrome coronavirus (SARS-CoV-2) differ between sexes, and whether such differences correlate with the sex difference in the disease course of COVID-19, is currently unknown. Here we examined sex differences in viral loads, SARS-CoV-2-specific antibody titres, plasma cytokines and blood-cell phenotyping in patients with moderate COVID-19 who had not received immunomodulatory medications. Male patients had higher plasma levels of innate immune cytokines such as IL-8 and IL-

18 along with more robust induction of non-classical monocytes. By contrast, female patients had more robust T cell activation than male patients during SARS-CoV-2 infection. Notably, we found that a poor T cell response negatively correlated with patients' age and was associated with worse disease outcome in male patients, but not in female patients. By contrast, higher levels of innate immune cytokines were associated with worse disease progression in female patients, but not in male patients. These findings provide a possible explanation for the observed sex biases in COVID-19, and provide an important basis for the development of a sex-based approach to the treatment and care of male and female patients with COVID-19.

[Download PDF](#)

Main

SARS-CoV-2 is the novel coronavirus first detected in Wuhan, China, in November 2019 that causes COVID-19⁶. On 11 March 2020, the World Health Organization (WHO) declared COVID-19 a pandemic⁷. A growing body of evidence reveals that male sex is a risk factor for a more severe disease, including death. Globally, approximately 60% of deaths from COVID-19 are reported in men⁵, and a cohort study of 17 million adults in England reported a strong association between male sex and the risk of death from COVID-19 (hazard ratio 1.59, 95% confidence interval 1.53–1.65)⁸.

Past studies have shown that sex has a considerable effect on the outcome of infections and has been associated with underlying differences in immune responses to infection^{9,10}. For example, the prevalence of hepatitis A and tuberculosis are notably higher in men than in women¹¹. Viral loads are consistently higher in male patients with hepatitis C virus and human immunodeficiency virus (HIV)^{12,13}. By contrast, women mount a more robust immune response to vaccines¹⁴. These findings collectively suggest a more robust ability among women to control infectious agents. However, the mechanism by which SARS-CoV-2 causes more severe disease in male patients than in female patients remains unknown.

To determine the immune responses against SARS-CoV-2 infection in male and female patients, we performed detailed analyses on the sex differences in immune phenotypes by the assessment of viral loads, levels of SARS-CoV-2-specific antibodies, plasma cytokines or chemokines, and blood-cell phenotypes.

Overview of the study design

Patients who were admitted to the Yale-New Haven Hospital between 18 March and 9 May 2020 and were confirmed positive for SARS-CoV-2 by RT-PCR from nasopharyngeal and/or oropharyngeal swabs in CLIA-certified laboratories were enrolled through the IMPACT biorepository study¹⁵. In the IMPACT study, biospecimens including blood, nasopharyngeal swabs, saliva, urine and stool samples were collected at study enrolment (baseline denotes the first time point) and longitudinally on average every 3 to 7 days (serial time points). The detailed demographics and clinical characteristics of these 98 participants are shown in Extended Data Table 1. Plasma and peripheral blood mononuclear cells (PBMCs) were isolated from whole blood, and plasma was used for titre measurements of SARS-CoV-2 spike S1 protein-specific IgG and IgM antibodies (anti-S1-IgG and -IgM) and cytokine or chemokine measurements. Freshly isolated PBMCs were stained and analysed by flow cytometry¹⁵. We obtained longitudinal serial time-point samples from a subset of these 98 study participants ($n = 48$; information in Extended Data Table 1). To compare the immune phenotypes between sexes, two sets of data analyses were performed in parallel—baseline and longitudinal, as described below. As a control group, healthcare workers (HCWs) from Yale-New Haven Hospital were enrolled who were uninfected with COVID-19. Demographics and background information for the HCW group and the demographics of HCWs for cytokine assays and flow cytometry assays for the primary analyses are in Extended Data Table 1. Demographic data, time-point information of the samples defined by the days from the symptom onset (DFSO) in each patient, treatment information, and raw data used to generate figures and tables is in Supplementary Table 1.

Baseline analysis

The baseline analysis was performed on samples from the first time point of patients who met the following criteria: not in intensive care unit (ICU), had not received tocilizumab, and had not received high doses of corticosteroids (prednisone equivalent of more than 40 mg) before the first sample collection date. This patient group, cohort A, consisted of 39 patients (17 male and 22 female) (Extended Data Tables 1, 2). Intersex and transgender individuals were not represented in this study. Figures 1–4 represent analyses of baseline raw values obtained from patients in cohort A. In cohort A patients, male and female patients were matched in terms of age, body mass index (BMI), and DFSO at the first time point sample collection (Extended Data Fig. 1a). However, there were significant differences in age and BMI between HCW controls and patients (patients had higher age and BMI values) (Extended Data Table 1), and therefore an age- and BMI-adjusted difference-in-differences analysis was also performed in parallel (Extended Data Table 3).

Fig. 1: Comparison of viral RNA concentrations, titres of anti-SARS-CoV-2 antibodies, and plasma cytokines and chemokine levels at the first sampling of cohort A patients.

 [figure1](#)

a, Comparison of viral RNA measured from nasopharyngeal (Np) swab and saliva. $n = 14$ for male and female patients (M_Pt and F_Pt, respectively) for nasopharyngeal samples, and $n = 9$ and 12, respectively, for saliva samples. Dotted lines indicate the detection limit of the assay (5,610 copies ml^{-1}), and negatively tested data are shown on the x axis. ND, not detected. **b**, Titres of specific IgG and

IgM antibodies against SARS-CoV-2 S1 protein were measured. $n = 13, 74, 15$ and 20 for IgG, and $n = 3, 18, 15$ and 20 for IgM, for male HCW (M_HCW), female HCW (F_HCW), M_Pt and F_Pt, respectively. The cut-off values for positivity are shown by the dotted lines. **c**, Comparison of the plasma levels of representative innate immune cytokines and chemokines. $n = 15, 28, 16$ and 19 for M_HCW, F_HCW, M_Pt and F_Pt, respectively. P values were determined by unpaired two-tailed t -test (**a**) or one-way analysis of variance (ANOVA) with Bonferroni multiple comparison test (**b, c**). All P values < 0.10 are shown. Data are mean \pm s.e.m. The results of all the cytokines or chemokines measured can be found in Extended Data Fig. 1b.

[Full size image](#)

Fig. 2: Differences in composition of PBMCs between male and female patients in cohort A at the first sampling.

 figure2

a, Comparison on the proportion of B cells (top) and T cells (bottom) in live PBMCs. $n = 6, 42, 16$ and 21 for M_HCW, F_HCW, M_Pt and F_Pt, respectively. **b**, Representative 2D plots for CD14 and CD16 in monocytes gate

(live/singlets/CD19⁻CD3⁻/CD56⁻CD66b⁻). Numbers in red indicate the percentages of each population in the parent monocyte gate. **c**, Comparison between percentages of total monocytes, classical monocytes (cMono), intermediate monocytes (intMono) and non-classical monocytes (ncMono) in the live PBMCs. $n = 6, 42, 16$ and 21 for M_HCW, F_HCW, M_Pt and F_Pt, respectively. **d**, Comparison of age, BMI, DFSO, T cells (percentage of live PBMCs) and plasma IL-18 and CCL5 levels between male patients who had high non-classical monocytes and low-intermediate non-classical monocytes. $n = 13$ and 4 for ‘low-int’ and ‘high’ group, respectively, for age, BMI and DFSO. $n = 12$ and 4 for ‘low-int’ and ‘high’ group, respectively, for T cells and IL-18 or CCL5 levels. **e**, Correlation between plasma CCL5 levels and non-classical monocytes (percentage of live cells). Pearson correlation coefficients (R) and P values for each sex are shown. Lines represent linear regression lines and shading represents 95% confidence intervals for each sex. ncMono-high male patients ($n = 4$) are shown with orange open squares, and ncMono-low-int male patients ($n = 11$) are shown with orange closed squares. $n = 19$ for female patients (purple circles). Data are mean \pm s.e.m. in **a**, **c** and **d**. P values were determined by one-way ANOVA with Bonferroni multiple comparison test (**a**, **c**) or unpaired two-tailed t -test (**d**). All P values < 0.10 are shown.

[Full size image](#)

Fig. 3: Sex difference in T cell phenotype at the first sampling of cohort A patients.



a, Percentages of CD4 and CD8 in the CD3-positive cells. **b**, Representative 2D plots for CD38 and HLA-DR in the CD4 and CD8 T cells. Numbers in red indicate the percentages of CD38⁺HLA-DR⁺ populations in the parent gate (live/singlets/CD3⁺/CD4⁺ or CD8⁺). **c**, Percentages of CD38⁺HLA-DR⁺ CD4 or CD8 cells in CD3-positive cells. **d**, Representative 2D plots for PD-1 and TIM-3 in the CD4 and CD8 T cells. Numbers in red indicate the percentages of PD-1⁺TIM-3⁺ populations in the parent gate (live/singlets/CD3⁺/CD4⁺ or CD8⁺/CD45RA⁻). **e**, Percentages of PD-1⁺TIM-3⁺ CD4 or CD8 cells in CD3-positive cells. $n = 6, 45, 16$ and 22 for M_HCW, F_HCW, M_Pt and F_Pt, respectively. P values were determined by one-way ANOVA with Bonferroni multiple comparison test. Data are mean \pm s.e.m. All P values < 0.10 are shown.

[Full size image](#)

Fig. 4: Differential immune phenotypes at the first sampling and disease progression between sexes in cohort A patients.

 **figure4**

a, b, Sex-aggregated (**a**) and sex-disaggregated (**b**) comparison of age, BMI, RNA concentration in nasopharyngeal swab and saliva, and anti-S1-IgG antibodies between the stabilized and deteriorated group. $n = 11, 6, 16$ and 6 for age and BMI, $n = 9, 5, 9$ and 5 for nasopharyngeal swab, $n = 6, 3, 8$ and 4 for saliva, and $n = 10, 5, 14$ and 6 for anti-S1-IgG antibodies, for M_stabilized, M_deteriorated, F_stabilized and F_deteriorated group, respectively. Dotted lines in the viral concentration and

anti-S1-IgG panels indicate the detection limit and cut-off value for positivity, respectively. **c**, Cytokine or chemokine comparison between stabilized and deteriorated groups. $n = 10, 6, 14$ and 5 for the M_stabilized, M_deteriorated, F_stabilized and F_deteriorated groups, respectively. **d**, Comparisons in the proportions of activated ($CD38^+HLA-DR^+$) and terminally differentiated ($PD-1^+TIM-3^+$) CD4 or CD8 T cells, and $IFN\gamma^+CD8$ T cells in $CD3$ -positive T cells are shown. $n = 10, 6, 16$ and 6 for M_stabilized, M_deteriorated, F_stabilized and F_deteriorated group, respectively. **e**, Pearson correlation heat maps of the indicated parameters are shown for each sex. For viral RNA concentrations and cytokine or chemokine levels, log-transformed values were used for the calculation of the correlations. The size and colour of the circles indicate the correlation coefficient (R), and only statistically significant correlations ($P < 0.05$) are shown. Clinical deterioration from the first time point was scored by $C_{max} - C_1$. $n = 17$ and 22 for male and female, respectively. **f**, Correlation between age and $CD38^+HLA-DR^+$ CD8 T cells (left) and $IFN\gamma^+CD8$ T cells (right). Pearson correlation coefficient (R) and P values for each correlation and sex are shown. Lines represent linear regression lines and shading represents 95% confidence intervals for each sex. P values were determined by unpaired two-tailed t -test in **a–d**. Data are mean \pm s.e.m. All P values < 0.10 are shown.

[Full size image](#)

Longitudinal analysis

As parallel secondary analyses, we performed longitudinal analysis on a total patient cohort (cohort B) to evaluate the difference in immune response over the course of the disease between male and female patients. Cohort B included all patient samples from cohort A (including several time-point samples from the cohort A patients) as well as an additional 59 patients who did not meet the inclusion criteria for cohort A. Because cohort B included more severely affected patients in ICU, the average clinical scores were higher in cohort B than in cohort A (mean \pm s.d.: 1.3 ± 0.5 (female) and 1.4 ± 0.5 (male) for cohort A, and 2.5 ± 1.5 (female) and 2.7 ± 1.3 (male) for cohort B) (Extended Data Table 1). This analysis included several time-point samples from 98 participants in total. Data from cohort B were analysed for sex differences in immune responses among patients using longitudinal analysis, controlling for potential confounding by age, BMI, receipt of immunomodulatory treatment (tocilizumab or corticosteroids), DFSO and ICU status. Second, we conducted a longitudinal analysis that compared male and female patients with COVID-19 to male and female HCWs, controlling for age and BMI. Adjusted least square means difference over time in immune responses between male and female patients with COVID-19 (Extended Data Table 4) and adjusted least square means

difference over time in immune responses between male and female patients with COVID-19 and male and female HCWs (Extended Data Table 5) were calculated.

Sex differences in cytokines and chemokines

We first compared the concentrations of viral RNA of male and female patients. For both cohorts A and B, there was no difference by sex in terms of the viral RNA concentrations in nasopharyngeal swab and saliva (Fig. 1a, Extended Data Tables 3, 4).

Anti-SARS-CoV-2 S1-specific IgG and IgM (anti-S1-IgG and -IgM) antibodies were comparable in infected male and female in cohort A (Fig. 1b) and in cohort B (Extended Data Tables 4, 5). Thus, at baseline and during the course of the disease, there were no clear differences in the amount of IgG or IgM generated against the S1 protein between male and female patients.

Next, we analysed the levels of 71 cytokines and chemokines in the plasma. Levels of many pro-inflammatory cytokines, chemokines and growth factors, including IL-1 β , IL-6, IL-8, TNF, CCL2, CXCL10 and G-CSF, are increased in the plasma of patients with COVID-19¹⁶. In line with previous reports, levels of inflammatory cytokine or chemokine were generally higher in patients than in controls (Fig. 1c, Extended Data Figs. 1b, 2a, Extended Data Table 3). The levels of type-I, -II or -III interferon (IFN) were comparable between the sexes in cohort A (Extended Data Fig. 1b, Extended Data Table 3). However, we found higher levels of IFN α 2 in female patients than in male patients in cohort B (Extended Data Table 4). The levels of many cytokines, chemokines and growth factors were increased in patients compared to HCWs in both sexes, and the levels between sexes were comparable (Fig. 1c, Extended Data Fig. 1b, Extended Data Table 3). However, levels of IL-8 and IL-18 were significantly higher in male patients than in female patients in cohort A (Fig. 1c). In age- and BMI-adjusted analyses of cohort A, we found that although IL-8 and IL-18 were no longer significantly higher among male patients than in female patients, IL-8 and CXCL10 were significantly increased in male patients compared to male HCWs than in female patients compared to female HCWs (difference-in-differences, Extended Data Table 3). In adjusted analyses of cohort B, although we did not see significant sex differences in the levels of IL-8 and IL-18, we found significantly higher levels of CCL5 in male patients than in female patients over the course of the disease (Extended Data Table 4) and significantly increased levels of CCL5 in male patients compared to male HCWs than in female patients compared to female HCWs (Extended Data Table 5, difference-in-differences). These data indicated that, although levels of most of the innate inflammatory cytokines and chemokines were comparable, there were a few

factors that are more robustly increased at the baseline (IL-8 and IL-18) and during the course of the disease (CCL5) in male patients than in female patients.

Monocyte differences by sex

Next, we examined the immune cell phenotype by flow cytometry. Freshly isolated PBMCs were stained with specific antibodies to identify T cells, B cells, natural killer T cells, natural killer cells, monocytes, macrophages and dendritic cells to investigate the composition of PBMCs (Extended Data Fig. 2b). Consistent with a previous report on a decrease in T cells in patients¹⁶, in cohort A, the proportion of T cells in the live cells was significantly lower in patients, whereas the proportion of B cells was higher in both male and female patients than in HCWs (Fig. 2a, Extended Data Table 3). There was no difference in the numbers of B cells across all groups, but the numbers of T cells were lower in patients of both sexes (data not shown). By contrast, in cohort B, we found that male patients had significantly lower numbers of T cells, both total counts and as a proportion of live cells, over the course of the disease than female patients (Extended Data Table 4). Next, we found higher populations of monocytes in both sexes in cohort A (Fig. 2b,c, Extended Data Fig. 2b) compared to HCWs. Although CD14⁺CD16⁻ classical monocytes were comparable across all groups, levels of CD14⁺CD16⁺ intermediate monocytes were increased in patients compared with HCWs, and this increase was more robust in female patients (Fig. 2b,c). By contrast, male patients had higher levels of CD14^{lo}CD16⁺ non-classical monocytes than controls and female patients (Fig. 2b,c). These differences were observed in age- and BMI-adjusted analyses, too, but were not significant (Extended Data Table 3).

We then divided the 17 cohort A male patients into two groups, namely, a ‘high’ group who had high percentages of non-classical monocytes (upper quartile 4 patients, all had more than 5% of non-classical monocytes) and a ‘low-intermediate’ group (others, 13 patients). We compared age, BMI, DFSO, T cells, and plasma levels of IL-18 and CCL5. Although we found no differences in age, BMI or DFSO (Fig. 2d), we noted that the group with high levels of non-classical monocytes had significantly lower levels of T cells and higher levels of CCL5 in plasma (Fig. 2d). In addition, we found a significant correlation between CCL5 levels and abundance in non-classical monocytes only in male patients (Fig. 2e). These findings suggest that the progression from classical to non-classical monocytes may be arrested at the intermediate stage in female patients, and that increased innate inflammatory cytokines and chemokines are associated with more robust activation of innate immune cells at the baseline as well as more robust longitudinal T cell decrease in male patients.

Higher T cell activation in female

We further examined the T cell phenotype in patients with COVID-19. The composition of overall CD4-positive and CD8-positive cells among T cells were similar between all groups in cohort A (Fig. 3a, Extended Data Fig. 2c, Extended Data Table 3). Detailed phenotyping of T cells for naive T cells, central or effector memory T (T_{CM}/T_{EM}) cells, follicular helper T (T_{FH}) cells, regulatory T (T_{reg}) cells revealed no remarkable differences in the frequency of these subsets between sexes (Extended Data Fig. 2c). However, we observed higher levels of CD38 and HLA-DR-positive activated T cells in female patients than in male patients (Fig. 3b,c). In parallel, PD-1- and TIM-3-positive terminally differentiated T cells were more prevalent among female patients than male patients (Fig. 3d,e). These findings were seen in both CD4 and CD8 T cells, but the differences were more robust in CD8 T cells (Fig. 3c,e, Extended Data Table 3). We also stained for intracellular cytokines such as IFN γ , granzyme B (GzB), TNF, IL-6 and IL-2 in CD8 T cells, and IFN γ , TNF, IL-17A, IL-6 and IL-2 in CD4 T cells. Levels of these cytokines were higher in patients than in controls, and were generally comparable between sexes in the patients (Extended Data Fig. 2d). Analyses of T cell phenotypes in cohort B did not reveal any significant differences between sexes (Extended Data Tables 4 and 5). Therefore, female patients with COVID-19 had more abundant activated and terminally differentiated T cell populations than male patients at baseline in unadjusted analyses.

Sex-dependent immunity and disease course

We investigated whether certain immune phenotypes were correlated with disease trajectory, and whether these phenotypes and factors differed between the sexes. To this end, we evaluated the disease course of patients in cohort A. The clinical scores at the first sample collection (C_1) were 1 or 2 for all of the patients in cohort A. The patients were categorized into a ‘deteriorated’ group if the patients marked a score of 3 or higher after the first sample collection date as their maximum clinical scores during admission (C_{max}). By contrast, if the patients maintained the score of 1 or 2, they were categorized as ‘stabilized’ (Extended Data Table 2). Both in male ($n = 17$) and female ($n = 22$) patients from cohort A, 6 patients of each sex deteriorated during the course of the disease (35.3% and 27.3%, respectively), and the intervals between the dates at which the patients reached C_{max} (DFSO at C_{max}) and the first sample collection (DFSO at C_1) were not significantly different between deteriorated male and female patients (mean \pm s.d. = 3.7 ± 4.1 and 4.2 ± 2.7 , respectively; $P = 0.81$ by unpaired two-tailed t -test).

We first examined age, BMI, viral loads and titres of anti-S1-IgG antibodies between the stabilized and deteriorated groups in a sex-aggregated manner. We found that the deteriorated group had on average a higher BMI than the stabilized group. Although the age was not statistically different, the stabilized group spanned a larger age range than the deteriorated group, who were generally of a more advanced age. The viral load and antibody titres were comparable (Fig. 4a). Next, we examined these factors in a sex-disaggregated manner, and found that the deteriorated male (M_deteriorated) group was on average significantly older than the stabilized male (M_stabilized) group, whereas the two female groups (F_deteriorated and F_stabilized) were comparable in age (Fig. 4b). In addition, BMI was higher for the M_deteriorated than the M_stabilized group, whereas there was no difference in BMI between the F_deteriorated and F_stabilized groups (Fig. 4b). By contrast, the F_deteriorated group had higher viral load in saliva than the F_stabilized group, whereas there was no difference in the male groups (Fig. 4b). The levels of antibodies were comparable between the deteriorated and stabilized groups both in male and female, but stabilized female tended to have higher antibody levels (Fig. 4b).

We further investigated whether the key factors identified in the previous analyses correlated with disease progression in male and female patients. We observed that regardless of sex, some chemokines and growth factors, such as CXCL10 (also known as IP-10) and M-CSF, were increased in patients that went on to develop worse disease. However, there were some innate immune factors, such as CCL5, TNFSF10 (also known as TRAIL) and IL-15, that were specifically increased only in female patients that subsequently progressed to worse disease, but this difference was not observed in male patients (Fig. 4c). In the age- and DFSO-adjusted analysis of cohort A, we also found that CCL5 was only increased in female patients that progressed to worse disease compared to the stabilized patients, but no such correlation was found in male patients (Extended Data Table 6).

T cell phenotypes in these groups showed that male patients whose disease worsened had a significantly lower proportion of activated T cells ($CD38^+HLA-DR^+$) and terminally differentiated T cells ($PD-1^+TIM-3^+$) and tendencies for fewer IFNy⁺ CD8 T cells at the first sample collection, compared with their counterpart male who did not progressed to worse disease (Fig. 4d). However, in female patients, the deteriorated group had similar levels of these types of CD8 T cells compared with the stabilized group (Fig. 4d).

We finally examined the correlations between age, BMI, viral loads, anti-S1 antibodies, cytokines or chemokines, activated or terminally differentiated or IFNy-producing CD8 T cells, and clinical disease course (' $C_{max} - C_1$ ' was used for the

deterioration score). The correlation matrix showed that in female patients, higher levels of innate immunity cytokines, such as TNFSF10 and IL-15, were positively correlated with disease progression, whereas there was no association between CD8 T cell status and deterioration (Fig. 4e, results of age- and DSO-adjusted analysis in Extended Data Table 6). In particular, CXCL10, M-CSF and IL-15 were positively correlated with IFNy⁺CD8 T cells in female patients (Fig. 4d).

By contrast, in male patients, progressive disease was associated with higher age, higher BMI, and poor CD8 T cell activation (Fig. 4e). Poor CD8 T cell activation and poor production of IFNy by CD8 T cells were significantly correlated with patients' age, whereas these correlations were not seen in female patients (Fig. 4e, f). These differences seemed to highlight the differences between the sexes in the immune responses against SARS-CoV-2 as well as the difference of the potential prognostic or predictive factors for clinical deterioration of COVID-19.

Discussion

Our results revealed key differences in immune responses during the disease course of SARS-CoV-2 infection in male and female patients. First, we found that the levels of several important pro-inflammatory innate immunity chemokines and cytokines such as IL-8, IL-18 (at baseline) and CCL5 (longitudinal analysis) were higher in male patients, which correlated with higher non-classical monocytes (at baseline). Second, we observed a more robust T cell response among female patients than male patients at baseline. In particular, activated CD8 T cells were significantly increased only in female patients but not in male patients compared with healthy volunteers. Analysis of their clinical trajectory showed that, although poor T cell responses were associated with future progression of disease in male patients, higher levels of innate immune cytokines were associated with worsening of COVID-19 disease in female patients. Notably, the T cell response was significantly and negatively correlated with patients' age in male, but not female, patients. These data indicate key differences in the baseline immune capabilities in male and female patients during the early phase of SARS-CoV-2 infection, and suggest a potential immunological underpinning of the distinct mechanisms of disease progression between sexes. These analyses also provide a potential basis for taking sex-dependent approaches to prognosis, prevention, care, and therapy for patient with COVID-19.

Although our study provides a strong basis for further investigation into how COVID-19 disease dynamics may differ between male and female patients, it is important to note that there are some limitations to the analyses presented in this Article. First, we acknowledge that the healthy HCWs used as the control

population were not matched to patients on the basis of age, BMI or underlying risk factors. To account for this, we performed adjusted analyses for the baseline and longitudinal comparisons between patients (cohort A and the full patient population, cohort B) and HCWs, controlling for age and BMI. However, we cannot rule out residual confounding due to underlying risk factors not available for the HCW controls.

Collectively, these data suggest that vaccines and therapies to increase T cell immune responses to SARS-CoV-2 might be warranted for male patients, whereas female patients might benefit from therapies that dampen innate immune activation early during disease. The immune landscape in patients with COVID-19 is considerably different between the sexes, and these differences may underlie heightened disease vulnerability in men.

Methods

No statistical methods were used to predetermine sample size. The experiments were not randomized. Investigators were blinded during experiments in terms of the sex or other clinical background information, with the sample labels having de-identified patient IDs that did not contain any of this information.

Ethics statement

This study was approved by Yale Human Research Protection Program Institutional Review Boards (FWA00002571, Protocol ID. 2000027690). Informed consent was obtained from all enrolled patients and healthcare workers.

Patients and HCWs

Adult patients (≥ 18 years old) admitted to Yale-New Haven Hospital between 18 March and 9 May 2020, positive for SARS-CoV-2 by RT-PCR from nasopharyngeal and/or oropharyngeal swabs, and able to provide informed consent (surrogate consent accepted) were eligible for the Yale IMPACT Biorepository study, and 198 patients were enrolled in this period. All patients necessitated hospitalization for their symptoms and had an WHO score¹⁷ of at least 3 at admission (denoting hospitalized, mild disease). At the initial screening, clinical PCR tests were performed in CLIA-certified laboratory and only the PCR-positive patients were enrolled. Only after the confirmation of PCR-positivity, the patients were enrolled and the first time point samples for this study were collected for each patient. The first time point samples were collected at 11.4 ± 8.1 , 10.2 ± 6.3 ,

11.7 ± 7.2 and 12.1 ± 7.3 (mean \pm s.d.) DFSO in cohort A female, cohort A male, cohort B female and cohort B male, respectively (Extended Data Fig. 1a, right panel for cohort A, Extended Data Table 1).

Among these patients, we could obtain whole blood for flow cytometry analysis using fresh PBMCs, plasma for cytokine or chemokine measurements, anti-S1 antibody measurements and nasopharyngeal swab and saliva from total of 98 individuals for the present study. For longitudinal analyses, biospecimens (blood, nasopharyngeal swabs, saliva, urine, and/or stool) were collected at study enrolment (baseline) and on average every 3 to 7 days while in the hospital in 48 of these 98 patients.

The patients were assessed with a locally developed clinical scoring system for disease severity; (1): admitted and observed without supplementary oxygen; (2) required ≤ 3 l supplementary oxygen via nasal canal to maintain $\text{SpO}_2 > 92\%$; (3) received tocilizumab, which per hospital treatment protocol required that the patient to require >3 l supplementary oxygen to maintain $\text{SpO}_2 > 92\%$, or, required >2 l supplementary oxygen to maintain $\text{SpO}_2 > 92\%$ and had a high-sensitivity C-reactive protein (CRP) > 70 ; (4) the patient required ICU-level care; (5) the patient required intubation and mechanical ventilation. In relation to the WHO scoring¹⁷, our clinical scores 1, 2/3, 4 and 5 largely correspond to WHO scores 3, 4, 5 and 6/7, respectively. Detailed demographic information for the entire cohort (98 cohort B patients, and several time-point samples from 54 patients among them) and of cohort A (39 patients) are shown in Extended Data Tables 1–3. For the patients who are 90 years old or older, their ages were protected health information, and ‘90’ was put as the surrogate value for the analyses. Among 198 total patients enrolled in IMPACT study in this period, we obtained whole blood, nasopharyngeal swabs or saliva samples from 98 patients for the present study. Individuals with active chemotherapy against cancers, pregnant patients, patients with background haematological abnormalities, patients with autoimmune diseases and patients with a history of organ transplantation and on immunosuppressive agents, were excluded from this study.

As a control group, COVID-19-uninfected HCWs from Yale-New Haven Hospital were enrolled. HCWs were tested every 2 weeks for PCR and serology. For the control group, the PBMCs and plasma analysis were done when both tests were negative. That is, if either or both of these tests were positive, these samples were excluded from the analyses. In some HCWs, samples were collected for the assays at up to two time points. In these cases, if the data for a certain type of assay were available for both of these time points, only the first time point data were used and otherwise data for either time point were used in the main analyses with cohort A.

Viral RNA measurement

SARS-CoV-2 RNA concentrations were measured from nasopharyngeal samples and saliva samples by RT-PCR as previously described^{18,19}. In short, total nucleic acid was extracted from 300 µl of viral transport media from the nasopharyngeal swab or 300 µl of whole saliva using the MagMAX Viral/Pathogen Nucleic Acid Isolation kit (ThermoFisher Scientific) using a modified protocol and eluted into 75 µl of elution buffer¹⁹. For SARS-CoV-2 RNA detection, 5 µl of RNA template was tested as previously described¹⁸, using the US CDC real-time RT-PCR primer/probe sets for 2019-nCoV_N1, 2019-nCoV_N2, and the human RNase P (RP) as an extraction control. Virus RNA copies were quantified using a tenfold dilution standard curve of RNA transcripts that we previously generated¹⁸. If the RNA concentration was lower than the limit of detection (ND) that was determined previously¹⁸, the value was set to 0 and used for the analyses.

Isolation of plasma

Plasma samples were collected after whole blood centrifugation at 400g for 10 min at room temperature with brake off. The plasma was then carefully transferred to 15-ml conical tubes and then aliquoted and stored at -80 °C for subsequent analysis.

SARS-CoV-2 specific antibody measurement

ELISAs were performed as previously described²⁰. In short, Triton X-100 and RNase A were added to serum samples at final concentrations of 0.5% and 0.5 mg ml⁻¹ respectively and incubated at room temperature for 30 min before use to reduce risk from any potential virus in serum. Then, 96-well MaxiSorp plates (Thermo Scientific 442404) were coated with 50 µl per well of recombinant SARS-CoV-2 S1 protein (ACROBiosystems S1N-C52H3-100 µg) at a concentration of 2 µg ml⁻¹ in PBS and were incubated overnight at 4 °C. The coating buffer was removed, and plates were incubated for 1 h at room temperature with 200 µl of blocking solution (PBS with 0.1% Tween-20, 3% milk powder). Serum was diluted 1:50 in dilution solution (PBS with 0.1% Tween-20, 1% milk powder) and 100 µl of diluted serum was added for two hours at room temperature. Plates were washed three times with PBS-T (PBS with 0.1% Tween-20) and 50 µl of HRP anti-Human IgG Antibody (GenScript A00166, 1:5,000) or anti-Human IgM-Peroxidase Antibody (Sigma-Aldrich A6907, 1:5,000) diluted in dilution solution were added to each well. After 1 h of incubation at room temperature, plates were washed six times with PBS-T. Plates were developed with 100 µl of TMB Substrate Reagent Set (BD Biosciences

555214) and the reaction was stopped after 12 min by the addition of 100ul of 2 N sulfuric acid. Plates were then read at a wavelength of 450 nm and 570 nm.

The cut-off values for sero-positivity were determined as 0.392 and 0.436 for anti-S1-IgG and anti-S1 IgM, respectively. Eighty pre-pandemic plasma samples were assayed to establish the negative baselines, and these values were statistically determined with confidence level of 99%.

Cytokine and chemokine measurement

Patients' sera isolated as above were stored in -80 °C until the measurement of the cytokines. The sera were shipped to Eve Technologies on dry ice, and levels of 71 cytokines and chemokines were measured with Human Cytokine Array/Chemokine Array 71-Plex Panel (HD71). All the samples were measured upon the first thaw.

The shipment of the samples and measurements were done in two separate batches, but the measurements were performed with the same assay kits using the same standard curves, therefore minimizing the batch effects between the measurements.

For the out of range values of the measurements, either the lowest highest extrapolatable values or the lowest or highest standard curve were recorded following the instructions of HD71 assay, and included in the analyses. Among all the samples measured, we found that two samples had outlier values (beyond 1.5× interquartile range) in more than half of the 71 cytokines or chemokines measured, suggesting the technical error and/or poor sample qualities in the measurements. Therefore, cytokine or chemokine data of these individuals were excluded from the analyses.

Isolation of PBMCs

The PBMCs were isolated from heparinized whole blood using Histopaque density gradient under the biosafety level 2+ facility. To isolate PBMCs, blood 1:1 diluted in PBS was layered over in Histopaque in a SepMate tube and centrifuged for 10 min at 1,200g. The PBMC layer was collected by quickly pouring the content into a new 50-ml tube. The cells were washed twice with PBS to remove any remaining histopaque and to remove platelets. The pelleted cells were treated with ACK buffer for red cell lysis and then counted. The percentage viability was estimated using Trypan blue staining.

Flow cytometry

Using the freshly isolated PBMCs, the staining was performed in three separate panels for (1) PBMC cell composition, (2) T cell surface staining, and (3) T cell intracellular staining. Exact antibody clones and vendors that were used for flow cytometric analysis are as follows: BB515 anti-HLA-DR (G46-6), BV785 anti-CD16 (3G8), PE-Cy7 anti-CD14 (HCD14), BV605 anti-CD3 (UCHT1), BV711 anti-CD19 (SJ25C1), BV421 anti-CD11c (3.9), AlexaFluor647 anti-CD1c (L161), Biotin anti-CD141 (M80), PE anti-CD304 (12C2), APCFire750 anti-CD11b (ICRF44), PerCP/Cy5.5 anti-CD66b (G10F5), BV785 anti-CD4 (SK3), APCFire750 or PE-Cy7 or BV711 anti-CD8 (SK1), BV421 anti-CCR7 (G043H7), AlexaFluor 700 anti-CD45RA (HI100), PE anti-PD1 (EH12.2H7), APC anti-TIM-3 (F38-2E2), BV711 anti-CD38 (HIT2), BB700 anti-CXCR5 (RF8B2), PE-Cy7 anti-CD127 (HIL-7R-M21), PE-CF594 anti-CD25 (BC96), BV711 anti-CD127 (HIL-7R-M21), BV421 anti-IL-17a (N49-653), AlexaFluor 700 anti-TNF (MAb11), PE or APC/Fire750 anti-IFNy (4S.B3), FITC anti-GranzymeB (GB11), AlexaFluor 647 anti-IL-4 (8D4-8), BB700 anti-CD183/CXCR3 (1C6/CXCR3), PE-Cy7 anti-IL-6 (MQ2-13A5), PE anti-IL-2 (5344.111), BV785 anti-CD19 (SJ25C1), BV421 anti-CD138 (MI15), AlexaFluor700 anti-CD20 (2H7), AlexaFluor 647 anti-CD27 (M-T271), PE/Dazzle594 anti-IgD (IA6-2), PE-Cy7 anti-CD86 (IT2.2), APC/Fire750 anti-IgM (MHM-88), BV605 anti-CD24 (M1/69), APC/Fire 750 anti-CD10 (HI10a), BV421 anti-CD15 (SSEA-1), AlexaFluor 700 Streptavidin (ThermoFisher). Freshly isolated PBMCs were plated at 1×10^6 – 2×10^6 cells in a 96-well U-bottom plate. Cells were resuspended in Live/Dead Fixable Aqua (ThermoFisher) for 20 min at 4 °C. Following a wash, cells were then blocked with Human TruStan FcX (BioLegend) for 10 min at room temperature. Cocktails of desired staining antibodies were directly added to this mixture for 30 min at room temperature. For secondary stains, cells were washed and supernatant aspirated; to each cell pellet, a cocktail of secondary markers was added for 30 min at 4 °C. Before analysis, cells were washed and resuspended in 100 µl of 4% paraformaldehyde for 30 min at 4 °C. For intracellular cytokine staining following stimulation, cells were resuspended in 200 µl cRPMI (RPMI-1640 supplemented with 10% FBS, 2 mM l-glutamine, 100 U ml⁻¹ penicillin, and 100 mg ml⁻¹ streptomycin, 1 mM sodium pyruvate, and 50 µM 2-mercaptoethanol) and stored at 4 °C overnight. Subsequently, these cells were washed and stimulated with 1× Cell Stimulation Cocktail (eBioscience) in 200 µl cRPMI for 1 h at 37 °C. Directly to this, 50 µl of 5× Stimulation Cocktail (plus protein transport inhibitor) (eBioscience) was added for an additional 4 h of incubation at 37 °C. After stimulation, cells were washed and resuspended in 100 µl of 4% paraformaldehyde for 30 min at 4 °C. To quantify intracellular cytokines, these samples were permeabilized with 1× Permeabilization Buffer from the FOXP3/Transcription Factor Staining Buffer Set (eBioscience) for 10 min at 4 °C. All further staining cocktails were made in this buffer. Permeabilized cells were then washed and resuspended in a cocktail

containing Human TruStan FcX (BioLegend) for 10 min at 4 °C. Finally, intracellular staining cocktails were directly added to each sample for 1 h at 4 °C. After this incubation, cells were washed and prepared for analysis on an Attune NXT (ThermoFisher). Data were analysed using FlowJo software v.10.6 software (Tree Star).

Set of markers used to identify each subset of cells are summarized in Extended Data Table 7, and gating strategies for the key cell populations presented in the main figures are shown in Extended Data Fig. 3a–c. For most samples, all available staining panels were implemented and analysed. The few exceptions pertained to those samples during which a mechanical malfunction occurred, which depleted the sample before acquisition, or to the samples with poor staining qualities. In these cases, data for these samples or panels were missing and not available. All the data available were used for the analyses, and the data used to generate figures and tables can be found in Supplementary Table 1, and the raw fcs files are available at ImmPort as described in the 'Data Availability' section.

Statistical analysis for the primary analyses

For the primary analyses shown in the main figures, Graph Pad Prism (v.8.0) was used for all statistical analysis. Unless otherwise noted, one-way ANOVA with Bonferroni's multiple comparison test was used for the comparisons between M_Pt versus F_Pt, M_Pt versus M_HCW, F_Pt versus F_HCW, and M_HCW versus F_HCW for the comparisons. For two-group comparisons including the comparison between stabilized group and deteriorated group in each sex (Fig. 4a–d), two-sided unpaired *t*-test was used for the comparison. Bioconductor R (v.3.6.3) package ggplot2 (v.3.3.0) was used to generate heat maps (Extended Data Fig. 2), X–Y graphs for correlation analyses (Figs. 2e, 4f), and Pearson correlation heat maps (Fig. 4e).

Statistical analysis for the secondary analyses

All multivariable analyses were conducted using R v.3.6.1 (for data cleaning) and SAS version 9.4 (Cary, NC; for data analysis). The code used for data cleaning and data analysis is available at https://github.com/muhellingson/covid_immresp. We conducted longitudinal analyses of the differences in immune response by sex for patients with COVID-19 and differences in immune response between patients with COVID-19 and HCWs by sex and adjusted linear regression to evaluate differences in immune response by sex at baseline and the differences in immune response by sex and patient trajectory.

Longitudinal difference in immune response in all patients positive for COVID-19 (cohort B) by sex

A marginal linear model was fitted to evaluate the difference in various immune responses (outcome) in patients by sex (exposure). We used an auto-regressive correlation structure to account for correlation between repeated observations in an individual over time. To account for the small sample size and unequal follow-up between participants, we used the Morel–Bokossa–Neerchal (MBN) correction. In addition to sex, the model contained time-independent terms for age (in years) and BMI and time-dependent terms for days from symptom onset (self-reported), ICU status (as a proxy for disease severity) and treatment with either tocilizumab or corticosteroids. A patient was defined as ‘on tocilizumab’ at a given time point if they had received the treatment within 14 days before the time the sample was taken. Patients were defined as ‘on corticosteroids’ if they had received the treatment on the same day the sample was taken. The resulting regression coefficients were interpreted as the difference in the adjusted least square means immune response between female and male patients.

Difference in immune response between patients with COVID-19 (cohort A) and HCWs by sex at baseline

We used linear regression to evaluate the difference in immune response between female and male patients at the first time point for those patients who had not received corticosteroids or tocilizumab before enrolment (cohort A). The model contained terms for sex, patient trajectory (worsened versus stable), age, BMI, and an interaction term for sex and group (patient versus HCWs). We calculated the least square means for each group (female patients who worsened, female patients who stabilized, male patients who worsened and male patients who stabilized) and evaluated the differences in the least square means of the different immune response outcomes by group and sex. *P* values and 95% confidence intervals were calculated with a Tukey correction for multiple pairwise comparisons. The regression coefficient of the interaction term between sex and group was interpreted as the difference-in-differences of the two comparisons by sex or by group (for example, the difference-in-differences between female and male patients and female and male HCWs).

Longitudinal difference in immune response between all patients with COVID-19 (cohort B) and HCWs by sex

We used a marginal linear model with a compound symmetric correlation structure and the MBN correction to evaluate the difference in immune responses between patients and HCWs by sex, controlling for age and BMI. We calculated the least square means for each group (female patients, female HCWs, male patient, male HCWs) and evaluated the differences in adjusted least square means to compare study groups by sex (female patients versus male patients, female HCWs versus male HCWs, female patients versus female HCWs and male patients versus male HCWs). *P* values and 95% confidence intervals were corrected using the Tukey correction for multiple pairwise comparisons. The regression coefficient of the interaction term between sex and study group was interpreted as the difference-in-differences between the two comparisons by sex or by group.

Multivariable patient trajectory analysis

We used linear regression to evaluate the difference in baseline immune response between patients who worsened after the baseline sample was taken and those who stabilized by sex. The model contained terms for sex, patient trajectory (worsened versus stable), age, days from symptom onset and an interaction term for sex and patient trajectory. We calculated the adjusted least square means for each group (female patients who worsened, female patients who stabilized, male patients who worsened and male patients who stabilized) and evaluated the differences in least square means of the different immune responses by patient trajectory and sex using the Tukey correction for multiple comparisons. The regression coefficient of the interaction term between sex and patient trajectory was interpreted as the difference-in-differences between the two patient trajectories by sex or sex by the two patient trajectories.

Reporting summary

Further information on research design is available in the [Nature Research Reporting Summary](#) linked to this paper.

Data availability

All of the background information of HCWs, clinical information of patients, and raw data used in this study are included in the Supplementary Table 1. In addition, all of the raw fcs files for the flow cytometry analysis are uploaded in ImmPort (<https://www.immport.org/shared/home>, study ID: SDY1648).

References

1. 1.

Chen, N. et al. Epidemiological and clinical characteristics of 99 cases of 2019 novel coronavirus pneumonia in Wuhan, China: a descriptive study. *Lancet* **395**, 507–513 (2020).

[CAS](#) [Article](#) [Google Scholar](#)

2. 2.

Li, Q. et al. Early transmission dynamics in Wuhan, China, of novel coronavirus-infected pneumonia. *N. Engl. J. Med.* **382**, 1199–1207 (2020).

[CAS](#) [Article](#) [Google Scholar](#)

3. 3.

Yang, X. et al. Clinical course and outcomes of critically ill patients with SARS-CoV-2 pneumonia in Wuhan, China: a single-centered, retrospective, observational study. *Lancet Respir. Med.* **8**, 475–481 (2020).

[CAS](#) [Article](#) [Google Scholar](#)

4. 4.

Meng, Y. et al. Sex-specific clinical characteristics and prognosis of coronavirus disease-19 infection in Wuhan, China: a retrospective study of 168 severe patients. *PLoS Pathog.* **16**, e1008520 (2020).

[Article](#) [Google Scholar](#)

5. 5.

Gebhard, C., Regitz-Zagrosek, V., Neuhauser, H. K., Morgan, R. & Klein, S. L. Impact of sex and gender on COVID-19 outcomes in Europe. *Biol. Sex Differ.* **11**, 29 (2020).

[CAS](#) [Article](#) [Google Scholar](#)

6. 6.

Zhu, N. et al. A novel coronavirus from patients with pneumonia in China, 2019. *N. Engl. J. Med.* **382**, 727–733 (2020).

[CAS](#) [Article](#) [Google Scholar](#)

7. 7.

WHO. WHO Director-General's Opening Remarks at the Media Briefing on COVID-19 - 11 March 2020 <https://www.who.int/dg/speeches/detail/who-director-general-s-opening-remarks-at-the-media-briefing-on-covid-19---11-march-2020> (2020).

8. 8.

Williamson, E. J. et al. Factors associated with COVID-19-related death using OpenSAFELY. *Nature* **584**, 430–436 (2020).

[CAS](#) [Article](#) [Google Scholar](#)

9. 9.

Klein, S. L. & Flanagan, K. L. Sex differences in immune responses. *Nat. Rev. Immunol.* **16**, 626–638 (2016).

[CAS](#) [Article](#) [Google Scholar](#)

10. 10.

Fischer, J., Jung, N., Robinson, N. & Lehmann, C. Sex differences in immune responses to infectious diseases. *Infection* **43**, 399–403 (2015).

[CAS](#) [Article](#) [Google Scholar](#)

11. 11.

Guerra-Silveira, F. & Abad-Franch, F. Sex bias in infectious disease epidemiology: patterns and processes. *PLoS One* **8**, e62390 (2013).

[CAS](#) [Article](#) [ADS](#) [Google Scholar](#)

12. 12.

Moore, A. L. et al. Virologic, immunologic, and clinical response to highly active antiretroviral therapy: the gender issue revisited. *J. Acquir. Immune Defic. Syndr.* **32**, 452–461 (2003).

[Article](#) [Google Scholar](#)

13. 13.

Collazos, J., Asensi, V. & Cartón, J. A. Sex differences in the clinical, immunological and virological parameters of HIV-infected patients treated with HAART. *AIDS* **21**, 835–843 (2007).

[Article](#) [Google Scholar](#)

14. 14.

Fink, A. L., Engle, K., Ursin, R. L., Tang, W. Y. & Klein, S. L. Biological sex affects vaccine efficacy and protection against influenza in mice. *Proc. Natl Acad. Sci. USA* **115**, 12477–12482 (2018).

[CAS](#) [Article](#) [Google Scholar](#)

15. 15.

Lucas, C. et al. Longitudinal analyses reveal immunological misfiring in severe COVID-19. *Nature* **584**, 463–469 (2020).

[CAS](#) [Article](#) [Google Scholar](#)

16. 16.

Huang, C. et al. Clinical features of patients infected with 2019 novel coronavirus in Wuhan, China. *Lancet* **395**, 497–506 (2020).

[CAS](#) [Article](#) [Google Scholar](#)

17. 17.

WHO. *R&D Blueprint Novel Coronavirus COVID-19 Therapeutic Trial Synopsis* https://www.who.int/blueprint/priority-diseases/key-action/COVID-19_Treatment_Trial_Design_Master_Protocol_synopsis_Final_18022020.pdf (2020).

18. 18.

Vogels, C. B. F. et al. Analytical sensitivity and efficiency comparisons of SARS-CoV-2 RT-qPCR primer–probe sets. *Nat. Microbiol.* **5**, 1299–1305

(2020)

[Article](#) [Google Scholar](#)

19. 19.

Wyllie, A. L. et al. Saliva or nasopharyngeal swab specimens for detection of SARS-CoV-2. *N. Engl. J. Med.* <https://doi.org/10.1056/NEJMc2016359> (2020).

20. 20.

Amanat, F. et al. A serological assay to detect SARS-CoV-2 seroconversion in humans. *Nat. Med.* **26**, 1033–1036 (2020).

[CAS](#) [Article](#) [Google Scholar](#)

[Download references](#)

Acknowledgements

We thank M. Linehan for technical and logistical assistance. This work was supported by the Women’s Health Research at Yale Pilot Project Program (A.I., A.M.R.), Fast Grant from Emergent Ventures at the Mercatus Center, Mathers Foundation, the Beatrice Kleinberg Neuwirth Fund, Yale Institute for Global Health, and the Ludwig Family Foundation. IMPACT received support from the Yale COVID-19 Research Resource Fund. A.I. is an Investigator of the Howard Hughes Medical Institute. CBFV is supported by NWO Rubicon 019.181EN.004. A.M. is supported by NIH grant R37AI041699.

Author information

Author notes

1. These authors contributed equally: Takehiro Takahashi, Mallory K. Ellingson, Patrick Wong, Benjamin Israelow, Carolina Lucas, Jon Klein, Julio Silva, Tianyang Mao

Affiliations

1. Department of Immunobiology, Yale University School of Medicine, New Haven, CT, USA

Takehiro Takahashi, Patrick Wong, Benjamin Israelow, Carolina Lucas, Jon Klein, Julio Silva, Tianyang Mao, Ji Eun Oh, Maria Tokuyama, Peiwen Lu, Arvind Venkataraman, Annsea Park, Feimei Liu, Eric Y. Wang, Molly L. Bucklin, Yiyun Cao, William Khoury-Hanold, Daniel Kim, Eriko Kudo, Melissa Linehan, Alice Lu-Culligan, Anjelica Martin, Tyler Rice, Eric Song, Nicole Sonnert, Yixin Yang, Aaron M. Ring & Akiko Iwasaki

2. Department of Epidemiology of Microbial Diseases, Yale School of Public Health, New Haven, CT, USA

Mallory K. Ellingson, Arnau Casanovas-Massana, Anne L. Wyllie, Chantal B. F. Vogels, Rebecca Earnest, Sarah Lapidus, Isabel M. Ott, Adam J. Moore, Kristina Brower, Chaney Kalinich, M. Catherine Muenker, Isabel Ott, Mary Petrone, Annie Watkins, Elizabeth B. White, Nathan D. Grubaugh, Albert I. Ko & Saad B. Omer

3. Department of Medicine, Section of Infectious Diseases, Yale University School of Medicine, New Haven, CT, USA

Benjamin Israelow, Melissa Campbell, Rupak Datta, Subhasis Mohanty, Haowei Wang, Albert Shaw, John B. Fournier, Camila D. Odio, Shelli Farhadian & Saad B. Omer

4. Department of Biomedical Engineering, Yale School of Engineering & Applied Science, New Haven, CT, USA

Feimei Liu

5. Boyer Center for Molecular Medicine, Department of Microbial Pathogenesis, Yale University, New Haven, CT, USA

Amit Meir

6. Department of Comparative Medicine, Yale University School of Medicine, New Haven, CT, USA

Jonathan Sun

7. Department of Ecology and Evolutionary Biology, Yale University, New Haven, CT, USA

Isabel M. Ott

8. Department of Medicine, Section of Pulmonary and Critical Care Medicine,
Yale University School of Medicine, New Haven, CT, USA

Giuseppe DeIuliis, Lokesh Sharma & Charles Dela Cruz

9. Department of Laboratory Medicine, Yale University School of Medicine, New
Haven, CT, USA

Wade L. Schulz

10. Center for Outcomes Research and Evaluation, Yale-New Haven Hospital,
New Haven, CT, USA

Wade L. Schulz

11. Yale Institute for Global Health, Yale University, New Haven, CT, USA

Amyn A. Malik & Saad B. Omer

12. Yale School of Nursing, Yale University, Orange, CT, USA

Saad B. Omer

13. Howard Hughes Medical Institute, Chevy Chase, MD, USA

Akiko Iwasaki

14. Yale Center for Clinical Investigation, Yale University School of Medicine,
New Haven, CT, USA

Kelly Anastasio, Staci Cahill & Maxine Kuang

15. Department of Neurology, Yale University School of Medicine, New Haven,
CT, USA

Michael H. Askenase & Sofia Velazquez

16. Yale School of Medicine, New Haven, CT, USA

Maria Batsu, Hannah Beatty, Santos Bermejo, Bertie Geng, Laura Glick, Ryan
Handoko, Lynda Knaggs, Irene Matos, David McDonald, Maksym
Minasyan, Nida Naushad, Allison Nelson, Jessica Nouws, Abeer Obaid, Hong-
Jai Park, Xiaohua Peng, Harold Rahming, Kadi-Ann Rose, Lorenzo

Sewanan, Denise Shepard, Erin Silva, Michael Simonov, Mikhail Smolgovsky, Yvette Strong, Codruta Todeasa, Jordan Valdez & Pavithra Vijayakumar

17. Department of Biochemistry and of Molecular Biology, Yale University School of Medicine, New Haven, CT, USA

Sean Bickerton & Edward Courchaine

18. Yale Viral Hepatitis Program, Yale University School of Medicine, New Haven, CT, USA

Joseph Lim

19. Equity Research and Innovation Center, Yale University, New Haven, CT, USA

Marcella Nunez-Smith

20. Department of Molecular, Cellular and Developmental Biology, Yale University School of Medicine, New Haven, CT, USA

Sarah Prophet

Authors

1. Takehiro Takahashi

[View author publications](#)

You can also search for this author in [PubMed](#) [Google Scholar](#)

2. Mallory K. Ellingson

[View author publications](#)

You can also search for this author in [PubMed](#) [Google Scholar](#)

3. Patrick Wong

[View author publications](#)

You can also search for this author in [PubMed](#) [Google Scholar](#)

4. Benjamin Israelow

[View author publications](#)

You can also search for this author in [PubMed](#) [Google Scholar](#)

5. Carolina Lucas

[View author publications](#)

You can also search for this author in [PubMed](#) [Google Scholar](#)

6. Jon Klein

[View author publications](#)

You can also search for this author in [PubMed](#) [Google Scholar](#)

7. Julio Silva

[View author publications](#)

You can also search for this author in [PubMed](#) [Google Scholar](#)

8. Tianyang Mao

[View author publications](#)

You can also search for this author in [PubMed](#) [Google Scholar](#)

9. Ji Eun Oh

[View author publications](#)

You can also search for this author in [PubMed](#) [Google Scholar](#)

10. Maria Tokuyama

[View author publications](#)

You can also search for this author in [PubMed](#) [Google Scholar](#)

11. Peiwen Lu

[View author publications](#)

You can also search for this author in [PubMed](#) [Google Scholar](#)

12. Arvind Venkataraman

[View author publications](#)

You can also search for this author in [PubMed](#) [Google Scholar](#)

13. Annsea Park

[View author publications](#)

You can also search for this author in [PubMed](#) [Google Scholar](#)

14. Feimei Liu

[View author publications](#)

You can also search for this author in [PubMed](#) [Google Scholar](#)

15. Amit Meir

[View author publications](#)

You can also search for this author in [PubMed](#) [Google Scholar](#)

16. Jonathan Sun

[View author publications](#)

You can also search for this author in [PubMed](#) [Google Scholar](#)

17. Eric Y. Wang

[View author publications](#)

You can also search for this author in [PubMed](#) [Google Scholar](#)

18. Arnau Casanovas-Massana

[View author publications](#)

You can also search for this author in [PubMed](#) [Google Scholar](#)

19. Anne L. Wyllie

[View author publications](#)

You can also search for this author in [PubMed](#) [Google Scholar](#)

20. Chantal B. F. Vogels

[View author publications](#)

You can also search for this author in [PubMed](#) [Google Scholar](#)

21. Rebecca Ernest

[View author publications](#)

You can also search for this author in [PubMed](#) [Google Scholar](#)

22. Sarah Lapidus

[View author publications](#)

You can also search for this author in [PubMed](#) [Google Scholar](#)

23. Isabel M. Ott

[View author publications](#)

You can also search for this author in [PubMed](#) [Google Scholar](#)

24. Adam J. Moore

[View author publications](#)

You can also search for this author in [PubMed](#) [Google Scholar](#)

25. Albert Shaw

[View author publications](#)

You can also search for this author in [PubMed](#) [Google Scholar](#)

26. John B. Fournier

[View author publications](#)

You can also search for this author in [PubMed](#) [Google Scholar](#)

27. Camila D. Odio

[View author publications](#)

You can also search for this author in [PubMed](#) [Google Scholar](#)

28. Shelli Farhadian

[View author publications](#)

You can also search for this author in [PubMed](#) [Google Scholar](#)

29. Charles Dela Cruz

[View author publications](#)

You can also search for this author in [PubMed](#) [Google Scholar](#)

30. Nathan D. Grubaugh

[View author publications](#)

You can also search for this author in [PubMed](#) [Google Scholar](#)

31. Wade L. Schulz

[View author publications](#)

You can also search for this author in [PubMed](#) [Google Scholar](#)

32. Aaron M. Ring

[View author publications](#)

You can also search for this author in [PubMed](#) [Google Scholar](#)

33. Albert I. Ko

[View author publications](#)

You can also search for this author in [PubMed](#) [Google Scholar](#)

34. Saad B. Omer

[View author publications](#)

You can also search for this author in [PubMed](#) [Google Scholar](#)

35. Akiko Iwasaki

[View author publications](#)

You can also search for this author in [PubMed](#) [Google Scholar](#)

Consortia

Yale IMPACT Research Team

- Kelly Anastasio
- , Michael H. Askenase
- , Maria Batsu
- , Hannah Beatty
- , Santos Bermejo
- , Sean Bickerton
- , Kristina Brower
- , Molly L. Bucklin
- , Staci Cahill
- , Melissa Campbell
- , Yiyun Cao

- , Edward Courchaine
- , Rupak Datta
- , Giuseppe DeIuliis
- , Bertie Geng
- , Laura Glick
- , Ryan Handoko
- , Chaney Kalinich
- , William Khoury-Hanold
- , Daniel Kim
- , Lynda Knaggs
- , Maxine Kuang
- , Eriko Kudo
- , Joseph Lim
- , Melissa Linehan
- , Alice Lu-Culligan
- , Amyn A. Malik
- , Anjelica Martin
- , Irene Matos
- , David McDonald
- , Maksym Minasyan
- , Subhasis Mohanty
- , M. Catherine Muenker
- , Nida Naushad
- , Allison Nelson
- , Jessica Nouws
- , Marcella Nunez-Smith
- , Abeer Obaid
- , Isabel Ott
- , Hong-Jai Park
- , Xiaohua Peng
- , Mary Petrone
- , Sarah Prophet
- , Harold Rahming
- , Tyler Rice
- , Kadi-Ann Rose
- , Lorenzo Sewanan
- , Lokesh Sharma
- , Denise Shepard
- , Erin Silva
- , Michael Simonov
- , Mikhail Smolgovsky

- , Eric Song
- , Nicole Sonnert
- , Yvette Strong
- , Codruta Todeasa
- , Jordan Valdez
- , Sofia Velazquez
- , Pavithra Vijayakumar
- , Haowei Wang
- , Annie Watkins
- , Elizabeth B. White
- & Yixin Yang

Contributions

A.I., S.B.O. and A.I.K. conceived the study. C.L., P.W., J.K., J. Silva, T.M. and J.E.O. defined parameters for flow cytometry experiments, collected and processed patient PBMC samples. P.W. acquired and analysed the flow cytometry data. B.I., J.K., C.L. and C.D.O. collected epidemiological and clinical data. F.L., A.M., J. Sun, E.Y.W. and A.M.R. acquired and analysed ELISA data. A.L.W., C.B.F.V., I.M.O., R.E., S.L., P.L., A.V., A.P. and M.T. performed the virus RNA concentration assays. N.D.G. supervised viral RNA concentration assays. A.C.-M. and A.J.M. processed and stored patient specimens, J.B.F., C.D.C. and S.F. assisted in patient recruitment, W.L.S. supervised clinical data management, A.S. coordinated and secured funding for PBMC collection. T.T. designed the analysis scheme, analysed and interpreted the data for the baseline analyses. M.K.E. and S.B.O. designed the analysis scheme, and interpreted the data for the longitudinal analyses. M.K.E. analysed the longitudinal data. T.T., M.K.E. and A.I. drafted the manuscript. A.I., A.M.R. and S.B.O. revised the manuscript. A.I. secured funds and supervised the project. Authors from the Yale IMPACT Research Team contributed to collection and storage of patient samples, as well as the collection of the patients' epidemiological and clinical data.

Corresponding author

Correspondence to [Akiko Iwasaki](#).

Ethics declarations

Competing interests

The authors declare no competing interests.

Additional information

Peer review information *Nature* thanks Petter Brodin, Malik Peiris and the other, anonymous, reviewer(s) for their contribution to the peer review of this work. Peer reviewer reports are available.

Publisher's note Springer Nature remains neutral with regard to jurisdictional claims in published maps and institutional affiliations.

Extended data figures and tables

[Extended Data Fig. 1 Comparison of basic clinical parameters of cohort A patient samples and plasma levels of 71 cytokines and chemokines at the first sampling of cohort A.](#)

a, Comparisons of age, BMI and DFSO at the first sampling between male and female patients in cohort A. $n = 17$ and 22 for M_Pt and F_Pt, respectively. **b**, Comparison of the plasma levels of 71 cytokines and chemokines. $n = 15$, 28, 16 and 19 for M_HCW, F_HCW, M_Pt and F_Pt, respectively. Data are mean \pm s.e.m. P values were determined by unpaired two-tailed t -test (**a**) or one-way ANOVA with Bonferroni multiple comparison test (**b**). All P values < 0.10 are shown.

[Extended Data Fig. 2 Heat maps of cytokines and chemokines, PBMC composition, T cell subsets, and T cell cytokine expression at the first sampling of cohort A patients.](#)

a, A heat map of the plasma levels (pg ml^{-1}) of 71 cytokines and chemokines. $n = 15$, 28, 16 and 19 for M_HCW, F_HCW, M_Pt and F_Pt, respectively. **b**, A heat map for the composition of PBMCs (percentage in live PBMCs). $n = 6$, 42, 16 and 21 for M_HCW, F_HCW, M_Pt and F_Pt, respectively. **c**, A heat map for the T cell subsets (percentage in CD3^+ cells). $n = 6$, 45, 16 and 22 for M_HCW, F_HCW, M_Pt and F_Pt, respectively. **d**, A heat map for the intracellular cytokine staining of T cells (percentage in CD3^+ cells). $n = 6$, 43, 16 and 22 for M_HCW, F_HCW, M_Pt and F_Pt, respectively. In all of these heat maps, log-transformed values were used for heat map generation.

[Extended Data Fig. 3 Flow cytometry gating strategy.](#)

a–c, Gating strategy used for monocytes (**a**), CD38⁺HLA-DR⁺ and PD-1⁺TIM-3⁺ CD4 or CD8 T cells (**b**), and T cell intracellular staining for IFNγ⁺ CD8 T cells (**c**).

Extended Data Table 1 Demographic and clinical characteristics of cohort A, cohort B and HCW comparison groups

[Full size table](#)

Extended Data Table 2 Background and sample information of 39 cohort A patients

[Full size table](#)

Extended Data Table 3 Adjusted least square means difference in immune response at baseline between male and female patients with COVID-19 in cohort A and male and female HCW controls

[Full size table](#)

Extended Data Table 4 Adjusted least square means difference over time in immune response between male and female patients with COVID-19 in cohort B

[Full size table](#)

Extended Data Table 5 Adjusted least square means difference over time in immune response between male and female patients with COVID-19 in cohort B and male and female healthy HCW controls

[Full size table](#)

Extended Data Table 6 Adjusted least square means difference between male and female patients with COVID-19 in cohort A by patient trajectory

[Full size table](#)

Extended Data Table 7 Definitions of each cell subset in flow cytometry with specific markers

[Full size table](#)

Supplementary information

[**Supplementary Table 1**](#)

Detailed clinical and immunological data for each patient.

[**Reporting Summary**](#)

[**Peer Review File**](#)

Rights and permissions

Reprints and Permissions

About this article



Check for
updates

Cite this article

Takahashi, T., Ellingson, M.K., Wong, P. *et al.* Sex differences in immune responses that underlie COVID-19 disease outcomes. *Nature* **588**, 315–320 (2020).
<https://doi.org/10.1038/s41586-020-2700-3>

Download citation

- Received: 04 June 2020
- Accepted: 19 August 2020
- Published: 26 August 2020
- Issue Date: 10 December 2020
- DOI: <https://doi.org/10.1038/s41586-020-2700-3>

Further reading

- [**Vaccinomics and Adversomics in the Era of Precision Medicine: A Review Based on HBV, MMR, HPV, and COVID-19 Vaccines**](#)

- Jasna Omersel
 - & Nataša Karas Kuželički

Journal of Clinical Medicine (2020)

- [**A Minimalist Strategy Towards Temporarily Defining Protection for COVID-19**](#)

- Nevio Cimolai

SN Comprehensive Clinical Medicine (2020)

- [Higher mortality of COVID-19 in males: sex differences in immune response and cardiovascular comorbidities](#)

- Laura A Bienvenu
- , Jonathan Noonan
- , Xiaowei Wang
- & Karlheinz Peter

Cardiovascular Research (2020)

- [Sex-disaggregated data confirm serum ferritin as an independent predictor of disease severity both in male and female COVID-19 patients](#)

- O. Gandini
- , A. Criniti
- , M.C. Gagliardi
- , L. Ballesio
- , S. Giglio
- , A. Balena
- , A. Caputi
- , A. Angeloni
- & C. Lubrano

Journal of Infection (2020)

- [Ist die Corona-Krise eine Lehrmeisterin für die Zukunft? Italienische Erfahrungen im Rahmen weltweiter Diskurse](#)

- Silvana Mirella Aliberti
- , Francesco De Caro
- , Giovanni Boccia
- & Mario Capunzo

Zeitschrift für Evidenz, Fortbildung und Qualität im Gesundheitswesen (2020)

Comments

By submitting a comment you agree to abide by our [Terms](#) and [Community Guidelines](#). If you find something abusive or that does not comply with our terms or guidelines please flag it as inappropriate.

[Download PDF](#)

This article was downloaded by **calibre** from <https://www.nature.com/articles/s41586-020-2700-3>

| [Section menu](#) | [Main menu](#) |

- Article
- [Published: 28 October 2020](#)

Tunable dynamics of B cell selection in gut germinal centres

- [Carla R. Nowosad^{1,2 na1},](#)
- [Luka Mesin^{1 na1},](#)
- [Tiago B. R. Castro ORCID: orcid.org/0000-0002-0359-0611^{1,2},](#)
- [Christopher Wichmann ORCID: orcid.org/0000-0002-2591-2810^{2,3},](#)
- [Gregory P. Donaldson ORCID: orcid.org/0000-0002-8551-374X²,](#)
- [Tatsuya Araki¹,](#)
- [Ariën Schiepers ORCID: orcid.org/0000-0002-5185-364X¹,](#)
- [Ainsley A. K. Lockhart²,](#)
- [Angelina M. Bilate²,](#)
- [Daniel Mucida ORCID: orcid.org/0000-0002-0000-0452² &](#)
- [Gabriel D. Victora ORCID: orcid.org/0000-0001-8807-348X¹](#)

[Nature](#) volume 588, pages321–326(2020) [Cite this article](#)

- 5303 Accesses
- 216 Altmetric
- [Metrics details](#)

Subjects

- [Antimicrobial responses](#)
- [Clonal selection](#)
- [Germinal centres](#)

Abstract

Germinal centres, the structures in which B cells evolve to produce antibodies with high affinity for various antigens, usually form transiently in lymphoid organs in response to infection or immunization. In lymphoid organs associated with the gut, however, germinal centres are chronically present. These gut-associated germinal centres can support targeted antibody responses to gut infections and immunization¹. But whether B cell selection and antibody affinity maturation take place in the face of the chronic and diverse antigenic stimulation characteristic of these structures under steady state is less clear^{2,3,4,5,6,7,8}. Here, by combining multicolour ‘Brainbow’ cell-fate mapping and sequencing of immunoglobulin genes from single cells, we find that 5–10% of gut-associated germinal centres from specific-pathogen-free (SPF) mice contain highly dominant ‘winner’ B cell clones at steady state, despite rapid turnover of germinal-centre B cells. Monoclonal antibodies derived from these clones show increased binding, compared with their unmutated precursors, to commensal bacteria, consistent with antigen-driven selection. The frequency of highly selected gut-associated germinal centres is markedly higher in germ-free than in SPF mice, and winner B cells in germ-free germinal centres are enriched in ‘public’ clonotypes found in multiple individuals, indicating strong selection of B cell antigen receptors even in the absence of microbiota. Colonization of germ-free mice with a defined microbial consortium (Oligo-MM¹²) does not eliminate germ-free-associated clonotypes, yet does induce a concomitant commensal-specific B cell response with the hallmarks of antigen-driven selection. Thus, positive selection of B cells can take place in steady-state gut-associated germinal centres, at a rate that is tunable over a wide range by the presence and composition of the microbiota.

[Access through your institution](#)

[Change institution](#)

[Buy or subscribe](#)

Access options

Subscribe to Journal

Get full journal access for 1 year

185,98 €

only 3,58 € per issue

[Subscribe](#)

All prices are NET prices.

VAT will be added later in the checkout.

Rent or Buy article

Get time limited or full article access on ReadCube.

from \$8.99

[Rent or Buy](#)

All prices are NET prices.

Additional access options:

- [Log in](#)
- [Access through your institution](#)
- [Learn about institutional subscriptions](#)

Fig. 1: Kinetics of clonal selection in steady-state gaG Cs.

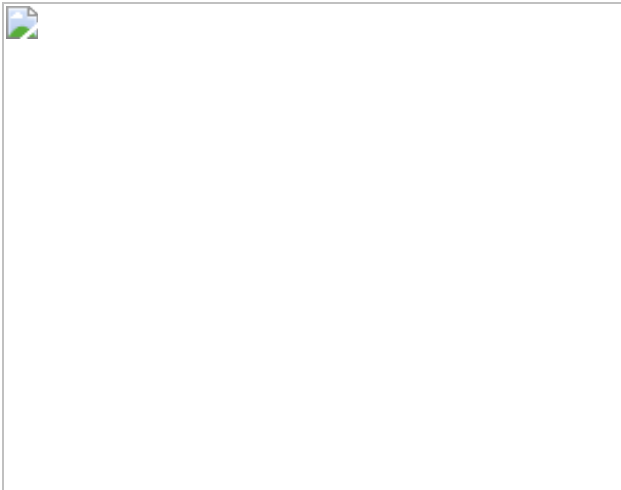


Fig. 2: Selection of commensal-binding clones in steady-state gaGCs.

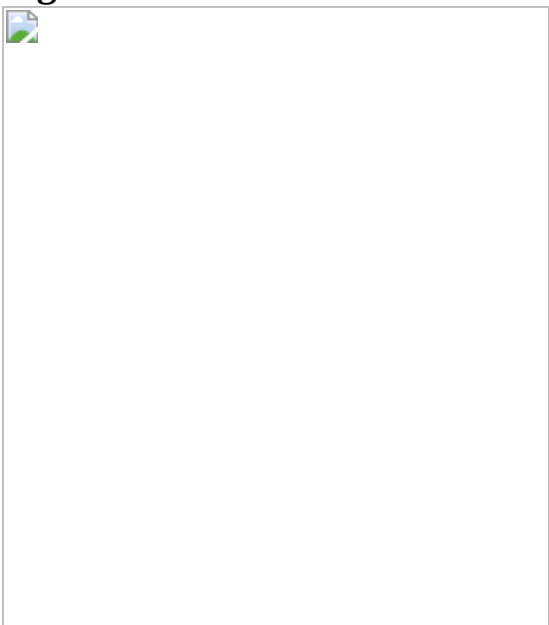


Fig. 3: Accelerated selection in gaGCs of germ-free and Oligo-MM¹²-colonized mice.



Fig. 4: Prominent public clonotypes in gaGCs of germ-free and Oligo-MM¹²-colonized mice.



Data availability

Incidence-based sequencing raw and processed data are available through BioProject (<https://www.ncbi.nlm.nih.gov/bioproject/>; identification code PRJNA647715); the analysis pipeline is available at <https://github.com/victoraLab/MIBS>.

References

1. 1.

Bergqvist, P. et al. Re-utilization of germinal centers in multiple Peyer's patches results in highly synchronized, oligoclonal, and affinity-matured gut IgA responses. *Mucosal Immunol.* **6**, 122–135 (2013).

[CAS](#) [Article](#) [Google Scholar](#)

2. 2.

Casola, S. et al. B cell receptor signal strength determines B cell fate. *Nat. Immunol.* **5**, 317–327 (2004).

[CAS](#) [Article](#) [Google Scholar](#)

3. 3.

Yeap, L. S. et al. Sequence-intrinsic mechanisms that target AID mutational outcomes on antibody genes. *Cell* **163**, 1124–1137 (2015).

[CAS](#) [Article](#) [Google Scholar](#)

4. 4.

Bunker, J. J. et al. Natural polyreactive IgA antibodies coat the intestinal microbiota. *Science* **358**, eaan6619 (2017).

[Article](#) [Google Scholar](#)

5. 5.

Reboldi, A. & Cyster, J. G. Peyer's patches: organizing B cell responses at the intestinal frontier. *Immunol. Rev.* **271**, 230–245 (2016).

[CAS](#) [Article](#) [Google Scholar](#)

6. 6.

Bemark, M. et al. Somatic hypermutation in the absence of DNA-dependent protein kinase catalytic subunit (DNA-PK(cs)) or recombination-activating gene (RAG)1 activity. *J. Exp. Med.* **192**, 1509–1514 (2000).

[CAS](#) [Article](#) [Google Scholar](#)

7. 7.

Biram, A. et al. B cell diversification is uncoupled from SAP-mediated selection forces in chronic germinal centers within Peyer's patches. *Cell Rep.* **30**, 1910–1922 (2020).

[CAS](#) [Article](#) [Google Scholar](#)

8. 8.

Bunker, J. J. & Bendelac, A. IgA responses to microbiota. *Immunity* **49**, 211–224 (2018).

[CAS](#) [Article](#) [Google Scholar](#)

9. 9.

Casola, S. & Rajewsky, K. B cell recruitment and selection in mouse GALT germinal centers. *Curr. Top. Microbiol. Immunol.* **308**, 155–171 (2006).

[CAS](#) [PubMed](#) [Google Scholar](#)

10. 10.

Biram, A. et al. BCR affinity differentially regulates colonization of the subepithelial dome and infiltration into germinal centers within Peyer's patches. *Nat. Immunol.* **20**, 482–492 (2019).

[CAS](#) [Article](#) [Google Scholar](#)

11. 11.

Tas, J. M. et al. Visualizing antibody affinity maturation in germinal centers. *Science* **351**, 1048–1054 (2016).

[ADS](#) [CAS](#) [Article](#) [Google Scholar](#)

12. 12.

Victora, G. D. et al. Germinal center dynamics revealed by multiphoton microscopy with a photoactivatable fluorescent reporter. *Cell* **143**, 592–605 (2010).

[CAS](#) [Article](#) [Google Scholar](#)

13. 13.

Livet, J. et al. Transgenic strategies for combinatorial expression of fluorescent proteins in the nervous system. *Nature* **450**, 56–62 (2007).

[ADS](#) [CAS](#) [Article](#) [Google Scholar](#)

14. 14.

Shinnakasu, R. et al. Regulated selection of germinal-center cells into the memory B cell compartment. *Nat. Immunol.* **17**, 861–869 (2016).

[CAS](#) [Article](#) [Google Scholar](#)

15. 15.

Meyer-Hermann, M., Binder, S. C., Mesin, L. & Victora, G. D. Computer simulation of multi-color Brainbow staining and clonal evolution of B cells in germinal centers. *Front. Immunol.* **9**, 2020 (2018).

[Article](#) [Google Scholar](#)

16. 16.

Tiller, T., Busse, C. E. & Wardemann, H. Cloning and expression of murine Ig genes from single B cells. *J. Immunol. Methods* **350**, 183–193 (2009).

[CAS](#) [Article](#) [Google Scholar](#)

17. 17.

Meffre, E. et al. Surrogate light chain expressing human peripheral B cells produce self-reactive antibodies. *J. Exp. Med.* **199**, 145–150 (2004).

[CAS](#) [Article](#) [Google Scholar](#)

18. 18.

Pollard, M. in *Germinal Centers in Immune Responses* (eds Odartchenko, N. et al.) 343–348 (Springer, 1967).

19. 19.

Brugiroux, S. et al. Genome-guided design of a defined mouse microbiota that confers colonization resistance against *Salmonella enterica* serovar Typhimurium. *Nat. Microbiol.* **2**, 16215 (2016).

[CAS](#) [Article](#) [Google Scholar](#)

20. 20.

Esterházy, D. et al. Compartmentalized gut lymph node drainage dictates adaptive immune responses. *Nature* **569**, 126–130 (2019).

[ADS](#) [Article](#) [Google Scholar](#)

21. 21.

Greiff, V. et al. Systems analysis reveals high genetic and antigen-driven predetermination of antibody repertoires throughout B cell development. *Cell Rep.* **19**, 1467–1478 (2017).

[CAS](#) [Article](#) [Google Scholar](#)

22. 22.

Chen, H. et al. BCR selection and affinity maturation in Peyer's patch germinal centres. *Nature* **582**, 421–425 (2020).

[ADS](#) [CAS](#) [Article](#) [Google Scholar](#)

23. 23.

Madisen, L. et al. A robust and high-throughput Cre reporting and characterization system for the whole mouse brain. *Nat. Neurosci.* **13**, 133–140 (2010).

[CAS](#) [Article](#) [Google Scholar](#)

24. 24.

Dogan, I. et al. Multiple layers of B cell memory with different effector functions. *Nat. Immunol.* **10**, 1292–1299 (2009).

[CAS](#) [Article](#) [Google Scholar](#)

25. 25.

Liu, K. et al. In vivo analysis of dendritic cell development and homeostasis. *Science* **324**, 392–397 (2009).

[ADS](#) [CAS](#) [Article](#) [Google Scholar](#)

26. 26.

Shulman, Z. et al. T follicular helper cell dynamics in germinal centers. *Science* **341**, 673–677 (2013).

[ADS](#) [CAS](#) [Article](#) [Google Scholar](#)

27. 27.

Trombetta, J. J. et al. Preparation of single-cell RNA-seq libraries for next generation sequencing. *Curr. Protoc. Mol. Biol.* **107**, 4.22.1-17 (2014).

[Article](#) [Google Scholar](#)

28. 28.

Mesin, L. et al. Restricted clonality and limited germinal center reentry characterize memory B cell reactivation by boosting. *Cell* **180**, 18–20 (2020).

[Article](#) [Google Scholar](#)

29. 29.

Lefranc, M. P. et al. IMGT, the international ImMunoGeneTics information system. *Nucleic Acids Res.* **37**, D1006–D1012 (2009).

[CAS](#) [Article](#) [Google Scholar](#)

30. 30.

Masella, A. P., Bartram, A. K., Truszkowski, J. M., Brown, D. G. & Neufeld, J. D. PANDAseq: paired-end assembler for illumina sequences. *BMC Bioinformatics* **13**, 31 (2012).

[CAS](#) [Article](#) [Google Scholar](#)

31. 31.

Retter, I., Althaus, H. H., Münch, R. & Müller, W. VBASE2, an integrative V gene database. *Nucleic Acids Res.* **33**, D671–D674 (2005).

[CAS](#) [Article](#) [Google Scholar](#)

32. 32.

DeWitt, W. S., III, Mesin, L., Victora, G. D., Minin, V. N. & Matsen, F. A., IV. Using genotype abundance to improve phylogenetic inference. *Mol. Biol. Evol.* **35**, 1253–1265 (2018).

[CAS](#) [Article](#) [Google Scholar](#)

33. 33.

Notredame, C., Higgins, D. G. & Heringa, J. T-Coffee: a novel method for fast and accurate multiple sequence alignment. *J. Mol. Biol.* **302**, 205–217 (2000).

[CAS](#) [Article](#) [Google Scholar](#)

34. 34.

Crooks, G. E., Hon, G., Chandonia, J. M. & Brenner, S. E. WebLogo: a sequence logo generator. *Genome Res.* **14**, 1188–1190 (2004).

[CAS](#) [Article](#) [Google Scholar](#)

35. 35.

Gupta, N. T. et al. Change-O: a toolkit for analyzing large-scale B cell immunoglobulin repertoire sequencing data. *Bioinformatics* **31**, 3356–3358 (2015).

[CAS](#) [Article](#) [Google Scholar](#)

36. 36.

Krzywinski, M. et al. Circos: an information aesthetic for comparative genomics. *Genome Res.* **19**, 1639–1645 (2009).

[CAS](#) [Article](#) [Google Scholar](#)

37. 37.

Pasqual, G., Angelini, A. & Victora, G. D. Triggering positive selection of germinal center B cells by antigen targeting to DEC-205. *Methods Mol. Biol.* **1291**, 125–134 (2015).

[CAS](#) [Article](#) [Google Scholar](#)

38. 38.

Palm, N. W. et al. Immunoglobulin A coating identifies colitogenic bacteria in inflammatory bowel disease. *Cell* **158**, 1000–1010 (2014).

[CAS](#) [Article](#) [Google Scholar](#)

39. 39.

Mouquet, H. et al. Polyreactivity increases the apparent affinity of anti-HIV antibodies by heterooligation. *Nature* **467**, 591–595 (2010).

[ADS](#) [CAS](#) [Article](#) [Google Scholar](#)

40. 40.

Chao, A. Nonparametric-estimation of the number of classes in a population. *Scand. J. Stat.* **11**, 265–270 (1984).

[MathSciNet](#) [Google Scholar](#)

41. 41.

Colwell, R. K. EstimateS: Statistical estimation of species richness and shared species from samples. Version 9. <http://purl.oclc.org/estimates> (2013).

[Download references](#)

Acknowledgements

We thank all members of the Victora and Mucida laboratories, past and present, for assistance with experiments, fruitful discussions and critical reading of the manuscript. In particular we thank: A. Rogoz and G. Fayzikhodjaeva for maintaining gnotobiotic mice; S. Gonzalez for maintaining SPF mice; K. Gordon and K. Chhospel for FACS; the Rockefeller University Genomics Center for RNA sequencing; and employees of the Rockefeller University for continuous assistance. We thank A. Vale (Universidade Federal do Rio de Janeiro, Brazil) for help with analysis of public clonotypes; K. McCoy (University of Calgary, Canada), S. Y. Wong and K. Cadwell (New York University, USA) for providing Oligo-MM¹² strains; J. Faith (Mount Sinai School of Medicine, USA) for other bacterial strains; and J Däbritz and E. Wirthgen (University of Rostock, Germany) for contributing to the training and supervision of C.W. This work was supported by National Institutes of Health (NIH)/National Institute of Allergy and Infectious Diseases (NIAID) grants R01AI119006 and R01AI139117 (to G.D.V.), and NIH/NIAID/National Institute of Diabetes and Digestive and Kidney Diseases (NIDDK) grants R01DK093674, R01DK113375 and R21AI144827 (to D.M.), with additional support from NIH grant DP1AI144248 (Pioneer Award) and from the Robertson Foundation to G.D.V. and NIH grant R01DK116646 (Transformative Award) to D.M. C.R.N. is a Human Frontier of Science Program postdoctoral fellow. G.P.D. is a Robert Black Fellow of the Damon Runyon Cancer Research Foundation. A.S. is a Boehringer-Ingelheim Fonds PhD fellow. G.D.V. and D.M. are Burroughs-Wellcome Investigators in the Pathogenesis of Infectious Disease. G.D.V. is a Searle Scholar, a Pew-Stewart Scholar, and a MacArthur Fellow.

Author information

Author notes

1. These authors contributed equally: Carla R. Nowosad, Luka Mesin

Affiliations

1. Laboratory of Lymphocyte Dynamics, The Rockefeller University, New York, NY, USA

Carla R. Nowosad, Luka Mesin, Tiago B. R. Castro, Tatsuya Araki, Ariën Schiepers & Gabriel D. Victora

2. Laboratory of Mucosal Immunology, The Rockefeller University, New York, NY, USA

Carla R. Nowosad, Tiago B. R. Castro, Christopher Wichmann, Gregory P. Donaldson, Ainsley A. K. Lockhart, Angelina M. Bilate & Daniel Mucida

3. Mucosal Immunology Group, Department of Pediatrics, University Medical Center Rostock, Rostock, Germany

Christopher Wichmann

Authors

1. Carla R. Nowosad

[View author publications](#)

You can also search for this author in [PubMed](#) [Google Scholar](#)

2. Luka Mesin

[View author publications](#)

You can also search for this author in [PubMed](#) [Google Scholar](#)

3. Tiago B. R. Castro

[View author publications](#)

You can also search for this author in [PubMed](#) [Google Scholar](#)

4. Christopher Wichmann

[View author publications](#)

You can also search for this author in [PubMed](#) [Google Scholar](#)

5. Gregory P. Donaldson

[View author publications](#)

You can also search for this author in [PubMed](#) [Google Scholar](#)

6. Tatsuya Araki

[View author publications](#)

You can also search for this author in [PubMed](#) [Google Scholar](#)

7. Ariën Schiepers

[View author publications](#)

You can also search for this author in [PubMed](#) [Google Scholar](#)

8. Ainsley A. K. Lockhart

[View author publications](#)

You can also search for this author in [PubMed](#) [Google Scholar](#)

9. Angelina M. Bilate

[View author publications](#)

You can also search for this author in [PubMed](#) [Google Scholar](#)

10. Daniel Mucida

[View author publications](#)

You can also search for this author in [PubMed](#) [Google Scholar](#)

11. Gabriel D. Victora

[View author publications](#)

You can also search for this author in [PubMed](#) [Google Scholar](#)

Contributions

C.R.N. and L.M. performed all mouse and antibody-sequencing experiments, with help from T.A. C.W. and C.R.N. produced and assayed

the reactivity of monoclonal antibodies by ELISA, with help from A.S. G.P.D. stained monoclonal antibodies in cultured bacteria and carried out and dot and western blots. A.M.B. optimized and performed flow cytometry of faecal bacteria. A.A.K.L. established the protein-free-diet protocol. L.M. and T.B.R.C. designed and performed all bioinformatics analyses. C.R.N., D.M. and G.D.V. conceptualized the study, designed all experiments, and wrote the manuscript with input from all authors.

Corresponding authors

Correspondence to [Daniel Mucida](#) or [Gabriel D. Victora](#).

Ethics declarations

Competing interests

The authors declare no competing financial interests.

Additional information

Peer review information *Nature* thanks Ramy Arnaout, Rachael Bashford-Rogers and Hai Qi for their contribution to the peer review of this work.

Publisher's note Springer Nature remains neutral with regard to jurisdictional claims in published maps and institutional affiliations.

Extended data figures and tables

[Extended Data Fig. 1 Clonal replacement in steady-state gaGCs.](#)

- a, Gating strategy for PA-GFP mice used in Fig. [1a–d](#). GC, germinal centre.
- b, Gating strategy and efficiency of labelling in germinal centres of AID-Confetti mice seven days after the administration of tamoxifen, as in Fig. [1e](#). The labelling efficiency is calculated as 100% minus the product of the

percentage of unlabelled cells in the GFP/YFP, RFP and CFP channels. **c**, Gating strategy for the *S1pr2*^{CreERT2}/tdTomato fate-mapping experiments shown in **g** and Fig. [1h](#). All flow plots are representative of multiple experiments. **d**, Multiphoton images of Peyer's patches from SPF mice at different times after tamoxifen treatment (see Fig. [1f](#)). Values in parentheses in images are NDS values. **e**, Quantification of multiple images as exemplified in **d** (see also Fig. [1g](#)). Data are from three to five mice per time point at days 14–35, and one to two mice per time point for day 7 and later times. **f**, Size of germinal centres in Peyer's patches (PPs) versus mLNs, calculated from samples obtained seven days after tamoxifen treatment as in **d** and Fig. [1f](#), plotted as the cross-sectional area of the largest available z-section. Each symbol represents one germinal centre. Lines show medians; *P* values are from two-tailed Mann–Whitney *U* tests. Data are pooled from multiple mLNs and Peyer's patches of two mice from two independent experiments. **g**, Turnover of B cell clones in germinal centres of Peyer's patches from *S1pr2*^{CreERT2} × *Rosa26*^{Stop-tdTomato} mice (see Fig. [1h](#)).

[Extended Data Fig. 2 Binding characteristics of ‘winner’ gaGC clones from SPF mice.](#)

a, Gating strategy for isolating AID-Confetti single germinal centres shown in **b**, **c**, Figs. [2a](#), [3d](#), [e](#) and Extended Data Figs. [6a](#), [b](#), [8a](#). CR, CFP and/or RFP; non CR, non-CFP, non-RFP, GY, GFP and/or YFP. **b**, **c**, Additional *Igh* sequence relationships among B cells from high-NDS germinal centres (**b**) and one low-NDS germinal centre (**c**) (see Fig. [2a](#)). Scale bars, 50 μm. In **c**, each tree is for a separate clone (defined as a unique V(D)J rearrangement). Only clones with more than five cells are shown (grey slices in pie charts). **d**, Gating strategy for bacterial flow cytometry, performed in **e**, Figs. [2b](#), [3f](#), [h](#), [i](#) and Extended Data Fig. [6d](#). **e**, Flow-cytometry analysis of the binding of recombinant monoclonal antibodies to faecal bacteria isolated from SPF mice. Plots gated as in **d**. All plots are representative of data obtained from at least two separate experiments. **f**, Summary of the reactivity of SPF monoclonal antibodies, assayed by ELISA against food protein extracts, autoantigens (anti-nuclear antibody, ANA), and a five-antigen polyreactivity panel comprising single-stranded DNA, double-stranded DNA, keyhole limpet haemocyanin (KLH), insulin

and LPS. Shown are background-subtracted OD₄₅₀ values. Data representative of assays repeated in at least three separate experiments.

Extended Data Fig. 3 Stable vertical transmission of the Oligo-MM¹² consortium.

a–c, qPCR of total (**a**) and strain-specific (**b, c**) 16S DNA from faecal samples of mice stably colonized with the Oligo-MM¹² consortium. In **a**, ΔC_t values were calculated in respect to a reference SPF sample, marked by the black filled symbols, with which all other values were compared. In **c**, C_t values were used to quantify the relative abundance of each species (see [Methods](#)). LOD, limit of detection. F₁ refers to the first generation after the parental strain (P, colonized by gavage). Note that *Bifidobacterium animalis* (YL2) is usually undetectable in faeces^{[19](#)}.

Extended Data Fig. 4 Frequency and isotype distribution of gaGCs in germ-free and Oligo-MM¹²-colonized mice.

a, Gating strategy for analysing the frequency of germinal centres and distribution of isotypes (results shown in **b–d**). **b**, Frequency of cells with the phenotype of germinal centres (CD38[−] FAS^{hi}) among total B220⁺ B cells in the indicated organs of mice raised under the indicated conditions. Each symbol represents one mouse. SPF, n = 25; germ-free (GF), n = 16; Oligo-MM¹², n = 11. **c**, Frequency of germinal-centre B cells positive for the indicated surface BCR isotype in different organs of mice raised under the indicated conditions. Data are from at least three mice per group, as in **d**. Data are presented as means ± s.e.m. **d**, Statistical analysis of selected isotypes and anatomical locations, using data from **c**. Each symbol represents one mouse. Lines indicate medians; P values are obtained from two-tailed Kruskall–Wallis tests carried out on each trio, with Dunn’s multiple comparisons post-test. All P values below 0.05 are reported.

Extended Data Fig. 5 Clonal selection in germ-free and Oligo-MM¹²-colonized mice.

a, Gating strategy for germ-free AID-Confetti single germinal centres used in **b–d**. **b–d**, Sequencing of *Igh* genes from B cells obtained from individual mLNs germinal centres. Germinal-centre B cells were single-cell-sorted from fragments of vibratome slices containing single germinal centres. To avoid biased selection of germinal centres based on NDS or loss of germinal centres with a low density of coloured cells, mLNs were harvested at five to seven days after treatment with tamoxifen, before extensive selection or clonal turnover; both fluorescent and non-fluorescent cells were included in the sample. This unbiased selection ensures that data are comparable to those obtained using *in situ* photoactivation (Fig. [1a–d](#)), which we could not perform because the photoactivatable GFP-transgenic strain is not available under germ-free status. **b**, Clonal composition of individual germinal centres from five mice (GF1–GF5). C, caecal-colonic mLNs; J, jejunal mLNs. **c**, Quantification of data from **b**. Each symbol represents one germinal centre. **d**, Proportion of germinal centres in which the largest clone accounts for more than 50% of all B cells in mLNs of SPF mice (data from Fig. [1b](#)) and germ-free mice (data from **b**). *P* values are from two-tailed Fisher's exact tests. Centre bars represent the proportion in the sample; error bars show the exact binomial 95% confidence interval. **e**, Multiphoton images of Oligo-MM¹² mLNs and Peyer's patches at different times after treatment with tamoxifen. Blue represents collagen (second harmonics); white shows autofluorescence; other colours are from the Confetti allele. Scale bars, 200 µm (overviews), 50 µm (close-ups). N/D, NDS not determined owing to a low density of coloured cells. **f**, Quantification of images as in **e** for mLNs (top) and Peyer's patches (bottom). Each symbol represents one germinal centre. Medians are indicated. Only germinal centres with a density of more than 0.4 fluorescent cells per 100 µm² are included in the NDS calculations. **g**, Proportion of germinal centres with NDS values of more than 0.75 in mLNs (top) and more than 0.5 in Peyer's patches (bottom) under SPF, germ-free and Oligo-MM¹² conditions at 20–23 days after tamoxifen; SPF and germ-free data are as in Fig. [3c](#). For SPF, Oligo-MM¹² and germ-free mLNs gaGCs, *n* = 57, 16 and 27, respectively; for gaGCs from Peyer's patches, *n* = 20, 10 and 9, respectively. *P* values obtained by two-tailed Fisher's exact tests. Error bars represent exact binomial 95% confidence intervals. All data are from three to five mice per time point.

Extended Data Fig. 6 Characteristics of ‘winner’ gaGC clones from germ-free and Oligo-MM¹²-colonized mice.

a, b, Additional *Igh* sequence relationships among B cells from high-NDS germinal centres of germ-free (**a**) and Oligo-MM¹²-colonized (**b**) mice. Details are as in Fig. 2a. Scale bars, 50 µm. **c,** Reactivity summary of germ-free monoclonal antibodies assayed by ELISA against food protein extracts, autoantigens (anti-nuclear antibody, ANA), and a five-antigen polyreactivity panel. Shown are background subtracted OD₄₅₀ values. **d,** Flow-cytometry analysis of the binding of monoclonal antibodies from germ-free mice to faecal bacteria from SPF mice. Details are as in Fig. 2b. **e,** ELISA analysis of the binding of monoclonal antibodies from germ-free mice to faecal bacterial fractions from SPF mice. MG053 was assayed at three dilutions only. Other monoclonal antibodies were assayed at dilutions indicated on the x-axis. Lines show the means of two assays. **f,** Western blot (WB) analysis of the binding of monoclonal antibodies from germ-free mice to a protein extract from mouse ileum tissue, run on a single-well 4–15% gel and blotted using a multiwell mask. Monoclonal antibody 3H9 is a DNA-specific negative control. Data in c–f are representative of two or more independent experiments.

Extended Data Fig. 7 Mutational patterns in germ-free/Oligo-MM¹² public clonotypes.

a, Dendrograms showing the sequence relationships between V_H1–47 and V_H1–12 clones in different mice. All clones with up to two-amino-acid differences from the public-clonotype CDR_H3 motifs are included. **b,** Heat maps showing the frequency of amino-acid replacements along the V_H1–47 and V_H1–12 families in germ-free (blue) and Oligo-MM¹² (green) mice, using the same data as in Fig. 4b. Only mice with more than two cells within the specified clone were included in the analysis. The number of cells analysed per mouse is indicated at the top of each column. Only those amino acids mutated in at least three (V_H1–47) or two (V_H1–12) mice are listed on the left, using Immunogenetics (IMGT; <http://www.imgt.org>)

numbering; to the right, the most frequent amino-acid replacement in each mouse is given. Arrows indicate recurrent amino-acid mutations found in five of six mice (V_H 1–47) or three of three mice (V_H 1–12).

Extended Data Fig. 8 Stereotypical germ-free IgH clonotypes are present in Oligo-MM¹² and germ-free/dietary-protein-free conditions.

a, Massive expansion of a public V_H 1–12 clonotype across different secondary lymphoid organs of mouse MM¹² 1 (from Fig. 4b), at 21 days after tamoxifen treatment. Multiphoton images show all three germinal centres sequenced from this mouse (yellow dotted boxes), magnified in the side panels. Scale bars, 200 μm (overviews) and 50 μm (close-ups). mLNs close-ups are from different image acquisitions of the same germinal centre. A clonal tree of all cells from this clone is shown at the bottom right. Arrowheads indicate clonal bursts and the organ of origin of cells with that particular sequence. **b**, Frequency of cells with a germinal-centre phenotype ($CD38^{\text{dim}} FAS^{\text{hi}}$) among total $B220^+$ B cells in the indicated organs of mice raised on protein-free chow (PFC). Data for SPF and germ-free mice are reproduced from Extended Data Fig. 4b. Each symbol represents one mouse. For PFC, $n = 8$ mice. **c**, Clonal distribution of germinal-centre B cells sequenced from the indicated tissues of three separate mice (PFC1–3), with public clonotypes colour-coded. See also Fig. 4b. C, caecal colonic mLNs; D, duodenal mLNs; I, ileal mLNs; PP, Peyer's patches.

Extended Data Fig. 9 Multiwell incidence-based *Igh* sequencing reveals clonal overlap among individual mice and between microbial colonization conditions.

a, Overview of the incidence-based *Igh* sequencing method used for c–g and Fig. 4c, d. To identify expanded public clonotypes among gaGC samples from multiple mice with high confidence, we developed an incidence-based sequencing strategy based on repeated sampling of the same germinal-centre B cell population. We sorted multiple samples of 100 germinal-centre B cells (usually 32 for mLNs and 16 for Peyer's patches)

from 6 germ-free, 6 SPF, and 7 Oligo-MM¹²-colonized mice, and sequenced all BCRs in each sample, for a total of roughly 80 thousand input B cells, plus 32 wells each of non-germinal-centre B cells from the mLN of 3 germ-free and 3 SPF mice as controls. To avoid counting as ‘public’ sequences that were spuriously present in different mice owing to barcode misassignment or DNA contamination, we included in our analysis only those clones that were represented by more than five reads in any single well and found in at least two wells from the same sample. Key bioinformatics steps are described in the figure; see [Methods](#) for a full description of the bioinformatic pipeline. **b**, Gating strategy used for data in **c–g** and Fig. [4c, d](#), described in **a**. **c**, Number of distinct clones per well, after collapsing sequences with matching V_H, J_H, and CDR_H3 nucleotide sequences. Each symbol represents one well. Boxes represent medians and interquartile ranges. As expected, non-germinal-centre B cell samples had many more total clones per well than did germinal-centre B cells. **d**, Proportion of expanded clones (present in more than one well per sample) in germinal-centre and non-germinal-centre samples from mLNs and Peyer’s patches of mice held under the specified conditions. **e**, Histograms showing Levenshtein distances between the indicated consensus CDR_H3 sequence and the CDR_H3 sequence of all clones in the indicated category. For ARGSNYXXXXDY, distances are plotted for clones carrying the ‘correct’ V_H1–47 gene or two ‘control’ V_H regions with similar usage frequency in our sample. *P* values were obtained by Kruskall–Wallis test comparing all three conditions. Owing to the very low number of total V_H1–12 clones outside of the germ-free condition, distances to the AREGFAY CDR_H3 are compared between V_H1–12 clones and all clones. *P* values obtained by two-tailed Mann–Whitney *U* test. **f**, Fraction of clone*wells containing public clonotypes in each condition, pooled from all mice. *P* values were obtained by Fisher’s exact test. **g**, Venn diagram showing the number of clones per condition (pooled from all mice) and overlap between conditions. The clone in the centre of the graph (SPF/Oligo-MM¹²/germ-free overlap) corresponds to the V_H1–47 public clonotype. In **f, g**, data are as in Fig. [4d](#).

Supplementary information

Supplementary Data

Supplementary Spreadsheet 1. *Ig* sequence information for single-cell sequences used throughout the manuscript, organized in labeled tabs according to colonization status/sequence use (for monoclonal antibody production, for clonal trees etc).

Reporting Summary

Supplementary Information

PDF containing further information under the following headings: Use of the AID-Confetti model to estimate the rate of GC selection, Supplementary discussion and Supplementary text references.

Supplementary Table

Supplementary Table S1. List of mABs produced and their characteristics.

Supplementary Table

Supplementary Table S2. Ingredients in protein-free chow.

Supplementary Table

Supplementary Table S3. Antibodies used for flow cytometry.

Supplementary Table

Supplementary Table S4. Bacterial strains/isolates used.

Supplementary Table

Supplementary Table S5. Primers used for QPCR amplification of individual Oligo-MM¹² bacteria.

Rights and permissions

[Reprints and Permissions](#)

About this article



Check for
updates

Cite this article

Nowosad, C.R., Mesin, L., Castro, T.B.R. *et al.* Tunable dynamics of B cell selection in gut germinal centres. *Nature* **588**, 321–326 (2020).
<https://doi.org/10.1038/s41586-020-2865-9>

[Download citation](#)

- Received: 07 March 2020
- Accepted: 29 July 2020
- Published: 28 October 2020
- Issue Date: 10 December 2020
- DOI: <https://doi.org/10.1038/s41586-020-2865-9>

Comments

By submitting a comment you agree to abide by our [Terms](#) and [Community Guidelines](#). If you find something abusive or that does not comply with our terms or guidelines please flag it as inappropriate.

[Access through your institution](#)

[Change institution](#)

Buy or subscribe

This article was downloaded by **calibre** from <https://www.nature.com/articles/s41586-020-2865-9>

| [Section menu](#) | [Main menu](#) |

Receptor binding and priming of the spike protein of SARS-CoV-2 for membrane fusion

[Download PDF](#)

- Article
- [Published: 17 September 2020](#)

Receptor binding and priming of the spike protein of SARS-CoV-2 for membrane fusion

- [Donald J. Benton](#) [ORCID: orcid.org/0000-0001-6748-9339^{1 na1}](#),
- [Antoni G. Wrobel](#) [ORCID: orcid.org/0000-0002-6680-5587^{1 na1}](#),
- [Pengqi Xu^{2,3}](#),
- [Chloë Rouston⁴](#),
- [Stephen R. Martin¹](#),
- [Peter B. Rosenthal](#) [ORCID: orcid.org/0000-0002-0387-2862⁵](#),
- [John J. Skehel¹](#) &
- [Steven J. Gamblin](#) [ORCID: orcid.org/0000-0001-5331-639X¹](#)

[Nature](#) volume 588, pages327–330(2020)[Cite this article](#)

- 27k Accesses
- 9 Citations
- 210 Altmetric
- [Metrics details](#)

Subjects

- [Cryoelectron microscopy](#)
- [SARS-CoV-2](#)

Abstract

Infection with severe acute respiratory syndrome coronavirus 2 (SARS-CoV-2) is initiated by virus binding to the ACE2 cell-surface receptors^{1,2,3,4}, followed by fusion of the virus and cell membranes to release the virus genome into the cell. Both receptor binding and membrane fusion activities are mediated by the virus spike glycoprotein^{5,6,7}. As with other class-I membrane-fusion proteins, the spike protein is post-translationally cleaved, in this case by furin, into the S1 and S2 components that remain associated after cleavage^{8,9,10}. Fusion activation after receptor binding is proposed to involve the exposure of a second proteolytic site (S2'), cleavage of which is required for the release of the fusion peptide^{11,12}. Here we analyse the binding of ACE2 to the furin-cleaved form of the SARS-CoV-2 spike protein using cryo-electron microscopy. We classify ten different molecular species, including the unbound, closed spike trimer, the fully open ACE2-bound trimer and dissociated monomeric S1 bound to ACE2. The ten structures describe ACE2-binding events that destabilize the spike trimer, progressively opening up, and out, the individual S1 components. The opening process reduces S1 contacts and unshields the trimeric S2 core, priming the protein for fusion activation and dissociation of ACE2-bound S1 monomers. The structures also reveal refolding of an S1 subdomain after ACE2 binding that disrupts interactions with S2, which involves Asp614^{13,14,15} and leads to the destabilization of the structure of S2 proximal to the secondary (S2') cleavage site.

[Download PDF](#)

Main

Recognition of the ACE2 receptor by the membrane spike glycoprotein of SARS-CoV-2 is a major determinant of virus infectivity, pathogenesis and host range. Previous structural studies on the spike glycoproteins of coronaviruses^{6,16,17,18,19,20,21,22} have shown that the spike trimer consists of a central helical stalk—comprising three interacting S2 components—that is covered at the top by S1. Each S1 component consists of two large domains, the N-terminal domain (NTD) and receptor-binding domain (RBD), each associated with a smaller intermediate subdomain. In virus membranes, spike glycoproteins exist in a closed form, in which the RBDs cap the top of the S2 core and are inaccessible to ACE2, and in an open form, in which one S1 component has opened to expose the RBD for ACE2 binding^{6,16,18,23}. Recent structural studies^{7,24,25} on the isolated RBD of the SARS-CoV-2 spike protein in complex with ACE2 have provided a molecular description of the receptor-binding interface. Although some comparisons can be inferred from the previous cryo-electron microscopy studies on the spike protein of SARS-CoV^{12,18,19,23}, structures of intact trimeric SARS-CoV-2 spike with bound

ACE2 are needed to determine the effects of binding on the overall spike conformation.

To examine this interaction between the SARS-CoV-2 spike protein and its receptor, we mixed the ectodomains of furin-cleaved spike with the ectodomains of ACE2 and incubated them for around 60 s before plunge-freezing the mixture in liquid ethane for examination by cryo-electron microscopy. In the images that we obtained, we could resolve ten distinct species of spike and spike–ACE2 complexes (Fig. 1 and Extended Data Fig. 1), ranging from tightly closed, unbound trimers to open trimers that formed complexes with three ACE2 molecules and dissociated monomeric S1–ACE2 complexes. Of the spike trimers analysed, two thirds were bound to ACE2 (Extended Data Fig. 1). Of the unbound species, we observe good-quality particles in the closed unbound conformation, equally compact to those reported in our previous study²⁶ and slightly more so than those described in previous reports^{6,16}. There are also considerable numbers (16% of all trimers) of unbound particles with one erect RBD, as well as some (4%) in an intermediate conformation, a less-compact closed form, with a single disordered RBD, which have also been reported in a previous study of the furin-cleaved spike protein²⁶.

Fig. 1: Sequential steps in ACE2 binding of the SARS-CoV-2 spike protein.

 **figure1**

Surface representation of the spike, with monomers coloured in blue, rosy brown and gold, and ACE2 coloured in green. Each step shows two views of the spike complexes: a trimer axis vertical view (left) and an orthogonal top-down view along the axis (right). Clockwise from the top, we show structures for closed, open but unbound RBD, followed by sequential ACE2-binding events until reaching the fully open, three-ACE2-bound spike protein state. From this final trimeric species, we show dissociation into monomeric S1–ACE2, which may also occur for the one- or two-ACE2-bound species.

[Full size image](#)

Of the spike trimers bound to the receptor, half accommodate one ACE2 receptor. As previously reported for the SARS-CoV spike protein^{12,23}, the ACE2-bound RBD occupies a range of tilts with respect to the long axis of the trimer (Extended Data Fig. 2a). Of the two RBDs per trimer that are not engaged with the receptor, either both are closed or one of the RBDs remains closed and one (either clockwise or anticlockwise to the bound S1 (Extended Data Fig. 1)) is in the open conformation.

We were also able to identify, reconstruct and refine trimers to which two or three ACE2 receptors were bound, in successively more open structures (Fig. 1 and Extended Data Fig. 1).

Comparison of the trimers with one erect RBD that is either bound or unbound by an ACE2 receptor revealed two things. First, ACE2 binding alters the position of the open RBD by a rigid-body rotation of the domain that moves its centre of mass on average a further approximately 5.5 Å away from the trimer axis, the NTD-associated and RBD-associated subdomains of the same monomer shift around 1.9 Å and about 2.3 Å, respectively (Extended Data Fig. 2c), and at the same time the NTDs of all three S1 components move by around 1.5–3.0 Å (Extended Data Fig. 2d). Similar changes in the domain orientation are observed in the recent structure of the SARS-CoV-2 spike complex with C105 Fab²⁷ (Extended Data Fig. 2e), which binds at the ACE2-binding site. However, the molecular basis of both of these sets of changes remains unclear. Binding of more than one ACE2 molecule does not induce any substantial further changes in the average positioning of the RBD (Extended Data Fig. 2e). Second, our data suggest that ACE2 binding favours the open conformation of the RBD. The relatively high-affinity interaction of RBD with ACE2 generates an RBD–ACE2 structure that cannot be accommodated in a closed trimer—the bound state does not have access to the closed conformation. In addition, the fact that ACE2 binding induces a more-open conformation of the spike RBD suggests that some of the binding energy is used to drive the new conformation of S1, which is then further excluded from a closed state.

The successive steps, from closed unbound trimer to the fully open, three-ACE2-bound trimer, are associated with a substantial reduction in the contact area that each S1 makes with both its neighbouring S1 monomers and with the S2 trimeric core (Extended Data Table 1). For the fully, three-ACE2-bound species, each S1 makes 1,400 Å² less contact with both its S1 trimer neighbours and 1,300 Å² less contact with the S2 core than in the fully closed trimer conformation; all of these rearrangements are driven by the energetics of the three ACE2-binding events. The movements of the RBD and NTD domains of S1 that are associated with the opening of the structure and stabilization of the new arrangement by ACE2 binding, as described above, leave a trimeric ring of S1 molecules that are attached to the S2 core only through contacts with its two small intermediate subdomains (Fig. 2a). Comparing the ACE2-bound, open form (the open-unbound structure is similar but of poorer local resolution) with the fully closed trimer, the RBD-associated intermediate subdomain moves about 8 Å, whereas the NTD-associated intermediate subdomain moves by 3 Å (Fig. 2a). The latter also undergoes a partial restructuring with possibly important implications for the mechanism of fusion activation of spike. In the closed form, one edge of the NTD-associated intermediate subdomain

interacts with a short helix and a loop from S2 of the neighbouring monomer (Fig. 2b). Notably, two components of this interaction comprise a series of side-chain π-stacking interactions in the closed structure²⁶: Tyr636, Phe318 and Arg634 of S1 with Tyr837 of S2; and a salt bridge formed by Asp614 of S1 with Lys854 of S2. By contrast, in the ACE2-bound form, Tyr636, Phe318 and Trp633 refold to the side of the domain further away from the symmetry axis (as viewed in Fig. 2c), leaving a channel to accommodate a new segment of α-helix that forms downstream of Asp614 from polypeptide chain that was previously disordered. As a consequence, the interactions between S1 and S2 described above for the closed form are lost in the ACE2-bound form and the segment comprising residues 827–855 of S2 becomes disordered (Fig. 2c). This part of S2 is immediately C-terminal to the putative fusion peptide of S2¹¹, the N terminus of which is defined by Arg815 at the S2' cleavage site^{9,11}. The opening of the ACE2-stabilized S1 therefore leads to the destabilization of the S2 structure just after the putative fusion peptide, potentially activating it for exposure in the next stages of membrane fusion. Notably, Asp614, which forms salt bridges to Lys854 of S2 in the closed form, is frequently substituted^{13,14,15} by a glycine residue and it has been suggested that this substitution reduces shedding of S1 (and increases the number of spike proteins on the virus surface)¹³. We also propose that this substitution would remove a key salt bridge, and that the unique stereochemistry available to glycine may facilitate the formation of the new segment of α-helix, which is also incompatible with the S2 interaction. Furthermore, it could lead to reduced stability of the closed form of the spike protein, which in turn would increase the likelihood of the RBDs adopting the open conformation and hence the ability of the spike protein to bind to ACE2.

Fig. 2: Structural rearrangements between the closed and the ACE2-bound states of the spike protein.

 **figure2**

a, Surface representation of a monomer of S2 in the one-ACE2-bound, two-RBD-closed state coloured in light pink with the S1 subunit of the adjacent monomer in ribbon representation; the S1 of the one-ACE2-bound, two-RBD-closed state is shown in green and the three-RBD-closed state (PDB 6ZGE²⁶) is shown in blue. The atoms on the surface of S2 that contact the S1 intermediate domains are coloured in red. The arrows indicate the direction of movements of the intermediate domains, and of the RBD, between the closed and ACE2-bound conformations of the spike. **b**, Ribbon representations of the NTD-associated intermediate domain in blue and the moiety of the S2 chain that it interacts with (in red) in the closed conformation of the spike. Essential residues that participate in the interaction are labelled; of particular note is the salt bridge between Asp614 (S1, chain A) and Lys854 (S2, chain B). **c**, Ribbon representation of the same intermediate domain as in **b**, but in the conformation observed in the ACE2-bound structure of the spike (in green), in which the movement and refolding of the domain leads to a loss of interaction with S2, which becomes disordered. The putative fusion peptide (FP) and the S2' site of the second protease cleavage at R815 adjacent to the region that undergoes unfolding are shown in dark red.

[Full size image](#)

The opening up, and out, from the trimer axis of the S1 domains after ACE2 binding gives rise to an unshielding of the top surface of the helix–loop–helix (approximately residues 980–990 within the HR1 region^{20,22,28,29}) at the top of the S2 domain (Fig. 3). In the closed form, these helices and their connecting turns are tightly shielded by the RBDs; each S2 monomer is predominantly covered by its anticlockwise-related S1 trimer neighbour. In the fully open state, the S1 domains move in such a way as to generate a cavity with a diameter of 50 Å around the trimer axis that is about 65 Å deep. At the bottom of this cavity is the now solvent-exposed, central portion of HR1. For membrane fusion to occur—in comparison with other class-I fusion proteins and as described in coronavirus post-fusion structures^{22,28,29}—the S2 component is likely to undergo a major helical rearrangement, in which the long trimer interface helix (spanning residues 990–1035) grows and extends, by incorporating the refolded turn and helix from the N-terminal portion of HR1, and projects the fusion peptide towards the host cell membrane. In this process, opening up of all three S1 monomers and their subsequent dissociation would enable the concerted helical refolding, as the cooperative displacement of the capping portions of the protein will probably be required for the extension of the helical coil, as has recently been observed for the haemagglutinin protein of influenza³⁰. The stoichiometry of S1 subunit–ACE2 interactions required for effective cell-surface contact or for priming is not addressed by our experiments. However, as the affinity of individual monomers for ACE2 appears to be sufficient for cellular association, it may be that more than one subunit is required to be in the open form for efficient priming of these rearrangements in S2 that occur in the process of membrane fusion. It seems reasonable to propose that the likelihood of triggering the fusion conformation increases with the number of ACE2 receptors bound.

Fig. 3: Structural basis of S2 unsheathing by ACE2 binding.

 **figure3**

The spike protein is shown as a space-filling representation for S1, with each monomer coloured blue, rosy brown and gold, and as a ribbon representation for S2 coloured in red for all three monomers. Left, top-down and side-on views of the

trimer in the closed conformation. Right, the same views for the fully open three-ACE2-bound species.

[Full size image](#)

In addition to the range of species of trimeric spike described above, the largest single population of particles that we were able to identify and reconstruct represent ACE2 bound to a S1 monomer (Fig. 4). The interaction between ACE2 and the RBD, and the interaction of the latter with its associated intermediate subdomain, are very similar between the monomeric and trimer versions and with previously determined crystal and electron microscopy structures of ACE2 and RBD^{7,24,25}. However, there are increasingly large rearrangements between the two intermediate subdomains and then with the NTD. By applying non-uniform refinement, the highest resolution was achieved for the reconstruction of the ACE2–RBD interaction (Extended Data Fig. 4), in part because of the tight interaction but also probably because of the dominant influence of this part of the structure on the alignment process. Nevertheless, it is clear that there are both increasingly large changes in the interfaces between domains on moving towards the NTD and a range of subpopulations of related but variable conformations. The high proportion of ACE2–S1 monomers, and the limited contact areas between the trimeric S1 ring interactions with S2, suggest that the fully open ACE2-bound spike complex is probably metastable.

Fig. 4: ACE2-bound S1 subunit as a part of the spike trimer and as an isolated monomer.

 **figure4**

Space-filling representations of the spike protein with one monomer coloured polychromatically. NTD, yellow; NTD-associated subdomain, blue; RBD-associated subdomain, pink; RBD, rosy brown; S2, red; ACE2, green. The remainder of the trimer on the left is coloured grey. The structure on the right is aligned on the RBD:ACE2 moiety of the trimer complex on the left. The arrow indicates the direction of movement of the NTD and NTD-associated subdomain on the transition from the trimer (left) to the monomer species (right).

[Full size image](#)

Taken together, our structural data enable mechanistic suggestions for the early stages of SARS-CoV-2 infection of cells. The SARS-CoV-2 spike protein is produced in a compact closed form in which the helices in the S2 membrane fusion

component are capped by the RBD of neighbouring monomers. After cleavage by furin between the S1 and S2 domains, the proportion of the spike trimers that is able to accommodate RBD in an open, ACE2-binding conformation increases²⁶. Binding of the ACE2 receptor to an open RBD leads to a more-open trimer conformation. The geometry of ACE2 binding is incompatible with the RBD adopting a closed conformation and leads to our observation of several two-open-RBD conformations as well as the three-RBD-bound conformation. Successive RBD opening and ACE2 binding lead to a fully open and ACE2-bound form in which the trimeric S1 ring remains bound to the core S2 trimer by limited contacts through the intermediate subdomains of S1. This arrangement leaves the top of the S2 helices fully exposed. In the process, the interaction of the closed form of S1 with a segment of the S2 chain that precedes the putative fusion peptide region, in the open form, is lost. We suggest that in this form the S trimer is primed for the helical rearrangements of S2 that are required for fusion of the viral and host cell membranes²⁸.

Methods

Constructs design, protein expression and purification

The ectodomains of ACE2 (19–615) and stabilized, ‘2P’ mutant (K986P and V987P) of SARS-CoV-2 spike (residues 1–1208) with intact furin-cleavage site were prepared as described in a recent study²⁶. In brief, the proteins were expressed in Expi293F cells (Gibco), collected twice after 3–4 and 6–7 days, and purified with affinity chromatography (spike using CoNTA resin from TAKARA, ACE2 with Streptactin XT resin from IBA Lifesciences), followed by gel filtration into a buffer containing 20 mM Tris pH 8.0 and 150 mM NaCl. As previously described²⁶, the purified spike was then incubated for 5 h with exogenous furin (New England Biolabs), after which the reaction was stopped by addition of EDTA.

Electron microscopy sample preparation and data collection

R2/2 200-mesh Quantifoil grids were glow-discharged for 30 s at 25 mA to prepare them for freezing. The furin-treated SARS-CoV-2 spike was mixed with octyl glucoside as previously described²⁶ and, 45–60 s before ultimately plunge-freezing the grid, with concentrated ACE2 at a 1:2 final molar ratio of trimeric spike:ACE2, aiming to obtain a final concentration of spike of 0.5 mg ml⁻¹ and octyl glucoside of 0.1%. Then, 4 µl of the obtained reaction mixture was applied on a grid pre-equilibrated at 4 °C in 100% humidity, blotted with filter paper for 4–4.5 s using Vitrobot Mark III, and plunge-frozen in liquid ethane.

Data were collected using EPU software on a Titan Krios microscope operating at 300 kV. Micrographs were collected using a Gatan K2 detector mounted on a Gatan GIF Quantum energy filter operating in zero-loss mode with a slit width of 20 eV. Exposures were 8 s, fractionated into 32 frames with an accumulated dose of $54.4 \text{ e}^- \text{\AA}^{-2}$, with a calibrated pixel size of 1.08 Å. Images were collected at a range of defoci between 1.5 and 3.0 μm.

Electron microscopy data processing

Movies were aligned using MotionCor2³¹ implemented in RELION³², followed by contrast transfer function (CTF) estimation using Ctffind4³³. Particles were picked using crYOLO³⁴ using a manually trained model. Particles were subjected to multiple rounds of two-dimensional classification using cryoSPARC³⁵. Classes that displayed a clear secondary structure were retained and split into subsets, which either resembled spike trimers or S1 monomers bound to ACE2. Initial models were made using the ab initio reconstruction in cryoSPARC. Different species containing trimeric spike proteins were separated by extensive three-dimensional classification in RELION as shown in Extended Data Fig. 3. Before the final refinement, particles corresponding to each of these species were subjected to Bayesian polishing in RELION³⁶ followed by homogeneous refinement in cryoSPARC coupled to CTF refinement. The monomeric S1–ACE2 complex was classified as in Extended Data Fig. 4a and refined using non-uniform refinement in cryoSPARC coupled to CTF refinement. The final particles from the S1–ACE2 complex were subjected to an unmasked refinement in RELION to better resolve less-ordered domains, with an overall lower global resolution (Extended Data Fig. 4b,c). Local resolution was estimated using blocres³⁷ implemented in cryoSPARC. Maps were locally filtered and globally sharpened³⁸ in cryoSPARC (Extended Data Figs. 5, 6).

Model building

The model for the monomeric S1–ACE2 complex was based on the previously determined crystal structure (PDB: 6M0J²⁴, with additional parts of the RBD and intermediate domain taken from a previous structure of the closed trimer (PDB: 6ZGE)²⁶. Models of the trimer structures were built using structures from our previous study²⁶ for the closed trimer (PDB: 6ZGE) and the one-erect-RBD structure (PDB: 6ZGG). The RBD–ACE2 parts of the model were built using the structure from the high resolution S1–ACE2 complex from this study. Models were manually adjusted using COOT³⁹. The models of S1–ACE2 and the one-ACE2-bound closed structure were refined and validated using PHENIX real space refine⁴⁰. The other, lower resolution models were refined using NAMDINATOR⁴¹.

and geometry minimization and validation in PHENIX (Extended Data Table 2). Measurements were made using Chimera⁴², CCP4MG⁴³ and PISA⁴⁴, with structures aligned on the large helix of S2 (residues 986–1032).

Reporting summary

Further information on research design is available in the [Nature Research Reporting Summary](#) linked to this paper.

Data availability

Maps and models have been deposited in the Electron Microscopy Data Bank (EMD) and the Protein Data Bank (PDB) with the following accession codes: [EMD-11681](#) and PDB [7A91](#) (dissociated S1 domain bound to ACE2 (non-uniform refinement)); [EMD-11682](#) and PDB [7A92](#) (dissociated S1 domain bound to ACE2 (unmasked refinement)); [EMD-11683](#) and PDB [7A93](#) (SARS-CoV-2 spike with two RBDs erect); [EMD-11684](#) and PDB [7A94](#) (SARS-CoV-2 spike with one ACE2 bound); [EMD-11685](#) and PDB [7A95](#) (SARS-CoV-2 spike with one ACE2 bound and one RBD erect in clockwise direction); [EMD-11686](#) and PDB [7A96](#) (SARS-CoV-2 spike with one ACE2 bound and one RBD erect in anticlockwise direction); [EMD-11687](#) and PDB [7A97](#) (SARS-CoV-2 spike with two ACE2 bound); [EMD-11688](#) and PDB [7A98](#) (SARS-CoV-2 spike with three ACE2 bound).

References

1. 1.

Zhou, P. et al. A pneumonia outbreak associated with a new coronavirus of probable bat origin. *Nature* **579**, 270–273 (2020).

[ADS](#) [CAS](#) [Article](#) [Google Scholar](#)

2. 2.

Wan, Y., Shang, J., Graham, R., Baric, R. S. & Li, F. Receptor recognition by the novel coronavirus from Wuhan: an analysis based on decade-long structural studies of SARS coronavirus. *J. Virol.* **94**, e00127-20 (2020).

[PubMed](#) [PubMed Central](#) [Google Scholar](#)

3. 3.

Li, F., Li, W., Farzan, M. & Harrison, S. C. Structure of SARS coronavirus spike receptor-binding domain complexed with receptor. *Science* **309**, 1864–1868 (2005).

[ADS](#) [CAS](#) [Article](#) [Google Scholar](#)

4. 4.

Li, W. et al. Angiotensin-converting enzyme 2 is a functional receptor for the SARS coronavirus. *Nature* **426**, 450–454 (2003).

[ADS](#) [CAS](#) [Article](#) [Google Scholar](#)

5. 5.

Li, F. Structure, function, and evolution of coronavirus spike proteins. *Annu. Rev. Virol.* **3**, 237–261 (2016).

[CAS](#) [Article](#) [Google Scholar](#)

6. 6.

Walls, A. C. et al. Structure, function, and antigenicity of the SARS-CoV-2 spike glycoprotein. *Cell* **181**, 281–292 (2020).

[CAS](#) [Article](#) [Google Scholar](#)

7. 7.

Shang, J. et al. Structural basis of receptor recognition by SARS-CoV-2. *Nature* **581**, 221–224 (2020).

[ADS](#) [CAS](#) [Article](#) [Google Scholar](#)

8. 8.

Belouzard, S., Chu, V. C. & Whittaker, G. R. Activation of the SARS coronavirus spike protein via sequential proteolytic cleavage at two distinct sites. *Proc. Natl Acad. Sci. USA* **106**, 5871–5876 (2009).

[ADS](#) [CAS](#) [Article](#) [Google Scholar](#)

9. 9.

Millet, J. K. & Whittaker, G. R. Host cell entry of Middle East respiratory syndrome coronavirus after two-step, furin-mediated activation of the spike protein. *Proc. Natl Acad. Sci. USA* **111**, 15214–15219 (2014).

[ADS](#) [CAS](#) [Article](#) [Google Scholar](#)

10. 10.

Hoffmann, M. et al. SARS-CoV-2 cell entry depends on ACE2 and TMPRSS2 and is blocked by a clinically proven protease inhibitor. *Cell* **181**, 271–280 (2020).

[CAS](#) [Article](#) [Google Scholar](#)

11. 11.

Lai, A. L., Millet, J. K., Daniel, S., Freed, J. H. & Whittaker, G. R. The SARS-CoV fusion peptide forms an extended bipartite fusion platform that perturbs membrane order in a calcium-dependent manner. *J. Mol. Biol.* **429**, 3875–3892 (2017).

[CAS](#) [Article](#) [Google Scholar](#)

12. 12.

Song, W., Gui, M., Wang, X. & Xiang, Y. Cryo-EM structure of the SARS coronavirus spike glycoprotein in complex with its host cell receptor ACE2. *PLoS Pathog.* **14**, e1007236 (2018).

[Article](#) [Google Scholar](#)

13. 13.

Zhang, L. et al. The D614G mutation in the SARS-CoV-2 spike protein reduces S1 shedding and increases infectivity. Preprint at <https://doi.org/10.1101/2020.06.12.148726> (2020).

14. 14.

Hu, J. et al. D614G mutation of SARS-CoV-2 spike protein enhances viral infectivity. Preprint at <https://doi.org/10.1101/2020.06.20.161323> (2020).

15. 15.

Korber, B. et al. Tracking changes in SARS-CoV-2 spike: evidence that D614G increases infectivity of the COVID-19 virus. *Cell* **182**, 812–827 (2020).

[CAS](#) [Article](#) [Google Scholar](#)

16. 16.

Wrapp, D. et al. Cryo-EM structure of the 2019-nCoV spike in the prefusion conformation. *Science* **367**, 1260–1263 (2020).

[ADS](#) [CAS](#) [Article](#) [Google Scholar](#)

17. 17.

Tortorici, M. A. et al. Structural basis for human coronavirus attachment to sialic acid receptors. *Nat. Struct. Mol. Biol.* **26**, 481–489 (2019).

[Article](#) [Google Scholar](#)

18. 18.

Yuan, Y. et al. Cryo-EM structures of MERS-CoV and SARS-CoV spike glycoproteins reveal the dynamic receptor binding domains. *Nat. Commun.* **8**, 15092 (2017).

[ADS](#) [CAS](#) [Article](#) [Google Scholar](#)

19. 19.

Kirchdoerfer, R. N. et al. Stabilized coronavirus spikes are resistant to conformational changes induced by receptor recognition or proteolysis. *Sci. Rep.* **8**, 15701 (2018).

[ADS](#) [Article](#) [Google Scholar](#)

20. 20.

Pallesen, J. et al. Immunogenicity and structures of a rationally designed prefusion MERS-CoV spike antigen. *Proc. Natl Acad. Sci. USA* **114**, E7348–E7357 (2017).

[CAS](#) [Article](#) [Google Scholar](#)

21. 21.

Walls, A. C. et al. Cryo-electron microscopy structure of a coronavirus spike glycoprotein trimer. *Nature* **531**, 114–117 (2016).

[ADS](#) [CAS](#) [Article](#) [Google Scholar](#)

22. 22.

Cai, Y. et al. Distinct conformational states of SARS-CoV-2 spike protein. *Science* **369**, 1586–1592 (2020).

[ADS](#) [CAS](#) [PubMed](#) [Google Scholar](#)

23. 23.

Gui, M. et al. Cryo-electron microscopy structures of the SARS-CoV spike glycoprotein reveal a prerequisite conformational state for receptor binding. *Cell Res.* **27**, 119–129 (2017).

[CAS](#) [Article](#) [Google Scholar](#)

24. 24.

Lan, J. et al. Structure of the SARS-CoV-2 spike receptor-binding domain bound to the ACE2 receptor. *Nature* **581**, 215–220 (2020).

[ADS](#) [CAS](#) [Article](#) [Google Scholar](#)

25. 25.

Yan, R. et al. Structural basis for the recognition of SARS-CoV-2 by full-length human ACE2. *Science* **367**, 1444–1448 (2020).

[ADS](#) [CAS](#) [Article](#) [Google Scholar](#)

26. 26.

Wrobel, A. G. et al. SARS-CoV-2 and bat RaTG13 spike glycoprotein structures inform on virus evolution and furin-cleavage effects. *Nat. Struct. Mol. Biol.* **27**, 763–767 (2020).

[CAS](#) [Article](#) [Google Scholar](#)

27. 27.

Barnes, C. O. et al. Structures of human antibodies bound to SARS-CoV-2 spike reveal common epitopes and recurrent features of antibodies. *Cell* **182**, 828–842 (2020).

[CAS](#) [Article](#) [Google Scholar](#)

28. 28.

Walls, A. C. et al. Tectonic conformational changes of a coronavirus spike glycoprotein promote membrane fusion. *Proc. Natl Acad. Sci. USA* **114**, 11157–11162 (2017).

[CAS](#) [Article](#) [Google Scholar](#)

29. 29.

Fan, X., Cao, D., Kong, L. & Zhang, X. Cryo-EM analysis of the post-fusion structure of the SARS-CoV spike glycoprotein. *Nat. Commun.* **11**, 3618 (2020).

[ADS](#) [CAS](#) [Article](#) [Google Scholar](#)

30. 30.

Benton, D. J., Gamblin, S. J., Rosenthal, P. B. & Skehel, J. J. Structural transitions in influenza haemagglutinin at membrane fusion pH. *Nature* **583**, 150–153 (2020).

[ADS](#) [CAS](#) [Article](#) [Google Scholar](#)

31. 31.

Zheng, S. Q. et al. MotionCor2: anisotropic correction of beam-induced motion for improved cryo-electron microscopy. *Nat. Methods* **14**, 331–332 (2017).

[CAS](#) [Article](#) [Google Scholar](#)

32. 32.

Scheres, S. H. W. RELION: implementation of a Bayesian approach to cryo-EM structure determination. *J. Struct. Biol.* **180**, 519–530 (2012).

[CAS](#) [Article](#) [Google Scholar](#)

33. 33.

Rohou, A. & Grigorieff, N. CTFFIND4: fast and accurate defocus estimation from electron micrographs. *J. Struct. Biol.* **192**, 216–221 (2015).

[Article](#) [Google Scholar](#)

34. 34.

Wagner, T. et al. SPHIRE-crYOLO is a fast and accurate fully automated particle picker for cryo-EM. *Commun. Biol.* **2**, 218 (2019).

[Article](#) [Google Scholar](#)

35. 35.

Punjani, A., Rubinstein, J. L., Fleet, D. J. & Brubaker, M. A. cryoSPARC: algorithms for rapid unsupervised cryo-EM structure determination. *Nat. Methods* **14**, 290–296 (2017).

[CAS](#) [Article](#) [Google Scholar](#)

36. 36.

Zivanov, J., Nakane, T. & Scheres, S. H. W. A Bayesian approach to beam-induced motion correction in cryo-EM single-particle analysis. *IUCrJ* **6**, 5–17 (2019).

[CAS](#) [Article](#) [Google Scholar](#)

37. 37.

Cardone, G., Heymann, J. B. & Steven, A. C. One number does not fit all: mapping local variations in resolution in cryo-EM reconstructions. *J. Struct. Biol.* **184**, 226–236 (2013).

[Article](#) [Google Scholar](#)

38. 38.

Rosenthal, P. B. & Henderson, R. Optimal determination of particle orientation, absolute hand, and contrast loss in single-particle electron cryomicroscopy. *J. Mol. Biol.* **333**, 721–745 (2003).

[CAS](#) [Article](#) [Google Scholar](#)

39. 39.

Emsley, P., Lohkamp, B., Scott, W. G. & Cowtan, K. Features and development of Coot. *Acta Crystallogr. D* **66**, 486–501 (2010).

[CAS](#) [Article](#) [Google Scholar](#)

40. 40.

Adams, P. D. et al. PHENIX: a comprehensive Python-based system for macromolecular structure solution. *Acta Crystallogr. D* **66**, 213–221 (2010).

[CAS](#) [Article](#) [Google Scholar](#)

41. 41.

Kidmose, R. T. et al. Namdinator - automatic molecular dynamics flexible fitting of structural models into cryo-EM and crystallography experimental maps. *IUCrJ* **6**, 526–531 (2019).

[CAS](#) [Article](#) [Google Scholar](#)

42. 42.

Pettersen, E. F. et al. UCSF Chimera—a visualization system for exploratory research and analysis. *J. Comput. Chem.* **25**, 1605–1612 (2004).

[CAS](#) [Article](#) [Google Scholar](#)

43. 43.

McNicholas, S., Potterton, E., Wilson, K. S. & Noble, M. E. M. Presenting your structures: the CCP4mg molecular-graphics software. *Acta Crystallogr. D* **67**, 386–394 (2011).

[CAS](#) [Article](#) [Google Scholar](#)

44. 44.

Krissinel, E. & Henrick, K. Inference of macromolecular assemblies from crystalline state. *J. Mol. Biol.* **372**, 774–797 (2007).

[CAS Article](#) [Google Scholar](#)

[Download references](#)

Acknowledgements

We thank A. Nans of the Structural Biology Science Technology Platform for assistance with data collection, P. Walker and A. Purkiss of the Structural Biology Science Technology Platform and the Scientific Computing Science Technology Platform for computational support, and L. Calder, P. Cherepanov, G. Kassiotis and S. Kjaer for discussions. This work was funded by the Francis Crick Institute, which receives its core funding from Cancer Research UK (FC001078 and FC001143), the UK Medical Research Council (FC001078 and FC001143) and the Wellcome Trust (FC001078 and FC001143). P.X. is also supported by the 100 Top Talents Program of Sun Yat-sen University, the Sanming Project of Medicine in Shenzhen (SZSM201911003) and the Shenzhen Science and Technology Innovation Committee (grant no. JCYJ20190809151611269).

Author information

Author notes

1. These authors contributed equally: Donald J. Benton, Antoni G. Wrobel

Affiliations

1. Strutural Biology of Disease Processes Laboratory, Francis Crick Institute, London, UK

Donald J. Benton, Antoni G. Wrobel, Stephen R. Martin, John J. Skehel & Steven J. Gamblin

2. Precision Medicine Center, The Seventh Affiliated Hospital, Sun Yat-sen University, Shenzhen, China

Pengqi Xu

3. Francis Crick Institute, London, UK

Pengqi Xu

4. Structural Biology Science Technology Platform, Francis Crick Institute, London, UK

Chloë Roustan

5. Structural Biology of Cells and Viruses Laboratory, Francis Crick Institute, London, UK

Peter B. Rosenthal

Authors

1. Donald J. Benton

[View author publications](#)

You can also search for this author in [PubMed](#) [Google Scholar](#)

2. Antoni G. Wrobel

[View author publications](#)

You can also search for this author in [PubMed](#) [Google Scholar](#)

3. Pengqi Xu

[View author publications](#)

You can also search for this author in [PubMed](#) [Google Scholar](#)

4. Chloë Roustan

[View author publications](#)

You can also search for this author in [PubMed](#) [Google Scholar](#)

5. Stephen R. Martin

[View author publications](#)

You can also search for this author in [PubMed](#) [Google Scholar](#)

6. Peter B. Rosenthal

[View author publications](#)

You can also search for this author in [PubMed](#) [Google Scholar](#)

7. John J. Skehel
[View author publications](#)

You can also search for this author in [PubMed](#) [Google Scholar](#)

8. Steven J. Gamblin
[View author publications](#)

You can also search for this author in [PubMed](#) [Google Scholar](#)

Contributions

D.J.B., A.G.W., P.X., C.R. and S.R.M. performed research, collected and analysed data; D.J.B., A.G.W., P.B.R., J.J.S. and S.J.G. conceived and designed research and wrote the paper.

Corresponding authors

Correspondence to [Donald J. Benton](#) or [Antoni G. Wrobel](#) or [Steven J. Gamblin](#).

Ethics declarations

Competing interests

The authors declare no competing interests.

Additional information

Peer review information *Nature* thanks Stephen Harrison and the other, anonymous, reviewer(s) for their contribution to the peer review of this work.

Publisher's note Springer Nature remains neutral with regard to jurisdictional claims in published maps and institutional affiliations.

Extended data figures and tables

[Extended Data Fig. 1 Surface representation of obtained structures.](#)

The three monomers of S in each trimer are coloured in blue, rosy brown and gold with ACE2 shown in green. Relative percentages of all trimeric S particles used to calculate electron microscopy maps are shown.

Extended Data Fig. 2 Features of the obtained spike structures.

a, Two three-dimensional classes, obtained by further classification of the one-ACE2-bound closed state from Fig. 1, representative of the range of motion of the RBD with bound ACE2, tilting away from the trimer axis of the spike trimer. The tilt of the RBD and ACE2 is indicated with a dashed line. **b**, Representative density of different obtained electron microscopy maps for residues 996–1030 of S2. Built model shown in pink, with EM density shown as a mesh. **c**, **d**, Comparison of spike structures for the open one-erect-RBD structure (purple) with the one-ACE2-bound structure (orange). **c**, S1 domains shown to highlight domain shifts of the RBD and RBD-associated intermediate domain. **d**, Outwards movements of spike domains (excluding RBDs). **e**, Comparison of RBD displacements of one-bound, two-bound and three-bound RBDs after binding of ACE2 to the unbound open structure of the spike protein (beige). These are compared to the RBD displacement after binding of the C105 Fab fragment²⁷, which binds at the ACE2 interface of the RBD (PDB: 6XCM).

Extended Data Fig. 3 Cryo-electron microscopy data processing scheme.

Classes of particles used to obtain the final spike trimer structures, unbound and in complex with ACE2, are surrounded by a box of the same colour as the final maps shown at the bottom. The global resolution, final particle number and percentage for each trimer species are shown at the bottom.

Extended Data Fig. 4 Monomeric S1 bound to ACE2.

a, Classification scheme for the S1–ACE2 complex. **b**, **c**, Maps are shown of orthogonal views of the non-uniform refinement (**b**) and unmasked refinement (**c**) of the final particles. Domains are coloured as follows: green, ACE2; yellow, NTD; rosy brown, RBD; pink, RBD ganymede; blue, NTD ganymede; cream, disseminated S1 density in **b**.

Extended Data Fig. 5 Fourier shell correlation graphs for each of the determined structures.

FSC, Fourier shell correlation.

[Extended Data Fig. 6 Maps and models of determined structures.](#)

Top, orthogonal views of electron microscopy density (grey) and ribbon diagram representation of the models. Bottom, electron microscopy maps coloured by local resolution shown below.

Extended Data Table 1 Buried interface surface area between monomers in different conformations

[Full size table](#)

Extended Data Table 2 Cryo-electron microscopy data collection, refinement and validation statistics

[Full size table](#)

Supplementary information

[Reporting Summary](#)

Rights and permissions

[Reprints and Permissions](#)

About this article



Check for
updates

Cite this article

Benton, D.J., Wrobel, A.G., Xu, P. *et al.* Receptor binding and priming of the spike protein of SARS-CoV-2 for membrane fusion. *Nature* **588**, 327–330 (2020).
<https://doi.org/10.1038/s41586-020-2772-0>

[Download citation](#)

- Received: 01 July 2020

- Accepted: 11 September 2020
- Published: 17 September 2020
- Issue Date: 10 December 2020
- DOI: <https://doi.org/10.1038/s41586-020-2772-0>

Further reading

- **Structural basis of severe acute respiratory syndrome coronavirus 2 infection**

- Jiwan Ge
- , Senyan Zhang
- , Linqi Zhang
- & Xinquan Wang

Current Opinion in HIV and AIDS (2021)

- **The SARS-CoV-2 spike protein: balancing stability and infectivity**

- Imre Berger
- & Christiane Schaffitzel

Cell Research (2020)

- **The SARS-CoV-2 Spike Glycoprotein as a Drug and Vaccine Target: Structural Insights into Its Complexes with ACE2 and Antibodies**

- Anastassios C. Papageorgiou
- & Imran Mohsin

Cells (2020)

- **Characterization of Structural and Energetic Differences between Conformations of the SARS-CoV-2 Spike Protein**

- Rodrigo A. Moreira

- , Horacio V. Guzman
- , Subramanian Boopathi
- , Joseph L. Baker
- & Adolfo B. Poma

Materials (2020)

- **Spike Glycoprotein-Mediated Entry of SARS Coronaviruses**

- Lin Wang
- & Ye Xiang

Viruses (2020)

Comments

By submitting a comment you agree to abide by our [Terms](#) and [Community Guidelines](#). If you find something abusive or that does not comply with our terms or guidelines please flag it as inappropriate.

[Download PDF](#)

This article was downloaded by **calibre** from <https://www.nature.com/articles/s41586-020-2772-0>

| [Section menu](#) | [Main menu](#) |

- Article
- [Published: 09 December 2020](#)

A metastasis map of human cancer cell lines

- [Xin Jin](#) [ORCID: orcid.org/0000-0003-4167-1743](#)¹,
- [Zelalem Demere](#)¹,
- [Karthik Nair](#)¹,
- [Ahmed Ali](#)^{1,2},
- [Gino B. Ferraro](#) [ORCID: orcid.org/0000-0002-1587-4259](#)³,
- [Ted Natoli](#)¹,
- [Amy Deik](#)¹,
- [Lia Petronio](#)¹,
- [Andrew A. Tang](#)¹,
- [Cong Zhu](#)¹,
- [Li Wang](#)¹,
- [Danny Rosenberg](#)¹,
- [Vamsi Mangena](#) [ORCID: orcid.org/0000-0003-2662-0366](#)⁴,
- [Jennifer Roth](#)¹,
- [Kwanghun Chung](#) [ORCID: orcid.org/0000-0002-8167-3340](#)^{1,4},
- [Rakesh K. Jain](#) [ORCID: orcid.org/0000-0001-7571-3548](#)^{3,5},
- [Clary B. Clish](#) [ORCID: orcid.org/0000-0001-8259-9245](#)¹,
- [Matthew G. Vander Heiden](#) [ORCID: orcid.org/0000-0002-6702-4192](#)^{1,2,6} &
- [Todd R. Golub](#) [ORCID: orcid.org/0000-0003-0113-2403](#)^{1,5,6}

[Nature](#) volume 588, pages331–336(2020)[Cite this article](#)

- 197 Altmetric

- [Metrics details](#)

Subjects

- [Breast cancer](#)
- [Cancer genomics](#)
- [Cancer models](#)
- [Metastasis](#)

Abstract

Most deaths from cancer are explained by metastasis, and yet large-scale metastasis research has been impractical owing to the complexity of in vivo models. Here we introduce an in vivo barcoding strategy that is capable of determining the metastatic potential of human cancer cell lines in mouse xenografts at scale. We validated the robustness, scalability and reproducibility of the method and applied it to 500 cell lines^{1,2} spanning 21 types of solid tumour. We created a first-generation metastasis map (MetMap) that reveals organ-specific patterns of metastasis, enabling these patterns to be associated with clinical and genomic features. We demonstrate the utility of MetMap by investigating the molecular basis of breast cancers capable of metastasizing to the brain—a principal cause of death in patients with this type of cancer. Breast cancers capable of metastasizing to the brain showed evidence of altered lipid metabolism. Perturbation of lipid metabolism in these cells curbed brain metastasis development, suggesting a therapeutic strategy to combat the disease and demonstrating the utility of MetMap as a resource to support metastasis research.

[Access through your institution](#)

[Change institution](#)

[Buy or subscribe](#)

Access options

Subscribe to Journal

Get full journal access for 1 year

185,98 €

only 3,58 € per issue

[Subscribe](#)

All prices are NET prices.

VAT will be added later in the checkout.

Rent or Buy article

Get time limited or full article access on ReadCube.

from \$8.99

[Rent or Buy](#)

All prices are NET prices.

Additional access options:

- [Log in](#)
- [Access through your institution](#)
- [Learn about institutional subscriptions](#)

Fig. 1: Scalable in vivo metastatic potential mapping with barcoded cell line pools.



Fig. 2: Drafting MetMap for 500 human cancer cell lines.



Fig. 3: Clinical correlates of metastatic potential.



Fig. 4: An altered lipid-metabolism state associates with brain metastatic potential in basal-like breast cancer.



Fig. 5: Investigation of lipid-metabolism genes in breast cancer brain metastasis.



Data availability

MetMap data and interactive visualization can be accessed at <https://pubs.broadinstitute.org/metmap>. RNA-seq data generated from this study have been deposited in the Gene Expression Omnibus (GEO) under accession numbers [GSE148283](#) and [GSE148372](#). Additional datasets used in this study include METABRIC, TCGA and MSK-targeted-sequencing breast cancer datasets from cBioPortal, the EMC-MSK dataset (GSE2035, GSE2603, GSE5327 and GSE12276), the 65-metastasis-sample dataset (GSE14020), paired primary tumour and brain metastasis RNA-seq from ref. ³⁶, and GSE52604. [Source data](#) are provided with this paper.

Code availability

Custom codes used for this study are accessible at the MetMap portal (<https://pubs.broadinstitute.org/metmap>).

References

1. 1.

Barretina, J. et al. The Cancer Cell Line Encyclopedia enables predictive modelling of anticancer drug sensitivity. *Nature* **483**, 603–607 (2012).

[ADS](#) [CAS](#) [PubMed](#) [PubMed Central](#) [Google Scholar](#)

2. 2.

Ghandi, M. et al. Next-generation characterization of the Cancer Cell Line Encyclopedia. *Nature* **569**, 503–508 (2019).

[ADS](#) [CAS](#) [PubMed](#) [PubMed Central](#) [Google Scholar](#)

3. 3.

Garnett, M. J. et al. Systematic identification of genomic markers of drug sensitivity in cancer cells. *Nature* **483**, 570–575 (2012).

[ADS](#) [CAS](#) [PubMed](#) [PubMed Central](#) [Google Scholar](#)

4. 4.

Behan, F. M. et al. Prioritization of cancer therapeutic targets using CRISPR–Cas9 screens. *Nature* **568**, 511–516 (2019).

[ADS](#) [CAS](#) [Google Scholar](#)

5. 5.

Kang, Y. et al. A multigenic program mediating breast cancer metastasis to bone. *Cancer Cell* **3**, 537–549 (2003).

[CAS](#) [PubMed](#) [PubMed Central](#) [Google Scholar](#)

6. 6.

Chen, S. et al. Genome-wide CRISPR screen in a mouse model of tumor growth and metastasis. *Cell* **160**, 1246–1260 (2015).

[CAS](#) [PubMed](#) [PubMed Central](#) [Google Scholar](#)

7. 7.

Malladi, S. et al. Metastatic latency and immune evasion through autocrine inhibition of WNT. *Cell* **165**, 45–60 (2016).

[CAS](#) [PubMed](#) [PubMed Central](#) [Google Scholar](#)

8. 8.

van der Weyden, L. et al. Genome-wide in vivo screen identifies novel host regulators of metastatic colonization. *Nature* **541**, 233–236 (2017).

[ADS](#) [PubMed](#) [PubMed Central](#) [Google Scholar](#)

9. 9.

Tasdogan, A. et al. Metabolic heterogeneity confers differences in melanoma metastatic potential. *Nature* **577**, 115–120 (2020).

[ADS](#) [CAS](#) [Google Scholar](#)

10. 10.

Robinson, D. R. et al. Integrative clinical genomics of metastatic cancer. *Nature* **548**, 297–303 (2017).

[ADS](#) [CAS](#) [PubMed](#) [PubMed Central](#) [Google Scholar](#)

11. 11.

Kennecke, H. et al. Metastatic behavior of breast cancer subtypes. *J. Clin. Oncol.* **28**, 3271–3277 (2010).

[PubMed](#) [PubMed Central](#) [Google Scholar](#)

12. 12.

Yu, C. et al. High-throughput identification of genotype-specific cancer vulnerabilities in mixtures of barcoded tumor cell lines. *Nat. Biotechnol.* **34**, 419–423 (2016).

[CAS](#) [PubMed](#) [PubMed Central](#) [Google Scholar](#)

13. 13.

Budczies, J. et al. The landscape of metastatic progression patterns across major human cancers. *Oncotarget* **6**, 570–583 (2015).

[PubMed](#) [PubMed Central](#) [Google Scholar](#)

14. 14.

Müller, C. et al. Hematogenous dissemination of glioblastoma multiforme. *Sci. Transl. Med.* **6**, 247ra101 (2014).

[PubMed](#) [PubMed Central](#) [Google Scholar](#)

15. 15.

Fonkem, E., Lun, M. & Wong, E. T. Rare phenomenon of extracranial metastasis of glioblastoma. *J. Clin. Oncol.* **29**, 4594–4595 (2011).

[PubMed](#) [PubMed Central](#) [Google Scholar](#)

16. 16.

Stone, K. R., Mickey, D. D., Wunderli, H., Mickey, G. H. & Paulson, D. F. Isolation of a human prostate carcinoma cell line (DU 145). *Int. J. Cancer* **21**, 274–281 (1978).

[CAS](#) [PubMed](#) [PubMed Central](#) [Google Scholar](#)

17. 17.

Ramaswamy, S., Ross, K. N., Lander, E. S. & Golub, T. R. A molecular signature of metastasis in primary solid tumors. *Nat. Genet.*

33, 49–54 (2003).

[CAS](#) [PubMed](#) [Google Scholar](#)

18. 18.

Zhang, X. H.-F. et al. Selection of bone metastasis seeds by mesenchymal signals in the primary tumor stroma. *Cell* **154**, 1060–1073 (2013).

[CAS](#) [PubMed](#) [PubMed Central](#) [Google Scholar](#)

19. 19.

Campbell, P. J. et al. The patterns and dynamics of genomic instability in metastatic pancreatic cancer. *Nature* **467**, 1109–1113 (2010).

[ADS](#) [CAS](#) [PubMed](#) [PubMed Central](#) [Google Scholar](#)

20. 20.

Witzel, I., Oliveira-Ferrer, L., Pantel, K., Müller, V. & Wikman, H. Breast cancer brain metastases: biology and new clinical perspectives. *Breast Cancer Res.* **18**, 8 (2016).

[PubMed](#) [PubMed Central](#) [Google Scholar](#)

21. 21.

Kodack, D. P., Askoxylakis, V., Ferraro, G. B., Fukumura, D. & Jain, R. K. Emerging strategies for treating brain metastases from breast cancer. *Cancer Cell* **27**, 163–175 (2015).

[CAS](#) [PubMed](#) [PubMed Central](#) [Google Scholar](#)

22. 22.

Curtis, C. et al. The genomic and transcriptomic architecture of 2,000 breast tumours reveals novel subgroups. *Nature* **486**, 346–352 (2012).

[CAS](#) [PubMed](#) [PubMed Central](#) [Google Scholar](#)

23. 23.

Cancer Genome Atlas Network. Comprehensive molecular portraits of human breast tumours. *Nature* **490**, 61–70 (2012).

[ADS](#) [Google Scholar](#)

24. 24.

Razavi, P. et al. The Genomic Landscape of Endocrine-Resistant Advanced Breast Cancers. *Cancer Cell* **34**, 427–438 (2018).

[CAS](#) [PubMed](#) [PubMed Central](#) [Google Scholar](#)

25. 25.

Gatza, M. L. et al. A pathway-based classification of human breast cancer. *Proc. Natl Acad. Sci. USA* **107**, 6994–6999 (2010).

[ADS](#) [CAS](#) [PubMed](#) [PubMed Central](#) [Google Scholar](#)

26. 26.

Creighton, C. J. et al. Proteomic and transcriptomic profiling reveals a link between the PI3K pathway and lower estrogen-receptor (ER) levels and activity in ER+ breast cancer. *Breast Cancer Res.* **12**, R40 (2010).

[PubMed](#) [PubMed Central](#) [Google Scholar](#)

27. 27.

Ricoult, S. J. H., Yecies, J. L., Ben-Sahra, I. & Manning, B. D. Oncogenic PI3K and K-Ras stimulate de novo lipid synthesis through mTORC1 and SREBP. *Oncogene* **35**, 1250–1260 (2016).

[CAS](#) [PubMed](#) [PubMed Central](#) [Google Scholar](#)

28. 28.

Cai, Y. et al. Loss of chromosome 8p governs tumor progression and drug response by altering lipid metabolism. *Cancer Cell* **29**, 751–766 (2016).

[CAS](#) [PubMed](#) [PubMed Central](#) [Google Scholar](#)

29. 29.

Li, H. et al. The landscape of cancer cell line metabolism. *Nat. Med.* **25**, 850–860 (2019).

[CAS](#) [PubMed](#) [PubMed Central](#) [Google Scholar](#)

30. 30.

Patra, K. C. & Hay, N. The pentose phosphate pathway and cancer. *Trends Biochem. Sci.* **39**, 347–354 (2014).

[CAS](#) [PubMed](#) [PubMed Central](#) [Google Scholar](#)

31. 31.

Jain, M. et al. A systematic survey of lipids across mouse tissues. *Am. J. Physiol. Endocrinol. Metab.* **306**, E854–E868 (2014).

[CAS](#) [PubMed](#) [PubMed Central](#) [Google Scholar](#)

32. 32.

Piomelli, D., Astarita, G. & Rapaka, R. A neuroscientist's guide to lipidomics. *Nat. Rev. Neurosci.* **8**, 743–754 (2007).

[CAS](#) [PubMed](#) [PubMed Central](#) [Google Scholar](#)

33. 33.

Paget, S. The distribution of secondary growths in cancer of the breast. 1889. *Cancer Metastasis Rev.* **8**, 98–101 (1989).

[CAS](#) [PubMed](#) [PubMed Central](#) [Google Scholar](#)

34. 34.

Dempster, J. M. et al. Agreement between two large pan-cancer CRISPR–Cas9 gene dependency data sets. *Nat. Commun.* **10**, 5817 (2019).

[ADS](#) [CAS](#) [PubMed](#) [PubMed Central](#) [Google Scholar](#)

35. 35.

Horton, J. D., Goldstein, J. L. & Brown, M. S. SREBPs: activators of the complete program of cholesterol and fatty acid synthesis in the liver. *J. Clin. Invest.* **109**, 1125–1131 (2002).

[CAS](#) [PubMed](#) [PubMed Central](#) [Google Scholar](#)

36. 36.

Varešlija, D. et al. Transcriptome characterization of matched primary breast and brain metastatic tumors to detect novel actionable targets. *J. Natl. Cancer Inst.* **111**, 388–398 (2019).

[PubMed](#) [PubMed Central](#) [Google Scholar](#)

37. 37.

Angelova, M. et al. Evolution of metastases in space and time under immune selection. *Cell* **175**, 751–765 (2018).

[CAS](#) [PubMed](#) [PubMed Central](#) [Google Scholar](#)

38. 38.

Zhang, M. et al. Adipocyte-derived lipids mediate melanoma progression via FATP proteins. *Cancer Discov.* **8**, 1006–1025 (2018).

[CAS](#) [PubMed](#) [PubMed Central](#) [Google Scholar](#)

39. 39.

Zou, Y. et al. Polyunsaturated fatty acids from astrocytes activate PPAR γ signaling in cancer cells to promote brain metastasis. *Cancer Discov.* **9**, 1720–1735 (2019).

[CAS](#) [PubMed](#) [PubMed Central](#) [Google Scholar](#)

40. 40.

Pascual, G. et al. Targeting metastasis-initiating cells through the fatty acid receptor CD36. *Nature* **541**, 41–45 (2017).

[ADS](#) [CAS](#) [PubMed](#) [PubMed Central](#) [Google Scholar](#)

41. 41.

Sullivan, M. R. et al. Quantification of microenvironmental metabolites in murine cancers reveals determinants of tumor nutrient availability. *eLife* **8**, e44235 (2019).

[CAS](#) [PubMed](#) [PubMed Central](#) [Google Scholar](#)

42. 42.

Zhang, C., Lowery, F. J. & Yu, D. Intracarotid cancer cell injection to produce mouse models of brain metastasis. *J. Vis. Exp.* **120**, e55085 (2017).

[Google Scholar](#)

43. 43.

Ozawa, T. & James, C. D. Establishing intracranial brain tumor xenografts with subsequent analysis of tumor growth and response to therapy using bioluminescence imaging. *J. Vis. Exp.* **41**, e1986 (2010).

[Google Scholar](#)

44. 44.

Tirosh, I. et al. Dissecting the multicellular ecosystem of metastatic melanoma by single-cell RNA-seq. *Science* **352**, 189–196 (2016).

[ADS](#) [CAS](#) [PubMed](#) [PubMed Central](#) [Google Scholar](#)

45. 45.

Langmead, B. & Salzberg, S. L. Fast gapped-read alignment with Bowtie 2. *Nat. Methods* **9**, 357–359 (2012).

[CAS](#) [PubMed](#) [PubMed Central](#) [Google Scholar](#)

46. 46.

Ritchie, M. E. et al. limma powers differential expression analyses for RNA-sequencing and microarray studies. *Nucleic Acids Res.* **43**, e47 (2015).

[PubMed](#) [PubMed Central](#) [Google Scholar](#)

47. 47.

Li, B. & Dewey, C. N. RSEM: accurate transcript quantification from RNA-seq data with or without a reference genome. *BMC Bioinformatics* **12**, 323 (2011).

[CAS](#) [PubMed](#) [PubMed Central](#) [Google Scholar](#)

48. 48.

Robinson, M. D., McCarthy, D. J. & Smyth, G. K. edgeR: a Bioconductor package for differential expression analysis of digital gene expression data. *Bioinformatics* **26**, 139–140 (2010).

[CAS](#) [PubMed](#) [PubMed Central](#) [Google Scholar](#)

49. 49.

Korotkevich, G., Sukhov, V. & Sergushichev, A. Fast gene set enrichment analysis. Preprint at <https://doi.org/10.1101/060012> (2019).

50. 50.

Hänzelmann, S., Castelo, R. & Guinney, J. GSVA: gene set variation analysis for microarray and RNA-seq data. *Bmc Bioinformatic* **14**, 7 (2013).

[Google Scholar](#)

51. 51.

Hosios, A., Li, Z., Lien, E. & Heiden, M. Preparation of lipid-stripped serum for the study of lipid metabolism in cell culture. *Bio Protoc.* **8**, e2876 (2018).

[CAS](#) [Google Scholar](#)

52. 52.

Cerami, E. et al. The cBio cancer genomics portal: an open platform for exploring multidimensional cancer genomics data. *Cancer Discov.* **2**, 401–404 (2012).

[PubMed](#) [PubMed Central](#) [Google Scholar](#)

[Download references](#)

Acknowledgements

We thank J. L. Goldstein for suggestions; A. Regev, N. Marjanovic and A. Bankapur for assistance with single-cell RNA-seq and analysis; Z. Herbert for assistance with RNA-seq; T. Mason for assistance with next-generation sequencing; S. Kim and S. Roberge for assistance with animal work; B. Wong for suggestions on figure and portal designs; and G. Wei, U. Ben-David, S. Corsello, P. Tsvetkov, I. Tirosh, R. Hosking and C. Mader for discussions. X.J. and G.B.F. were Susan G. Komen Fellows. A.A. is a HHMI Medical Research Fellow. This work was supported by BroadNext10, Broad SharkTank grants (X.J.), HHMI (T.R.G.), and in part by Koch Institute/DFHCC Bridge project grant (M.G.V.H. and R.K.J.). R.K.J. acknowledges support from the NIH (R35CA197742, R01CA208205 and U01CA224173), National Foundation for Cancer Research; the Ludwig Center at Harvard; the Jane's Trust Foundation; the Advanced Medical Research Foundation and by the U.S Department of Defense Breast Cancer Research Program Innovator Award W81XWH-10-1-0016.

Author information

Affiliations

1. Broad Institute of MIT and Harvard, Cambridge, MA, USA

Xin Jin, Zelalem Demere, Karthik Nair, Ahmed Ali, Ted Natoli, Amy Deik, Lia Petronio, Andrew A. Tang, Cong Zhu, Li Wang, Danny Rosenberg, Jennifer Roth, Kwanghun Chung, Clary B. Clish, Matthew G. Vander Heiden & Todd R. Golub

2. Koch Institute for Integrative Cancer Research, Department of Biology, Massachusetts Institute of Technology, Cambridge, MA, USA

Ahmed Ali & Matthew G. Vander Heiden

3. Edwin L. Steele Laboratories, Department of Radiation Oncology, Massachusetts General Hospital, Boston, MA, USA

Gino B. Ferraro & Rakesh K. Jain

4. Institute for Medical Engineering and Science, Picower Institute for Learning and Memory, Department of Chemical Engineering, Massachusetts Institute of Technology, Cambridge, MA, USA

Vamsi Mangena & Kwanghun Chung

5. Harvard Medical School, Boston, MA, USA

Rakesh K. Jain & Todd R. Golub

6. Dana-Farber Cancer Institute, Boston, MA, USA

Matthew G. Vander Heiden & Todd R. Golub

Authors

1. Xin Jin

[View author publications](#)

You can also search for this author in [PubMed](#) [Google Scholar](#)

2. Zelalem Demere

[View author publications](#)

You can also search for this author in [PubMed](#) [Google Scholar](#)

3. Karthik Nair

[View author publications](#)

You can also search for this author in [PubMed](#) [Google Scholar](#)

4. Ahmed Ali

[View author publications](#)

You can also search for this author in [PubMed](#) [Google Scholar](#)

5. Gino B. Ferraro

[View author publications](#)

You can also search for this author in [PubMed](#) [Google Scholar](#)

6. Ted Natoli

[View author publications](#)

You can also search for this author in [PubMed](#) [Google Scholar](#)

7. Amy Deik

[View author publications](#)

You can also search for this author in [PubMed](#) [Google Scholar](#)

8. Lia Petronio

[View author publications](#)

You can also search for this author in [PubMed](#) [Google Scholar](#)

9. Andrew A. Tang

[View author publications](#)

You can also search for this author in [PubMed](#) [Google Scholar](#)

10. Cong Zhu

[View author publications](#)

You can also search for this author in [PubMed](#) [Google Scholar](#)

11. Li Wang

[View author publications](#)

You can also search for this author in [PubMed](#) [Google Scholar](#)

12. Danny Rosenberg

[View author publications](#)

You can also search for this author in [PubMed](#) [Google Scholar](#)

13. Vamsi Mangena

[View author publications](#)

You can also search for this author in [PubMed](#) [Google Scholar](#)

14. Jennifer Roth

[View author publications](#)

You can also search for this author in [PubMed](#) [Google Scholar](#)

15. Kwanghun Chung

[View author publications](#)

You can also search for this author in [PubMed](#) [Google Scholar](#)

16. Rakesh K. Jain

[View author publications](#)

You can also search for this author in [PubMed](#) [Google Scholar](#)

17. Clary B. Clish

[View author publications](#)

You can also search for this author in [PubMed](#) [Google Scholar](#)

18. Matthew G. Vander Heiden

[View author publications](#)

You can also search for this author in [PubMed](#) [Google Scholar](#)

19. Todd R. Golub

[View author publications](#)

You can also search for this author in [PubMed](#) [Google Scholar](#)

Contributions

X.J. conceptualized the project, conducted experiments, collected data and analysed results. Z.D. assisted with experiments. K.N. and T.N. assisted with bioinformatic and RNA-seq analysis. A.A., A.D., C.B.C. and M.G.V.H. performed lipidomics and data interpretation. G.B.F. and R.K.J. performed intracranial injection experiments and data analysis. L.P. and

A.A.T. assisted with petal plot and portal development. C.Z., L.W., D.R. and J.R. assisted with PRISM assay and data generation. V.M. and K.C. performed tissue imaging, data acquisition and analysis. T.R.G. supervised the research. X.J. and T.R.G. wrote the manuscript.

Corresponding authors

Correspondence to [Xin Jin](#) or [Todd R. Golub](#).

Ethics declarations

Competing interests

T.R.G. receives research funding unrelated to this project from Bayer HealthCare, Novo Ventures and Calico Life Sciences; holds equity in FORMA Therapeutics; is a consultant to GlaxoSmithKline; and is a founder of Sherlock Biosciences. M.G.V.H. is a scientific advisory board member for Agios Pharmaceuticals, Aeglea Biotherapeutics, Auron Therapeutics and iTeos Therapeutics. R.K.J. received a honorarium from Amgen; consultant fees from Chugai, Merck, Ophthotech, Pfizer, SPARC and SynDevRx; owns equity in Accurius, Enlight, Ophthotech and SynDevRx; and serves on the Boards of Trustees of Tekla Healthcare Investors, Tekla Life Sciences Investors, Tekla Healthcare Opportunities Fund and Tekla World Healthcare Fund. No reagents or funding from these organizations were used in this study. X.J. and T.R.G. are named as inventors on pending PCT Patent Application No. PCT/US20/29584 filed by The Broad Institute, which describes compositions and methods for characterizing the metastatic potential of cancer cell lines. The other authors declare no competing interests.

Additional information

Peer review information *Nature* thanks Roger Gomis, Jason Locasale, Ultan McDermott and the other, anonymous, reviewer(s) for their contribution to the peer review of this work.

Publisher's note Springer Nature remains neutral with regard to jurisdictional claims in published maps and institutional affiliations.

Extended data figures and tables

[Extended Data Fig. 1 An in vivo barcoding approach to establish multiplexed cancer metastasis xenografts and validation using orthogonal assays.](#)

a, Principal component analysis (PCA) of transcriptomic expression of the breast cancer collection from CCLE, and the pooling schemes focusing on basal-like breast cancer. G, GFP; R, mCherry. The linked numbers indicate the labelling barcodes. **b**, Real-time BLI monitoring of the overall metastasis progression from pilot, group1, group2 cell line pools. Data are mean \pm s.e.m. $n = 5$ (pilot), $n = 8$ (group1), $n = 7$ (group2) mice. **c**, Total cancer cell numbers isolated by FACS from each target organ from pilot, group1, group2 pools. Each dot represents an animal. Box plots display quartiles of the data. **d**, Cancer cell composition of metastases from different organs as determined by barcode abundance from pilot, group1, group2 pools. pilot: G portion samples are highlighted in green, R portion samples are highlighted in red. preinj, pre-injected population. Data **c**, **d** were used to quantify the metastatic potential presented in Fig. [1b](#). **e**, An example of the gating strategy to isolate GFP+ barcoded cancer cells for the pilot pool. Infected cell lines expressed GFP at different levels as shown in the histogram, and a fixed gate was used to enrich cells with closer expression level. Numbers correspond to cell percentages within the gate. **f**, An example of barcode mapping result visualized by Integrative Genomics Viewer (IGV). **g**, Distribution of the barcode read counts versus all gene transcript counts. Barcodes are among the top 10% highly expressed genes, allowing robust quantification. **h**, An example of barcode read quantification in the pre-injected and metastasis samples from pilot pool. Barcodes are listed as in **a**. cpk, counts per thousand. **i**, Taqman assay on in vitro cultured barcoded cell lines from the pilot pool. The signal is very specific to each barcode and there is no cross detection. **j**, Quantification of barcode abundance and cancer cell composition using the Taqman RT-qPCR assay in the pre-injected and metastasis samples from the pilot pool.

The results agree with barcode quantification from bulk RNA-Seq (Extended Data Fig. 1d). **k**, Single cell RNA-Seq of metastases from different organs from the pilot pool. Single cancer cells isolated from each organ were sorted into 96-well plates, with 90 cells per plate (rest 6 wells for positive and negative controls), and subjected to Smart-Seq2. PCA revealed that PC1 maximally separated the cancer cells into 2 clusters (CLs), with CL1 enriched in cells isolated from brain, and CL2 enriched in cells isolated from lung, liver and bone. Heat map on the right shows gene expression that associates with PC1 and clustering of cells. Based on marker expression, CL1 corresponds to HCC1954 (ERBB2+, CDH1+) and CL2 corresponds to MDAMB231 (CDKN2A loss, VIM+). **l**, Projection of marker gene expression on the PCA plot. **m**, Cancer cell composition based on single cell RNA-Seq data. The results agree with barcode quantification from bulk RNA-Seq (Extended Data Fig. 1d). **n**, Real-time BLI monitoring of metastasis progression of the 8 cell lines that were individually tested. Each plot highlights one of the 8 lines. Data are mean \pm s.e.m. Each group contains 4 mice. **o**, Scatter plot showing the correlation of overall metastatic potential (5 organs combined) from pooled cell line experiments with whole body BLI of metastases measured individually. Pearson's correlation coefficient and its test *P* value are presented. [Source data](#)

[Extended Data Fig. 2 Using PRISM cell line pools for metastatic potential profiling.](#)

a, Optimizing the workflow of metastatic potential mapping using PRISM. A PRISM pool of 25 cell lines was used for testing the need of GFP labelling and cancer cell purification. The barcode abundance altered compared to the unlabelled population after GFP labelling as shown by the pie chart. **b**, A detailed line-by-line view of barcode abundance before and after GFP labelling. The unlabelled cell pool had more even distribution. Post labelling, several lines showed noticeable dropout, but all lines were detectable. **c**, Scatter plot comparing barcode enrichment after normalizing to the pre-injected input from the two experiments. Pearson's correlation coefficient and its test *P* value are presented. Strong positive correlation is observed, with the exception of one cell line U2OS. **d**, Quality control of MetMap500 and MetMap125 datasets showing initial barcode abundance in the pre-injected populations. MetMap500, 1 large pool containing 498 cell

lines was profiled, with 10 cell lines showing low initial abundance. These 10 cell lines were not detected in any in vivo sample, and were excluded from subsequent analysis. MetMap125, 5 pools of 25 cell lines were profiled separately and data were combined for analysis. **e**, Quality control of MetMap500 and MetMap125 datasets showing scatter plots of raw barcode abundance from in vivo organs versus the data normalized to the pre-injected input (in **d**). A strong linear relationship was observed. [Source data](#)

Extended Data Fig. 3 Subcutaneous injection of PRISM cell line pool.

a, The same PRISM pool of 498 cell lines used for MetMap500 profiling was tested using subcutaneous injection on a cohort of 6 mice. Survival curves compare animal survival difference between subcutaneous and intracardiac (IC) injections, *P* value calculated using two-sided, log-rank test. **b**, Total numbers of cell lines detected in animals from the subcutaneous and IC injections. Detected lines are coloured in pink and non-detected lines are coloured in light-blue. *P* value calculated using two-sided *t*-test. **c**, Scatter plot showing barcode-quantified tumorigenic potential and metastatic potential from subcutaneous and IC experiments respectively. **d**, Group1 of basal breast cancer pool (Extended Data Fig. 1a) was subjected to mammary fat pad injection, barcode quantitation through RNA-Seq, and cell number inference. [Source data](#)

Extended Data Fig. 4 Association of overall metastatic potential with clinical parameters.

a. Bar plots showing significance of single variate and multi variate association analysis with metastatic potential in MetMap500. *P* values are calculated using linear regression and Anova (type II) of the linear models. The dotted lines indicate 0.05 cutoff. **b**. Box plots showing metastatic potential of cell lines stratified by metastasis status in the corresponding patients and cancer lineage. Box plots display quartiles of the data. Outlier points extend beyond $1.5 \times$ interquartile ranges from either hinge. **c**, Scatter plots showing correlation of metastatic potential with patient age, stratified

by cancer lineage. An inverse correlation was observed in several cancer types. **d–g**, Correlation of overall metastatic potential with derived site (**d**), time length in culture to derive the cell lines (**e**), mutation burden (**f**) and cell doubling (**g**) in the 21 basal breast cancer cohort. **d**, *P* value calculated using two-sided *t*-test. **e–g**, Pearson's correlation coefficients and test *P* values are presented. [Source data](#)

[Extended Data Fig. 5 Genetic correlates of brain metastatic potential in basal-like breast cancer.](#)

a, A line-by-line view of brain metastatic potential and its associated features at genetic, expression, metabolite, and gene dependency levels. Mutation: mutant (MUT), wild-type (WT). Copy number: data are binarized, with deletion (DEL) cutoff ≤ -1 and amplification (AMP) cutoff ≥ 1 . Expression signatures: 1. Hallmark: PI3K/AKT/MTOR signalling, 2. GO: ERBB signalling pathway, 3. GO: ERBB2 signalling pathway, 4. Burton: adipogenesis peak at 8hr, 5. GO: carnitine metabolic process, 6. Reactome: mitochondrial fatty acid beta oxidation, 7. GO: short chain fatty acid metabolic process. Data not available for the cell lines are marked with X. **b, c**, Scatter plots showing the correlation of SREBF1 in vitro dependency and brain metastatic potential in MetMap500 (a) and MetMap125 (b). Strong inverse correlation was observed for breast cancer in both datasets. Each dot represents a cell line. [Source data](#)

[Extended Data Fig. 6 Association of chr 8p gene copy number status and PI3K-response signatures with brain metastasis in clinical breast cancer specimens.](#)

a, Heat maps showing coordinated expression of chr 8p genes mirrored their copy number status in the two large breast cancer datasets, METABRIC and TCGA. The 8p^{low} cluster is defined by CNA data. The right panel shows distribution of 8p^{low} cluster in different breast cancer subtypes and its association with disease specific survival. *P* values calculated using two-sided, log-rank tests. CNA, Copy Number Alteration. Exp, RNA-Seq Expression. **b**, Hierarchical clustering of primary breast tumours by 8p gene expression in the EMC-MSK dataset. The 8p^{low} cluster

is enriched in tumours that developed brain metastasis, but not lung or bone metastasis. The right panel shows organ-specific metastasis free survival curves stratified by 8p^{low} status. The 8p^{low} cluster displays poorer brain metastasis compared to the 8p^{WT} cluster. Brain metastasis free survival curves stratified by 8p^{low} status in different subtypes is also presented. *P* values calculated using two-sided, log-rank tests. **c**, Hierarchical clustering of breast cancer metastases by 8p gene expression, with the 8p^{low} cluster being enriched in brain metastases. **d**, Chr 8p CNA status determined by Targeted Seq in the MSK metastatic breast cancer dataset. Brain metastases are enriched in chr 8p deletion compared to primary tumour, local recurrence and metastases at other sites. The 8p^{low} cluster predicts poor brain metastasis free survival. *P* values calculated using two-sided, log-rank tests. LN, lymph node. **e**, Heat maps showing co-regulated patterns of two independent PI3K-response signatures in METABRIC and TCGA breast cancer datasets. PI3Ksig.1 was generated by overexpression of PIK3CA^{mut} in breast epithelial cells. PI3Ksig.2 was generated by PI3K inhibitor treatment in the CMap database. The right panel shows distribution of PI3Ksig^{high} cluster in different breast cancer subtypes and its association with disease specific survival. *P* values calculated using two-sided, log-rank tests. **f**, Hierarchical clustering of primary breast tumours by PI3K signatures in the EMC-MSK dataset. The PI3Ksig^{high} cluster is enriched in tumours that developed brain metastasis. The right panel shows organ-specific metastasis free survival curves stratified by PI3K signatures. The PI3Ksig^{high} cluster displayed poorer brain metastasis. Brain metastasis free survival curves stratified by PI3K signatures in different subtypes is also presented. *P* values calculated using two-sided, log-rank tests. **g**, Hierarchical clustering of breast cancer metastases by PI3K signatures, with the PI3Ksig^{high} cluster being enriched in brain metastases. **h**, Heat maps showing significant yet non-complete overlap between 8p^{low} and PI3Ksig^{high} clusters in the EMC-MSK dataset. 8p^{low} and PI3Ksig^{high} clusters co-capture a subset of patients with the worst brain metastasis prognosis. *P* values calculated using two-sided, log-rank tests. The lower panel presents a Cox proportional-hazards model of brain metastasis free survival using multi variates – 8p, PI3Ksig, and breast cancer subtype. The 8p^{low}/PI3Ksig^{high} cluster is the most associated with brain metastasis. **i**.

$8p^{low}$ and PI3Ksig high clusters co-capture the majority of brain metastasis samples. [Source data](#)

Extended Data Fig. 7 Lipid metabolite profile changes upon SREBF1 knockout.

Heat maps showing relative lipid abundance in cells cultured in medium supplemented with serum or delipidated serum. SREBF1-WT and SREBF1-KO of JIMT1 (PIK3CA mut) and HCC1806 ($8p^{low}$) were used. Lipid species groupings and lipid desaturation levels are also presented. WT, wild-type; KO, knockout. [Source data](#)

Extended Data Fig. 8 Analysis of multiplexed breast cancer metastasis in vivo transcriptomes.

a, A schematic of the differential analysis approach for in vivo transcriptomes with mixed cancer cell lines. An in silico transcriptome was modelled based on single cell line in vitro transcriptomes and cell line composition (comp.) of the metastasis sample. The in silico profile was then compared with the actual in vivo data in a paired-wise manner. **b**, Comparison of in silico modelled profiles to the actual pre-injected or in vivo metastasis sample profiles. The pre-injected populations are direct mixtures of in vitro cell lines and show tight correlation with in silico data. In vivo samples show large fold changes. **c**, Box plots showing \log_2 fold changes of MUCL1 and SCGB2A2 in in vivo metastasis samples and pre-injected cells. Each point represents a sample. Box plots display quartiles of the data. Outlier points extend beyond $1.5 \times$ interquartile ranges from either hinges. **d**, Heat map showing \log_2 fold change of lung metastasis genes (Minn et al.) in lung, liver, kidney and bone metastasis samples from the pilot study, where MDAMB231 dominated the population. **e**, Correlation of gene expression changes in different metastasis sites. Pre-injected population had no expression change and thus showed no correlation with in vivo samples. Brain metastases showed weaker correlations with extracranial metastases. **f**, Bubble plot showing enrichment of Hallmark gene pathways (MSigDB) comparing in vivo expression of metastases at different organ sites to their in vitro counterparts. **g**, Bubble plot showing in

vivo upregulation of SREBF1, SCD and SREBF1-response signature in brain metastases. **h, i**, GSEA analysis of lipid metabolism gene sets using in vivo RNA-Seq profiles combined by metastasis organ sites irrespective of sample or cell line composition (**h**). Gene sets related to lipid metabolism are selectively enriched on top in the brain but not in other organs or in vitro. Restricting analysis to JIMT1-dominant samples revealed a similar result. No enrichment was seen in normal brain when analysis was performed on GTEx normal tissue (**i**). Each tick represents a lipid metabolism gene set from MSigDB. ***, $P = 0.001$; ** = 0.01. [Source data](#)

Extended Data Fig. 9 Expression of TGF β signalling, EMT status, inflammatory response and lipid metabolism genes in clinical breast cancer metastasis specimens.

a, Comparison of brain metastasis versus extracranial metastasis clinical samples. Lower expression of TGF β signature genes and EMT signature genes in brain metastases than other metastasis sites. Enriched expression of selective SREBF1 target genes (including FASN, SCD, SREBF1 itself) and Pentose Phosphate Pathway (PPP) genes in brain metastases. **b, c**, A strategy to remove brain stroma contamination effect from brain metastasis expression profiles when performing comparison of paired primary breast tumour and brain metastasis clinical specimens. A gene signature indicating brain stroma contamination was derived from comparison of brain with breast and breast cancer brain metastasis (**b**). Arrowheads indicate a few brain metastasis samples with noticeable brain stroma contamination. A brain contamination score was calculated and its effect was regressed out in the RNASeq data of matched primary tumours and brain metastases (**c**). The heat map shows expression of brain stroma indicator before and after removal of the contamination effect. **d, e**, Paired comparison of primary breast tumour and brain metastasis clinical specimens after removal of brain stroma contamination. **d**, Lipid metabolism genes and PPP genes. **e**, Signature scores were projected for each sample using the corrected RNA-Seq profiles. P, Primary breast tumour; M, brain Metastasis; upregulation in red, downregulation in blue. P values calculated using paired, two-sided t -tests. [Source data](#)

Extended Data Fig. 10 In vivo and in vitro effects of SREBF1 knockout.

a, Growth kinetics of SREBF1-WT and -KO cells in in vitro culture medium with 10% serum or 10% delipidated serum. Cell growth was monitored by Incucyte real-time imaging. WT, wild-type, in black; KO, knockout, in red. Two independent guides were used per group. **b**, Fluorescence imaging of metastases in serial brain sections from mice receiving intracardiac injection of JIMT1 SREBF1-WT or -KO cells (Fig. 5d). Confocal tile scans of representative sections are presented at the lower panel. GFP+ signals indicate cancer lesions. Circles highlight macro-metastatic lesions and arrows indicate micro lesions. **c, d**, One-by-one assessment of lipid metabolism gene fitness in additional brain metastatic cell lines through intracranial injection. SREBF1 was tested for HCC1954, MDAMB231 (**c**) and HCC1806. Additional genes were tested for HCC1806 (**d**). Cell outgrowth in brain metastasis was monitored by real-time BLI. Two independent guides per gene were tested, in a one guide one mouse fashion. **e–g**, Outgrowing (HCC1806) or residual (JIMT1) SREBF1-KO cells from brain metastases were derived for CRISPR-seq (**e**), western blot (**f**), and RT-qPCR (**g**) assays. **e**, CRISPR-seq quantifying SREBF1 gene editing efficiencies of brain-derived and pre-injected cells. **f**, Western blot quantifying SREBF1 protein levels. **g**, RT-qPCR quantifying relative expression of SREBF1, SCD, CD36, FABP6 in brain-derived versus pre-injected cells. Pre-injected WT HCC1806 was used as reference. **h, i**, Brain-derived and pre-injected HCC1806 cells were cultured in brain-slice-conditioned medium (CM) or medium supplemented with cerebrospinal fluid, or serum, or delipidated serum, or SM1 supplement, and western blot (**h**) or RT-qPCR was performed (**i**). SREBF1, SCD and CD36 were upregulated when cells were cultured in brain slice CM, cerebrospinal fluid, and delipidated serum. Brain-derived SREBF1-KO cells were better at inducing SCD and CD36, in comparison to pre-injected SREBF1-KO cells. Experiments were performed twice independently with similar results.

[Source data](#)

Supplementary information

Supplementary Information

Supplementary Notes 1-4.

Life Sciences Reporting Summary

Supplementary Figure 1

Uncropped raw western blot images.

Supplementary Table 1

Basal-like breast cancer cell line and barcode information.

Supplementary Table 2

Metastatic potential of basal-like breast cancer.

Supplementary Table 3

MetMap cell line, pooling scheme, and updated annotation.

Supplementary Table 4

Metastatic potential in MetMap500.

Supplementary Table 5

Metastatic potential in MetMap125.

Supplementary Table 6

Signature gene list of Chr 8p genes, PI3K-response signatures, and brain stroma indicator.

Supplementary Table 7

Differential analysis of RNA-Seq of SREBF1-KO versus -WT cells.

Supplementary Table 8

Differential analysis of RNA-Seq of *in vivo* metastases versus *in-silico*-modeled *in vitro* profiles from breast cancer pools.

Supplementary Table 9

Tissue dissociation buffers and programs.

Supplementary Table 10

Guide sequences used for gene perturbation in CRISPR screen and validation; data count of mini-pool screen; CRISPR-seq primers.

Source data

Source Data Fig. 1

Source Data Fig. 2

Source Data Fig. 3

Source Data Fig. 4

Source Data Fig. 5

Source Data Extended Data Fig. 1

Source Data Extended Data Fig. 2

Source Data Extended Data Fig. 3

Source Data Extended Data Fig. 4

[Source Data Extended Data Fig. 5](#)

[Source Data Extended Data Fig. 6](#)

[Source Data Extended Data Fig. 7](#)

[Source Data Extended Data Fig. 8](#)

[Source Data Extended Data Fig. 9](#)

[Source Data Extended Data Fig. 10](#)

Rights and permissions

[Reprints and Permissions](#)

About this article



Check for
updates

Cite this article

Jin, X., Demere, Z., Nair, K. *et al.* A metastasis map of human cancer cell lines. *Nature* **588**, 331–336 (2020). <https://doi.org/10.1038/s41586-020-2969-2>

[Download citation](#)

- Received: 17 December 2018
- Accepted: 26 August 2020
- Published: 09 December 2020

- Issue Date: 10 December 2020
- DOI: <https://doi.org/10.1038/s41586-020-2969-2>

Comments

By submitting a comment you agree to abide by our [Terms](#) and [Community Guidelines](#). If you find something abusive or that does not comply with our terms or guidelines please flag it as inappropriate.

[Access through your institution](#)

[Change institution](#)

[Buy or subscribe](#)

Associated Content

Collection

[Cancer at Nature Research](#)

This article was downloaded by **calibre** from <https://www.nature.com/articles/s41586-020-2969-2>

| [Section menu](#) | [Main menu](#) |

- Article
- [Published: 25 November 2020](#)

A map of *cis*-regulatory elements and 3D genome structures in zebrafish

- [Hongbo Yang^{1 na1}](#),
- [Yu Luan^{1 na1}](#),
- [Tingting Liu^{1 na1}](#),
- [Hyung Joo Lee](#) ORCID: orcid.org/0000-0002-7030-5390²,
- [Li Fang](#) ORCID: orcid.org/0000-0001-5456-0255³,
- [Yanli Wang⁴](#),
- [Xiaotao Wang¹](#),
- [Bo Zhang⁴](#),
- [Qiushi Jin¹](#),
- [Khai Chung Ang](#) ORCID: orcid.org/0000-0001-7695-9953⁵,
- [Xiaoyun Xing²](#),
- [Juan Wang¹](#),
- [Jie Xu¹](#),
- [Fan Song⁴](#),
- [Iyyanki Sriranga¹](#),
- [Chachrit Khunsriraksakul⁴](#),
- [Tarik Salameh⁴](#),
- [Daofeng Li](#) ORCID: orcid.org/0000-0001-7492-3703²,
- [Mayank N. K. Choudhary²](#),
- [Jacek Topczewski](#) ORCID: orcid.org/0000-0001-6023-9556^{6,7},
- [Kai Wang³](#),
- [Glenn S. Gerhard⁸](#),
- [Ross C. Hardison](#) ORCID: orcid.org/0000-0003-4084-7516⁹,

- [Ting Wang²](#),
- [Keith C. Cheng⁵](#) &
- [Feng Yue](#) [ORCID: orcid.org/0000-0002-7954-5462^{1,10}](#)

[Nature](#) volume **588**, pages337–343(2020)[Cite this article](#)

- 4753 Accesses
- 85 Altmetric
- [Metrics details](#)

Subjects

- [Chromatin structure](#)
- [Epigenomics](#)
- [Sequence annotation](#)

Abstract

The zebrafish (*Danio rerio*) has been widely used in the study of human disease and development, and about 70% of the protein-coding genes are conserved between the two species¹. However, studies in zebrafish remain constrained by the sparse annotation of functional control elements in the zebrafish genome. Here we performed RNA sequencing, assay for transposase-accessible chromatin using sequencing (ATAC-seq), chromatin immunoprecipitation with sequencing, whole-genome bisulfite sequencing, and chromosome conformation capture (Hi-C) experiments in up to eleven adult and two embryonic tissues to generate a comprehensive map of transcriptomes, *cis*-regulatory elements, heterochromatin, methylomes and 3D genome organization in the zebrafish Tübingen reference strain. A comparison of zebrafish, human and mouse regulatory elements enabled the identification of both evolutionarily conserved and species-specific regulatory sequences and networks. We observed enrichment of evolutionary breakpoints at topologically associating domain boundaries, which were correlated with strong histone H3 lysine 4 trimethylation (H3K4me3) and CCCTC-binding factor (CTCF) signals. We performed

single-cell ATAC-seq in zebrafish brain, which delineated 25 different clusters of cell types. By combining long-read DNA sequencing and Hi-C, we assembled the sex-determining chromosome 4 de novo. Overall, our work provides an additional epigenomic anchor for the functional annotation of vertebrate genomes and the study of evolutionarily conserved elements of 3D genome organization.

[Access through your institution](#)

[Change institution](#)

[Buy or subscribe](#)

Access options

Subscribe to Journal

Get full journal access for 1 year

185,98 €

only 3,58 € per issue

[Subscribe](#)

All prices are NET prices.

VAT will be added later in the checkout.

Rent or Buy article

Get time limited or full article access on ReadCube.

from \$8.99

[Rent or Buy](#)

All prices are NET prices.

Additional access options:

- [Log in](#)
- [Access through your institution](#)
- [Learn about institutional subscriptions](#)

Fig. 1: Identification of *cis*-regulatory elements in the zebrafish genome.



Fig. 2: Characterization of tissue-specific *cis*-regulatory elements.



Fig. 3: Analysis of heterochromatin and repetitive elements and de novo assembly of zebrafish chromosome 4.



Fig. 4: Conservation of zebrafish *cis*-regulatory elements and transcriptional networks.



Fig. 5: Higher-order chromatin structure and zebrafish genome evolution.



Data availability

All the sequencing data are deposited in the NCBI Gene Expression Omnibus under accession code [GSE134055](#). All the genomic data generated in this study can be visualized in the WashU Epigenome Browser (<https://epigenome.wustl.edu/zebrafishENCODE/>). The human histone-modification ChIP-seq data were downloaded from the ROADMAP Project. The mouse histone modification ChIP-seq data were downloaded from the mouse ENCODE Consortium. The human tissue transcriptome data were downloaded from the GTEx Consortium. The public zebrafish ChIP-seq and ATAC-seq data used in this study are listed in Supplementary Table [6](#). The human h1-ESC Hi-C data were downloaded from GSE52457. GM12878 and K562 GRO-seq data were downloaded from GSE60456. GM12878 and K562 CTCF ChIP-seq were downloaded from GSE31477. GM12878 and K562 Pol2 ChIP-seq were downloaded from GSE91426 and GSE31477. [Source data](#) are provided with this paper.

References

1. 1.

Howe, K. et al. The zebrafish reference genome sequence and its relationship to the human genome. *Nature* **496**, 498–503 (2013).

[ADS](#) [CAS](#) [PubMed](#) [PubMed Central](#) [Google Scholar](#)

2. 2.

Gerhard, G. S. et al. Life spans and senescent phenotypes in two strains of Zebrafish (*Danio rerio*). *Exp. Gerontol.* **37**, 1055–1068 (2002).

[PubMed](#) [Google Scholar](#)

3. 3.

Lamason, R. L. et al. SLC24A5, a putative cation exchanger, affects pigmentation in zebrafish and humans. *Science* **310**, 1782–1786 (2005).

[ADS](#) [CAS](#) [Google Scholar](#)

4. 4.

Vastenhoud, N. L. et al. Chromatin signature of embryonic pluripotency is established during genome activation. *Nature* **464**, 922–926 (2010).

[ADS](#) [CAS](#) [PubMed](#) [PubMed Central](#) [Google Scholar](#)

5. 5.

Bogdanovic, O. et al. Dynamics of enhancer chromatin signatures mark the transition from pluripotency to cell specification during embryogenesis. *Genome Res.* **22**, 2043–2053 (2012).

[CAS](#) [PubMed](#) [PubMed Central](#) [Google Scholar](#)

6. 6.

Kaaij, L. J. et al. Enhancers reside in a unique epigenetic environment during early zebrafish development. *Genome Biol.* **17**, 146 (2016).

[PubMed](#) [PubMed Central](#) [Google Scholar](#)

7. 7.

Aday, A. W., Zhu, L. J., Lakshmanan, A., Wang, J. & Lawson, N. D. Identification of *cis* regulatory features in the embryonic zebrafish genome through large-scale profiling of H3K4me1 and H3K4me3 binding sites. *Dev. Biol.* **357**, 450–462 (2011).

[CAS](#) [PubMed](#) [PubMed Central](#) [Google Scholar](#)

8. 8.

Vesterlund, L., Jiao, H., Unneberg, P., Hovatta, O. & Kere, J. The zebrafish transcriptome during early development. *BMC Dev. Biol.* **11**, 30 (2011).

[CAS](#) [PubMed](#) [PubMed Central](#) [Google Scholar](#)

9. 9.

Buenrostro, J. D., Giresi, P. G., Zaba, L. C., Chang, H. Y. & Greenleaf, W. J. Transposition of native chromatin for fast and sensitive epigenomic profiling of open chromatin, DNA-binding proteins and nucleosome position. *Nat. Methods* **10**, 1213–1218 (2013).

[CAS](#) [PubMed](#) [PubMed Central](#) [Google Scholar](#)

10. 10.

ENCODE Project Consortium. An integrated encyclopedia of DNA elements in the human genome. *Nature* **489**, 57–74 (2012).

[ADS](#) [Google Scholar](#)

11. 11.

Yue, F. et al. A comparative encyclopedia of DNA elements in the mouse genome. *Nature* **515**, 355–364 (2014).

[CAS](#) [PubMed](#) [PubMed Central](#) [Google Scholar](#)

12. 12.

Anderson, J. L. et al. Multiple sex-associated regions and a putative sex chromosome in zebrafish revealed by RAD mapping and population genomics. *PLoS ONE* **7**, e40701 (2012).

[ADS](#) [CAS](#) [PubMed](#) [PubMed Central](#) [Google Scholar](#)

13. 13.

Klemm, S. L., Shipony, Z. & Greenleaf, W. J. Chromatin accessibility and the regulatory epigenome. *Nat. Rev. Genet.* **20**, 207–220 (2019).

[CAS](#) [PubMed](#) [Google Scholar](#)

14. 14.

Meuleman, W. et al. Index and biological spectrum of human DNase I hypersensitive sites. *Nature* **584**, 244–251 (2020).

[CAS](#) [PubMed](#) [PubMed Central](#) [Google Scholar](#)

15. 15.

Quillien, A. et al. Robust identification of developmentally active endothelial enhancers in zebrafish using FANS-assisted ATAC-seq. *Cell Rep.* **20**, 709–720 (2017).

[CAS](#) [PubMed](#) [PubMed Central](#) [Google Scholar](#)

16. 16.

Letelier, J. et al. Evolutionary emergence of the *rac3b/rfng/sgca* regulatory cluster refined mechanisms for hindbrain boundaries

formation. *Proc. Natl Acad. Sci. USA* **115**, E3731–E3740 (2018).

[CAS](#) [PubMed](#) [Google Scholar](#)

17. 17.

Liu, G., Wang, W., Hu, S., Wang, X. & Zhang, Y. Inherited DNA methylation primes the establishment of accessible chromatin during genome activation. *Genome Res.* **28**, 998–1007 (2018).

[CAS](#) [PubMed](#) [PubMed Central](#) [Google Scholar](#)

18. 18.

Marlétaz, F. et al. Amphioxus functional genomics and the origins of vertebrate gene regulation. *Nature* **564**, 64–70 (2018).

[ADS](#) [PubMed](#) [PubMed Central](#) [Google Scholar](#)

19. 19.

Meier, M. et al. Cohesin facilitates zygotic genome activation in zebrafish. *Development* **145**, dev156521 (2018).

[PubMed](#) [Google Scholar](#)

20. 20.

Torbey, P. et al. Cooperation, *cis*-interactions, versatility and evolutionary plasticity of multiple *cis*-acting elements underlie krox20 hindbrain regulation. *PLoS Genet.* **14**, e1007581 (2018).

[PubMed](#) [PubMed Central](#) [Google Scholar](#)

21. 21.

Paik, E. J. et al. A Cdx4–Sall4 regulatory module controls the transition from mesoderm formation to embryonic hematopoiesis. *Stem Cell Reports* **1**, 425–436 (2013).

[CAS](#) [PubMed](#) [PubMed Central](#) [Google Scholar](#)

22. 22.

Kang, J. et al. Modulation of tissue repair by regeneration enhancer elements. *Nature* **532**, 201–206 (2016).

[ADS](#) [CAS](#) [PubMed](#) [PubMed Central](#) [Google Scholar](#)

23. 23.

Kaufman, C. K. et al. A zebrafish melanoma model reveals emergence of neural crest identity during melanoma initiation. *Science* **351**, aad2197 (2016).

[PubMed](#) [PubMed Central](#) [Google Scholar](#)

24. 24.

Goldman, J. A. et al. Resolving heart regeneration by replacement histone profiling. *Dev. Cell* **40**, 392–404 (2017).

[CAS](#) [PubMed](#) [PubMed Central](#) [Google Scholar](#)

25. 25.

Pérez-Rico, Y. A. et al. Comparative analyses of super-enhancers reveal conserved elements in vertebrate genomes. *Genome Res.* **27**, 259–268 (2017).

[PubMed](#) [PubMed Central](#) [Google Scholar](#)

26. 26.

Lister, R. et al. Global epigenomic reconfiguration during mammalian brain development. *Science* **341**, 1237905 (2013).

[PubMed](#) [PubMed Central](#) [Google Scholar](#)

27. 27.

Visel, A. et al. Ultraconservation identifies a small subset of extremely constrained developmental enhancers. *Nat. Genet.* **40**, 158–160 (2008).

[CAS](#) [PubMed](#) [PubMed Central](#) [Google Scholar](#)

28. 28.

Dimitrieva, S. & Bucher, P. UCNEbase—a database of ultraconserved non-coding elements and genomic regulatory blocks. *Nucleic Acids Res.* **41**, D101–D109 (2013).

[CAS](#) [PubMed](#) [Google Scholar](#)

29. 29.

Visel, A., Minovitsky, S., Dubchak, I. & Pennacchio, L. A. VISTA Enhancer Browser—a database of tissue-specific human enhancers. *Nucleic Acids Res.* **35**, D88–D92 (2007).

[CAS](#) [PubMed](#) [Google Scholar](#)

30. 30.

Corces, M. R. et al. The chromatin accessibility landscape of primary human cancers. *Science* **362**, eaav1898 (2018).

[ADS](#) [PubMed](#) [PubMed Central](#) [Google Scholar](#)

31. 31.

Neph, S. et al. Circuitry and dynamics of human transcription factor regulatory networks. *Cell* **150**, 1274–1286 (2012).

[CAS](#) [PubMed](#) [PubMed Central](#) [Google Scholar](#)

32. 32.

Yang, T. et al. HiCRep: assessing the reproducibility of Hi-C data using a stratum-adjusted correlation coefficient. *Genome Res.* **27**, 1939–1949 (2017).

[CAS](#) [PubMed](#) [PubMed Central](#) [Google Scholar](#)

33. 33.

Krefting, J., Andrade-Navarro, M. A. & Ibn-Salem, J. Evolutionary stability of topologically associating domains is associated with conserved gene regulation. *BMC Biol.* **16**, 87 (2018).

[PubMed](#) [PubMed Central](#) [Google Scholar](#)

34. 34.

Lazar, N. H. et al. Epigenetic maintenance of topological domains in the highly rearranged gibbon genome. *Genome Res.* **28**, 983–997 (2018).

[CAS](#) [PubMed](#) [PubMed Central](#) [Google Scholar](#)

35. 35.

Fishman, V. et al. 3D organization of chicken genome demonstrates evolutionary conservation of topologically associated domains and highlights unique architecture of erythrocytes' chromatin. *Nucleic Acids Res.* **47**, 648–665 (2019).

[CAS](#) [PubMed](#) [Google Scholar](#)

36. 36.

Dixon, J. R. et al. Topological domains in mammalian genomes identified by analysis of chromatin interactions. *Nature* **485**, 376–380 (2012).

[ADS](#) [CAS](#) [PubMed](#) [PubMed Central](#) [Google Scholar](#)

37. 37.

Smagulova, F. et al. Genome-wide analysis reveals novel molecular features of mouse recombination hotspots. *Nature* **472**, 375–378 (2011).

[ADS](#) [CAS](#) [PubMed](#) [PubMed Central](#) [Google Scholar](#)

38. 38.

Canela, A. et al. Genome organization drives chromosome fragility. *Cell* **170**, 507–521 (2017).

[CAS](#) [PubMed](#) [PubMed Central](#) [Google Scholar](#)

39. 39.

Gothe, H. J. et al. Spatial chromosome folding and active transcription drive DNA fragility and formation of oncogenic *MLL* translocations. *Mol. Cell* **75**, 267–283 (2019).

[CAS](#) [PubMed](#) [Google Scholar](#)

40. 40.

Canela, A. et al. Topoisomerase II–induced chromosome breakage and translocation is determined by chromosome architecture and transcriptional activity. *Mol. Cell* **75**, 252–266 (2019).

[CAS](#) [PubMed](#) [Google Scholar](#)

41. 41.

Postlethwait, J. H. et al. Vertebrate genome evolution and the zebrafish gene map. *Nat. Genet.* **18**, 345–349 (1998).

[CAS](#) [PubMed](#) [Google Scholar](#)

42. 42.

Pedroso, G. L. et al. Blood collection for biochemical analysis in adult zebrafish. *J. Vis. Exp.* **3865**, e3865 (2012).

[Google Scholar](#)

43. 43.

Rao, S. S. et al. A 3D map of the human genome at kilobase resolution reveals principles of chromatin looping. *Cell* **159**, 1665–1680 (2014).

[CAS](#) [PubMed](#) [PubMed Central](#) [Google Scholar](#)

44. 44.

Xie, W. et al. Epigenomic analysis of multilineage differentiation of human embryonic stem cells. *Cell* **153**, 1134–1148 (2013).

[CAS](#) [PubMed](#) [PubMed Central](#) [Google Scholar](#)

45. 45.

Kim, D. et al. TopHat2: accurate alignment of transcriptomes in the presence of insertions, deletions and gene fusions. *Genome Biol.* **14**, R36 (2013).

[PubMed](#) [PubMed Central](#) [Google Scholar](#)

46. 46.

Trapnell, C. et al. Transcript assembly and quantification by RNA-Seq reveals unannotated transcripts and isoform switching during cell differentiation. *Nat. Biotechnol.* **28**, 511–515 (2010).

[CAS](#) [PubMed](#) [PubMed Central](#) [Google Scholar](#)

47. 47.

Wang, L. et al. CPAT: Coding-Potential Assessment Tool using an alignment-free logistic regression model. *Nucleic Acids Res.* **41**, e74

(2013).

[CAS](#) [PubMed](#) [PubMed Central](#) [Google Scholar](#)

48. 48.

Dobin, A. et al. STAR: ultrafast universal RNA-seq aligner. *Bioinformatics* **29**, 15–21 (2013).

[CAS](#) [PubMed](#) [PubMed Central](#) [Google Scholar](#)

49. 49.

Li, B. & Dewey, C. N. RSEM: accurate transcript quantification from RNA-Seq data with or without a reference genome. *BMC Bioinformatics* **12**, 323 (2011).

[CAS](#) [PubMed](#) [PubMed Central](#) [Google Scholar](#)

50. 50.

Maertin, M. Cutadapt removes adapter sequences from high-throughput sequencing reads. *EMBnet J.* **17**, 10–12 (2011).

[Google Scholar](#)

51. 51.

Langmead, B. & Salzberg, S. L. Fast gapped-read alignment with Bowtie 2. *Nat. Methods* **9**, 357–359 (2012).

[CAS](#) [PubMed](#) [PubMed Central](#) [Google Scholar](#)

52. 52.

Li, Z. et al. Identification of transcription factor binding sites using ATAC-seq. *Genome Biol.* **20**, 45 (2019).

[PubMed](#) [PubMed Central](#) [Google Scholar](#)

53. 53.

Korhonen, J., Martinmäki, P., Pizzi, C., Rastas, P. & Ukkonen, E. MOODS: fast search for position weight matrix matches in DNA sequences. *Bioinformatics* **25**, 3181–3182 (2009).

[CAS](#) [PubMed](#) [PubMed Central](#) [Google Scholar](#)

54. 54.

Kulakovskiy, I. V. et al. HOCOMOCO: towards a complete collection of transcription factor binding models for human and mouse via large-scale ChIP-seq analysis. *Nucleic Acids Res.* **46** (D1), D252–D259 (2018).

[CAS](#) [PubMed](#) [Google Scholar](#)

55. 55.

Gerstein, M. B. et al. Integrative analysis of the *Caenorhabditis elegans* genome by the modENCODE project. *Science* **330**, 1775–1787 (2010).

[ADS](#) [CAS](#) [PubMed](#) [PubMed Central](#) [Google Scholar](#)

56. 56.

Li, H. et al. The Sequence Alignment/Map format and SAMtools. *Bioinformatics* **25**, 2078–2079 (2009).

[PubMed](#) [PubMed Central](#) [Google Scholar](#)

57. 57.

Liu, T. Use model-based Analysis of ChIP-Seq (MACS) to analyze short reads generated by sequencing protein-DNA interactions in embryonic stem cells. *Methods Mol. Biol.* **1150**, 81–95 (2014).

[CAS](#) [PubMed](#) [Google Scholar](#)

58. 58.

Hiller, M. et al. Computational methods to detect conserved non-genic elements in phylogenetically isolated genomes: application to zebrafish. *Nucleic Acids Res.* **41**, e151 (2013).

[CAS](#) [PubMed](#) [PubMed Central](#) [Google Scholar](#)

59. 59.

Lee, H. J. et al. Regenerating zebrafish fin epigenome is characterized by stable lineage-specific DNA methylation and dynamic chromatin accessibility. *Genome Biol.* **21**, 52 (2020).

[CAS](#) [PubMed](#) [PubMed Central](#) [Google Scholar](#)

60. 60.

Krueger, F. & Andrews, S. R. Bismark: a flexible aligner and methylation caller for Bisulfite-Seq applications. *Bioinformatics* **27**, 1571–1572 (2011).

[CAS](#) [PubMed](#) [PubMed Central](#) [Google Scholar](#)

61. 61.

Zhou, X., Li, D., Lowdon, R. F., Costello, J. F. & Wang, T. methylC Track: visual integration of single-base resolution DNA methylation data on the WashU EpiGenome Browser. *Bioinformatics* **30**, 2206–2207 (2014).

[CAS](#) [PubMed](#) [PubMed Central](#) [Google Scholar](#)

62. 62.

Burger, L., Gaidatzis, D., Schübeler, D. & Stadler, M. B. Identification of active regulatory regions from DNA methylation data. *Nucleic Acids Res.* **41**, e155 (2013).

[PubMed](#) [PubMed Central](#) [Google Scholar](#)

63. 63.

Wu, H. et al. Detection of differentially methylated regions from whole-genome bisulfite sequencing data without replicates. *Nucleic Acids Res.* **43**, e141 (2015).

[PubMed](#) [PubMed Central](#) [Google Scholar](#)

64. 64.

Hansen, K. D., Langmead, B. & Irizarry, R. A. BSmooth: from whole genome bisulfite sequencing reads to differentially methylated regions. *Genome Biol.* **13**, R83 (2012).

[PubMed](#) [PubMed Central](#) [Google Scholar](#)

65. 65.

Ramírez, F. et al. deepTools2: a next generation web server for deep-sequencing data analysis. *Nucleic Acids Res.* **44** (W1), W160–W165 (2016).

[PubMed](#) [PubMed Central](#) [Google Scholar](#)

66. 66.

Koren, S. et al. Canu: scalable and accurate long-read assembly via adaptive k -mer weighting and repeat separation. *Genome Res.* **27**, 722–736 (2017).

[CAS](#) [PubMed](#) [PubMed Central](#) [Google Scholar](#)

67. 67.

Walker, B. J. et al. Pilon: an integrated tool for comprehensive microbial variant detection and genome assembly improvement. *PLoS ONE* **9**, e112963 (2014).

[ADS](#) [PubMed](#) [PubMed Central](#) [Google Scholar](#)

68. 68.

Dudchenko, O. et al. De novo assembly of the *Aedes aegypti* genome using Hi-C yields chromosome-length scaffolds. *Science* **356**, 92–95 (2017).

[ADS](#) [CAS](#) [PubMed](#) [PubMed Central](#) [Google Scholar](#)

69. 69.

Kundaje, A. et al. Integrative analysis of 111 reference human epigenomes. *Nature* **518**, 317–330 (2015).

[CAS](#) [PubMed](#) [PubMed Central](#) [Google Scholar](#)

70. 70.

Heinz, S. et al. Simple combinations of lineage-determining transcription factors prime *cis*-regulatory elements required for macrophage and B cell identities. *Mol. Cell* **38**, 576–589 (2010).

[CAS](#) [PubMed](#) [PubMed Central](#) [Google Scholar](#)

71. 71.

Grant, C. E., Bailey, T. L. & Noble, W. S. FIMO: scanning for occurrences of a given motif. *Bioinformatics* **27**, 1017–1018 (2011).

[CAS](#) [PubMed](#) [PubMed Central](#) [Google Scholar](#)

72. 72.

Servant, N. et al. HiC-Pro: an optimized and flexible pipeline for Hi-C data processing. *Genome Biol.* **16**, 259 (2015).

[PubMed](#) [PubMed Central](#) [Google Scholar](#)

73. 73.

Durand, N. C. et al. Juicer provides a one-click system for analyzing loop-resolution Hi-C experiments. *Cell Syst.* **3**, 95–98 (2016).

[CAS](#) [PubMed](#) [PubMed Central](#) [Google Scholar](#)

74. 74.

Robinson, J. T. et al. Juicebox.js provides a cloud-based visualization system for Hi-C data. *Cell Syst.* **6**, 256–258 (2018).

[CAS](#) [PubMed](#) [PubMed Central](#) [Google Scholar](#)

75. 75.

Abdennur, N. & Mirny, L. A. Cooler: scalable storage for Hi-C data and other genomically labeled arrays. *Bioinformatics* **36**, 311–316 (2020).

[CAS](#) [PubMed](#) [Google Scholar](#)

76. 76.

Crane, E. et al. Condensin-driven remodelling of X chromosome topology during dosage compensation. *Nature* **523**, 240–244 (2015).

[ADS](#) [CAS](#) [PubMed](#) [PubMed Central](#) [Google Scholar](#)

77. 77.

Giorgetti, L. et al. Structural organization of the inactive X chromosome in the mouse. *Nature* **535**, 575–579 (2016).

[ADS](#) [CAS](#) [PubMed](#) [PubMed Central](#) [Google Scholar](#)

78. 78.

Imakaev, M. et al. Iterative correction of Hi-C data reveals hallmarks of chromosome organization. *Nat. Methods* **9**, 999–1003 (2012).

[CAS](#) [PubMed](#) [PubMed Central](#) [Google Scholar](#)

79. 79.

Darling, A. E., Mau, B. & Perna, N. T. progressiveMauve: multiple genome alignment with gene gain, loss and rearrangement. *PLoS ONE* **5**, e11147 (2010).

[ADS](#) [PubMed](#) [PubMed Central](#) [Google Scholar](#)

80. 80.

Li, H. & Durbin, R. Fast and accurate short read alignment with Burrows–Wheeler transform. *Bioinformatics* **25**, 1754–1760 (2009).

[CAS](#) [PubMed](#) [PubMed Central](#) [Google Scholar](#)

81. 81.

Johansen, N. & Quon, G. scAlign: a tool for alignment, integration, and rare cell identification from scRNA-seq data. *Genome Biol.* **20**, 166 (2019).

[PubMed](#) [PubMed Central](#) [Google Scholar](#)

82. 82.

Schep, A. N., Wu, B., Buenrostro, J. D. & Greenleaf, W. J. chromVAR: inferring transcription-factor-associated accessibility from single-cell epigenomic data. *Nat. Methods* **14**, 975–978 (2017).

[CAS](#) [PubMed](#) [PubMed Central](#) [Google Scholar](#)

[Download references](#)

Acknowledgements

This work was supported by NIH grants R35GM124820, R01HG009906, R24DK106766 (R.C.H. and F.Y.) and R01DK107735 (G.S.G.). F.Y. is also supported by U01CA200060. T.W. is supported by NIH grants R01HG007175, R01HG007354, R01ES024992, U24ES026699 and U01HG009391. We thank J. A. Stamatoyannopoulos for discussion and suggestions; H. Lyu for proof reading and other Yue lab members for discussion; and E. DeForest, S. Stella, P. Hubley and Penn State Zebrafish Functional Genomics Core for fish husbandry and embryo collection.

Author information

Author notes

1. These authors contributed equally: Hongbo Yang, Yu Luan, Tingting Liu

Affiliations

1. Department of Biochemistry and Molecular Genetics, Feinberg School of Medicine Northwestern University, Chicago, IL, USA

Hongbo Yang, Yu Luan, Tingting Liu, Xiaotao Wang, Qiushi Jin, Juan Wang, Jie Xu, Iyyanki Sriranga & Feng Yue

2. Department of Genetics, The Edison Family Center for Genome Sciences and Systems Biology, Washington University School of Medicine, St Louis, MO, USA

Hyung Joo Lee, Xiaoyun Xing, Daofeng Li, Mayank N. K. Choudhary & Ting Wang

3. Raymond G. Perelman Center for Cellular and Molecular Therapeutics, Children's Hospital of Philadelphia, Philadelphia, PA, USA

Li Fang & Kai Wang

4. Bioinformatics and Genomics Program, The Pennsylvania State University, State College, PA, USA

Yanli Wang, Bo Zhang, Fan Song, Chachrit Khunsriraksakul & Tarik Salameh

5. Department of Pathology and Penn State Zebrafish Functional Genomics Core, College of Medicine, The Pennsylvania State University, Hershey, PA, USA

Khai Chung Ang & Keith C. Cheng

6. Department of Pediatrics, Northwestern University Feinberg School of Medicine, Chicago, IL, USA

Jacek Topczewski

7. Stanley Manne Children's Research Institute, Ann and Robert H. Lurie Children's Hospital of Chicago, Chicago, IL, USA

Jacek Topczewski

8. Department of Medical Genetics and Molecular Biochemistry, Lewis Katz School of Medicine at Temple University, Philadelphia, PA, USA

Glenn S. Gerhard

9. Department of Biochemistry and Molecular Biology, Pennsylvania State University, University Park, PA, USA

Ross C. Hardison

10. Robert H. Lurie Comprehensive Cancer Center of Northwestern University, Chicago, IL, USA

Feng Yue

Authors

1. Hongbo Yang

[View author publications](#)

You can also search for this author in [PubMed](#) [Google Scholar](#)

2. Yu Luan

[View author publications](#)

You can also search for this author in [PubMed](#) [Google Scholar](#)

3. Tingting Liu

[View author publications](#)

You can also search for this author in [PubMed](#) [Google Scholar](#)

4. Hyung Joo Lee

[View author publications](#)

You can also search for this author in [PubMed](#) [Google Scholar](#)

5. Li Fang

[View author publications](#)

You can also search for this author in [PubMed](#) [Google Scholar](#)

6. Yanli Wang

[View author publications](#)

You can also search for this author in [PubMed](#) [Google Scholar](#)

7. Xiaotao Wang

[View author publications](#)

You can also search for this author in [PubMed](#) [Google Scholar](#)

8. Bo Zhang

[View author publications](#)

You can also search for this author in [PubMed](#) [Google Scholar](#)

9. Qiushi Jin

[View author publications](#)

You can also search for this author in [PubMed](#) [Google Scholar](#)

10. Khai Chung Ang

[View author publications](#)

You can also search for this author in [PubMed](#) [Google Scholar](#)

11. Xiaoyun Xing

[View author publications](#)

You can also search for this author in [PubMed](#) [Google Scholar](#)

12. Juan Wang

[View author publications](#)

You can also search for this author in [PubMed](#) [Google Scholar](#)

13. Jie Xu

[View author publications](#)

You can also search for this author in [PubMed](#) [Google Scholar](#)

14. Fan Song

[View author publications](#)

You can also search for this author in [PubMed](#) [Google Scholar](#)

15. Iyyanki Sriranga

[View author publications](#)

You can also search for this author in [PubMed](#) [Google Scholar](#)

16. Chachrit Khunsriraksakul

[View author publications](#)

You can also search for this author in [PubMed](#) [Google Scholar](#)

17. Tarik Salameh

[View author publications](#)

You can also search for this author in [PubMed](#) [Google Scholar](#)

18. Daofeng Li

[View author publications](#)

You can also search for this author in [PubMed](#) [Google Scholar](#)

19. Mayank N. K. Choudhary

[View author publications](#)

You can also search for this author in [PubMed](#) [Google Scholar](#)

20. Jacek Topczewski

[View author publications](#)

You can also search for this author in [PubMed](#) [Google Scholar](#)

21. Kai Wang

[View author publications](#)

You can also search for this author in [PubMed](#) [Google Scholar](#)

22. Glenn S. Gerhard

[View author publications](#)

You can also search for this author in [PubMed](#) [Google Scholar](#)

23. Ross C. Hardison

[View author publications](#)

You can also search for this author in [PubMed](#) [Google Scholar](#)

24. Ting Wang

[View author publications](#)

You can also search for this author in [PubMed](#) [Google Scholar](#)

25. Keith C. Cheng

[View author publications](#)

You can also search for this author in [PubMed](#) [Google Scholar](#)

26. Feng Yue

[View author publications](#)

You can also search for this author in [PubMed](#) [Google Scholar](#)

Contributions

F.Y. conceived and supervised the project. H.Y. and T.L. collected tissue and conducted experiments. Y.L. led the data analysis. Y.L., H.Y., H.J.L., Y.W., X.W., B.Z., L.F. and J.W. conducted analyses. D.L. and T.W. provided the website for data presentation. K.C.A. and K.C.C. provided animal support. Q.J., X.X., J.X., F.S., I.S., C. K., T.S., M.N.K.C., J.T., K.W., G.S.G., R.C.H., T.W. and K.C.C. helped with data interpretation. H.Y., Y.L., T.L. and F.Y. prepared the manuscript with input from all authors.

Corresponding author

Correspondence to [Feng Yue](#).

Ethics declarations

Competing interests

The authors declare no competing interests.

Additional information

Peer review information *Nature* thanks Michael Beer, Jesse Dixon and the other, anonymous, reviewer(s) for their contribution to the peer review of this work.

Publisher's note Springer Nature remains neutral with regard to jurisdictional claims in published maps and institutional affiliations.

Extended data figures and tables

[Extended Data Fig. 1 Tissue-specific gene expression in zebrafish.](#)

a, Clustering analysis of transcripts from RNA-seq data in embryonic and adult tissues ($n = 31,842$). **b, c**, Gene Ontology and KEGG pathway analysis for the tissue-specific genes in adult brain, heart and testis (the number of tissue-specific genes in these two figures are, Brain = 3,693, Heart = 392, Testis = 1,605). **d**, Distribution of H3K4me3 signals surrounding the known and predicted novel transcripts. **e**, Human orthologues of zebrafish tissue-specific genes were more tissue-specific compared to human orthologues of non-tissue-specific zebrafish genes ($n = 14,764, 3,739, 6,043$, Mann–Whitney U Test, two-sided, *** $P < 2.2 \times 10^{-16}$). [Source data](#)

[Extended Data Fig. 2 Comparative analysis of zebrafish cis-regulatory elements.](#)

a, Comparison of the predicted regulatory elements identified with previous data. Enhancers were based on H3K27ac signals in the same four tissues

(brain, heart, intestine, testis) from Perez-Rico et al. 2017. The data we generated are from Tübingen zebrafish strain and the published results were from the AB strain. **b**, Number of predicted *cis*-regulatory elements in each tissue. E-brain stands for 1 dpf embryonic neuron cells. E-trunk stands for 1 dpf zebrafish whole trunk region. **c**, An example showing genes with active promoters have higher expression level. Blue hollow bar indicates the known *mrpl39* promoter. Orange hollow bar indicates the potential novel promoter. The *mrpl39* promoter has H3K4me3 peaks in both muscle and brain, but only has strong H3K27ac signals in muscle and its expression is higher (4.43-fold). **d**, Gene Ontology results for the muscle-specific enhancers and skin-specific enhancers. We used the GREAT tool for this analysis (the numbers of tissue-specific enhancers used in this figure are muscle = 813, skin = 512). [Source data](#)

Extended Data Fig. 3 Enhancer reporter assay for tissue-specific enhancers.

In total, 28 of 32 predicted tissue-specific enhancers showed consistent GFP signals in the corresponding tissues. For the eight brain enhancers tested, 63/95, 51/86, 85/119, 112/143, 27/45, 34/48, 27/41, 62/77, and 37/45 embryos, respectively, had green signals in the brain region. For the six tested heart enhancers, 64/94, 52/85, 79/121, 20/41, 51/95, 32/55 and 20/31 embryos, respectively, had green signals in the heart region. For the six tested muscle enhancers, 52/57, 26/30, 107/124, 53/63, 93/114, 61/67 and 66/78 embryos, respectively, had green signals in the trunk muscle. For the four selected kidney enhancers, 47/82, 35/67, 44/62, 15/42 and 56/110 embryos, respectively, had green signals in the kidney region. [Source data](#)

Extended Data Fig. 4 Single-cell ATAC-seq in zebrafish brain.

a, Barcode selection of single cell ATAC-seq. The x-axis represents the log value of the number of unique molecular identifiers (UMI); the y axis represents the ratio of fragments in promoter regions; the red lines represent threshold, and the grey shadows represent that the barcode passed the filter. **b**, Genomic distribution of all differentially accessible (DA) peaks. **c**, Overlap of all differentially accessible peaks with enhancers predicted in bulk brain. **d**, Top, the cluster distribution in the tSNE projection. Bottom

left, pileups of differentially accessible ATAC-seq signals for each cluster. Shown in the figure is the +/- 10kb flanking region surrounding peak centres. Bottom right, most significantly enriched transcription factor motif for each cluster. **e**, t-SNE projection of all scATAC-seq cells colored by Z-score of peak enrichment. **f**, Motif enrichment of known neuron-specific TFs in scATAC-seq predicted clusters ($n = 19,955$). [Source data](#)

[Extended Data Fig. 5 Heterochromatin annotation in adult tissues.](#)

a, WashU Epigenome Browser screenshot of H3K9me3 and H3K9me2 histone ChIP-seq signals in 11 zebrafish adult tissues. The values on the y-axis were input-normalized. **b**, Distribution of H3K9me3 and H3K9me2 sites in the zebrafish genome. **c**, Venn diagram shows the overlap between H3K9me3 and H3K9me2 sites in zebrafish genome. **d**, Overlapping percentile of H3K9me3 and H3K9me2 peaks in adult tissues. **e**, H3K9me3 and H3K9me2 sites were depleted of ATAC-seq, H3K4me3 and H3K27ac ChIP-seq signals ($n = 68,789$ H3K9me3 sites and $n = 73,777$ H3K9me2 sites). **f**, Overlap of H3K9me3 sites, H3K9me2 sites, and ATAC-seq peaks with repetitive elements (The total number of each bar, from left to right, 68,789, 73,777 and 436,036). **g**, Examples of H3K9me3 sites in one tissue found to be active regions in other tissues. Horizontal scale 0-20 for H3K27ac and H3K4me3, 0-10 for RNA-seq, 0-5 for H3K9me3 and H3K9me2.

[Extended Data Fig. 6 DNA methylation level and distribution in adult tissues.](#)

a, Fraction of total CpGs with low (<25%), medium (≥25% and <75%), and high (≥75%) methylation levels and mean CpG methylation levels (mCG(CG) in zebrafish adult tissues (the mCG/CG ratio, from left to right, 0.788, 0.859, 0.790, 0.777, 0.791, 0.797, 0.781, 0.777, 0.804, 0.789, 0.781). **b**, Distribution of CpG methylation levels across zebrafish adult tissues. **c**, The distribution of non CpG methylation in 11 adult tissues. **d**, Mean methylation levels of the tissue-specific gene promoters. n represents the number of tissue-specific gene promoter. **e**, Mean methylation level of

CpGs overlapping different genomic features or repetitive element classes. CDS, coding sequence. **f**, Number of UMRs and LMRs in zebrafish tissues and their overlap with enhancer and promoters (left panel) (number of UMR and LMR, from top to bottom, 14,990, 10,569, 14,569, 14,587, 14,831, 14,289, 13,842, 13,569, 14,424, 14,374, 13,908, 30,009, 7,916, 19,038, 21,411, 22,591, 16,796, 14,961, 16,268, 17,481, 15,932, 15,665) and ATAC-seq peaks (right panel)(numbers of UMR and LMR are the same with left panel). **g**, Clustering of tissue-specific hypoDMRs. Values in the heat map are mean methylation levels of hypoDMRs ($n = 17,654$, number of tissue-specific hypoDMRs). [Source data](#)

Extended Data Fig. 7 De novo assembly of zebrafish chromosome 4 of the Tübingen strain.

a, WashU Epigenome Browser snapshot showing that heterochromatic marks H3K9me2 and H3K9me3 signals were enriched on chromosome 4 in zebrafish testis. The values on the y-axis were input-normalized. **b**, H3K9me2, H3K9me3, and DNA methylation level on chr4 long arm are significantly higher than other regions in all tissues ($n = 11$, two-sided, *t*-test). **c**, Overall strategy of de novo assembly of the Tübingen chr4 by integrating 10X, Nanopore, Bionano, and Hi-C data. **d**, Bionano long molecule sequencing data shows that there were many SVs on chr4 when mapped to the GRCz11 reference genome. **e**, SVs on chr4 detected by Bionano when the data were mapped to the de novo assembled chr4. [Source data](#)

Extended Data Fig. 8 Conservation of *cis*-regulatory elements from zebrafish to other vertebrates.

a, Percentage of zebrafish enhancers whose sequences were conserved in human (the number of each bar, from left to right, 13,307, 7,018, 11,940, 7,499, 14,783, 14,272, 8,995, 13,777, 10,757, 15,505, 1,734, 4,011, 5,247). **b, c**, Similar to Fig. [4a](#). Percentage of zebrafish exons and *cis*-regulatory elements that have orthologous sequences in mouse and other fish species. Total number of each bar, from left to right: 1,000, 25,593, 58,065, 1,000. For exons and random, we randomly sample 1000 elements and computed

their conservation percentage. The simulations were performed 20 times and the average percentage was presented. **d**, Another example of ultra-conserved noncoding element (UCNE). This element (FOXP1_Finn_1) is predicted to be a muscle enhancer in zebrafish, mouse, and human. Grey vertical bar marks the ultra-conserved region. Red vertical bar is the enhancer sequence in the human genome that was validated as a limb enhancer by transgenic mouse reporter assay in the VISTA Enhancer Browser (#hs956). [Source data](#)

Extended Data Fig. 9 Distal ATAC-seq peak-to-gene pairs, enhancer-to-gene pairs, and transcriptional regulation network.

a, b, Distance distribution of *cis*-regulatory elements to their linked gene TSS. **c**, Correlation of ATAC-seq peak-to-gene pairs and Enhancer-to-gene pairs (n from left to right = 3,292, 3,827, 3,544, 3,281, 3,008, 2,795, 2,357, 2,001, 1,106). **d**, Validation of predicted enhancer-to-gene pairs by Hi-C interaction counts in muscle. **e**, *mef2d* is a regulator in both zebrafish muscle and heart, but it regulates different downstream targets by motif prediction analysis. **f**, The overall structure of the regulatory network is conserved between human and zebrafish. FFL connection analysis was performed, in this analysis, there are three types of nodes: A, driver node that regulates B and C; B, middle node, regulated by A but regulating node C; C, passenger node, regulated by both A and B. [Source data](#)

Extended Data Fig. 10 Compartment and TADs in zebrafish.

a, Heat map of genome-wide Hi-C interaction matrices in zebrafish brain (blue) and muscle (red). **b**, Active marks (H3K4me3, H3K27ac, and ATAC-seq) were enriched in compartment A and depleted in compartment B. Repressive marks (H3K9me2 and H3K9me3) were enriched in compartment B. Error bands represent standard error of the mean. **c**, Genome browser snapshot of A/B compartment in brain and muscle. The blue vertical shaded area marks a region that is located in compartment B in brain but in compartment A in muscle. As expected, A compartment which is associated with more ATAC-seq peaks, H3K27ac and RNA-seq signals.

d, Examples of shared TADs between zebrafish brain and muscle. **e**, Average DI scores surrounding TAD boundaries identified in brain (upper panel) and muscle (lower panel). **f**, ChIP-seq data shows that CTCF binding sites were enriched at TAD boundaries. **g**, Footprint analysis of ATAC-seq peaks in the TAD boundaries shows enrichment of CTCF binding motif (number of each bar, from left to right, 0.213, 0.24, 0.22, 0.237, 0.251, 0.232, 0.24, 0.262, 0.271, 0.281, 0.37, 0.27, 0.253, 0.25, 0.252, 0.253, 0.26, 0.23, 0.238, 0.24, 0.22). **h**, Repetitive elements enriched at TAD boundaries (left panel) and loop anchors (right panel). [Source data](#)

Extended Data Fig. 11 Comparing zebrafish evolutionary breakpoints with TAD annotation.

a, Similar to Fig. 5d. Enrichment of evolutionary breakpoints at TAD boundaries. Relative positions of evolutionary breakpoints to TADs in 15 vertebrates. In all cases, we found that the evolutionary breakpoints were enriched at zebrafish TAD boundaries and depleted from the centre of TADs. Grey vertical bar labels the TAD body area. **b**, By comparing zebrafish with 17 vertebrates, H3K4me3 signals were found to be more enriched at TAD boundaries with breakpoints than those without breakpoints. Orange vertical bar labels the TAD boundaries. **c**, Higher H3K4me3 levels at breakpoint-containing TAD boundaries when using TADs annotation from zebrafish muscle were found as well, similar to Fig. 5g. **d**, H3K4me3 enrichment in human ESCs (H1) TAD boundaries with or without zebrafish-to-human breakpoints. **e**, H3K4me3 enrichment in mouse ESCs TAD boundaries with or without zebrafish-to-mouse breakpoints. **f**, H3K4me3 enrichment in human ESCs (H1) TAD boundaries with or without mouse-to-human breakpoints.

Extended Data Fig. 12 TADs with and without breakpoints.

a, H3K27ac and ATAC-seq signals do not show differences at TAD boundaries with breakpoints compared to those without breakpoints. Orange vertical bar labels the TAD boundaries. **b**, Sizes of TADs with and without evolutionary breakpoints were similar ($n = 573, 777$, two-sided, t -test). **c**, Enrichment of transcription at breakpoints (BP) that overlap with CTCF TAD boundaries in K562 cells (the number of breakpoints in blue line is 639, red line is 625). **d**, In 17 vertebrates, TADs without evolutionary breakpoints (bottom panel) have stronger interaction frequencies in the middle than TADs with evolutionary breakpoints (upper panel). Breakpoints in these 17 vertebrates were defined by comparing their genomes to the zebrafish genome. **e**, Distribution of correlations between the expression pattern of each pair of paralogs across 11 adult zebrafish tissues. **f**, Correlations between pairs of paralogs located on the same chromosome. Among them, 17 pairs were located within the same TAD, and the rest of the 65 pairs were located in different TADs. As a control, we

randomly sampled 100 genes. Number of each bar, from left to right, 17, 65, 100. [Source data](#)

Supplementary information

[Supplementary Information](#)

This file contains a guide to the Supplementary Tables 1-19.

[Reporting Summary](#)

[Supplementary Tables](#)

This zip file contains Supplementary Tables 1-19.

[Supplementary Data](#)

This zip file contains Supplementary Dataset 1.

Source data

[Source Data Fig. 1](#)

[Source Data Fig. 2](#)

[Source Data Fig. 3](#)

[Source Data Fig. 4](#)

[Source Data Fig. 5](#)

[Source Data Extended Data Fig. 1](#)

[Source Data Extended Data Fig. 2](#)

[Source Data Extended Data Fig. 3](#)

[Source Data Extended Data Fig. 4](#)

[Source Data Extended Data Fig. 6](#)

[Source Data Extended Data Fig. 7](#)

[Source Data Extended Data Fig. 8](#)

[Source Data Extended Data Fig. 9](#)

[Source Data Extended Data Fig. 10](#)

[Source Data Extended Data Fig. 12](#)

Rights and permissions

[Reprints and Permissions](#)

About this article



Check for
updates

Cite this article

Yang, H., Luan, Y., Liu, T. *et al.* A map of *cis*-regulatory elements and 3D genome structures in zebrafish. *Nature* **588**, 337–343 (2020).
<https://doi.org/10.1038/s41586-020-2962-9>

[Download citation](#)

- Received: 20 July 2019
- Accepted: 17 September 2020
- Published: 25 November 2020
- Issue Date: 10 December 2020
- DOI: <https://doi.org/10.1038/s41586-020-2962-9>

Comments

By submitting a comment you agree to abide by our [Terms](#) and [Community Guidelines](#). If you find something abusive or that does not comply with our terms or guidelines please flag it as inappropriate.

[Access through your institution](#)

[Change institution](#)

[Buy or subscribe](#)

This article was downloaded by **calibre** from <https://www.nature.com/articles/s41586-020-2962-9>

| [Section menu](#) | [Main menu](#) |

- Article
- [Published: 19 August 2020](#)

Structure of LRRK2 in Parkinson's disease and model for microtubule interaction

- [C. K. Deniston¹](#) na1 nAff7,
- [J. Salogiannis^{1,2}](#) na1,
- [S. Mathea³](#) na1,
- [D. M. Snead](#) [ORCID: orcid.org/0000-0001-7839-452X¹](#),
- [I. Lahiri¹](#) nAff8,
- [M. Matyszewski¹](#),
- [O. Donosa](#) [ORCID: orcid.org/0000-0002-1871-447X²](#),
- [R. Watanabe⁴](#) nAff9,
- [J. Böhning](#) [ORCID: orcid.org/0000-0002-6242-1041⁴](#) nAff10,
- [A. K. Shiao^{5,6}](#),
- [S. Knapp](#) [ORCID: orcid.org/0000-0001-5995-6494³](#),
- [E. Villa](#) [ORCID: orcid.org/0000-0003-4677-9809⁴](#),
- [S. L. Reck-Peterson](#) [ORCID: orcid.org/0000-0002-1553-465X^{1,2,6}](#)
&
- [A. E. Leschziner](#) [ORCID: orcid.org/0000-0002-7732-7023^{1,4}](#)

[Nature](#) volume 588, pages344–349(2020) [Cite this article](#)

- 9055 Accesses
- 4 Citations
- 183 Altmetric

- [Metrics details](#)

Subjects

- [Cryoelectron microscopy](#)
- [Motor proteins](#)
- [Parkinson's disease](#)

Abstract

Leucine-rich repeat kinase 2 (*LRRK2*) is the most commonly mutated gene in familial Parkinson's disease¹ and is also linked to its idiopathic form². *LRRK2* has been proposed to function in membrane trafficking³ and colocalizes with microtubules⁴. Despite the fundamental importance of *LRRK2* for understanding and treating Parkinson's disease, structural information on the enzyme is limited. Here we report the structure of the catalytic half of *LRRK2*, and an atomic model of microtubule-associated *LRRK2* built using a reported cryo-electron tomography *in situ* structure⁵. We propose that the conformation of the *LRRK2* kinase domain regulates its interactions with microtubules, with a closed conformation favouring oligomerization on microtubules. We show that the catalytic half of *LRRK2* is sufficient for filament formation and blocks the motility of the microtubule-based motors kinesin 1 and cytoplasmic dynein 1 *in vitro*. Kinase inhibitors that stabilize an open conformation relieve this interference and reduce the formation of *LRRK2* filaments in cells, whereas inhibitors that stabilize a closed conformation do not. Our findings suggest that *LRRK2* can act as a roadblock for microtubule-based motors and have implications for the design of therapeutic *LRRK2* kinase inhibitors.

[Access through your institution](#)

[Change institution](#)

[Buy or subscribe](#)

Access options

Subscribe to Journal

Get full journal access for 1 year

185,98 €

only 3,58 € per issue

[Subscribe](#)

All prices are NET prices.

VAT will be added later in the checkout.

Rent or Buy article

Get time limited or full article access on ReadCube.

from \$8.99

[Rent or Buy](#)

All prices are NET prices.

Additional access options:

- [Log in](#)
- [Access through your institution](#)
- [Learn about institutional subscriptions](#)

Fig. 1: Cryo-EM structure of LRRK2^{RCKW}.

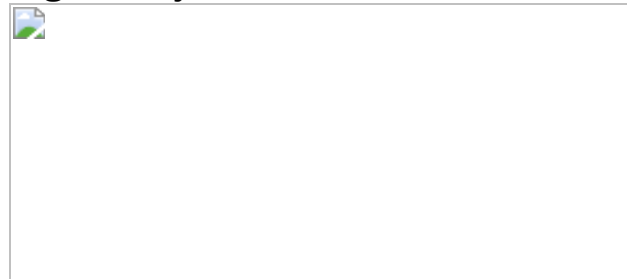


Fig. 2: Modelling the microtubule-associated LRRK2 filaments.



Fig. 3: LRRK2^{RCKW} forms WD40- and COR-mediated dimers outside the filaments.



Fig. 4: LRRK2^{RCKW} inhibits the motility of kinesin and dynein.



Fig. 5: Type II, but not type I, kinase inhibitors rescue kinesin and dynein motility and reduce LRRK2 filament formation in cells.



Data availability

All reagents and data will be made available upon request. Model coordinates for the LRRK2^{RCKW} structure are deposited in the PDB as follows: (1) PDB accession code [6VP6](#): LRRK2^{RCKW} with the adjacent COR-B and WD40 domains (from the trimer) used to optimize residues at those interfaces during refinement in Rosetta, with GDP-Mg²⁺ bound; (2) PDB accession code [6VNO](#): the top 10 models for LRRK2^{RCKW} without adjacent domains, with GDP-Mg²⁺ bound; (3) PDB accession code [6VP8](#): LRRK2^{RCKW} with the adjacent COR-B and WD40 domains (from the trimer) used to optimize residues at those interfaces during refinement in Rosetta, no GDP-Mg²⁺; (4) PDB accession code [6VP7](#): the top 10 models for LRRK2^{RCKW} without adjacent domains, no GDP-Mg²⁺ bound. Cryo-EM maps for the different LRRK2^{RCKW} structures are deposited at the EMDB as follows: (1) Electron Microscopy Data Bank (EMDB) accession code [EMD-21250](#): this deposition contains both the 3.5 Å map of LRRK2^{RCKW} trimer (used to build the COR-B, kinase and WD40 domains) and the 3.8 Å map of the signal-subtracted LRRK2^{RCKW} trimer (used to build the ROC and COR-A domains); (2) EMDB accession code [EMD-21306](#): 8.1 Å map of LRRK2^{RCKW} monomer; (3) EMD accession code 21309: 9.5 Å map of COR-mediated LRRK2^{RCKW} dimer in the absence of kinase ligand (apo); (4) EMDB accession code [EMD-21310](#): 13.4 Å map of WD40-mediated LRRK2^{RCKW} dimer in the absence of kinase ligand (apo); (5) EMDB accession code [EMD-21311](#): 9.0 Å map of COR-mediated LRRK2^{RCKW} dimer in the presence of MLi-2; (6) EMDB accession code [EMD-21312](#): 10.2 Å map of WD40-mediated LRRK2^{RCKW} dimer in the presence of MLi-2. All other data that support the findings of this study are available from the corresponding authors upon reasonable request.

References

1. 1.

Monfrini, E. & Di Fonzo, A. Leucine-rich repeat kinase (LRRK2) genetics and parkinson's disease. *Adv. Neurobiol.* **14**, 3–30 (2017).

[PubMed](#) [Google Scholar](#)

2. 2.

Di Maio, R. et al. LRRK2 activation in idiopathic Parkinson's disease. *Sci. Transl. Med.* **10**, eaar5429 (2018).

[PubMed](#) [PubMed Central](#) [Google Scholar](#)

3. 3.

Abeliovich, A. & Gitler, A. D. Defects in trafficking bridge Parkinson's disease pathology and genetics. *Nature* **539**, 207–216 (2016).

[ADS](#) [PubMed](#) [Google Scholar](#)

4. 4.

Gloeckner, C. J. et al. The Parkinson disease causing LRRK2 mutation I2020T is associated with increased kinase activity. *Hum. Mol. Genet.* **15**, 223–232 (2006).

[CAS](#) [PubMed](#) [Google Scholar](#)

5. 5.

Watanabe, R. et al. The *in situ* structure of Parkinson's disease-linked LRRK2. *Cell* **182**, 1508–1518.e16 (2020).

[CAS](#) [PubMed](#) [Google Scholar](#)

6. 6.

Gotthardt, K., Weyand, M., Kortholt, A., Van Haastert, P. J. M. & Wittinghofer, A. Structure of the Roc-COR domain tandem of C. tepidum, a prokaryotic homologue of the human LRRK2 Parkinson kinase. *EMBO J.* **27**, 2239–2249 (2008).

[CAS](#) [PubMed](#) [PubMed Central](#) [Google Scholar](#)

7. 7.

Deyaert, E. et al. Structure and nucleotide-induced conformational dynamics of the *Chlorobium tepidum* Roco protein. *Biochem. J.* **476**, 51–66 (2019).

[CAS](#) [PubMed](#) [Google Scholar](#)

8. 8.

Deng, J. et al. Structure of the ROC domain from the Parkinson's disease-associated leucine-rich repeat kinase 2 reveals a dimeric GTPase. *Proc. Natl Acad. Sci. USA* **105**, 1499–1504 (2008).

[ADS](#) [CAS](#) [PubMed](#) [Google Scholar](#)

9. 9.

Zhang, P. et al. Crystal structure of the WD40 domain dimer of LRRK2. *Proc. Natl Acad. Sci. USA* **116**, 1579–1584 (2019).

[CAS](#) [PubMed](#) [Google Scholar](#)

10. 10.

Guaitoli, G. et al. Structural model of the dimeric Parkinson's protein LRRK2 reveals a compact architecture involving distant interdomain contacts. *Proc. Natl Acad. Sci. USA* **113**, E4357–E4366 (2016).

[CAS](#) [PubMed](#) [Google Scholar](#)

11. 11.

Sejwal, K. et al. Cryo-EM analysis of homodimeric full-length LRRK2 and LRRK1 protein complexes. *Sci. Rep.* **7**, 8667 (2017).

[ADS](#) [PubMed](#) [PubMed Central](#) [Google Scholar](#)

12. 12.

Kett, L. R. et al. LRRK2 Parkinson disease mutations enhance its microtubule association. *Hum. Mol. Genet.* **21**, 890–899 (2012).

[CAS](#) [PubMed](#) [Google Scholar](#)

13. 13.

Steger, M. et al. Phosphoproteomics reveals that Parkinson's disease kinase LRRK2 regulates a subset of Rab GTPases. *eLife* **5**, e12813 (2016).

[PubMed](#) [PubMed Central](#) [Google Scholar](#)

14. 14.

Steger, M. et al. Systematic proteomic analysis of LRRK2-mediated Rab GTPase phosphorylation establishes a connection to ciliogenesis. *eLife* **6**, e31012 (2017).

[PubMed](#) [PubMed Central](#) [Google Scholar](#)

15. 15.

Ito, G. et al. GTP binding is essential to the protein kinase activity of LRRK2, a causative gene product for familial Parkinson's disease. *Biochemistry* **46**, 1380–1388 (2007).

[CAS](#) [PubMed](#) [Google Scholar](#)

16. 16.

West, A. B. et al. Parkinson's disease-associated mutations in LRRK2 link enhanced GTP-binding and kinase activities to neuronal toxicity. *Hum. Mol. Genet.* **16**, 223–232 (2007).

[CAS](#) [PubMed](#) [Google Scholar](#)

17. 17.

Lietha, D. et al. Structural basis for the autoinhibition of focal adhesion kinase. *Cell* **129**, 1177–1187 (2007).

[CAS](#) [PubMed](#) [PubMed Central](#) [Google Scholar](#)

18. 18.

Terheyden, S., Ho, F. Y., Gilsbach, B. K., Wittinghofer, A. & Kortholt, A. Revisiting the Roco G-protein cycle. *Biochem. J.* **465**, 139–147 (2015).

[CAS](#) [PubMed](#) [Google Scholar](#)

19. 19.

Cheng, K.-Y. et al. The role of the phospho-CDK2/cyclin A recruitment site in substrate recognition. *J. Biol. Chem.* **281**, 23167–23179 (2006).

[CAS](#) [PubMed](#) [Google Scholar](#)

20. 20.

Pungaliya, P. P. et al. Identification and characterization of a leucine-rich repeat kinase 2 (LRRK2) consensus phosphorylation motif. *PLoS ONE* **5**, e13672 (2010).

[ADS](#) [PubMed](#) [PubMed Central](#) [Google Scholar](#)

21. 21.

Hui, K. Y. et al. Functional variants in the *LRRK2* gene confer shared effects on risk for Crohn's disease and Parkinson's disease. *Sci. Transl. Med.* **10**, eaai7795 (2018).

[PubMed](#) [PubMed Central](#) [Google Scholar](#)

22. 22.

Scott, J. D. et al. Discovery of a 3-(4-pyrimidinyl) indazole (MLi-2), an orally available and selective leucine-rich repeat kinase 2 (LRRK2) inhibitor that reduces brain kinase activity. *J. Med. Chem.* **60**, 2983–2992 (2017).

[CAS](#) [PubMed](#) [Google Scholar](#)

23. 23.

Fell, M. J. et al. MLi-2, a potent, selective, and centrally active compound for exploring the therapeutic potential and safety of LRRK2 kinase inhibition. *J. Pharmacol. Exp. Ther.* **355**, 397–409 (2015).

[CAS](#) [PubMed](#) [Google Scholar](#)

24. 24.

Case, R. B., Pierce, D. W., Hom-Booher, N., Hart, C. L. & Vale, R. D. The directional preference of kinesin motors is specified by an element outside of the motor catalytic domain. *Cell* **90**, 959–966 (1997).

[CAS](#) [PubMed](#) [Google Scholar](#)

25. 25.

Redwine, W. B. et al. The human cytoplasmic dynein interactome reveals novel activators of motility. *eLife* **6**, e28257 (2017).

[PubMed](#) [PubMed Central](#) [Google Scholar](#)

26. 26.

Dixit, R., Ross, J. L., Goldman, Y. E. & Holzbaur, E. L. F. Differential regulation of dynein and kinesin motor proteins by tau. *Science* **319**, 1086–1089 (2008).

[ADS](#) [CAS](#) [PubMed](#) [PubMed Central](#) [Google Scholar](#)

27. 27.

Monroy, B. Y. et al. A combinatorial MAP Code dictates polarized microtubule transport. *Dev. Cell* **53**, 60–72.e4 (2020).

[CAS](#) [PubMed](#) [Google Scholar](#)

28. 28.

Reck-Peterson, S. L. et al. Single-molecule analysis of dynein processivity and stepping behavior. *Cell* **126**, 335–348 (2006).

[CAS](#) [PubMed](#) [PubMed Central](#) [Google Scholar](#)

29. 29.

Qiu, W. et al. Dynein achieves processive motion using both stochastic and coordinated stepping. *Nat. Struct. Mol. Biol.* **19**, 193–200 (2012).

[CAS](#) [PubMed](#) [PubMed Central](#) [Google Scholar](#)

30. 30.

DeWitt, M. A., Chang, A. Y., Combs, P. A. & Yildiz, A. Cytoplasmic dynein moves through uncoordinated stepping of the AAA+ ring domains. *Science* **335**, 221–225 (2012).

[ADS](#) [CAS](#) [PubMed](#) [Google Scholar](#)

31. 31.

Liu, M. et al. Type II kinase inhibitors show an unexpected inhibition mode against Parkinson’s disease-linked LRRK2 mutant G2019S. *Biochemistry* **52**, 1725–1736 (2013).

[CAS](#) [PubMed](#) [PubMed Central](#) [Google Scholar](#)

32. 32.

Canning, P. et al. Inflammatory signaling by NOD-ripk2 is inhibited by clinically relevant type II kinase inhibitors. *Chem. Biol.* **22**, 1174–1184 (2015).

[CAS](#) [PubMed](#) [PubMed Central](#) [Google Scholar](#)

33. 33.

Ren, X. et al. Identification of GZD824 as an orally bioavailable inhibitor that targets phosphorylated and nonphosphorylated breakpoint cluster region-Abelson (Bcr-Abl) kinase and overcomes clinically acquired mutation-induced resistance against imatinib. *J. Med. Chem.* **56**, 879–894 (2013).

[CAS](#) [PubMed](#) [Google Scholar](#)

34. 34.

Deng, X. et al. Characterization of a selective inhibitor of the Parkinson’s disease kinase LRRK2. *Nat. Chem. Biol.* **7**, 203–205 (2011).

[CAS](#) [PubMed](#) [PubMed Central](#) [Google Scholar](#)

35. 35.

Gilsbach, B. K. et al. Structural characterization of LRRK2 inhibitors. *J. Med. Chem.* **58**, 3751–3756 (2015).

[CAS](#) [PubMed](#) [Google Scholar](#)

36. 36.

Godena, V. K. et al. Increasing microtubule acetylation rescues axonal transport and locomotor deficits caused by LRRK2 Roc-COR domain mutations. *Nat. Commun.* **5**, 5245 (2014).

[ADS](#) [CAS](#) [PubMed](#) [PubMed Central](#) [Google Scholar](#)

37. 37.

Blanca Ramírez, M. et al. GTP binding regulates cellular localization of Parkinson's disease-associated LRRK2. *Hum. Mol. Genet.* **26**, 2747–2767 (2017).

[PubMed](#) [PubMed Central](#) [Google Scholar](#)

38. 38.

Schmidt, S. H. et al. The dynamic switch mechanism that leads to activation of LRRK2 is embedded in the DFG ψ motif in the kinase domain. *Proc. Natl Acad. Sci. USA* **116**, 14979–14988 (2019).

[CAS](#) [PubMed](#) [Google Scholar](#)

39. 39.

Wang, Y. et al. CRACR2a is a calcium-activated dynein adaptor protein that regulates endocytic traffic. *J. Cell Biol.* **218**, 1619–1633 (2019).

[CAS](#) [PubMed](#) [PubMed Central](#) [Google Scholar](#)

40. 40.

Etoh, K. & Fukuda, M. Rab10 regulates tubular endosome formation through KIF13A and KIF13B motors. *J. Cell Sci.* **132**, jcs226977 (2019).

[CAS](#) [PubMed](#) [Google Scholar](#)

41. 41.

Horgan, C. P., Hanscom, S. R., Jolly, R. S., Futter, C. E. & McCaffrey, M. W. Rab11-FIP3 links the Rab11 GTPase and cytoplasmic dynein to mediate transport to the endosomal-recycling compartment. *J. Cell Sci.* **123**, 181–191 (2010).

[CAS](#) [PubMed](#) [Google Scholar](#)

42. 42.

Niwa, S., Tanaka, Y. & Hirokawa, N. KIF1B β - and KIF1A-mediated axonal transport of presynaptic regulator Rab3 occurs in a GTP-dependent manner through DENN/MADD. *Nat. Cell Biol.* **10**, 1269–1279 (2008).

[CAS](#) [PubMed](#) [Google Scholar](#)

43. 43.

Matanis, T. et al. Bicaudal-D regulates COPI-independent Golgi-ER transport by recruiting the dynein-dynactin motor complex. *Nat. Cell Biol.* **4**, 986–992 (2002).

[CAS](#) [PubMed](#) [Google Scholar](#)

44. 44.

Sui, H. & Downing, K. H. Structural basis of interprotofilament interaction and lateral deformation of microtubules. *Structure* **18**, 1022–1031 (2010).

[CAS](#) [PubMed](#) [PubMed Central](#) [Google Scholar](#)

45. 45.

Wagner, T. et al. SPHIRE-crYOLO is a fast and accurate fully automated particle picker for cryo-EM. *Commun. Biol.* **2**, 218 (2018).

[Google Scholar](#)

46. 46.

Woehlke, G. et al. Microtubule interaction site of the kinesin motor. *Cell* **90**, 207–216 (1997).

[CAS](#) [PubMed](#) [Google Scholar](#)

47. 47.

Suloway, C. et al. Automated molecular microscopy: the new Leginon system. *J. Struct. Biol.* **151**, 41–60 (2005).

[CAS](#) [PubMed](#) [PubMed Central](#) [Google Scholar](#)

48. 48.

Zheng, S. Q. et al. MotionCor2: anisotropic correction of beam-induced motion for improved cryo-electron microscopy. *Nat. Methods* **14**, 331–332 (2017).

[CAS](#) [PubMed](#) [PubMed Central](#) [Google Scholar](#)

49. 49.

Lis, P. et al. Development of phospho-specific Rab protein antibodies to monitor *in vivo* activity of the LRRK2 Parkinson’s disease kinase. *Biochem. J.* **475**, 1–22 (2018).

[CAS](#) [PubMed](#) [PubMed Central](#) [Google Scholar](#)

50. 50.

Lander, G. C. et al. Appion: an integrated, database-driven pipeline to facilitate EM image processing. *J. Struct. Biol.* **166**, 95–102 (2009).

[CAS](#) [PubMed](#) [PubMed Central](#) [Google Scholar](#)

51. 51.

Roseman, A. M. FindEM—a fast, efficient program for automatic selection of particles from electron micrographs. *J. Struct. Biol.* **145**, 91–99 (2004).

[CAS](#) [PubMed](#) [Google Scholar](#)

52. 52.

Zivanov, J. et al. New tools for automated high-resolution cryo-EM structure determination in RELION-3. *eLife* **7**, e42166 (2018).

[PubMed](#) [PubMed Central](#) [Google Scholar](#)

53. 53.

Punjani, A., Rubinstein, J. L., Fleet, D. J. & Brubaker, M. A. cryoSPARC: algorithms for rapid unsupervised cryo-EM structure determination. *Nat. Methods* **14**, 290–296 (2017).

[CAS](#) [PubMed](#) [Google Scholar](#)

54. 54.

Henderson, R. et al. Outcome of the first electron microscopy validation task force meeting. *Structure* **20**, 205–214 (2012).

[CAS](#) [PubMed](#) [Google Scholar](#)

55. 55.

Scheres, S. H. W. & Chen, S. Prevention of overfitting in cryo-EM structure determination. *Nat. Methods* **9**, 853–854 (2012).

[CAS](#) [PubMed](#) [PubMed Central](#) [Google Scholar](#)

56. 56.

Rosenthal, P. B. & Henderson, R. Optimal determination of particle orientation, absolute hand, and contrast loss in single-particle electron cryomicroscopy. *J. Mol. Biol.* **333**, 721–745 (2003).

[CAS](#) [PubMed](#) [Google Scholar](#)

57. 57.

Chen, S. et al. High-resolution noise substitution to measure overfitting and validate resolution in 3D structure determination by single particle electron cryomicroscopy. *Ultramicroscopy* **135**, 24–35 (2013).

[CAS](#) [PubMed](#) [PubMed Central](#) [Google Scholar](#)

58. 58.

Wang, R. Y.-R. et al. Automated structure refinement of macromolecular assemblies from cryo-EM maps using Rosetta. *eLife* **5**, 352 (2016).

[Google Scholar](#)

59. 59.

Emsley, P. & Cowtan, K. Coot: model-building tools for molecular graphics. *Acta Crystallogr. D* **60**, 2126–2132 (2004).

[PubMed](#) [Google Scholar](#)

60. 60.

Söding, J., Biegert, A. & Lupas, A. N. The HHpred interactive server for protein homology detection and structure prediction. *Nucleic Acids Res.* **33**, W244–W248 (2005).

[PubMed](#) [PubMed Central](#) [Google Scholar](#)

61. 61.

Greggio, E. et al. The Parkinson's disease kinase LRRK2 autophosphorylates its GTPase domain at multiple sites. *Biochem. Biophys. Res. Commun.* **389**, 449–454 (2009).

[CAS](#) [PubMed](#) [PubMed Central](#) [Google Scholar](#)

62. 62.

Pettersen, E. F. et al. UCSF Chimera—a visualization system for exploratory research and analysis. *J. Comput. Chem.* **25**, 1605–1612 (2004).

[CAS](#) [Google Scholar](#)

63. 63.

Charrier, J.-D. et al. Discovery and structure-activity relationship of 3-aminopyrid-2-ones as potent and selective interleukin-2 inducible T-cell kinase (Itk) inhibitors. *J. Med. Chem.* **54**, 2341–2350 (2011).

[CAS](#) [PubMed](#) [Google Scholar](#)

64. 64.

Nicholas, M. P., Rao, L. & Gennrich, A. An improved optical tweezers assay for measuring the force generation of single kinesin molecules. *Methods Mol. Biol.* **1136**, 171–246 (2014).

[CAS](#) [PubMed](#) [PubMed Central](#) [Google Scholar](#)

65. 65.

Htet, Z. M. et al. LIS1 promotes the formation of activated cytoplasmic dynein-1 complexes. *Nat. Cell Biol.* **22**, 518–525 (2020).

[CAS](#) [PubMed](#) [PubMed Central](#) [Google Scholar](#)

66. 66.

Kendrick, A. A. et al. Hook3 is a scaffold for the opposite-polarity microtubule-based motors cytoplasmic dynein-1 and KIF1C. *J. Cell Biol.* **218**, 2982–3001 (2019).

[CAS](#) [PubMed](#) [PubMed Central](#) [Google Scholar](#)

67. 67.

Deniston, C. K. Parkinson's disease-linked LRRK2 structure and model for microtubule interaction. PhD thesis, Univ. California, San Diego (2020).

[Download references](#)

Acknowledgements

We thank S. Taylor for her role in initiating this collaborative work, which was partially supported by multi-investigator grants from the Michael J. Fox Foundation: grants: 11425 and 11425.02 (PI: S. Taylor) and 18321 (PIs: A.E.L. and S.L.R.-P.). We also thank the UC San Diego Cryo-EM Facility, the Nikon Imaging Center at UC San Diego, where the confocal microscopy was performed, the use of instruments at the Electron Imaging Center for NanoMachines supported by NIH (1S10RR23057, 1S10OD018111, and 1U24GM116792), NSF (DBI-1338135) and CNSI at UCLA; J. P. Gillies and A. Kendrick for technical support with protein purifications, and A. Dickey for feedback on the manuscript. C.K.D. was initially supported by the Molecular Biophysics Training Grant (NIH grant T32 GM008326) and subsequently by a Predoctoral Fellowship from the Visible Molecular Cell Consortium and Center for Trans-scale Structural Biology (UC San Diego). D.S. is supported by an A. P. Giannini Foundation postdoctoral fellowship. A.K.S. receives salary and support from the Ludwig Institute for Cancer Research. E.V. is supported by a NIH Director's New Innovator Award DP2GM123494. S.L.R.-P. is an investigator of the Howard Hughes Medical institute and is also supported by R01GM121772. A.E.L. is supported by R01GM107214. S.K. is grateful for support from the SGC, a registered charity that receives funds from AbbVie, Bayer Pharma AG, Boehringer Ingelheim, Canada Foundation for Innovation, Eshelman Institute for Innovation, Genome Canada, Innovative Medicines Initiative EUbOPEN (agreement No 875510), Janssen, Merck KGaA, MSD, Ontario Ministry of Economic Development and Innovation, Pfizer, São Paulo Research Foundation-FAPESP, Takeda, and the Wellcome, as well as Boehringer Ingelheim for funding initial structural studies of this project. Most of this work is described in the thesis⁶⁷ by C.K.D.

Author information

Author notes

1. C. K. Deniston

Present address: Genomics Institute of the Novartis Research Foundation, La Jolla, CA, USA

2. I. Lahiri

Present address: Department of Biological Sciences, Indian Institute of Science Education and Research Mohali, Mohali, India

3. R. Watanabe

Present address: La Jolla Institute for Immunology, La Jolla, CA, USA

4. J. Böhning

Present address: Sir William Dunn School of Pathology, Oxford University, Oxford, UK

5. These authors contributed equally: C. K. Deniston, J. Salogiannis, S. Mathea

Affiliations

1. Department of Cellular and Molecular Medicine, University of California San Diego, La Jolla, CA, USA

C. K. Deniston, J. Salogiannis, D. M. Snead, I. Lahiri, M. Matyszewski, S. L. Reck-Peterson & A. E. Leschziner

2. Howard Hughes Medical Institute, Chevy Chase, MD, USA

J. Salogiannis, O. Donosa & S. L. Reck-Peterson

3. Institute of Pharmaceutical Chemistry, Goethe-Universität, Frankfurt, Germany

S. Mathea & S. Knapp

4. Division of Biological Sciences, Molecular Biology Section, University of California San Diego, La Jolla, CA, USA

R. Watanabe, J. Böhning, E. Villa & A. E. Leschziner

5. Small Molecule Discovery Program, Ludwig Institute for Cancer Research, La Jolla, CA, USA

A. K. Shiao

6. Division of Biological Sciences, Cell and Developmental Biology Section, University of California San Diego, La Jolla, CA, USA

A. K. Shiao & S. L. Reck-Peterson

Authors

1. C. K. Deniston

[View author publications](#)

You can also search for this author in [PubMed](#) [Google Scholar](#)

2. J. Salogiannis

[View author publications](#)

You can also search for this author in [PubMed](#) [Google Scholar](#)

3. S. Mathea

[View author publications](#)

You can also search for this author in [PubMed](#) [Google Scholar](#)

4. D. M. Snead

[View author publications](#)

You can also search for this author in [PubMed](#) [Google Scholar](#)

5. I. Lahiri

[View author publications](#)

You can also search for this author in [PubMed](#) [Google Scholar](#)

6. M. Matyszewski

[View author publications](#)

You can also search for this author in [PubMed](#) [Google Scholar](#)

7. O. Donosa

[View author publications](#)

You can also search for this author in [PubMed](#) [Google Scholar](#)

8. R. Watanabe

[View author publications](#)

You can also search for this author in [PubMed](#) [Google Scholar](#)

9. J. Böhning

[View author publications](#)

You can also search for this author in [PubMed](#) [Google Scholar](#)

10. A. K. Shiau

[View author publications](#)

You can also search for this author in [PubMed](#) [Google Scholar](#)

11. S. Knapp

[View author publications](#)

You can also search for this author in [PubMed](#) [Google Scholar](#)

12. E. Villa

[View author publications](#)

You can also search for this author in [PubMed](#) [Google Scholar](#)

13. S. L. Reck-Peterson

[View author publications](#)

You can also search for this author in [PubMed](#) [Google Scholar](#)

14. A. E. Leschziner

[View author publications](#)

You can also search for this author in [PubMed](#) [Google Scholar](#)

Contributions

C.K.D. collected and processed the cryo-EM data. J.S. performed the single-molecule and cellular assays with the help of O.D. S.M. designed the LRRK2^{RCKW} construct and purified the protein. C.K.D. and I.L. built the molecular model of LRRK2^{RCKW}. D.M.S. performed the SEC–MALS and phosphorylation assays. M.M. collected and analysed the LRRK2^{RCKW} and microtubule cryo-EM data. R.W. and J.B. performed the cellular cryo-ET. A.K.S. contributed to the structural analysis and provided advice on the selection of kinase inhibitors. S.K., E.V., S.L.R.-P. and A.E.L. directed and supervised the research. C.K.D., J.S., S.L.R.-P. and A.E.L. wrote the manuscript and S.M., D.S., M.M., O.D., A.K.S., S.K. and E.V. edited it.

Corresponding authors

Correspondence to [S. L. Reck-Peterson](#) or [A. E. Leschziner](#).

Ethics declarations

Competing interests

The authors declare no competing interests.

Additional information

Peer review information *Nature* thanks Asa Abelovich, Henning Stahlberg and the other, anonymous, reviewer(s) for their contribution to the peer review of this work.

Publisher's note Springer Nature remains neutral with regard to jurisdictional claims in published maps and institutional affiliations.

Extended data figures and tables

[Extended Data Fig. 1 Optimization of LRRK2 constructs and cryo-EM analysis of a LRRK2^{RCKW} trimer.](#)

a, We systematically scanned domain boundaries (amino acid numbers of boundaries noted above domain names) to generate LRRK2 constructs that expressed well in baculovirus-infected insect cells and yielded stable and soluble protein. These attempts included full-length LRRK2, the kinase domain alone or with the WD40 domain, and other isolated domains. In this approach, only the GTPase domain on its own expressed well. Next, we gradually shortened LRRK2 from its amino terminus. Red asterisks indicate constructs that were soluble. **b**, After identifying domain boundaries yielding constructs that expressed soluble protein, additional fine tuning of boundaries was performed. A Coomassie-stained SDS-PAGE gel shows systematic N-terminal truncations at the ROC domain resulting in the identification of a construct with the highest expression levels: amino acids 1327–2527 (red asterisk, ‘LRRK2^{RCKW}’ here). **c**, A Coomassie-stained SDS-PAGE gel of purified LRRK2^{RCKW} after elution from an S200 gel filtration column. As predicted by its primary structure, LRRK2^{RCKW} runs at approximately 140 kDa. **d**, Electron micrograph of LRRK2^{RCKW}. **e**, 2D class averages of the LRRK2^{RCKW} trimer. **f**, 2D/3D classification scheme used to obtain the 3.5 Å structure of the LRRK2^{RCKW} trimer. **g, h**, Fourier shell correlations (from Cryosparc) (**d**) and Euler angle distribution (**e**) for the LRRK2^{RCKW} trimer.

[Extended Data Fig. 2 Cryo-EM analysis of a signal-subtracted LRRK2^{RCKW} trimer and map-to-model fit.](#)

a, Processing strategy used to obtain a 3.8 Å structure of LRRK2^{RCKW} generated from a signal-subtracted trimer where only one monomer contains the ROC and COR-A domains. This structure improved the resolution of the ROC and COR-A domains relative to the full trimer (Extended Data Fig. 1). **b–d**, 2D class averages (**b**), Fourier shell correlations (from Relion) (**c**), and Euler angle distribution (from Relion) (**d**) for the 3.8 Å resolution signal-subtracted LRRK2^{RCKW} structure. **e**, Close-ups (**f–l**) of different parts of the final model fit into the map. **f**, Section of the WD40 domain. **g**, C-terminal helix and its interface with the kinase domain. **h**, Active site of the kinase. Residues in the DYG motif are labelled. G2019, the site of a major PD-associated mutation (G2019S) and the last residue of the activation loop seen in our structure, is highlighted by a black rounded square. **i**, Interface between COR-B and the α C helix of the N-lobe of the kinase domain. **j**, Interface between the ROC and COR-B domains. R1441 and Y1699, two residues mutated in Parkinson’s disease, are labelled. **k, l**, Two different views of the ROC and COR-A domains with GDP-Mg²⁺ modelled into the density. Side chains were omitted in these two panels, corresponding to the lowest-resolution parts of the map. **m**, Map-to-model FSC plots for the top-ranked LRRK2^{RCKW} models, with (left) or without (right) GDP-Mg²⁺ (right) in the ROC domain. The 0.143 FSC values are reported in Supplementary Table 1. **n**, Size exclusion chromatography–multiple angle light scattering (SEC–MALS) analysis of LRRK2^{RCKW} under the conditions used for cryo-EM (Fig. 1). The table shows the calculated molecular weights (MW) of LRRK2^{RCKW} according to SEC standards and MALS.

[Extended Data Fig. 3 Comparisons between LRRK2 and other kinases and modelling of the LRR into LRRK2^{RCKW}.](#)

a, View of the LRRK2^{RCKW} atomic model with COR-A, COR-B and kinase domains coloured. The N- and C-lobes of the kinase are labelled, as is the α C helix in the N-lobe. **b, c**, The FAK-FERM (PDB code 2J0J)¹⁷ (**b**) and CDK2-cyclin A (PDB code 2CCH)¹⁹ (**c**) complexes, shown in the same orientation as the kinase in **a**. The α C helix of CDK2 is also labelled. **d**, Same view as in **a** with only the kinase domain and the C-terminal helix coloured. **e**, Rotated view of the LRRK2 kinase domain with the C-terminal

helix facing the viewer. **f**, **g**, CDKL3 (PDB code 3ZDU) (**f**) and RIPK2 (PDB code 4C8B)³² (**g**) shown in the same orientation as the LRRK2 kinase in **e**, with alpha helices with the same general location as the LRRK2 C-terminal helix coloured in green. **h**, KSR2-MEK1 complex (PDB code 2Y4I), with the kinase oriented as in **e** (left) and after removing KSR2 for clarity (right). The alpha helix associated with the kinase is shown in green. **i**, HCK (PDB code 2HCK) in complex with its SH2 and SH3 domains with the kinase oriented as in **e** (left), and after removal of the SH2 and SH3 domains for clarity (right). A remaining alpha helix from the SH2 domain is shown in yellow. **j**, Front view of the LRRK2 kinase with the C-spine and R-spine residues coloured in grey and white, respectively. **k**, Close-up of the DYG motif and neighbouring R-spine residues. A putative hydrogen bond between Y2018 and the backbone carbonyl of I1933 is shown (O–O distance: 2.7 Å). This interaction provides a structural explanation for the hyperactivation of the kinase resulting from a Y2018F mutation³⁸, which would release the activation loop. **l**, Crystal structure of the LRR–ROC–COR(A/B) domains from *C. tepidum* Roco (PDB code 6HLU)⁷. **m**, Homology model for human LRR–ROC–COR(A/B) based on the *C. tepidum* Roco structure (from SWISS-MODEL). **n**, Chimeric model combining LRRK2^{RCKW} and the homology model for the LRR domain from **m** obtained by aligning their ROC–COR(A/B) domains. **o**, **p**, Two views of the hybrid LRRK2^{LRCKW} model. **q**, Close-up showing the proximity between the active site of the kinase (with the side chains of its DYG motif shown) and the S1292 autophosphorylation site on the LRR. The close-up also highlights the proximity between N2081, a residue implicated in Crohn’s disease, and the LRR.

Extended Data Fig. 4 Comparison between LRRK2^{RCKW} and integrative models built into cryo-ET maps of LRRK2 filaments in cells and docking of LRRK2^{RCKW} into those maps.

a, Root-mean-square deviation (r.m.s.d.) between the atomic model of LRRK2^{RCKW} and each of the 1,167 integrative models previously generated⁵. r.m.s.d. values were calculated in Chimera⁶² using 100%

residue similarity and with pruning iterations turned off. r.m.s.d. values are grouped into 53 clusters of related models (see ref. [5](#) for details), with the mean and standard deviation shown whenever the cluster contains two or more models. Integrative models that gave the lowest, median and highest r.m.s.d. values are shown. The models are coloured according to the per-residue r.m.s.d. with the atomic model of LRRK2^{RCKW}. **b**, The WD40s in the crystal structure of a dimer of the LRRK2 WD40 (PDB code: 6DLP)[9](#) were replaced with the WD40s from our cryo-EM structure of LRRK2^{RCKW}. **c**, The resulting dimer was fitted into the 14 Å cryo-ET map of cellular microtubule-associated LRRK2 filaments[5](#). **d**, Two views of the same fitting shown in **c**, displayed with a higher threshold for the map to highlight the fitting of the WD40 β-propellers into the density. The white arrows point towards the holes at the centre of the β-propellers densities. **e**, Four copies of LRRK2^{RCKW} were docked into the cryo-ET map by aligning their WD40 domains to the docked WD40 dimer. **f**, Model containing the four aligned LRRK2^{RCKW}. **g–j**, Modelling of the kinase-closed form of LRRK2^{RCKW}. **g, h**, The structure of ITK bound to an inhibitor (PDB code 3QGY)[63](#), which is in a closed conformation, was aligned to LRRK2^{RCKW} using only the C-lobes of the two kinases. **i**, The N-terminal portion of LRRK2^{RCKW}, comprising ROC, COR-A, COR-B and the N-lobe of the kinase, was aligned to ITK using only the N-lobes of the kinases. ROC, COR-A and COR-B were moved as a rigid body in this alignment. **j**, Kinase-closed model of LRRK2^{RCKW}.

Extended Data Fig. 5 Ab initio models for cryo-EM of LRRK2^{RCKW} dimers and cryo-EM analysis of WD40- and COR-mediated dimers of LRRK2^{RCKW} in the presence of the inhibitor MLi-2.

a, An initial dataset was collected from a sample of LRRK2^{RCKW} incubated in the presence of the kinase inhibitor MLi-2 and dimers were selected. **b**, Representative two-dimensional class averages used for ab initio model building. **c**, Ab initio models with the structure of LRRK2^{RCKW} docked in. **d**, Volumes generated from the molecular models in **b**, filtered to 30 Å resolution. **e**, Projections of the volumes in **d** shown in the same order as

their corresponding 2D class averages in **b**. **f**, Data processing strategy for obtaining cryo-EM structures of WD40- and COR-mediated dimers of LRRK2^{RCKW} in the presence of the inhibitor MLi-2. The models used during this processing (Methods) are those shown in **d** along with an additional linear trimer (Methods) used for particle sorting.

Extended Data Fig. 6 Cryo-EM analysis of a monomer and WD40- and COR-mediated dimers of LRRK2^{RCKW} in the absence of inhibitor (apo) and dimerization of LRRK2^{RCKW} outside the filaments.

a, Data-processing strategy for obtaining cryo-EM structures of a monomer and WD40- and COR-mediated dimers of LRRK2^{RCKW} in the absence of inhibitor. The models used during the processing of the dimers (Methods) are those shown in Extended Data Fig. [5d](#), along with an additional linear trimer (Methods) used for particle sorting. The models used for processing of the monomer (Methods) were the same dimer models as in Extended Data Fig. [5d](#) (used for particle sorting) in addition to a monomer model generated from our LRRK2^{RCKW} model (used for refinement). **b**, Two-dimensional (2D) class averages of WD40- and COR-mediated LRRK2^{RCKW} dimers obtained in the absence of inhibitors (apo) or in the presence of either ponatinib or MLi-2. The same molecular models of the two dimers shown in Fig. [3](#) are shown on the left but in orientations similar to those represented by the 2D class averages shown here. For each class average, a projection from the corresponding model in the best-matching orientation is shown to its left. **c**, Two copies of the LRRK2^{RCKW} structure were aligned to the ROC–COR domains of the LRR–ROC–COR structure from the *C. tepidum* Roco protein (PDB code 6HLU) to replicate the interface observed in the bacterial homologue in the context of the human protein. This panel shows a comparison between the dimer modelled based on the *C. tepidum* LRR–ROC–COR structure and the dimer observed for LRRK2^{RCKW} in this work. Although the bacterial structure shows a dimerization interface that involves the GTPase (ROC), LRRK2^{RCKW} interacts exclusively through its COR-A and -B domains, with the ROC

domains located away from this interface. The two arrangements are shown schematically in cartoon form below the structures.

Extended Data Fig. 7 Properties of the microtubule-associated LRRK2^{RCKW} filaments.

a, b, The LRRK2^{RCKW} structure solved in this work (**a**) was split at the junction between the N- and C-lobes of the kinase domain (L1949-A1950) (**b**). **c,** Docking of the two halves of LRRK2^{RCKW} into a cryo-EM map of a LRRK2^{RCKW} dimer solved in the presence of MLi-2. The dimer map is the same one shown in Fig. 3 and Extended Data Figs. 10 and 11. **d,** The model obtained in **c** was docked into cryo-EM maps of either WD40- or COR-mediated dimers obtained in the presence of MLi-2. **e,** Molecular models resulting from the docking in **d**. **f,** Aligning, in alternating order, copies of the dimer models generated in **d** and **e** results in a right-handed filament with dimensions compatible with those of a microtubule, and its ROC domains pointing inwards (see Fig. 3g, h for more details). **g,** Docking of the two halves of LRRK2^{RCKW} into a cryo-EM map of a LRRK2^{RCKW} monomer solved in the absence of inhibitor (apo). The map is the one shown in Fig. 1g and Extended Data Fig. 6. **h,** Three-way comparison of LRRK2^{RCKW} (with domain colours) and the models resulting from the dockings into the MLi-2 WD40-mediated dimer map (**c**) (dark blue) and apo monomer map (**g**) (light blue). The three structures were aligned using the C-lobes of their kinases and the WD40 domain. The superposition illustrates that the docking into the apo map results in a structure very similar to that obtained from the trimer (Fig. 1) and that the presence of MLi-2 leads to a closing of the kinase. **i,** Molecular model of the microtubule-associated LRRK2^{RCKW} filament obtained by docking a fragment of a microtubule structure (PDB code 6O2S) into the corresponding density in the sub-tomogram average (Fig. 2a). **j,** Same view as in **i** with the models shown as surface representations coloured by their Coulomb potential. **k, l,** ‘Peeling off’ of the structure shown in **j**, with the LRRK2^{RCKW} filament seen from the perspective of the microtubule surface (**k**) and the microtubule surface seen from the perspective of the LRRK2^{RCKW} filament (**l**). Note that the acidic C-terminal tubulin tails are not ordered in the microtubule structure and are therefore not included in

the surface charge distributions. The Coulomb potential colouring scale is shown on the right.

Extended Data Fig. 8 Inhibition of motor motility by wild-type and I2020T mutant LRRK2^{RCKW}.

a, Example kymographs showing that increasing concentrations of LRRK2^{RCKW} reduce kinesin runs. **b**, Example kymographs showing that 25 nM LRRK2^{RCKW} reduces dynein runs. **c**, Representative kymographs of kinesin motility in the presence or absence of wild-type and I2020T mutant LRRK2^{RCKW}. **d**, The percentage of motile kinesin events per microtubule in the absence of LRRK2 or in the presence of 25 nM wild-type or I2020T mutant LRRK2^{RCKW}. Data are mean \pm s.d. ($n = 12$ microtubules per condition quantified from two independent experiments). There is a significant difference between 0 nM and both 25 nM RCKW conditions ($P < 0.0001$), but no significant (ns) difference between the inhibitory effects of wild-type LRRK2^{RCKW} versus I2020T mutant LRRK2^{RCKW} as calculated using the Kruskal–Wallis test with Dunn’s posthoc for multiple comparisons (compared to no LRRK2^{RCKW}).

Extended Data Fig. 9 Type II kinase inhibitors rescue kinesin and dynein motility.

a–e, Ponatinib is a type II, ‘DFG out’ inhibitor. **a**, Superposition of the structures of Ponatinib-bound RIPK2 (PDB code 4C8B)³² and IRAK4 (PDB code 6EG9). Ponatinib is shown in yellow, and the DYG motif residues are shown in white. **b**, **c** For comparison, the structures of Roco4 bound to LRRK2-IN-1 (PDB code 4YZM)³⁵, a LRRK2-specific type I, ‘DFG in’ inhibitor (**b**), and a model of MAPK1 bound to MLi-2 (PDB code 5U6I)²², another LRRK2-specific type I, ‘DFG in’ inhibitor (**c**) are shown. The inhibitor and DFG residues are coloured as in **a**. **d**, The structures in **a–c**, as well as the kinase from LRRK2^{RCKW} are shown superimposed. The colour arrowheads point to the N-lobe β -sheet to highlight the difference in conformation between kinases bound to the two different types of inhibitors. Note that the LRRK2^{RCKW} kinase is even more open than the

two ponatinib-bound kinases. **e**, Rotated view of **d**, now highlighting the position of the N-lobe α C helix. An additional alpha helix in the N-lobe of MAPK1 was removed from this view for clarity. **f**, The kinase inhibitors MLi-2 (1 μ M), LRRK2-IN-1 (1 μ M), ponatinib (10 μ M) and GZD-824 (10 μ M) all inhibit the LRRK2^{RCKW} kinase activity in vitro compared to a DMSO control. A western blot using a phospho-specific antibody to Rab8A at the indicated time points is shown. **g**, A dose–response curve showing the percentage of motile kinesin events per microtubule as a function of ponatinib concentration with LRRK2^{RCKW} (25 nM) or without LRRK2^{RCKW}. Data are mean \pm s.d. (from left to right: $n = 12, 18, 16, 14$ and 9 microtubules quantified from one experiment). *** $P < 0.0001$, Kruskal–Wallis test with Dunn’s posthoc for multiple comparisons, compared to DMSO without LRRK2^{RCKW}. **h**, Dose–response curve of run lengths from data in **g** represented as a cumulative frequency distribution. From top to bottom: $n = 654, 173, 584, 293$ and 129 motile kinesin events. Mean decay constants (τ) \pm confidence interval are (from top to bottom) $2.736 \pm 0.113, 1.291 \pm 0.181, 2.542 \pm 0.124, 2.285 \pm 0.134$, and 1.653 ± 0.17 . **i**, Representative kymographs of kinesin and dynein with DMSO or type II inhibitors with or without LRRK2^{RCKW}. **j**, The type II kinase inhibitors ponatinib and GZD-824 rescue kinesin run length, represented as a cumulative frequency distribution of run lengths with LRRK2^{RCKW} (25 nM) or without LRRK2^{RCKW}. From top to bottom: $n = 893, 355, 507, 499, 524$ and 529 runs from two independent experiments. Mean decay constants (τ) \pm 95% confidence intervals are (from top to bottom) $2.070 \pm 0.058, 0.8466 \pm 0.091, 1.938 \pm 0.065, 2.075 \pm 0.07, 1.898 \pm 0.065$ and 1.718 ± 0.064 . Data were resampled with bootstrapping analysis and statistical significance was established using a one-way ANOVA with Dunnett’s test for multiple comparisons. DMSO run lengths were significantly different ($P < 0.0001$) between conditions (0 vs 25 nM RCKW). Ponatinib (0 vs 25 nM RCKW) and GZD-824 (0 vs 25 nM LRRK2) were not significant. **k**, As in **j** but with dynein. From top to bottom: $n = 659, 28, 289, 306, 254$ and 339 runs from two independent experiments. Mean decay constants (τ) \pm 95% confidence intervals; micrometres are $4.980 \pm 0.147, 0.846 \pm 0.415, 4.686 \pm 0.142, 4.445 \pm 0.172, 3.156 \pm 0.09, 3.432 \pm 0.188$ (from top to bottom). Statistical significance as in **j** and run lengths were significantly different ($P < 0.0001$) between DMSO conditions (0 vs 25 nM RCKW), and not significant for

ponatinib or GZD0824 conditions. The DMSO conditions are reproduced from Fig. 4f for comparison. **l**, Expression levels of GFP-LRRK2 (I2020T) in 293T cells treated with either DMSO or GZD-824 (5 μ M). An immunoblot with anti-GFP (LRRK2) and anti-GADPH (loading control), which is a representative image from three replicates, is shown. **m**, Quantification of GFP–LRRK2 (I2020T) expression levels from western blots similar to l. Data are mean \pm s.d. ($n = 3$ per condition). GZD-824 is not significantly different from the DMSO-treated control (Mann–Whitney test). **n**, 293T cells immunostained for tubulin showing that the microtubule architecture is not affected by GZD-824 or MLi-2 compared to DMSO treatment. See Supplementary Table 1 for all source data and replicate information.

Extended Data Table 1 Cryo-EM data collection and model refinement statistics

[Full size table](#)

Supplementary information

[Supplementary Figure 1](#)

Western blots shown in Extended Data Fig. 9.

[Reporting Summary](#)

[Supplementary Table 1](#)

Data for statistics and replicate information

[Video 1](#)

| LRRK2^{RCKW} Structure Overview of the cryo-EM structure of LRRK2^{RCKW} with close-ups of its domains.

[Video 2](#)

| Parkinson's Disease mutations in LRRK2^{RCKW} Structure Close-ups of the residues most commonly mutated in PD. I2020 (mutated to T2020 in PD) is disordered in our structure and this is indicated by the square brackets around its name.

Video 3

| The C-terminal helix of LRRK2^{RCKW} Close-up of the C-terminal helix of LRRK2^{RCKW} showing the residues involved in electrostatic and hydrophobic interactions between it and the kinase domain.

Rights and permissions

Reprints and Permissions

About this article



Check for
updates

Cite this article

Deniston, C.K., Salogiannis, J., Mathea, S. *et al.* Structure of LRRK2 in Parkinson's disease and model for microtubule interaction. *Nature* **588**, 344–349 (2020). <https://doi.org/10.1038/s41586-020-2673-2>

Download citation

- Received: 10 November 2019
- Accepted: 12 August 2020
- Published: 19 August 2020
- Issue Date: 10 December 2020

- DOI: <https://doi.org/10.1038/s41586-020-2673-2>

Further reading

- [**Kinase Domain Is a Dynamic Hub for Driving LRRK2 Allostery**](#)

- Susan S. Taylor
- , Pallavi Kaila-Sharma
- , Jui-Hung Weng
- , Phillip Aoto
- , Sven H. Schmidt
- , Stefan Knapp
- , Sebastian Mathea
- & Friedrich W. Herberg

Frontiers in Molecular Neuroscience (2020)

- [**“Opening” New Insights into LRRK2 Conformation and the Microtubule**](#)

- Diana A. Olszewska
- & Anthony E. Lang

Movement Disorders (2020)

- [**The 14-3-3 Proteins as Important Allosteric Regulators of Protein Kinases**](#)

- Veronika Obsilova
- & Tomas Obsil

International Journal of Molecular Sciences (2020)

- [**Allosteric inhibition of LRRK2, where are we now**](#)

- Ahmed Soliman
- , Fatma Nihan Cankara
- & Arjan Kortholt

Biochemical Society Transactions (2020)

Comments

By submitting a comment you agree to abide by our [Terms](#) and [Community Guidelines](#). If you find something abusive or that does not comply with our terms or guidelines please flag it as inappropriate.

[Access through your institution](#)

[Change institution](#)

[Buy or subscribe](#)

This article was downloaded by **calibre** from <https://www.nature.com/articles/s41586-020-2673-2>

| [Section menu](#) | [Main menu](#) |

- Article
- [Published: 04 November 2020](#)

Structures and pH-sensing mechanism of the proton-activated chloride channel

- [Zheng Ruan ORCID: orcid.org/0000-0002-4412-4916^{1 na1}](#),
- [James Osei-Owusu^{2 na1}](#),
- [Juan Du ORCID: orcid.org/0000-0003-1467-1203¹](#),
- [Zhaozhu Qiu ORCID: orcid.org/0000-0002-9122-6077^{2,3}](#) &
- [Wei Lü ORCID: orcid.org/0000-0002-3009-1025¹](#)

[Nature](#) volume 588, pages350–354(2020)[Cite this article](#)

- 4815 Accesses
- 136 Altmetric
- [Metrics details](#)

Subjects

- [Chloride channels](#)
- [Cryoelectron microscopy](#)

Abstract

The proton-activated chloride channel (PAC) is active across a wide range of mammalian cells and is involved in acid-induced cell death and tissue injury^{1,2,3}. PAC has recently been shown to represent a novel and

evolutionarily conserved protein family^{4,5}. Here we present two cryo-electron microscopy structures of human PAC in a high-pH resting closed state and a low-pH proton-bound non-conducting state. PAC is a trimer in which each subunit consists of a transmembrane domain (TMD), which is formed of two helices (TM1 and TM2), and an extracellular domain (ECD). Upon a decrease of pH from 8 to 4, we observed marked conformational changes in the ECD–TMD interface and the TMD. The rearrangement of the ECD–TMD interface is characterized by the movement of the histidine 98 residue, which is, after acidification, decoupled from the resting position and inserted into an acidic pocket that is about 5 Å away. Within the TMD, TM1 undergoes a rotational movement, switching its interaction partner from its cognate TM2 to the adjacent TM2. The anion selectivity of PAC is determined by the positively charged lysine 319 residue on TM2, and replacing lysine 319 with a glutamate residue converts PAC to a cation-selective channel. Our data provide a glimpse of the molecular assembly of PAC, and a basis for understanding the mechanism of proton-dependent activation.

[Access through your institution](#)

[Change institution](#)

[Buy or subscribe](#)

Access options

Subscribe to Journal

Get full journal access for 1 year

185,98 €

only 3,58 € per issue

[Subscribe](#)

All prices are NET prices.

VAT will be added later in the checkout.

Rent or Buy article

Get time limited or full article access on ReadCube.

from \$8.99

[Rent or Buy](#)

All prices are NET prices.

Additional access options:

- [Log in](#)
- [Access through your institution](#)
- [Learn about institutional subscriptions](#)

Fig. 1: Overall architecture of PAC.

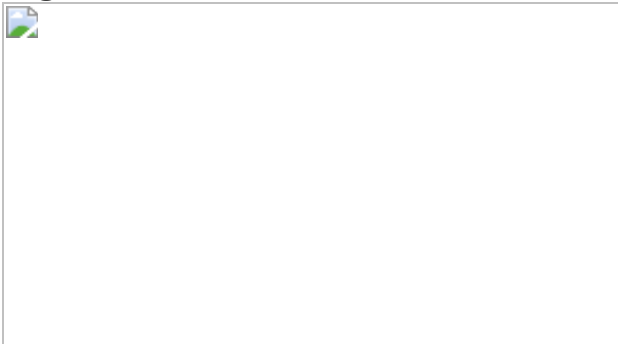


Fig. 2: Intersubunit interfaces.

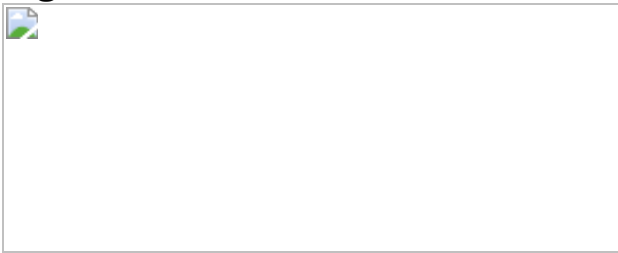


Fig. 3: Ion-conducting pathways and anion selectivity.

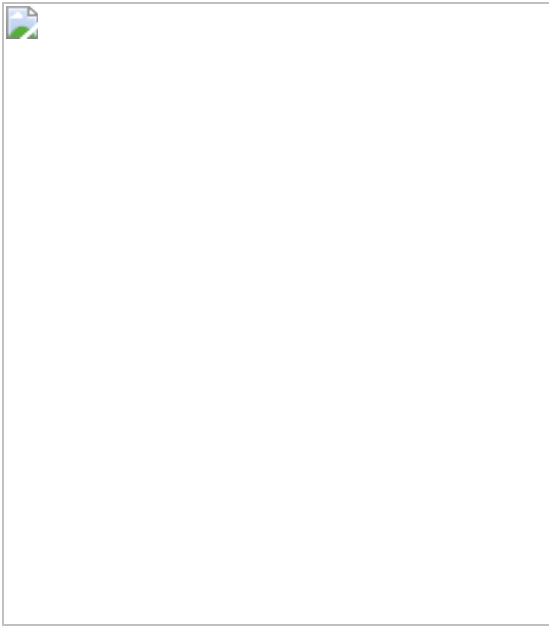
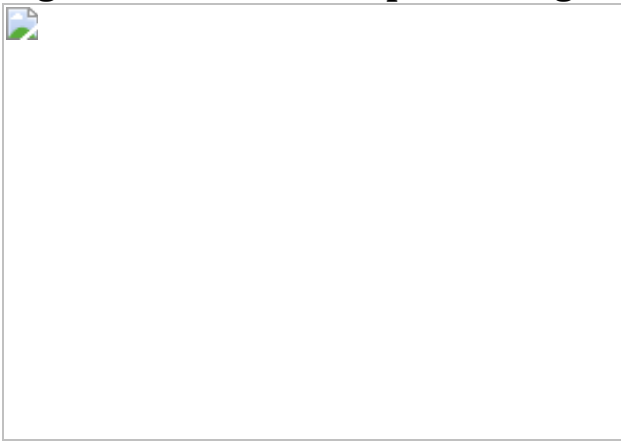


Fig. 4: Mechanisms of pH sensing and channel activation.



Data availability

The cryo-EM density maps and coordinates of pH8-PAC and pH4-PAC have been deposited in the Electron Microscopy Data Bank (EMDB) under accession numbers [EMD-22403](#) and [EMD-22404](#) and in the RCSB Protein Data Bank (PDB) under accession codes [7JNA](#) and [7JNC](#).

References

1. 1.

Capurro, V. et al. Functional analysis of acid-activated Cl⁻ channels: properties and mechanisms of regulation. *Biochim. Biophys. Acta* **1848**, 105–114 (2015).

[CAS](#) [PubMed](#) [Google Scholar](#)

2. 2.

Wang, H. Y., Shimizu, T., Numata, T. & Okada, Y. Role of acid-sensitive outwardly rectifying anion channels in acidosis-induced cell death in human epithelial cells. *Pflugers Arch.* **454**, 223–233 (2007).

[CAS](#) [PubMed](#) [Google Scholar](#)

3. 3.

Sato-Numata, K., Numata, T. & Okada, Y. Temperature sensitivity of acid-sensitive outwardly rectifying (ASOR) anion channels in cortical neurons is involved in hypothermic neuroprotection against acidotoxic necrosis. *Channels* **8**, 278–283 (2014).

[PubMed](#) [PubMed Central](#) [Google Scholar](#)

4. 4.

Yang, J. et al. PAC, an evolutionarily conserved membrane protein, is a proton-activated chloride channel. *Science* **364**, 395–399 (2019).

[ADS](#) [CAS](#) [PubMed](#) [PubMed Central](#) [Google Scholar](#)

5. 5.

Ullrich, F. et al. Identification of TMEM206 proteins as pore of PAORAC/ASOR acid-sensitive chloride channels. *eLife* **8**, e49187 (2019).

[CAS](#) [PubMed](#) [PubMed Central](#) [Google Scholar](#)

6. 6.

Osei-Owusu, J., Yang, J., Del Carmen Vitery, M., Tian, M. & Qiu, Z. PAC proton-activated chloride channel contributes to acid-induced cell death in primary rat cortical neurons. *Channels* **14**, 53–58 (2020).

[PubMed](#) [PubMed Central](#) [Google Scholar](#)

7. 7.

Jasti, J., Furukawa, H., Gonzales, E. B. & Gouaux, E. Structure of acid-sensing ion channel 1 at 1.9 Å resolution and low pH. *Nature* **449**, 316–323 (2007).

[ADS](#) [CAS](#) [PubMed](#) [Google Scholar](#)

8. 8.

Noreng, S., Bharadwaj, A., Posert, R., Yoshioka, C. & Baconguis, I. Structure of the human epithelial sodium channel by cryo-electron microscopy. *eLife* **7**, e39340 (2018).

[PubMed](#) [PubMed Central](#) [Google Scholar](#)

9. 9.

Gonzales, E. B., Kawate, T. & Gouaux, E. Pore architecture and ion sites in acid-sensing ion channels and P2X receptors. *Nature* **460**, 599–604 (2009).

[ADS](#) [CAS](#) [PubMed](#) [PubMed Central](#) [Google Scholar](#)

10. 10.

Baconguis, I., Bohlen, C. J., Goehring, A., Julius, D. & Gouaux, E. X-ray structure of acid-sensing ion channel 1-snake toxin complex reveals open state of a Na^+ -selective channel. *Cell* **156**, 717–729 (2014).

[CAS](#) [PubMed](#) [PubMed Central](#) [Google Scholar](#)

11. 11.

Yoder, N. & Gouaux, E. Divalent cation and chloride ion sites of chicken acid sensing ion channel 1a elucidated by X-ray crystallography. *PLoS ONE* **13**, e0202134 (2018).

[PubMed](#) [PubMed Central](#) [Google Scholar](#)

12. 12.

Yoder, N., Yoshioka, C. & Gouaux, E. Gating mechanisms of acid-sensing ion channels. *Nature* **555**, 397–401 (2018).

[ADS](#) [CAS](#) [PubMed](#) [PubMed Central](#) [Google Scholar](#)

13. 13.

Mansoor, S. E. et al. X-ray structures define human P2X₃ receptor gating cycle and antagonist action. *Nature* **538**, 66–71 (2016).

[ADS](#) [CAS](#) [PubMed](#) [PubMed Central](#) [Google Scholar](#)

14. 14.

Vullo, S. et al. Conformational dynamics and role of the acidic pocket in ASIC pH-dependent gating. *Proc. Natl Acad. Sci. USA* **114**, 3768–3773 (2017).

[CAS](#) [PubMed](#) [Google Scholar](#)

15. 15.

Gao, C. et al. Roles of the lateral fenestration residues of the P2X₄ receptor that contribute to the channel function and the deactivation effect of ivermectin. *Purinergic Signal.* **11**, 229–238 (2015).

[CAS](#) [PubMed](#) [PubMed Central](#) [Google Scholar](#)

16. 16.

Lambert, S. & Oberwinkler, J. Characterization of a proton-activated, outwardly rectifying anion channel. *J. Physiol.* **567**, 191–213 (2005).

[CAS](#) [PubMed](#) [PubMed Central](#) [Google Scholar](#)

17. 17.

Liechti, L. A. et al. A combined computational and functional approach identifies new residues involved in pH-dependent gating of ASIC1a. *J. Biol. Chem.* **285**, 16315–16329 (2010).

[CAS](#) [PubMed](#) [PubMed Central](#) [Google Scholar](#)

18. 18.

Smith, E. S. J., Zhang, X., Cadiou, H. & McNaughton, P. A. Proton binding sites involved in the activation of acid-sensing ion channel ASIC2a. *Neurosci. Lett.* **426**, 12–17 (2007).

[CAS](#) [PubMed](#) [Google Scholar](#)

19. 19.

Paukert, M., Chen, X., Polleichtner, G., Schindelin, H. & Gründer, S. Candidate amino acids involved in H^+ gating of acid-sensing ion channel 1a. *J. Biol. Chem.* **283**, 572–581 (2008).

[CAS](#) [PubMed](#) [Google Scholar](#)

20. 20.

Goehring, A. et al. Screening and large-scale expression of membrane proteins in mammalian cells for structural studies. *Nat. Protoc.* **9**, 2574–2585 (2014).

[CAS](#) [PubMed](#) [PubMed Central](#) [Google Scholar](#)

21. 21.

Haley, E. et al. Expression and purification of the human lipid-sensitive cation channel TRPC3 for structural determination by single-particle cryo-electron microscopy. *J. Vis. Exp.* **143**, e58754 (2019).

[Google Scholar](#)

22. 22.

Mastronarde, D. N. Automated electron microscope tomography using robust prediction of specimen movements. *J. Struct. Biol.* **152**, 36–51 (2005).

[PubMed](#) [Google Scholar](#)

23. 23.

Zheng, S. Q. et al. MotionCor2: anisotropic correction of beam-induced motion for improved cryo-electron microscopy. *Nat. Methods* **14**, 331–332 (2017).

[CAS](#) [PubMed](#) [PubMed Central](#) [Google Scholar](#)

24. 24.

Zhang, K. Gctf: real-time CTF determination and correction. *J. Struct. Biol.* **193**, 1–12 (2016).

[ADS](#) [CAS](#) [PubMed](#) [PubMed Central](#) [Google Scholar](#)

25. 25.

Rohou, A. & Grigorieff, N. CTFFIND4: fast and accurate defocus estimation from electron micrographs. *J. Struct. Biol.* **192**, 216–221 (2015).

[PubMed](#) [PubMed Central](#) [Google Scholar](#)

26. 26.

Scheres, S. H. W. RELION: implementation of a Bayesian approach to cryo-EM structure determination. *J. Struct. Biol.* **180**, 519–530 (2012).

[CAS](#) [PubMed](#) [PubMed Central](#) [Google Scholar](#)

27. 27.

Punjani, A., Rubinstein, J. L., Fleet, D. J. & Brubaker, M. A. cryoSPARC: algorithms for rapid unsupervised cryo-EM structure determination. *Nat. Methods* **14**, 290–296 (2017).

[CAS](#) [PubMed](#) [Google Scholar](#)

28. 28.

Zivanov, J., Nakane, T. & Scheres, S. H. W. A Bayesian approach to beam-induced motion correction in cryo-EM single-particle analysis. *IUCrJ* **6**, 5–17 (2019).

[CAS](#) [PubMed](#) [PubMed Central](#) [Google Scholar](#)

29. 29.

Emsley, P. & Cowtan, K. Coot: model-building tools for molecular graphics. *Acta Crystallogr. D* **60**, 2126–2132 (2004).

[PubMed](#) [Google Scholar](#)

30. 30.

Drozdetskiy, A., Cole, C., Procter, J. & Barton, G. J. JPred4: a protein secondary structure prediction server. *Nucleic Acids Res.* **43**, W389–W394 (2015).

[CAS](#) [PubMed](#) [PubMed Central](#) [Google Scholar](#)

31. 31.

Afonine, P. V. et al. New tools for the analysis and validation of cryo-EM maps and atomic models. *Acta Crystallogr. D* **74**, 814–840 (2018).

[CAS](#) [Google Scholar](#)

32. 32.

Wang, R. Y. R. et al. Automated structure refinement of macromolecular assemblies from cryo-EM maps using Rosetta. *eLife* **5**, e17219 (2016).

[PubMed](#) [PubMed Central](#) [Google Scholar](#)

33. 33.

Pettersen, E. F. et al. UCSF Chimera—a visualization system for exploratory research and analysis. *J. Comput. Chem.* **25**, 1605–1612 (2004).

[CAS](#) [Google Scholar](#)

34. 34.

Goddard, T. D. et al. UCSF ChimeraX: meeting modern challenges in visualization and analysis. *Protein Sci.* **27**, 14–25 (2018).

[CAS](#) [PubMed](#) [Google Scholar](#)

35. 35.

The PyMOL Molecular Graphics System, v.2.1. (Schrödinger, LLC, 2020).

36. 36.

Dolinsky, T. J., Nielsen, J. E., McCammon, J. A. & Baker, N. A. PDB2PQR: an automated pipeline for the setup of Poisson–Boltzmann electrostatics calculations. *Nucleic Acids Res.* **32**, W665–W667 (2004).

[CAS](#) [PubMed](#) [PubMed Central](#) [Google Scholar](#)

37. 37.

Olsson, M. H. M. Søndergaard, C. R., Rostkowski, M. & Jensen, J. H. PROPKA3: consistent treatment of internal and surface residues in empirical pK_a predictions. *J. Chem. Theory Comput.* **7**, 525–537 (2011).

[CAS](#) [PubMed](#) [Google Scholar](#)

38. 38.

Lomize, M. A., Pogozheva, I. D., Joo, H., Mosberg, H. I. & Lomize, A. L. OPM database and PPM web server: resources for positioning of proteins in membranes. *Nucleic Acids Res.* **40**, D370–D376 (2012).

[CAS](#) [PubMed](#) [Google Scholar](#)

39. 39.

Jo, S., Kim, T., Iyer, V. G. & Im, W. CHARMM-GUI: a web-based graphical user interface for CHARMM. *J. Comput. Chem.* **29**, 1859–1865 (2008).

[CAS](#) [PubMed](#) [PubMed Central](#) [Google Scholar](#)

40. 40.

Abraham, M. J. et al. Gromacs: high performance molecular simulations through multi-level parallelism from laptops to supercomputers. *SoftwareX* **1–2**, 19–25 (2015).

[ADS](#) [Google Scholar](#)

41. 41.

Huang, J. et al. CHARMM36m: an improved force field for folded and intrinsically disordered proteins. *Nat. Methods* **14**, 71–73 (2017).

[CAS](#) [PubMed](#) [Google Scholar](#)

42. 42.

Hess, B. P-LINCS: a parallel linear constraint solver for molecular simulation. *J. Chem. Theory Comput.* **4**, 116–122 (2008).

[CAS](#) [PubMed](#) [Google Scholar](#)

43. 43.

Leaver-Fay, A., Kuhlman, B. & Snoeyink, J. An adaptive dynamic programming algorithm for the side chain placement problem. *Pac. Symp. Biocomput.* **10**, 16–27 (2005).

[Google Scholar](#)

44. 44.

Yang, H. et al. TMEM16F forms a Ca^{2+} -activated cation channel required for lipid scrambling in platelets during blood coagulation. *Cell* **151**, 111–122 (2012).

[CAS](#) [PubMed](#) [PubMed Central](#) [Google Scholar](#)

45. 45.

Zhang, Y. & Skolnick, J. TM-align: a protein structure alignment algorithm based on the TM-score. *Nucleic Acids Res.* **33**, 2302–2309 (2005).

[CAS](#) [PubMed](#) [PubMed Central](#) [Google Scholar](#)

[Download references](#)

Acknowledgements

We thank G. Zhao and X. Meng for support with data collection at the David Van Andel Advanced Cryo-Electron Microscopy Suite; the HPC team of VARI for computational support; and D. Nadziejka for technical editing. W.L. is supported by National Institutes of Health (NIH) grants R56HL144929 and R01NS112363; Z.Q. is supported by a McKnight Scholar Award, a Klingenstein-Simon Scholar Award, a Sloan Research Fellowship in Neuroscience and NIH grants R35GM124824 and R01NS118014; Z.R. is supported by an American Heart Association (AHA) postdoctoral fellowship (grant 20POST35120556); J.O.-O. is supported by an AHA predoctoral fellowship (grant 18PRE34060025); and J.D. is supported by a McKnight Scholar Award, a Klingenstein-Simon Scholar Award, a Sloan Research Fellowship in Neuroscience, a Pew Scholar in the Biomedical Sciences and NIH grant R01NS111031.

Author information

Author notes

1. These authors contributed equally: Zheng Ruan, James Osei-Owusu

Affiliations

1. Department of Structural Biology, Van Andel Institute, Grand Rapids, MI, USA

Zheng Ruan, Juan Du & Wei Lü

2. Department of Physiology, Johns Hopkins University School of Medicine, Baltimore, MD, USA

James Osei-Owusu & Zhaozhu Qiu

3. Solomon H. Snyder Department of Neuroscience, Johns Hopkins University School of Medicine, Baltimore, MD, USA

Zhaozhu Qiu

Authors

1. Zheng Ruan

[View author publications](#)

You can also search for this author in [PubMed](#) [Google Scholar](#)

2. James Osei-Owusu

[View author publications](#)

You can also search for this author in [PubMed](#) [Google Scholar](#)

3. Juan Du

[View author publications](#)

You can also search for this author in [PubMed](#) [Google Scholar](#)

4. Zhaozhu Qiu

[View author publications](#)

You can also search for this author in [PubMed](#) [Google Scholar](#)

5. Wei Lü

[View author publications](#)

You can also search for this author in [PubMed](#) [Google Scholar](#)

Contributions

W.L. and Z.Q. supervised the project. Z.R. purified PAC, prepared and screened cryo-EM samples, performed cryo-EM data collection and processing and performed computational simulation. J.O.-O. cloned the PAC constructs and performed electrophysiological studies. Z.R., J.O.-O., J.D., Z.Q. and W.L. contributed to data analysis and manuscript preparation.

Corresponding authors

Correspondence to [Zhaozhu Qiu](#) or [Wei Lü](#).

Ethics declarations

Competing interests

The authors declare no competing interests.

Additional information

Peer review information *Nature* thanks Lily Jan, Stephan Kellenberger and Kenton Swartz for their contribution to the peer review of this work.

Publisher's note Springer Nature remains neutral with regard to jurisdictional claims in published maps and institutional affiliations.

Extended data figures and tables

[Extended Data Fig. 1 Purification of PAC and biochemical and biophysical analysis.](#)

a, Fluorescence size-exclusion chromatography (FSEC) of PAC–GFP solubilized in GDN detergent. **b**, SDS–PAGE gel of purified PAC–GFP protein after metal affinity chromatography. The uncropped source gel of the image can be found in Supplementary Fig. [1a](#). The gel was repeated three times from different batches of purification and similar results were obtained. **c**, SEC profile of PAC in MSP3D1 nanodiscs. **d**, A deglycosylation assay of PAC–GFP with or without PNGase F treatment. The GFP and far-red signal (Alexa 488 and Alexa 680) of the gel was detected and merged using ChemiDoc imaging system (BioRad). The uncropped source gel of the image can be found in Supplementary Fig. [1b](#). The deglycosylation assay was repeated twice with similar results. **e**, F196 mediates intersubunit interactions by forming a cation–π interaction with Arg237' and hydrophobic interactions with Tyr267' and Phe282' from the adjacent subunit. The two subunits are in green and blue. **f**, FSEC traces of GFP-tagged wild-type PAC and the F196 mutant solubilized using GDN detergent. The peak position of F196A is shifted and is broader compared to

the wild type, suggesting that F196A interferes with the proper assembly of PAC. **g**, The whole-cell current density of wild-type PAC and PAC(F196A) recorded at pH 4.6 with a holding potential of 100 mV. The centre error bar represents mean and s.e.m. Two-tailed unpaired *t*-test was used to determine the difference in current density between F196A and the wild type ($P = 3.09 \times 10^{-6}$). D'Agostino & Pearson omnibus test was performed to check the normality of the data (P values are 0.846 and 0.349 for wild type ($n = 10$) and F196A ($n = 11$), respectively). ***denotes $P < 0.001$.

Extended Data Fig. 2 Workflow for cryo-EM data-processing of pH8-PAC and data statistics.

a, A total of 16,733 raw movies stacks were collected and processed with motion correction, CTF estimation and particle picking. Particles were subjected to two rounds of 2D classification and a 3D classification run to obtain a homogeneous particle set. To further sort out conformational heterogeneity, we attempted to subtract and classify (1) particles without nanodiscs and (2) the ECD of PAC (residues 72–317) by using a mask. Subsequent refinement allowed us to obtain a map at 3.60-Å resolution for the entire PAC protein and 3.36-Å resolution for the ECD. **b**, Representative micrograph, 2D class averages, Fourier shell correlation (FSC) curves and angular distribution of particles used for 3D reconstruction for the pH8-PAC dataset. The gold-standard 0.143 threshold was used to determine map resolution based on the FSC curve. The threshold for model versus map correlation was 0.5 to determine the resolution.

Extended Data Fig. 3 Workflow for cryo-EM data-processing of pH4-PAC and data statistics.

a, A total of 26,689 raw movie stacks were collected and processed with motion correction, CTF estimation and particle picking. Two rounds of 2D classification were performed to clean up junk particles. Subsequently, particles belonging to the 2D class averages with clear features were subjected to three rounds of 3D classification. The initial 3D classification was conducted by using the pH8-PAC map low-pass filter set to 50 Å as the

reference. No symmetry operator was imposed in this step. After refinement with C_3 symmetry, a 5.8-Å-resolution map for pH4-PAC was obtained. Subsequently, the second 3D classification job was conducted by using the 5.8-Å map as the reference and the low-pass filter set to 50 Å. We imposed C_3 symmetry at this step to increase the classification efficiency. This allowed us to obtain a map at 4.6 Å after refinement. Finally, a third 3D classification job was launched by using the 4.6-Å pH4-PAC map as the reference and the low-pass filter set to 7 Å. The C_3 symmetry was also imposed. This classification pushed the resolution of the pH4-PAC map to 4.2 Å. In an effort to obtain a more homogeneous particle set, we subtracted the ECD of the pH4-PAC map (residues 72–317) and classified the refined particles without image alignment. In the end, we obtained a reconstruction of the pH4-PAC map at 3.73-Å resolution and a pH4-PAC ECD map at 3.66-Å resolution. **b**, Representative micrograph, 2D class averages, Fourier shell correlation (FSC) curves and angular distribution of particles used for 3D reconstruction for the pH4-PAC dataset. The gold-standard 0.143 threshold was used to determine map resolution based on the FSC curve. The threshold for model versus map correlation was 0.5 to determine the resolution.

Extended Data Fig. 4 Local-resolution cryo-EM maps, representative densities of cryo-EM maps and domain organization of human PAC.

a, The local resolution of the pH8-PAC map. A non-sliced (left) and a sliced (right) view of the map viewed parallel to the membrane are shown. The unit for the colour key is Å. **b**, Representative densities of several secondary structural elements of pH8-PAC. The atomic model is overlaid with the density to show the side chain information. **c**, The local resolution of the pH4-PAC map. A non-sliced (left) and a sliced (right) view of the map viewed parallel to the membrane are shown. The unit for the colour key is Å. **d**, Representative densities of several secondary structural elements of pH4-PAC. The atomic model is overlaid with the density to show the side chain information. **e**, The pH8-PAC single subunit viewed parallel to the membrane. The wrist, palm, thumb, finger and β-ball domains are highlighted. **f**, The pH4-PAC single subunit viewed in the same

orientation as the right image of panel **e**. **g**, Domain organization of PAC. Clusters of secondary structure that form the palm, finger, thumb and β -ball domains are labelled.

Extended Data Fig. 5 Comparison of the structures of PAC and ASIC.

a–d, Structural comparison of human PAC (**a, c**) with chicken ASIC1a (**b, d**) viewed parallel to the membrane (**a, b**) and from the extracellular side (**c, d**). The acidic pocket of human PAC and chicken ASIC1a are in different locations. **e**, Overlay of the pH8-PAC (blue) and pH4-PAC (red) single subunit with the chicken ASIC1a (green) subunit. The ECD of ASICa is composed of a β -sheet core and the exterior helical structure. Although the β -sheet core shares high similarity with the human PAC structure, the chicken ASIC1a TMD is organized differently from that of the human PAC.

Extended Data Fig. 6 Sequence alignment of PAC homologues and ASIC.

Sequence alignment of PAC homologues (from human, frog (XENLA) and zebrafish (DANRE)) and chicken ASIC1. The ASIC1 sequence is aligned with PAC based on the structural alignment using TMalign⁴⁵. Secondary structural (SS) elements of PAC are labelled at the top, whereas the SS elements of ASIC1 are indicated at the bottom. Cysteine residues mediating disulfide bonds in the extracellular domain of PAC are marked with yellow dots. Putative N-linked glycosylation sites of PAC are highlighted with green dots. Lys319 of PAC is marked with red dots. The pre-TM2 helix observed in the pH4-PAC structure is indicated with a red frame. PAC lacks the α 1, α 2, α 3, α 4 and α 5 helices that form the ECD exterior helical structure in chicken ASIC1a, whereas the α A and α B helices are unique to PAC.

Extended Data Fig. 7 PAC channel desensitization.

a, A representative whole-cell current trace of PAC in wild-type HEK293 cells upon extracellular acidification at pH 4.6 and pH 4.0 with a holding

potential at 100 mV. Substantial desensitization was observed during the prolonged exposure to the pH 4.0 solution (position 4 versus position 3), but not to the pH 4.6 solution (position 2 versus position 1). **b**, Quantification of PAC desensitization (pH 4.6 ($n = 12$) and pH 4.0 ($n = 11$) as shown in **a**. Activation and desensitization currents are normalized to the initial PAC currents. The x axis numbers correspond to the red marker location in **a**. Each data point is represented by a solid dot. The mean and s.e.m. are represented by the bar graph. **c**, Representative whole-cell current-voltage traces of PAC at the beginning (position 3 in **a**) and the end (position 4 in **a**) of pH 4.0 treatment. **d**, Reversal potential of PAC at the beginning and the end of pH 4.6 and pH 4.0 treatment, respectively ($n = 9$). Two-tailed paired *t*-test was used to determine significance (*P* values are 0.361 and 0.077 for pH 4.6 and pH 4.0, respectively). D'Agostino & Pearson omnibus test was performed to check the normality of the data (*P* values are 0.673 and 0.335 for pH 4.6 and pH 4.0 conditions, respectively). NS indicates *P* > 0.05. **e**, Whole-cell patch-clamp recording configuration with 50 mM NaCl pipette solution and 150 mM bath solutions (scheme depicted on the left). This creates the concentration gradient necessary to observe any potential PAC current at 0 mV. Owing to the small amplitude of endogenous PAC current at 0 mV, we transfected PAC cDNA in PAC knockout HEK293 cells. The representative whole-cell current trace of PAC upon acidification at 0 mV is shown on the right. Location 1 and 3 represent initial activation of PAC immediately after acidic buffer treatment. Location 2 and 4 represent desensitized PAC after prolonged acidic buffer treatment. **f**, The desensitized currents (position 2 and 4 in **e**) are normalized to the initial PAC currents (position 1 and 3 in **e**). The desensitized data currents are represented by the normalized average ± s.e.m.

Extended Data Fig. 8 Lateral fenestration and ion selectivity of PAC.

a, The reversal potential (V_{rev}) of wild-type PAC, PAC(K325E) and PAC(K329E) at 150 mM NaCl (black) or 15 mM NaCl (red) in the bath solution (internal solution contains 150 mM NaCl). The bar graph represents the mean and s.e.m. ($n = 16$ (wild type), $n = 8$ (K325E) and $n = 6$ (K329E)). Individual data points are shown as dots. The same data points for the wild type were also used in Fig. [3i](#) for comparison with K319E. **b**,

The relative Cl^-/Na^+ permeability for wild-type PAC ($n = 16$), and K325E ($n = 8$) and K329E ($n = 6$) mutants calculated from the pH-5-induced current at 100 mV. The centre and error bar represent the mean and s.e.m of the permeability ratio. Individual data points are shown as solid dots. The same data points for the wild type were also used in Fig. 3j for comparison with K319E. The average $P_{\text{Cl}}/P_{\text{Na}}$ permeability values are indicated for each construct. **c**, The current density of wild-type PAC ($n = 10$), and K325E ($n = 10$) and K329E mutants ($n = 10$) at pH 4.6 with a holding potential of 100 mV. The bar graph shows the average normalized current density \pm s.e.m. One-way ANOVA with Bonferroni post-hoc test was used to determine the significance (P values are 0.832 and 0.416 for K325E and K329E, respectively). D'Agostino & Pearson omnibus test was performed to check the normality of the data (P values are 0.255, 0.153 and 0.293 for the wild type and K325E and K329E mutants, respectively). NS indicates $P > 0.05$. **d**, The pH dose-response curve of wild-type PAC, PAC(K325E) and PAC(K329E). The currents are normalized to those at pH 4.6 ($n = 8$ (wild-type PAC), $n = 6$ PAC(K325E) and $n = 7$ (PAC(K329E)). The currents at different pH are represented by the average normalized currents \pm s.e.m. A nonlinear fitting to a sigmoidal dose-response curve is generated for each construct. **e**, Representative whole-cell patch-clamp recording at pH 5.0 with 150 mM NaCl pipette solution and 150 mM (black) or 15 mM NaCl (red) bath solutions. The current-voltage relationship of wild-type (left), K325E (middle) and K329E (right) PAC in two different bath solutions are plotted. The same wild-type traces were also shown in Fig. 3j (left) for comparison with K319E. **f, i**, The pH8-PAC and pH4-PAC extracellular fenestration viewed from the extracellular side (left) and parallel to the membrane (right), respectively. Residues forming the fenestration are shown in sticks, including three negatively charged residues (Asp91, Glu94 and Glu250) for pH8-PAC and two positively charged residues (Arg93 and Lys294) for pH4-PAC. **g, j**, Radius of the fenestration tunnel, estimated by CAVER v.3.0, for pH8-PAC (**g**) and pH4-PAC (**j**). The horizontal line marks the smallest radius along the tunnel. The residues lining the fenestration tunnel are marked. **h, k**, Fenestration water-density plot for pH8-PAC (**h**) and pH4-PAC (**k**) from a 100-ns MD simulation. Water molecules in the Z range of the side fenestration site are projected to the X/Y plane and are shown as a 2D histogram.

Extended Data Fig. 9 His98 is involved in PAC pH sensing.

a, p*K*_a prediction of titratable residues for the pH8 and pH4 structures of human PAC. The mean and error bar (standard deviation) are calculated based on 1,000 fixed-backbone rotamer ensembles generated from each structure (see [Methods](#)). **b**, SDS gel of GFP-tagged wild-type PAC, PAC(H98C/Q296C) and PAC(H98S/Q296S). A dimeric band is observed for the H98C/Q296C mutant, but not for the wild type and the H98S/Q296S mutant. The unedited source gel of the image can be found in Supplementary Fig. [1c](#). The gel was independently repeated twice with similar results. **c**, The FSEC profile of GFP-tagged wild-type PAC, PAC(H98C/Q296C) and PAC(H98S/Q296S) solubilized using GDN detergent. **d**, The whole-cell current density of wild-type PAC, PAC(H98C/Q296C) and PAC(H98S/Q296S) recorded at pH 5.0 at 100 mV. The bar graph shows the average current density (nA/pF) ± s.e.m. Each individual data point represents a cell (*n* = 8 (wild type), *n* = 10 (H98C/Q296C) and *n* = 12 (H98S/Q296S)). Two-tailed unpaired *t*-test was used to determine the difference in current density compared to the wild type (*P* values are 1.08×10^{-6} for H98C/Q296C and 0.321 for H98S/Q296S). D'Agostino & Pearson omnibus test was performed to check the normality of the data (*P* values are 0.328, 0.154 and 0.727 for the wild type and the H98C/Q296C and H98S/Q296S mutants, respectively). **e**, The pH dose-response curve of wild-type PAC and PAC(H98S/Q296S). The currents are normalized to those at pH 4.6 (*n* = 5 (wild-type PAC); *n* = 6 (PAC(H98S/Q296S))). A nonlinear fitting to a sigmoidal dose-response curve is generated for each construct. Bar plot shows the mean ± s.e.m. **f**, The pH₅₀ of wild-type PAC and PAC(H98S/Q296S) estimated from the pH dose-response curve. The centre and bar represent the estimated pH₅₀ and s.e.m. from the nonlinear fitting in **e**. Two-tailed Mann-Whitney test was used to determine the significance (*P* = 0.0087). **g**, The proposed pH-sensing mechanism for PAC. At high pH, the deprotonated His98 residue is surrounded by Gln296, Ser102 and Iso298, and TM1 pairs with TM2 from the same subunit. At low pH, the protonated His98 residue undergoes a conformational change and moves into an acidic pocket. As a result, TM1 dissociates from the resting interface and rotates to interact with TM2 of the adjacent subunit. For all panels, NS indicates *P* > 0.05, ** denotes a *P* value

between 0.01 and 0.001 and *** denotes $P < 0.001$; n represents measurements from biologically independent cells.

Extended Data Table 1 Cryo-EM data collection, refinement and validation statistics

[Full size table](#)

Supplementary information

Supplementary Figure

Supplementary Figure 1: The raw gel images. a, The marker and the PAC–GFP lane are cropped to make Extended Data Fig. 1b. b, The Extended Data Fig. 1d is made by cropping the marker, and PAC–GFP lanes w/o PNGase F treatment. c, The Extended Fig. 9b is made by cropping the GFP-tagged WT, H98C/Q296C, H98S/Q296S lanes. The brightness of the image is adjusted globally to increase contrast but without biasing the data. Both gels in (b) and (c) are imaged by detecting the GFP (480 nm) and far red (680nm) signal.

Reporting Summary

Video 1

A video showing the conformational change between pH8–PAC and pH4–PAC.

Rights and permissions

[Reprints and Permissions](#)

About this article



Check for
updates

Cite this article

Ruan, Z., Osei-Owusu, J., Du, J. *et al.* Structures and pH-sensing mechanism of the proton-activated chloride channel. *Nature* **588**, 350–354 (2020). <https://doi.org/10.1038/s41586-020-2875-7>

[Download citation](#)

- Received: 04 April 2020
- Accepted: 14 August 2020
- Published: 04 November 2020
- Issue Date: 10 December 2020
- DOI: <https://doi.org/10.1038/s41586-020-2875-7>

Comments

By submitting a comment you agree to abide by our [Terms](#) and [Community Guidelines](#). If you find something abusive or that does not comply with our terms or guidelines please flag it as inappropriate.

[Access through your institution](#)

[Change institution](#)

[Buy or subscribe](#)

This article was downloaded by **calibre** from <https://www.nature.com/articles/s41586-020-2875-7>

- Matters Arising
- [Published: 09 December 2020](#)

Crop asynchrony stabilizes food production

- [Lukas Egli](#) ORCID: [orcid.org/0000-0001-7617-3272^{1,2}](https://orcid.org/0000-0001-7617-3272),
- [Matthias Schröter¹](#),
- [Christoph Scherber](#) ORCID: [orcid.org/0000-0001-7924-8911^{3,4}](https://orcid.org/0000-0001-7924-8911),
- [Teja Tscharntke^{5,6}](#) &
- [Ralf Seppelt](#) ORCID: [orcid.org/0000-0002-2723-7150^{1,7}](https://orcid.org/0000-0002-2723-7150)

[Nature](#) volume **588**, pages E7–E12 (2020) [Cite this article](#)

- 63 Altmetric
- [Metrics details](#)

Subjects

- [Agroecology](#)
- [Sustainability](#)

[Matters Arising](#) to this article was published on 09 December 2020

The [Original Article](#) was published on 19 June 2019

[Access through your institution](#)

[Change institution](#)

[Buy or subscribe](#)

Access options

Subscribe to Journal

Get full journal access for 1 year

185,98 €

only 3,58 € per issue

[Subscribe](#)

All prices are NET prices.

VAT will be added later in the checkout.

Rent or Buy article

Get time limited or full article access on ReadCube.

from \$8.99

[Rent or Buy](#)

All prices are NET prices.

Additional access options:

- [Log in](#)
- [Access through your institution](#)
- [Learn about institutional subscriptions](#)

Fig. 1: Crop asynchrony as a function of crop diversity and determinants of national caloric production stability.

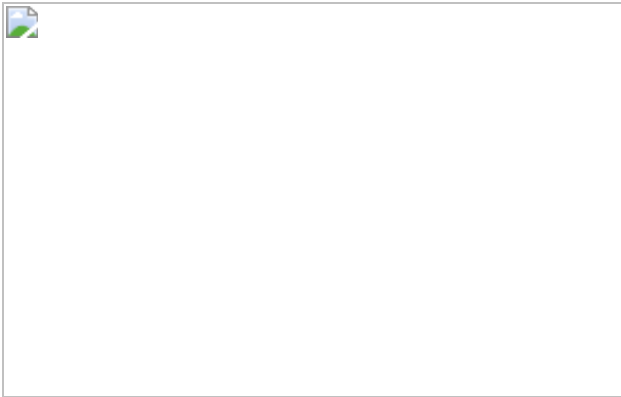
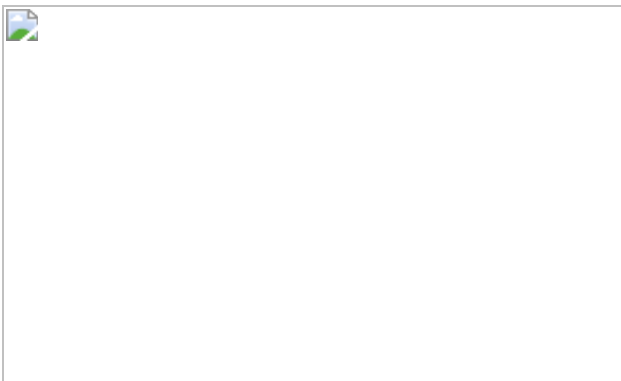


Fig. 2: National crop asynchrony and caloric production stability worldwide.



Data availability

All datasets used and generated during this study are provided in a public repository: <https://github.com/legli/AgriculturalStability>.

Code availability

The codes used for data preparation and analyses are provided in a public repository: <https://github.com/legli/AgriculturalStability>.

References

1. 1.

- Renard, D. & Tilman, D. National food production stabilized by crop diversity. *Nature* **571**, 257–260 (2019).

[CAS](#) [Article](#) [Google Scholar](#)

2. 2.

Mehrabi, Z. & Ramankutty, N. Synchronized failure of global crop production. *Nat. Ecol. Evol.* **3**, 780–786 (2019).

[Article](#) [Google Scholar](#)

3. 3.

Cottrell, R. S. et al. Food production shocks across land and sea. *Nat. Sustain.* **2**, 130–137 (2019).

[Article](#) [Google Scholar](#)

4. 4.

The Food and Agriculture Organization of the United Nations Statistics (FAO, accessed 22 November 2019);
<https://www.fao.org/faostat/en/#data/>.

5. 5.

Marshall, M. G. *Codebook: Major Episodes of Political Violence (MEPV) and Conflict Regions, 1946–2015*.
<http://www.systemicpeace.org/inscr/MEPVcodebook2016.pdf> (2016).

6. 6.

Klein Goldewijk, K., Beusen, A., Doelman, J. & Stehfest, E. New anthropogenic land use estimates for the Holocene – HYDE 3.2. *Earth Syst. Sci. Data* **9**, 927–953 (2017).

[ADS](#) [Article](#) [Google Scholar](#)

7. 7.

Sacks, W. J., Deryng, D. & Foley, J. A. Crop planting dates: an analysis of global patterns. *Glob. Ecol. Biogeogr.* **19**, 607–620 (2010).

[Google Scholar](#)

8. 8.

Willmott, C. J. & Matsuura, K. *Terrestrial Air Temperature and Precipitation: Monthly and Annual Time Series (1950–1999)*.
http://climate.geog.udel.edu/~climate/html_pages/README.ghcn_ts2.html (2001).

9. 9.

Food balance sheets: A handbook (FAO, 2001).

10. 10.

R Core Team. R: A Language and Environment for Statistical Computing (R Foundation for Statistical Computing, 2019).

11. 11.

Loreau, M. & de Mazancourt, C. Species synchrony and its drivers: neutral and nonneutral community dynamics in fluctuating environments. *Am. Nat.* **172**, E48–E66 (2008).

[Article](#) [Google Scholar](#)

12. 12.

Hallett, L. M. et al. codyn : An R package of community dynamics metrics. *Methods Ecol. Evol.* **7**, 1146–1151 (2016).

[Article](#) [Google Scholar](#)

13. 13.

Khoury, C. K. et al. Increasing homogeneity in global food supplies and the implications for food security. *Proc. Natl Acad. Sci. USA* **111**, 4001–4006 (2014).

[ADS](#) [CAS](#) [Article](#) [Google Scholar](#)

14. 14.

Bates, D., Mächler, M., Bolker, B. M. & Walker, S. C. Fitting linear mixed-effects models using lme4. *J. Stat. Softw.* **67**, 1–48 (2015).

[Article](#) [Google Scholar](#)

15. 15.

Knapp, S. & van der Heijden, M. G. A. A global meta-analysis of yield stability in organic and conservation agriculture. *Nat. Commun.* **9**, 3632 (2018).

[ADS](#) [Article](#) [Google Scholar](#)

[Download references](#)

Acknowledgements

L.E. acknowledges funding from the Helmholtz Association (Research School ESCALATE, VH-KO-613). We thank V. Grimm for discussions; M. Wu for statistical support and D. Renard for discussions and the exchange of code to make our analysis clearer and more consistent. The FAOSTAT database is maintained and regularly updated by FAO with regular support from its Member States.

Author information

Affiliations

1. UFZ - Helmholtz Centre for Environmental Research, Leipzig,
Germany

Lukas Egli, Matthias Schröter & Ralf Seppelt

2. University of Potsdam, Institute of Biochemistry and Biology,
Potsdam, Germany

Lukas Egli

3. University of Münster, Institute of Landscape Ecology, Münster,
Germany

Christoph Scherber

4. Centre for Biodiversity Monitoring, Zoological Research Museum
Alexander Koenig, Bonn, Germany

Christoph Scherber

5. University of Göttingen, Agroecology, Department of Crop Sciences,
Göttingen, Germany

Teja Tscharntke

6. University of Göttingen, Centre of Biodiversity and Sustainable Land
Use (CBL), Göttingen, Germany

Teja Tscharntke

7. Institute of Geoscience and Geography, Martin-Luther-University
Halle-Wittenberg, Halle (Saale), Germany

Ralf Seppelt

Authors

1. Lukas Egli
[View author publications](#)

You can also search for this author in [PubMed](#) [Google Scholar](#)

2. Matthias Schröter

[View author publications](#)

You can also search for this author in [PubMed](#) [Google Scholar](#)

3. Christoph Scherber

[View author publications](#)

You can also search for this author in [PubMed](#) [Google Scholar](#)

4. Teja Tscharntke

[View author publications](#)

You can also search for this author in [PubMed](#) [Google Scholar](#)

5. Ralf Seppelt

[View author publications](#)

You can also search for this author in [PubMed](#) [Google Scholar](#)

Contributions

L.E., M.S., T.T. and R.S. designed the study. L.E. and C.S. performed the analysis. All authors wrote the manuscript.

Corresponding author

Correspondence to [Lukas Egli](#).

Ethics declarations

Competing interests

The authors declare no competing interests.

Additional information

Publisher's note Springer Nature remains neutral with regard to jurisdictional claims in published maps and institutional affiliations.

Extended data figures and tables

[Extended Data Fig. 1 Main determinants of national caloric production stability.](#)

a–h, Effects of crop diversity (**a**), crop asynchrony (**b**), irrigation (**c**), nitrogen use intensity (**d**), temperature instability (**e**), precipitation instability (**f**), warfare (**g**) and time (**h**) on caloric production stability. Results are shown for the linear regression models including crop diversity (green), crop asynchrony (blue) and both (orange) ($n = 590$). Irrigation and nitrogen use intensity were back-transformed from square-root-transformation, predicted values were back-transformed from log-transformation. Predictions were calculated using the observed range of the focal predictor, while keeping all the other predictors at their mean values. Shaded areas represent 95% confidence intervals. The figure was created with the statistical software package R 3.6.1¹⁰.

Extended Data Table 1 Data sources underlying the analyses

[Full size table](#)

Extended Data Table 2 Determinants of national caloric production stability

[Full size table](#)

Supplementary information

[Supplementary Methods.](#)

[Reporting Summary](#)

Rights and permissions

[Reprints and Permissions](#)

About this article



Check for
updates

Cite this article

Egli, L., Schröter, M., Scherber, C. *et al.* Crop asynchrony stabilizes food production. *Nature* **588**, E7–E12 (2020). <https://doi.org/10.1038/s41586-020-2965-6>

[Download citation](#)

- Received: 12 February 2020
- Accepted: 30 September 2020
- Published: 09 December 2020
- Issue Date: 10 December 2020
- DOI: <https://doi.org/10.1038/s41586-020-2965-6>

Comments

By submitting a comment you agree to abide by our [Terms](#) and [Community Guidelines](#). If you find something abusive or that does not comply with our terms or guidelines please flag it as inappropriate.

[Access through your institution](#)

[Change institution](#)

[Buy or subscribe](#)

This article was downloaded by **calibre** from <https://www.nature.com/articles/s41586-020-2965-6>

| [Section menu](#) | [Main menu](#) |

- Matters Arising
- [Published: 09 December 2020](#)

Reply to: Crop asynchrony stabilizes food production

- [Delphine Renard](#) ORCID: orcid.org/0000-0002-3228-4269¹ &
- [David Tilman](#) ORCID: orcid.org/0000-0001-6395-7676^{2,3}

[Nature](#) volume 588, page E13(2020) [Cite this article](#)

- 1 Altmetric
- [Metrics details](#)

Subjects

- [Agroecology](#)
- [Biodiversity](#)

The [Original Article](#) was published on 09 December 2020

[Access through your institution](#)

[Change institution](#)

[Buy or subscribe](#)

Access options

Subscribe to Journal

Get full journal access for 1 year

185,98 €

only 3,58 € per issue

[Subscribe](#)

All prices are NET prices.
VAT will be added later in the checkout.

Rent or Buy article

Get time limited or full article access on ReadCube.

from \$8.99

[Rent or Buy](#)

All prices are NET prices.

Additional access options:

- [Log in](#)
- [Access through your institution](#)
- [Learn about institutional subscriptions](#)

References

1. 1.

Egli, L., Schröter, M., Scherber, C., Tscharntke, T. & Seppelt, R. Crop asynchrony stabilizes food production. *Nature* <https://doi.org/10.1038/s41586-020-2965-6> (2020).

2. 2.

Renard, D. & Tilman, D. National food production stabilized by crop diversity. *Nature* **571**, 257–260 (2019).

[CAS](#) [Article](#) [Google Scholar](#)

3. 3.

Doak, D. F. et al. The statistical inevitability of stability–diversity relationships in community ecology. *Am. Nat.* **151**, 264–276 (1998).

[CAS](#) [Article](#) [Google Scholar](#)

4. 4.

Loreau, M. & De Mazancourt, C. Species asynchrony and its drivers: neutral and nonneutral community dynamics in fluctuating environments. *Am. Nat.* **172**, E48–E66 (2008).

[Article](#) [Google Scholar](#)

5. 5.

The Food and Agriculture Organization of the United Nations Statistics (FAO, accessed January 2019);
<https://www.fao.org/faostat/en/#data/>.

[Download references](#)

Acknowledgements

We thank the Bren School of Environment Science and Management of the University of California Santa Barbara for support leading to the initial publication. This work was also supported by a grant overseen by the French ‘Programme Investissement d’Avenir’ as part of the ‘Make Our Planet Great Again’ programme (reference: 17-MPGA-0004) and by a National Science Foundation grant (LTER-1831944).

Author information

Affiliations

1. CEFE, CNRS, Univ. Montpellier, University Paul Valéry Montpellier
3, EPHE, IRD, Montpellier, France

Delphine Renard

2. Bren School of Environmental Science and Management, University
of California Santa Barbara, Santa Barbara, CA, USA

David Tilman

3. Department of Ecology, Evolution and Behavior, University of
Minnesota, St Paul, MN, USA

David Tilman

Authors

1. Delphine Renard

[View author publications](#)

You can also search for this author in [PubMed](#) [Google Scholar](#)

2. David Tilman

[View author publications](#)

You can also search for this author in [PubMed](#) [Google Scholar](#)

Contributions

D.R. and D.T. wrote the paper.

Corresponding author

Correspondence to [Delphine Renard](#).

Ethics declarations

Competing interests

The authors declare no competing interests.

Additional information

Publisher's note Springer Nature remains neutral with regard to jurisdictional claims in published maps and institutional affiliations.

Rights and permissions

[Reprints and Permissions](#)

About this article



Check for
updates

Cite this article

Renard, D., Tilman, D. Reply to: Crop asynchrony stabilizes food production. *Nature* **588**, E13 (2020). <https://doi.org/10.1038/s41586-020-2966-5>

[Download citation](#)

- Published: 09 December 2020
- Issue Date: 10 December 2020
- DOI: <https://doi.org/10.1038/s41586-020-2966-5>

Comments

By submitting a comment you agree to abide by our [Terms](#) and [Community Guidelines](#). If you find something abusive or that does not comply with our terms or guidelines please flag it as inappropriate.

[Access through your institution](#)

[Change institution](#)

[Buy or subscribe](#)

Associated Content

Nature | Letter

[National food production stabilized by crop diversity](#)

- Delphine Renard
- & David Tilman

This article was downloaded by **calibre** from <https://www.nature.com/articles/s41586-020-2966-5>

| [Section menu](#) | [Main menu](#) |

Amendments & Corrections

- [**Author Correction: Area-based conservation in the twenty-first century**](#) [18 November 2020]
Author Correction •
- [**Author Correction: Elephant shark genome provides unique insights into gnathostome evolution**](#) [19 November 2020]
Author Correction •
- [**Author Correction: Determination of RNA structural diversity and its role in HIV-1 RNA splicing**](#) [20 November 2020]
Author Correction •
- [**Author Correction: Innovations present in the primate interneuron repertoire**](#) [24 November 2020]
Author Correction •
- [**Publisher Correction: Room-temperature superconductivity in a carbonaceous sulfur hydride**](#) [20 November 2020]
Publisher Correction •
- [**Publisher Correction: Large Chinese land carbon sink estimated from atmospheric carbon dioxide data**](#) [24 November 2020]
Publisher Correction •

Author Correction: Area-based conservation in the twenty-first century
[Download PDF](#)

- Author Correction
- [Published: 18 November 2020](#)

Author Correction: Area-based conservation in the twenty-first century

- [Sean L. Maxwell](#)¹,
- [Victor Cazalis](#) [ORCID: orcid.org/0000-0003-0850-883X](#)²,
- [Nigel Dudley](#)^{1,3},
- [Michael Hoffmann](#) [ORCID: orcid.org/0000-0003-4785-2254](#)⁴,
- [Ana S. L. Rodrigues](#)²,
- [Sue Stoltz](#)³,
- [Piero Visconti](#) [ORCID: orcid.org/0000-0001-6823-2826](#)^{5,6,7},
- [Stephen Woodley](#) [ORCID: orcid.org/0000-0003-3074-6578](#)⁸,
- [Naomi Kingston](#)⁹,
- [Edward Lewis](#)⁹,
- [Martine Maron](#) [ORCID: orcid.org/0000-0002-5563-5789](#)¹,
- [Bernardo B. N. Strassburg](#) [ORCID: orcid.org/0000-0002-8598-3020](#)^{10,11,12},
- [Amelia Wenger](#)^{1,13},
- [Harry D. Jonas](#)^{8,14},
- [Oscar Venter](#)¹⁵ &
- [James E. M. Watson](#) [ORCID: orcid.org/0000-0003-4942-1984](#)^{1,16}

[Nature](#) volume 588, page E14 (2020) [Cite this article](#)

- 660 Accesses

- 1 Altmetric
- [Metrics details](#)

The [Original Article](#) was published on 07 October 2020

[Download PDF](#)

Correction to: *Nature* <https://doi.org/10.1038/s41586-020-2773-z> Published online 07 October 2020.

In this Review, the affiliation to which authors Victor Cazalis and Ana S. L. Rodrigues are attributed (affiliation 2) should be corrected from ‘Centre d’Ecologie Fonctionnelle et Evolutive CEFE UMR 5175, CNRS, Univ. de Montpellier, Univ. Paul-Valéry Montpellier, EPHE, Montpellier, France’ to ‘CEFE, Univ. Montpellier, CNRS, EPHE, IRD, Univ. Paul Valéry Montpellier 3, Montpellier, France’. This error has been corrected online.

Author information

Affiliations

1. Centre for Biodiversity and Conservation Science, School of Earth and Environmental Sciences, University of Queensland, St Lucia, Queensland, Australia

Sean L. Maxwell, Nigel Dudley, Martine Maron, Amelia Wenger & James E. M. Watson

2. CEFE, Univ. Montpellier, CNRS, EPHE, IRD, Univ. Paul Valéry Montpellier 3, Montpellier, France

Victor Cazalis & Ana S. L. Rodrigues

3. Equilibrium Research, Bristol, UK

Nigel Dudley & Sue Stolton

4. Conservation and Policy, Zoological Society of London, London, UK

Michael Hoffmann

5. Institute of Zoology, Zoological Society of London, London, UK

Piero Visconti

6. Centre for Biodiversity and Environment Research, University College London, London, UK

Piero Visconti

7. International Institute for Applied Systems Analysis (IIASA), Laxenburg, Austria

Piero Visconti

8. World Commission on Protected Areas, International Union for Conservation of Nature, Gland, Switzerland

Stephen Woodley & Harry D. Jonas

9. UN Environment Programme World Conservation Monitoring Centre (UNEP-WCMC), Cambridge, UK

Naomi Kingston & Edward Lewis

10. Rio Conservation and Sustainability Science Centre, Department of Geography and the Environment, Pontifícia Universidade Católica, Rio de Janeiro, Brazil

Bernardo B. N. Strassburg

11. International Institute for Sustainability, Rio de Janeiro, Brazil

Bernardo B. N. Strassburg

12. Programa de Pós Graduação em Ecologia, Universidade Federal do Rio de Janeiro, Rio de Janeiro, Brazil

Bernardo B. N. Strassburg

13. Global Marine Program, Wildlife Conservation Society, New York, NY, USA

Amelia Wenger

14. Future Law, Kota Kinabalu, Malaysia

Harry D. Jonas

15. Ecosystem Science and Management, University of Northern British Columbia, Prince George, British Columbia, Canada

Oscar Venter

16. Global Conservation Program, Wildlife Conservation Society, New York, NY, USA

James E. M. Watson

Authors

1. Sean L. Maxwell

[View author publications](#)

You can also search for this author in [PubMed](#) [Google Scholar](#)

2. Victor Cazalis

[View author publications](#)

You can also search for this author in [PubMed](#) [Google Scholar](#)

3. Nigel Dudley

[View author publications](#)

You can also search for this author in [PubMed](#) [Google Scholar](#)

4. Michael Hoffmann

[View author publications](#)

You can also search for this author in [PubMed](#) [Google Scholar](#)

5. Ana S. L. Rodrigues

[View author publications](#)

You can also search for this author in [PubMed](#) [Google Scholar](#)

6. Sue Stoltz

[View author publications](#)

You can also search for this author in [PubMed](#) [Google Scholar](#)

7. Piero Visconti

[View author publications](#)

You can also search for this author in [PubMed](#) [Google Scholar](#)

8. Stephen Woodley

[View author publications](#)

You can also search for this author in [PubMed](#) [Google Scholar](#)

9. Naomi Kingston

[View author publications](#)

You can also search for this author in [PubMed](#) [Google Scholar](#)

10. Edward Lewis

[View author publications](#)

You can also search for this author in [PubMed](#) [Google Scholar](#)

11. Martine Maron

[View author publications](#)

You can also search for this author in [PubMed](#) [Google Scholar](#)

12. Bernardo B. N. Strassburg
[View author publications](#)

You can also search for this author in [PubMed](#) [Google Scholar](#)

13. Amelia Wenger
[View author publications](#)

You can also search for this author in [PubMed](#) [Google Scholar](#)

14. Harry D. Jonas
[View author publications](#)

You can also search for this author in [PubMed](#) [Google Scholar](#)

15. Oscar Venter
[View author publications](#)

You can also search for this author in [PubMed](#) [Google Scholar](#)

16. James E. M. Watson
[View author publications](#)

You can also search for this author in [PubMed](#) [Google Scholar](#)

Corresponding author

Correspondence to [Sean L. Maxwell](#).

Rights and permissions

[Reprints and Permissions](#)

About this article



Check for
updates

Cite this article

Maxwell, S.L., Cazalis, V., Dudley, N. *et al.* Author Correction: Area-based conservation in the twenty-first century. *Nature* **588**, E14 (2020).
<https://doi.org/10.1038/s41586-020-2952-y>

[Download citation](#)

- Published: 18 November 2020
- Issue Date: 10 December 2020
- DOI: <https://doi.org/10.1038/s41586-020-2952-y>

Comments

By submitting a comment you agree to abide by our [Terms](#) and [Community Guidelines](#). If you find something abusive or that does not comply with our terms or guidelines please flag it as inappropriate.

[Download PDF](#)

This article was downloaded by **calibre** from <https://www.nature.com/articles/s41586-020-2952-y>.

Author Correction: Elephant shark genome provides unique insights into gnathostome evolution

[Download PDF](#)

- Author Correction
- [Published: 19 November 2020](#)

Author Correction: Elephant shark genome provides unique insights into gnathostome evolution

- [Byrappa Venkatesh](#) ORCID: orcid.org/0000-0003-3620-0277^{1,2},
- [Alison P. Lee](#)¹,
- [Vydianathan Ravi](#)¹,
- [Ashish K. Maurya](#)³,
- [Michelle M. Lian](#)¹,
- [Jeremy B. Swann](#)⁴,
- [Yuko Ohta](#)⁵,
- [Martin F. Flajnik](#)⁵,
- [Yoichi Sutoh](#)⁶,
- [Masanori Kasahara](#)⁶,
- [Shawn Hoon](#)⁷,
- [Vamshidhar Gangu](#)⁷,
- [Scott W. Roy](#)⁸,
- [Manuel Irimia](#)⁹,
- [Vladimir Korzh](#)¹⁰,
- [Igor Kondrychyn](#)¹⁰,
- [Zhi Wei Lim](#)¹,
- [Boon-Hui Tay](#)¹,
- [Sumantry Tohari](#)¹,
- [Kiat Whye Kong](#)⁷,

- [Shufen Ho⁷](#),
- [Belen Lorente-Galdos^{11,12}](#),
- [Javier Quilez^{11,12}](#),
- [Tomas Marques-Bonet^{11,12}](#),
- [Brian J. Raney¹³](#),
- [Philip W. Ingham³](#),
- [Alice Tay¹](#),
- [LaDeana W. Hillier¹⁴](#),
- [Patrick Minx¹⁴](#),
- [Thomas Boehm⁴](#),
- [Richard K. Wilson¹⁴](#),
- [Sydney Brenner¹](#) &
- [Wesley C. Warren¹⁴](#)

[Nature volume 588](#), page E15(2020) [Cite this article](#)

- 595 Accesses
- 3 Altmetric
- [Metrics details](#)

Subjects

- [Cellular immunity](#)
- [Comparative genomics](#)
- [Development](#)
- [Molecular evolution](#)

The [Original Article](#) was published on 08 January 2014

[Download PDF](#)

Correction to: *Nature* <https://doi.org/10.1038/nature12826> Published online
08 January 2014

In this Article, the Author Information section should have stated that the miRNA reads for 17 tissues have been deposited at the Sequence Read Archive (SRA) under accession numbers: [SRR12545166](#)–[SRR12545182](#). The original Article has not been corrected.

Author information

Affiliations

1. Comparative Genomics Laboratory, Institute of Molecular and Cell Biology, A*STAR, Biopolis, Singapore, 138673

Byrappa Venkatesh, Alison P. Lee, Vyidianathan Ravi, Michelle M. Lian, Zhi Wei Lim, Boon-Hui Tay, Sumanty Tohari, Alice Tay & Sydney Brenner

2. Department of Paediatrics, Yong Loo Lin School of Medicine, National University of Singapore, Singapore, Singapore, 119228

Byrappa Venkatesh

3. Developmental and Biomedical Genetics Laboratory, Institute of Molecular and Cell Biology, A*STAR, Biopolis, Singapore, Singapore, 138673

Ashish K. Maurya & Philip W. Ingham

4. Department of Developmental Immunology, Max-Planck-Institute of Immunobiology and Epigenetics, Stuebeweg 51, 79108, Freiburg, Germany

Jeremy B. Swann & Thomas Boehm

5. Department of Microbiology and Immunology, University of Maryland, Baltimore, Maryland, 21201, USA

Yuko Ohta & Martin F. Flajnik

6. Department of Pathology, Hokkaido University Graduate School of Medicine, Sapporo, 060-8638, Japan

Yoichi Sutoh & Masanori Kasahara

7. Molecular Engineering Laboratory, Biomedical Sciences Institutes, A*STAR, Biopolis, Singapore, 138673

Shawn Hoon, Vamshidhar Gangu, Kiat Whye Kong & Shufen Ho

8. Department of Biology, San Francisco State University, San Francisco, California, 94132, USA

Scott W. Roy

9. Banting and Best Department of Medical Research and DonnellyCentre, University of Toronto, Toronto, Ontario, M5S 3E1, Canada

Manuel Irimia

10. Fish Developmental Biology Laboratory, Institute of Molecular and Cell Biology, A*STAR, Biopolis, Singapore, 138673

Vladimir Korzh & Igor Kondrychyn

11. Institut de Biologia Evolutiva (UPF-CSIC), PRBB, 08003, Barcelona, Spain

Belen Lorente-Galdos, Javier Quilez & Tomas Marques-Bonet

12. Institució Catalana de Recerca i Estudis Avançats (ICREA), 08010, Barcelona, Catalonia, Spain

Belen Lorente-Galdos, Javier Quilez & Tomas Marques-Bonet

13. Center for Biomolecular Science and Engineering, School of Engineering, University of California Santa Cruz, Santa Cruz, California, 95064, USA

Brian J. Raney

14. The Genome Institute at Washington University, St Louis, Missouri, 63108, USA

LaDeana W. Hillier, Patrick Minx, Richard K. Wilson & Wesley C. Warren

Authors

1. Byrappa Venkatesh

[View author publications](#)

You can also search for this author in [PubMed](#) [Google Scholar](#)

2. Alison P. Lee

[View author publications](#)

You can also search for this author in [PubMed](#) [Google Scholar](#)

3. Vyidianathan Ravi

[View author publications](#)

You can also search for this author in [PubMed](#) [Google Scholar](#)

4. Ashish K. Maurya

[View author publications](#)

You can also search for this author in [PubMed](#) [Google Scholar](#)

5. Michelle M. Lian

[View author publications](#)

You can also search for this author in [PubMed](#) [Google Scholar](#)

6. Jeremy B. Swann

[View author publications](#)

You can also search for this author in [PubMed](#) [Google Scholar](#)

7. Yuko Ohta

[View author publications](#)

You can also search for this author in [PubMed](#) [Google Scholar](#)

8. Martin F. Flajnik

[View author publications](#)

You can also search for this author in [PubMed](#) [Google Scholar](#)

9. Yoichi Sutoh

[View author publications](#)

You can also search for this author in [PubMed](#) [Google Scholar](#)

10. Masanori Kasahara

[View author publications](#)

You can also search for this author in [PubMed](#) [Google Scholar](#)

11. Shawn Hoon

[View author publications](#)

You can also search for this author in [PubMed](#) [Google Scholar](#)

12. Vamshidhar Gangu

[View author publications](#)

You can also search for this author in [PubMed](#) [Google Scholar](#)

13. Scott W. Roy

[View author publications](#)

You can also search for this author in [PubMed](#) [Google Scholar](#)

14. Manuel Irimia

[View author publications](#)

You can also search for this author in [PubMed](#) [Google Scholar](#)

15. Vladimir Korzh

[View author publications](#)

You can also search for this author in [PubMed](#) [Google Scholar](#)

16. Igor Kondrychyn

[View author publications](#)

You can also search for this author in [PubMed](#) [Google Scholar](#)

17. Zhi Wei Lim

[View author publications](#)

You can also search for this author in [PubMed](#) [Google Scholar](#)

18. Boon-Hui Tay

[View author publications](#)

You can also search for this author in [PubMed](#) [Google Scholar](#)

19. Sumanty Tohari

[View author publications](#)

You can also search for this author in [PubMed](#) [Google Scholar](#)

20. Kiat Whye Kong

[View author publications](#)

You can also search for this author in [PubMed](#) [Google Scholar](#)

21. Shufen Ho

[View author publications](#)

You can also search for this author in [PubMed](#) [Google Scholar](#)

22. Belen Lorente-Galdos

[View author publications](#)

You can also search for this author in [PubMed](#) [Google Scholar](#)

23. Javier Quilez

[View author publications](#)

You can also search for this author in [PubMed](#) [Google Scholar](#)

24. Tomas Marques-Bonet

[View author publications](#)

You can also search for this author in [PubMed](#) [Google Scholar](#)

25. Brian J. Raney

[View author publications](#)

You can also search for this author in [PubMed](#) [Google Scholar](#)

26. Philip W. Ingham

[View author publications](#)

You can also search for this author in [PubMed](#) [Google Scholar](#)

27. Alice Tay

[View author publications](#)

You can also search for this author in [PubMed](#) [Google Scholar](#)

28. LaDeana W. Hillier

[View author publications](#)

You can also search for this author in [PubMed](#) [Google Scholar](#)

29. Patrick Minx

[View author publications](#)

You can also search for this author in [PubMed](#) [Google Scholar](#)

30. Thomas Boehm

[View author publications](#)

You can also search for this author in [PubMed](#) [Google Scholar](#)

31. Richard K. Wilson

[View author publications](#)

You can also search for this author in [PubMed](#) [Google Scholar](#)

32. Sydney Brenner

[View author publications](#)

You can also search for this author in [PubMed](#) [Google Scholar](#)

33. Wesley C. Warren

[View author publications](#)

You can also search for this author in [PubMed](#) [Google Scholar](#)

Corresponding authors

Correspondence to [Byrappa Venkatesh](#) or [Wesley C. Warren](#).

Rights and permissions

[Reprints and Permissions](#)

About this article



Check for
updates

Cite this article

Venkatesh, B., Lee, A.P., Ravi, V. *et al.* Author Correction: Elephant shark genome provides unique insights into gnathostome evolution. *Nature* **588**, E15 (2020). <https://doi.org/10.1038/s41586-020-2967-4>

[Download citation](#)

- Published: 19 November 2020
- Issue Date: 10 December 2020
- DOI: <https://doi.org/10.1038/s41586-020-2967-4>

Comments

By submitting a comment you agree to abide by our [Terms](#) and [Community Guidelines](#). If you find something abusive or that does not comply with our terms or guidelines please flag it as inappropriate.

[Download PDF](#)

This article was downloaded by **calibre** from <https://www.nature.com/articles/s41586-020-2967-4>

| [Section menu](#) | [Main menu](#) |

Author Correction: Determination of RNA structural diversity and its role in HIV-1 RNA splicing

[Download PDF](#)

- Author Correction
- [Published: 20 November 2020](#)

Author Correction: Determination of RNA structural diversity and its role in HIV-1 RNA splicing

- [Phillip J. Tomezsko](#)^{1,2,3 na1},
- [Vincent D. A. Corbin](#) [ORCID: orcid.org/0000-0003-1155-0959](#)^{4,5 na1},
- [Paromita Gupta](#)^{1 na1},
- [Harish Swaminathan](#)¹,
- [Margalit Glasgow](#)^{1,6},
- [Sitara Persad](#)^{1,6},
- [Matthew D. Edwards](#)⁷,
- [Lachlan McIntosh](#)^{4,8,9},
- [Anthony T. Papenfuss](#) [ORCID: orcid.org/0000-0002-1102-8506](#)^{4,5,8,9,10},
- [Ann Emery](#)^{11,12,13},
- [Ronald Swanstrom](#)^{12,13,14},
- [Trinity Zang](#)¹⁵,
- [Tammy C. T. Lan](#)¹,
- [Paul Bieniasz](#)^{15,16},
- [Daniel R. Kuritzkes](#)^{3,17},
- [Athe Tsibris](#)^{3,17} &
- [Silvi Rouskin](#) [ORCID: orcid.org/0000-0003-2042-6642](#)¹

- 874 Accesses
- 2 Altmetric
- [Metrics details](#)

Subjects

- [Bioinformatics](#)
- [Retrovirus](#)
- [RNA](#)

The [Original Article](#) was published on 06 May 2020

[Download PDF](#)

Correction to: *Nature* <https://doi.org/10.1038/s41586-020-2253-5> Published online 6 May 2020

In the ‘Code availability’ section of this Article, the URL from which the DREEM clustering algorithm can be accessed was incorrect. The correct URL is <https://codeocean.com/capsule/6175523/tree/v1>. The Article has been corrected online.

Author information

Author notes

1. These authors contributed equally: Phillip J. Tomezsko, Vincent D. A. Corbin, Paromita Gupta

Affiliations

1. Whitehead Institute for Biomedical Research, Cambridge, MA, USA

Phillip J. Tomezsko, Paromita Gupta, Harish Swaminathan, Margalit Glasgow, Sitara Persad, Tammy C. T. Lan & Silvi Rouskin

2. Program in Virology, Harvard Medical School, Boston, MA, USA

Phillip J. Tomezsko

3. Brigham and Women's Hospital, Boston, MA, USA

Phillip J. Tomezsko, Daniel R. Kuritzkes & Athe Tsibris

4. Bioinformatics Division, Walter and Eliza Hall Institute, Parkville, Victoria, Australia

Vincent D. A. Corbin, Lachlan McIntosh & Anthony T. Papenfuss

5. Department of Medical Biology, The University of Melbourne, Melbourne, Victoria, Australia

Vincent D. A. Corbin & Anthony T. Papenfuss

6. Massachusetts Institute of Technology, Cambridge, MA, USA

Margalit Glasgow & Sitara Persad

7. Computer Science and Artificial Intelligence Laboratory, Massachusetts Institute of Technology, Cambridge, MA, USA

Matthew D. Edwards

8. Peter MacCallum Cancer Centre, Melbourne, Victoria, Australia

Lachlan McIntosh & Anthony T. Papenfuss

9. Department of Mathematics and Statistics, University of Melbourne, Melbourne, Victoria, Australia

Lachlan McIntosh & Anthony T. Papenfuss

10. Sir Peter MacCallum Department of Oncology, The University of Melbourne, Melbourne, Victoria, Australia

Anthony T. Papenfuss

11. Curriculum in Genetics and Molecular Biology, University of North Carolina at Chapel Hill, Chapel Hill, NC, USA

Ann Emery

12. Lineberger Comprehensive Cancer Center, University of North Carolina at Chapel Hill, Chapel Hill, NC, USA

Ann Emery & Ronald Swanstrom

13. Department of Microbiology and Immunology, University of North Carolina at Chapel Hill, Chapel Hill, NC, USA

Ann Emery & Ronald Swanstrom

14. Department of Biochemistry and Biophysics, University of North Carolina at Chapel Hill, Chapel Hill, NC, USA

Ronald Swanstrom

15. Laboratory of Retrovirology, The Rockefeller University, New York, NY, USA

Trinity Zang & Paul Bieniasz

16. Howard Hughes Medical Institute, The Rockefeller University, New York, NY, USA

Paul Bieniasz

17. Department of Medicine, Harvard Medical School, Boston, MA, USA

Daniel R. Kuritzkes & Athé Tsibris

Authors

1. Phillip J. Tomezsko

[View author publications](#)

You can also search for this author in [PubMed](#) [Google Scholar](#)

2. Vincent D. A. Corbin

[View author publications](#)

You can also search for this author in [PubMed](#) [Google Scholar](#)

3. Paromita Gupta

[View author publications](#)

You can also search for this author in [PubMed](#) [Google Scholar](#)

4. Harish Swaminathan

[View author publications](#)

You can also search for this author in [PubMed](#) [Google Scholar](#)

5. Margalit Glasgow

[View author publications](#)

You can also search for this author in [PubMed](#) [Google Scholar](#)

6. Sitara Persad

[View author publications](#)

You can also search for this author in [PubMed](#) [Google Scholar](#)

7. Matthew D. Edwards

[View author publications](#)

You can also search for this author in [PubMed](#) [Google Scholar](#)

8. Lachlan McIntosh

[View author publications](#)

You can also search for this author in [PubMed](#) [Google Scholar](#)

9. Anthony T. Papenfuss

[View author publications](#)

You can also search for this author in [PubMed](#) [Google Scholar](#)

10. Ann Emery

[View author publications](#)

You can also search for this author in [PubMed](#) [Google Scholar](#)

11. Ronald Swanstrom

[View author publications](#)

You can also search for this author in [PubMed](#) [Google Scholar](#)

12. Trinity Zang

[View author publications](#)

You can also search for this author in [PubMed](#) [Google Scholar](#)

13. Tammy C. T. Lan

[View author publications](#)

You can also search for this author in [PubMed](#) [Google Scholar](#)

14. Paul Bieniasz

[View author publications](#)

You can also search for this author in [PubMed](#) [Google Scholar](#)

15. Daniel R. Kuritzkes

[View author publications](#)

You can also search for this author in [PubMed](#) [Google Scholar](#)

16. Athé Tsibris

[View author publications](#)

You can also search for this author in [PubMed](#) [Google Scholar](#)

17. Silvi Rouskin

[View author publications](#)

You can also search for this author in [PubMed](#) [Google Scholar](#)

Corresponding author

Correspondence to [Silvi Rouskin](#).

Rights and permissions

[Reprints and Permissions](#)

About this article



Check for
updates

Cite this article

Tomezsko, P.J., Corbin, V.D.A., Gupta, P. *et al.* Author Correction: Determination of RNA structural diversity and its role in HIV-1 RNA splicing. *Nature* **588**, E16 (2020). <https://doi.org/10.1038/s41586-020-2949-6>

[Download citation](#)

- Published: 20 November 2020
- Issue Date: 10 December 2020
- DOI: <https://doi.org/10.1038/s41586-020-2949-6>

Comments

By submitting a comment you agree to abide by our [Terms](#) and [Community Guidelines](#). If you find something abusive or that does not comply with our terms or guidelines please flag it as inappropriate.

[Download PDF](#)

This article was downloaded by **calibre** from <https://www.nature.com/articles/s41586-020-2949-6>

| [Section menu](#) | [Main menu](#) |

Author Correction: Innovations present in the primate interneuron repertoire

[Download PDF](#)

- Author Correction
- [Published: 24 November 2020](#)

Author Correction: Innovations present in the primate interneuron repertoire

- [Fenna M. Krienen](#) ORCID: orcid.org/0000-0002-1400-6820^{1,2},
- [Melissa Goldman](#)^{1,2},
- [Qiangge Zhang](#)^{2,3},
- [Ricardo C. H. del Rosario](#) ORCID: orcid.org/0000-0002-7038-9598²,
- [Marta Florio](#)^{1,2},
- [Robert Machold](#)⁴,
- [Arpiar Saunders](#)^{1,2},
- [Kirsten Levandowski](#)^{2,3},
- [Heather Zaniewski](#)^{2,3},
- [Benjamin Schuman](#)⁴,
- [Carolyn Wu](#)³,
- [Alyssa Lutservitz](#)^{1,2},
- [Christopher D. Mullally](#)^{1,2},
- [Nora Reed](#)^{1,2},
- [Elizabeth Bien](#)^{1,2},
- [Laura Bortolin](#)^{1,2},
- [Marian Fernandez-Otero](#)^{2,5},
- [Jessica D. Lin](#) ORCID: orcid.org/0000-0002-4093-0005²,
- [Alec Wysoker](#)²,
- [James Nemesh](#)²,

- [David Kulp](#)²,
- [Monika Burns](#)⁵,
- [Victor Tkachev](#) [ORCID: orcid.org/0000-0001-6011-0576](#)^{6,7,8},
- [Richard Smith](#)^{9,10},
- [Christopher A. Walsh](#) [ORCID: orcid.org/0000-0002-0156-2238](#)^{9,10},
- [Jordane Dimidschstein](#)²,
- [Bernardo Rudy](#)^{4,11},
- [Leslie S. Kean](#)^{6,7,8},
- [Sabina Berretta](#)^{5,12,13},
- [Gord Fishell](#)^{2,14},
- [Guoping Feng](#) [ORCID: orcid.org/0000-0002-8021-277X](#)^{2,3} &
- [Steven A. McCarroll](#) [ORCID: orcid.org/0000-0002-6954-8184](#)^{1,2}

[Nature](#) volume **588**, page E17(2020) [Cite this article](#)

- 616 Accesses
- 2 Altmetric
- [Metrics details](#)

Subjects

- [Evolutionary biology](#)
- [Genetics of the nervous system](#)
- [Transcriptomics](#)

The [Original Article](#) was published on 30 September 2020

[Download PDF](#)

Correction to: *Nature* <https://doi.org/10.1038/s41586-020-2781-z> Published online 30 September 2020

In Figure 2b of this Article, two labels were inadvertently swapped: the brown dot should be labelled ‘*PVALB*⁺’, and the yellow dot should be labelled ‘*SST*⁺’. In addition, the y-axis label of Fig. 4g should read “Percentage of striatal interneurons” not “Striatal interneurons (%)” and the numbers on the axis should be 0, 10, 20, 30, 40 (rather than 0, 0.1, 0.2, 0.3, 0.4). In the sentence “The *TAC3*⁺ interneuron population appeared to be shared between marmosets and humans (Fig. 4g), and constituted 30% and 38% of the interneurons sampled in marmoset and human striatum, respectively”, ‘38%’ should read ‘34%’. These errors have been corrected online.

Author information

Affiliations

1. Department of Genetics, Harvard Medical School, Boston, MA, USA

Fenna M. Krienen, Melissa Goldman, Marta Florio, Arpiar Saunders, Alyssa Lutservitz, Christopher D. Mullally, Nora Reed, Elizabeth Bien, Laura Bortolin & Steven A. McCarroll

2. Stanley Center for Psychiatric Research, Broad Institute of MIT and Harvard, Cambridge, MA, USA

Fenna M. Krienen, Melissa Goldman, Qiangge Zhang, Ricardo C. H. del Rosario, Marta Florio, Arpiar Saunders, Kirsten Levandowski, Heather Zaniewski, Alyssa Lutservitz, Christopher D. Mullally, Nora Reed, Elizabeth Bien, Laura Bortolin, Marian Fernandez-Otero, Jessica D. Lin, Alec Wysoker, James Nemesh, David Kulp, Jordane Dimidschstein, Gord Fishell, Guoping Feng & Steven A. McCarroll

3. McGovern Institute for Brain Research, Department of Brain and Cognitive Sciences, Massachusetts Institute of Technology, Cambridge, MA, USA

Qiangge Zhang, Kirsten Levandowski, Heather Zaniewski, Carolyn Wu & Guoping Feng

4. NYU Neuroscience Institute, Langone Medical Center, New York University, New York, NY, USA

Robert Machold, Benjamin Schuman & Bernardo Rudy

5. Division of Comparative Medicine, Department of Biological Engineering, Massachusetts Institute of Technology, Cambridge, MA, USA

Marian Fernandez-Otero, Monika Burns & Sabina Berretta

6. Division of Hematology/Oncology, Boston Children's Hospital, Boston, MA, USA

Victor Tkachev & Leslie S. Kean

7. Department of Pediatric Oncology, Dana-Farber Cancer Institute, Boston, MA, USA

Victor Tkachev & Leslie S. Kean

8. Department of Pediatrics, Harvard Medical School, Boston, MA, USA

Victor Tkachev & Leslie S. Kean

9. Department of Pediatrics, Boston Children's Hospital, Boston, MA, USA

Richard Smith & Christopher A. Walsh

10. Division of Genetics and Genomics, Boston Children's Hospital, Boston, MA, USA

Richard Smith & Christopher A. Walsh

11. Department of Anesthesiology, Perioperative Care and Pain Medicine,
New York University School of Medicine, New York, NY, USA

Bernardo Rudy

12. McLean Hospital, Belmont, MA, USA

Sabina Berretta

13. Department of Psychiatry, Harvard Medical School, Boston, MA, USA

Sabina Berretta

14. Program in Neuroscience, Harvard Medical School, Boston, MA, USA

Gord Fishell

Authors

1. Fenna M. Krienen

[View author publications](#)

You can also search for this author in [PubMed](#) [Google Scholar](#)

2. Melissa Goldman

[View author publications](#)

You can also search for this author in [PubMed](#) [Google Scholar](#)

3. Qiangge Zhang

[View author publications](#)

You can also search for this author in [PubMed](#) [Google Scholar](#)

4. Ricardo C. H. del Rosario

[View author publications](#)

You can also search for this author in [PubMed](#) [Google Scholar](#)

5. Marta Florio

[View author publications](#)

You can also search for this author in [PubMed](#) [Google Scholar](#)

6. Robert Machold

[View author publications](#)

You can also search for this author in [PubMed](#) [Google Scholar](#)

7. Arpiar Saunders

[View author publications](#)

You can also search for this author in [PubMed](#) [Google Scholar](#)

8. Kirsten Levandowski

[View author publications](#)

You can also search for this author in [PubMed](#) [Google Scholar](#)

9. Heather Zaniewski

[View author publications](#)

You can also search for this author in [PubMed](#) [Google Scholar](#)

10. Benjamin Schuman

[View author publications](#)

You can also search for this author in [PubMed](#) [Google Scholar](#)

11. Carolyn Wu

[View author publications](#)

You can also search for this author in [PubMed](#) [Google Scholar](#)

12. Alyssa Lutservitz

[View author publications](#)

You can also search for this author in [PubMed](#) [Google Scholar](#)

13. Christopher D. Mullally
[View author publications](#)

You can also search for this author in [PubMed](#) [Google Scholar](#)

14. Nora Reed
[View author publications](#)

You can also search for this author in [PubMed](#) [Google Scholar](#)

15. Elizabeth Bien
[View author publications](#)

You can also search for this author in [PubMed](#) [Google Scholar](#)

16. Laura Bortolin
[View author publications](#)

You can also search for this author in [PubMed](#) [Google Scholar](#)

17. Marian Fernandez-Otero
[View author publications](#)

You can also search for this author in [PubMed](#) [Google Scholar](#)

18. Jessica D. Lin
[View author publications](#)

You can also search for this author in [PubMed](#) [Google Scholar](#)

19. Alec Wysoker
[View author publications](#)

You can also search for this author in [PubMed](#) [Google Scholar](#)

20. James Nemesh
[View author publications](#)

You can also search for this author in [PubMed](#) [Google Scholar](#)

21. David Kulp

[View author publications](#)

You can also search for this author in [PubMed](#) [Google Scholar](#)

22. Monika Burns

[View author publications](#)

You can also search for this author in [PubMed](#) [Google Scholar](#)

23. Victor Tkachev

[View author publications](#)

You can also search for this author in [PubMed](#) [Google Scholar](#)

24. Richard Smith

[View author publications](#)

You can also search for this author in [PubMed](#) [Google Scholar](#)

25. Christopher A. Walsh

[View author publications](#)

You can also search for this author in [PubMed](#) [Google Scholar](#)

26. Jordane Dimidschstein

[View author publications](#)

You can also search for this author in [PubMed](#) [Google Scholar](#)

27. Bernardo Rudy

[View author publications](#)

You can also search for this author in [PubMed](#) [Google Scholar](#)

28. Leslie S. Kean

[View author publications](#)

You can also search for this author in [PubMed](#) [Google Scholar](#)

29. Sabina Berretta

[View author publications](#)

You can also search for this author in [PubMed](#) [Google Scholar](#)

30. Gord Fishell

[View author publications](#)

You can also search for this author in [PubMed](#) [Google Scholar](#)

31. Guoping Feng

[View author publications](#)

You can also search for this author in [PubMed](#) [Google Scholar](#)

32. Steven A. McCarroll

[View author publications](#)

You can also search for this author in [PubMed](#) [Google Scholar](#)

Corresponding authors

Correspondence to [Fenna M. Krienen](#) or [Steven A. McCarroll](#).

Rights and permissions

[Reprints and Permissions](#)

About this article



Check for
updates

Cite this article

Krienen, F.M., Goldman, M., Zhang, Q. *et al.* Author Correction: Innovations present in the primate interneuron repertoire. *Nature* **588**, E17 (2020). <https://doi.org/10.1038/s41586-020-2874-8>

[Download citation](#)

- Published: 24 November 2020
- Issue Date: 10 December 2020
- DOI: <https://doi.org/10.1038/s41586-020-2874-8>

Comments

By submitting a comment you agree to abide by our [Terms](#) and [Community Guidelines](#). If you find something abusive or that does not comply with our terms or guidelines please flag it as inappropriate.

[Download PDF](#)

This article was downloaded by **calibre** from <https://www.nature.com/articles/s41586-020-2874-8>

Publisher Correction: Room-temperature superconductivity in a carbonaceous sulfur hydride

[Download PDF](#)

- Publisher Correction
- [Published: 20 November 2020](#)

Publisher Correction: Room-temperature superconductivity in a carbonaceous sulfur hydride

- [Elliot Snider^{1 na1}](#),
- [Nathan Dasenbrock-Gammon](#) [ORCID: orcid.org/0000-0002-0298-8513^{2 na1}](#),
- [Raymond McBride^{1 na1}](#),
- [Mathew Debessai³](#),
- [Hiranya Vindana²](#),
- [Kevin Vencatasamy²](#),
- [Keith V. Lawler](#) [ORCID: orcid.org/0000-0003-1087-5815⁴](#),
- [Ashkan Salamat⁵](#) &
- [Ranga P. Dias](#) [ORCID: orcid.org/0000-0002-0830-4928^{1,2}](#)

[Nature](#) volume 588, page E18(2020) [Cite this article](#)

- 1612 Accesses
- 2 Altmetric
- [Metrics details](#)

Subjects

- [Superconducting properties and materials](#)
- [Superconductors](#)

The [Original Article](#) was published on 14 October 2020

[Download PDF](#)

Correction to: *Nature* <https://doi.org/10.1038/s41586-020-2801-z> Published online 14 October 2020

In this Article, owing to an error in the production process, the received date was incorrectly stated as 31 August 2020 instead of 21 July 2020. This error has been corrected online.

Author information

Author notes

1. These authors contributed equally: Elliot Snider, Nathan Dasenbrock-Gammon, Raymond McBride

Affiliations

1. Department of Mechanical Engineering, School of Engineering and Applied Sciences, University of Rochester, Rochester, NY, USA

Elliot Snider, Raymond McBride & Ranga P. Dias

2. Department of Physics and Astronomy, University of Rochester, Rochester, NY, USA

Nathan Dasenbrock-Gammon, Hiranya Vindana, Kevin Vencatasamy & Ranga P. Dias

3. Intel Corporation, Hillsboro, OR, USA

Mathew Debessai

4. Department of Chemistry and Biochemistry, University of Nevada Las Vegas, Las Vegas, NV, USA

Keith V. Lawler

5. Department of Physics and Astronomy, University of Nevada Las Vegas, Las Vegas, NV, USA

Ashkan Salamat

Authors

1. Elliot Snider

[View author publications](#)

You can also search for this author in [PubMed](#) [Google Scholar](#)

2. Nathan Dasenbrock-Gammon

[View author publications](#)

You can also search for this author in [PubMed](#) [Google Scholar](#)

3. Raymond McBride

[View author publications](#)

You can also search for this author in [PubMed](#) [Google Scholar](#)

4. Mathew Debessai

[View author publications](#)

You can also search for this author in [PubMed](#) [Google Scholar](#)

5. Hiranya Vindana

[View author publications](#)

You can also search for this author in [PubMed](#) [Google Scholar](#)

6. Kevin Vencatasamy

[View author publications](#)

You can also search for this author in [PubMed](#) [Google Scholar](#)

7. Keith V. Lawler

[View author publications](#)

You can also search for this author in [PubMed](#) [Google Scholar](#)

8. Ashkan Salamat

[View author publications](#)

You can also search for this author in [PubMed](#) [Google Scholar](#)

9. Ranga P. Dias

[View author publications](#)

You can also search for this author in [PubMed](#) [Google Scholar](#)

Corresponding author

Correspondence to [Ranga P. Dias](#).

Rights and permissions

[Reprints and Permissions](#)

About this article



Check for
updates

Cite this article

Snider, E., Dasenbrock-Gammon, N., McBride, R. *et al.* Publisher Correction: Room-temperature superconductivity in a carbonaceous sulfur hydride. *Nature* **588**, E18 (2020). <https://doi.org/10.1038/s41586-020-2955-8>

[Download citation](#)

- Published: 20 November 2020
- Issue Date: 10 December 2020
- DOI: <https://doi.org/10.1038/s41586-020-2955-8>

Comments

By submitting a comment you agree to abide by our [Terms](#) and [Community Guidelines](#). If you find something abusive or that does not comply with our terms or guidelines please flag it as inappropriate.

[Download PDF](#)

This article was downloaded by **calibre** from <https://www.nature.com/articles/s41586-020-2955-8>

Publisher Correction: Large Chinese land carbon sink estimated from atmospheric carbon dioxide data

[Download PDF](#)

- Publisher Correction
- [Published: 24 November 2020](#)

Publisher Correction: Large Chinese land carbon sink estimated from atmospheric carbon dioxide data

- [Jing Wang](#) ORCID: [orcid.org/0000-0002-7149-5157^{1,2,3,4}](https://orcid.org/0000-0002-7149-5157),
- [Liang Feng^{3,4}](#),
- [Paul I. Palmer](#) ORCID: [orcid.org/0000-0002-1487-0969^{3,4}](https://orcid.org/0000-0002-1487-0969),
- [Yi Liu](#) ORCID: [orcid.org/0000-0001-9305-5358^{1,2}](https://orcid.org/0000-0001-9305-5358),
- [Shuangxi Fang](#) ORCID: [orcid.org/0000-0002-2104-5721^{5,6}](https://orcid.org/0000-0002-2104-5721),
- [Hartmut Bösch⁷](#),
- [Christopher W. O'Dell⁸](#),
- [Xiaoping Tang⁹](#),
- [Dongxu Yang^{1,2}](#),
- [Lixin Liu⁶](#) &
- [ChaoZong Xia⁹](#)

[Nature](#) volume 588, page E19 (2020) [Cite this article](#)

- 709 Accesses
- 3 Altmetric
- [Metrics details](#)

Subjects

- [Atmospheric science](#)
- [Carbon cycle](#)

The [Original Article](#) was published on 28 October 2020

[Download PDF](#)

Correction to: *Nature* <https://doi.org/10.1038/s41586-020-2849-9> Published online 28 October 2020

In the legend of Fig. 2 of this Article, owing to an error during the production process, panels a and b were inadvertently labelled ‘northeast China (within 38–54° N, 120–135° E)’ and panels c and d were inadvertently labelled ‘southwest China (within 18–30° N, 95–110° E)’, rather than the other way around. The figure was correct. This error has been corrected online.

Author information

Affiliations

1. Institute of Atmospheric Physics, Chinese Academy of Sciences, Beijing, China

Jing Wang, Yi Liu & Dongxu Yang

2. University of Chinese Academy of Sciences, Beijing, China

Jing Wang, Yi Liu & Dongxu Yang

3. National Centre for Earth Observation, University of Edinburgh, Edinburgh, UK

Jing Wang, Liang Feng & Paul I. Palmer

4. School of GeoSciences, University of Edinburgh, Edinburgh, UK

Jing Wang, Liang Feng & Paul I. Palmer

5. College of Environment, Zhejiang University of Technology,
Hangzhou, China

Shuangxi Fang

6. Meteorological Observation Centre, China Meteorological
Administration, Beijing, China

Shuangxi Fang & Lixin Liu

7. National Centre for Earth Observation, University of Leicester,
Leicester, UK

Hartmut Bösch

8. Colorado State University, Fort Collins, CO, USA

Christopher W. O'Dell

9. Academy of Forest Inventory and Planning, State Forestry
Administration, Beijing, China

Xiaoping Tang & ChaoZong Xia

Authors

1. Jing Wang

[View author publications](#)

You can also search for this author in [PubMed](#) [Google Scholar](#)

2. Liang Feng

[View author publications](#)

You can also search for this author in [PubMed](#) [Google Scholar](#)

3. Paul I. Palmer

[View author publications](#)

You can also search for this author in [PubMed](#) [Google Scholar](#)

4. Yi Liu

[View author publications](#)

You can also search for this author in [PubMed](#) [Google Scholar](#)

5. Shuangxi Fang

[View author publications](#)

You can also search for this author in [PubMed](#) [Google Scholar](#)

6. Hartmut Bösch

[View author publications](#)

You can also search for this author in [PubMed](#) [Google Scholar](#)

7. Christopher W. O'Dell

[View author publications](#)

You can also search for this author in [PubMed](#) [Google Scholar](#)

8. Xiaoping Tang

[View author publications](#)

You can also search for this author in [PubMed](#) [Google Scholar](#)

9. Dongxu Yang

[View author publications](#)

You can also search for this author in [PubMed](#) [Google Scholar](#)

10. Lixin Liu

[View author publications](#)

You can also search for this author in [PubMed](#) [Google Scholar](#)

11. ChaoZong Xia

[View author publications](#)

You can also search for this author in [PubMed](#) [Google Scholar](#)

Corresponding authors

Correspondence to [Paul I. Palmer](#) or [Yi Liu](#) or [Shuangxi Fang](#).

Rights and permissions

[Reprints and Permissions](#)

About this article



Check for
updates

Cite this article

Wang, J., Feng, L., Palmer, P.I. *et al.* Publisher Correction: Large Chinese land carbon sink estimated from atmospheric carbon dioxide data. *Nature* **588**, E19 (2020). <https://doi.org/10.1038/s41586-020-2986-1>

[Download citation](#)

- Published: 24 November 2020
- Issue Date: 10 December 2020
- DOI: <https://doi.org/10.1038/s41586-020-2986-1>

Comments

By submitting a comment you agree to abide by our [Terms](#) and [Community Guidelines](#). If you find something abusive or that does not comply with our terms or guidelines please flag it as inappropriate.

[Download PDF](#)

This article was downloaded by **calibre** from <https://www.nature.com/articles/s41586-020-2986-1>

| [Section menu](#) | [Main menu](#) |

Collections